Air entrainment and air-water separation in hydraulic air compressors

by

Alex Hutchison

A thesis submitted in partial fulfillment
of the requirements for the degree of
Doctor of Philosophy (PhD) in Natural
Resources Engineering

The Faculty of Graduate Studies
Laurentian University
Sudbury, Ontario, Canada

THESIS DEFENCE COMMITTEE/COMITÉ DE SOUTENANCE DE THÈSE
Laurentian Université/Université Laurentienne
Faculty of Graduate Studies/Faculté des études supérieures

Title of Thesis Titre de la thèse	Air entrainment and air-water separation in hydraulic air compressors		
Name of Candidate Nom du candidat	Hutchison, Alex		
Degree Diplôme	Doctor of Philosophy Science		
Department/Program Département/Programme	Natural Resource Engineering	Date of Defence Date de la soutenance	August 16, 2018

APPROVED/APPROUVÉ

Thesis Examiners/Examinateurs de thèse:

Dr. Dean Millar
(Supervisor/Directeur de thèse)

Dr. Martin Hudyma
(Committee member/Membre du comité)

Dr. Turgut Yelsin
(Committee member/Membre du comité)

Dr. Ramesh Subramanian
(Committee member/Membre du comité)

Dr. David Nobles Dean, Faculty of Graduate Studies
(External Examiner/Examinateur externe)

Dr. Charles Ramcharan
(Internal Examiner/Examinateur interne)

Approved for the Faculty of Graduate Studies
Approuvé pour la Faculté des études supérieures
Dr. David Lesbarrères
Monsieur David Lesbarrères

Doyen, Faculté des études supérieures

ACCESSIBILITY CLAUSE AND PERMISSION TO USE

I, **Alex Hutchison**, hereby grant to Laurentian University and/or its agents the non-exclusive license to archive and make accessible my thesis, dissertation, or project report in whole or in part in all forms of media, now or for the duration of my copyright ownership. I retain all other ownership rights to the copyright of the thesis, dissertation or project report. I also reserve the right to use in future works (such as articles or books) all or part of this thesis, dissertation, or project report. I further agree that permission for copying of this thesis in any manner, in whole or in part, for scholarly purposes may be granted by the professor or professors who supervised my thesis work or, in their absence, by the Head of the Department in which my thesis work was done. It is understood that any copying or publication or use of this thesis or parts thereof for financial gain shall not be allowed without my written permission. It is also understood that this copy is being made available in this form by the authority of the copyright owner solely for the purpose of private study and research and may not be copied or reproduced except as permitted by the copyright laws without written authority from the copyright owner.

Abstract

A hydraulic air compressor (HAC) is an isothermal gas compressor that uses hydropower to compress air, originally developed by Charles Taylor in the 1890s to supply industry with compressed air. In the modern revival of this technology, the hydropower will be provided by pumps rather than natural sources. As such, energy efficiency is an important driver of component design; all of the hydropower is consumed either to overcome irreversibility or to compress air. The compressor relies on the increasing pressure of water flowing downward in a downcomer to compress air in the form of bubbles being dragged along with the flow. The air entrainment process at the top of the downcomer is facilitated by a mixing head. At the bottom of the downcomer, the bubbles are separated from the flow in a separator vessel. The objective of this thesis is to develop the design methodology for the air entrainment and air-water separation components on either end of the downcomer process.

Several mixing heads were tested on a small (4.5 m height) prototype HAC. The test without a mixing head successfully entrained air, confirming that air entrainment is a system effect. Two heads with dissimilar geometry were associated with the lowest irreversibility, leading to the conclusion that the best design at that scale is a mixing head incorporating some form of vortex breaker. Air entrainment is driven by a system energy balance and not exclusively by a local Venturi geometry.

The fraction of the air successfully captured in the plenum of the separator is called the separator effectiveness. Mechanistic models have been created to characterize both the irreversibility and separator effectiveness of two types of gravity separator (horizontal and vertical orientation) for

the design of separators for future commercial-scale compressors. The separator effectiveness models require as input the flow field information from computational fluid dynamics analysis and the bubble size distribution at inlet. The bubble size distribution was measured on the small prototype and used to select a bubble size prediction model for testing on a much larger scale (29 m height) demonstrator HAC. The displacement model for horizontal separators matched the actual performance at the prototype scale well, particularly at high flow rate. The vertical velocity model produced a good match for the separator on the demonstrator HAC, but not for the same bubble size model identified on the small prototype.

Keywords: hydraulic air compressor, minimum work air entrainment, separator design, flow irreversibility, bubble size distribution

Acknowledgments

I would like to thank Dean Millar for his guidance and supervision over the course of the research presented in this thesis and the thesis committee for their efforts to read and review the material: Ramesh Subramanian, Marty Hudyma, Turgut Yalcin, Charles Ramcharan, and David Nobes. I would also like to thank the Ultra Deep Mine Network for funding my research and the Northern Ontario Heritage Fund Corporation and the Independent Energy System Operator for providing additional funding for the project.

Additionally, I would like to express gratitude to the following people for providing additional support: David Vitone, the project manager for the Dynamic Earth HAC build; Justin Sivret, who was responsible for data collection on Dynamic Earth HAC; Adam Walli, who made recommendations on sensors for Baby HAC and assisted with troubleshooting and soldering; Greg Lakanen, who provided 3D printing services, facilitated the modification of the Baby HAC scaffold, and lent tools for construction and maintenance of both experimental platforms; and Arnaud Kottas for performing the bubble measurement on Baby HAC.

Lastly, I acknowledge the current and former members of the research team for their contributions to the project: Dean Millar, Caterina Noula, Stephen Young, Justin Sivret, Valeria Pavese, Javier Rico, David Vitone, Sujit Sengupta, Peter Moutsatsos, Arnaud Kottas, and Tom Clifford.

Table of Contents

List of Figures

List of Tables

List of Appendices

Nomenclature

A	surface area, m^2
A_p	projected area perpendicular to direction of motion, m^2
b	dissolved salt concentration, mol/kg
B	width of pump bay, m
c_i	dissolved equilibrium concentration of species i, mol/m^3
C_d	drag coefficient, dimensionless
d	bubble diameter (equivalent sphere), m
d_{max}	maximum stable bubble diameter, m
d_x	x percentile bubble diameter, m
$\bar{d}$	mean bubble diameter as defined by Rosin-Rammler distribution, m
D	pipe or vessel hydraulic mean diameter, m
Eo	Eötvös (Bond) number, dimensionless
f	Darcy friction factor, dimensionless
F_b	buoyancy force, N
F_d	drag force, N
Fr	Froude number, dimensionless
g	acceleration from gravity, m/s^2
g_c	centrifugal component of field force, m/s^2
g_f	acceleration from field force, m/s^2
h	elevation difference between tailrace and forebay water levels ($z_{forebay} - z_{tailrace}$), m

h_i	elevation at position i, m
h_{inlet}	level of water over mixing head, m
h_{mix}	head loss from entrainment irreversibility, m H_2O
h_s	snorkel offset, m
Δh	head loss across system component, m H_2O
$\Delta_{soln}H$	enthalpy of solution, J/mol
I	turbulent intensity, dimensionless
j_g	volume flux (superficial velocity) of gas phase, m/s
j_l	volume flux (superficial velocity) of liquid phase, m/s
k	heat transfer coefficient, $W/m^2 \cdot K$
k_H	adjusted Henry's constant, $m^3 \cdot Pa/mol$
$k_{H,0}$	pure fluid Henry's constant, $m^3 \cdot Pa/mol$
$k_{H,i}$	Henry's constant for species i, $m^3 \cdot Pa/mol$
k_s	Sechenov constant, kg/mol
KE_i	kinetic energy at position i
l	plane interval, m
L	characteristic length, m
L_B	length of pump bay, m
L_p	pipe or vessel length, m
$\dot{m}_g$	mass flow rate of gas, kg/s
$\dot{m}_l$	mass flow rate of liquid, kg/s
Mo	Morton number, dimensionless

n	Rosin-Rammler spread parameter, dimensionless
N_r	circulation number, dimensionless
p_i	Henry's constant for species i, Pa
P	pressure, Pa
P_i	pressure at point i, Pa
P_{sh}	minor loss, Pa
PE_i	potential energy at position i
PrE_i	pressure energy at position i
ΔP	pressure drop across system component, Pa
q	heat transfer rate, W
Q_g	gas flow rate, m^3/s
Q_l	liquid flow rate, m^3/s
r	radial distance from centrifugal separator centre, m
R	universal gas constant, J/mol·K
$\mathcal{R}$	Atkinson resistance, kg/m^7
Re	Reynolds number, dimensionless
Re_p	particle Reynolds number, dimensionless
Δs	vertical displacement, m
t	residence time for a single cell, s
T	temperature, K
T_0	reference temperature at which Henry's constant is valid, K
ΔT	temperature difference between bubble surface and bulk fluid, K

U_i	internal energy at position i
$U_{transfer}$	interphase heat transfer
v	total flow velocity, m/s
v_b	bubble velocity, m/s
v_h	horizontal velocity component along separator length, m/s
v_i	velocity at position i, m/s
v_r	relative (terminal) velocity, m/s
v_t	tangential velocity, m/s
v_v	vertical velocity component, m/s
v_w	water velocity, m/s
V	volume, m^3
V_b	bubble volume, m^3
We_{crit}	critical Weber number, dimensionless
x	constant, dimensionless
X	loss coefficient, dimensionless
X_f	combined loss coefficient function, dimensionless
y	gas yield due to solubility, dimensionless
Y	fraction of bubbles with diameter less than d, dimensionless
z_x	elevation of water surface in tank x, m

Greek Letters

$\acute{\alpha}$	angle of approach velocity, radians
ε	absolute surface roughness, m

η_x	x component of efficiency, dimensionless
μ	dynamic viscosity of continuous (liquid) phase, Pa·s
ρ_g	gas density, kg/m^3
ρ_l	liquid density, kg/m^3
σ	surface tension, N/m
τ	turbulent shear, Pa

Chapter 1

1. Introduction

A hydraulic air compressor (HAC) is a gas compressor that uses hydropower to compress air. Air is inducted into a stream of water flowing vertically downward as bubbles. The pressure increase created by the conversion of gravitational potential energy is transmitted from the water to the air and the heat generated by the compression process is simultaneously transmitted from the air to the water. At the end of the compression process, the high pressure air bubbles are separated from the water stream.

Figure 1.1 is a schematic representation of a HAC that operates using hydropower provided by a watercourse, called a 'run-of-river HAC' (Millar, 2014). Water flows from the forebay down to the separator then back up to the tailrace. Air is entrained at the top of the downcomer pipe and the bubbles are compressed by the increasing weight of water in the downcomer. The bubbles are separated from the water in the separator vessel at the bottom. The water stream returns to the tailrace along with any air that failed to separate. The elevation difference between the forebay and the tailrace (h) provides the driving head and the column of water between the tailrace and the separator ($z_{tailrace} - z_{separator}$) determines the delivery pressure. In this case, the driving head is maintained by a natural hydropower source. It can otherwise employ an artificial hydropower source (e.g. mine service water loop) or recirculating pumps. The delivery pressure can be reduced by flow losses in the riser shaft, but those are typically designed to be small by employing large diameter riser shafts (Schulze, 1954). An advantage is that there are no moving parts anywhere in the system except control valves and any recirculation pumps.

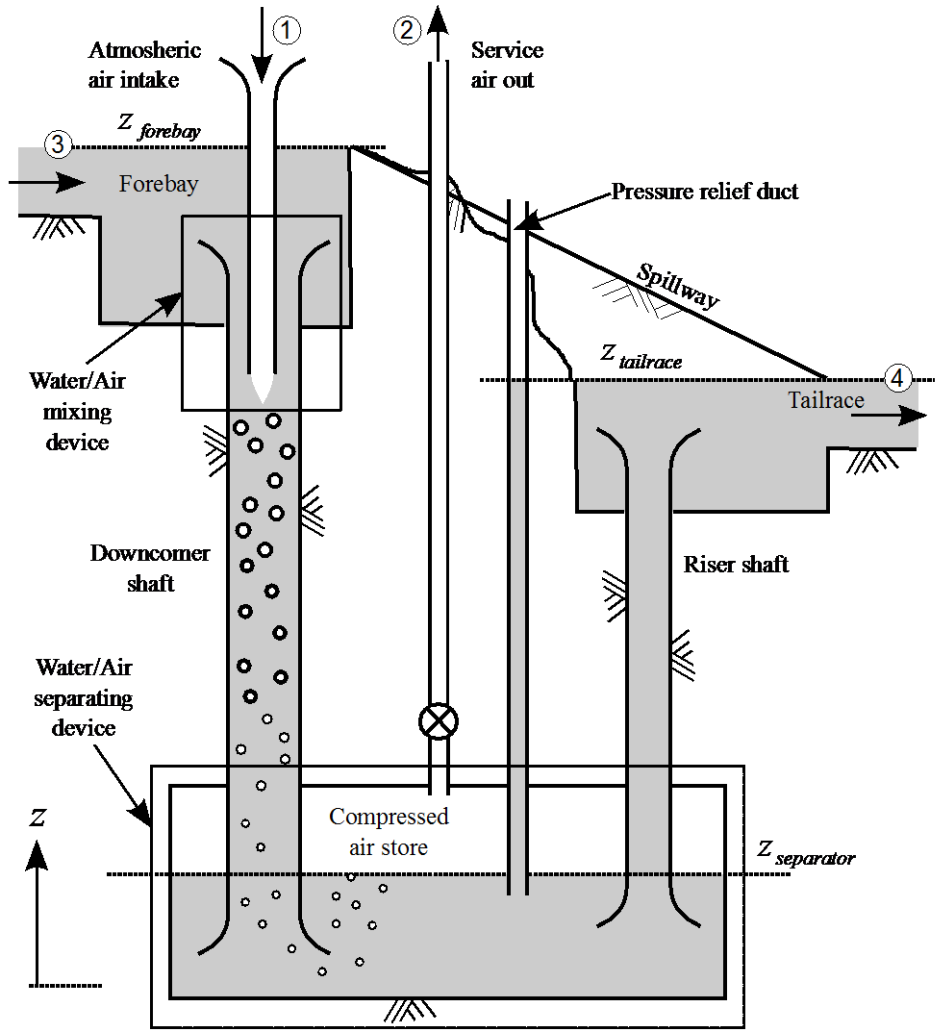

Figure 1.1: Schematic of a HAC employing a natural watercourse (Young et al., 2015)

There were 18 historic commercial scale installations built between 1896 and 1929 with mechanical efficiencies ranging from 45-88% (Millar, 2014). Schulze (1954) produced a historical review of HAC technology describing the construction, application, and performance of each of these HACs, where that information was available. Some of these installations remain in place to this day, but none are currently operating. Neither the design methodology for HACs and their components nor the method by which they were operated have survived, motivating

this programme of work. Some original documents on the mechanical performance of HACs have survived. For example, McNair and Koenig (1911) reported a study of oxygen depletion by gas dissolution at a HAC in Cobalt, Ontario. Several of these documents were written in German and were subsequently translated and integrated into the review by Schulze (1954).

The technology was first developed by Charles Havelock Taylor and installed at the Dominion Cotton Mills at Magog, Quebec, in 1896. All of the largest HACs were formed in rock; the largest one (and the last constructed by Taylor) built at Ragged Chutes in Cobalt in 1909 supplied 18.9 m^3/s free air delivery (FAD) at a pressure of 807 kPa gauge (Millar, 2014). Millar (2014) and Young (2015) have summarized the performance details of the historic HACs from data and descriptions in Schulze (1954).The traditional control system is simple. The compressor is designed to produce more air than is required by the consumer. Storage capacity in the separator accounts for short duration compressor shutdowns and buffers irregular demand. Net air production causes the gas pocket in the separator to expand, pushing down the water surface. When the bottom of the blow-off pipe is exposed (labeled “pressure relief duct” in Figure 1.1), the water column falls into the separator until the pressure in the separator overcomes the weight of that column and air and water are vented. All of these compressors used gravity separators, some of which doubled as compressed air storage vessels (Schulze, 1954).This blow-off pipe is a necessary safety mechanism. If the pipe is not placed correctly or is blocked, then the air can vent up the downcomer at high speed. Ice blockage of the blow-off pipe has been known to cause blow-back in the downcomer, damaging the mixing head(s) and compressor house (Schulze, 1954). Air vented by the blow-off pipe is a form of waste. Controlling the separator water level

with a control valve converts the blow-off from the primary control mechanism to a safety back-up.

1.1 The modern revival of the HAC is as an energy efficiency technology

Unlike a run-of-river HAC, where the cost of power is effectively zero, electrical power is required to run a pumped HAC. Therefore, there is a greater emphasis on energy efficiency for pumped HACs. In a HAC, hydropower is consumed in five categories (Millar and Muller, 2017): (i) irreversibility associated with air entrainment, (ii) friction loss in pipes and tanks, (iii) dynamic (minor) losses created by changing flow direction of cross-sectional area, (iv) drag between bubbles and water, and (v) compressing air. Air compression is the only useful component, comprising the numerator of the mechanical efficiency equation (1.1). The indicated air power is the product of the mass flow of air ($\dot{m}_g$) and the integral of volume (V) with pressure (dP). Hydropower is the product of the mass flow of water ($\dot{m}_l$) and the specific potential energy consumed in the process, which is the product of the acceleration due to gravity (g) and the difference in elevation between the forebay and tailrace water levels (h). In the modern revival of the technology, the reduction of energy required to compress air is achieved when each source of wasted hydropower (i)-(iv) is addressed.

$$\eta_{mech} = \frac{\text{indicated air power}}{\text{hydropower}} = \frac{\dot{m}_g \cdot \int V dP}{\dot{m}_l \cdot g \cdot h} \tag{1.1}$$

Indicated air power is a function of the mass flow rate of air and the compression process. In energy terms, the advantage of a HAC over mechanical compression is that a HAC employs the ideal (isothermal) process for gas compression. According to Millar and Muller (2017), there are further advantages that are related to the simplicity and operation of the machine. The relative

lack of moving parts reduces the maintenance requirement and improves system reliability. The seals on low head, high flow pumps have long lifespans and are not prone to failure.

None of the other components are subject to significant wear, except for corrosion in salt water service, which is controllable with proper materials selection. Lubricating oils are unnecessary and do not contaminate the compressed air delivered downstream. The air delivered by a HAC is cooler, drier, and cleaner (Millar, 2014) than that delivered by a conventional compressor, which reduces corrosion and fouling in the delivery pipeline and tools powered by the compressed air. Low maintenance and high reliability contribute lower labour costs and longer service life of the equipment between major overhauls. Several of the historic installations were known to operate continuously for decades (Schulze, 1954).

1.1.1 A real isothermal compression process

The isothermal compression process is the minimum work compression process (see: Figure 1.2). A perfect isothermal compression is not achievable, because the air increases in temperature and some differential temperature is required to drive heat transfer to the surroundings. The "nearly isothermal" process (Pavese, 2015) is one where there is a temperature increase, but only a negligible one. A typical HAC has a mass flow of water more than 1000 times that of air, because the density of water is ~850 times higher than that of air under atmospheric conditions and the volumetric water flow rate at the inlet is higher than the volumetric air flow rate (Millar, 2014). Water has a specific heat capacity around 4 times that of air. By this logic, a hypothetical compression process that would normally increase the temperature of the air stream by 200 K would increase the combined air-water stream in a HAC by only up to 0.05 K. Measurements by a very sensitive differential temperature instrument on Dynamic Earth HAC (see: chapter 5)

show that the temperature increase in the downcomer is on the order of 10 mK (Sivret, 2018), confirming the nearly isothermal process is achievable.

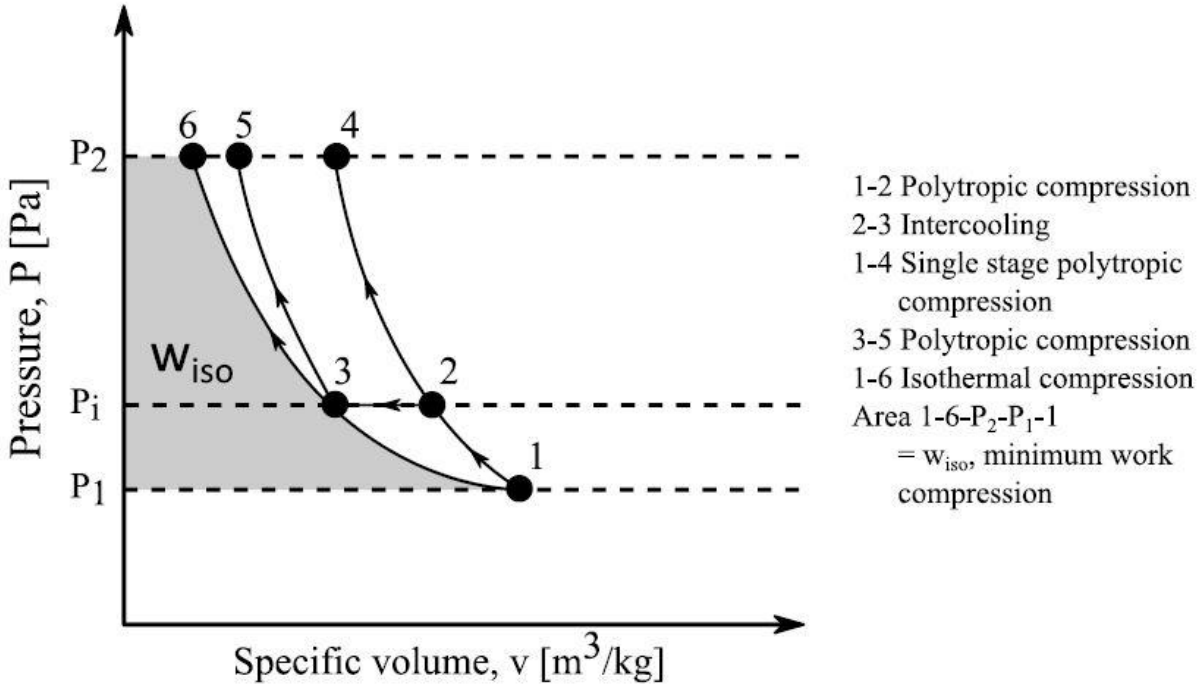

Figure 1.2: Isothermal compression is associated with the minimum area to the left of the process curve, representing the total compression work. Intercooling stages in conventional compressors reduce the process work requirement for compression (Young, 2017)

Bubbly two-phase flows of the type occurring in the downcomer of a HAC have ample interfacial surface area for heat transfer between the bubbles and the water. By Newton's law of cooling (1.2), the rate of heat transfer (q) is proportional to both the surface contact area (A) and the temperature difference (ΔT) between the surface and the bulk fluid. With very large surface area, significant heat transfer can maintain small temperature gradients within the bulk fluid.

$$q = k \cdot A \cdot \Delta T \tag{1.2}$$

1.1.2 Improving overall efficiency of HACs

Given that the thermodynamic process of compression in a HAC is ideal, it is useful to rephrase the mechanical efficiency in terms of sources of irreversibility (1.3). All of the hydropower not consumed overcoming irreversibility is available for air compression. Therefore, the target for efficiency improvement of HACs should be to reduce irreversibility from all sources. The sources addressed in this thesis are those generated by air entrainment and in the separator.

$$\eta_{mech} = \frac{\text{hydropower} - \text{air entrainment} - \text{separator} - \text{other sources}}{\text{hydropower}} \tag{1.3}$$

In a pumped HAC, the conversion is from electrical power to compressed air power. The total HAC efficiency breakdown is presented below:

$$\eta_{HAC} = \eta_{VFD} \cdot \eta_{motor} \cdot \eta_{pump} \cdot \eta_{mech} \cdot y \cdot \eta_{separator} \tag{1.4}$$

The terms added ahead of the mechanical efficiency comprise the efficiency of the conversion of electrical power to hydropower. The demonstrator HAC at Dynamic Earth has a variable frequency drive (VFD), which is useful for experimentation in that the flow rate can be adjusted on both pumps for performance testing. In commercial models, this component is unlikely to be included in the design. The motor efficiency (η_{motor}) represents the conversion of electrical power after the VFD to mechanical shaft power going into the pump. The pump efficiency term (η_{pump}) represents the conversion efficiency from shaft power to hydropower. This term necessarily includes the flow losses from the inlet of the pump suction line to the outlet of the

pump delivery line and the pump itself. Each of these components is critical to the design of commercial pumped HACs, but they are not the subject of this thesis.

The remaining undefined terms modify the quantity of air delivered. Because the mechanical efficiency (η_{mech}) of a HAC is proportional to the mass flow rate of air ($\dot{m}_g$), any fraction of the air flow rate at the intake that is not delivered at the outlet reduces the overall HAC efficiency. This 'air productivity' fraction is the product (Equation (1.4)) of two terms: air yield due to dissolution (y) and separator effectiveness ($\eta_{separator}$). These are addressed in the following two sections.

1.1.3 Compressed air yield

Compressed air yield in a HAC due to dissolution was the subject of recent work on this project by Dean Millar (2014), Valeria Pavese (2015), and Stephen Young (2017). Beyond this section, solubility yield is not specifically addressed in this thesis. Air that is dissolved in the downcomer during the course of compression cannot be captured by the separator at the bottom. The energy that compressed that portion of the air to the point at which it dissolves and joins the water stream is lost. This effect was described in the historic literature by McNair and Koenig (1911), who used candle flame height to measure the oxygen concentration of mine ventilation air provided by the HAC at Ragged Chutes at 17.7% by volume (normally 20.9%). They state that these results are consistent with previous (uncited) measurements made of air from the HAC at Victoria mine. Oxygen, being more soluble than nitrogen, preferentially dissolves in the water, reducing its concentration in the remaining gas (Millar, 2014).

At high pressure, gases become more soluble in water. The equilibrium concentration of each gas species depends on partial pressure and temperature. The equation below (1.5) is a combination of the Henry and van 't Hoff equations from Sander (2015). For the purposes of the discussion here, Henry's constant ($k_{H,i}$) is cited in $m^3 \cdot Pa/mol$. In other sources, the name "Henry's constant" may refer to either this measure or its inverse (Young, 2017). The dissolved equilibrium concentration of the species (c_i) is proportional to its partial pressure (p_i). The relationship with temperature is more complex; the enthalpy of solution ($\Delta_{soln}H$) follows the chemistry sign convention of negative values for exothermic reactions, such as those for gas. Therefore, there is a negative exponent when the fluid temperature (T) is greater than the reference temperature (T_0), reducing the equilibrium concentration. According to Millar (2014), the equilibrium concentration of air is approximately halved when the temperature increases from 25°C (298 K) to 80°C (353 K).

$$c_i = \frac{p_i}{k_{H,i}} \cdot \exp\left[-\frac{\Delta_{soln}H}{R} \cdot \left(\frac{1}{T} - \frac{1}{T_0}\right)\right] \tag{1.5}$$

This relationship with temperature introduces the means to control the gas solubility mechanics. By reducing the equilibrium concentration of dissolved gases, the rate and capacity of gas dissolution is reduced (Young, 2017). Therefore, increasing the water temperature is one way in which the gas solubility can be impeded. In a run-of-river HAC, the water chemistry and temperature cannot be adjusted. One of the key advantages of a pumped HAC is that both of these parameters can be controlled. Simply by running a pumped HAC over time, the water temperature increases from irreversibility in the fluid circuit and internal energy heat transfer from the air. Figure 1.3 shows a modeled increase in temperature and gas yield over the course

of several days in a hypothetical large, insulated HAC. Once a threshold temperature is reached (after 12 days, in this case), it would be necessary to add cooling to the system, because the ambient cooling rate is insufficient to meet the demand.

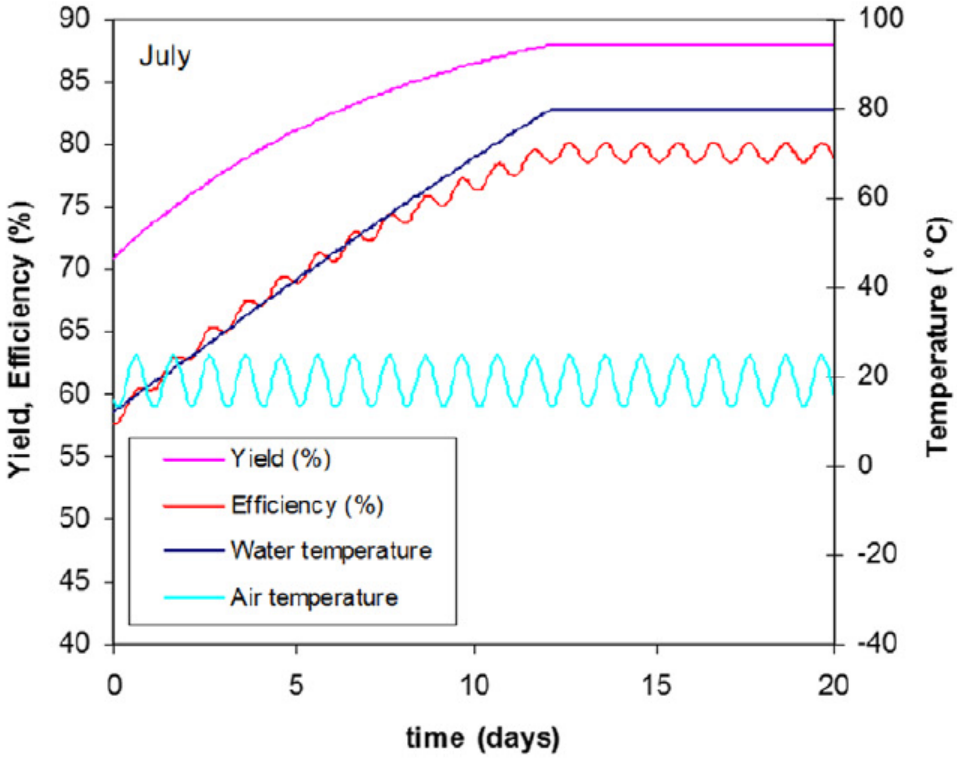

Figure 1.3: Yield improves as the solubility losses are decreased by increasing temperature. The water temperature is increased by the heat of compression over time to the equilibrium point of heat transfer to the surrounding environment. The efficiency reported in this figure is the mechanical efficiency including solubility yield (Millar, 2014)

Another control mechanism is to employ co-solutes in the water. The presence of co-solutes generally reduces the capacity of the water to dissolve gases from the air (Young, 2017). Equation (1.6) below, based on the formulation of Sechenov's equation from Sander (2015), is

used to adjust Henry's constant for the salinity of the water. As the dissolved salt concentration (b) increases, the adjusted Henry's constant (k_H) also increases. From (1.5), the equilibrium concentration is proportional to the inverse of Henry's constant, meaning that an increase in Henry's constant leads to a decrease in equilibrium concentration. According to Millar (2014), a 1 mol/kg solution of sodium sulphate has the effect of doubling Henry's constant for both nitrogen and oxygen, halving the capacity of the water to dissolve the predominant gases in air.

$$\log\left(\frac{k_H}{k_{H,0}}\right) = k_s \cdot b \tag{1.6}$$

The HAC at Victoria Mine ran on river water with no possibility of temperature or salinity control. It delivered air at a temperature of 4°C (277 K) and an absolute pressure of 888 kPa (Millar, 2014). Based on oxygen concentration measurements taken in March, 1907, Millar (2014) calculated the yield due to solubility at just over 75% by mass. By heating and salting water in a recirculating HAC as described above to cut the equilibrium concentration by a factor four, the same system would improve its yield to 94%. Because solution of gas into the water stream is occurring in the context of a fluid flowing in changing pressure conditions, the equilibrium point is constantly shifting. The dynamics of solubility are analogous to those of heat transfer (1.2). It uses a different coefficient and the driving force is a concentration difference rather than a temperature difference, but the equation follows the same form and the same logarithmic convergence on equilibrium when integrated over time.

According to Young (2017), the absolute humidity (kg water vapour/kg dry air) at 100% relative humidity (saturation humidity) represents a significant fraction of the total mass in the upper end of the temperature range. In small air bubbles submerged in water, it is reasonable to assume that

the relative humidity holds at or around 100%. In the temperature range of 5°C (278 K) to 45°C (318 K), his models with and without psychrometry agreed within 1% of each other. At higher temperatures, however, the psychrometric model deviated significantly. As pressure increases in the downcomer, the saturation (absolute) humidity falls rapidly. The water vapour crashes out (i.e. condenses) as liquid because the compressed air has a substantially lower capacity to hold it in vapour form than it did at lower pressure. Any energy expended to compress the vapour to that point is lost. Water vapour crashing out should be treated similarly to solubility yield of other gases in that the energy effect is similar. This behaviour suggests an optimum temperature for a HAC based on the dependence of psychrometry and gas solubility on water temperature.

Finally, there is a special application of solubility yield in HACs: carbon capture is possible because the equilibrium solubility of carbon dioxide is two orders of magnitude greater than that of nitrogen (Millar, 2014). In atmospheric air, the concentration of carbon dioxide is low enough that its dissolved molar concentration would be less than that of nitrogen. However, in gases with high concentrations of carbon dioxide, such as flue gas from a coal power plant, the dissolved gases would more heavily favour carbon dioxide. The gas comes out of solution as the pressure decreases in the riser, releasing low pressure carbon-enriched gas for capture at the tailrace (Millar, 2014).

1.1.4 Separator effectiveness

Of the air that remains in gas form, the separator does not perfectly separate the gas from the water stream. Some fraction of the air remains with the water stream as separator underflow. Some energy may be recovered in the form of an air lift effect in the riser pipe, but it is less than the energy spent to entrain and drag that air down the downcomer due to irreversibility in the

compression process, so separator underflow is undesirable. The fraction of gas at the separator level that is recovered into the plenum is defined as the separator effectiveness ($\eta_{separator}$).

Bubbles are separated from the water either by slowing the flow down and allowing enough time for the air to rise out of suspension in a gravity separator or by generating a large centrifugal acceleration by rapidly turning the flow, driving the lighter medium towards the axis of a centrifugal separator. The high velocity and large velocity gradients in a centrifugal separator create more flow irreversibility, making them more difficult to apply to a HAC, where hydraulic head is at a premium (see: section 4.1). The focus in this thesis is on modeling the separator effectiveness of gravity separators.

1.2 Research questions and hypotheses

This research is intended to describe the mixing and separation processes to contribute to the performance prediction model. Once the performance can be predicted reliably, the mixing and separation devices can be optimized to maximize efficiency or to fulfill other objectives and meet constraints specific to each commercial application. The questions in this section represent what knowledge is required to build an understanding of air entrainment, bubble size prediction, and separation sufficient for HAC engineering design. Where possible, hypotheses are included below each question. Each of these questions is relevant to the objective of this work to develop the design methodology for the air entrainment and air-water separation components of HACs, but it has not been feasible to fully answer all of them. Although not all of these questions are answered in this thesis, each one is at least addressed.

1.2.1 Air entrainment

1. What drives air entrainment in a HAC?

   The steady flow energy balance (see: section 3.5) and observations of air entrainment by vortex formation without designed mixing head geometry at the Baby HAC prototype suggest that the HAC inducts air as a natural consequence of the system geometry.

2. Can a HAC in the closed loop configuration (i.e. no forebay tank) induct air without the Venturi effect?

   There is nothing in the steady flow energy equation that suggests the system would operate differently in a closed loop configuration if the pipe is opened to atmosphere using holes instead of a free water surface in a tank (see: section 3.7). Changing the position of the holes should also predictably change the operating point on the recirculation pumps by changing the driving head of the compression loop.

3. Does air entrainment without a vortex create less flow irreversibility? Is any difference between vortex entrainment and other processes significant to engineering design?

   The sharp velocity gradient moving out from the wall of a vortex creates flow irreversibility. Similarly, a sparger or air manifold of any design intended to prevent vortex formation or snorkel air into a water flow below the surface will create flow irreversibility from friction and sudden expansion minor (shock) loss (see: section 2.2). Large vortices have been observed to be lossy and unstable (described in section 7.3), so those at least are undesirable.

4. Under what conditions is a vortex likely to form?

   Experimental evidence reported in the literature suggests that a vortex naturally forms

whenever the free surface nearest the suction pressure zone is sufficiently large to support it (see: section 2.2.2) except under conditions where the local geometry favors impinging jet entrainment (see: section 2.2.1).

1.2.2 Air-water separation

1. How does one predict the size distribution of bubbles entering the separator without a reliable coalescence model?

   Using a bubble size distribution prediction at the mixing head and assuming no coalescence or breakup interactions in the downcomer should result in a misestimation of bubble size (see: sections 2.3.7 and 2.3.8). One of several empirical models (see: section 4.3.2) should result in a reasonable estimate of bubble size, to be confirmed by manual measurement (see: section 6.4.1).

2. How much do dissolved salts affect separator effectiveness?

   The presence of dissolved salts shrinks the bubble size distribution by preventing coalescence (see: section 6.6). The presence of salt is expected to reduce separator effectiveness.

3. What is the effect of swirling flow in gravity separators?

   Vertical separators with full admission inlets will have swirling flow. The centrifugal force term is expected to be small enough that it would not significantly change the magnitude of the field force inside the separator (see: section 2.3.1).

4. Under what economic conditions, if any, is the selection of a centrifugal separator preferable over a gravity separator?

   The centrifugal separator option was rejected for the Dynamic Earth HAC because the

head loss across the separator would have consumed a significant fraction of the total driving head available for the compression loop (see: section 4.1).

1.2.3 Control and operation

1. What is the cause of the extreme flow surging observed at Baby HAC in the headless configuration at high water flow rate?

   The large vortex formed without a mixing head appears to be unstable and oscillates between entraining and non-entraining (see: section 7.3).

2. What is the effect of gas solubility on bubble size distribution?

   In bubbly flows where the coalescence rate is low, the bubble size should be uniformly decreased down the downcomer in the same fashion as increasing pressure causes the same effect.

1.3 Chapter list

Chapter 2 is divided into three parts: concepts of two-phase flow, air entrainment mechanisms, and bubble mechanics for separator effectiveness modeling. Section 2.1 introduces the concepts and terminology that are used in the remainder of this thesis. Section 2.2 identifies the air entrainment mechanisms that are expected to be relevant for a HAC and comments on how they compare to one another in terms of flow irreversibility. The irreversibility associated with air entrainment is the key parameter for mixing head design. Section 2.3 describes the bubble mechanics and variables that contribute to bubble diameter, which control how the bubbles move within a fluid flow and are used later in the thesis to model two gravity separators.

Chapter 3 describes what, physically, is responsible for air entrainment and develops an equation intended to model the critical water level at which air entrainment can begin, which is relevant for the design of HAC inlets in reservoirs. Understanding the physical basis for air entrainment is necessary to develop the design criteria of mixing heads for future installations.

Chapter 4 describes the two components of the separator performance model: head loss (irreversibility) and separator effectiveness. The head loss associated with a separator design is simple to evaluate, but improperly selected design elements that increase head loss can measurably reduce the energy available for air compression in limited head applications. Separator effectiveness is more difficult to calculate and relies on accurate modeling of the internal flow field, the inlet bubble size distribution, and how the bubble separates from the flow. An accurate prediction of separator effectiveness saves capital cost, where the safety factor on separator size can be reduced if the model is reliable.

The prototype (Baby HAC) and demonstrator (Dynamic Earth HAC) are described in detail in chapter 5. The physical description, instrumentation scheme, experimental methodology, and the rationale for various experimental design decisions are included in this chapter. Experiments on mixing heads and separators have been performed on both HACs.

Chapter 6 presents the results from the experiments designed to characterize the air entrainment and air-water separation processes on both HACs. The greater part of the experimental programme was performed on Baby HAC, which has been operational for a longer period of time.

Chapter 7 synthesizes the experimental results into the design consequences of the findings. The best design practices for mixing heads and the likely reasons why the others failed to meet expectations are identified. The limitations of the separator effectiveness models are described.

Chapter 8 concludes the work by responding to the research questions presented in section 1.2, describing the original contributions presented in this thesis, and outlining some future work that naturally expands on the work already completed.

Chapter 2

2. Literature Review

This chapter describes the literature relevant to characterizing the air entrainment and separation processes to develop the design methodology for the air-water mixing head and separator components of HACs. For entrainment, the objective is to determine how air entrains in water and which local entrainment mechanisms might be preferable on the basis of reducing irreversibility. For separation, the objective is to identify which variables contribute to separation effectiveness and determine how to evaluate them for the purposes of design modeling.

2.1 Concepts of two-phase bubbly flow

The two-phase (liquid-gas) flow in the downcomer consists predominantly of water, with large numbers of air bubbles dispersed throughout. Modeling air entrainment, downward transport, and separation occurs in this context. Several key definitions are required to describe bubbly flow:

Bubble diameter: Diameter is the most commonly used measure of bubble size and it assumes a spherical shape. Bubbles are not perfectly spherical (see: Figure 2.1), so this measure is the diameter of an equivalent sphere. The Sauter mean diameter is used for heat and mass transfer and is defined as the diameter of a sphere with the same surface area to volume ratio as the bubble (Brennen, 2005). Clift et al. (1978) use a hydraulic equivalent sphere diameter for mechanical calculations, defined as the diameter of a sphere with the same density and relative velocity of the actual bubble.

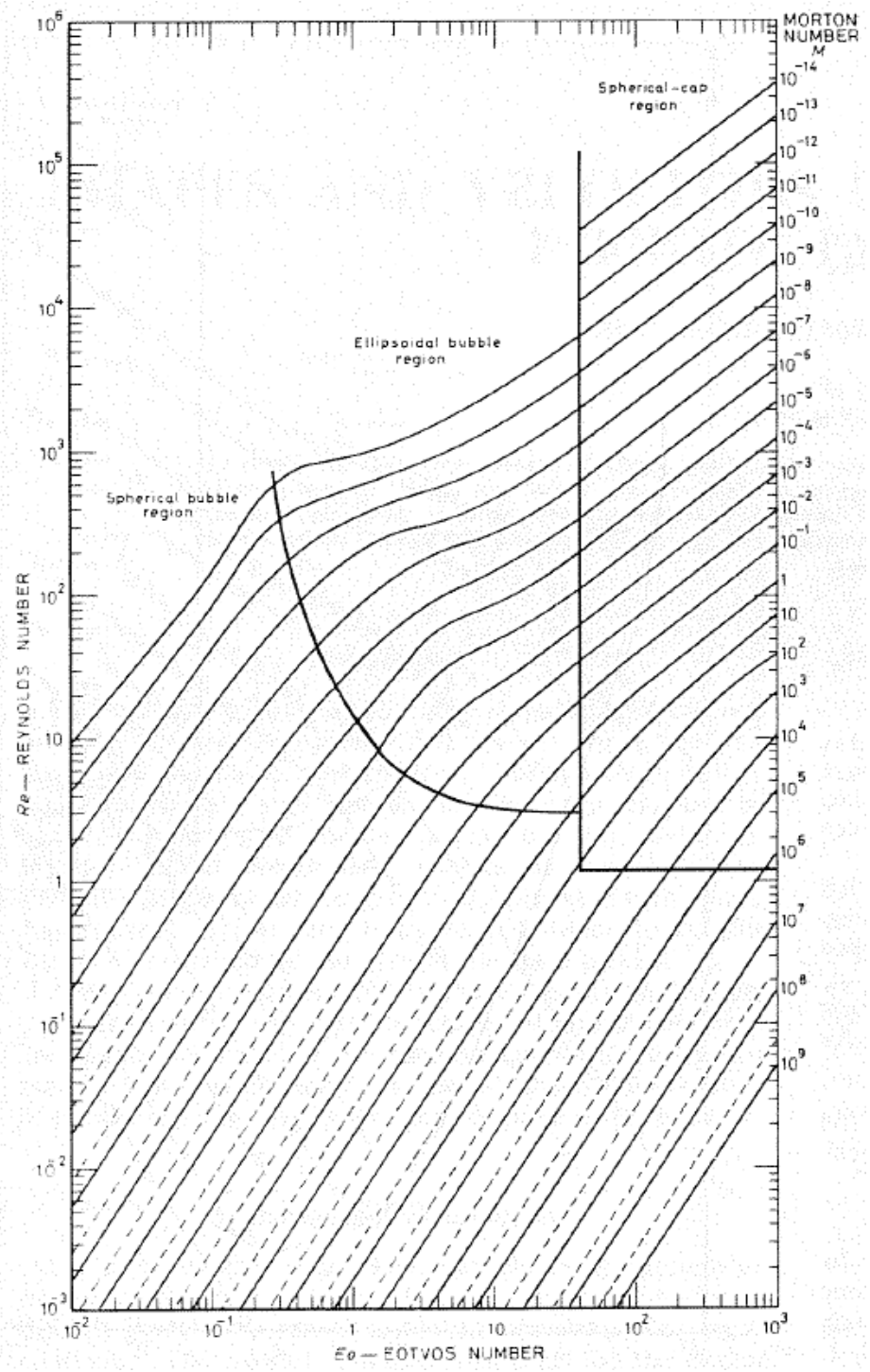

Figure 2.1: Smaller bubbles have the lower Reynolds and Eötvös numbers because the length scale appears in the numerator of both, so these tend to be more spherical than larger bubbles (Grace, 1973)

Bubble size distribution: Bubbles are not created with a uniform size; they fall into an approximately lognormal size distribution of mass fraction based on diameter. The Rosin-Rammler distribution (2.1) is convenient, because it defines the mass fraction of the distribution smaller than a given diameter (d) using only two parameters: the mean bubble diameter ($\bar{d}$) and an empirical spread parameter (n). It has been found to be sufficiently accurate for modeling (Laleh et al., 2012a). More accurate distributions exist (Taya et al., 2012), but these rely on multiple empirical parameters that are not as well-established.

$$Y = 1 - \exp\left[-\left(\frac{d}{\bar{d}}\right)^{n}\right] \tag{2.1}$$

Bubble swarm: When the gas volume fraction increases above 10%, the bubbles begin to concentrate in swarms (Brennen, 2005). The effect is increased in flows where the continuous phase is turbulent, as in the downcomer of a HAC, because the turbulent vorticity tends to concentrate the bubble swarms (Aliseda and Lasheras, 2011). The literature is unclear about the effect of bubble swarms. According to Roghair et al. (2011), bubble swarms increase the dragand therefore decrease bubble velocity. According to Wilkinson and van Dierendonck (1990), the bubble swarm has the opposite effect, resulting in a higher velocity than for individual bubbles. In a HAC downcomer, the gas volume fraction at inlet (top) may be up to 50% (Millar, 2014) and at the inlet to the separator (bottom) will be substantially lower, decreasing with increasing delivery pressure.

Coalescence/Breakup: Bubbles in motion are subject to shear forces and collisions. Colliding bubbles have a chance to merge or coalesce. When shear forces exceed the strength of the bubble surface provided by surface tension, the bubble can rupture or break up. Other effects can cause

bubble breakup (Clift et al., 1978), but these are not relevant to this application. The balance of coalescence and breakup generates the bubble size distribution.

Continuous phase: When a multiphase flow is dominated by one of the phases, the dominant material is referred to as the continuous phase. Bubbly flows are dominated by the liquid phase.

Dispersed phase: In this case, the dispersed phase consists of discrete bubbles spread throughout the continuous liquid phase.

Drag coefficient: The effects of drag and impact are combined into a single dimensionless parameter called the drag coefficient (treated in more detail in section 2.3.3), which depends on the particle Reynolds number. It is empirically-derived, so it also accounts for effects of lesser importance. Bubbles change shape with Reynolds number and are proposed to exhibit slightly different behavior than settling particles, so there are adjustments to drag coefficients specific to bubble motion (Karamanev and Nikolov, 1992) and changes to the flow field created by the formation of bubble swarms (Roghair et al., 2011).

Detrainment: The removal of bubbles from a bubbly mixture by coalescence with an air plenum or large void is referred to as detrainment.

Entrainment: The process where bubbles are created by rupturing the water-air surface and drawing air into the flow as a bubbly mixture is referred to as entrainment.

Eötvös (Bond) number: The Eötvös number is a dimensionless ratio of buoyancy forces to surface tension (σ) forces (2.2). It contributes to the prediction of the flow regime (Usui, 1989), bubble shape (Grace, 1973), and the correction of the drag coefficient to compensate for the

effect of bubble swarms (Roghair et al., 2011). The characteristic length term (L) in (2.2) can refer to the pipe diameter or bubble diameter, depending on the source. Buoyancy is also related to the difference in density between the displaced liquid (ρ_l) and the gas (ρ_g) and the field force acceleration (e.g. by gravity, g_f).

$$Eo = \frac{(\rho_l - \rho_g) \cdot g_f \cdot L^2}{\sigma} \tag{2.2}$$

Flow regime: There are two types of flow may occur in a HAC: bubbly and slug. There is a wide transition zone between the two (Martin, 1976). The HAC downcomer process sits within that transition zone, based on the ratio of gas volume flux (j_g) to liquid volume flux (j_l) between 1.0 and less than 0.1. Figure 2.2 illustrates that there is an uncertain boundary between the bubbly and slug flow regimes, where different researchers disagree over which flow regime is being observed within the transition zone. In the separator, the flux ratio is low and dropping, pushing the flow regime into a more bubbly form.

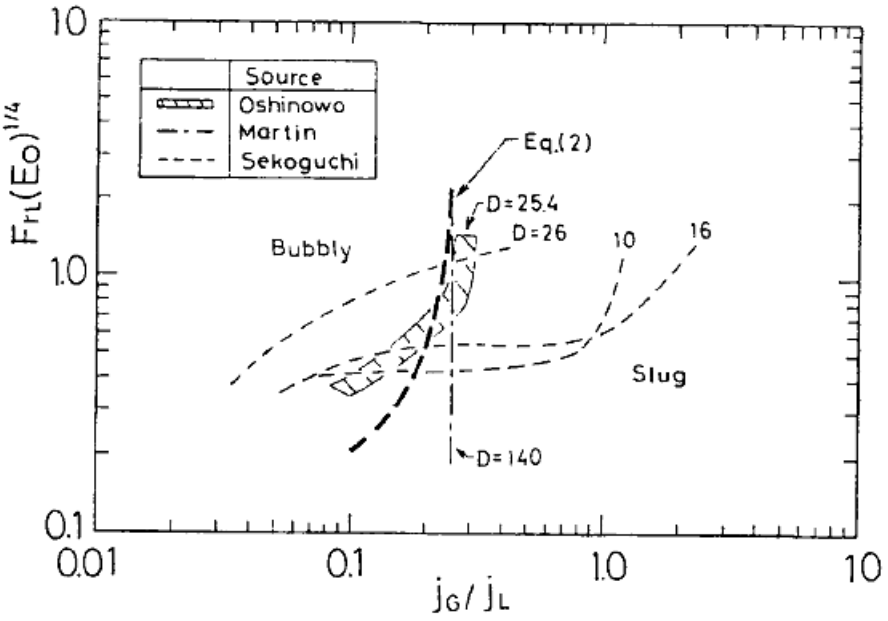

Figure 2.2: A flow regime map for the bubbly-slug zone of vertical downward two-phase flow. The horizontal axis is the ratio of gas volume flux over liquid volume flux and the vertical axis is a function of the Froude and Eötvös numbers (Usui, 1989)

Froude number: The Froude number is a dimensionless ratio of inertial forces to gravitational forces. Equation (2.3) represents the densimetric Froude number, which treats both phases as media with nonzero densities. Inertial forces are represented here by liquid volume flux (j_l) rather than velocity for ease of calculation. It is a reasonable approximation for flows where the water if dominant. The Froude number contributes to the prediction of the flow regime (Usui, 1989) and appears in bubble size prediction equations (Akita and Yoshida, 1974; Wilkinson et al., 1994).

$$Fr = \frac{j_l}{\sqrt{g_f \cdot D \cdot \frac{\rho_l - \rho_g}{\rho_l}}} \tag{2.3}$$

Gas volume fraction (void fraction): Gas volume fraction is a dimensionless ratio of the volume of gas to the volume of liquid in a two-phase flow. This is the property that actually determines the flow regime, but it is difficult to evaluate reliably (Bhagwat and Ghajar, 2012; Usui and Sato, 1989). Gas volume fraction also contributes to the adjustment of bubble drag coefficient to account for bubble swarm interference (Roghair et al., 2011). In a HAC downcomer, gas volume fraction is lowest at the bottom where it exits into the separator because it is at higher pressure than above. It further decreases in the separator as air is removed from the flow.

Particle Reynolds number: The particle Reynolds number is a dimensionless ratio of inertial forces to viscous (μ) forces as they apply to a bubble or particle within a flow field (2.4). It differs from the standard Reynolds number in that the difference in media densities is used in place of fluid density, the relative velocity of the bubble with respect to the continuous medium velocity (v_r) is used in place of absolute velocity, and the characteristic length is the bubble diameter (d). This number is used to calculate the drag coefficient (Brown and Lawler, 2003; Cheng, 2009) and bubble shape regime (Grace, 1973).

$$Re_p = \frac{(\rho_l - \rho_g) \cdot v_r \cdot d}{\mu} \tag{2.4}$$

Relative velocity: When a two-phase bubbly fluid is subject to an acceleration field, the bubbles will tend to migrate opposite the field direction, due to buoyancy. In a gravitational field, the bubbles move upward with respect to the motion of the continuous medium. In a centrifugal field, the bubbles will move radially inward toward the centre of rotation. Relative velocity (2.5) is used to back-calculate the absolute velocity of a bubble (v_b) in space when the local water

velocity (v_w) is known. For a separation process, the intent is to allow the bubbles to detrain so the gas may be siphoned off. In a HAC downcomer, the intent is to drag the bubbles down to the bottom; the flow velocity of the continuous phase must exceed the relative velocity.

$$v_r = v_b - v_w \tag{2.5}$$

Shear: Bubble breakup occurs when the shear forces acting on it exceed the cohesive surface tension forces holding it together. In general, the shear is generated by turbulent eddies and velocity gradients. According to Clift et al. (1978), only turbulent eddies on a scale smaller than the bubble size are relevant to breakup. Larger eddies serve to transport rather than break up the bubble. Significant velocity gradients act to break up bubbles near the flow boundary at the pipe wall (see: Figure 2.3).

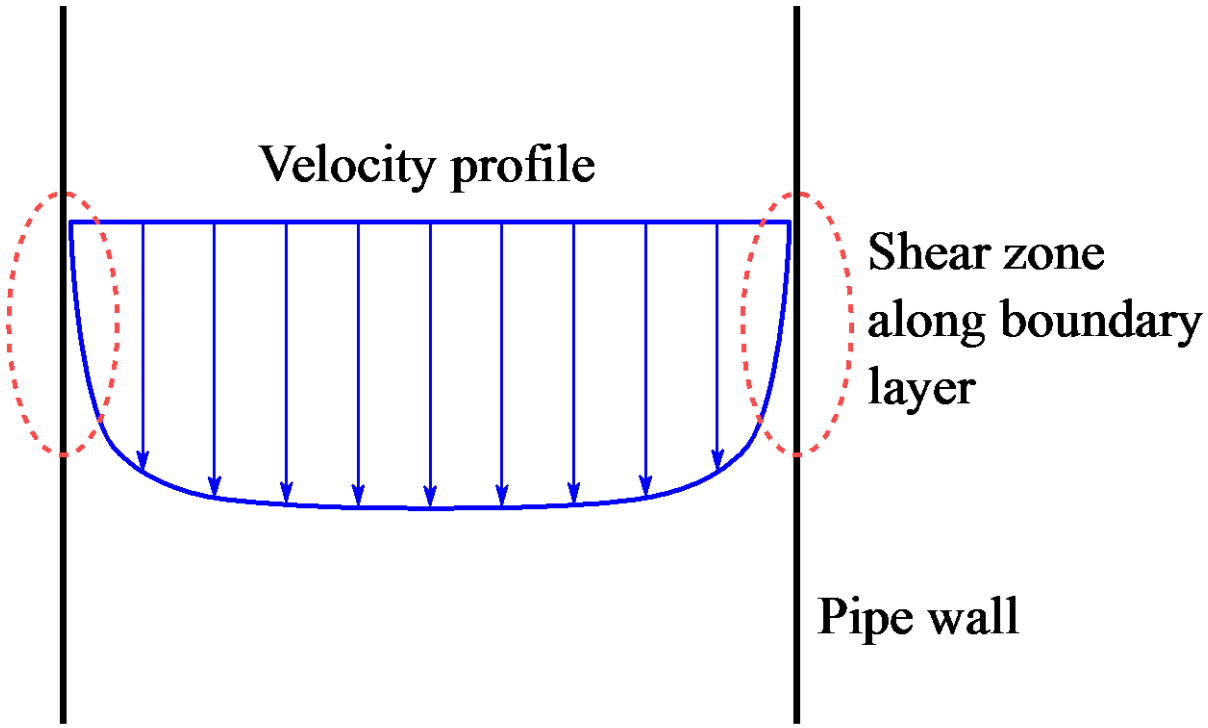

Figure 2.3: Fully-developed turbulent pipe flow velocity gradients at the pipe wall

Surface tension: This is a surface effect generated by unequal forces of molecular attraction between the two phases. The surface tension of water tends to increase at low temperature (NIST, 2018) and when inorganic solvents are used and decrease with higher temperatures or organic solvents (Smits, 2000).

Volume flux (superficial velocity): Volume flux applies to the gas and liquid streams separately and is used to predict the flow regime (see: Figure 2.2). It is evaluated by dividing the volume flow rate of the phase divided by the total flow area available. These are preferred over other potential measures such as true velocity, because they can be evaluated explicitly. For a single

phase flow, this number is equal to the flow velocity. In a two-phase flow, this is what the velocity of one of the phases would be if that phase occupied the entire pipe area.

Weber number: The Weber number is a dimensionless ratio of inertial or shear (τ) forces to surface tension (σ). In the context of bubble mechanics, this number describes the balance of forces attempting to break apart a bubble and those holding it together. A critical Weber number (2.6) is used to describe the maximum stable bubble size (d_{max}) in a flow (Hesketh et al., 1987) in order to predict bubble breakup.

$$We_{crit} = \frac{\tau \cdot d_{max}}{\sigma} \cdot \left(\frac{\rho_g}{\rho_l}\right)^{1/3} \tag{2.6}$$

2.2 Air entrainment processes

As an energy efficiency technology, the HAC requires each process to incur as little energy loss as possible. Any energy required to overcome the irreversibility associated with the entrainment process is unavailable to the system for air compression downstream. Therefore, the objective of the mixing head in a HAC is to facilitate entrainment with minimum irreversibility. The intent of this section is to identify the common mechanisms involved in entrainment and which ones are most promising for mixing head design.

Chanson (1995) considers water aeration in simulated marine and river environments by the action of breaking waves. Kobus (1984) describes air entrainment in a generic form by several mechanisms (see: Table 2.1) in open channel flows. Hydraulic jump, jest striking, and breaking wave all refer to the same basic principle where a fast-moving water stream collides with a slower moving water stream or stationary object, producing a shear layer along which air is

entrained. This phenomenon will be referred to as impinging jet entrainment in this thesis. Vortex entrainment occurs where a slow-moving water body is accelerated into an opening near enough to the water surface that a vortex can bridge between the free surface and the intake. Venturi eductors should be added to the list for consideration in closed pipe entrainment scenarios. The common feature of all of these entrainment mechanisms is some surface disturbance generated by local flow conditions. In each case where entrainment occurs at a free surface or air pocket, bubbles are generated by shear acting on that surface created by velocity gradients in the local flow. According to Clift et al. (1978), the shearing eddies are of a size scale similar to the size of the bubbles being generated.

Table 2.1: Mechanisms of local air entrainment by self-aerating flow (Kobus, 1984)

Hydraulic jump	Jet striking		Vortex	Breaking wave
	Solid surface	Liquid surface		
Jump in conduits	Closed dissipation chamber	Sharp crested weirs	Dropshafts	Breakwaters
High head gates	Priming at siphons	Outlet structures	Suction pipe at pumps	
Regulating valves in pipes	Regulating valves in pipes	Dropshafts	Intakes	

Future iterations of the pumped HAC will be designs with no forebay tank but that will instead draw air directly into the downcomer pipe through an in-line mixing head. Removing the forebay tank from the design reduces complexity and weight at the top of the structure, reducing capital cost. Figure 2.4 illustrates the difference between the current format “open loop” HAC and a simpler “closed loop” format for pumped systems. These closed loop HACs will have the advantage of removing the cost and weight of the forebay tank and its water content, as well as

the flow irreversibility created by exit and inlet losses between the pipes and tank body. The value of investigating entrainment mechanisms specific to the type of open loop HAC that requires a tank and a free surface is to understand the phenomenon of entrainment irreversibility for early run pumped HACs in open loop configuration, retain the option of using hydropower, and unify the concepts of free surface and closed pipe entrainment into a single framework.

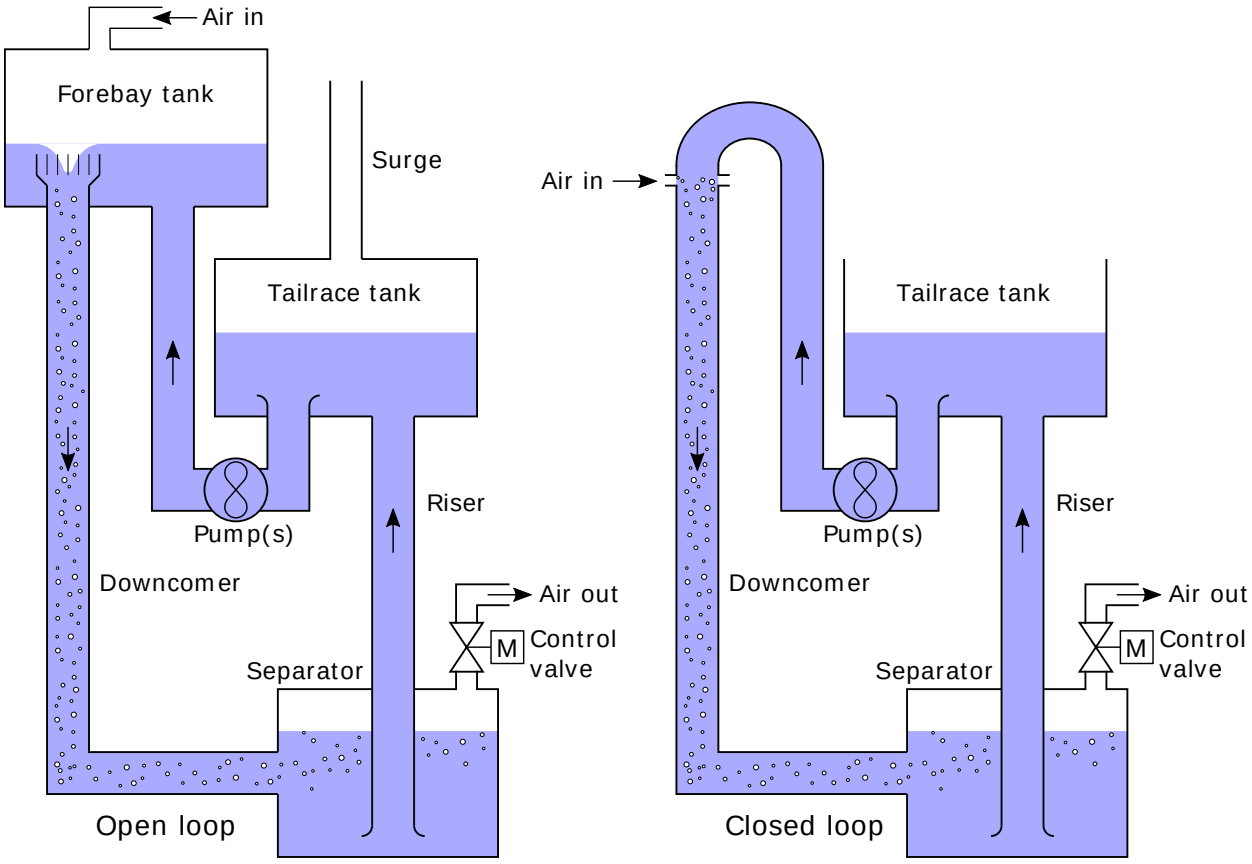

Figure 2.4: The open loop system was originally designed for hydropower resources and the closed loop system is a simplification for pumped systems

2.2.1 Impinging jet entrainment

The jet striking and hydraulic jump categories in Table 2.1 refer to a similar mechanism where a high speed water jet impacts stagnant or slower speed water body, causing a surface disturbance and air entrainment. This combined effect will be referred to as impinging jet entrainment. The momentum of the water jet striking the water surface creates a shear layer along the contact (Kobus, 1984). Figure 2.5 illustrates how the shear layer entrains air drawn in at the impact point as bubbles in the hydraulic jump case.

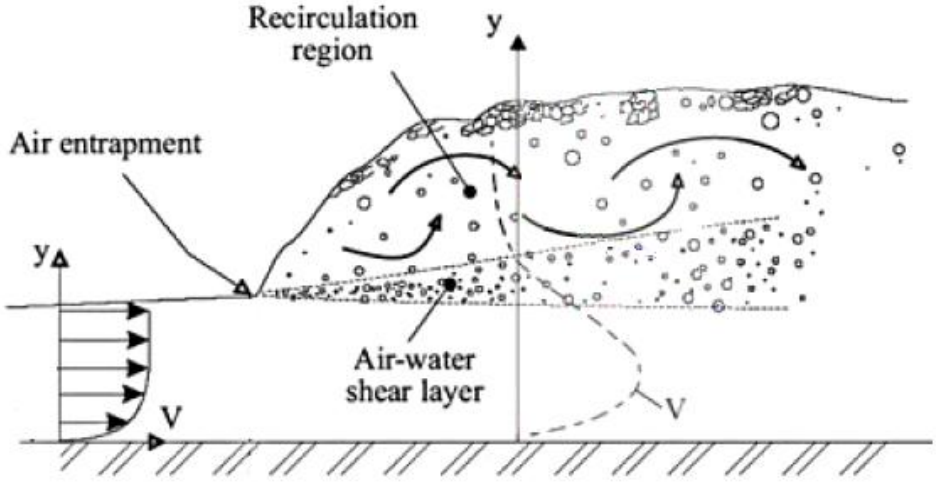

Figure 2.5: Air induction by hydraulic jump. The flow direction is from left to right (modified from Chanson, 2009)

In the open channel case, the impinging jet is generally either perpendicular to the bulk flow as with a plunging jet or in the flow direction as with hydraulic jump (Kobus, 1984). Vertical jets strike the surface with a greater differential velocity than do horizontal jets because the vertical component of velocity of the surface is essentially zero. This should increase the entrainment quantity for a jet of the same size and speed.

Horizontal jets collide with a surface moving slowly in the same direction as the jet, making the differential velocity lower. However, horizontal jets are associated with a surface roller that sits above the shear mixing layer and generates its own surface disturbance (Kobus, 1984).

Kobus (1984) presents data showing that in the case of jets striking an angled plate, a jet striking at a perpendicular angle entrains more air than one striking at a 45° angle. However, some of the kinetic energy of the jet striking the 45° plate would be recovered downstream. It is not clear which of these cases is associated with a larger air entrainment per unit of energy cost.

Chanson (2009) states that vorticity and air bubble movement are different in vertical and horizontal impinging jets, but that they depend on most of the same physical properties. The theoretical and numerical approach is made difficult by the requirement to simultaneously solve the continuity, energy, and momentum equations for each phase plus mass transfer in a three dimensional system. Extrapolation from experimental results using dynamic similarity is complicated by the large number of relevant dimensionless parameters to be accounted for. Attempts to simplify the analysis by using only Froude or Reynolds similarity have not adequately described the process (Chanson, 2009).

Of the original HAC installations by Charles Taylor, at least one used an impinging jet entrainment process which was located at Ragged Chutes in Cobalt, Ontario (Schulze, 1954). Figure 2.6 is a rare photograph of one of the two mixing head at Ragged Chutes in operation.

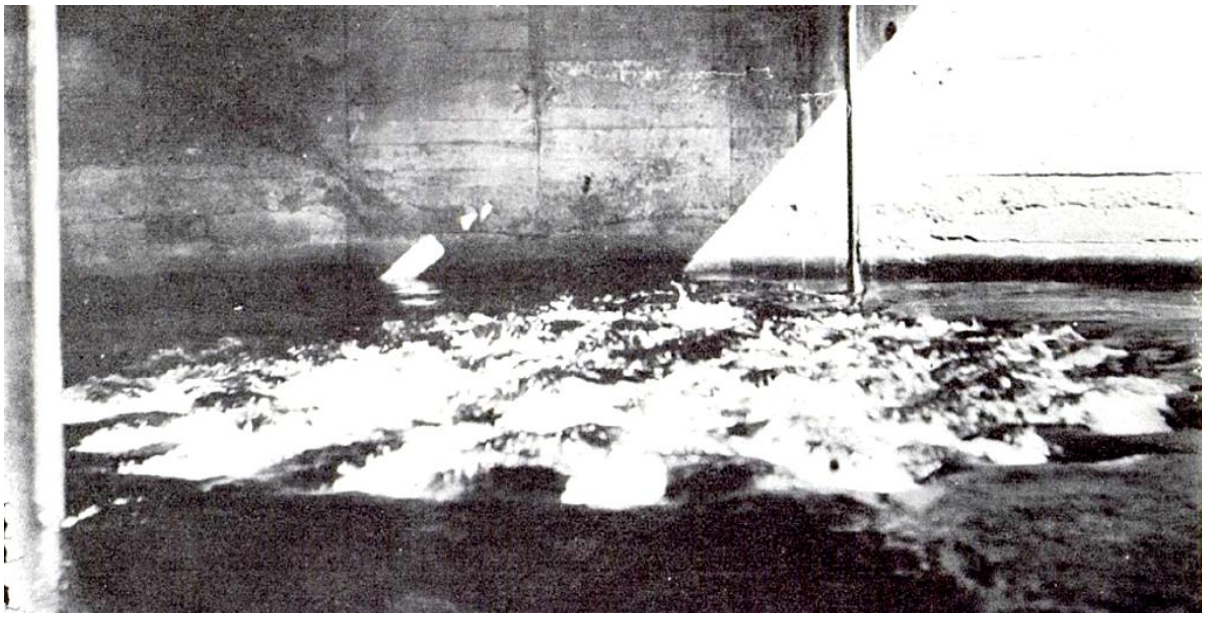

Figure 2.6: Photograph of Ragged Chutes head operating shows rolling breaker characteristic of non-vertical impinging jet entrainment mechanism (Schulze, 1954)

2.2.2 Vortex entrainment

A vortex is a local swirling flow within a larger flow field. For the purposes of this discussion, eddies within a turbulent flow are not considered vortices unless they join the pipe intake to a surface. Underwater vortices can also join the inlet to a rigid surface such as a tank wall or floor (Knauss, 1987). These are also not considered here.

A vortex with potential for air entrainment is a rotating disturbance between the water surface and pipe inlet. According to Knauss (1987), vortex formation at an intake is initiated by the creation of swirl in the flow created by upstream conditions. Stronger, steadier vortices are associated with more consistent and stronger swirl generation upstream. Upstream swirl generation is generally unavoidable, so vortex formation is a common feature at pipe inlets.

Not all surface vortices induct air. Those of lesser power will tend to create a visible surface swirl or dimple. Only the strongest vortices induct air (Knauss, 1987). Figure 2.7 shows the progression of vortex formation including non-inducting stages. Unstable inducting vortices cycle through these stages.

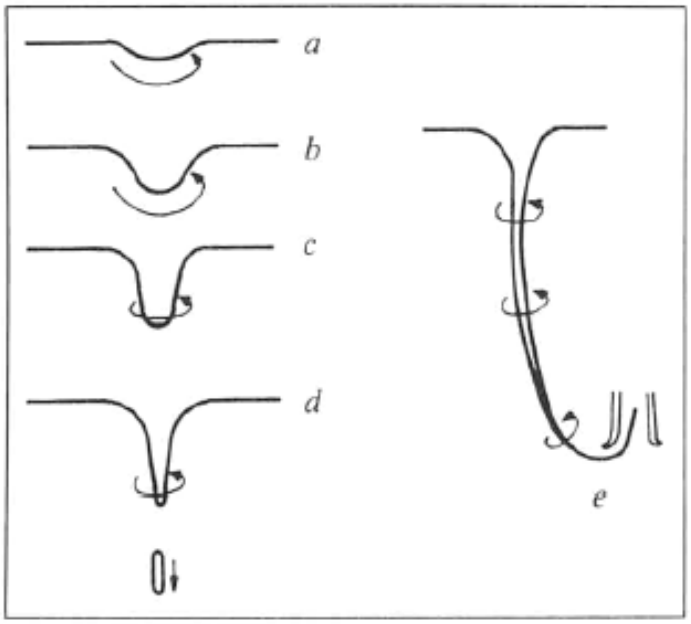

Figure 2.7: Stages of vortex development. Vortex "e" is entering the suction pipe of a pump; the tip is sitting near the lowest pressure point of the inlet (Chen, 1979)

For air entraining vortices, there is an air core at constant pressure in the centre of the vortex. This core is kept open by centrifugal force developed by high velocity swirling flow in the surrounding water (Chen, 1979). The tangential velocity within the vortex is a gradient from its highest level at the air contact to near zero in the surrounding free field. At the bottom of the vortex, the tip intermittently shears away (see: Figure 2.8), producing bubbles (Chanson, 1995).

Figure 2.8: An elongated air pocket breaks off an unstable vortex in this snorkel head

For inlets to sump pumps or hydroelectric turbines, vortices and air ingestion at the inlet create irreversibility in the flow and degrade performance of turbomachinery downstream. According to Knauss (1987), air ingestion of as little as 3% by volume creates a measureable decrease in pump efficiency.

Pipe intakes are best kept as close to the water surface as possible to lower cost, simplify operation, and reduce ingestion of sediments (Jain et al., 1978). However, air entraining vortices are more likely to form as the submergence of these inlets is reduced. Bhargava et al. (1984) and Cristofano et al. (2014) performed experiments to create empirical relationships to define the upstream conditions that were likely to result in air entraining vortices. This empirical work produced critical submergence criteria (i.e. submergence sufficient to prevent the formation of air-entraining vortices) based on a common set of dimensionless numbers: the ratio of water level (Cristofano et al., 2014) or channel width (Bhargava et al., 1984) to intake pipe diameter

(critical submergence ratio), Froude number, Reynolds number, and either Weber number (Cristofano et al., 2014) or an unnamed dimensionless number and the ratio of oncoming channel flow velocity to intake pipe velocity (Bhargava et al., 1984). Chen (1979), Gulliver and Rindels (1984), Jain et al. (1978), and Knauss (1987) used mixed experimental and theoretical models to accomplish the same task. One of the differences between this type of approach and the approach by Bhargava et al. (1984) or Cristofano et al. (2014) is that all of these models rely in part on a dimensionless parameter called the circulation number. Equation (2.7) is one variation of the circulation number from Werth and Frizzell (2009). This number is challenging to calculate, because it relies on accurate knowledge of the angle of the approach velocity ($\acute{\alpha}$), which is not possible for irregular approach geometries. Zheng and Werth (2008) showed that formed inlets reduce the minimum submergence requirement established for bellmouth pipe inlets.

$$N_r = \frac{\tan \acute{\alpha}}{[1 + (L_B/B) \cdot \tan \acute{\alpha}]} \tag{2.7}$$

2.2.3 Venturi effect entrainment

The Venturi effect relies on an exchange of static pressure for dynamic pressure created by a flow constriction that increases the local velocity. Equation (2.8) is a simplification of the Bernoulli equation with no change in elevation. If the velocity at position 2 (v_2) is increased to pass a flow through an aperture, then the static pressure (P_2) must drop below that at position 1 (P_1).

$$P_1 + \frac{1}{2}\rho v_1^2 = P_2 + \frac{1}{2}\rho v_2^2 \tag{2.8}$$

In the context of air entrainment in a HAC, that pressure is below atmospheric and connected to the atmosphere by a snorkel. The low pressure in the water flow provides motive force for the air to be drawn into the snorkel and down to the point of low pressure at the aperture. Figure 2.9 is a reproduction of the mixing head from the Peterborough Lift Lock (W.H.B., 1903), which operated by inducting air through a snorkel manifold into the water flow. At the point the air and water streams meet, the air stream is broken into bubbles and entrained by the turbulent action of the flowing water (Clift et al., 1978). This is the principle by which a Venturi eductor produces a bubbly flow.

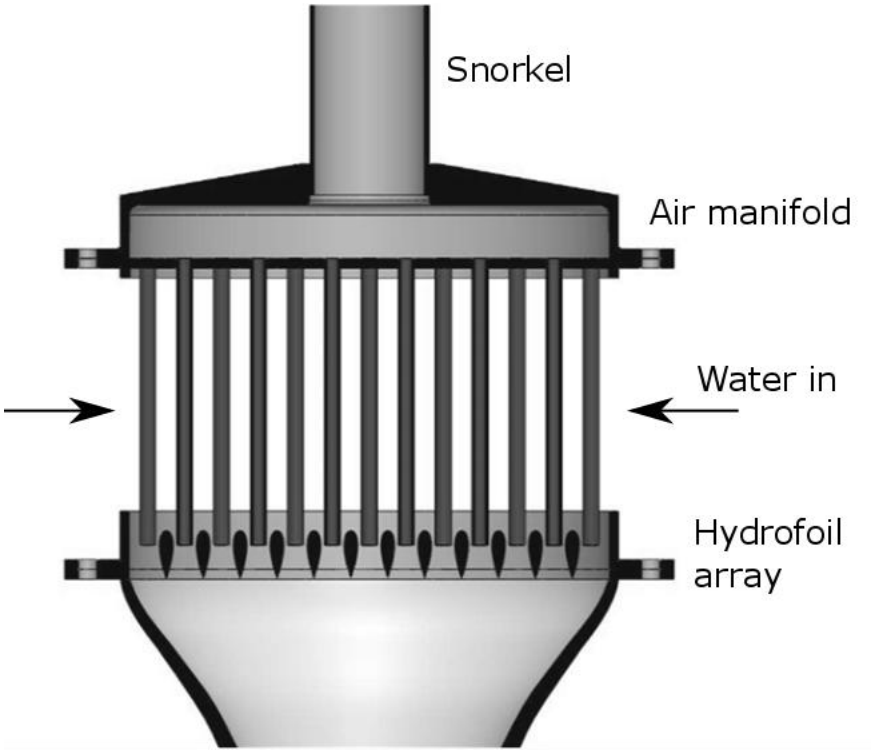

Figure 2.9: The air manifold of this mixing head is positioned to place the pipe ends in the narrowest part of the hydrofoil array

Charles Taylor and his contemporaries used this concept to drive the design of all of the mixing heads of the historic installations for which some evidence remains (Schulze, 1954; Taylor, 1897). In one case at Ragged Chutes (shown in operation in Figure 2.6), it is clear that the head did not function according to the original design. Figure 2.10 depicts both heads in their installed positions. Both are topped with an array of long pipes and have water inlet ports below. The air pipes are longer than would be necessary to generate the flow disturbance for impinging jet entrainment. It is clear that these heads were intended to operate with the large pipes protruding out from the water and acting as snorkels rather than the actual operation mode with water flowing over the top. Regardless of this design error, Ragged Chutes was one of the most mechanically efficient HACs (Millar, 2014).

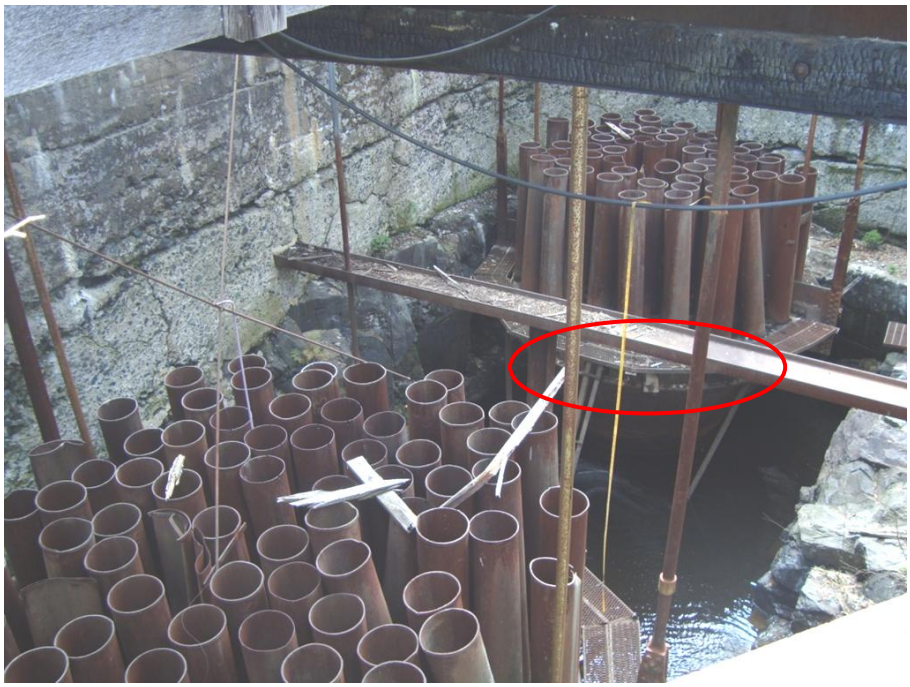

Figure 2.10: Ragged Chutes heads in their current condition. Circled in red are water entry ports

Venturi effect entrainment is also useful for closed pipe air induction. The HAC at the Royal Mines Inspection Plant (Clausthal) in Germany had a Venturi eductor mixing head installed at the top of the downcomer pipe (see: Figure 2.11) downstream from a sump outlet (Schulze, 1954).

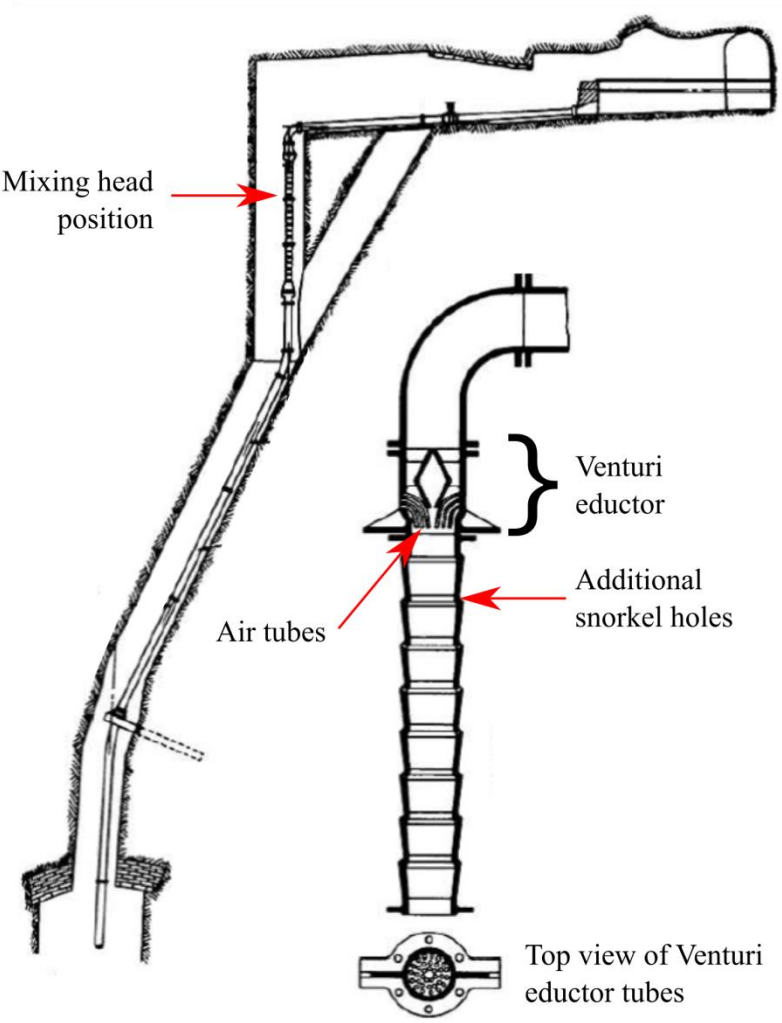

Figure 2.11: The mixing head at the Clausthal compressor was a closed pipe design that used shaped air tubes and an obstruction to generate negative gauge pressure by increasing flow velocity, per Bernoulli (modified from Schulze, 1954)

2.2.4 Relative irreversibility of entrainment mechanisms

The common thread of all entrainment mechanisms is that there must be some surface or interface disturbance and that the way this disturbance creates air bubbles within the water stream is by shearing action. Therefore, there is some inherent irreversibility associated with the entrainment process. This is not to say that all mechanisms are of equal value for application in a HAC but that they act in a similar fashion and so can be compared against one another to meet the objective of minimum work air entrainment for HAC design.

Beyond the potential impact to downstream turbomachinery in pumping and hydroelectric applications, there are further irreversibilities associated with air entraining vortices (Knauss, 1987): (i) vortex swirl shear, (ii) uneven intake flow creating locally high velocity, (iii) ingestion of floating debris, and (iv) minor losses associated with vortex control mechanisms installed on pipe.Vortex swirl shear is unique to that entrainment mechanism, but the other three are present to varying degrees in all mechanisms. The uneven intake flow is also a feature of the impinging jet and Venturi eduction has locally high velocity at the aperture. Floating debris should not be a problem for any closed system as in a pumped HAC where the water quality is controlled. Lastly, minor losses associated with vortex control would be similar to those that come from the features used to create the impinging jet or the obstruction created by the snorkel pipes in a Venturi eductor.

Impinging jet entrainment is initiated by high velocity, high shear fluid impact. The vertical plunging jet case is excluded from consideration owing to the cost in head necessary to accelerate the jet in free-fall. The horizontal case requires no free-fall acceleration and instead impacts either a slower-moving fluid body or solid obstruction, as was the case with the lips of

the protruding pipes at the Ragged Chutes. This mechanism is associated with substantial irreversibility but is, however, also associated with considerable air entrainment per unit length (Kobus, 1984).

In large, uncontrolled vortices, the swirl continues into the pipe beyond the inlet and creates downstream losses by increasing the wall shear for the same flow rate due to the tangential component of velocity. This can be controlled using swirl breaking vanes (Prosser, 1977), which adds pipe surface area for friction and minor losses but limits the downstream range. A vortex is also a large surface disturbance that entrains a packet of air by the tail shear-off mechanism described in section 2.2.2 that is small relative to the scale of the overall disturbance. This should eliminate the large, single vortex from consideration as a desirable entrainment mechanism. However, small vortices operating in parallel would not generate coherent swirl downstream and should be considered.

Venturi eduction uses local geometry to enhance the negative gauge pressure used to draw the air downward into the flow. The physical entrainment process is similar to the two other entrainment mechanisms where the flowing water shears the air-water interface to produce bubbles. If this offers superior performance by reducing the irreversibility associated with the surface disturbance component of entrainment, then it does so at the cost of increased intricacy of the mixing head and any associated flow costs created by the obstructions.

There are three remaining candidates for testing: (i) horizontal orientation impinging jet, (ii) small vortex, and (iii) Venturi eduction. These show the best promise of low irreversibility entrainment: vertical orientation impinging jets appear to be more undesirable than the horizontal equivalent because they are associated with head loss in free fall and large, deep vortices are

unstable and produce significant downstream irreversibility by generating coherent swirl in the pipe below the mixing head. The quantity of air entrained by any of these mechanisms and which mechanisms are likely to appear depend on the local conditions and geometry such that it is not feasible at this stage to compare between them on that basis. Chapter 3 continues the discussion of air entrainment to determine the effect of system parameters on air entrainment and how the entrainment mechanism is a reaction to the local geometry under the influence of these system effects.

2.3 Air-water separation removes entrained bubbles from the two-phase flow

The objective of air-water separator design is to remove the largest fraction of air practicable from the two-phase flow. Fundamentally, it is an optimization problem where large gravity separators offer superior performance over the more compact option, centrifugal separation, but do so at higher capital cost. This thesis is intended to quantify the performance of these separators so that design optimization can be performed for future commercial application.

There are two general classes of separator relevant to this application: gravity and centrifugal. Gravity separators work by slowing the flow down so that suspended bubbles can float free of the mixture under the force of gravity and merge with an air plenum above (see: Figure 2.12).

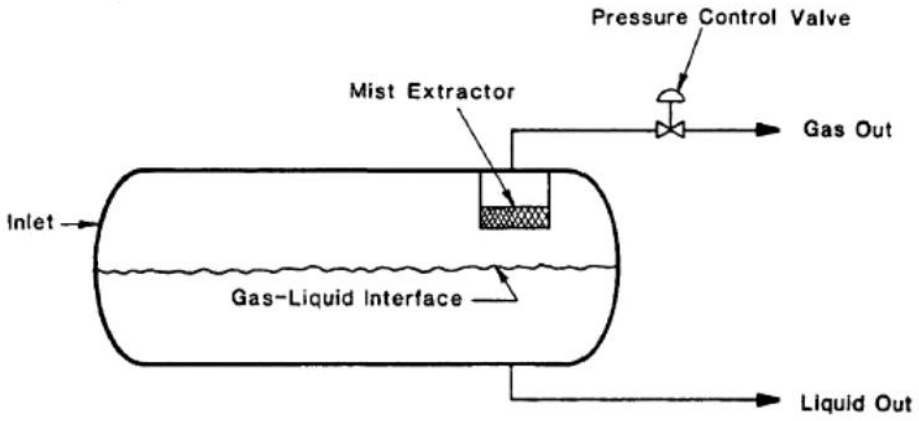

Figure 2.12: Schematic of a gravity separator from the oil and gas industry. Two-phase flows in that industry tend to be gas-dominated, so the inlet is indicated on the gas side of the gas-liquid interface (modified from Arnold and Stewart, 2008)

All of the historic HAC installations described by Schulze (1954) used gravity. These ranged from long separation galleries in rock that doubled as compressed air storage vessels to smaller iron separators intended for lower flow rates and little air storage capacity. The separator for the Peterborough Lift Lock HAC in Figure 2.13 is a relatively compact steel and cast iron design of the style also installed in HACs at Magog, Quebec and Dillingen Iron Works, Germany (Schulze, 1954).

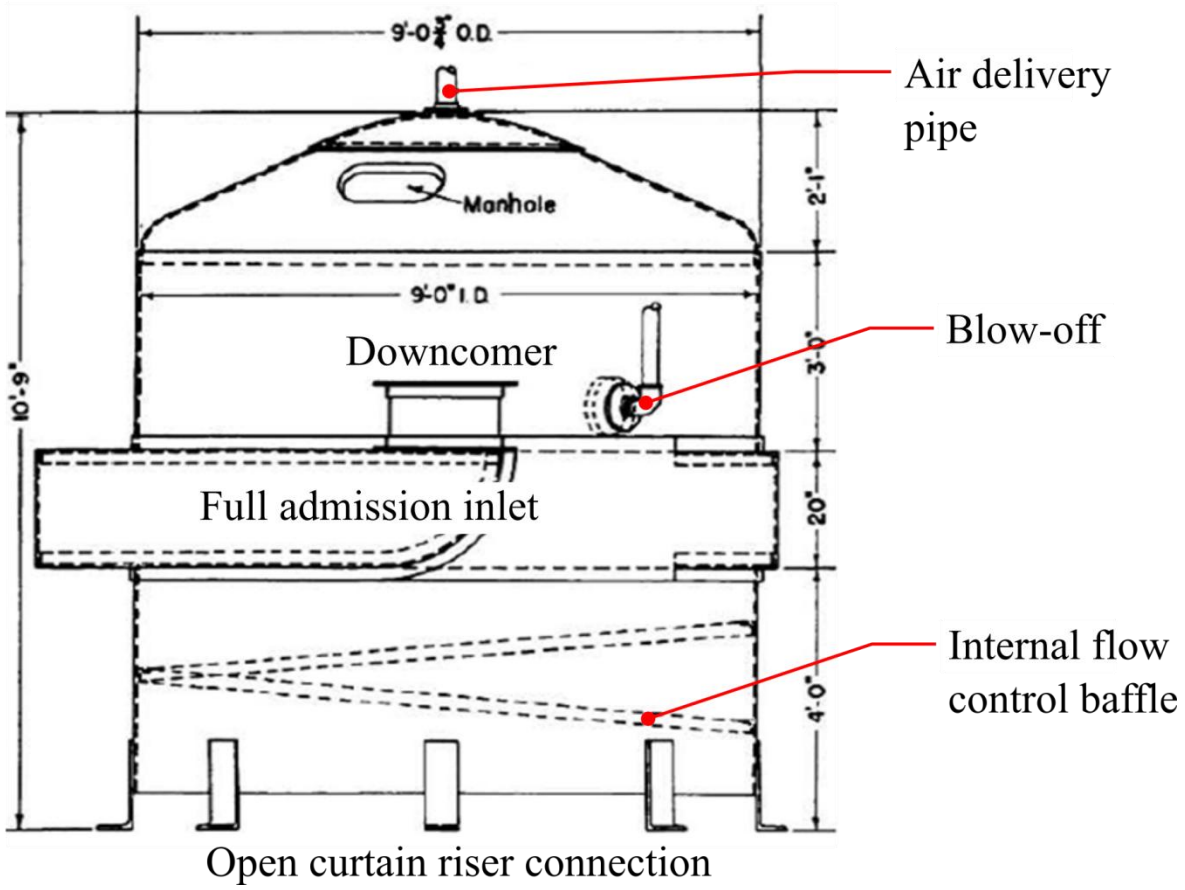

Figure 2.13: Vertical gravity separator at the Peterborough Lift Lock in Peterborough, Ontario. Water enters from the downcomer connection point shown above in the centre at mid-height and exits around the skirt at the bottom to flow out in the annular space around the separator (Schulze, 1954)

Centrifugal separators work by rapidly turning the flow, generating a centrifugal reaction force from the centripetal acceleration. Under this force, bubbles migrate inwards and merge with an air core along the separator axis. This thesis is chiefly concerned with gravity separators based on the high pressure drop associated with centrifugal separators described in section 4.1. However, centrifugal separators are a potential avenue of future research, so the formulation of mechanical principles below is, as much as possible, sufficiently generic to apply to both classes.

There are two performance parameters of interest for separators: pressure drop (irreversibility) and separator effectiveness. Pressure drop is determined by the friction losses in the wetted portion of the separator and separator effectiveness is determined by the motion of bubbles within the continuous medium. Pressure drop can be evaluated using single phase analysis with computational fluid dynamics (CFD) software or by a combined one dimensional pipe and channel flow analysis if the geometry is simple enough to allow it. Single phase analysis should ideally produce slightly conservative results if the combined air and water volume flow rate is assumed to be water only. The flow into the riser inlet (separator outlet) would be overestimated, since the separated fraction would still be included in the total flow rate quantity, resulting in a small overestimate of flow rate and therefore pressure drop in that leg of the separator. Separator effectiveness is a more complex problem to resolve and is the subject of the remainder of this literature review.

2.3.1 Bubble mechanics – buoyancy-drag balance

In a separator, the fluid is subject to either gravity or centrifugal acceleration (i.e. the reaction to centripetal acceleration from Newton's third law) or both. Resolving bubble motion in a centrifugal system is the same as for a gravitational system except the field acceleration is not uniform (see: Figure 2.14). The magnitude of the centrifugal acceleration (g_c) is inversely proportional to the radial distance of the bubble from the axis of its rotational path (r), so the acceleration is increased as the bubble moves to the centre of the separator (2.9). The strength of the centrifugal acceleration component increases as a bubble moves radially towards the vortex but decreases as it moves axially towards the outlet (Mantilla et al., 1999):

$$g_c = \frac{v_t^2}{r} \tag{2.9}$$

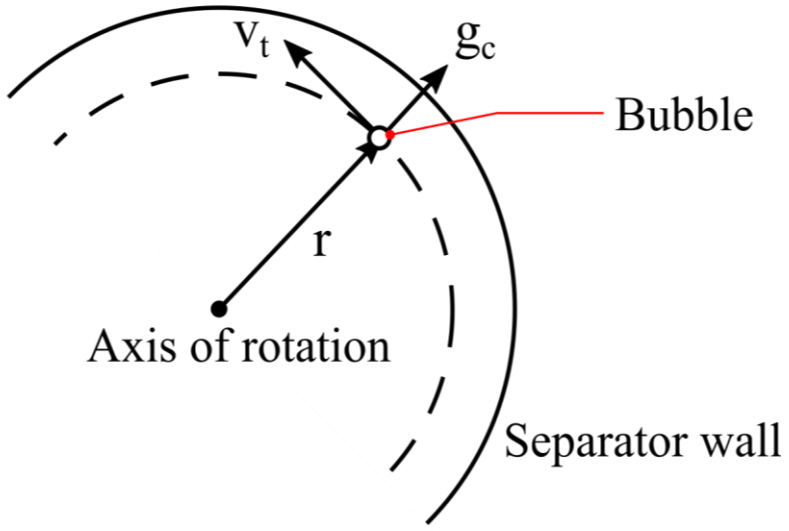

Figure 2.14: Centrifugal acceleration on a bubble in a centrifugal separator

The resultant of these components of field acceleration determines the direction of buoyancy and drag forces (see: Figure 2.15), which determine direction of bubble motion relative to motion of the continuous phase fluid. The field acceleration ($\vec{g}_f$) is calculated as the sum of the gravitational ($\vec{g}$) and centrifugal ($\vec{g}_c$) acceleration vectors (2.10). The magnitude of the field acceleration is subsequently used to calculate buoyancy, below. In a swirling gravity separator, there are components of both centrifugal acceleration and gravity present, but the centrifugal component is negligible and therefore not included in the model (see: section 4.3.3). For example, the maximum centrifugal acceleration in the vertical gravity separator at Dynamic Earth HAC (see: section 5.2) occurs at the outlet of the downcomer. At 0.4 m^3/s (close to maximum flow), the centrifugal acceleration at the centre of the pipe outlet as the flow is initially turned into the separator is 2.7 m/s^2, perpendicular to the direction of gravity. However, the

magnitude of the field acceleration when combined with gravity is only 10.2 m/s^2. This value should approach the magnitude of gravitational acceleration along the flow path below the inlet elevation as the swirl dissipates.

$$\vec{g}_f = \vec{g} + \vec{g}_c \tag{2.10}$$

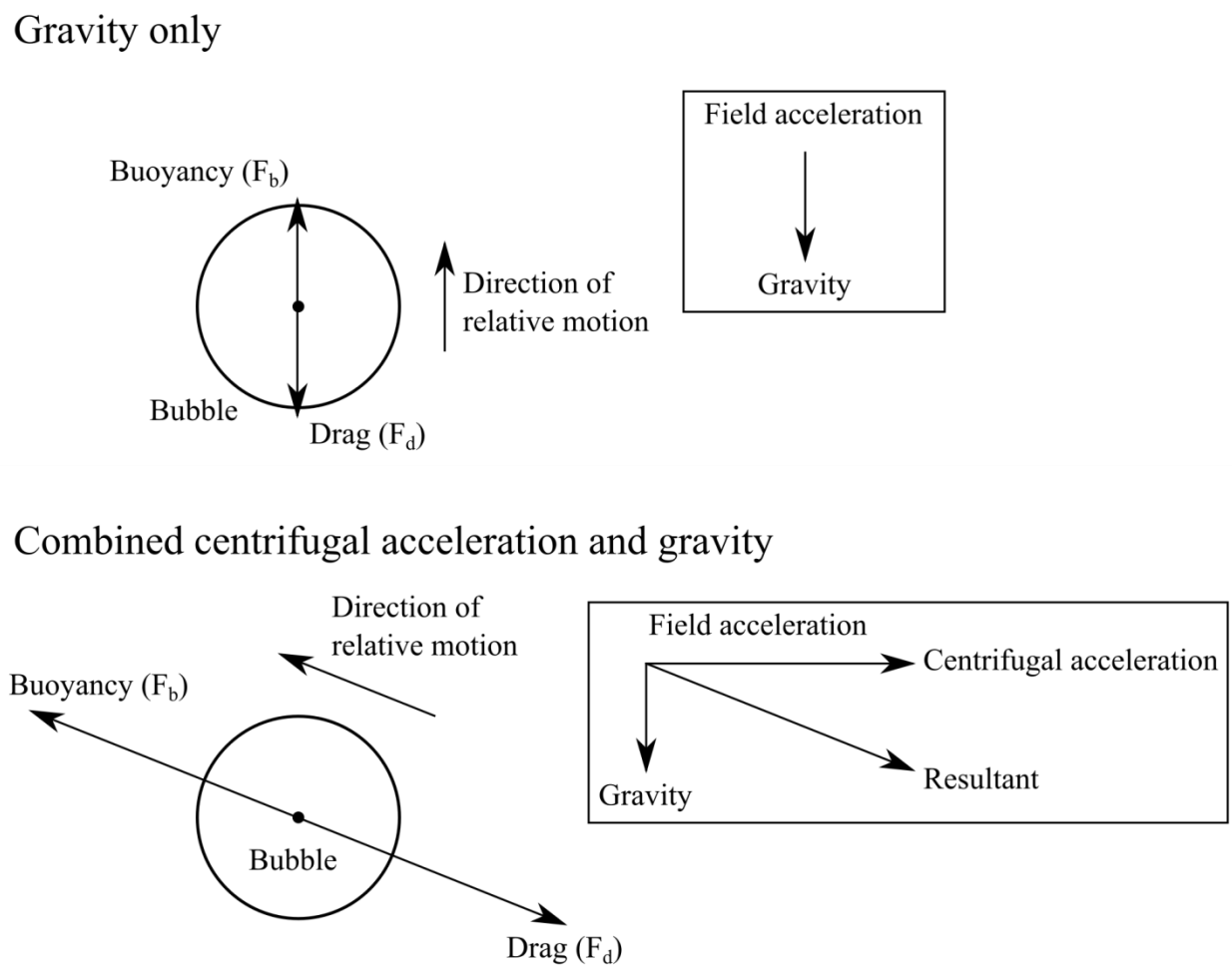

Figure 2.15: The bubble moves opposite the direction of the resultant field force. In a gravity separator, the centrifugal force is negligible

Buoyancy acts in the direction opposite the resultant of the field acceleration. It is the result of displacement of the denser medium by a lighter medium. In the case of a HAC, the air bubble displaces water volume and has a density two (e.g. for service air pressure, around 110 psig) or three (at atmospheric pressure) orders of magnitude lower than that of water, depending on pressure. The displacement of that volume of water by an air bubble creates the buoyancy force:

$$F_b = \left(\rho_l - \rho_g\right) \cdot g_f \cdot V_b \tag{2.11}$$

When describing bubbles, it is useful to characterize them using the diameter of an equivalent sphere (see: section 2.3.2):

$$F_b = \frac{\pi}{6} \cdot \left(\rho_l - \rho_g\right) \cdot g_f \cdot d^3 \tag{2.12}$$

In a typical gravity separator, the magnitude and direction of g_f are determined by gravity alone. In centrifugal separators, it is the acceleration by the resultant field force.

Drag opposes motion relative to the continuous medium. The bubble projects an area that obstructs the flow. The drag force is created by the kinetic energy of the continuous medium striking that area at the relative velocity of the bubble and adjusted by a drag coefficient to account for additional energy recovered or lost by flow around the obstruction (Clift et al., 1978):

$$F_d = \frac{1}{2} \cdot C_d \cdot A_p \cdot \rho_l \cdot v_r^2 \tag{2.13}$$

Similar to the buoyancy force, it is useful to characterize the bubble area using the diameter of the equivalent sphere:

$$F_d = \frac{\pi}{8} \cdot C_d \cdot d^2 \cdot \rho_l \cdot v_r^2 \tag{2.14}$$

Other forces acting on the bubble, such as turbulent transport (Karamanev and Nikolov, 1992), bubble swarm interference (Roghair et al., 2011; Wilkinson et al., 1992), and pressure gradients are accounted for as part of the drag force using an empirically-derived coefficient called the drag coefficient (Clift et al., 1978).

The value of interest is the terminal velocity of the bubble moving relative to the liquid medium. Terminal velocity is reached when the net force acting on the bubble is zero. The net force is zero when the magnitude of the buoyancy force is equal to that of the drag force. Under these conditions, the direction of the terminal velocity is opposite the direction of the resultant field force and the magnitude of the terminal velocity is resolved by rearranging equations (2.12) and (2.14):

$$v_r = \sqrt{\frac{4}{3} \cdot \frac{d \cdot g_f \cdot \left(\rho_l - \rho_g\right)}{C_d \cdot \rho_l}} \tag{2.15}$$

Relative velocity is a vector quantity (2.16), where v_r is the velocity of the bubble relative to that of the water, v_b is the absolute velocity of the bubble, and v_w is the water velocity. However, it can be treated as a scalar quantity for gravity separators because the direction of relative motion is vertical, which is one of the component directions.

$$\vec{v}_r = \vec{v}_b - \vec{v}_w \tag{2.16}$$

Because this occurs in the context of a flowing continuous medium, the terminal velocity is referred to in this thesis as relative velocity. This is not an explicit relationship, because relative velocity is an indirect component of the drag coefficient (see: section 2.3.3). Nevertheless, larger bubbles have a larger relative velocity than smaller bubbles and are therefore preferable for separation, because a higher relative velocity allows them to successfully separate even in the presence of faster moving water. The ratio of density difference over water density is close to unity across the relevant pressures for HACs because the density of water is large relative to that of air even at high pressure.

2.3.2 Bubble mechanics – bubble shape

Bubbles are not perfect spheres. Instead, bubble shape depends on the local flow conditions. Young (2017) found that bubble shape maps designed for bubbles rising in a stagnant water column are not useful for turbulent flows, such as the fully-developed pipe flow at the bottom of a HAC downcomer. The threshold for turbulent pipe flow is at a Reynolds number (2.17) of 2300 where the flow is fully-developed at least 5-10 pipe diameters downstream of bends, change in section, or inlets. The Reynolds number (Re) is a dimensionless ratio of inertial forces

consisting of the product of fluid density (ρ), flow velocity (v), and pipe diameter (D) to viscous (μ) forces.

$$Re = \frac{\rho \cdot v \cdot D}{\mu} \tag{2.17}$$

According to Çengel and Cimbala (2010), there remains some transitional behaviour in pipe flow above a Reynolds number of 2300 up to 4000.. For water, the ratio of density over viscosity is approximately 10^6. Therefore, in order to be turbulent, the flow velocity multiplied by the hydraulic mean diameter of the downcomer pipe must be at least 0.004. Even at the smallest scale of HACs, the velocity threshold for turbulent flow in the downcomer is very low. It is reasonable to expect that the flow at the separator inlet in a HAC is turbulent.

Bhagwat and Ghajar (2012) performed a series of experiments to characterize how bubble shape and size were affected by volume flux of the air and water streams in a turbulent downward pipe flow. The observed shapes tended to be spheroid and more regular than those plotted by Grace (1973) for bubbles rising in stagnant water. With increasing water flow rate, bubbles are smaller, more numerous, and more spherical (see: Figure 2.16). With increasing air flow rate, bubbles are larger, more numerous, and less spherical (see: Figure 2.17).

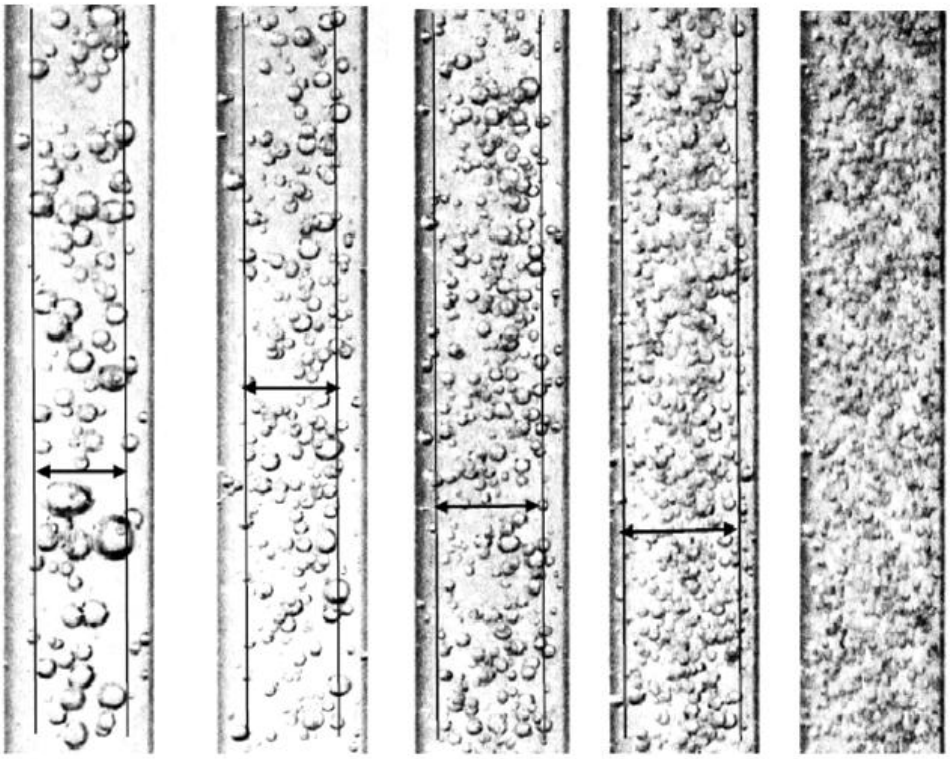

Figure 2.16: Increasing water volume flux from left to right at constant air volume flux

(Bhagwat and Ghajar, 2012)

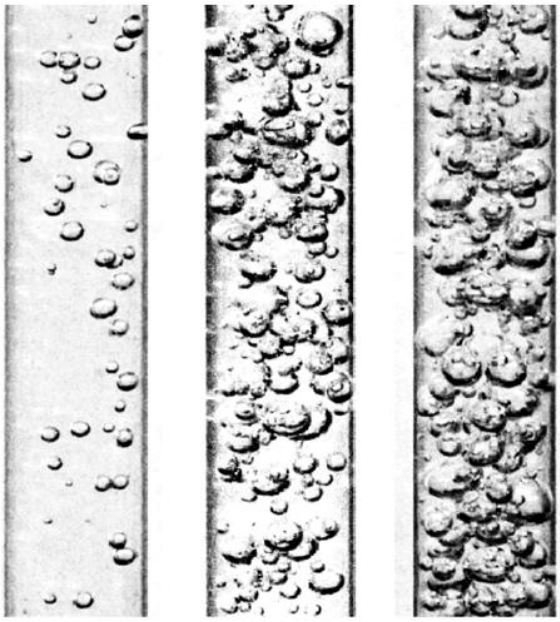

Figure 2.17: Increasing volume flux of air from left to right at constant water volume flux (Bhagwat and Ghajar, 2012)

Large bubbles tend to be less spherical than smaller bubbles, and bubbles in downward bubbly flows regardless of size appear to be more spherical than the shape maps for bubble columns would indicate (Grace, 1973). Although it would be more accurate to use volume and cross-sectional area to characterize bubbles to calculate relative velocity, it is more convenient to use a single number to describe the size of a bubble. Clift et al. (1978) use a hydraulic equivalent diameter to describe a sphere with the same relative velocity as the actual bubble. This number is produced by first calculating the relative velocity for the spheroid bubble and then calculating the diameter of a spherical bubble that would have the same relative velocity.

In the chemical engineering literature, it is more common to use the Sauter diameter, which is another equivalent sphere diameter based on the same volume to surface area ratio as the bubble. Frequently, bubble diameter numbers presented in the literature fail to specify the how the

measurement was performed. More spherical bubbles will have closer equivalent diameters by any method. Because bubbles in downward flows are more spherical than those in stagnant flows, the potential error created by using the wrong form of equivalent diameter is smaller for downward bubbly flows than for the less spherical bubbles in bubble columns. For the purposes of this thesis, published bubble diameter numbers will be taken to refer to hydraulic equivalent sphere diameter regardless of the actual method used to produce it.

2.3.3 Bubble mechanics – drag coefficient

The evaluation of drag coefficient for air bubbles moving in a bubbly flow is based on empirical correlations of free settling spheres in an infinite medium. Free settling refers to the settling of dense media unhindered and unforced by boundary effects, obstructions, or interactions with other particles. Brown and Lawler (2003) compiled results from the literature and their own experiments into a single relationship valid for particle Reynolds numbers (Re_p) up to 10^5. Cheng (2009) produced a closer fit relationship based on the same dataset:

$$C_d = \frac{24}{Re_p} \cdot \left(1 + 0.27 \cdot Re_p\right)^{0.43} + 0.47\left[1 - \exp\left(-0.04 \cdot Re_p^{0.38}\right)\right] \qquad (2.18)$$

There are three assumptions required to use this relationship unaltered for bubbly flows, none of which apply in the separator of a HAC: that the medium is infinite, that free rising is the same as free settling, and that the rising bubbles do not interact with one another. According to Clift et al. (1978), the wall effect creates a deviation of less than 2% from the predicted relative velocity for bubbles with a particle Reynolds number greater than 100 when the bubble diameter is less than 0.12 times the vessel diameter. This is true in a HAC separator, where the vessel diameter is large in the case of gravity separation and shear forces maintain small bubble sizes in centrifugal separators.

2.3.4 Bubble mechanics – free rising

Karamanev and Nikolov (1992) addressed the second assumption using low density solid particles, showing that the free rising case matches the free settling case up to a particle Reynolds number of around 130, where it was found that the drag coefficient stopped decreasing with increasing particle Reynolds number. Instead, it holds at 0.95 from that point up to the limits of the test (see: Figure 2.18). From equation (2.18), the drag coefficient reaches 0.95 at a particle Reynolds number of 135. In order to avoid discontinuity in the drag coefficient function, this particle Reynolds number will be used as the critical point for modeling.

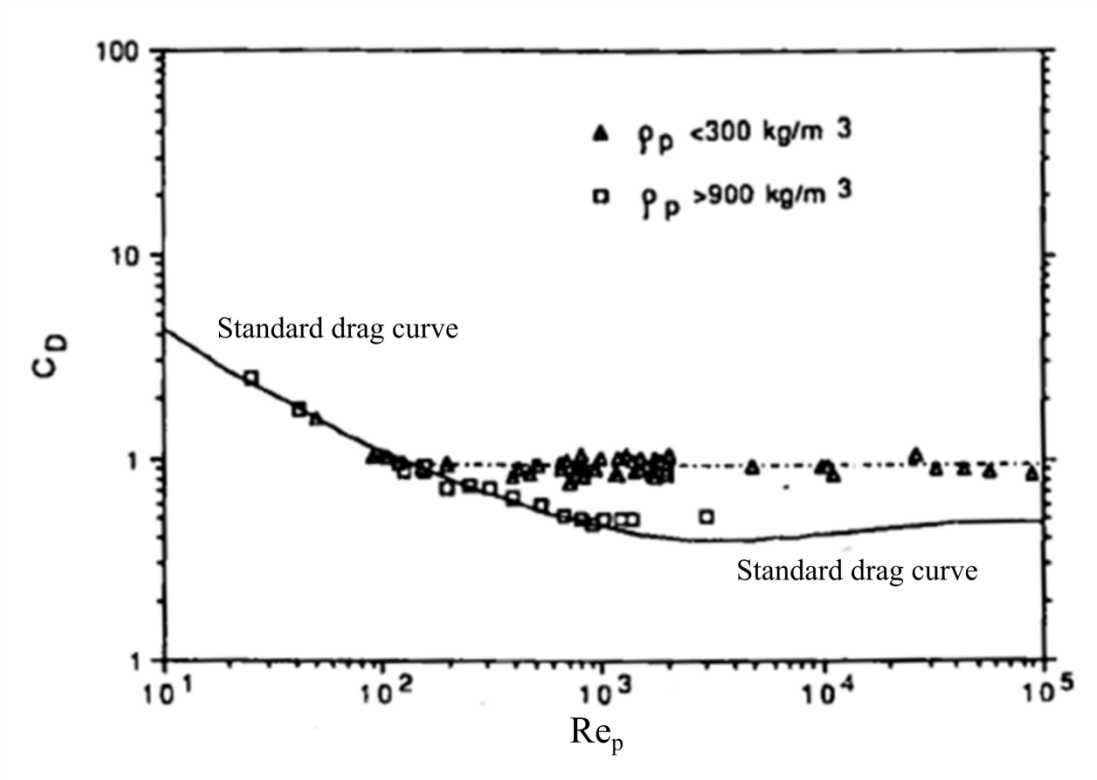

Figure 2.18: Drag coefficient with particle Reynolds number for two cases: when the density of the rising sphere is close to that of water (>900 kg/m^3), the relationship follows the free settling drag curve. When it is much lower than that of water (<300 kg/m^3), the free settling correlation does not match the behavior (Karamanev and Nikolov, 1992)

Karamanev and Nikolov (1992) used low density solid spheres rising in a stagnant water column. The mechanism they suspect as a cause of the difference from settling is a rocking, spiral trajectory created by wake shedding of rising spheres at higher particle Reynolds numbers. The question is whether bubbles in a separator follow the same pattern despite being non-spherical and in a downward flow. Bubbles rising in against a downward flow (e.g. in a vertical orientation separator) tend to be more spherical and regular in shape than those in a stagnant column (see: section 2.3.2). To the proposed mechanism, weather balloons are observed to exhibit the same

trajectory pattern rising through the atmosphere (Karamanev and Nikolov, 1992). It seems reasonable that this behavior would apply to bubble separation.

Table 2.2 illustrates the effect of this correction on relative velocity. These data were generated for a temperature of 15°C and an absolute pressure of 300 kPa. The relative velocity for a bubble of a given diameter is insensitive to changes in pressure for reasons described in section 2.3.1.

Table 2.2: Relative velocity and particle Reynolds number for a typical size range of bubbles in a gravity separator with and without the drag coefficient correction proposed by Karamanev and Nikolov (1992)

Bubble diameter (mm)	With correction		Without correction	
	Relative velocity (m/s)	Particle Reynolds number	Relative velocity (m/s)	Particle Reynolds number
0.500	0.051	22	0.051	22
0.750	0.079	52	0.079	52
1.000	0.107	94	0.107	94
1.204	**0.128**	**135**	**0.129**	**135**
1.250	0.131	143	0.133	146
1.500	0.143	188	0.158	208
1.750	0.155	237	0.182	278
2.000	0.166	290	0.204	357
2.500	0.185	405	0.244	534
3.000	0.203	533	0.279	734
4.000	0.234	820	0.340	1190
5.000	0.262	1146	0.390	1708

The critical diameter under only the force of gravity is 1.2 mm. This is a small bubble on the scale of what should be expected in a HAC separator. The effect of the correction is more pronounced for larger bubbles. If the separator is properly sized and the effectiveness is high, then only the small bubbles are failing to separate. In this case, the correction should not make a significant difference. However, for separators with lower effectiveness, larger bubbles are

failing to separate and this correction becomes more relevant, because the mass fraction of the smallest bubbles in the distribution on their own is not large enough to account for substantial loss in separation.

2.3.5 Bubble mechanics – bubble swarms

Rising bubbles tend to accumulate into swarms, especially where turbulent eddies are present (Aliseda and Lasheras, 2011). In experiments at high pressure with large bubbles, the relative velocity was found to increase due to a tendency of bubbles to coalesce when converged into a swarm (Wilkinson and Van Dierendonck, 1990). In simulations with smaller bubbles, the drag coefficient was found to increase (Roghair et al., 2011). Although it would seem that these findings are in conflict with one another, it is possible for the relative velocity to increase at the same time that the drag coefficient increases if, at the same time, the bubbles are coalescing and therefore increasing in size.

These effects are most pronounced when the gas volume fraction is high (see: Figure 2.19). There might be an effect where the gas volume fraction is locally high near the water surface at which the gas bubbles merge with the plenum. This could potentially become important for separators with low effectiveness or where coalescence is inhibited, as with the addition of salt co-solutes (Lessard and Zieminski, 1971). For the purposes of modeling where gas volume fraction is low, as in the main body of the separator, this effect will be ignored.

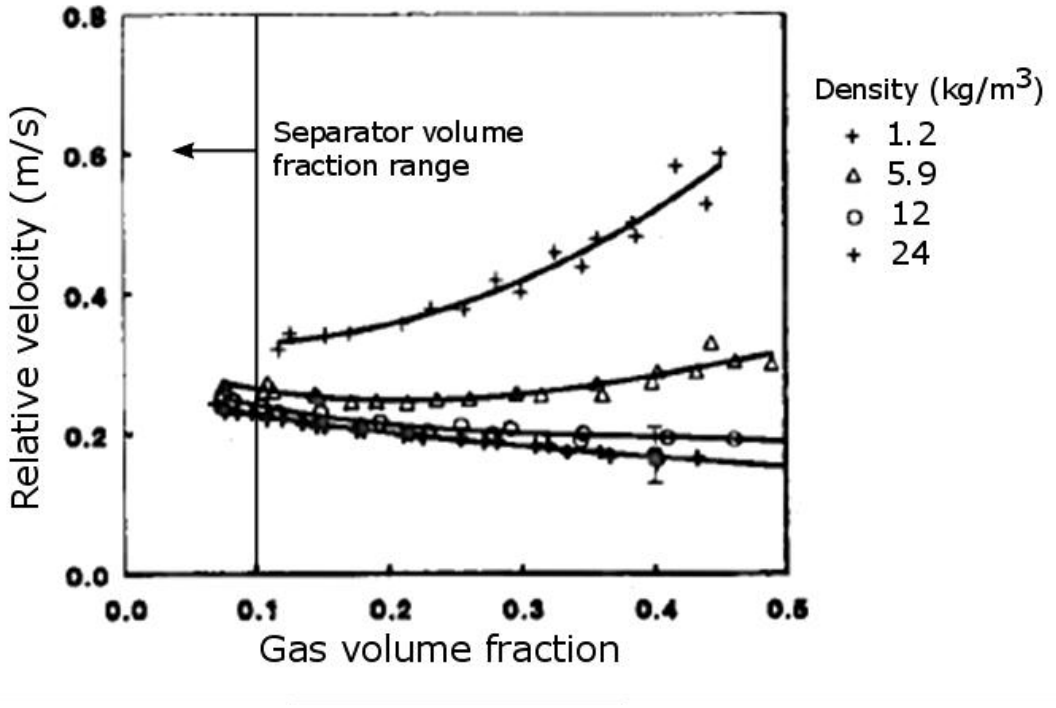

Figure 2.19: The effect of bubble swarming is small at low gas volume fraction (modified from Wilkinson et al., 1992)

2.3.6 Bubble size distribution

Like particles, a population of bubbles has a lognormal size distribution. The use of a distribution is relevant because different sizes of bubbles will separate at different rates under the same flow conditions. The portion of the air bubble population that is least likely to successfully separate is the smallest fraction owing to its lower relative velocity, which is the consequence of the balance of forces described in section 2.3.1.

Typically, the Rosin-Rammler distribution is used (Akita and Yoshida, 1974; Biswal et al., 1994; Burdin et al., 1999; Iida et al., 2010; Laleh, 2010; Wilkinson et al., 1994). Other distributions exist that can be tuned to fit better because they have additional parameters (Taya et al., 2012),

but these extra parameters are non-physical and less well established in the literature. The Rosin-Rammler distribution uses two parameters, the Rosin-Rammler mean bubble diameter ($\bar{d}$) and the spread parameter (n):

$$Y = 1 - \exp\left[-\left(\frac{d}{\bar{d}}\right)^{n}\right] \tag{2.19}$$

Substituting the Rosin-Rammler mean for the diameter in equation (2.19) results in the following evaluation:

$$0.623 = 1 - \exp[-1] \tag{2.20}$$

Where the Rosin-Rammler mean is the point at which 62.3% of the distribution by mass (or volume, for a material of constant density) is composed of bubbles smaller than this mean. The spread parameter (n) defines how wide the distribution is around the mean. Figure 2.20 illustrates the effect of spread parameter on a series of distributions corrected to the same mean.

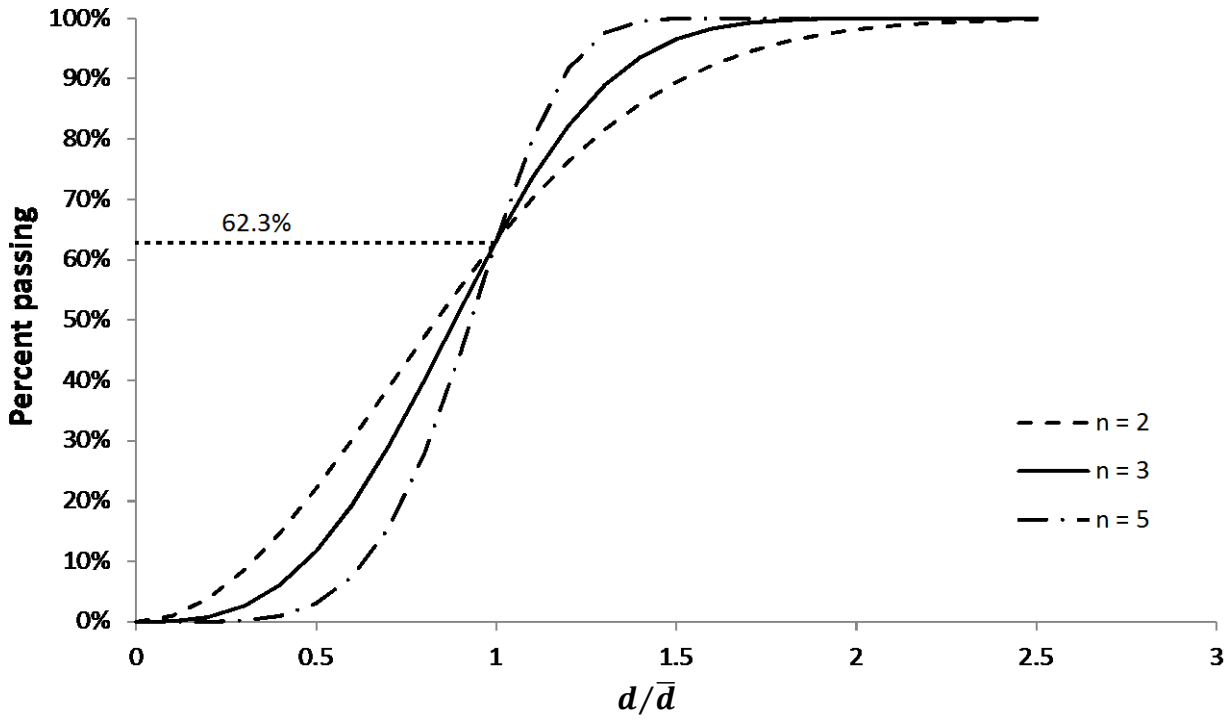

Figure 2.20: Increasing spread parameter corresponds to a narrower distribution

The Rosin-Rammler distribution is a continuous function where experimental data are typically organized as histograms. Where graphs are provided instead of tabulated histograms, plot digitization is used to extract the distribution (see: Figure 2.21). The imperfect fit leads to several possible methods to fit the distribution to the data. It is common practice to produce the parameters by setting d_{10} and d_{90} equal (the diameters at which 10% and 90% of the mass, respectively, is composed of smaller bubbles) for the Rosin-Rammler function and the measured distribution (Innopharma Technology, 2017). This creates good agreement in the upper and lower ends of the curve, but poorer agreement in the centre.

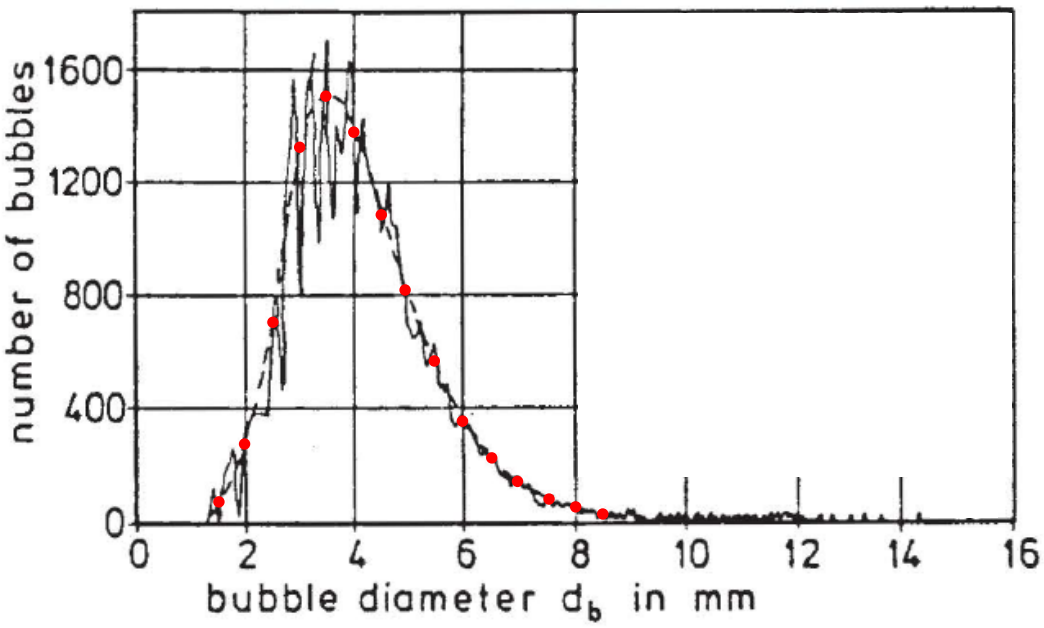

Figure 2.21: A lognormal distribution with digitization points for Rosin-Rammler distribution fit (modified from Kobus, 1984)

If the full histograms are available, a better fit is created using a root mean square (RMS) minimization using a nonlinear solver. This method was used where possible on several bubble distributions in water published in the literature (see: Table 2.3). Laleh (2010) and Kharoua et al. (2013) opted to use a static spread parameter at 2.6 based on an arithmetic average for the distribution and described fair agreement between the model and the actual performance. Table 2.3 shows that there is some variability to this number and Figure 2.20 shows that the relationship between spread parameter and distribution shape is non-linear. A more considered approach should be taken.

Table 2.3: Rosin-Rammler parameters from bubble size distribution measurements

Identifier (Figure 4.8)	Parameter		Source	Fit method
	$\bar{d}$ (mm)	n		
A	5.53	3.74	Kobus (1984), Figure 9	Minimize RMS on selected points from plot best fit line (see: Figure 2.21)
B	15.4	1.53	Akita and Yoshida (1974), Table IV	Minimize RMS on all points from table
C	6.00	2.65	Hesketh et al. (1987), Figure 1, Run #6	Evaluate d_{10} and d_{90} from fit line and set parameters to match
D	5.24	2.65	Hesketh et al. (1987), Figure 1, Run #3	Evaluate d_{10} and d_{90} from fit line and set parameters to match
E	0.962	5.18	Hesketh et al. (1987), Figure 1, Run #2	Evaluate d_{10} and d_{90} from fit line and set parameters to match
F	1.18	4.18	Hesketh et al. (1987), Figure 1, Run #7	Evaluate d_{10} and d_{90} from fit line and set parameters to match
G	1.28	4.02	Hesketh et al. (1987), Figure 1, Run #5	Evaluate d_{10} and d_{90} from fit line and set parameters to match
H	1.73	4.95	Hesketh et al. (1987), Figure 1, Run #4	Evaluate d_{10} and d_{90} from fit line and set parameters to match
I	2.65	3.19	Johansen et al. (2001), Figure 7.1.15, First count	Minimize RMS on all points from plot
J	3.00	3.15	Johansen et al. (2001), Figure 7.1.15, Second count	Minimize RMS on all points from plot
K	0.784	3.70	Majumder et al. (2006), Table 2, Location A	Minimize RMS on all nonzero points from table
L	1.28	3.75	Majumder et al. (2006), Table 2, Location B	Minimize RMS on all nonzero points from table
M	1.38	3.80	Majumder et al. (2006), Table 2, Location C	Minimize RMS on all nonzero points from table

There is a general consensus in the literature that the bubble size distribution in pipe flow along an extended length does not depend on the initial bubble size distribution at the entrainment position (Akita and Yoshida, 1974; Chen et al., 2005; Clift et al., 1978; Wilkinson et al., 1994). Unlike particles, the size distribution of bubbles shifts mean and increases or decreases spread by the action of coalescence and breakup.

2.3.7 Bubble breakup

Two general models exist that describe bubble breakup (Chen et al., 2005): the first assumes that when a bubble breaks up, the surface energy is minimized such that the daughter bubbles are likely to be of uneven size. The second model assumes that breakup occurs as a result of a force balance between shear and surface tension, which results in a greater probability of even sizes. According to Clift et al. (1978), bubble breakup tends to result in bubbles of roughly equal size with some very small bubbles occasionally appearing (see: Figure 2.22). Liquid “a” has a higher surface tension than “b” and results in more spherical bubbles. The numbered sketches show the progression of breakup over time for bubbles in liquid with high (a) and low (b) surface tension. Note that in particular for bubbles in liquids with high surface tension (e.g. water) that the result is two large bubbles and some very small bubbles at the site of the surface rupture.

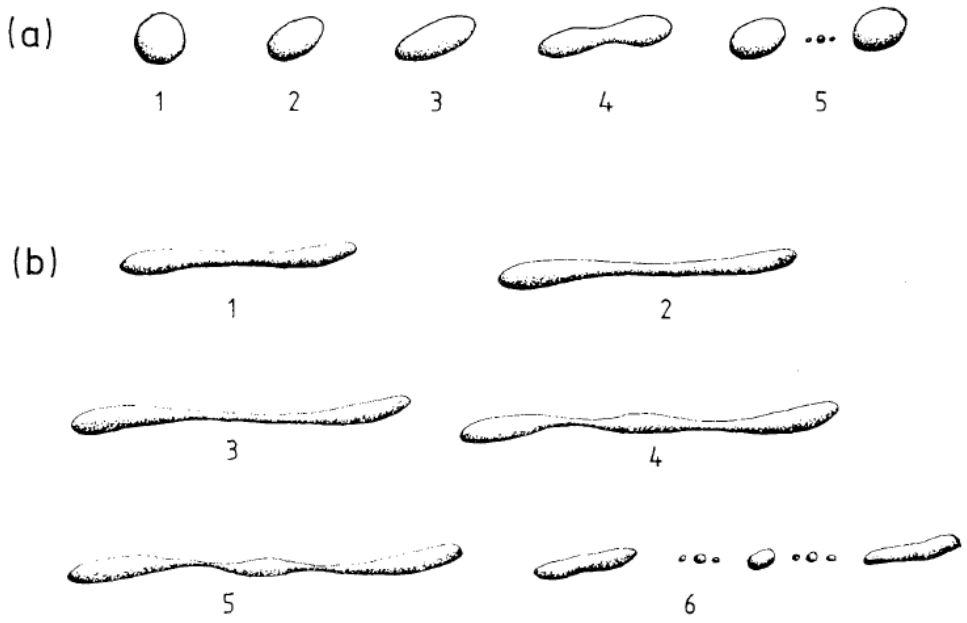

Figure 2.22: Bubble breakup in stages for gas in two different liquids (Clift et al., 1978)

The size of the turbulent eddies that generate breakup events are at the same scale as the bubbles (Chanson, 2009; Clift et al., 1978). Larger eddies tend to cause the bubbles to move around and smaller ones are incapable of rupturing the surface.

2.3.8 Bubble coalescence

Coalescence has a probability of occurring in the event of a bubble collision (see: Figure 2.23). When bubbles collide with one another, the liquid drains out of the contact region and the thickness of the film between them reduces over time. If the film thickness drops below a critical threshold, the surface ruptures and the bubbles coalesce. If the bubbles rebound away from one another before the liquid drainage is sufficient to cause surface rupture, the bubbles fail to coalesce. A higher speed collision results in a more likely coalescence event (Orvalho et al., 2015). The collision rate is increased by high gas volume fraction and the presence of large

turbulent eddies (Clift et al., 1978), which concentrate bubbles at the axis where pressure is slightly lower.

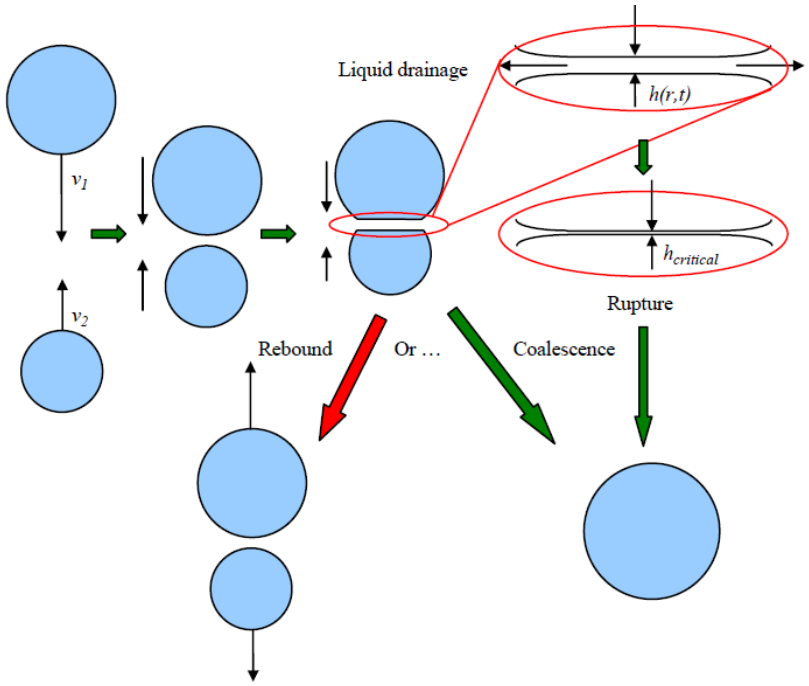

Figure 2.23: Colliding bubbles can coalesce or rebound (Chen et al., 2005)

Mechanistic models that are used to predict coalescence overestimate the rate by an order of magnitude (Chen et al., 2005; Nguyen et al., 2013). The individual mechanisms that affect coalescence are well documented, but attempts to synthesize these into a functional mechanistic model have met limited success. The solution proposed and adopted by Chen et al. (2005) is to artificially inflate the breakup frequency by a factor of ten to bring the equilibrium size distribution back into agreement with experimental evidence without creating numerical stability problems.

It is appropriate to use breakup alone to predict the bubble size distribution when the coalescence rate is high. Under this condition, the effect is to break up large, unstable bubbles generated by coalescence events to maintain the size distribution near its stable equilibrium as calculated by Hesketh et al. (1987). This assumption is valid for flows with lots of bubble interactions and high breakup and coalescence rates.

All of the coalescence models agree that low gas volume fraction corresponds to low coalescence rates (Nguyen et al., 2013). Liao and Lucas (2009) stated that breakup decreases when the gas volume fraction increases, but it seems likely that they were mistaking the effect of increased coalescence for decreased breakup.

Dissolved salts, such as those that might be used in a HAC to reduce yield loss by gas dissolution, inhibit coalescence by the action of bubble surface contamination preventing rupture (Lessard and Zieminski, 1971; Orvalho et al., 2015; Wilkinson et al., 1994).

2.3.9 Maximum bubble size

Reliable mechanistic models do not exist for either breakup or coalescence (Liao and Lucas, 2009). Hesketh et al. (1987) created an empirical equation to predict the 99th percentile bubble size based on the maximum stable size of bubbles breaking up in a horizontal pipeline:

$$d_{99} \approx d_{max} = 1.38 \cdot \left(\frac{We_{crit}}{2}\right)^{0.6} \cdot \frac{\sigma^{0.6} \cdot D^{0.5}}{\rho_l^{0.3} \cdot \rho_g^{0.2} \cdot \mu_l^{0.1} \cdot j_l^{1.1}} \tag{2.21}$$

Hesketh et al. (1987) evaluated the critical Weber number (We_{crit}) for bubble breakup at 1.1 from experimental data. For bubble breakup, Laleh (2010) used a modified version of this

equation to predict the maximum droplet size at inlet for a three-phase gravity separator model that matched measured values acceptably well.

Kobus (1984) presents an alternative that describes the bubble size distribution generated by continuous air jet injection into a stagnant body of water:

$$d_{99} \approx d_{max} = \frac{1.138}{172} \cdot \left(\frac{Q_g^2}{g_f}\right)^{1/5} \tag{2.22}$$

Using the same assumption as above, this number can be directly equated with the 99th percentile size for the distribution fit. These methods are likely to be less accurate with increasing pressure or the presence of co-solutes (e.g. Na_2SO_4) in the liquid medium, because coalescence is inhibited under both conditions. Because both methods model a coalescence-breakup balance that assumes a breakup-limited size distribution, the result is prone to error if the size distribution is instead coalescence-limited.

Akita and Yoshida (1974) (2.23) and Wilkinson et al. (1994) (2.24) created empirical equations to predict the Sauter mean diameter (d_{32}) in bubbly pipe flows. Akita and Yoshida (1974) related the ratio of bubble diameter over pipe diameter to the Eötvös, Galilei, and Froude numbers. Wilkinson et al. (1994) related the Eötvös number to the Capillary and inverted Morton numbers and the ratio of fluid densities. According to Wilkinson et al. (1994), the Sauter mean diameter prediction is accurate within ±20% for water, but the introduction of non-coalescing liquids (e.g. seawater) cause the equation to overestimate bubble size well outside this envelope. These relationships were generated using dimensional analysis and do not imply any mechanism by

which the distribution is created. Both of these correlations have been previously used for HAC solubility calculations in Millar (2014) and Young (2017).

$$d_{32} = 26 \cdot D \cdot \left(\frac{g_f \cdot D^2 \cdot \rho_l}{\sigma}\right)^{-0.5} \cdot \left(\frac{g_f \cdot D^3 \cdot \rho_l^2}{\mu}\right)^{-0.12} \cdot \left(\frac{j_g}{\sqrt{g_f \cdot D}}\right)^{-0.12} \tag{2.23}$$

$$d_{32} = 3 \cdot g_f^{-0.44} \cdot \sigma^{0.34} \cdot \mu^{0.22} \cdot \rho_l^{-0.45} \cdot \rho_g^{-0.11} \cdot j_g^{-0.02} \tag{2.24}$$

Hesketh et al. (1987) found that there is a constant ratio between the Sauter diameter and the 99th percentile at approximately 0.62 in pipe flows (see: Figure 2.24):

$$d_{99} = \frac{d_{32}}{0.62} \tag{2.25}$$

This figure was consistent with previous results from liquid-liquid dispersions.

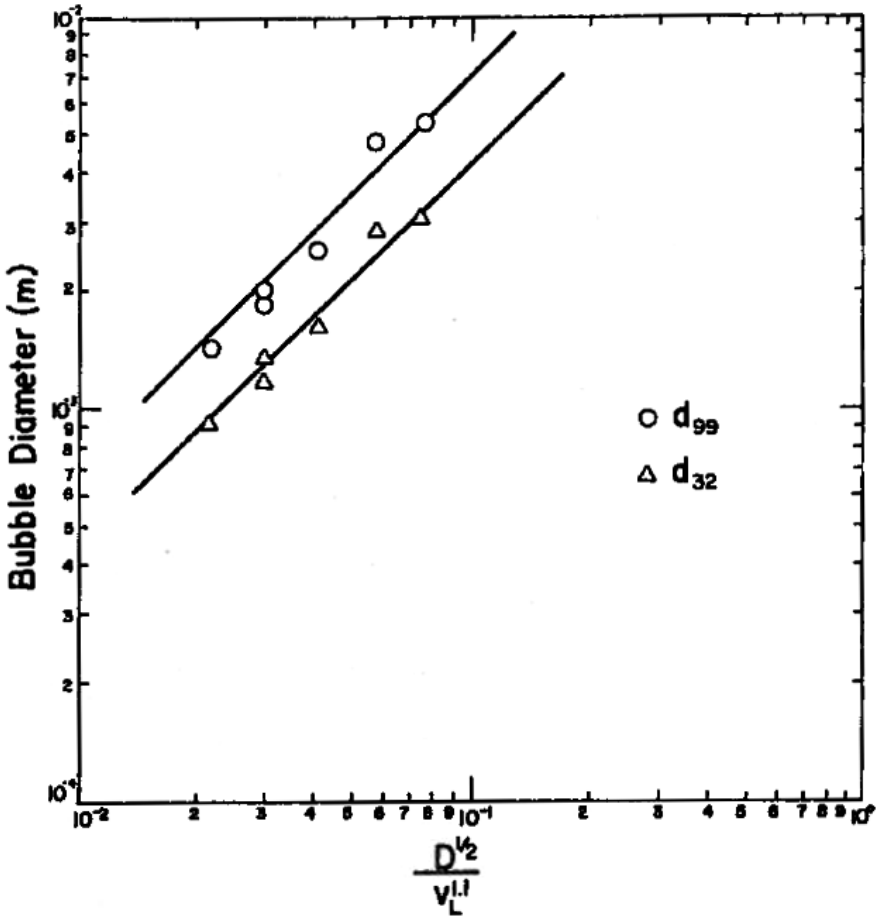

Figure 2.24: Relationship between Sauter mean diameter and 99th percentile diameter (Hesketh et al., 1987)

In a HAC downcomer, the maximum bubble size near the top where gas volume fraction is higher will tend to be near the coalescence-breakup equilibrium. There is some depth at which the gas volume fraction will drop below the point at which coalescence can maintain that equilibrium size. Below that point, bubbles will be smaller than predicted using breakup calculations. From there, bubbles will continue to compress, further reducing gas volume fraction and coalescence. Without a reliable coalescence model, it is not possible to predict

where and to what extent this will occur. Therefore, the bubble size distribution at the separator inlet may be unpredictable.

It was sensible for Laleh (2010) to use the breakup model alone to determine size distribution, because that system had an upstream flow of decreasing pressure. Even if the coalescence events were restricted, the stable breakup size would have been decreasing along the flow length due to an increase of velocity.

2.3.10 Centrifugal separation

The concept of centrifugal separation is to employ a larger field acceleration (see: section 2.3.1) to generate a larger relative velocity (larger field acceleration generates a larger buoyancy force per unit volume displacement, resulting in a larger relative velocity) to allow the bubbles to separate from the continuous medium more rapidly. This means a smaller centrifugal separator can have the same effectiveness as a larger gravity separator. The benefit is in the lower capital cost or in allowing it to fit into a smaller opening where space is limited for reasons other than cost.

The published work on centrifugal separation comes from the mineral processing and oil and gas industries. Gas-liquid cylindrical cyclone (GLCC) separators (see: Figure 2.25) come from developments in the oil and gas industry in the last 25 years (Mantilla Sanmiguel, 1998). These hold an advantage over other types of cyclone in that the tangential or radial outlet prevents the vortex from extending into the outlet and losing gas into the liquid stream (Kurokawa and Ohtaki, 1995).

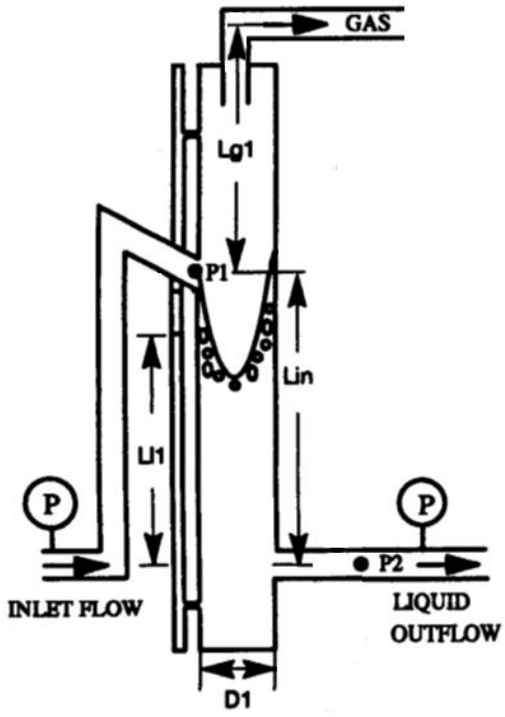

Figure 2.25: GLCC schematic (modified from Kouba et al., 1995)

The high velocity and steep velocity gradients come at the cost of a significant increase in flow losses across the separator and potential increase in bubble breakup compared to gravity separation. Recall that bubble breakup is the result of shear in the continuous medium, which is increased by increasing velocity (more turbulence) and strong velocity gradients. For application to HACs, centrifugal separation brings the advantage of a smaller, cheaper separation vessel at the cost of increased flow losses.

2.3.11 Summary

Separator effectiveness measures the mass fraction of the bubble population that successfully merges with the air plenum. The velocity of these bubbles is determined by the force balance

between buoyancy and drag and the bubbles move relative to the flow field inside the separator. If the downward component of velocity is too high or if the water leaves the separator with the air bubbles still entrained, then the energy expended to compress that fraction of the air has been wasted for no effective gain.

Larger bubbles move faster than smaller bubbles relative to the water. In order to effectively model separator effectiveness, it is necessary to model the water flow field and accurately predict the size distribution of the bubbles within the separator. The water flow field establishes the context in which the bubbles are moving and the size distribution of the bubbles determines how they move.

Figure 2.26 illustrates the importance of correct modeling for design. There is a small operating envelope for a gravity separator of a given size. Therefore, a small error in design can result in either high capital cost by over-engineering or poor effectiveness with a sharp drop-off with increasing flow rate. If the correction for rising by Karamanev and Nikolov (1992) proves accurate, then this envelope should be narrower because the relative velocity increases more slowly with increasing diameter than if the correction does not apply (see: Table 2.2). Kurokawa and Ohtaki (1995) observed that centrifugal separators have a similarly narrow operating envelope.

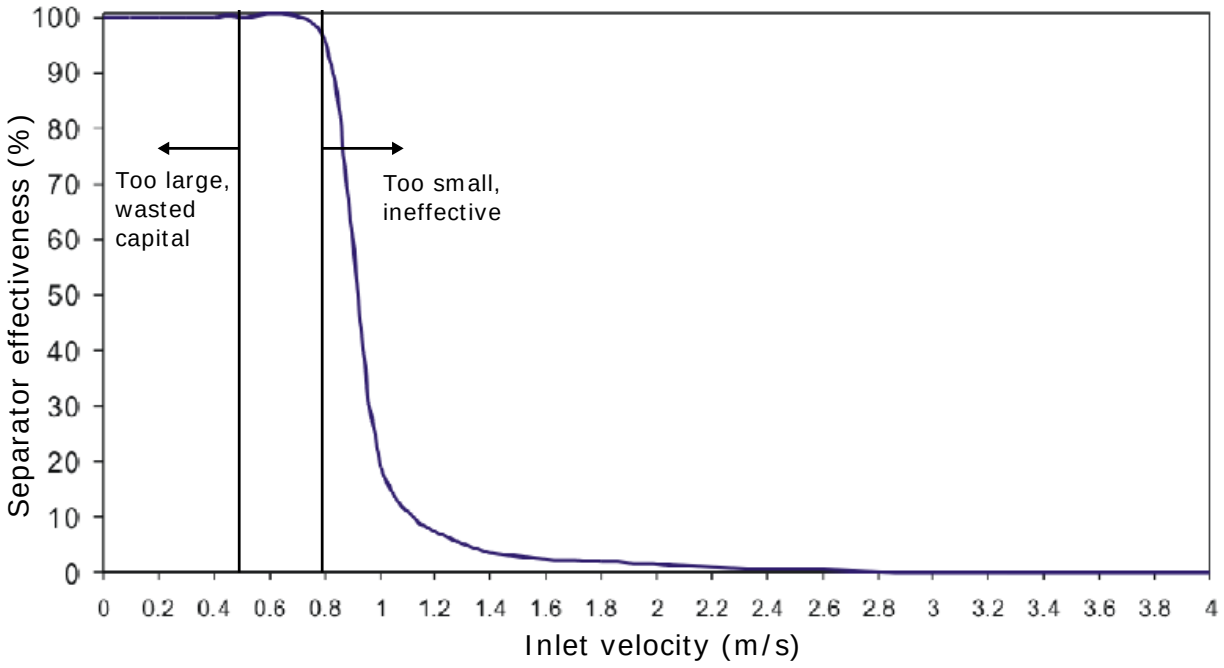

Figure 2.26: A separator has a small design window (modified from Laleh, 2010)

Chapter 3

3. Common driver of air induction across mechanisms

In a HAC, the source of energy for the compression loop is the difference of elevation between the water levels in the forebay and tailrace tanks. The flow moving through the loop from the forebay tank to the tailrace tank must consume all of the available head to thermodynamically balance the system. There are five energy sinks in the compression loop:

1. Major and minor losses
2. Air entrainment
3. Free fall flow
4. Other irreversibilities
5. Air compression

Major losses consist of internal flow friction, the result of pipe wall roughness and shear created by the velocity gradient of the flow near the pipe wall. Minor losses occur when the flow velocity is changed in magnitude or direction. In the case of a single phase flow, this component is the only source of energy consumption.

Air entrainment involves a surface discontinuity created by high velocity flow. The air is mixed with the water by shearing action to generate a bubbly flow. Shear and strong velocity gradients result in inherent irreversibility.

Free fall in the downcomer is the result of inadequate transport capacity (Kobus, 1984) to prevent bubble separation and coalescence into a continuous void inside the pipe. Along the

length of this void, the air is not compressing and at the end of the void, there is a zone of re-entrainment where the air is again converted into bubbles. In the case where a free fall flow exists in the downcomer, the energy cost of air entrainment is incurred twice: first at the top of the downcomer where the first entrainment occurs and second at the bottom of the free fall zone where re-entrainment occurs by means of a plunging jet. This phenomenon is addressed in sections 6.5 and 7.7.

Any unaccounted irreversibilities create a mismatch between the model and the experimental values. The purpose of evaluating irreversibilities is to account for enough sources of irreversibility that the mechanistic HAC model matches actual performance.

After all irreversibilities are subtracted from the driving head of the compression loop, the remainder is the energy available for air compression. The efficiency of the HAC is maximized when this number is maximized.

3.1 System-driven pressure gradient

For a single phase flow with no external source of energy between two points, the steady flow energy equation (SFEE) applies (3.1). The SFEE represents energy conservation in steady flow between two or more points (noted by i). It includes kinetic energy (KE), potential energy (PE), pressure energy (PrE), and internal energy (U). Within the compressor loop of a HAC from the forebay tank to the tailrace tank, this assumption is true.

$$KE_i + PE_i + PrE_i + U_i = \text{constant} \tag{3.1}$$

For a case where the water flow rate is enough to completely consume the available head, there is a complete conversion of potential energy into internal energy from the forebay surface to the tailrace surface (see: Figure 3.1).

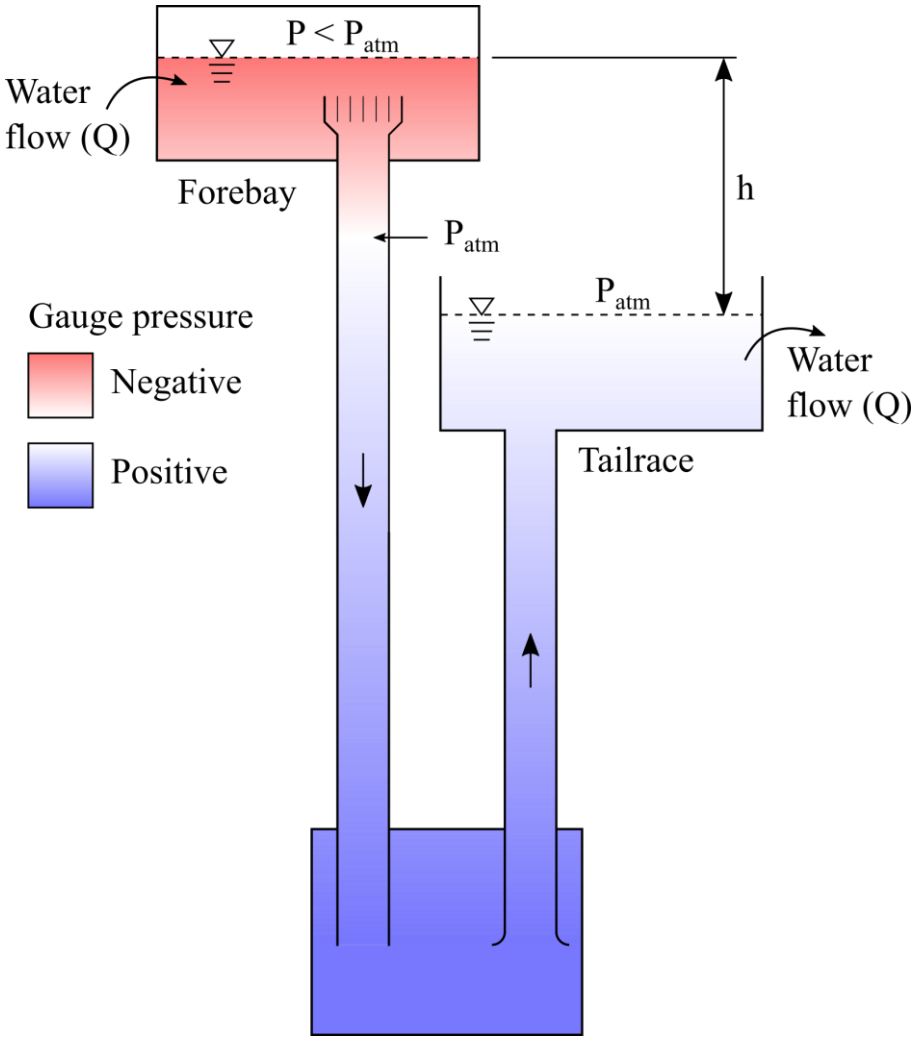

Figure 3.1: A single phase system with HAC geometry where the low fixed flow rate requires below-atmospheric pressure in the forebay tank

Irreversibility manifests as an increase of internal energy (temperature). The velocity at both surfaces in steady state flow is negligible and in a real system where both the forebay and tailrace are open to atmosphere, both share the same pressure reference. Therefore, the kinetic and pressure components of energy are the same at both positions. The reduction in potential energy is equally matched by an increase in internal energy:

$$PE_{forebay} + U_{forebay} = PE_{tailrace} + U_{tailrace} \tag{3.2}$$

For the case where there is insufficient water flow rate available to completely consume the available head by irreversibility sources alone (as in Figure 3.1), there must be another term to balance the equation. Kinetic energy remains at zero in both positions. Therefore, system geometry must generate low pressure in the forebay tank if the tailrace tank is fixed at atmospheric pressure:

$$\begin{aligned} PE_{forebay} - PE_{tailrace} \\ = \left(U_{tailrace} - U_{forebay}\right) + (PrE_{tailrace} - PrE_{forebay}) \end{aligned} \tag{3.3}$$

The difference in elevation between the position of the atmospheric pressure horizon in the downcomer and the level in the tailrace tank for a single phase system marks the fraction of driving head required to overcome the flow losses in the compression loop incurred after that point.

For a single phase system, it is possible to control either the head or the flow rate. Unless they are exactly matched, the other must be adjusted for energy to be conserved. For a HAC, it is

useful to recognize that any low pressure necessary to pull atmospheric air into the forebay tank and induct it into the downcomer is created by the system geometry and limited water flow rate.

3.2 Air induction is required to balance the energy equation

Energy transferred from the water stream into the air stream for the compression process is another means to balance the SFEE:

$$\begin{aligned} PE_{forebay} - PE_{tailrace} \\ = \left(U_{tailrace} - U_{forebay}\right) + \left(PrE_{tailrace} - PrE_{forebay}\right) \\ + \text{compression work} \end{aligned} \tag{3.4}$$

This relationship neglects the heat exchange between the air and water streams at the inlet caused by the air coming into the system at a different temperature from that of the water. It is an indicator of how the available potential energy is distributed into other forms, where the increase of internal energy ($U_{tailrace} - U_{forebay}$) represents the irreversibility of the system. Some negative gauge pressure is necessary to provide the motive force to entrain the air, but most of the potential negative pressure in the forebay tank (depicted in Figure 3.1) can be exchanged for air compression work. Equation (3.5) is the numerator of the HAC mechanical efficiency equation (1.1); the indicated air power (i.e. the compression power) is proportional to the mass flow rate of air. Therefore, reducing irreversibility in the system proportionally increases the air flow rate into it.

$$\text{indicated air power} = \dot{m}_g \cdot \text{air compression work} = \dot{m}_g \cdot \int VdP \tag{3.5}$$

This means that the air flow rate into the system is determined by the collective irreversibility in the compression loop and not by local geometry in the mixing head. Figure 3.2 shows the consequence of throttling the flow (i.e. increasing irreversibility) at a constant input rate of water. The flow in ‘a’ is unrestricted and the flow in ‘b’ is restricted by a valve positioned in the pipe immediately below the lower edge of the image. Note that case ‘b’ is drawing a narrower vortex and therefore less air. Note that irreversibility determines the quantity of air that is entrained but does not dictate whether air is entrained. This must hold true whether or not there is special local geometry to induce air entrainment.

Figure 3.2: Vortex formation above an unrestricted (a) and restricted (b) pipe intake (Shakerin, 2010)

3.3 Why doesn't it just pull more water?

If the energy balance can be satisfied with more water flow, then why does it induct air? In a pumped HAC, the forebay water level responds to the water flow rate. In a reservoir system where the forebay level is fixed, the proximity of the inlet lip of the mixing head to the water surface may serve to choke the water flow from around the sides of the mixing head into the downcomer (see: Figure 3.3). The curve represents the height of water over the lip of the mixing head necessary to admit sufficient water flow to meet the energy consumption requirement with

only water. If that lip is close to the water surface, then the flow rate into the pipe is limited by the area available for flow and the pressure gradient from outside to inside the mixing head, as in a horizontal channel flow.

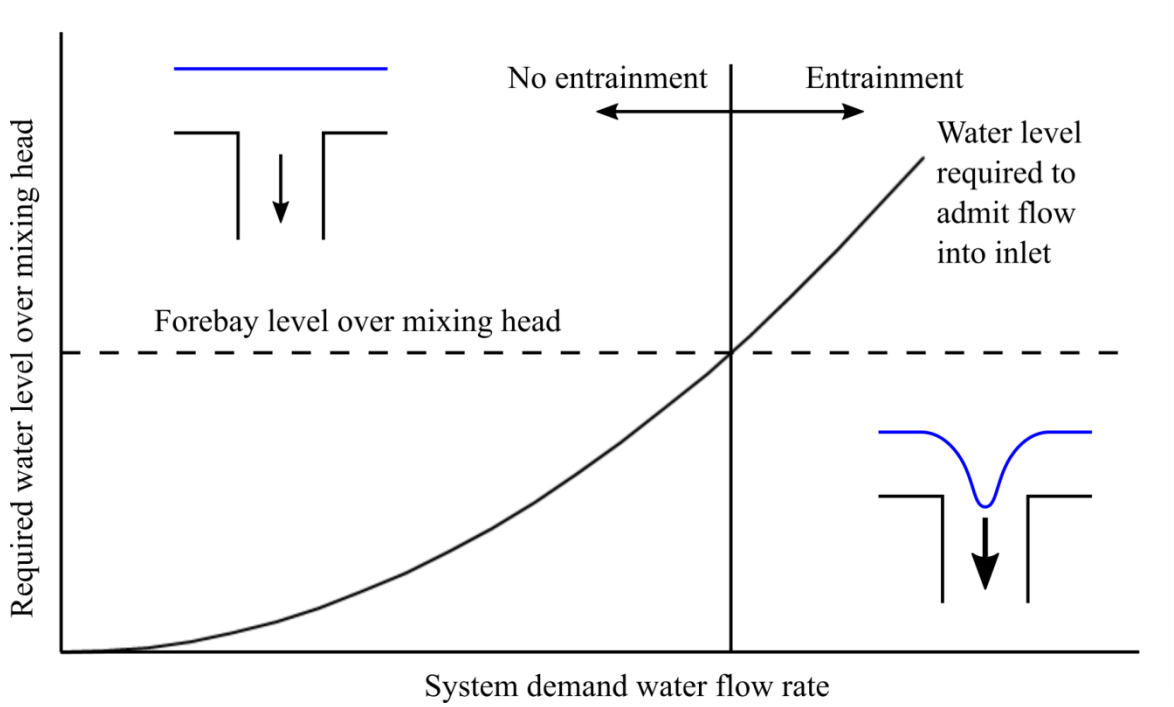

Figure 3.3: A downcomer inlet positioned too close to the water surface to ingest only water must also induct air to meet demand

Where the water level is high enough that the system can pull enough water into the inlet to meet the energy consumption requirement (demand for irreversibility), there is no entrainment necessary. If the water flow rate is insufficient to allow the demand for irreversibility to be met through the induced friction of the water flowing through the system, so that the energy equation is balanced, then some other energy consumption mechanism is required to balance the system. Air entrainment and compression and the additional irreversibilities incurred by a two-phase flow allow the system to rebalance with a lower water flow rate.

Generically, if, for whatever reason, air induction was precluded as a mechanism of introducing additional dissipation to balance the energy equation, a possible alternative mechanism could be the development of a non-entraining vortex. The presence of an organized structure in the water over the inlet, such as a non-entraining vortex, introduces velocity gradients and shear in addition to what would be present without, resulting in some additional viscous energy dissipation. Such a non-entraining vortex would be limited in size, because if yet more dissipation was required to cause it to grow, the 'tail' of the vortex would deepen to bring air into sufficient proximity with the inlet, such that air would be inducted (see: section 2.2.2).

According to Shields (G. Shields, personal communication, January 22, 2018), a former operator of the HAC at Ragged Chutes, two control systems were in place at that installation: gates linking the river and forebay could be opened or closed and the vertical position of the mixing heads could be adjusted. The gates were adjusted based on the season and the water flow rate over the dam. The water level in the forebay was lower than that of the river, so the gates worked to control the water flow rate. The mixing heads were set to maximize air delivery. Because the gates limited the flow rate into the forebay, the Ragged Chutes HAC acted like a pumped HAC.

3.4 A criterion for the threshold of air entrainment

If, in a pumped HAC, the system water flow rate is less than that required to completely consume the driving head, then air is inducted. The forebay water level responds to the water flow rate and the inlet geometry. If, in a run-of-river HAC, the water level is lower than a critical water level, then air is inducted. It is possible to use the SFEE to describe this critical water level or establish an upper bound for the water level in the forebay tank of a pumped water HAC.

With the understanding that there is a level threshold at which the flow will convert from single phase to two-phase (see: Figure 3.3), it is possible to define this threshold with an analytical relationship of the limiting single phase case. Figure 3.4 is a schematic of a single phase flow where there is potential for air flow along the streamline from position 1 at the water free surface with a defined reference absolute pressure (which may or may not be atmospheric) to position 2 immediately after the inlet.

Figure 3.4 illustrates how the pressure responds along the streamline from 1 to 2. All pressures represented in this chapter are gauge relative to the reference pressure at the water free surface. Each term represents part of the Bernoulli equation, in order of appearance in (3.6) below: (i) hydrostatic pressure is the conversion of potential energy into pressure; (ii) dynamic pressure is the kinetic energy component; (iii) gauge pressure is the sensible pressure relative to the reference pressure; and (iv) the final pressure profile in Figure 3.4 (not part of (3.6)) is the gauge pressure with the hydrostatic pressure removed (called static pressure) and is included to illustrate the exchange between this static pressure and dynamic pressure along the vertical streamline between 1 and 2. There is a discontinuity indicated at 2. This does not represent a physical discontinuity of the pressure profile, but is instead a schematic representation of the minor loss (P_{sh}) associated with the flow entering the pipe inlet.

$$\rho \cdot g \cdot h_1 + \frac{\rho \cdot v_1^2}{2} + P_1 = \rho \cdot g \cdot h_2 + \frac{\rho \cdot v_2^2}{2} + P_2 + P_{sh} \tag{3.6}$$

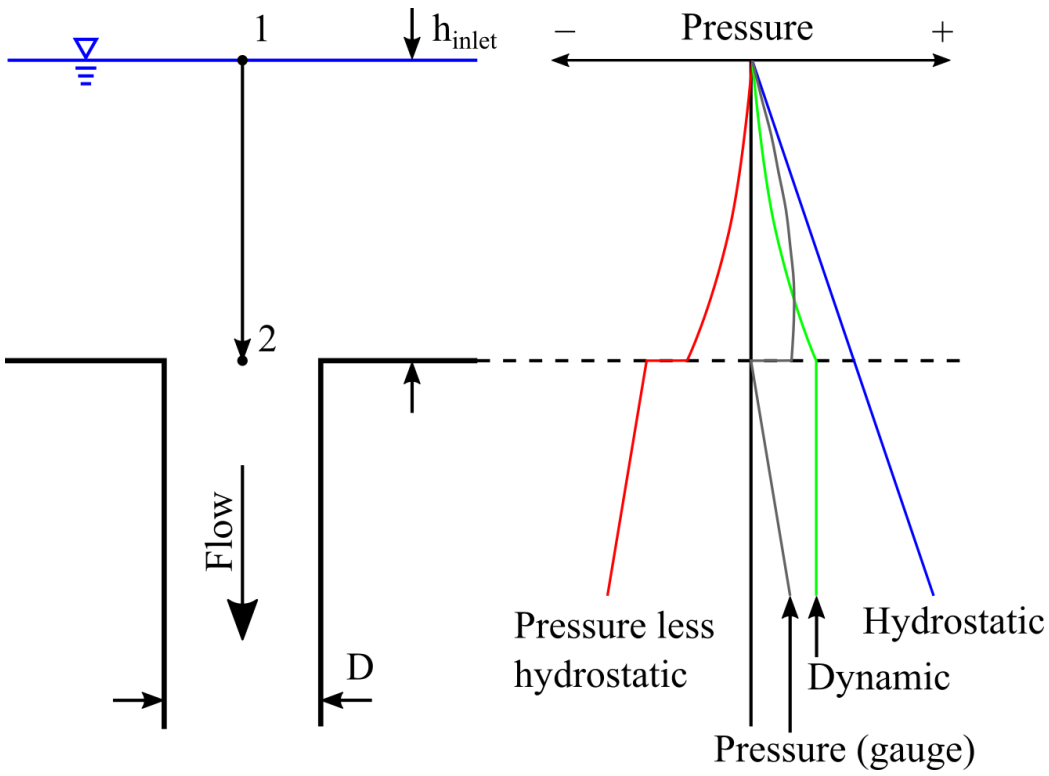

Figure 3.4: Schematic of a vertical pipe inlet at the critical point before air is inducted

From Torricelli's law (3.7), one would expect that the dynamic pressure would increase linearly along the streamline from 1 to 2. However, the assumption behind the law that the pressure at i is equal to the pressure at 1 is not true in this case, because of the inclusion of the minor loss component (P_{sh}). Therefore, the increase of dynamic pressure is nonlinear.

$$v_i^2 = 2 \cdot g \cdot (h_1 - h_i) \tag{3.7}$$

Note that the gauge pressure at 2 is equal to that at 1. This is the critical condition for air entrainment where any further reduction of pressure at 2 provides a pressure gradient for potential air flow into the pipe. In the ideal case (where there is no cost in irreversibility associated with the surface disturbance required to entrain air) the threshold occurs where the

combined static and hydrostatic pressure at 2 is equal to the reference pressure. The mass or volume flow of air inducted under such conditions will depend on the resistance of the flow path between the two locations. At the onset of induction, the air flow is nil. If the demanded water flow rate increases beyond the threshold value (established in Figure 3.3), the pressure at 2 drops below the reference pressure, providing a motive force for air to flow from 1 (reference pressure) to 2 (below reference pressure).Hydrostatic pressure increases linearly along the vertical streamline. Moving down the streamline from the water surface at 1, where the velocity is zero, there is an increase of dynamic pressure until it reaches the point of maximum velocity at 2 (the pipe inlet lip or bottom of bellmouth). Because there is no external source of energy between 1 and 2, the increase in dynamic pressure comes at an equal cost to static pressure. At the pipe inlet (around position 2), there is a minor loss incurred, which further reduces static pressure. After 2, the static pressure continues to decrease due to flow losses from friction and other irreversibilities. If the static pressure drops low enough to bring the gauge pressure below zero (i.e. the absolute pressure at 2 is lower than the reference pressure), then there is potential for air entrainment.

From Figure 3.4, the dynamic pressure at 1 is zero because the velocity (v_1) is zero. Using gauge pressure for both pressure terms makes the pressure at 1 (P_1) equal to zero. Major loss along the streamline is negligible because the forebay is large relative to the inlet pipe. For the critical condition, the minor loss is available in the literature for some inlet configurations or it can be determined empirically for unusual geometries. From these conditions, the equation is simplified:

$$\rho \cdot g \cdot h_1 = \rho \cdot g \cdot h_2 + \frac{\rho \cdot v_2^2}{2} + P_2 + P_{sh} \tag{3.8}$$

The equation is rearranged to isolate the critical pressure at 2:

$$\rho \cdot g \cdot h_1 - \rho \cdot g \cdot h_2 - \frac{\rho \cdot v_2^2}{2} - P_{sh} = P_2 \tag{3.9}$$

In the critical condition, the pressure at 2 is zero (air flow is nil, so no pressure drop from 1 to 2). This formulation is valid only for single phase fluid flows, so conditions where entrainment is occurring cannot directly be resolved. When the pressure at 2 is at or higher than atmospheric, there is no motive force for air entrainment. Conversely, air entrainment occurs when that motive force is present:

$$\rho \cdot g \cdot h_1 - \rho \cdot g \cdot h_2 - \frac{\rho \cdot v_2^2}{2} - P_{sh} < 0 \tag{3.10}$$

The minor loss component can be rephrased as the fraction of dynamic pressure consumed, where X is the minor loss coefficient:

$$P_{sh} = \frac{X \cdot \rho \cdot v_2^2}{2} \tag{3.11}$$

Substituting equation (3.11) into equation (3.10) and collecting terms eliminates the dependence on fluid density:

$$g \cdot (h_1 - h_2) < \frac{v_2^2 \cdot (1 + X)}{2} \tag{3.12}$$

The difference in elevation between 1 and 2 ($h_1 - h_2$) is the level of water over the inlet (h_{inlet}). This is a variable of interest and one that is straightforward to measure:

$$h_{inlet} < \frac{v_2^2 \cdot (1 + X)}{2 \cdot g} \tag{3.13}$$

Volume flow rate of water (Q_l) and pipe diameter (D) replace velocity because these values are two of the design parameters for a HAC:

$$v = \frac{4 \cdot Q_l}{\pi \cdot D^2} \tag{3.14}$$

For some mixing head designs, the cross-section area at 2 is not the same as the downcomer pipe cross-section and the section may not be circular. The pipe diameter (D) is diameter is calculated as an equivalent area circular diameter for the cross-section at 2 (i.e. the diameter of a circle with the same flow area as the mixing head inlet at 2). Hydraulic mean diameter would not be appropriate in this case, because it is the velocity that must be correct in the conversion and not

the pressure drop. Substituting equation (3.14) into equation (3.12) rephrases the equation using only variables relevant to the design of the HAC:

$$h_{inlet} < \frac{8 \cdot (1 + X) \cdot Q_l^2}{\pi^2 \cdot D^4 \cdot g} \tag{3.15}$$

Note that this is technically an implicit relationship for modeling and design because the forebay water level is included in the calculation of the system water flow rate, Q_l (h_{inlet} is referred generally to the elevation of the lip of the inlet). It is not unreasonable to expect that the range of h_{inlet} may be significant with respect to the total driving head of the system. If this was not the case, then it would be safer to neglect this component of irreversibility from the model formulation. For measurement, the loss coefficient (X) is the measure of interest. It is the characteristic property of the mixing head that is ideally minimized in design. When the loss coefficient is minimized, the water level over the lip of the inlet is reduced and the inlet irreversibility is minimized.

In historic compressors operating on river hydropower, it was typical to have adjustable intake heads that could be shifted vertically to accommodate the river conditions (Schulze, 1954). This estimate of h_{inlet} is useful to inform the range of the intake head elevation control system for a reservoir or run-of-river HAC design. For a pumped HAC, it gives an indication of the necessary size of the forebay tank for the range of flow rates.

3.5 Irreversibility attributed to entrainment

Even when operating on the single phase side of, but near to, the critical water flow rate, there is potential for additional loss. For the case of vortex entrainment, there are weaker (i.e. non-

entraining) vortex classes that nevertheless create pressure drop along the flow direction that is not fully recovered (Knauss, 1987). Whether entraining air or not, an additional term is required to account for the head loss between the water surface and the pipe inlet (h_{mix}):

$$h_{inlet} < \frac{8 \cdot (1 + X) \cdot Q_l^2}{\pi^2 \cdot D^4 \cdot g} + h_{mix} \tag{3.16}$$

Analytical evaluation of this term is beyond the scope of what is possible with a single phase, one dimensional analysis. It includes complex flow behavior in two and three dimensions. It is not possible to separate the irreversibility due to shock loss from other sources of irreversibility using only these variables. For convenience, the entrainment irreversibility is included into a loss coefficient function (X_f), which is not likely to be a single constant:

$$h_{inlet} < \frac{8 \cdot \left(1 + X_f\right) \cdot Q_l^2}{\pi^2 \cdot D^4 \cdot g} \tag{3.17}$$

The loss coefficient function represents the combined irreversibility due to the inlet loss and air entrainment. The intent of the mixing head design is to minimize this combined loss coefficient function, using whatever mechanism is appropriate.

At some position below the entrainment horizon, pressure returns to atmospheric and the compression process begins. Any head consumed to that position is unavailable for compression. Figure 3.5 shows the gauge pressure trend from the water surface into a bellmouth mixing head. This is a generic inlet geometry that better accounts for the complexity of a practical mixing head than the simplified sharp edge geometry represented in Figure 3.4. Between A and B, the flow accelerates and reduces the pressure rise created by loss of elevation (hydrostatic pressure).

Between B and C, there is a shock loss from the inlet. Depending on the geometry, there may be more than one position at which a minor loss occurs. From C to D, there is another acceleration of flow, which exceeds the hydrostatic pressure rise, creating a minimum pressure below the reference pressure at D (also 2). After D, the pressure rises down the downcomer. At E, the pressure has risen back to the reference pressure. The interval between D and E is called the entrainment zone.

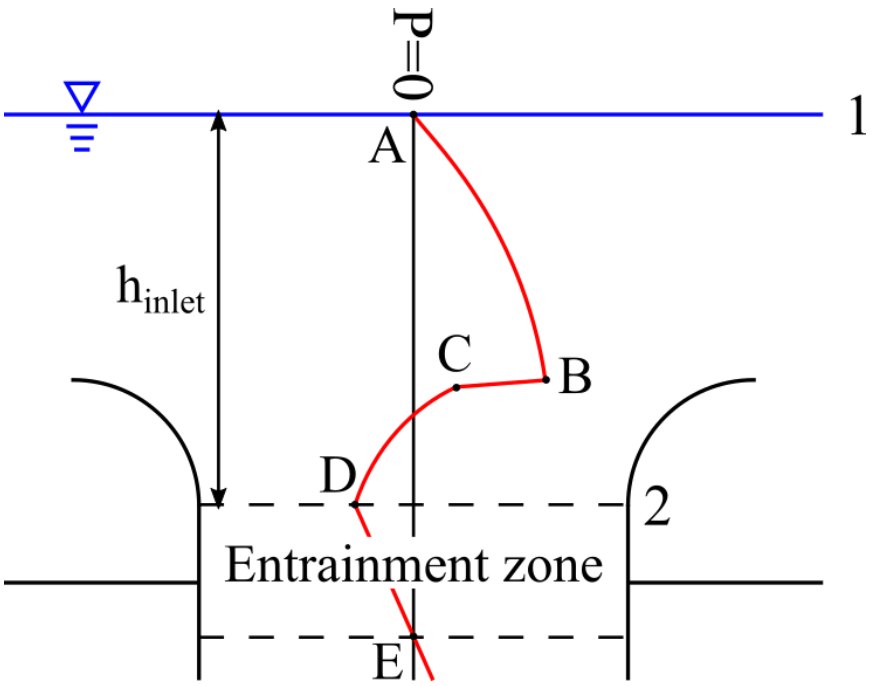

Figure 3.5: Exaggerated gauge pressure profile along the streamline in an air entrainment case

The pressure required to drive air flow is small (tens of Pa) relative to pressure required to drive water flow (order of kPa), so the gauge pressure at D would in that case be close to the reference pressure (at A). The vertical distance between D and E and the magnitude of the negative pressure at D would both vary with water flow rate. These effects should be equivalent at the

same flow rate between mixing heads, allowing the comparison to be made using the single variable approach described above.

It is infeasible to experimentally isolate the loss from entrainment alone, because the water level measurement captures the combined entrainment, inlet, bubble drag, and pipe flow losses between the free surface and the datum from which the level is measured (e.g. lip of mixing head). Any losses associated with the entrainment process or mixing head geometry that occur below this horizon are not captured in the measurement. These losses cannot be captured using this single variable approach. There is also potential for further downstream loss in the case of vortex entrainment if the swirl is allowed to continue down the pipe (see: section 2.2.2). In a mixing head with vortex breaking or vortex limiting geometry, this quantity is assumed to be small with respect to the losses above the entrainment zone and will be ignored.

The irreversibility of the entrainment process is characterized by the reduction in potential energy of the fluids between the free surface and the end of the entrainment zone below the inlet where the pressure is again equal to the reference pressure (position E in Figure 3.5). Between these points (A and E), no compression work has been performed (i.e. no pressure increase) and all of the energy has gone to accelerate the flow to the pipe velocity and overcome losses.

3.5.1 A direct measurement of entrainment irreversibility

The change in potential energy of the water stream from the free surface to the compression starting point can be calculated using the SFEE (3.18). Recall from above that the SFEE consists of potential energy (PE), internal energy (U), pressure energy (PrE), and kinetic energy (KE) terms.

$$(PE_E - PE_A) = \left(U_A - U_E + U_{transfer}\right) + (PrE_A - PrE_E) + (KE_A - KE_E) \quad (3.18)$$

The kinetic energy at the free surface (KE_A) is zero and he change in pressure energy is zero, by definition:

$$(PE_E - PE_A) = \left(U_A - U_E + U_{transfer}\right) - KE_E \quad (3.19)$$

Temperature and pressure measurements are required for thermodynamic property lookup. The temperature of air and water must be measured separately in the approach flow upstream of A. The forebay reference pressure must also be measured. It is not likely that the vertical position of E would coincide with the position of one of the measurement ports in the downcomer. Therefore, its position and any additional measurements described below should be interpolated between the two, ideally closely spaced, measurement positions that bracket the end of the entrainment zone as determined by gauge pressure measurement.

To accurately evaluate the change of internal energy, a precise measurement of differential temperature is required. Instruments capable of reading millikelvin-scale temperature difference are commercially available (Riventa Limited, 2017). Based on a total conversion of head to internal energy, a temperature rise of 1 mK in water at 20°C and 100 kPa corresponds to 0.427 m of head consumed (NIST, 2018). Temperature change of this scale could be obfuscated by heat transfer due to air and water entering the system at different temperatures. Therefore, it would be necessary to achieve equal or near-equal temperature of the incoming air and water streams at A to strictly limit heat transfer ($U_{transfer}$) in the process between A and E. The heat transfer term is a consequence of the air and water coming into the system at different temperatures. It

represents the total heat transferred between the air and water streams between the free surface and the entrainment horizon. There is no heat of compression included because there is no compression.

Kinetic energy can be measured or estimated in one of three ways: (i) using measured water flow rate (volumetric) and an estimate of gas volume fraction, (ii) direct measurement of dynamic pressure using a Pitot-static tube, or (iii) using the bubbly flow HAC downcomer model. Average water flow rate is measured at the pump(s). Average water velocity can be estimated using the measured volume flow rate of water, pipe internal area, and an estimate of gas volume fraction (i.e. fraction of the pipe area occupied by air and not available for water flow). Gas volume fraction can be estimated directly using a conductivity probe transit (Muñoz-Cobo et al., 2017) or indirectly by comparing pressure rise down the pipe below E to a flow model with varying density accounting for the displacement of dense water by light air. Velocity inside the pipe is uneven due in part to the two-phase flow and in part to the undeveloped flow near the inlet. The Pitot-static method would require a transit measurement across the pipe section. The final method relies on the accuracy of the HAC model. The measured mechanical efficiency of Dynamic Earth HAC (see: chapter 5) closely matched the modeled efficiency (including the prediction of the optimum) after a flat correction was made to the driving head value (Sivret, 2018), indicating that the bubbly flow downcomer model is a reasonable representation of the actual. The flow at position E should be bubbly, which should make the modeled values of velocity and gas volume fraction accurate. The kinetic energy of the air itself can be neglected due to its low fraction of total flowing mass.

The calculation of equation (3.19) has four likely sources of error: (i) incomplete heat transfer between the air and water upstream of A, (ii) measurement error of water temperature, (iii) error in estimation or measurement of kinetic energy, and (iv) interpolation error of the vertical position of E or of one of the other interpolated measurements. Error in temperature measurement and incomplete heat transfer are potentially serious problems. The former will be resolved by using precision temperature instruments to take measurements. The latter will depend on the magnitude of the temperature difference between the circulating water and incoming air.

In the best-case scenario, the kinetic energy term is of the same order as the entrainment loss (i.e. X_f of order 1), so error in the calculation of water velocity based on poor estimates of gas volume fraction would lead to significant error in the loss calculation.

The final problem of interpolation error is best remedied by having one or both of the measurement ports close to position E. Alternatively, a probe dropped down the downcomer pipe through the mixing head can be used to identify this position. There is potential for error in correctly locating the position of E due to the presence of free-fall within the entrainment zone. In that case, the differential temperature should be read between the approach flow and the position where the detrainment (or free-fall) zone begins, if possible.

3.5.2 A reasonable approximation of entrainment irreversibility

Directly evaluating irreversibility using temperature measurement requires expensive instrumentation. There are two ways to indirectly measure this irreversibility using a simpler instrumentation scheme: (i) the forebay water level over the mixing head and (ii) the quantity of

air inducted into the system or mechanical efficiency. Mechanical efficiency is proportional to the ratio of air flow rate to water flow rate (see: section 1.1), so reporting either value against water flow rate captures the same information.

The elevation difference between the free surface (A) and the end of the entrainment zone (E), where the compression process begins is an approximate measure of potential energy consumed to drive air into the system, including the downcomer inlet loss, the cost of air-water mixing, and the acceleration of the two-phase fluid from stationary to the pipe velocity. It is not possible to determine the position of the end of the entrainment zone (E) without pressure instruments in the downcomer. However, the position of the top of the entrainment zone (D) is more predictable, so that a water level measurement over the mixing head (A-D) can be made. If the length of the entrainment zone (between D and E) is small or follows the same trend and if the pressure required to induct the same air flow rate into the two-phase flow is similar across mixing head designs, then this water level measure is a good comparator. If the geometry and flow conditions downstream of D are the same, the intake geometry associated with the shortest vertical distance between the free surface (A) and top of the entrainment zone (D) is superior to all others. Because some mixing heads have complex geometry (i.e. not cylindrical) below the top of the entrainment horizon (D), the water level measure described above may not be a good characterization of the entrainment irreversibility.

If the irreversibility associated with one mixing head geometry is sufficiently different from another, then there should be a measureable difference in the air quantity inducted into the flow. For this to be measureable, it requires that the entrainment irreversibility is a significant fraction of the total irreversibility of the system. That total irreversibility determines the amount of

energy available for air compression, which controls the air intake flow rate. This measure, or the derived measure of mechanical efficiency, offers another coarse evaluation metric for mixing head selection.

The water level measure is a more direct indicator of irreversibility associated with the inlet loss and entrainment process where the downstream flow conditions are comparable across mixing head designs. The air flow measurement is a better measure of total irreversibility. It is especially useful when there is complex geometry or flow below the entrainment horizon, but only if the entrainment losses represent a significant fraction of the overall system irreversibility. These simpler methods should be sufficient to detect coarse differences between mixing heads. The more detailed potential energy balance may be necessary for fine-tuning.

3.6 Mixing head design objective

The optimum mixing head design is the one associated with minimum irreversibility. The total air flow rate inducted into the system is controlled by system effects and not by local geometry except by the effect of that local geometry on the system. Therefore, the design objective should be to facilitate rather than drive the entrainment process.

Beyond the design of the mixing head itself, is the design of the forebay. The water level equation (3.17) can be used to size the forebay. In a pumped system, the flow rate is set and the water level relaxes to equilibrium. In a reservoir system, the elevation of the water surface is set and the mixing head vertical position within the forebay is a design parameter to reach the desired flow rate.

3.7 Closed loop entrainment

In a closed loop system, the forebay tank is removed and replaced by a pipe loop to connect the pump directly to the downcomer pipe. If the mixing head pipe section is positioned above the water surface elevation of the tailrace tank, then there is no requirement to locally generate negative gauge pressure to induct air (see: Figure 3.6).

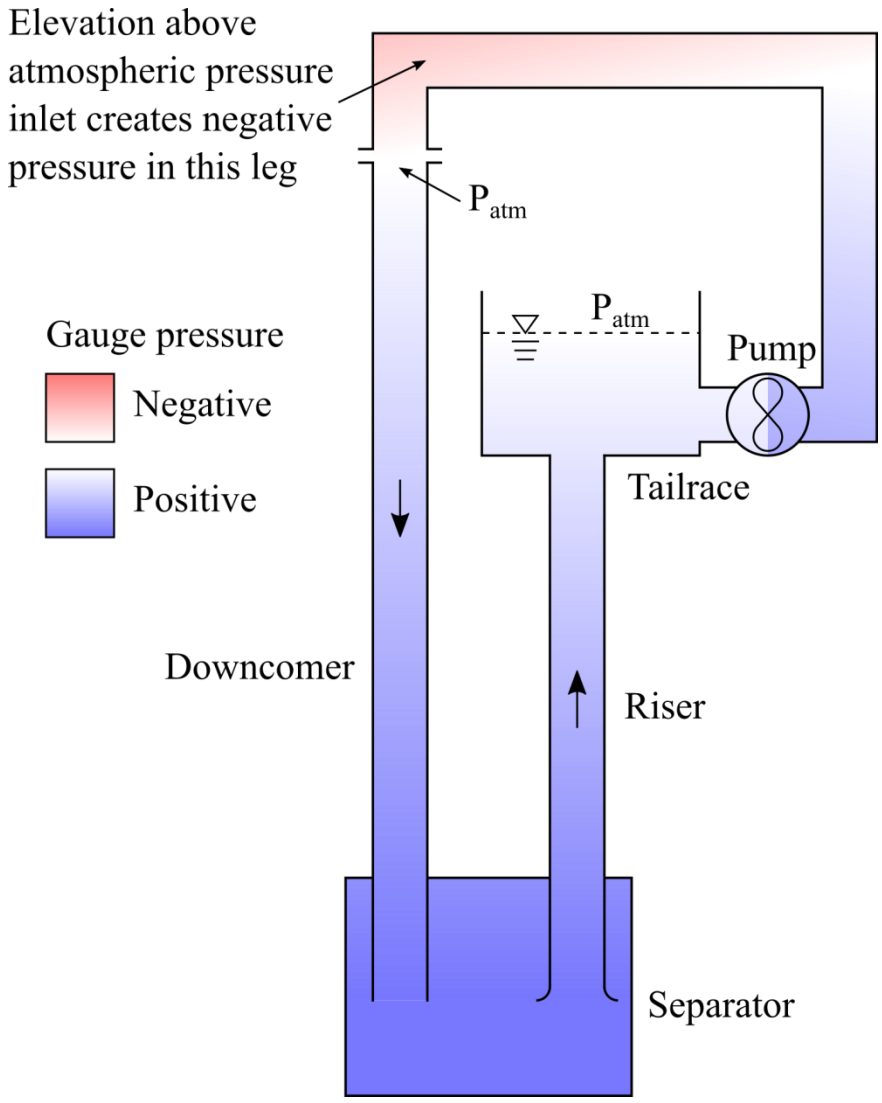

Figure 3.6: The pressure profile in closed loop is bounded by atmospheric pressure in the tailrace and at the air port inlets in the downcomer pipe

Fundamentally, the same system-driven pressure gradient drives air entrainment as in the open loop case. By removing the pipe outlet loss where the pump discharge pipe empties into the forebay tank and the part of the inlet loss at the mixing head associated with the flow contraction into the downcomer pipe, the closed loop case has a potential for higher overall mechanical efficiency than the open loop case.

3.8 Summary

The objective of the mixing head design is to facilitate the entrainment process with minimum irreversibility. The system creates the potential for air entrainment because it cannot fully consume the hydropower without air compression and the additional irreversibility generated in a two-phase flow. For each mixing head, an augmented loss coefficient function will describe how it performs against this metric.

The irreversibility can be measured directly using specialist differential temperature instrumentation to evaluate the increase of internal energy. Alternatively, it can be approximated using more conventional instrumentation by measuring water level over the entrainment horizon and the compression loop efficiency with water flow rate across mixing heads.

This thesis is intended to compare mixing head geometry options and identify which are preferable. Mixing heads with fewer internal features that might cause minor losses are expected to perform better than those with more. Vortex breaking geometry should prevent downstream losses due to swirl within the pipe and improve the efficiency of the compression loop. The system-generated low pressure zone (see: Figure 3.6) at the inlet is expected to drive air induction without the need for local geometry that increases velocity to reduce pressure by the Venturi effect.

Chapter 4

4. Separator performance model

The objective of the separator design is to minimize the cost of compressed air delivery, where a larger, more expensive separator offers equal or superior separator effectiveness over a smaller one. Fundamentally, separator design is an optimization between irreversibility, separator effectiveness, and capital cost. This chapter describes the models developed to predict the irreversibility (pressure drop across the separator) and separator effectiveness (fraction of air in gaseous form separated from two-phase flow) of a separator vessel. These models are tested in chapter 6 against the measured performance of two separators on prototype HACs with the intent of validating not only the models themselves but also the modeling strategies for the purposes of HAC design in the future.

Capital cost is a function of the size of the separator vessel. For vessels of the same type, increasing the size results in more engineering effort, more material, and a greater expense for fabrication and installation. The excavation at the bottom must be larger to accommodate a larger vessel and the shaft may need to be larger than strictly required for flow in order to lower components to the bottom. If the system is sufficiently large, the separator may be formed as an excavation of rock as at Ragged Chutes, constructed in 1909 (Schulze, 1954).

In several of the historic installations, thin-walled separators were constructed with open bottoms (Schulze, 1954). Figure 4.1 is a plate of one such separator installed at Magog (Taylor, 1897). If the HAC is constructed in a single shaft, the downcomer pipe is placed within the shaft and the riser is the annular space around the pipe. The flow from the downcomer is expanded to the full

diameter of the separator and then routed to flow out from under the skirt at the bottom. Because there is water on both sides of the separator skin, the differential pressure across the skin is negligible for separators of this type, particularly when compared to those where the separator is a pressure vessel surrounded by air at atmospheric pressure. The air plenum within the vessel results in differential pressure on the top surface of the separator of the order of 1 metre water gauge owing to the displacement of the water by the air. Under this condition, the vessel must be structurally sound against reaction forces, the weight of any pipework that it supports, and the limited differential pressure across the walls bounding the air plenum at the top of the vessel. This is a preferred case for construction of future installations because of the reduced underground development and simpler design of the vessel and pipework.

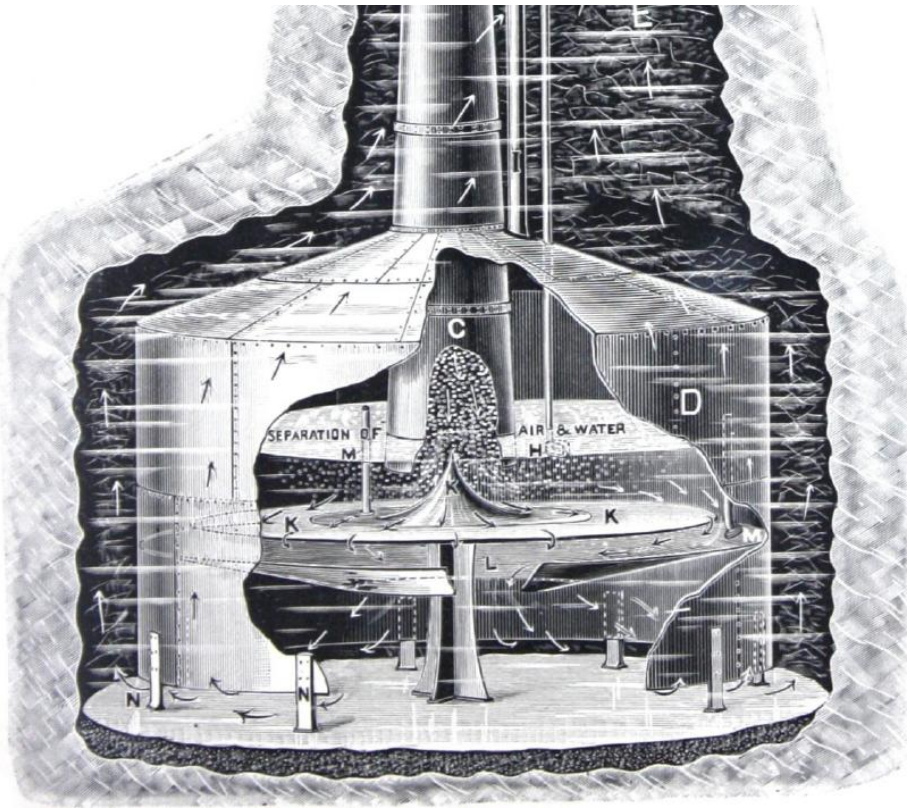

Figure 4.1: A thin-walled large separator under low differential pressure (Taylor, 1897)

Separators are broadly categorized into two categories: centrifugal and gravity. Centrifugal separators are smaller and rely on high velocity flow inside to create large values of centrifugal acceleration. They trade higher irreversibility for lower capital cost. Gravity separators are larger and require low velocity inside to allow bubbles to separate under the force of gravity alone. They trade higher capital cost for lower irreversibility.

4.1 Centrifugal separators

A centrifugal separator uses the reaction to radial acceleration generated by high tangential velocity to perform separation. The light medium (air bubbles) migrates towards the axis of rotation while the dense medium (water) migrates outwards from the axis. Because the velocity is necessarily high to generate substantial centrifugal acceleration and the velocity gradients and shear across the cross-section of the separator correspondingly large, this method of separation is inherently associated with more irreversibility than gravity separation.

The separator effectiveness of a centrifugal separator is controlled by three conditions: (i) bubble size distribution (larger bubbles have higher relative velocity), (ii) tangential velocity (higher tangential velocity results in higher centrifugal acceleration), and (iii) residence time (longer residence time allows bubbles with lower relative velocity to migrate further towards the central vortex). Equation (4.1), originally presented in section 2.3.1, represents the motion of a bubble within the flow field. Bubble size distribution (distribution of d) determines how the bubbles respond to the flow conditions within the separator. Tangential velocity creates the centrifugal component of the field force (g_f). A short residence time requires that the relative velocity (v_r) be higher than for the case of a longer residence time to allow a bubble to migrate the same distance from the wall to the axis of the separator.

$$v_r = \sqrt{\frac{4}{3} \cdot \frac{d \cdot g_f \cdot (\rho_l - \rho_g)}{C_d \cdot \rho_l}} \tag{4.1}$$

Pressure drop in a centrifugal separator requires a three-dimensional flow analysis to model. One- or two- dimensional simplifications reflect the actual system most poorly when there is a three-dimensional flow pattern. ANSYS Fluent computational fluid dynamics (CFD) software was used to perform preliminary checks for an order-of-magnitude estimate of pressure drop on a cylindrical cyclone (see: Figure 4.2) intended for the Dynamic Earth HAC conceptual design described in section 5.2. This design had an internal diameter of 0.88 metres and a height of 4 metres (Young et al., 2015). For a HAC design with a driving head of 5 metres and a designed flow rate of 400 kg/s of water, the separator irreversibility was found to consume from one third to one half of the total available head (see: Table 4.1).

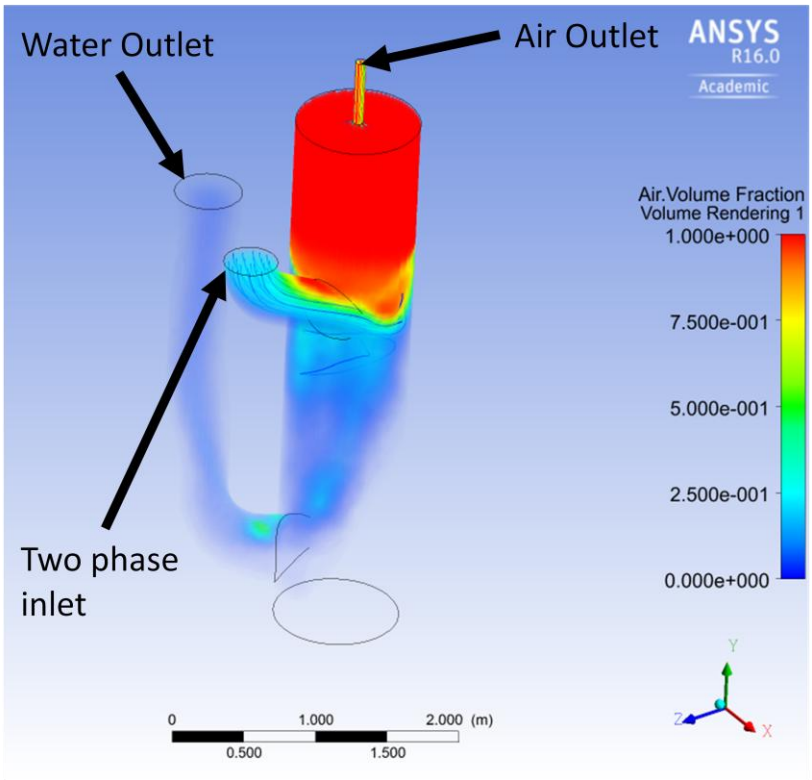

Figure 4.2: Eulerian two-phase CFD model for pressure drop of a cylindrical cyclone separator (Young et al., 2015)

Table 4.1: Pressure drop for centrifugal separator design for Dynamic Earth HAC (Young et al., 2015)

Water mass flow rate (kg/s)	Head loss (m H_2O)	Fraction of head available (%)
400	1.64	33
	1.99	40
	2.28	46
	2.40	48
350	1.59	32
	1.68	34
	1.88	38
	1.98	40
325	1.56	31
	1.44	29
	1.66	33
	1.86	37

The target efficiency for the compression loop of the Dynamic Earth HAC is 73% at 400 kg/s (Young et al., 2015). These results would cap that efficiency at between 52% and 67% before other irreversibilities were taken into account. This was a sufficiently poor result that further model refinement was deemed to be unnecessary to justify discarding the centrifugal separator as a viable option for the low head HAC at Dynamic Earth. A HAC running on a limited head budget cannot tolerate this level of head loss across a single component, so this design concept was rejected for the immediate future until the design of HACs with a much larger head budget

are considered. The remainder of this chapter is on the subject of gravity separators. Note, however, that the bubble motion models of separator effectiveness for gravity separators are generalizable and that the same principles of the relative velocity of bubbles in an acceleration field broadly apply in the case of centrifugal separation. Recall from section 2.3.1 that the model for the relative velocity of a bubble includes the centrifugal acceleration component in the derivation.

4.2 Predicting head loss in gravity separators

Gravity separators have low irreversibility compared to centrifugal separators. Low flow velocity inside the vessel results in low friction losses regardless of internal geometry features. This section describes the separator evaluation methodology and how it influences design. Two methods were used to calculate the head loss associated with the separator: pipe flow calculations and CFD modeling using ANSYS Fluent software. Pipe flow calculations are valid for single phase, one-dimensional systems. The CFD results presented in this section are for a single phase, three-dimensional model.

It is possible to use a two-phase CFD model, but these are more difficult, more complicated, and take more time to solve. Because the objective of this work is to develop a separator design methodology, relying on a slow and cumbersome process that requires more skill to utilize is sub-optimal. Building a simplified, high-speed model that produces a result with adequate accuracy for the design process is preferable to a model that is more accurate, but also slower, more complex, and more difficult to operate.

The inlet flow conditions for a gravity separator are the same as for a centrifugal separator. Two-phase flow modeling is similar between the two. The spread of results presented in Table 4.1 is the consequence of a model poorly matched to the system. The Eulerian model used in those simulations is the simplest one and is only applicable for flows with a dispersed secondary phase (ANSYS, 2009). The flow into the separator is dispersed but the flow inside the separator is a mixed form where some part is dispersed two-phase, some part has a high gas volume fraction, and some part is single-phase. Laleh (2010) used a combined model approach (described in section 4.3) to solve for separator effectiveness. His model was highly complex and required extensive solution time to converge and manual intervention to maintain the liquid level inside.

Pipe flow calculation is a simpler and faster but less accurate method to evaluate head loss. This is a one-dimensional calculation for pipe flow problems. Where the flow is more complex than the basic one-dimensional case (e.g. three-dimensional flow pattern inside a separator or where an elbow is positioned adjacent to an outlet), the accuracy of this calculation is reduced. It is, however, particularly useful to estimate the relative irreversibility associated with flow through a series of components (on an order-of-magnitude basis) to identify which of these components require the most attention in design. This calculation is based on friction loss along a pipe length:

$$\Delta h = \frac{f \cdot L_p \cdot v^2}{2 \cdot D \cdot g} \tag{4.2}$$

Frictional head loss is a conversion of kinetic energy into internal energy by action of shear on the pipe wall. The Darcy friction factor (f) is a dimensionless parameter solved implicitly in the Colebrook equation:

$$\frac{1}{\sqrt{f}} = -2.0 \cdot \log\left(\frac{\varepsilon/D}{3.7} + \frac{2.51}{Re \cdot \sqrt{f}}\right) \tag{4.3}$$

Changing flow conditions (e.g. velocity, direction) create additional irreversibility. These minor losses can account for the majority of the total loss across a pipe segment. The loss coefficient (X) characterizes the irreversibility created by a pipe geometry or flow condition change:

$$\Delta h = \frac{X \cdot v^2}{2 \cdot g} \tag{4.4}$$

A separator for a HAC consists of seven flow components: (i) section of downcomer pipe, (ii) flow turn, (iii) downcomer outlet, (iv) friction through main body of the separator, (v) flow turn, (vi) riser inlet, and (vii) section of riser pipe. Figure 4.3 shows these flow components in the context of the separator installed at the Dynamic Earth HAC (see: section 5.2).

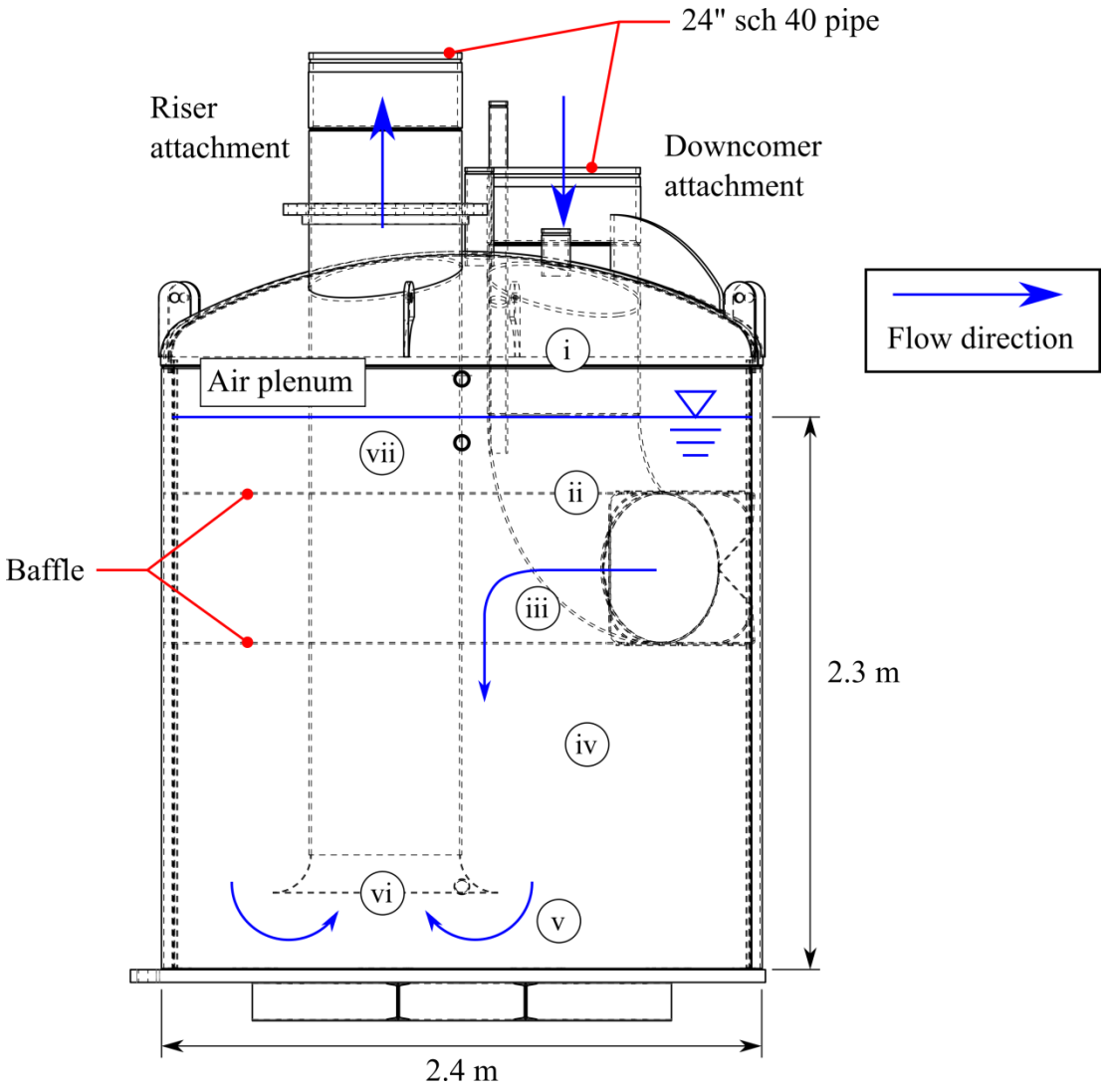

Figure 4.3: Dynamic Earth separator showing flow path through vessel

The flow components presented above are a generic breakdown used for these calculations for a HAC separator. Flow turns (ii, v), inlets (vi), outlets (iii), and any additional features within the main body (iv) or outside the separator envelope create minor losses. Table 4.2 contains the minor losses used for the Dynamic Earth separator head loss calculation.

Table 4.2: Minor losses in the Dynamic Earth HAC (Çengel and Cimbala, 2010)

Fitting type	Loss coefficient (X)
Short radius elbow (ii)	0.30
Outlet (iii)	1.05
12° conical diffuser	0.11
Bellmouth inlet (vi)[a]	0.03

[a] Treated as a rounded entry with radius of mouth curve > 0.2 times pipe diameter

In both the friction loss equation (4.2) and the minor loss equation (4.4), the head loss is proportional to the square of velocity. If the objective is to reduce head loss, it is more effective to reduce velocity than to reduce the loss coefficient. Figure 4.4 presents the comparison between the single phase, one dimensional model and the CFD model. All models assumed that the flow is single phase at the full combined volume of air and water. At high pressure, this assumption is more accurate. The air volume fraction decreases with increasing pressure, so the continuous phase is more dominant at the separator position. The horizontal axis in Figure 4.4 is the total combined flow rate of air and water at the inlet of the separator. The separation action within the separator reduces the volume flow rate in the main body through the riser (iv-vi), which means this analysis is slightly conservative.

The original downcomer design was to continue the 16" (nominal) downcomer pipe into the separator. From the pipe flow calculation (16" downcomer curve in Figure 4.4), the head loss associated with that design was less than that associated with the centrifugal separator model, but still too great (~0.9 m at the design water flow rate of 0.4 m^3/s). Increasing the pipe diameter to 24" (nominal) resulted in a 79% reduction to the head loss prediction (24" downcomer curve), even after accounting for the minor loss associated with the 12° conical diffuser (in Table 4.2)

immediately above the downcomer attachment point on the separator (see: Figure 4.3). The CFD model (CFD curve in Figure 4.4) was only calculated for this 24" downcomer case. Each point along the curve is a separate simulation on the same mesh. In a gravity separator, the main body head loss (iv-v) should be a small part of the total due to the low flow velocity and large section of the vessel.

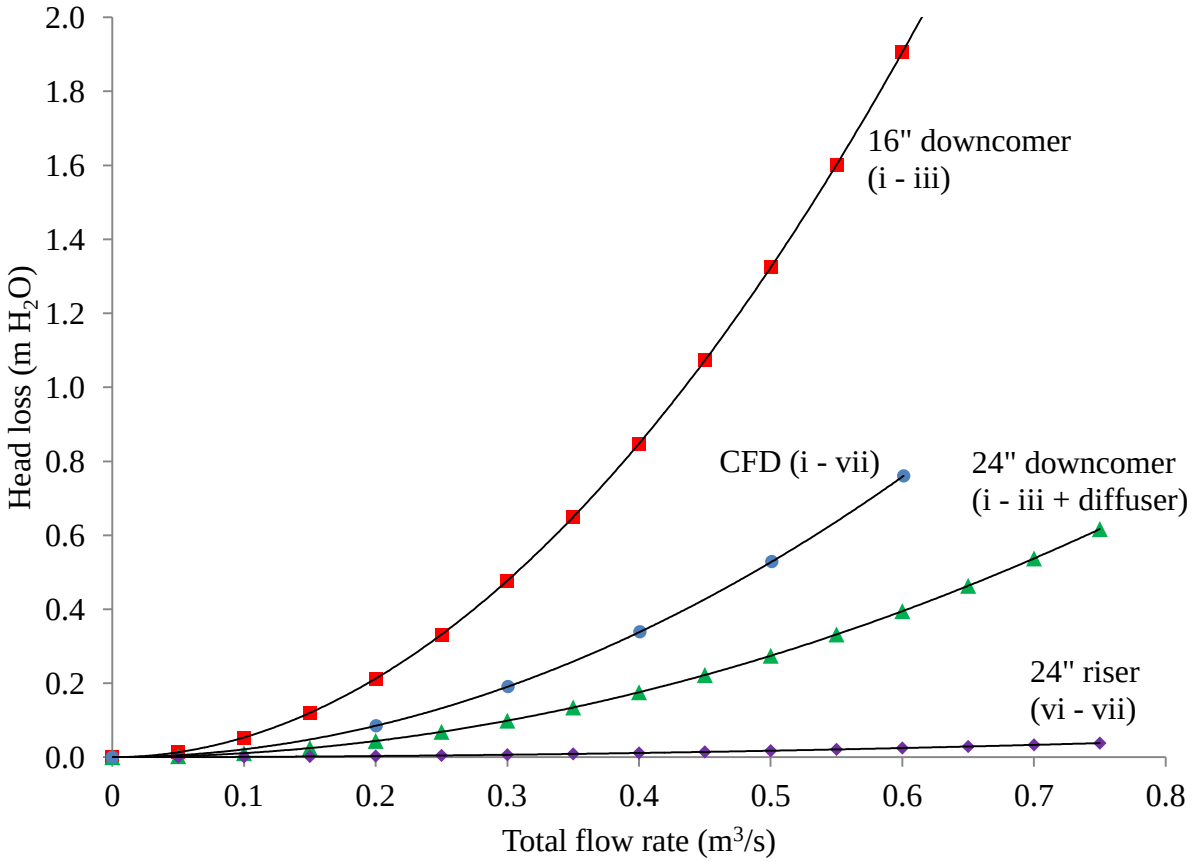

Figure 4.4: Design head loss associated with Dynamic Earth separator using pipe flow calculations and CFD. Fit curves are quadratic

The riser pipe curve (24” riser in Figure 4.4) is included to demonstrate the effect of minor loss in the separator. The pipe length in the riser is significantly longer than the one in the downcomer, but the loss coefficient is limited to the bellmouth inlet (see: Table 4.2), only. Most of the total head loss in the downcomer segment of the separator is composed of minor losses.

The CFD model should be taken as the best estimate. The discrepancy between the CFD model and the pipe flow calculation model is probably not in the complex geometry of the main body of the separator. The flow velocity inside that segment is small and therefore should not constitute a significant fraction of the total head loss. Therefore, the source of the discrepancy between CFD results and pipe flow calculations is likely to be in the minor loss components of the downcomer section (note the order-of-magnitude difference in head loss between the 24” downcomer and 24” riser curves in Figure 4.4). Interactions between closely-spaced flow features are known to amplify minor losses (see, e.g. Figure A5.10 from McPherson, 2003) with pipe flow calculations, that are implicitly accommodated in CFD simulations of the same systems.

4.3 Separator effectiveness

Over-sized gravity separators have high separator effectiveness, but come with a greater capital cost for engineering, fabrication, and installation. It is important to be able to accurately predict separator effectiveness in order to avoid unnecessary cost. There is a small target envelope for design (see: section 2.3.11) to achieve a reasonable separator effectiveness, so it is better to be slightly conservative with the separator effectiveness prediction than to risk under-sizing of the separator. The steep slope of the separator effectiveness curve with velocity (see: Figure 2.26) results in a large reduction of effectiveness for a small reduction in diameter. The objective of separator modeling in this context is to predict separator effectiveness so that the vessel size can

be designed. A model that accurately predicts separator effectiveness is ideal, but a slightly conservative (i.e. underestimated) prediction is also acceptable for design.

Laleh (2010) used a combined volume of fluid and discrete phase CFD model to track droplet motion in two gravity separators. The volume of fluid model represents the free surface and the discrete phase model represents the bubbles within the water component of the fluid volume. Combining these models was a complex operation; the computational time for a single parameter set exceeded 24 hours and the volume of fluid model required periodic manual correction to set the liquid level inside. Laleh (2010) also used very low under-relaxation factors for several of the solution parameters, suggesting problems with convergence (ANSYS, 2009) that would have required extensive troubleshooting to solve. The model had to be run several times to map the separator effectiveness with flow rate, droplet size, and oil quality. Overall, it was deemed that Laleh's approach, although hydrodynamically rigorous, was computationally expensive and impractical to be the design tool used to calculate separator effectiveness. Development of a more accessible, faster approach was needed for practical design.

The new approach first uses CFD to generate a single phase flow field and subsequently populates an overlaid, coarser grid with a bubble size distribution. The latter measure is implemented in Microsoft Excel. The input parameters used in the CFD model are described in section 4.3.1. Bubble motion is solved using the bubble size distribution entering the separator and the flow field velocities within the separator. The bubble size distribution is assumed not to change inside the separator. Physically, a separating bubble must coalesce with the air plenum at the top of a separator. There may be further coalescence interactions between bubbles where the gas volume fraction is high near the interface. Such complex interactions are not taken into

account in either Laleh's model or the near statistical model presented in this chapter nor are they available in the discrete particle model included in ANSYS Fluent (ANSYS, 2009).

The separator effectiveness model requires as input the separator geometry, air and water flow rates, temperature and pressure for thermodynamic property lookup, and bubble size distribution. Separator geometry is the design input. Air and water flow rates and temperature and pressure are calculated by an updated version of the HAC performance model originally presented in Millar (2014). Bubble size distribution is estimated by one of the methods presented in section 2.3.9.

Gravity separator orientation changes the modeling strategy. In a vertical separator, the separating bubble motion is opposite the water flow direction (see: Figure 4.5). The important parameter is the diameter of a bubble with a component of relative velocity in the vertical direction that equals the local vertical velocity of the flow field. Bubbles with diameters larger than that critical diameter value report to the separator's air plenum and those smaller than that critical value do not. In a horizontal separator, the motion of a separating bubble is perpendicular to the water flow direction (see: Figure 4.5). The bubble has a vertical relative velocity and is pulled along the separator length horizontally by the flow. If a bubble has enough time to reach the surface as it is pulled from the inlet to the outlet, then it separates. These models are described in more detail in sections 4.3.3 and 4.3.4, respectively.

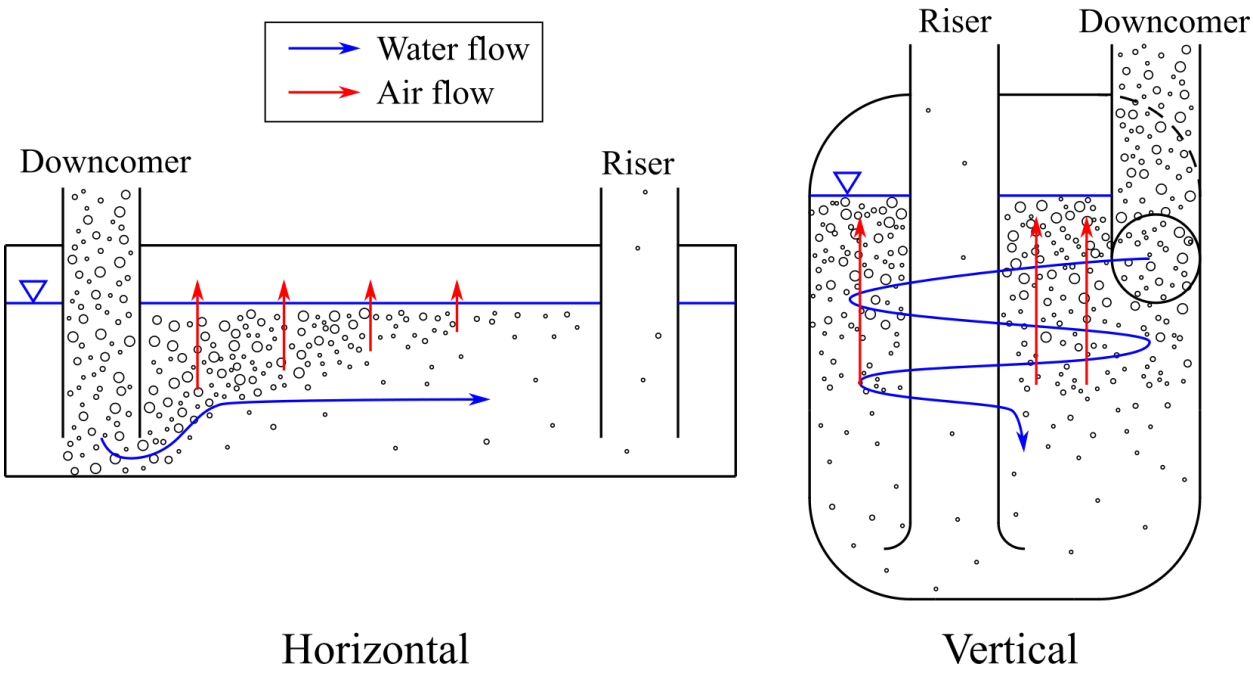

Figure 4.5: Horizontal and vertical separator orientations

In a HAC, a vertical separator is best applied in the case where the downcomer and riser share a single shaft. A horizontal separator is appropriate when the riser is a separate shaft from the downcomer or if there is a requirement for buffer storage of air. Beyond design restrictions on separator fit and HAC operation, vertical separators are cheaper, easier to install, and smaller, but do not work well at high flow rates (Laleh et al., 2012b). Based on this assessment, HACs at the largest scale are likely to use horizontal separators.

4.3.1 Flow field CFD model

The purpose behind solving for the flow field inside the separator is to define the environment against which the bubble distribution is tested. The parameters of interest are the flow velocity components for separator effectiveness and the difference in total pressure between the downcomer attachment (inlet) plane and the riser attachment (outlet) plane to evaluate head loss.

Figure 4.6 shows the meshed solids that feed the CFD model, which represent the water mass inside the horizontal gravity separator at Baby HAC and the vertical gravity separator at Dynamic Earth HAC (both of these prototypes are described further in chapter 5). In this section, all settings have been left as default except those that are specifically addressed below.

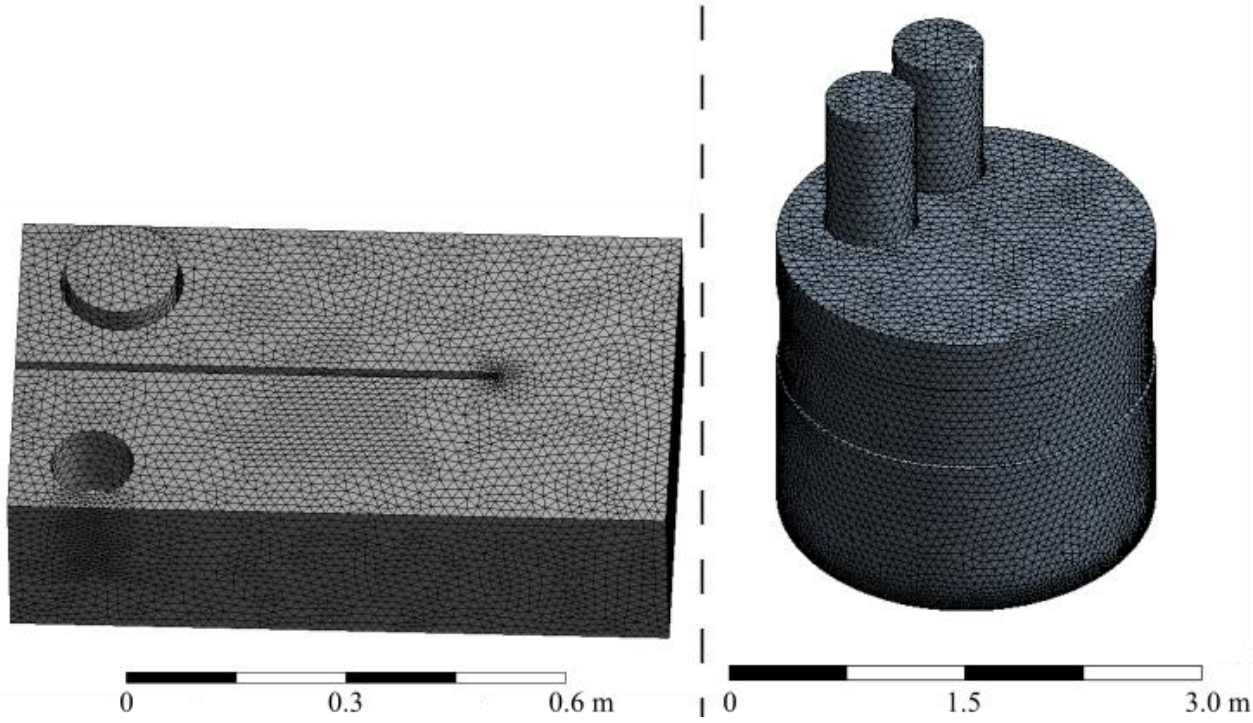

Figure 4.6: Fluent mesh for the Baby HAC horizontal gravity separator (left) and the Dynamic Earth HAC vertical gravity separator

Both meshes were generated in the ANSYS Workbench application (version 17) using the default settings for Fluent meshes with the exception of the following parameters:

- Mesh type: tetrahedral
- Relevance center: fine
- Element size: default
- Initial size seed: active assembly
- Smoothing: mediumTransition: slow
- Span angle center: fine
- Use advanced size function: on: proximity and curvature
- Transition ratio: 0.272
- Inflation algorithm: pre
- Collision avoidance: layer compression
- Shape checking: CFD
- Element midside nodes: dropped
- Straight sided elements: N/A
- Number of retries: 0
- Rigid body behaviour: dimensionally reduced

These parameters result in a finer mesh than would ordinarily be used to solve a problem of this type. A fine mesh was preferred in this case to place the mesh quality parameters well within safe limits (minimum orthogonal quality greater than 0.1 and maximum skewness less than 1, see: Table 4.3), but also because the solution time of this part of the problem is small compared to the potential solution time for separator effectiveness. The total solution time for the full span

of flow rates for one separator geometry with the finest mesh was approximately 8 hours (compared to ~1 hour for a coarse mesh). Because each set of solutions for one variation of separator geometry is subsequently used for hundreds of bubble model simulations, time-saving measures on mesh optimization do not improve the overall calculation time for separator effectiveness by any meaningful amount.

Skewness is a measure of how close each element is to the ideal equilateral or equiangular shape. Lower values represent less skewed elements. Orthogonal quality is evaluated for each cell face is a measure of how close the normal direction of a cell face is to the vector between the centroids of the two adjacent cells (ANSYS, 2009). The value reported for each cell is for the worst face (i.e. closest to perpendicular). Higher values represent better orthogonal quality. The solution process is slower, but there is better detail of the internal flow field for the separator effectiveness models; it tends to converge more reliably with fewer solution errors.

Table 4.3: Mesh quality parameters for both CFD models. The minimum orthogonal quality is low for the vertical separator in a small area of narrow geometry within the mesh

	Horizontal (Baby HAC)		Vertical (Dynamic Earth HAC)	
	Skewness	Ortho. quality	Skewness	Ortho. quality
Maximum	0.841	0.992	0.976	0.993
Average	0.230	0.769	0.232	0.767
Minimum	0.000	0.159	0.000	0.002

The meshed fluid body has been rounded-off in sharp corners where the geometry requires a finer mesh to define the boundary. Sharp features tend to degrade both measures of cell quality

for the cells that comprise them, increasing solution times and creating problems with numerical stability where the mesh size gradient is extreme (e.g. in corners generated by two curves approaching tangentially). Given that any such corners are along the boundary and that both the boundary layer and any regions immediately adjacent to more than one boundary layer will have low flow velocity, the effect on head loss and separator effectiveness estimation should be small. These locations are also places where moving bubbles are unlikely to be and where the assumption of free-field bubble motion is poor. For these reasons, this modification to the water body geometry is appropriate.

Both models are three-dimensional, double precision, single phase, and steady flow (i.e. not transient). Fluent always uses the continuity (one equation) and momentum equations (three equations for three-dimensional models). The flow at the separator inlet (i.e. downcomer outlet) is a fully-developed pipe flow and the largest source of pressure drop is expected to be at the end of the downcomer leg in the separator, based on the pipe flow calculation. No extreme pressure or velocity gradients are expected in either separator model, so the standard turbulent k-epsilon viscosity model (two equations) was used. Water was selected as the fluid medium with constant density at 998.2 kg/m^3 and viscosity at 0.001003 kg/m·s.

Four boundaries were set in the model: downcomer, riser, plenum interface, and wall. The downcomer and riser boundaries are the circular faces representing the separator connection to the respective pipes; the plenum interface is the face that represents the water surface within the separator; and the wall is all other faces collected together into a single boundary.

The downcomer boundary was set as a mass flow inlet. Both CFD models (Figure 4.6) were run once for each member of sets of defined water flow rates corresponding to experimental

conditions set out later in the work in Table 6.6 (Baby HAC) and Table 6.7 (Dynamic Earth HAC). The turbulent conditions at the inlet were defined using the intensity and hydraulic diameter model, where the hydraulic diameter was 0.102 m for Baby HAC and 0.575 m for Dynamic Earth HAC and the turbulent intensity is determined using the equation recommended in the Fluent user's guide (ANSYS, 2009):

$$I = 0.16 \cdot Re^{-1/8} \cdot 100\% \tag{4.5}$$

Substituting mass flow rate for velocity in the Reynolds equation results in a turbulent intensity equation fully determined by model parameters:

$$I = 0.16 \cdot \left(\frac{4 \cdot \dot{m}_l}{\pi \cdot D \cdot \mu}\right)^{-1/8} \cdot 100\% \tag{4.6}$$

The riser boundary was set as a pressure inlet with zero total pressure. There is no lookup for any property based on pressure, so total pressure is used to reference pressure drop from one cell or one face to another. Because the outlet is defined at zero total pressure, the separator pressure drop is equal to the total pressure evaluated at the inlet during post-processing. This boundary has turbulent condition properties assigned in the same fashion as for the inlet, for the case where there is backflow in one or more cells of the outlet. No outlet backflow occurred over the course of the CFD modeling process described in this thesis.

The plenum interface is a wall boundary with a zero shear condition, so that the velocity at the surface is not restricted by the presence of the edge. The wall boundary for all other faces has a zero slip condition, which sets velocity in all directions at the wall to zero.

The CFD model was initialized using the hybrid initialization method included in Fluent and solved with the SIMPLE model using the following settings:

- Gradient: least squares cell based
- Pressure: second order
- Momentum: second order upwind
- Turbulent kinetic energy: second order upwind
- Turbulent dissipation rate: second order upwind

The default convergence criteria were used where the scaled residuals for each of the equations must reach 10^{-3}. During the solution process, the continuity equation failed to meet this convergence criterion in nearly every case. The convergence was improved by reducing the under-relaxation factors for all of the variables to 0.2, but not corrected to the point that it would meet the default convergence requirements. An additional convergence monitor was added to monitor the area-weighted average of total pressure at the inlet, which converged to a constant value. This convergence problem was probably caused by the calculation of the scaled residual. The scaled residual is calculated as a fraction of the lowest (best) absolute residual from the first five iterations of the post-initialization solution (ANSYS, 2009). Because this model is relatively simple and the flow incompressible, the continuity equation may be converging well in the initialization or during the first five iterations of the solution so that the absolute residual being used to produce the scaled residuals is low. If this scaled residual does not reach 10^{-3}, then the automatic convergence detection does not flag the calculation as complete. Despite not reaching this scaled residual convergence target after 2000 iterations (Dynamic Earth HAC) or 1000 iterations (Baby HAC), the convergence of the continuity equation was deemed acceptable. To

verify that the mass flow continuity was okay, a manual check of the absolute residual mass flow difference between inlet and outlet was performed and passed (agreement within 10^{-6} of the total mass flow rate) for every model calculation.

Once the flow field has been solved in the CFD model, it must be extracted for use in the subsequent bubble motion model. The models described in sections 4.3.3 and 4.3.4 rely on area-weighted velocity components from the cells intersecting interrogation planes. One of the challenges involved in exporting data from the Fluent CFD model is the inability to extract the intersection area between the solution cells and an interrogation plane. It would be a mistake to equally weight all intersected cells, because the cells around the perimeter are both smaller and have lower velocity than those closer to the centre. The software can identify which cells are intersected by the plane and the velocity components associated with each one, and it can provide the cell volume. Equation (4.7) converts cell volume into an approximation of area.

$$A = x \cdot V^{2/3} \tag{4.7}$$

There is no reasonable analytical conversion method even for regular cell geometry. The constant (x) is solved to minimize the RMS of the error between the sum of areas generated with equation (4.7) and the actual area of each respective section. Table 4.4 shows that a single value results in a reasonable conversion on all planes. The individual error figures are not large, which is an indicator that this approximation should not create gross systematic error in the bubble motion solution.

Table 4.4: Comparison between summed cell area and actual area for interrogation planes in Baby HAC separator ($x = 0.69$)

Position	Area (m2)		Error (%)
	Converted	Actual	
200	0.0409	0.0439	-6.8
250	0.0426	0.0439	-2.8
300	0.0481	0.0439	9.7
350	0.0454	0.0439	3.5
400	0.0429	0.0439	-2.2
450	0.0454	0.0439	3.5
500	0.0461	0.0439	5.1
550	0.0443	0.0439	1.0
600	0.0423	0.0439	-3.6
650	0.0392	0.0439	-10.5

The simulated flow rate is the total flow rate through the separator. The design flow rate of a HAC is expressed as water flow rate. Because the simulation is single phase and the actual case is two-phase, the water flow rate should be down-rated by the gas volume fraction. For example, a modeled flow rate of 0.405 m^3/s in the Dynamic Earth HAC corresponds to a water flow rate of 0.385 m^3/s (see: section 6.4.3). This is a conservative assumption for both vertical and horizontal separators. In a vertical separator, the lower section of the vessel has a lower gas volume fraction and the flow velocity is lower than at the top. In a horizontal separator, the air content of the water reduces along the vessel length and the flow velocity should reduce. It is less conservative at higher pressures where the gas volume fraction is reduced.

4.3.2 Evaluating bubble size at inlet

In order to design separators for future HAC installations, a model that accurately predicts bubble size is required. The cost of inaccuracy in the bubble model is not low separator effectiveness, but more conservative separator design, increasing capital cost. From chapter 2, bubble size is characterized with the Rosin-Rammler distribution, which is described by two parameters: average diameter and spread. In section 2.3.9, four models were introduced that can be used to predict the 99th percentile bubble diameter:

Akita and Yoshida (1974):

$$d_{99} = 41.9 \cdot D \cdot \left(\frac{g_f \cdot D^2 \cdot \rho_l}{\sigma}\right)^{-0.5} \cdot \left(\frac{g_f \cdot D^3 \cdot \rho_l^2}{\mu}\right)^{-0.12} \cdot \left(\frac{j_g}{\sqrt{g_f \cdot D}}\right)^{-0.12} \tag{4.8}$$

Wilkinson et al. (1994):

$$d_{99} = 4.84 \cdot g_f^{-0.44} \cdot \sigma^{0.34} \cdot \mu^{0.22} \cdot \rho_l^{-0.45} \cdot \rho_g^{-0.11} \cdot j_g^{-0.02} \tag{4.9}$$

Hesketh et al. (1987):

$$d_{99} = 0.964 \cdot \frac{\sigma^{0.6} \cdot D^{0.5}}{\rho_l^{0.3} \cdot \rho_g^{0.2} \cdot \mu_l^{0.1} \cdot j_l^{1.1}} \tag{4.10}$$

Kobus (1984):

$$d_{99} = 0.00662 \cdot \left(\frac{Q_g^2}{g_f}\right)^{1/5} \tag{4.11}$$

Figure 4.7 illustrates the difference between these bubble size relationships. The conditions and pressure range were generated using the downcomer model produced by Young (2017) for the Dynamic Earth HAC. Note that none of these relationships agree with one another and the Akita and Yoshida (1974) relationship predicts an increasing diameter with pressure in contrast to the other three. Each of these relationships will be compared to a measured bubble size and separator effectiveness to determine which should be used for modeling in the future.

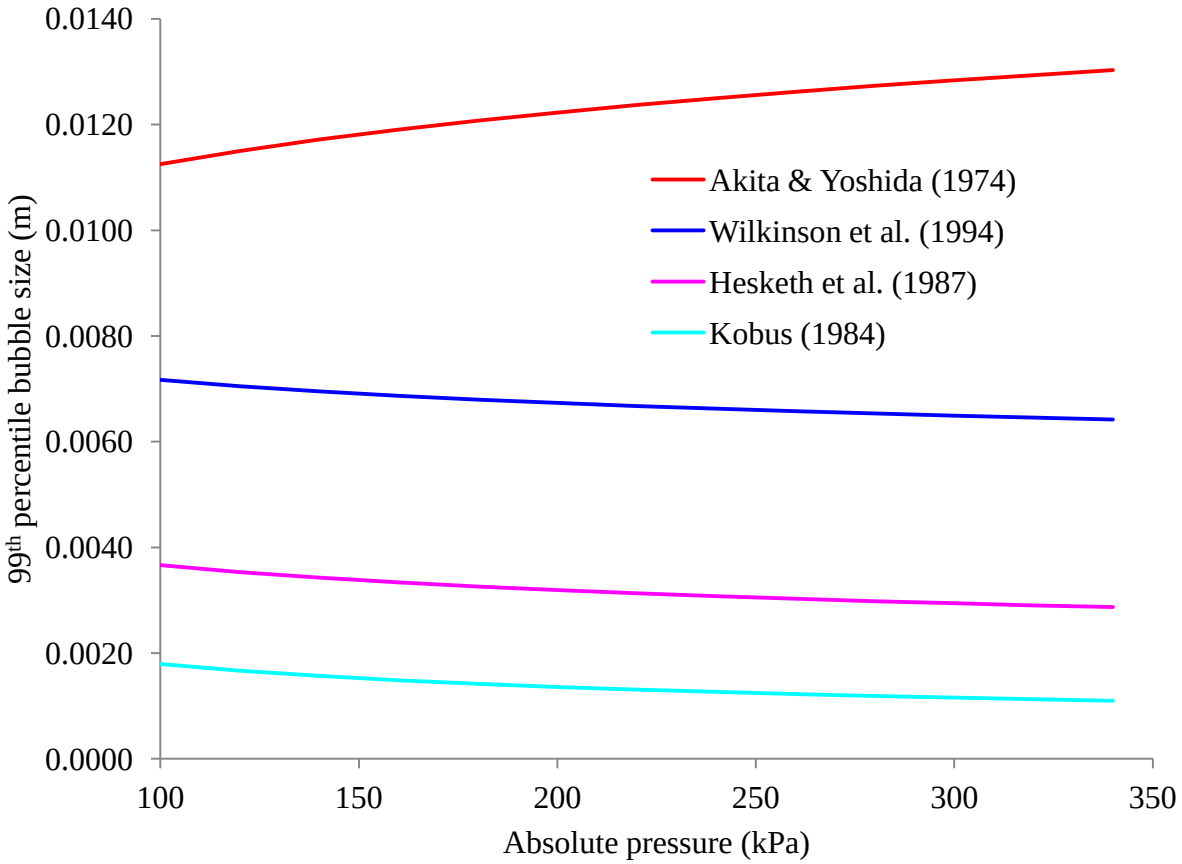

Figure 4.7: 99th percentile bubble size (d_{99}) prediction at 15°C at a water flow rate of 700 kg/s and air flow rate of 0.146 kg/s in a downcomer pipe with a diameter of 0.368 m

In order to convert these 99th percentile numbers into a distribution, the spread parameter and the Rosin-Rammler mean must be determined. It is common practice in the literature to calculate a single value for the spread parameter on all distributions (see: section 2.3.6). However, based on the literature distributions presented in Table 2.3, the spread parameter was found to vary by mean bubble diameter (see: Figure 4.8).

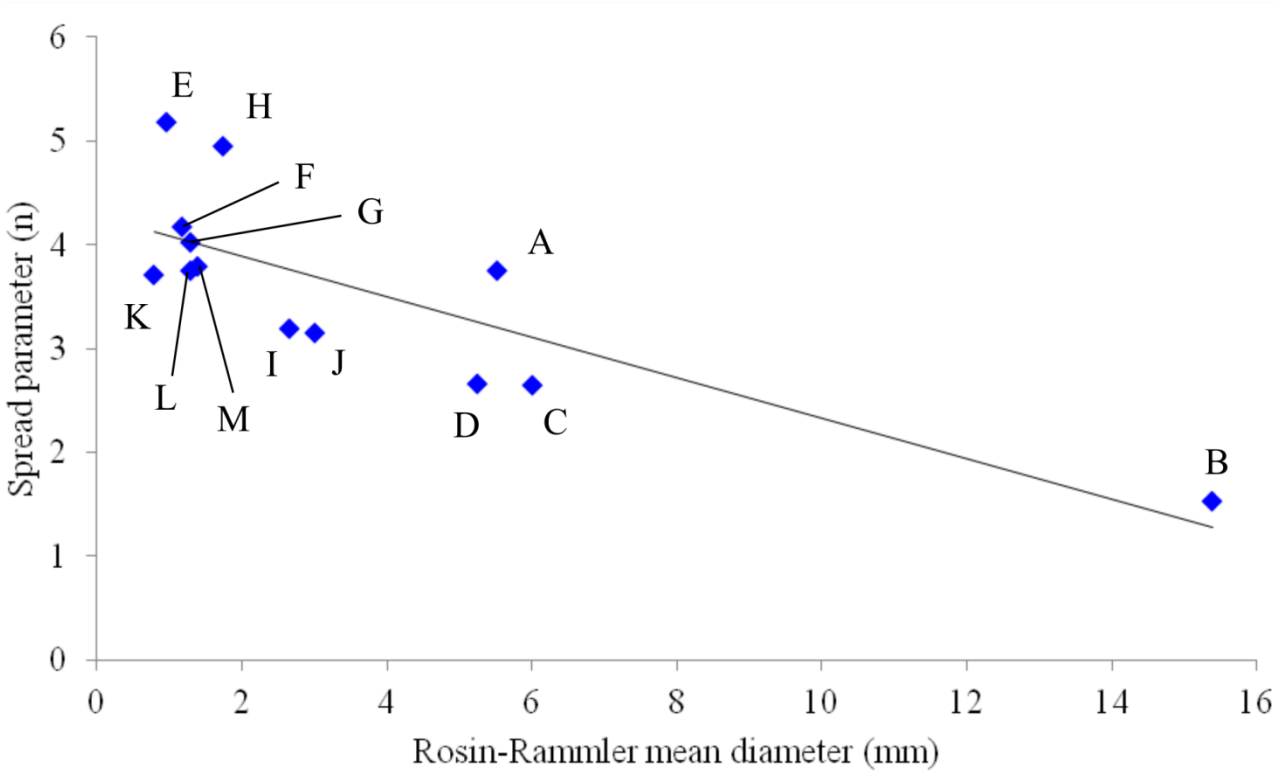

Figure 4.8: Relationship between Rosin-Rammler mean and spread parameter based on data presented in Table 2.3

From Figure 4.8, there is a relationship between Rosin-Rammler mean diameter ($\bar{d}$) and the spread parameter (n) in these natural bubble distributions, provisionally characterized for this dataset as linear (r^2 = 0.641). Equation (4.12) will be used in this thesis to calculate the spread

parameter of all distributions generated by one of the four models described above. Note that this equation takes the Rosin-Rammler mean in metres.

$$n = -195 \cdot \bar{d} + 4.27 \tag{4.12}$$

Using this relationship, the Rosin-Rammler distribution resolves to a single parameter fit:

$$Y = 1 - \exp\left[-\left(\frac{d}{\bar{d}}\right)^{-195\cdot\bar{d}+4.27}\right] \tag{4.13}$$

Using equation (4.13), the Rosin-Rammler mean can be computed using any percentile diameter. All four models have been tuned to produce the 99th percentile diameter. Because the Rosin-Rammler mean cannot be isolated in this single-parameter form of the equation, a numerical solver is necessary to compute it:

$$0.01 = \exp\left[-\left(\frac{d_{99}}{\bar{d}}\right)^{-195\cdot\bar{d}+4.27}\right] \tag{4.14}$$

4.3.3 Vertical velocity model for vertical separators

In a vertical separator, the net motion of the water is vertically downward. The horizontal component of flow is neglected. In order to separate from the water, the bubbles must have a relative velocity that is greater than the downward component of velocity within the water stream. Figure 4.9 illustrates a vertical gravity separator for a HAC where the downcomer outlet is away from the centerline and drives a swirling flow in the vessel. The swirling flow would contribute a small centrifugal force component, which is neglected in the separator effectiveness model.

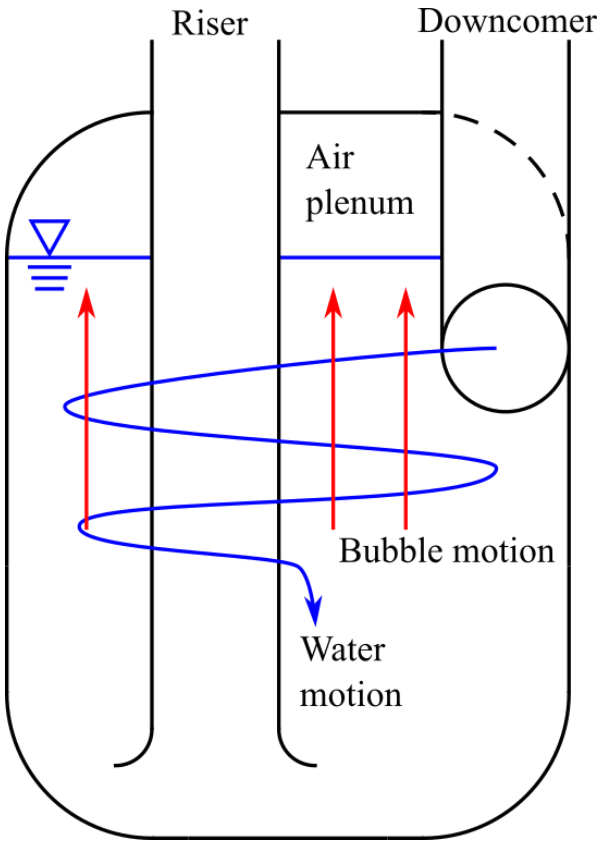

Figure 4.9: Bubble motion in a vertically-oriented separator opposes the motion of the water

The vertical velocity model is solved using the following procedure (steps 4-7 visually represented in Figure 4.10):

1. Generate interrogation planes and calculate area weights for each cell. This step only needs to be completed once for each mesh;
2. Use ANSYS Fluent CFD package to solve the flow field inside the separator. Solution settings are described in section 4.3.1;
3. Compute the Rosin-Rammler mean diameter for each of the four bubble size models presented in section 4.3.2;

4. Compute cut size for every cell on each plane (see below);
5. Convert cut size into separation effectiveness by cell using vertical velocity (see below);
6. Compute the overall separation effectiveness for each plane using area weighting;
7. Report separator effectiveness as the maximum separation effectiveness of all planes; and
8. Repeat steps 2-7 across the full range of flow rate.

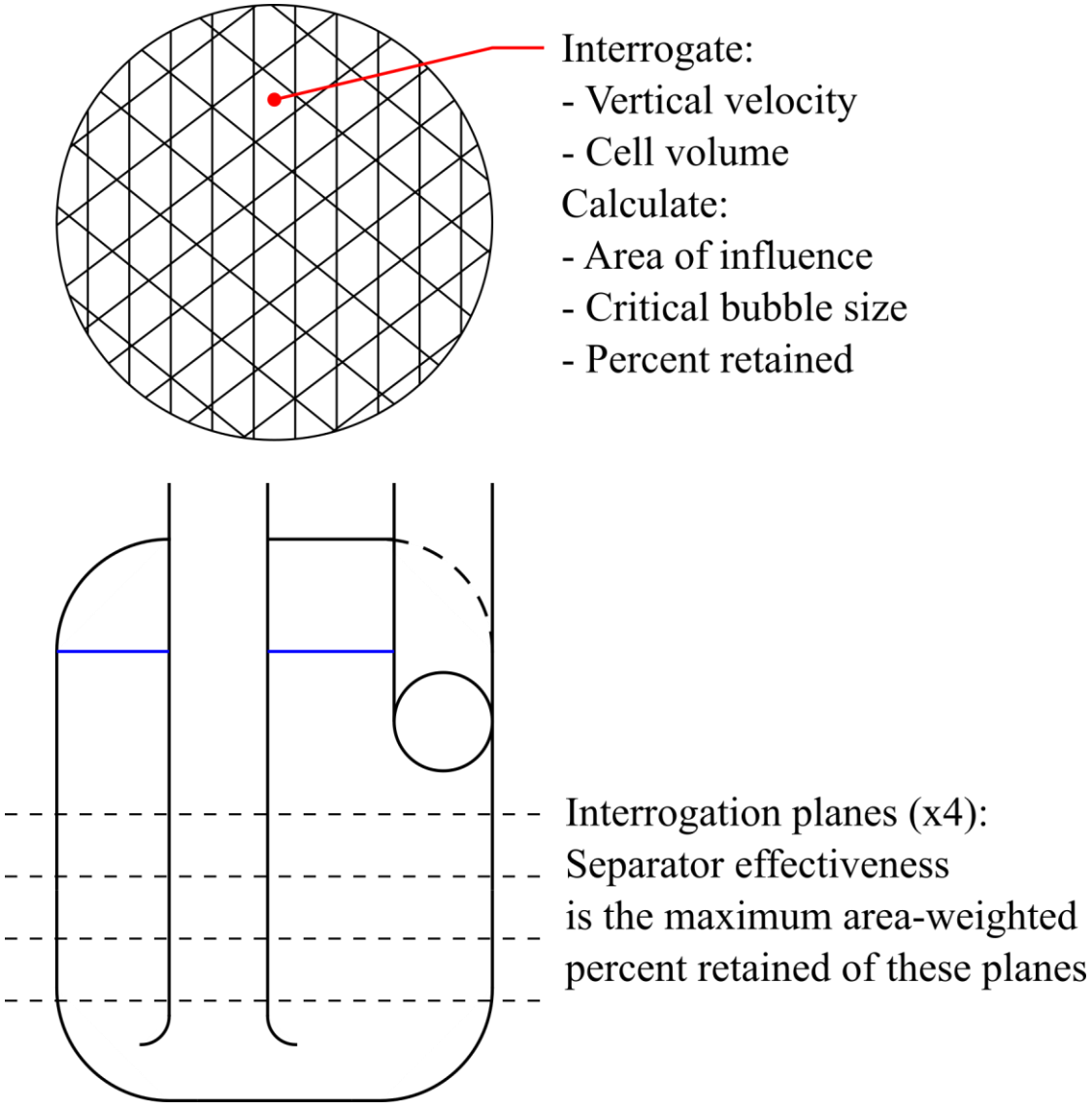

Figure 4.10: Vertical separator model calculation procedure

The mesh for a separator CFD model and the interrogation planes used to extract information from that mesh only need to be defined once for a given geometry. The interrogation planes are evenly spaced in the constant cross-section portion of the separator starting below the downcomer outlet and ending above the riser inlet. Figure 4.11 is a contour plot of the vertical component of velocity at the second interrogation plane down from the downcomer outlet on an early iteration of the Dynamic Earth HAC separator design. Note how the lower right-hand corner of the separator shows a flow short circuit, where water is flowing at high velocity down along that wall toward the separator bottom. This flow pattern was corrected in later iterations of the design by directing the downcomer outlet flow tangentially along the separator wall with a baffle to guide the flow into a more coherent swirl. Cell volumes are independent of the flow solution, so the area weights can also be calculated at this stage using the cell volume correction method described in section 4.3.1.

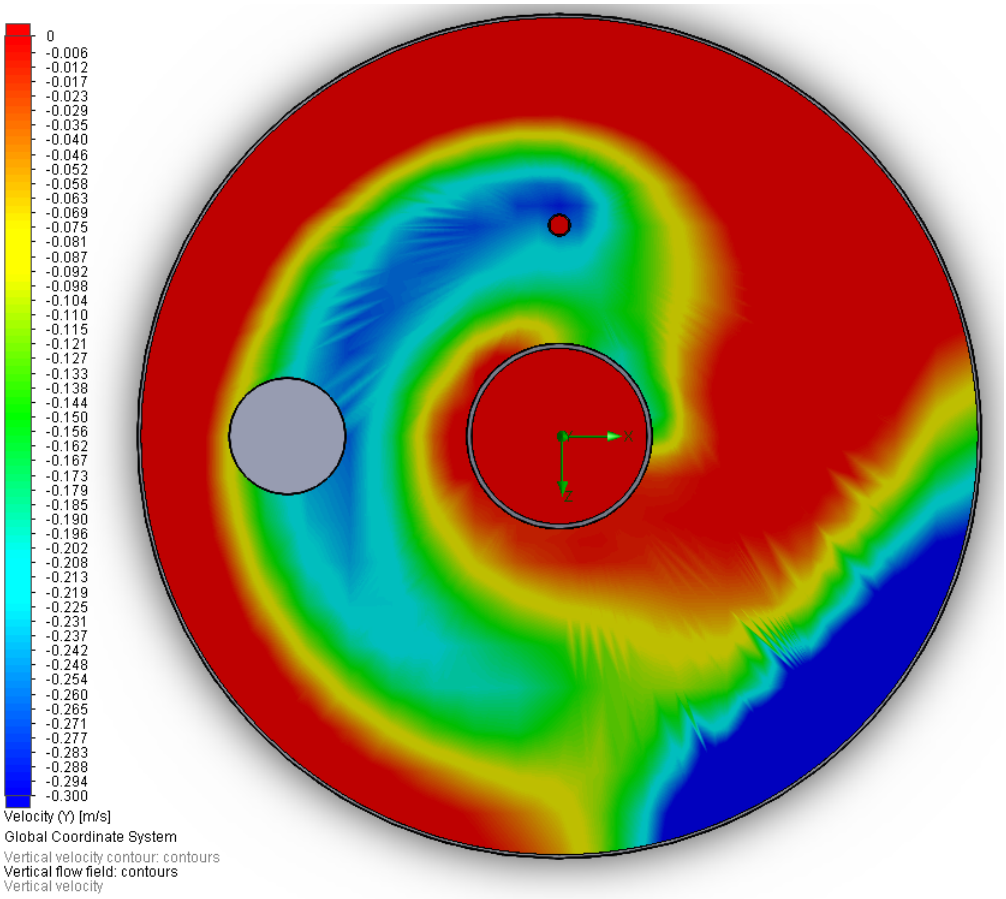

Figure 4.11: Cut plane of vertical velocity profile from an old design iteration of the Dynamic Earth HAC separator. The gradient represents the vertical component of velocity from red (zero or upward flow) to blue (downward flow in excess of 0.3 m/s)

The information required from the flow solution is the vertical component of velocity (Figure 4.11). If the velocity direction in the cell is upward or if the velocity is zero, then that separation effectiveness of that cell is set to 1. For cells with non-zero, downward velocity, the critical bubble diameter (i.e. the cut size) for that cell is determined using equation (4.1), where the magnitude of the vertical velocity in the cell is substituted for the relative velocity. The critical

diameter for each cell is converted to separation effectiveness as the volume fraction of bubbles larger than the critical diameter $(1 - Y)$ from equation (4.13).

An area-weighted average converts cell-specific separation effectiveness to separation effectiveness on each interrogation plane. This assumes that bubbles of all sizes are uniformly distributed across the entire cross-section of the separator. Once the separation effectiveness of each plane has been calculated, the maximum value is reported as the separator effectiveness. The maximum effectiveness is a better predictor than the average effectiveness, because the flow passes through all of the planes and there may be locally low effectiveness in the first plane in the sequence or where there is an unusual flow pattern along the separator length. This solution should result in a slightly conservative estimate of separator effectiveness. The vertical velocity in the lower planes should be slightly higher than actual, because the large bubbles should have already been removed by that point, resulting in slightly lower velocity.

4.3.4 Displacement model for horizontal separators

The displacement model is more complex than the vertical velocity model. Because the bubbles are moving perpendicular relative to the flow direction, it is not possible to use a simple check to determine whether or not a bubble of a given size will successfully separate. The displacement model tracks horizontal and vertical displacement along the separator length. In order to successfully separate, the bubble must migrate to a position above the water level before it reaches the riser inlet (see: Figure 4.12). This model also produces a more nuanced picture of how the bubble field should appear along the length of the separator, so that verification against an experiment does not solely rely on the overall separator effectiveness.

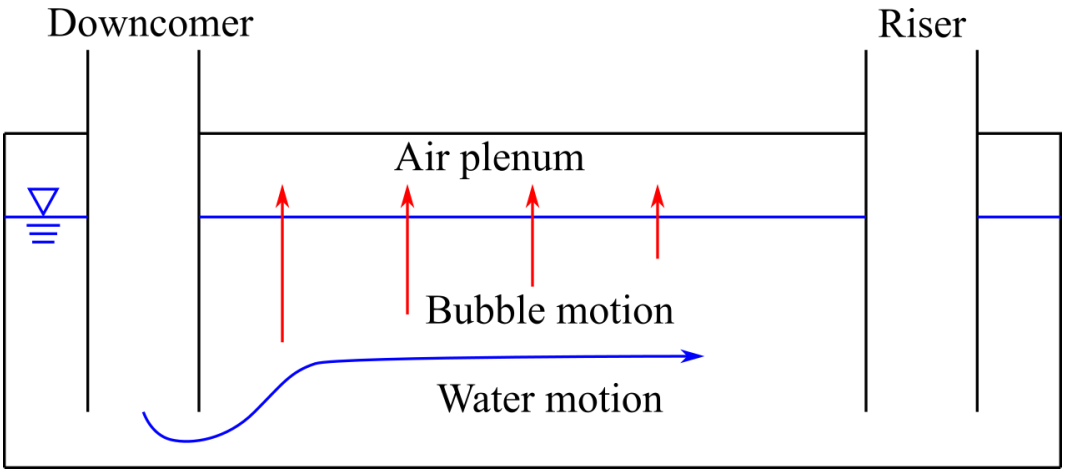

Figure 4.12: Bubbles in a horizontal separator are carried along its length by the flow and must rise to the surface before they reach the riser to separate

The displacement model is solved using the following procedure:

1. Generate interrogation planes and calculate area weights for each cell. This step only needs to be completed once for each mesh;
2. Divide the interrogation planes into evenly-placed segments (see: Figure 4.13);
3. Use ANSYS Fluent CFD package to solve the flow field inside the separator. Solution settings are described in section 4.3.1;
4. Compute the Rosin-Rammler mean diameter and spread parameter for a measured bubble size distribution;
5. Convert the Rosin-Rammler distribution from a function to a histogram;
6. Populate the lower segments (around the end of the downcomer pipe) of the initial interrogation plane with the bubble distribution. The distribution is tracked by the fraction of a bin present in each segment;

7. For each cell within a segment, calculate the vertical displacement for every bin in the bubble size histogram;
8. Using area weighting, move the fraction attributed for each bin into the segment nearest the displaced position at the next interrogation plane;
9. Repeat step 8 for all segments on the current plane;
10. Verify that bin fractions add to 1 at next interrogation plane;
11. Repeat steps 7-10 for all interrogation planes;
12. Compare model result to experimental observation; and
13. Repeat steps 3-12 across the full range of flow rate.

As in the case of the vertical velocity model, the CFD flow solution mesh and the interrogation planes used to extract information from that mesh only need to be defined once for a given geometry. The interrogation planes are evenly spaced in the constant cross-section portion of the separator starting at the center of the downcomer and ending before the turn in the separator. It was necessary to start the interrogation planes overlapping the downcomer, because the bubble plume is concentrated around the pipe at low and middle flow rates in the Baby HAC separator (see: section 6.4.2). Figure 4.13 shows both the interrogation planes after the downcomer pipe and the plane segments subsequently used in the displacement calculations. Cell volumes are independent of the flow solution, so the area weights can also be calculated at this stage using the cell volume correction method described in section 4.3.1.

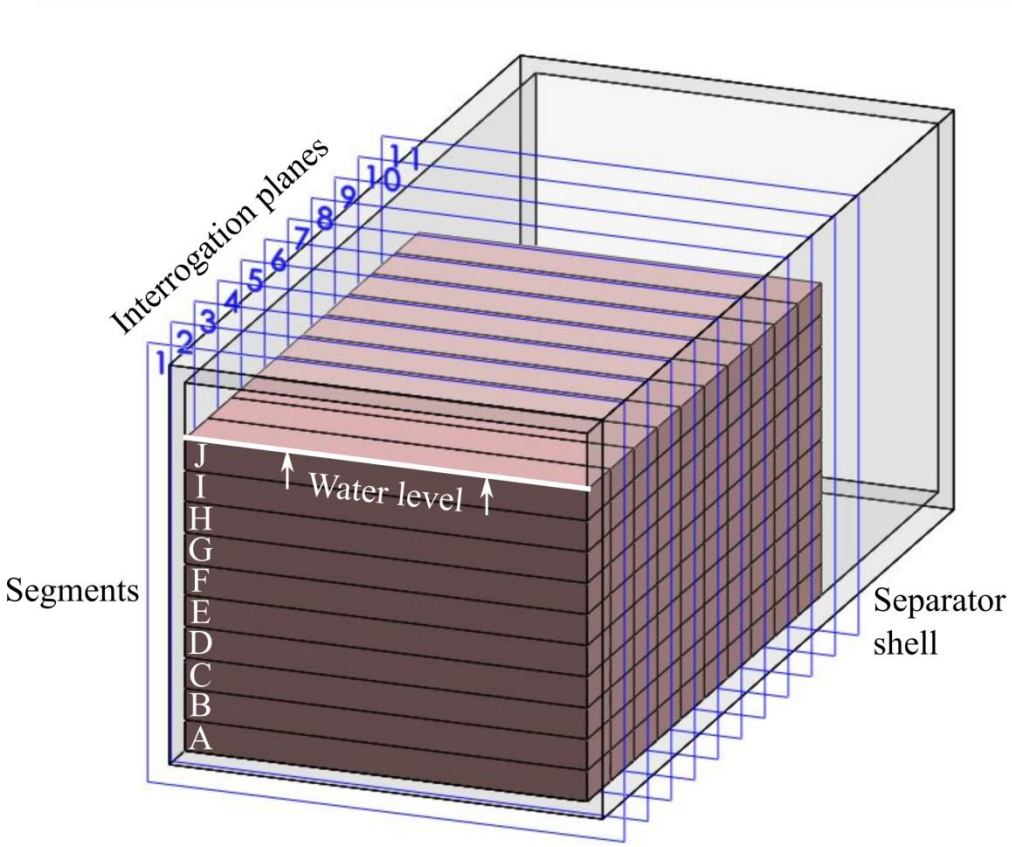

Figure 4.13: Schematic view of grid segments for displacement tracking vertically and along flow length

The Rosin-Rammler distribution of bubbles is converted into a histogram consisting of ten bins. The frequency for each bin is not used until the model has been solved. Instead each bin is divided into fractions and assigned to segments along the initial plane. These bin fractions add to 1 so that the checksum on each plane will immediately identify any problems. Within each segment, the bin fractions are further distributed into individual cells. Similar to the vertical velocity model, this distribution is area-weighted, assuming an even spread of the bin fraction across the segment into which it has been assigned. This is a probabilistic model, so the fact that the total volume of the bin fraction that exists in a cell at any time is likely to be significantly

smaller than the volume of a single bubble in the size range of that bin is immaterial. The bin fraction assigned to a cell or segment represents the probability that a bubble in that size range exists at that position at any given time.

The schematic in Figure 4.12 is a reasonable representation of how a downcomer exits into a horizontal separator. The downcomer outlet is positioned below the water surface to prevent backflow of compressed air up the pipe. The cross-section of flow along the separator length is also large with respect to the vertical pipe, sized in order to slow down the flow to allow separation to occur. Because of these conditions, the initial plane is best positioned after the flow turn at the pipe outlet in order to reduce the influence of uneven flow at the turn. The bubbles are not spread across all segments of the initial plane, but are spread evenly across the segments positioned at or below the downcomer outlet elevation. This leads to some unavoidable error in cases where there is significant bubble separation at the sides of or immediately after the downcomer outlet, which is most likely to occur at low flow rate.

Two velocity parameters are required from the flow field model: vertical velocity and velocity along the separator length. The horizontal velocity component perpendicular to the separator flow direction is neglected. The segments span the full width of the separator and motion along that direction is assumed to have only a small effect on the separator performance. For each cell, residence time (t) is calculated using equation (4.15), where the horizontal velocity (v_h) determines how long it takes for the fluid in that cell to reach the next plane, assuming that the velocity is constant along that line. This assumption potentially results in reduced accuracy unless the planes are closely-spaced.

$$t = \begin{cases} 0, & v_h < 0 \\ 5, & v_h = 0 \\ \dfrac{l}{v_h}, & v_h > 0 \end{cases} \tag{4.15}$$

The conditional explicit values in equation (4.15) are required by a few cases. Cells on wall boundaries of the CFD mesh have zero velocity, by definition. They are significantly smaller and fewer in number than the cells in the bulk flow away from the boundaries. This case was set to an arbitrary value of 5 seconds in order to allow the model to solve. When the bubble motion solution mesh is scaled up for simulations of larger separators, this number should also be scaled. Negative values of horizontal velocity would create negative residence time, which would again 'break' the model. Allowing the residence time to be 0 seconds passes the bubble distribution from that cell directly into the next plane without shifting the vertical position. Cells with reverse direction velocity only occur in plane with the downcomer and riser pipes or around the end of the baffle (if present in the design). Ideally, the planes should be selected to start close to but not penetrating the downcomer pipe and avoid the end of the baffle and riser pipe. An additional case not included here is one where the velocity of the cell is sufficiently low that the residence time exceeds 5 seconds. For the Baby HAC separator solution at 3 kg/s water flow rate (minimum flow), the fraction of cells for which this condition applied was 0.076%, which is not a large enough fraction to warrant special accommodation.

Vertical displacement is the absolute vertical velocity of a bubble of a given size multiplied by the time for which that velocity applies:

$$\Delta s = (v_r + v_v) \cdot t \tag{4.16}$$

If the vertical component of flow velocity (v_v) is positive in a cell, then the vertical displacement is boosted by that amount. If it is negative, then the vertical displacement is inhibited or may even reverse. A fluid moving slower horizontally, by equation (4.15), increases the time over which that vertical velocity condition applies. Bubbles with sufficient vertical displacement can jump multiple segments, and the velocity pattern from the skipped segment is ignored in the model. This behavior is expected to be most common for larger bubbles, where the vertical displacement is expected to be dominated by relative velocity.

Once the vertical displacement is calculated for a bin size in a cell, the bin fraction assigned to that cell is reassigned to the nearest segment on the next plane (see: Figure 4.14). If a bubble moves above the position of the water level inside the separator, the bubble is considered to have separated (i.e. merged with the air plenum) and is no longer tracked from that point except to verify the checksum at each plane. After the calculation for one plane is completed, the bin fractions are tallied on for the next plane. The segments to which the bin fractions have been assigned use the same area-weighting procedure as for the first plane. The potential error generated by this assumption is mitigated by the close spacing of the segments.

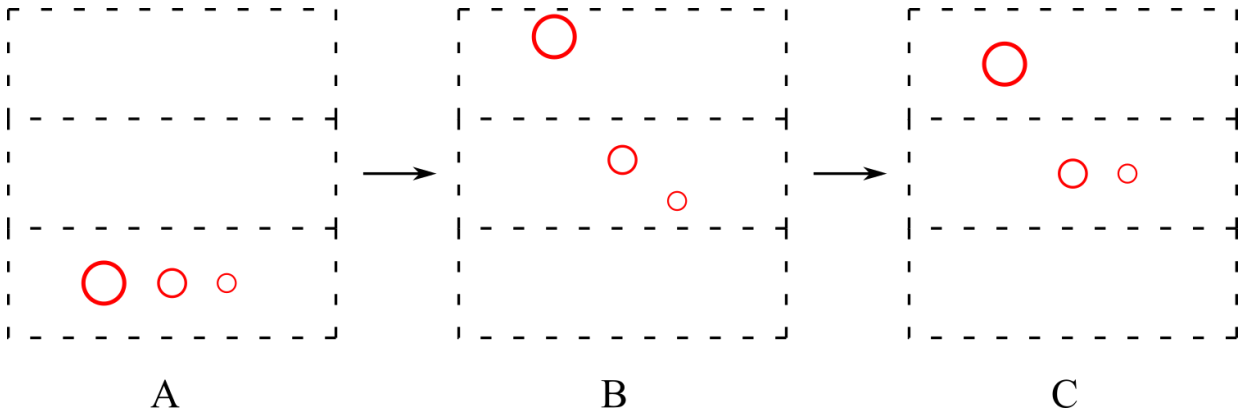

Figure 4.14: Progression of the displacement tracking model: (A) initial – bubbles of different sizes starting in the same initial segment; (B) displacement – vertical displacement calculated over time required to move horizontally to next slice; (C) final – bubble position assumption for next plane

4.4 Summary

The objective of this modeling effort is to produce a system of prediction of head loss and separator effectiveness for separators in HACs that is accurate enough for design, to be validated experimentally in chapter 6. Head loss across the separator reduces the work available for air compression. Accurate prediction of head loss identifies potential problems in the design before construction so that correction can be applied earlier in the project. Separator effectiveness contributes to the total air yield of the system. An undersized separator is likely to have an extremely poor effectiveness (see: section 2.3.11). If the separator effectiveness model is inaccurate, then the separator design must be conservative. A more accurate model allows the designer to shrink the separator closer to the model prediction, and thereby reduce capital cost.

In the first pass, head loss is evaluated using a one-dimensional pipe and channel flow analysis. Once the major design faults have been identified and corrected, then a second-pass CFD model

provides a more accurate estimate of head loss and is also used in the separator effectiveness models.

The separator effectiveness model is divided into two cases for vertically- and horizontally-oriented separators. The vertical model is a simple case, where the vertical component of velocity is matched to a critical bubble diameter (cut size) for each cell and converted into separation effectiveness. The displacement model calculates a cell-based residence time and the vertical displacement in that time for each bin fraction. It offers a more complete picture of where the bubbles in each bin appear along the flow length. Both models use an area-weighting assumption where bubbles are assumed to be evenly distributed across the plane or segment and the cell-by-cell analysis affects the whole in proportion to its fraction of the plane or segment area. This assumption and the unpredictability of the bubble size distribution at the separator inlet are the two most likely sources of error in the model, to be addressed in chapter 6. The Visual Basic code for both of these models is included in full in Appendix A. The results of these analyses are presented alongside the respective experimental results in sections 6.4.2 (Baby HAC) and 6.4.3 (Dynamic Earth HAC). Sample tables from the displacement model of the Baby HAC separator are presented in Appendix J.

Chapter 5

5. Experimental platforms and methodology

Two prototypes were constructed to complete the experimental work described in this thesis: an initial prototype ("Baby HAC") and a larger pre-commercial demonstrator ("Dynamic Earth HAC" or "demonstrator"). The Baby HAC prototype was constructed in December, 2014 as a relatively low-cost test bed to develop experimental protocols and establish the control methodology for the planned demonstrator HAC. Its construction in transparent PVC (see: Figure 5.1) opened the process up to observation and it led to a better overall understanding of HAC operation. Design faults in this prototype (the consequence of changing from run-of-rive to pumped operation and the lack of information available on HAC operations in the literature) and observations made of the process itself led to improvements in the design of the Dynamic Earth HAC demonstrator. Most of the experimental work presented in this thesis was completed on Baby HAC owing to significant delays in the construction of the demonstrator as well as the benefits of the transparent construction.

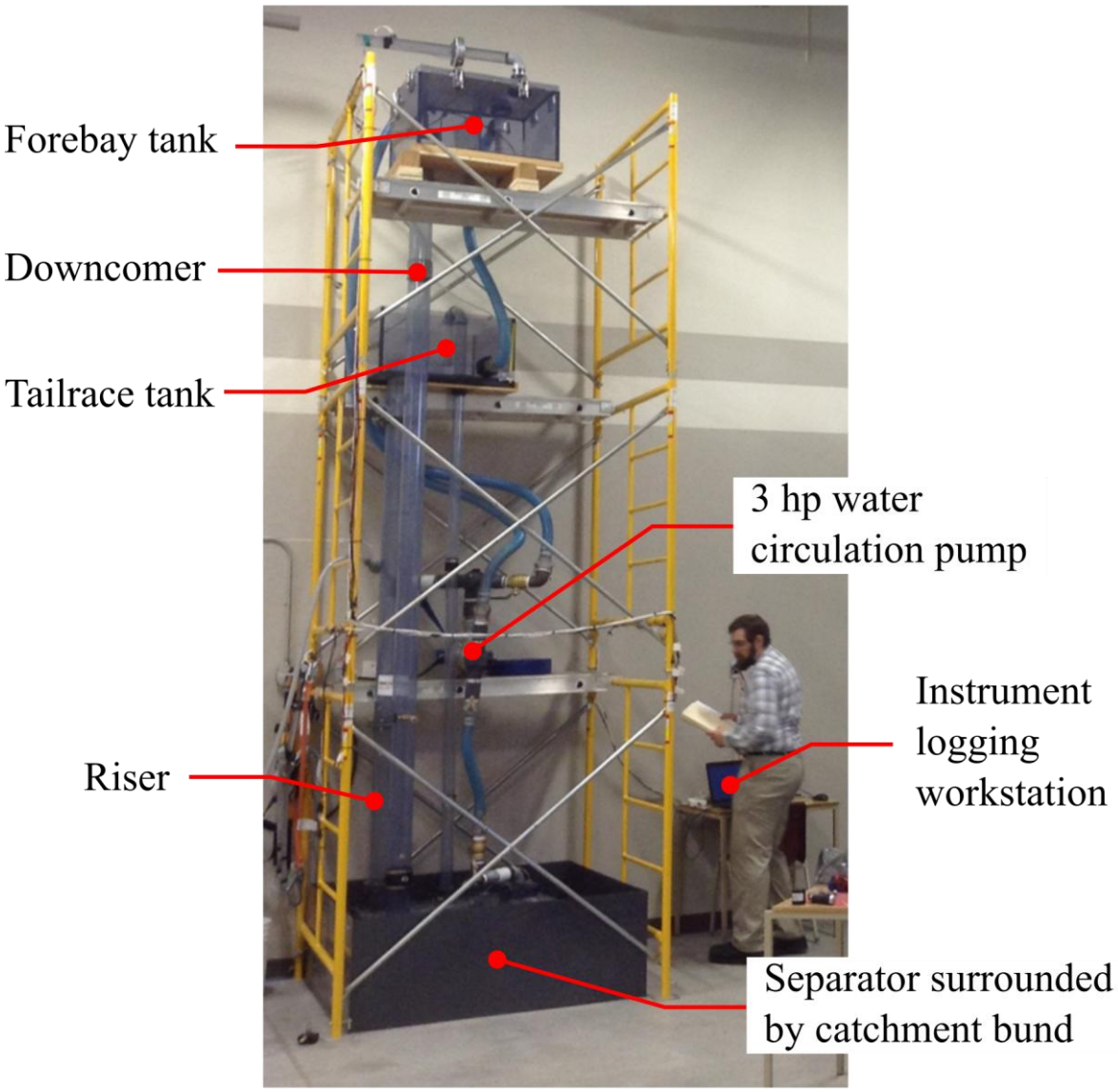

Figure 5.1: Baby HAC prototype located in the lab Cambrian College

The Dynamic Earth HAC demonstrator was completed in June, 2017. The enclosure shown in Figure 5.2 encompasses approximately half of the total height of the compressor. An advantage of the site was a pre-existing abandoned elevator shaft that houses the lower half of the compressor, including the separator. The demonstrator was intended for commercial-scale testing of components at a high enough pressure to generate a measureable signal of yield (i.e.

compressed gas not recovered on account of its being dissolved in the water) for gas solubility experiments by Young (2017), including air with no indicator gas (e.g. high CO_2 concentration). The pressure developed by Baby HAC was too low to dissolve enough of the components of air to change the composition (Young, 2017) and it was recognized early in the process that a higher pressure HAC would be required to perform the gas solubility experiments.

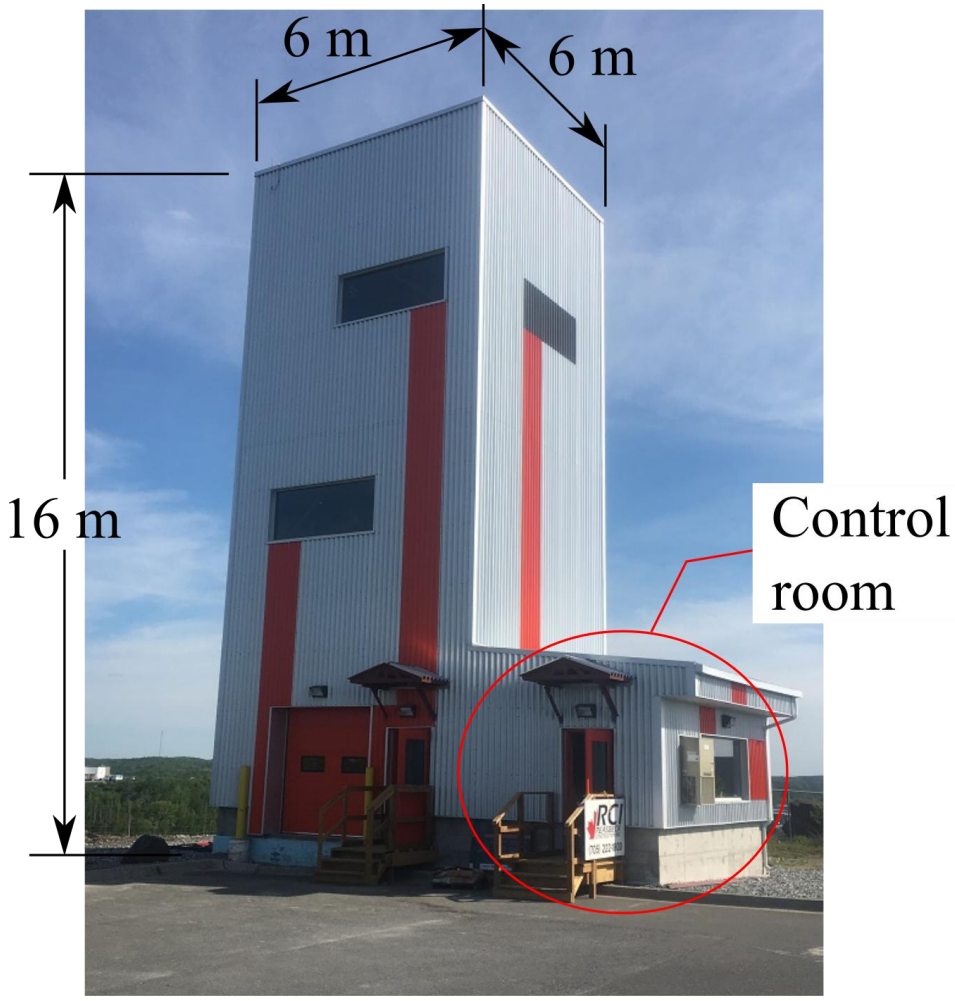

Figure 5.2: HAC enclosure at Dynamic Earth in Sudbury, Ontario (Electrale Innovation Limited, 2017)

5.1 Baby HAC prototype

The physical scale of Baby HAC (i.e. downcomer and riser diameters, water flow rate, and head) was based on a museum model of the HAC at Ragged Chutes in Cobalt, Ontario (Parks Canada, 2013), and was made to fit in a 1.5 m x 1.5 m (5 ft x 5 ft) footprint on a scaffold tower. It has a total height of 5 metres. This size was selected as the upper limit of what could be reasonably moved and assembled by hand, and which could be observed and controlled from ground level. Figure 5.3 shows the major components of Baby HAC from the design drawings. The catchment bund is not shown, which surrounds the separator on all sides and is capable of containing the total volume of water in the system with a generous allowance for splashing. The system is filled with water using a sink tap near ground level and does not require pressure boosting to reach the forebay tank. The full fabrication drawings for Baby HAC are presented in Appendix B.

The downcomer is a 4 inch (10 cm) schedule 40 PVC pipe. This dimension and the driving head (~1 m) were selected from the museum model. The design flow rate was set using the minimum practical flow velocity of 0.3 m/s identified for a HAC downcomer at prototype-scale (i.e. downcomer diameter on the order of 1 inch) presented in Rice (1976). In a 4 inch pipe, this corresponds to approximately 2 kg/s of water flow rate. The pump selected for Baby HAC was intended to deliver up to 10 kg/s, and actually delivers up to 8 kg/s according to the flow instruments at maximum flow rate on Baby HAC.

The riser is a 6 inch (15 cm) schedule 40 PVC pipe. This dimension is not critical to the function of the HAC except that flow losses in the riser consume energy that would otherwise be consumed in the compression process. A 6 inch pipe is convenient because it is the next standard

size up and not significantly more expensive than a 4 inch pipe, but consumes less than 5 centimetres of head even at the maximum design flow rate of 10 kg/s.

All other pipes and hoses were 2 inch (5 cm), which allows parts to be standardized across process connections. The maximum common size for national pipe thread (NPT) fittings and pipes is 2 inches and PVC glue-in socket fittings and adapters are available in the same size. The air outlet pipe is an exception, where it was necessary to use a small-bore control valve to achieve the fine control necessary to hold the separator water level steady during operation.

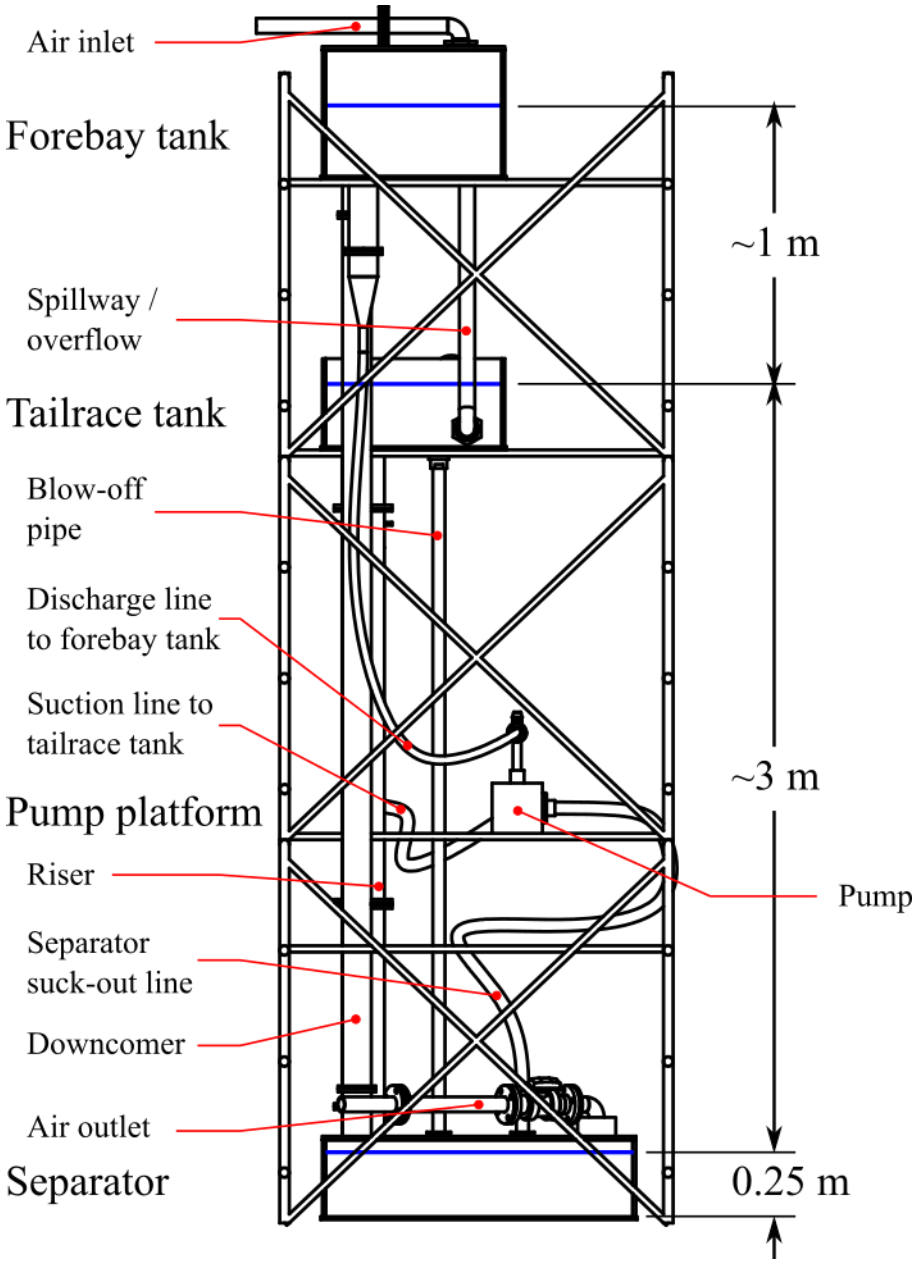

Figure 5.3: Labeled front view schematic of Baby HAC from design drawings. Not shown: fill/drain line, catchment bund, and electrical connection

5.1.1 Instrumentation

The measurement scheme for Baby HAC consists of several instruments divided into four categories: flow rate, temperature, pressure, and water level. Water and air flow rate are each measured at a single position using orifice plate flow meters with differential pressure (DP) instruments. Temperature and pressure are used for thermodynamic property lookups in REFPROP (NIST, 2018). Air temperature was measured in the forebay and water temperature is measured in the forebay and separator. Pressure is measured adjacent to the forebay tank and inside the separator. Water level is measured in the forebay and tailrace tanks with pressure sensors. The water level in the separator tank is calculated using those levels and the total quantity of water in the system. Each of these instruments is describes in detail at the end of this subsection.

Electrical measurement on the pump motor is not included, because the compression loop (i.e. flow from forebay tank to tailrace tank) can be treated as independent from the pumping leg. The pump could be controlled by a throttling valve to reduce the flow rate and the addition of instruments to measure electrical power use would have resulted in more cost for the instruments and additional DAQ space that could not be accommodated by the limited equipment budget. Electrical metering at low flow rate would show that most of the hydropower generated by the pump is dissipated across the throttling valve. This prototype was designed to be low-cost and easy to erect and operate. It was not designed for high efficiency.

Analog proportional voltage output instruments were selected to take advantage of the low cost, good availability, and high reliability of automotive instruments. All analog signals and instrument power are transmitted on 16 AWG (American wire gauge) wire, which has a low

resistance of 0.013 Ω/m (Daycounter, Inc., 2016). Voltage drop along the transmission wires has been neglected. The data acquisition unit (DAQ) used for Baby HAC is a National Instruments model USB-6211. It has a high analog to digital conversion resolution at 16 bits (National Instruments, 2014) and sufficient analog input ports to meet the needs of the instrumentation specification with spares available for expansion. The 16-bit conversion is applied to a range of either ±5 V or ±10 V, depending on the instrument. The other range options were not used for this project.

The digital signals from the DAQ are numerical values of measured voltage. These are converted live into physical values using a program written in LabVIEW. LabVIEW is a visual programming language by National Instruments, which is intended to interface with their data acquisition equipment. Figure 5.4 is a screen capture of the interface that controls logging and displays the status of the Baby HAC instrumentation. Key functions from this program are included in Appendix C.

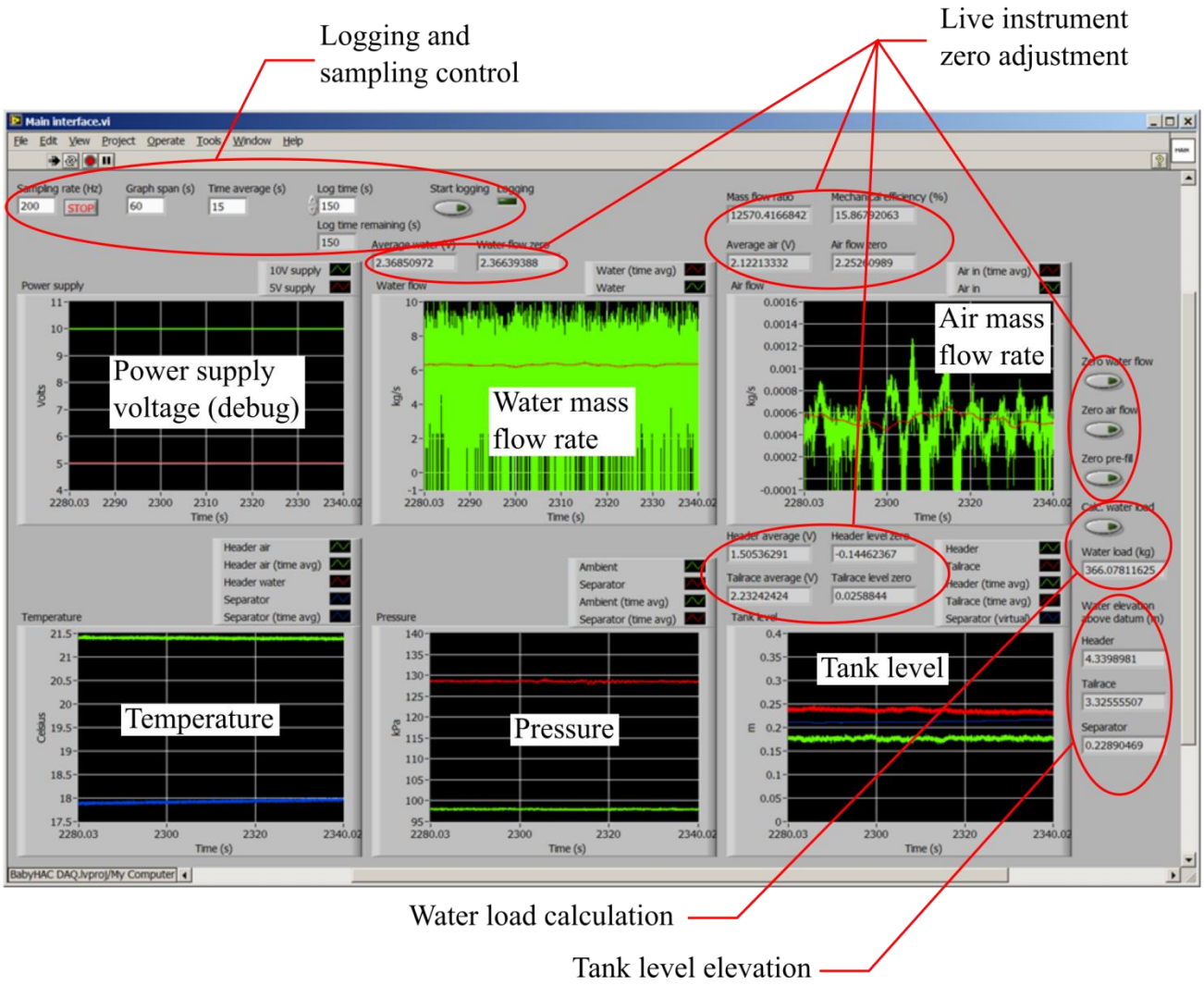

Figure 5.4: Instrumentation interface for Baby HAC

All instruments described in this section include nameplate information on accuracy and range and the calibration procedure. Voltage measurements for calibration were taken using a digital multimeter. The calibration tables are presented in Appendix D.

Water flow rate:

Flow rate on Baby HAC is measured using pressure drop across orifice plate flow meters for both water and air flow. An orifice meter is composed of three basic components: the orifice plate, DP sensor, and pressure tappings. Each of these components is matched to the application and to each other. For accurate measurement, an orifice meter requires at least five pipe diameters of straight pipe downstream and as much as possible upstream (Howe and Lipták, 2003). It was not possible in Baby HAC to position the orifice meters for maximum accuracy on straight pipe, but this requirement ruled out metering in hoses. The orifice flow conversion code in Visual Basic from an Excel converter (from DP to flow rate) is included in Appendix E. This was copied into the LabVIEW program, presented in Appendix C.

Water flow rate is measured in the riser pipe. Because it is present in the compression loop, there was a trade-off between unrecoverable head loss and flow meter accuracy. The orifice diameter is 9 cm, sitting inside a pipe with an internal diameter of 15 cm. This was selected to use as much of the DP sensor scale as possible without consuming so much head that the HAC didn't operate properly. With these dimensions, the maximum flow rate of Baby HAC at slightly over 8 kg/s roughly corresponds to a pressure drop of 2000 Pa (see: Figure 5.5), which is approximately 20% of the nominal head.

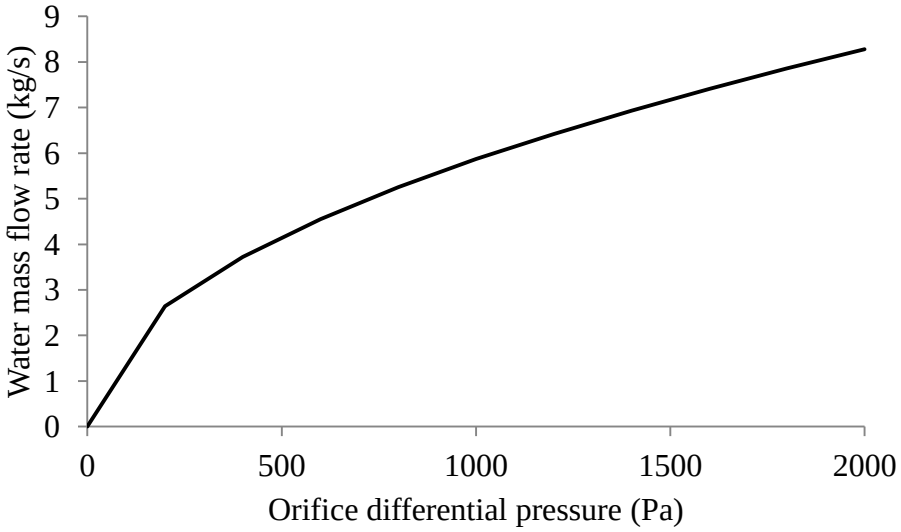

Figure 5.5: DP signal conversion to mass flow rate using the orifice meter calculator

The original sensor selected for this measurement survived less than 40 hours of operation before being rendered inoperable in a fashion consistent with damage due to water hammer (Omega, 2016). The Omega PX26 is a substantially cheaper alternative with a slightly larger minimum scale of ±7 kPa. At maximum flow, only 28% of the full scale is used, but no alternatives were available in a reasonable price range that included the possibility of more frequent replacement if additional sensors were to fail by water hammer. The instrument has an accuracy of ±1% of full scale, but its output voltage range is ±16.7 mV. The conversion from differential pressure to flow rate is nonlinear and the zero drifts rapidly, making the instrument particularly unreliable at low flow rate.

The instrument was calibrated using a static column of water over the high pressure port (P2) leaving the low pressure port (P1) open to air. First, the zero was established with both ports open to air and the voltage was recorded. The tube attached to P2 was filled to the full scale of

the instrument (69 cm H_2O). The water column was incrementally reduced and voltage recorded at each point until the column was emptied. The slope of the proportional response in calibration matched the expected slope from the datasheet (see: Appendix D). The instrument and its zero were stable during calibration, but during operation there is significant noise and zero drift. The frequency of noise peaked at 60 Hz (electrical noise and motor vibrations at 3500 rpm rotation speed), with lower peaks at 8 and 40 Hz (possibly due to transmission of harmonic vibrations through the rigid sensor mount). Zero drift is corrected in the procedure (see: section 5.1.3) and in the control program by resetting the zero frequently during the experiment. The measurement time period was limited to 2.5 minutes (150 seconds) so that the pump could be turned off and the zero reset between measurements.

The pressure tappings are located according to the radius taps method (Howe and Lipták, 2003), where the upstream tap is one pipe diameter from the plate and the downstream tap is half a pipe diameter from the plate. The flanges were too wide on the riser to be able to use the flange or corner taps method. Because the pipe is mounted vertically, there is potential for hydrostatic pressure to contribute to the signal. Static pressure difference across the DP sensor is eliminated by bleeding air from the lines so that the same static water column applies to both sides and the sensor itself is mounted horizontally (see: Figure 5.6). The friction losses along the pipe between the ports (23 cm apart) are expected to be small, so no correction has been applied.

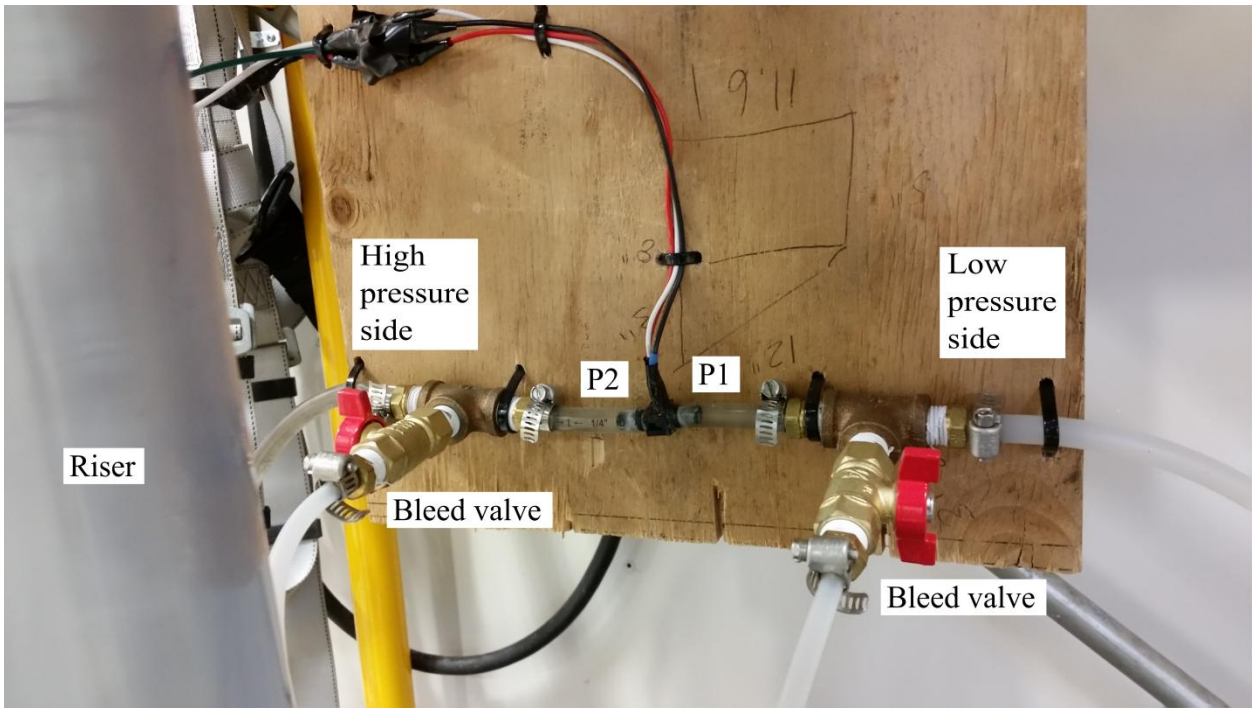

Figure 5.6: Water flow meter DP sensor board

Air flow rate:

Because there was no potential for measureable loss of air yield at the pressure developed by Baby HAC (Young, 2017) and because the separator was oversized, the air mass flow into the system at the forebay and out of the system at the separator should balance. Therefore, air flow rate was measured only at the intake pipe. This position was selected because an incorrect setting of the outlet valve position for perfect separator level control would tend to lead to a higher or lower reading than expected. If the separator water level increased over the logging period (limited to 150 seconds by the zero drift of the water flow meter), then there would have been a net decrease in the air stored in that tank. That would mean the total air vented would be equal to the total produced plus the difference in stored quantity over that time period. The disadvantage of air measurement at inlet is that the air flow is less steady than the separator outlet flow

because the periodic variation of water level in the forebay tank creates a mild piston effect, solved using a time average flow rate.

The orifice diameter is 1.3 cm, sitting inside a pipe with an internal diameter of 5.2 cm. This instrument carries less risk than the water flow meter of disrupting the process. The orifice was sized to slightly below the minimum recommended ratio with pipe diameter (Howe and Lipták, 2003) to maximize the pressure signal. At 2 inches, the pipe is at the minimum recommended size for orifice metering, but still slightly too large for perfect measurement of the air flow attained at Baby HAC.

An Allsensors 1 INCH-D sensor was selected to measure the pressure difference for this application. It has a scale of ±1 inch H_2O (249 Pa) corresponding to 0.5-4.5 V with an accuracy of ±0.25% of full scale, excluding temperature shift (Allsensors, 2014). The zero offset voltage and span have some variability between instruments, so calibration was required to determine both parameters.

The instrument was calibrated against a TSI DP-CALC Model 5815 digital micromanometer that had a resolution of 1 Pa. An air duct and fan assembly was used to create differential pressure for the instrument. At each operating point, the DP sensor was checked against the manometer in both directions (positive and negative pressure). The fan was not able to develop pressure below 70 Pa, so the calibration does not include points between 0-70 Pa and -70-0 Pa. Both the slope and intercept of the linear response found in calibration were within the respective ranges identified in the datasheet (see: Appendix D). The instrument was observed to exhibit slight zero drift over the course of hours or days, so the LabVIEW interface and experimental procedure include setting the zero at startup.

The pressure tappings are located according to the flange taps method (Howe and Lipták, 2003), where the upstream and downstream taps are located 1 inch (2.5 cm) from their respective orifice plate faces. The corner taps method could not be used because the flanges are wide and the connection to the pipe is too brittle for drilling through the contact.

Temperature:

Temperature measurement on Baby HAC is used for thermodynamic property lookups in REFPROP for air and water (i.e. density, viscosity) and to demonstrate isothermal compression. The prototype is located indoors in a temperature-controlled workshop, so the air temperature range is limited to around 20-25°C. The water is sourced from a sink tap; city water has a minimum temperature of around 10°C, but usually sits around 15°C. While the HAC is running, the temperature increases over time from pump inefficiency and internal energy heat transfer from air in the downcomer. The maximum rated temperature for the clear PVC material is 40°C. Therefore, the expected temperature range is between 10-40°C.

Temperature is measured on Baby HAC with thermistors. These are cheap and readily available components where resistance varies with temperature on a fixed curve. The curve is published by the manufacturer for each model of thermistor. Variable resistance was converted to a voltage signal using a voltage divider, where a known, fixed resistance was wired in series with the variable resistor. If the supply voltage is known, measuring voltage drop across the fixed resistor provides enough information to calculate the resistance of the thermistor.

USSensors PS103J2 thermistors were selected for this application. These came pre-embedded in brass pipe fittings for installation, enabling placement in the tank below the water level without

requiring special consideration for wiring. For this sensor, the resistance at 25°C is 10 kΩ (USSensor, 2014) and it has a rated accuracy of ±0.1°C in 0-70°C range (Dankert, 1997). The voltage dividers use 10 kΩ resistors on a 10 V power supply, so that the mid-range temperature (25°C) creates an even split that measures a drop of approximately 5 V across the fixed resistor.

The thermistors were spot-checked against one another and a thermometer by submerging them in a bucket of water. All three reported within 0.1°C of one another and within 0.2°C of the thermometer reading of 16.7°C. Thermodynamic property calculation is relatively tolerant to error in temperature evaluation. For example, to register an error of 0.1% in the density of water, at a pressure of 100 kPa and an actual temperature of 20.0°C, the thermistor would need to report a temperature of 24.4°C (low) or 14.4°C (high). To maintain agreement between thermistors for the verification of isothermal compression, the resistance of each fixed resistor in the voltage dividers was measured with a multimeter and that measurement was used in place of the nameplate value in the temperature calculation.

Pressure:

Absolute pressure measurement on Baby HAC is used for thermodynamic property lookups for air and water. Pressure is measured at the top of the scaffold tower near the air inlet and in the separator tank. The separator pressure is also used occasionally for troubleshooting. The air inlet sensor reads atmospheric pressure, which is usually around 98.5 kPa (abs) in Sudbury. The separator sensor reads atmospheric pressure when there is no water in the HAC up to an operating pressure around 130 kPa (abs).

Freescale Semiconductor MPX4250AP absolute pressure sensors were selected for this application. This sensor has a measurement range of 20-250 kPa (abs) at a rated maximum error of ±3.45 kPa (Freescale Semiconductor, 2009). Three of these sensors were purchased, but only two were installed.

Each of the three sensors was checked against a pressure standard measuring atmospheric pressure and all were found to agree within 0.3% of the measured value (see: Table 5.1), which is an order of magnitude better than the rated accuracy. Only the separator pressure sensor was calibrated for off-atmospheric measurement. The sensor was calibrated in-situ using a static column of water in the HAC above the water level in the separator. Pressure was evaluated using measures of the supply and output voltage taken with a digital multimeter and the transfer function from the datasheet. These measures were repeated at increments of increasing water column height up to a total pressure of 127 kPa (abs). The pressure calculated using the transfer function in the datasheet matched the measured column of water (see: Appendix D).

Table 5.1: Barometer single-point calibration of pressure sensors

Instrument location	Multimeter reading (V)	Converted pressure (kPa)	Barometer reading (kPa)	Error (%)
Spare	1.7800	99.00	99.001	0.00
Atmospheric reading	1.7740	98.70	99.001	-0.30
Separator	1.7745	98.725	99.001	-0.28

Water level:

Water level in the forebay and tailrace tanks is used to calculate the total water load inside the HAC and the difference in elevations between these levels during operation determines the hydraulic head that drives the compression process. The forebay water level is additionally used to evaluate the performance of the mixing heads (see: section 3.5.2). Each of these tanks is 30 cm in height, so sensitive level sensing instruments are required.

An Impress Sensors IMSL IP86 was selected for this application. It measures water level up to 0.5 m H_2O with an accuracy of ±0.1% of full scale (Impress Sensors & Systems, 2014). The sensor consists of a submersible probe connected to a tube embedded in the cable that exposes the low pressure side of the cell to atmospheric pressure. The output is 0-5 V proportional. It is important to note at this scale that the sensor does not measure tank level exactly but the water column above the pressure cell. When the probe is resting on the tank bottom, the cell is positioned 0.5 inches (13 mm) above. This is corrected in the code with a zero offset.

These instruments were calibrated together in a bucket with incremental increases in water level to a total depth of 30 cm. The proportional response matched the datasheet for both instruments (see: Appendix D).

The zero reading was slightly different between the two, so each required its own zero offset in addition to the cell position offset described above. Similar to the flow meter DP sensors, the instruments were observed to exhibit slight zero drift over the course of days, so the LabVIEW interface and experimental procedure include setting the zero prior to filling.

The forebay sensor reference pressure is outside the tank. It was not possible to insert the tube back into the tank to reference the internal pressure, because the tube is too small to effectively seal and leakage would affect the air flow measurement. At low air flow rate, the pressure drop along the intake pipe was small, so there was little error in the measurement. At higher flow rate, the difference was noticeable, where the pressure in the forebay tank was as much as 30 Pa (or 0.3 cm of water gauge) lower than atmospheric. Because the level sensor referenced atmospheric pressure instead of this lower pressure, the level measurement was reading lower than actual. The maximum observed error in the forebay during testing at full flow rate was an underestimation of water level of less than 0.5 cm, except in the case of the test with no mixing head, where the air intake was unstable and hard to quantify. The evaluation that is affected is the mixing head comparison. Mixing heads that result in more net air flow into the system would tend to underestimate water level more than others. The effect was to slightly amplify the differences between mixing heads, which would not cause a poorer mixing geometry to appear to outperform a better one.

5.1.2 Mixing head designs

The mixing heads tested on Baby HAC were made based on designs used by Charles Taylor (the original inventor) at Ragged Chutes and the Peterborough Lift Lock described in Schulze (1954) and the snorkel design described in Bidini et al. (1999):

1. Ragged Chutes head
2. Peterborough head
3. Snorkel head (snorkel position adjustable or removable)
4. No head (blank pipe)

Design drawings for each of these mixing heads are presented at the end of Appendix B.

Ragged Chutes head:

The Ragged Chutes head is based on a design used by Taylor at very large scale. From the design of the water ports around the perimeter of the head (not included in the Baby HAC version) and the length of the pipes at the top of the original, it is apparent that the design intent was that it would operate as a snorkel. However, it never actually worked by that mechanism (see: section 2.2.3). The Ragged Chutes head for Baby HAC, shown in Figure 5.7, was 3D printed in one piece. The straight section slides into the 4 inch (10 cm) downcomer pipe. It is a tight fit so the head does not move during operation. The cyan line at mid-level marks where the top lip of the downcomer pipe sits when the head is in place.

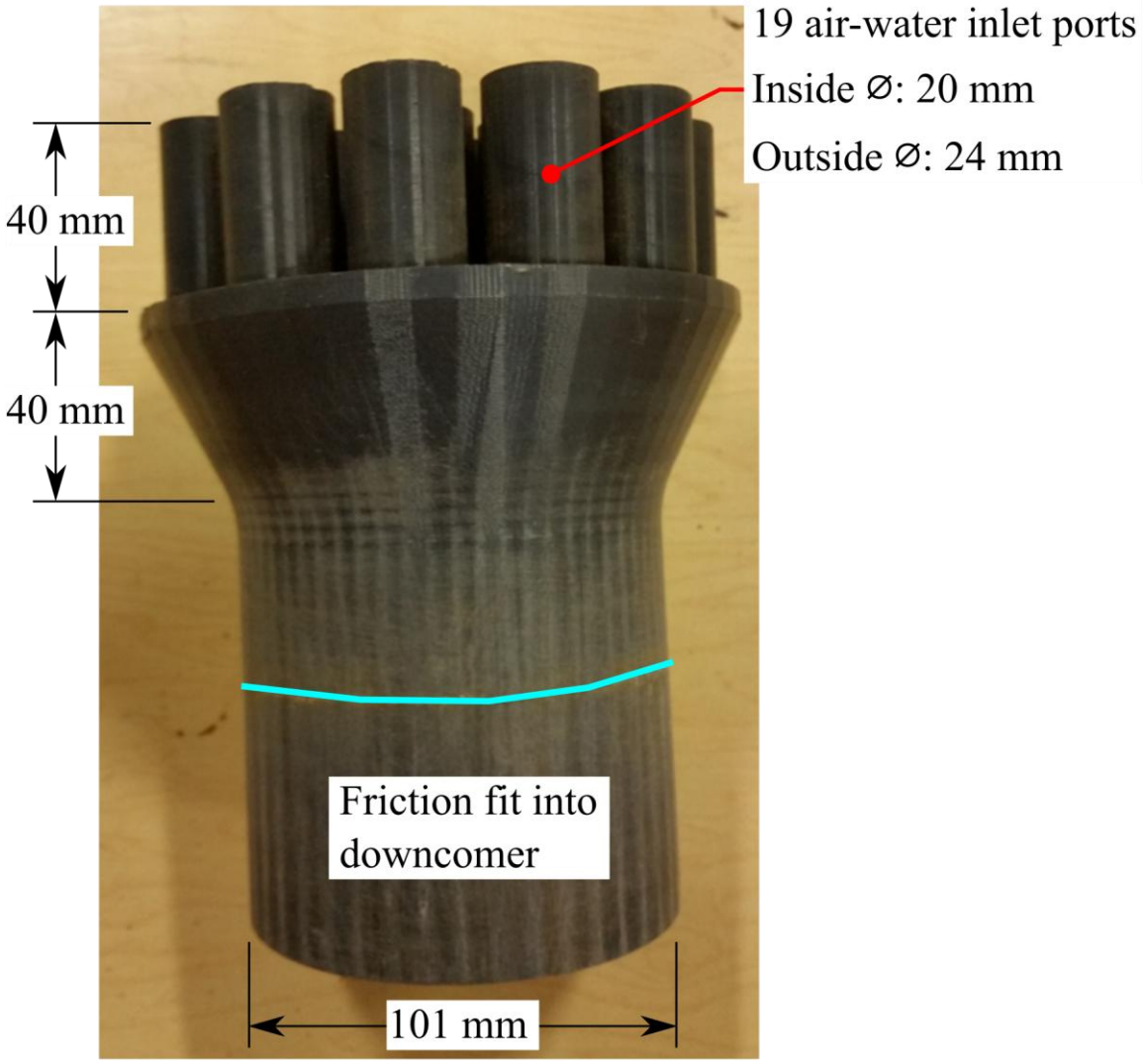

Figure 5.7: Ragged Chutes style mixing head

Peterborough head:

The Peterborough head is based on a different snorkel design. It consists of an air manifold lowered into an array of hydrofoils so that the ends of the air pipes are at the lowest pressure point in the assembly. This was not scaled down for Baby HAC so the same hydrofoil geometry used in the original Peterborough Lift Lock HAC mixing head could be tested. The same geometry was again reused for Dynamic Earth HAC (see: section 5.2.2). The Baby HAC version,

shown in Figure 5.8, was fabricated in two pieces, where the lower piece was 3D printed and the upper piece welded together. These were bolted together using threaded rod. To reduce the cost and overall height of the 3D printed piece, the head does not slide into the pipe, which instead slots into a lip at the bottom of the head.

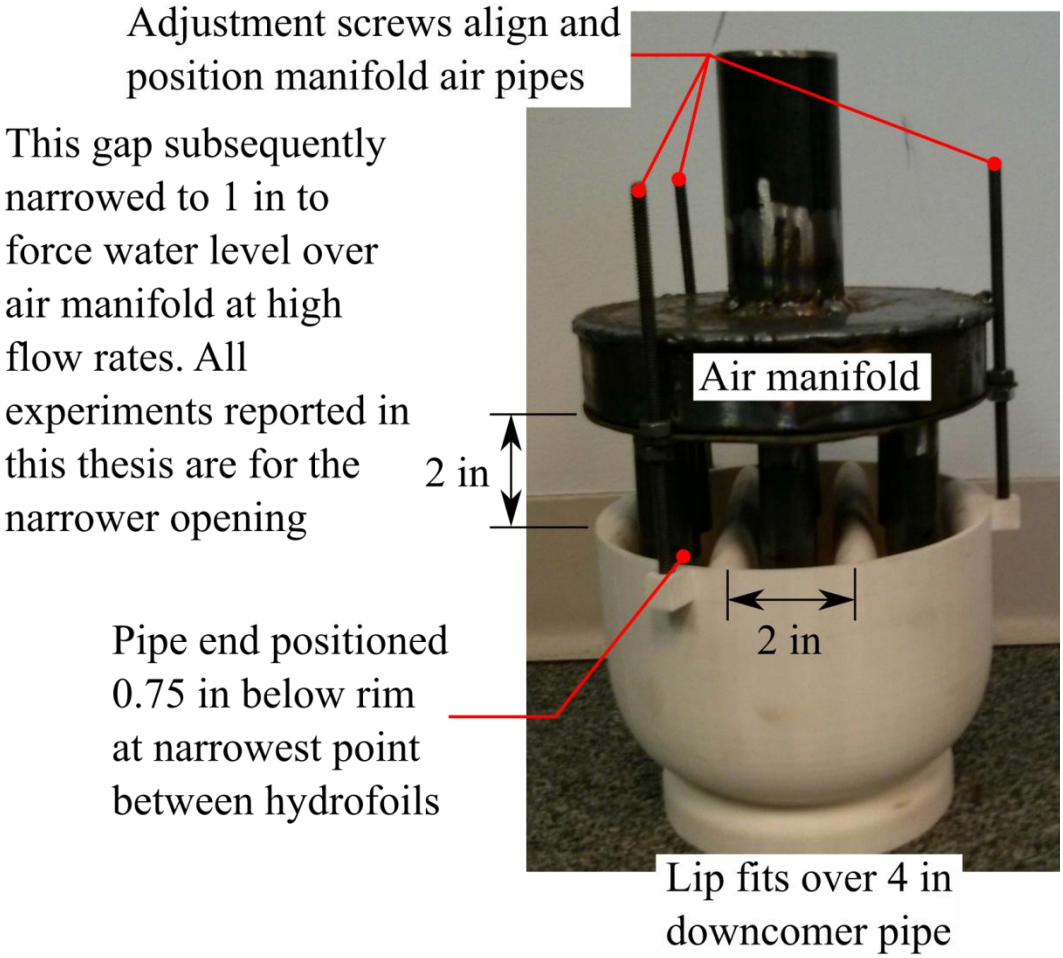

Figure 5.8: Close-up of the hydrofoils and air manifold of the Peterborough head

Snorkel head:

The snorkel head is based on illustrations of experimental HACs built by researchers investigating them for future development, most recently by Bidini et al. (1999). The initial snorkel concept didn't adjust properly and was tested once and subsequently replaced with a

steel pipe. The fins intended to hold the snorkel, however, act as an effective vortex breaker. The concept is simple: create a bellmouth inlet and find the optimal vertical position for the end of the snorkel. Figure 5.9 shows the components of the snorkel head. The snorkel has six possible positions and the head was additionally tested with the snorkel removed completely.

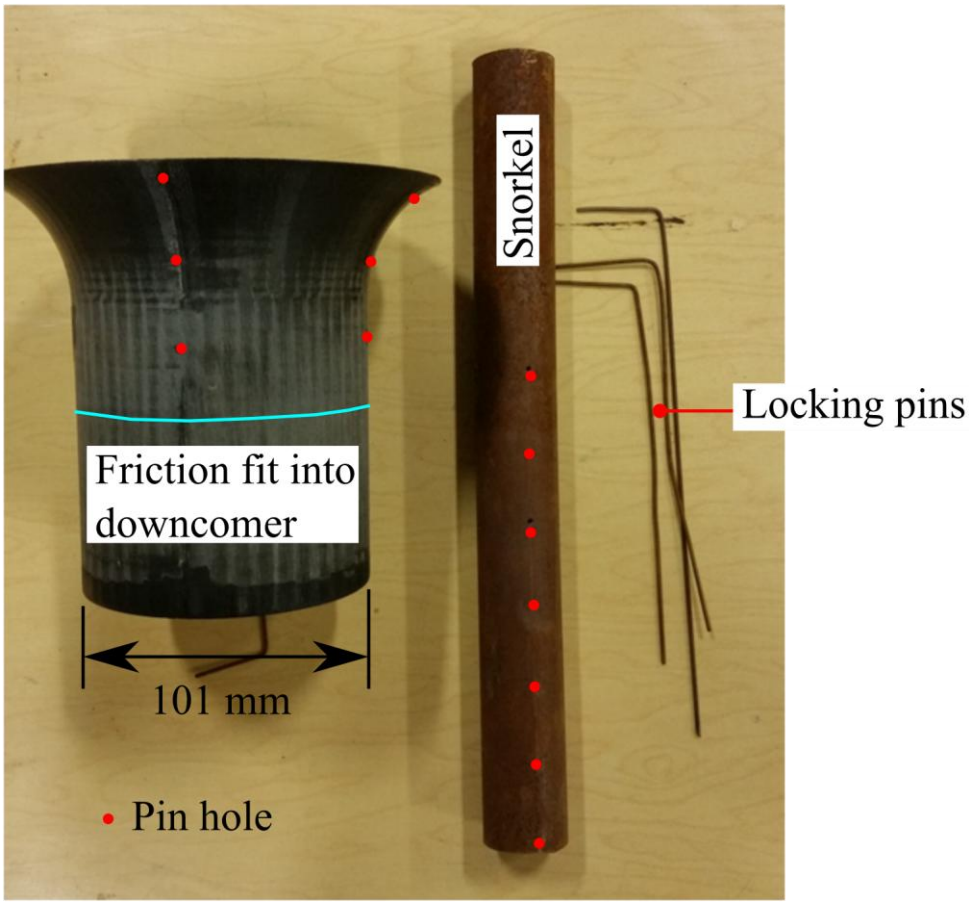

Figure 5.9: The snorkel of this head is installed by sliding the pipe into place and locking it into position with two pins

No head:

The final test is to see if and how the HAC works with no mixing head installed. This is the configuration that would most definitively prove that a HAC inducts air no matter what local geometry is employed at the top of the downcomer.

5.1.3 Measurement procedure – entrainment

The mixing head comparison is intended to determine which mixing geometry is associated with the least overall irreversibility. From chapter 3, the water level in the forebay over the lip of the mixing head (see: Figure 5.10) reflects the total energy required to accelerate the water flow, overcome inlet losses, and overcome the irreversibility associated with any air entrainment that occurs above that position. The second method identified is to check the air quantity entrained with water flow rate, assuming the total driving head is similar. The air quantity entrained is determined by the total system irreversibility for a given water flow rate and by changing the mixing head for the same set of system states, any difference in air flow is accounted for by the mixing head.

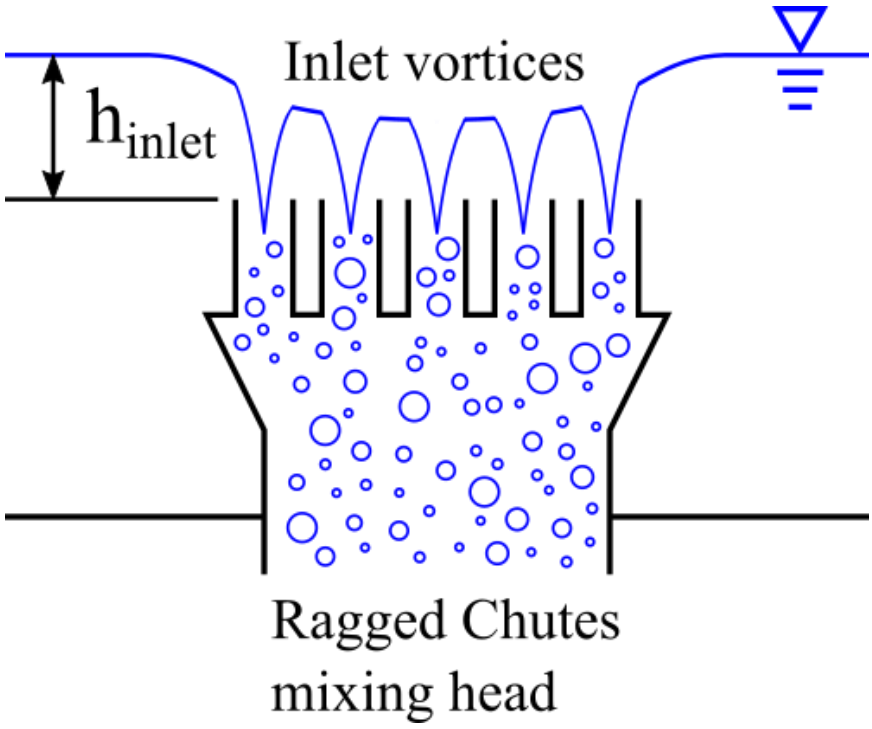

Figure 5.10: Water level measurement for an operating mixing head

All of the instruments were automatically logged in the LabVIEW code, including raw voltage, converted values, time averages, and secondary, calculated variables. Raw voltage readings are only used for troubleshooting. Time averages and secondary variables are used for troubleshooting, control of the separator water level, and to provide a visual indication of the state of the HAC in the control interface. Only the converted values in the log files were used to generate the data presented in section 6.1.

Instrument zero for the orifice flow DP and water level sensors is set inside the LabVIEW interface. To set zero, the process value must be held at zero (e.g. pump turned off and water levels equalized for water flow DP sensor) for at least the duration of the time averaging set prior to running the code. The time average voltage signal is used instead of the raw voltage in order to cancel noise, which can be substantive.

The experimental procedures described below focus on the steps required for measurement accuracy and logging and are somewhat abridged in terms of the physical operation of the HAC. The startup and shutdown procedures including filling, drainage, and logging setup can be found in Appendix F.

Pre-fill:

1. Install the mixing head for testing into the forebay tank;
2. Measure the position of the lip of the mixing head;
3. Latch and seal the forebay tank lid with duct tape to prevent air flow bypassing the inlet flow meter. Any leakage will degrade the accuracy of the air flow measurement; and
4. Zero the water level sensors. This only needs to be done once for a full day's testing.

Pre-start:

1. Add water to the HAC. Fill the separator completely and use the water load calculator to monitor the mass of water in the system. Stop when the water load is between 360-370 kg. This range provides adequate water across the entire flow rate range for all mixing heads without risk of spillover;
2. During filling, add at least 0.5 inches (13 mm) to the forebay tank. The forebay level sensor requires that its pressure cell is wetted for the hard-coded zero offset to be correct. This reading is required for the water load calculation described in step 1;
3. After filling, zero the air flow meter. Water in the tailrace tank prevents air from drifting from the inlet through the overflow (spillway) hose;
4. Bleed air from the lines leading to the water flow DP sensor; and
5. Set the choke valve after the pump to the minimum flow position.

Measurement:

1. Zero the water flow meter;
2. Turn on the pump;
3. After the bubbly flow reaches the separator, adjust the separator air valve to hold the level around 20-25 cm. If the level changes significantly during the logging period, the displacement of the water between the separator and tailrace tanks created by changes in air volume may affect the water flow measurement;
4. Start logging. It runs for 150 seconds and then automatically shuts off;
5. Close the air valve and stop the pump;

6. Check the water flow rate. If the time average settles at a value outside a ±2 kg/s envelope, reject the measurement and return to step 1. Ideally it should be well within this envelope and a smaller range should be used for measurements at low flow rate due to the nonlinear conversion from pressure. The logging duration for each run is intended to be short enough to minimize the number of measurements rejected at this step and long enough to flatten out the low frequency periodic air flow at intake;
7. Repeat steps 1-6 at least once for each position of the valve;
8. Nudge the pump throttle valve open a little to increment the water flow rate for the next test; and
9. Repeat steps 1-8 until the pump choke valve is fully open.

The measurement procedure above produces approximately 30 logs for each mixing head.

5.1.4 Separator design

Baby HAC has a horizontal gravity separator. The bubbly flow at the downcomer outlet is turned into a channel flow in the body of the separator. The water flows around a baffle and toward the riser inlet (see: Figure 5.11) as the air is separated into a plenum above the water surface. The baffle extends the flow path from the downcomer to the riser, allowing the downcomer and riser pipes to be placed close to one another. The 0.5 inch (13 mm) thick PVC is near the limit of its strength at 30 kPa gauge pressure, so the lid span is reduced by making the baffle the full height of the tank walls and bolting the lid onto it.

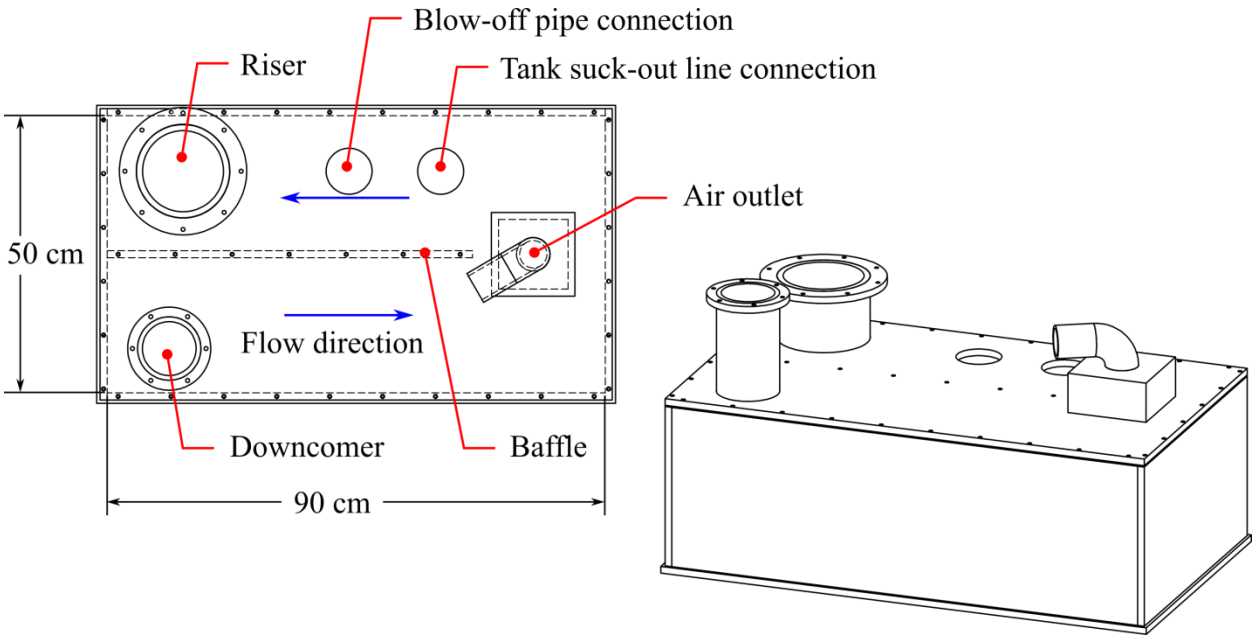

Figure 5.11: Baby HAC separator schematic from fabrication drawings. Tank bulkheads for the blow-off and tank suck-out and the air outlet valve assembly are not shown

5.1.5 Measurement procedure – separation

The separator was designed before the effectiveness model was developed, so it was deliberately oversized to guarantee near-perfect separator effectiveness at all flow rates. The design water level inside the separator is 20 cm, for a residence time of 9 s at the original design flow rate of 10 kg/s. The minimum bubble rise rate to clear the entire depth within the residence time is 2.2 cm/s. Rice (1976) asserted that the minimum flow velocity required to successfully drag bubbles down the downcomer of a HAC was 30 cm/s, an order of magnitude greater than the required rise rate in this separator. By this simplistic assessment (as no more sophisticated modeling framework had been developed at the time), the separator design was deemed fit for purpose. The water flow meter in the riser requires that the flow in that pipe be free of air. A consequence of this design choice is that the separator bubble tracking model cannot be checked against

separator effectiveness. Instead, a visual comparison must be made between the observed shape of the bubble plume and the model prediction.

The primary objective of the Baby HAC separator experiment is to validate the bubble displacement model of separator effectiveness for horizontal separators. The secondary objective is to identify which bubble size model (presented in section 4.3.2) best matches the actual bubble size distribution near the downcomer outlet at Baby HAC. Because the downcomer is transparent, the bubble size can be manually measured using a photograph of the bubbly flow. Comparing the measured distribution to the bubble sizes predicted by each of the empirical models identifies which model is the most promising candidate to predict the separator effectiveness of Dynamic Earth HAC.

Two controllable variables affect the flow field inside the separator: water flow rate and separator level. Water velocity is the controlling parameter in both separator models, so changing the flow rate or the area available for flow changes how the separator performs. The set-up is similar to the entrainment measurement procedure except instrument logging is not necessary in this case. The established performance data from the mixing head trials provide the air flow rate and pressure for the bubble size models. Temperature is assumed to be 20°C. The pre-fill and pre-start procedures are the same as for the mixing head experiment (see: section 5.1.3) except the separator should be lit from the side to make the inside more visible. Figure 5.12 shows the separator in a no-flow condition. The distance indicated between the thermistor port and close edge of the level tape (measured to the nearest 1/16”) is a convenient scale to be used for the photograph post processing.

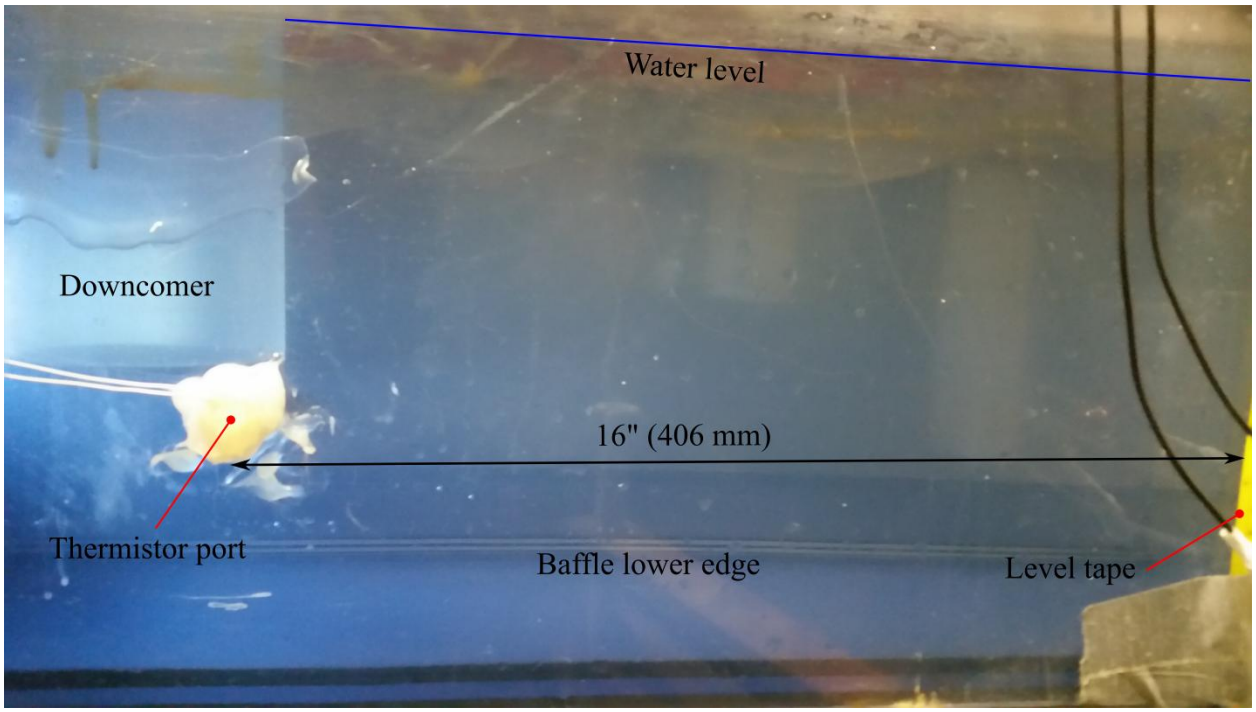

Figure 5.12: Photograph through the transparent side of the separator at Baby HAC with the pump stopped

Bubble size measurement:

1. Operate the HAC at a middle flow rate (5 kg/s). Higher flow rates are unsuitable because motion blur obscures the bubbles;
2. Take a several still images (in this case, frames from slow-motion video) of the downcomer above the separator under different lighting conditions. Include a scale to measure bubble diameter;
3. Identify the image with the largest area of clearly identifiable bubbles;
4. Measure the short and long axis for each bubble in that area. The bubbles are not spherical;

5. Use the average axis length to calculate the spherical diameter, which is the same procedure used by Akita and Yoshida (1974);
6. Produce a histogram of the bubble sizes;
7. Convert the result into a Rosin-Rammler distribution;
8. Compute the bubble size distribution for each of the empirical models; and
9. Identify which method produces the distribution with the closest Rosin-Rammler mean diameter to the measured value.

Bubble images were captured as frames from a slow-motion (high frame rate) video captured by a smart phone camera. In the frame was a measuring tape scale from which the image scale (pixels per millimetre) was determined. Long and short bubble axes were measured manually in image pixels and subsequently converted to millimetres. Based on the number of pixels across the short axis measurements, the bubble size error was on the order of 2-5% for each bubble.

Separator effectiveness measurement:

1. Zero the water flow meter;
2. Turn on the pump;
3. Select the water flow rate for the test (low, medium, and high corresponding to 3, 5, and 8 kg/s, respectively) and dial it in using the water flow meter reading and the pump choke valve;
4. Adjust the separator air valve to hold the level as close to 25 cm as possible. Changing level affects both the water flow measurement and the cross-sectional area available for flow in the separator channel;

5. Take enough photographs to ensure at least one clear image of the bubble plume inside the separator including the leading edge of the downcomer pipe and the two points used for scaling the image in post processing (centre of thermistor port to near edge of level tape);
6. Close the air valve and stop the pump; and
7. Repeat steps 1-6 for each flow rate.

Post processing (refer to Figure 5.13):

1. Select the clearest photograph that matches the criteria in step 5 above at the first flow rate;
2. Calculate the scale on that photograph;
3. Run the bubble displacement separator model for this condition;
4. Using linear interpolation, identify the vertical positions above which 95% and 99% of the bubble mass, respectively, lies for each interrogation plane;
5. Draw a line connecting those positions on the photograph;
6. Repeat steps 1-5 for each flow rate; and
7. Compare the model result to the observed bubble plume for each flow rate.

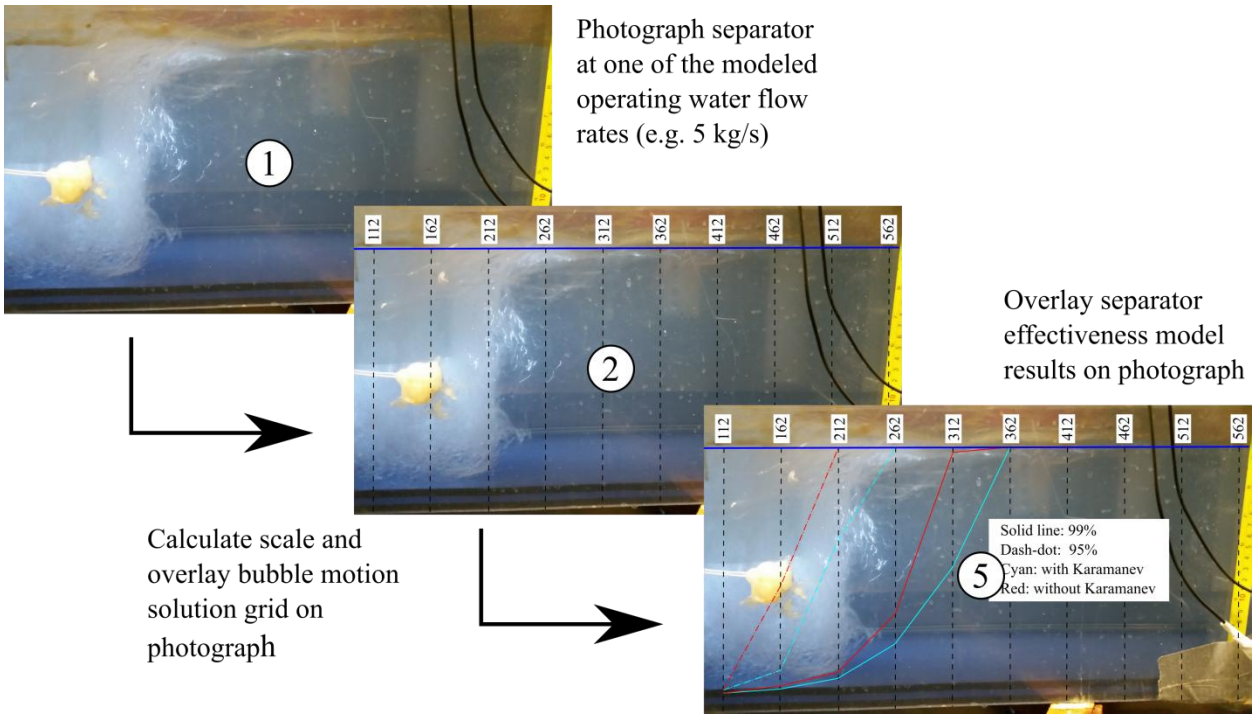

Figure 5.13: Post processing procedure stages for Baby HAC separator evaluation

The bubble displacement model is expected to be more accurate for higher flow rates; more planes are used because the higher horizontal velocity carries the bubble plume across more interrogation planes and water flow rate measurement is more reliable in the upper end of the scale. The low flow rate test is necessary to show that the model accurately reflects the pattern of change with increasing flow rate, even if its accuracy is poor at low flow.

5.2 Dynamic Earth HAC demonstrator

Dynamic Earth HAC was based on a HAC that Taylor embedded in one of the piers of the Peterborough lift lock on the Trent-Severn canal (Schulze, 1954). The dimensions of Dynamic Earth HAC were matched to the Peterborough design (see: Figure 5.14) as a working compressor at a reasonable scale large enough to validate the solubility yield model (Young, 2017).

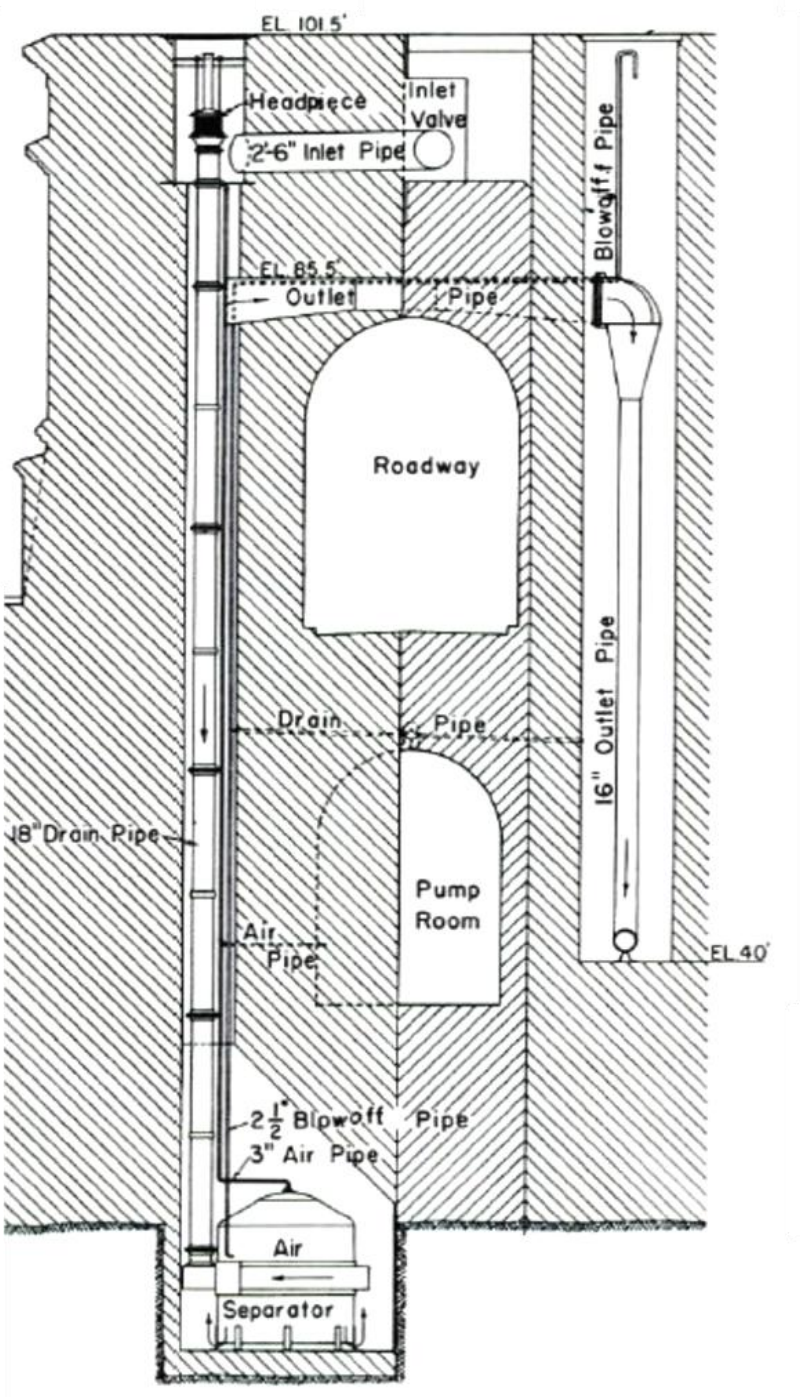

Figure 5.14: Section view of the HAC at the Peterborough lift lock. All dimensions are in feet and inches (reduced from Schulze, 1954)

Dynamic Earth HAC has a total height of 29 metres (95 feet), excluding the building envelope. The tailrace tank is positioned 22 metres (72 feet) above the separator and 5 metres (16 feet) below the forebay tank. Figure 5.15 is a pipes and tanks view of the Dynamic Earth design. Selected design and fabrication drawings of mechanical components relevant to this thesis are included in Appendix G.

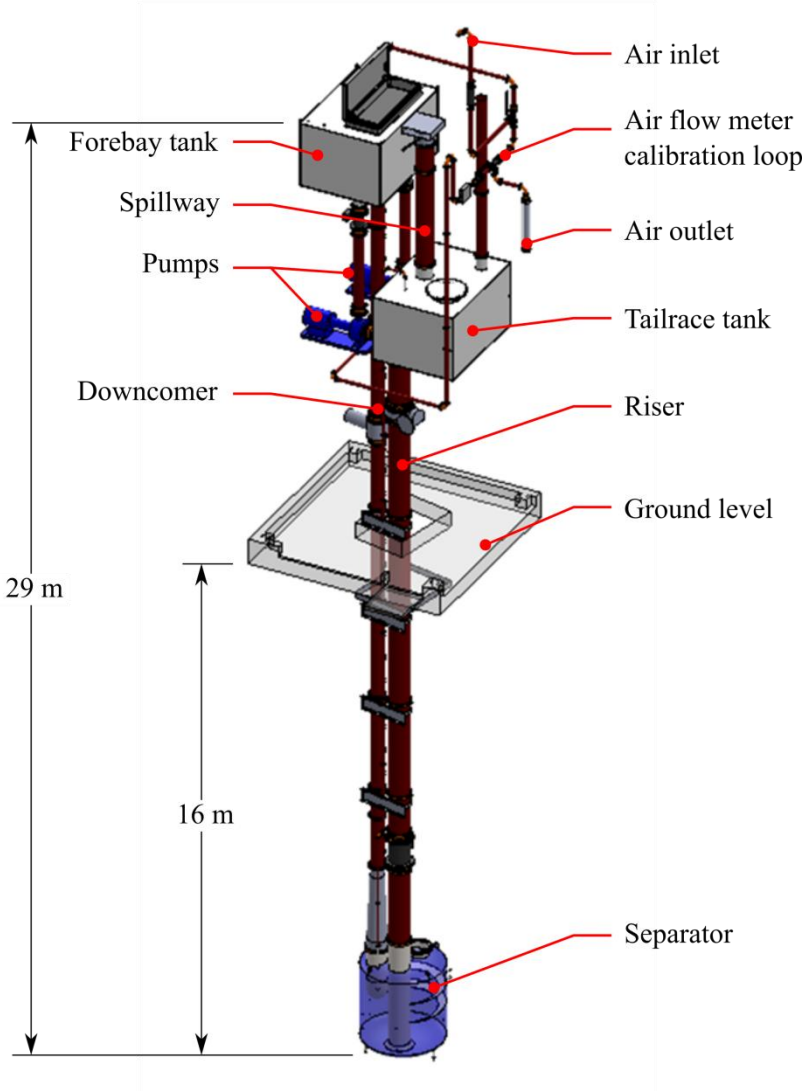

Figure 5.15: Labeled isometric view of Dynamic Earth HAC SolidWorks model. The building envelope and shaft surface are not shown

All pipes below the maximum water level in the system are either rubber lined or stainless steel. Adding salt and increasing temperature to control the gas solubility properties of the circulating water have the consequence of enhancing the corrosion rate of steel. Only the blow-off pipe is in stainless steel, because the rubber lining process was not practical for small pipes.

The downcomer is a 16 inch nominal (14.5 inch; 368 mm internal) standard weight steel pipe. The design flow rate was set at 400 kg/s to correspond to the maximum free air delivery predicted by the performance model summarized in Figure 5.16. Two pumps circulate the water, offering the possibility of extending the range into lower flow rates by running on a single pump configuration, where the overall HAC efficiency is expected to be higher.

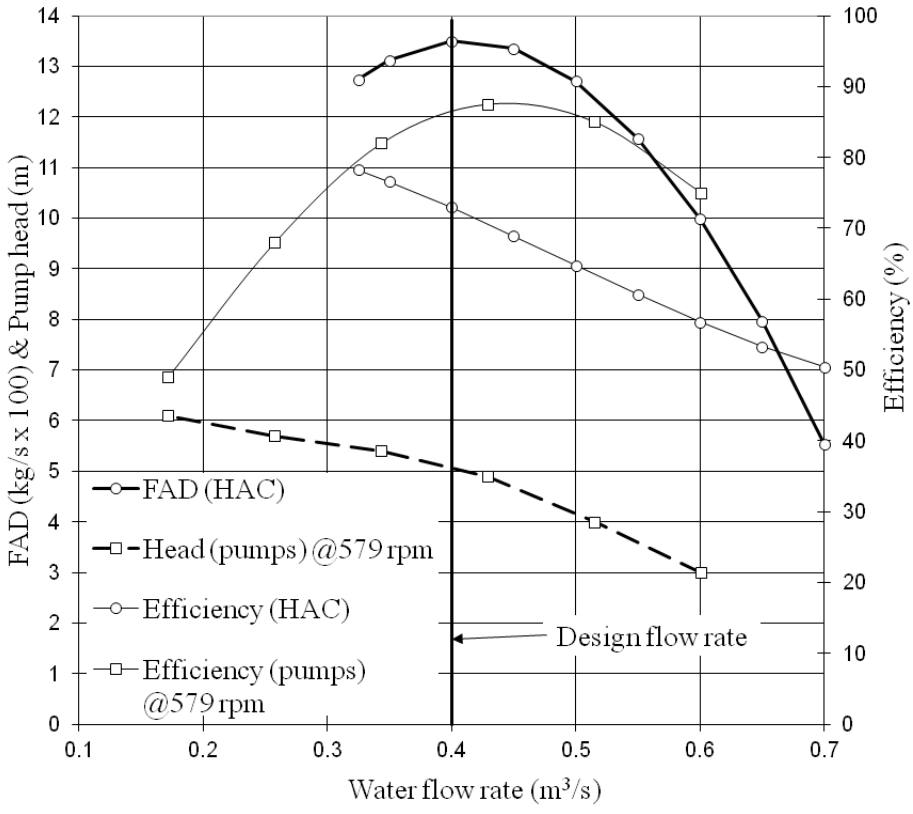

Figure 5.16: Predicted performance map for Dynamic Earth HAC (Young et al., 2015)

Unlike the Peterborough HAC, the returning water is enclosed in a riser pipe. Using the annular space in the shaft as a riser would require more water, prevent the use of the shaft for ventilation, and restrict access to the separator and pipework. Instead, the riser is a standard weight steel pipe with a nominal diameter of 24 inches (22.1 inches; 562 mm internal). The head loss in this pipe is small with respect to the total head available.

The air pipe is routed up to the top deck of the building so that water equalizing in this pipe in the event of a control valve failure (i.e. fail open case) does not flood the air mass flow sensor and control valve near the outlet. The blow-off pipe empties into the top of the tailrace tank.

The late completion of Dynamic Earth HAC has shifted most of the experimental work planned for this thesis onto Baby HAC. To date, only one mixing head has been installed, so no quantitative mixing head comparisons are possible. The placement of the separator in a tight elevator shaft has reduced its size enough that the separator effectiveness is low at the design flow rate but still almost perfect at the lowest flow rate. Recall from section 1.1.2 that the overall HAC efficiency is further reduced after accounting for the mechanical efficiency (η_{mech}) by the yield (y, a consequence of solubility) and the separator effectiveness ($\eta_{separator}$). These latter two variables combined are called the air productivity (5.1), which is the ratio of the compressed air mass flow delivered to the atmospheric air mass flow at intake. Because only air productivity can be measured and not separator effectiveness, the separator models were adjusted by a coarse evaluation of yield, described in section 6.4.3.

$$\text{Air productivity} = y \cdot \eta_{separator} \tag{5.1}$$

5.2.1 Relevant instrumentation

The instruments critical to the work presented in this thesis are the air and water flow meters, the water level sensors in the forebay and tailrace tanks, and the pressure sensors used to investigate air detrainment in the downcomer. For the purposes of this thesis, pressure and temperature measurement at the air inlet and in the separator are relevant only for thermodynamic property lookup, and are not described in any detail here. Recall from section 5.1.1 that the evaluation of these properties is insensitive even to substantial error in pressure and temperature measurement. Electrical power and pump measurement instruments are not relevant to this thesis. All instruments described below transmit a 4-20 mA analog signal to a centrally-located 16-bit digital to analog converter and are converted to physical values and logged to a database by the MATLAB control software. More complete information on instrumentation and data logging and processing is available in Sivret (2018).

Water flow rate:

Water flow rate is measured independently in each pump discharge pipe below the forebay tank. The Krohne OPTIFLUX 2300 is the magnetic flow meter selected for this application. In a 12 inch pipe (nominal, DN 300), it measures flows up to 0.85 m^3/s. The accuracy at 0.01 m^3/s is approximately ±1% and improves to ±0.2% at maximum flow. At the design flow rate of 0.2 m^3/s (each pump), the accuracy is ±0.5% (Krohne, 2016). The flow meters are installed near the top of the pump discharge pipe to maximize the length of the straight pipe section upstream (see: Figure 5.17).

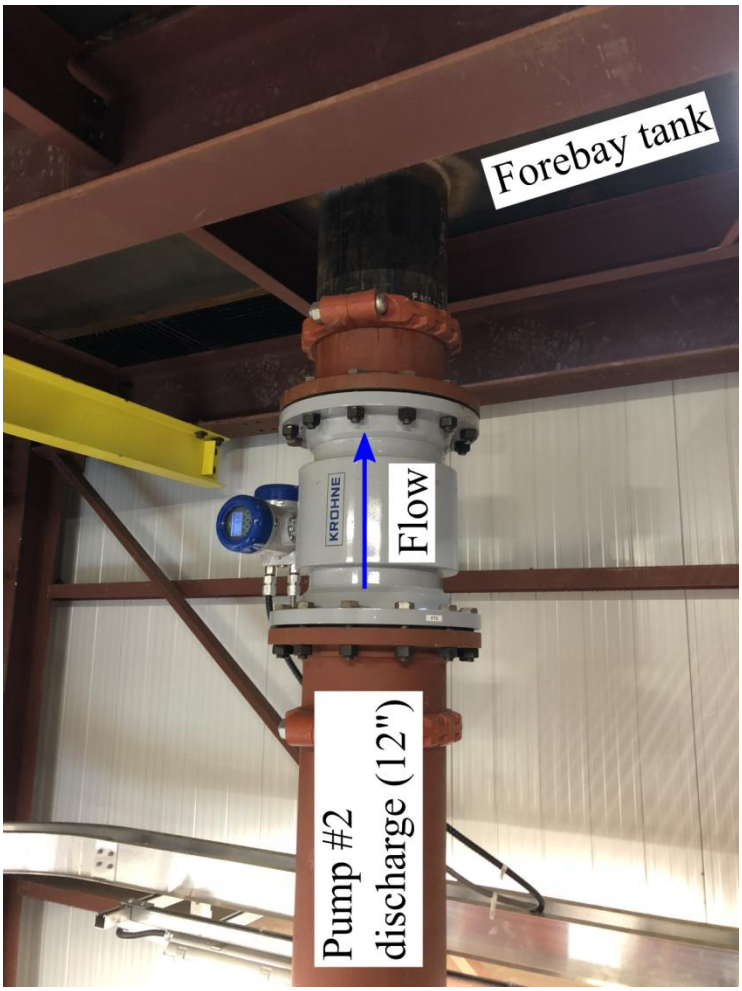

Figure 5.17: One of two identical magnetic flow meters positioned five pipe diameters upstream of the outlet in the forebay tank above

Air flow rate:

Air flow is measured at both the inlet and outlet. A Krohne OPTIMASS 6400 Coriolis meter was installed at the outlet before the control valve. It measures air flow rates up to 0.17 kg/s. The accuracy is ±0.9% at 0.05 kg/s and improves to ±0.5% at maximum flow (Krohne, 2017). The inlet flow meter is a Krohne OPTISONIC 7300, which has been calibrated against the Coriolis meter. The calibration pipe loop (see: Figure 5.18) allows the outlet flow from the separator to be

routed backwards through the ultrasonic meter. During the first calibration procedure, the ultrasonic meter was tested both forward and backward with the result that the flow meters agree closely with one another in both directions across the operating envelope of the HAC.

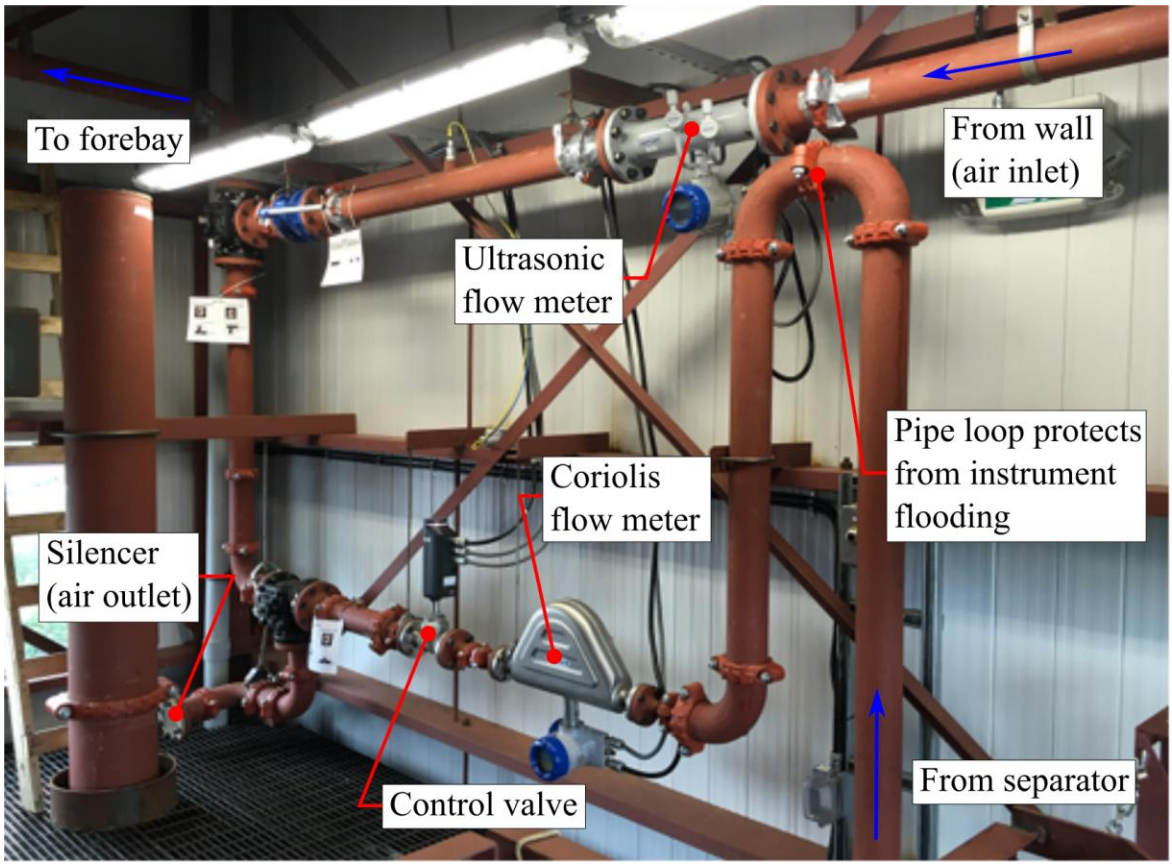

Figure 5.18: Air flow measurement wall at Dynamic Earth HAC. The outlet leg is connected to the inlet to calibrate the ultrasonic flow meter with the Coriolis meter

Water level:

Water level in the forebay and tailrace tanks is measured using a pair of Krohne OPTISOUND VU-30 ultrasonic level sensors. They measure accuracy to ±0.15% of full scale, corresponding to ±13 mm (Millar and Muller, 2017). For the purposes of the mixing head performance

experiment, the forebay level sensor provides a measurement of the water level over the lip of the mixing head. Together, the level sensors measure the driving head to evaluate hydropower for the compression loop.

Air detrainment pressure sensors:

The pressure sensors first installed to evaluate pump performance were repurposed to measure the pressure in the downcomer in the first four sampling ports downstream of the mixing head in the forebay tank (see: Figure 5.19). They were calibrated for pressures up to 300 kPa with an accuracy of ±0.1%. This translates to 3 cm H_2O, which makes them somewhat inaccurate for low pressure measurement on the order of 1 m H_2O. These sensors were used to measure the pressure profile in the downcomer during two benchmark tests (BM46 and BM47).

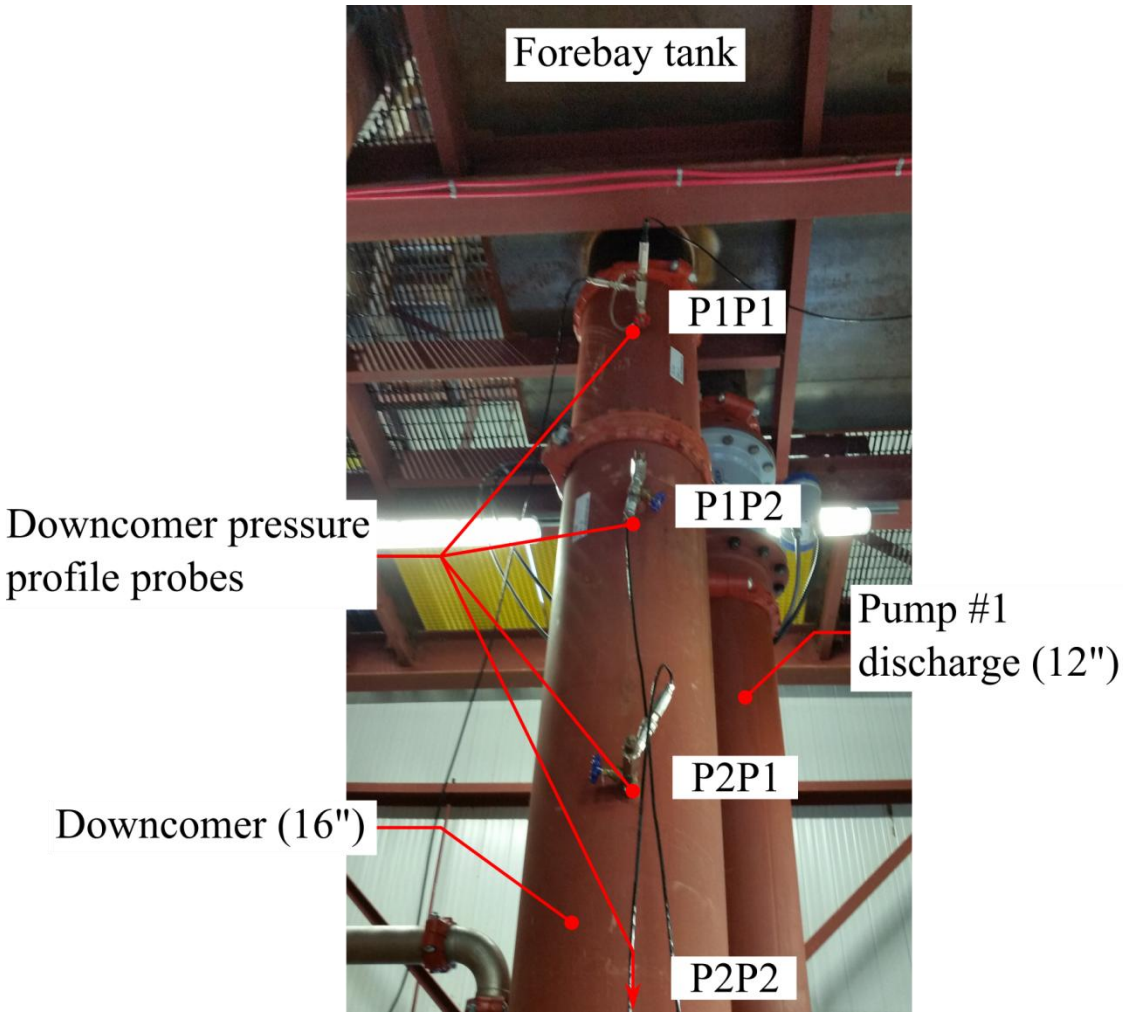

Figure 5.19: Top three pressure sensors in the downcomer intended to detect the detrainment zone

5.2.2 Mixing head design

At the time of writing, only one mixing head has been fabricated and installed at Dynamic Earth. The mixing head is a reproduction of the original design installed at the Peterborough lift lock HAC in 1903 (see: Figure 5.20). This head was fabricated by machining and welding students at Cambrian College in Sudbury, Ontario. Three positioning screws around the periphery position

the ends of the air pipes at the narrowest point between the hydrofoils, located 1.5 inches (41 mm) below the lip of the hydrofoil assembly. The hydrofoils, with the obstruction of the air manifold itself, locally reduce pressure and enhance air entrainment.

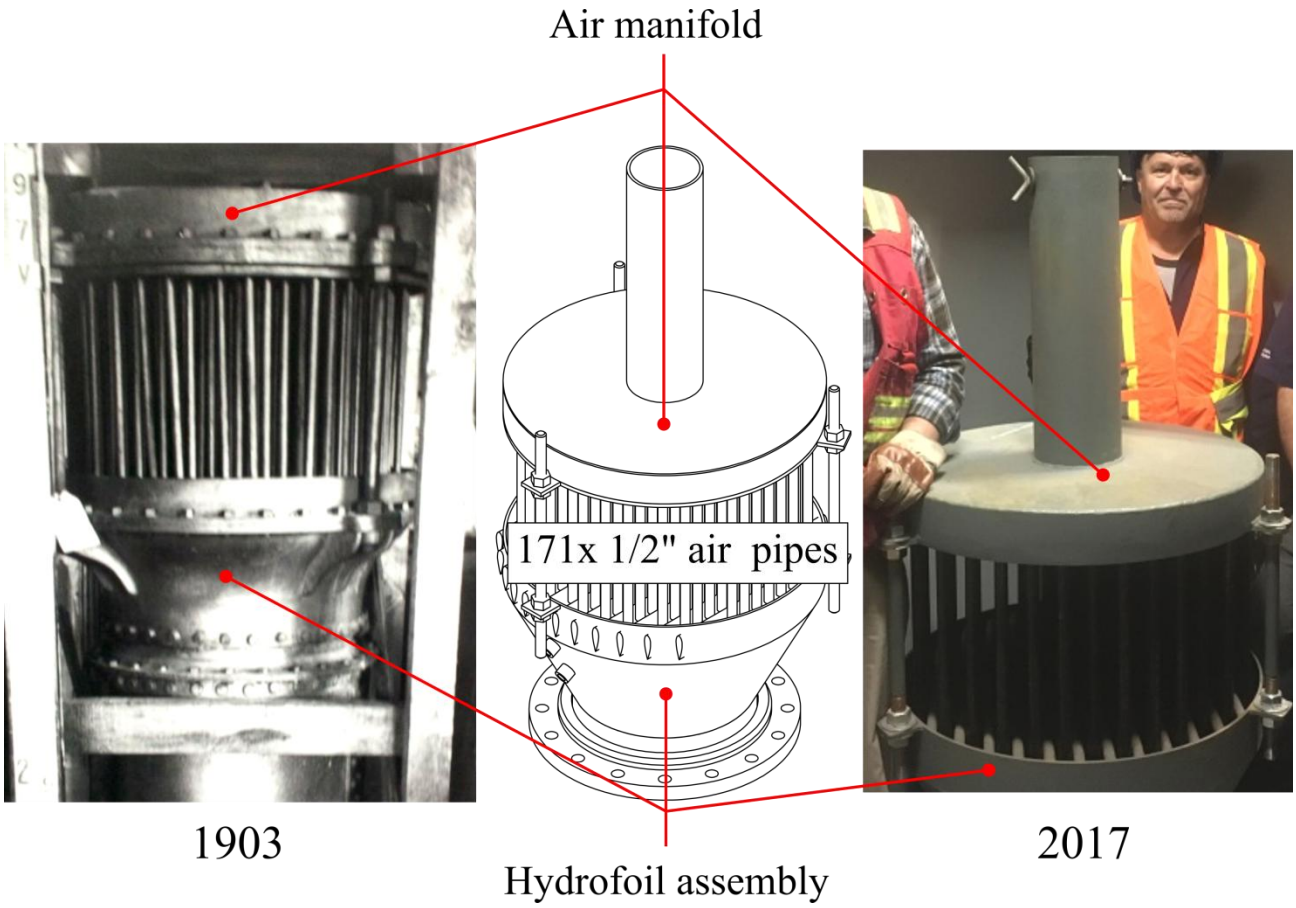

Figure 5.20: From left to right: original mixing head prior to installation at the Peterborough lift lock (modified from Parks Canada, 2013), design drawing of reproduction for Dynamic Earth HAC, reproduction head installed in forebay tank (modified from Electrale Innovation Limited, 2017)

5.2.3 Separator design

The separator at Dynamic Earth is a vertical gravity separator with a total height of 2.9 metres and an internal diameter of 2.4 metres. It was assembled from three pieces lowered separately into the shaft (see: Figure 5.21). The design was originally a simplified version of the Peterborough HAC separator, but was adjusted to be more similar to the original in subsequent design iterations to reduce head loss (downcomer outlet transition) and make the internal vertical velocity profile more uniform (internal guide baffles).

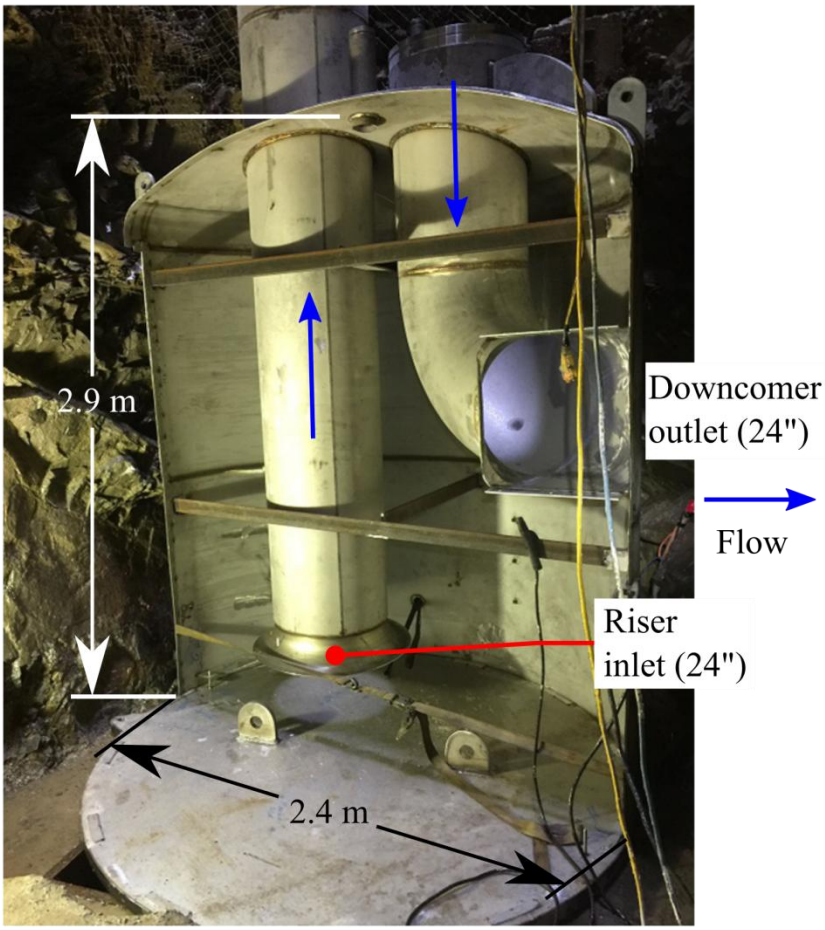

Figure 5.21: A cutaway view of the separator during reassembly at shaft bottom prior to the third piece of the assembly was lowered into place (Electrale Innovation Limited, 2017)

The site at Dynamic Earth had an old elevator shaft with a depth of 16 metres, which reduced the superstructure building height at the cost of limiting the available space at shaft bottom. The original design called for a taller separator with an internal diameter of 9 feet (2.7 metres). The space limitation forced the design to shrink in both dimensions. The reduction in diameter increased the vertical velocity by forcing the same volume flow rate through a vessel with smaller cross-sectional area. The reduction in height reduced the flow path length that would otherwise tend to develop the downward flow and reduce the variability of the vertical velocity profile. By shrinking the vessel, the vertical velocity was increased and made less uniform. The consequence was that the expected separator effectiveness was reduced. The expected head loss did not change significantly with these changes because the largest anticipated source of irreversibility was in the downcomer outlet (see: section 4.2), which remained unchanged with this design adjustment.

5.2.4 Experimental procedure

Three experimental datasets are of interest from the commissioning and benchmarking tests conducted on Dynamic Earth HAC: forebay water level against water flow rate with changing water load, air detrainment and re-entrainment in the downcomer, and separator effectiveness against water flow rate for the nominal water load. The rationale and procedures for each of these tests are listed below:

Benchmark test:

A benchmark test is a standardized procedure to capture the behaviour of the HAC across the full range of flow rates on a single pump or with both pumps.

1. Ensure the forebay tank is adequately sealed using the ultrasonic flow meter. If it reads nonzero velocity, then there is leakage in the forebay lid;
2. Assign a test number for logging;
3. Start the pump(s) at minimum speed;
4. Wait 3 minutes for the separator level controller and system parameters to stabilize;
5. Log for 5 minutes;
6. If the pump is not at maximum speed, increment the pump speed and return to step 4; and
7. Shut off the pump(s).

Mixing head:

Because only one mixing head has been fabricated, it is not possible to perform the same type of comparative experiments as were performed on Baby HAC. The driving head of Dynamic Earth is more flexible than that of Baby HAC. The mixing equation presented in section 3.5 is independent of driving head. Therefore, the forebay tank level should have the same relationship with flow rate for low head as it does for high head. There may be a small increase in water level at lower head, as the suction pressure at the air manifold required to entrain air is less when less air is being entrained.

1. Measure the level of the lip of the mixing head above the forebay tank floor;
2. Fill the HAC to a minimum safe water load for operation;

3. Run a benchmark test;
4. If the water load is not at maximum, increment the water load and return to step 3; and
5. Plot forebay water level above the mixing head lip against water flow rate for a representative sample of the water load increments.

Air detrainment zone:

An air detrainment zone is a region of flow in the downcomer where the bubbles coalesce and shift the flow regime to an annular flow, in which there is a continuous air pocket along the length of the zone and the water is in free-fall. Air is re-entrained into a bubbly or bubbly-slug transitional flow at the base of this zone where the free-falling water jet collides with the top of the slower-moving flow transition surface by the 'impinging jet' entrainment mechanism (see: section 2.2.1). It was suspected to exist in the downcomer below the mixing head because the air mass flow rate delivered by the HAC did not meet the expected value from the model and a similar zone was observed at Baby HAC (see: section 7.7). Any such discontinuity in the flow would be apparent in a pressure profile, so it was decided to move pressure instruments from the pumps to the downcomer pipe to look for this effect (see: Figure 5.19).

1. Install pressure instruments in the first four sampling ports of the downcomer below the forebay tank floor;
2. Under a static column of water, identify the zero offset for each of the four instruments;
3. Add these instruments to the benchmark test logging procedure;
4. Run one or more benchmark tests; and
5. Plot the pressure profiles for each of the benchmark tests.

Separator effectiveness:

Air productivity is measured using an air balance, where the difference between the air flow at inlet and the air not recovered from the separator must be the result of a combination of yield due to gas solubility and separator effectiveness. At low water flow rate, the separator effectiveness is expected to be nearly perfect, so the difference can be ascribed to gas solubility. As the separator underflow water stream is passed up the riser, the dropping pressure triggers dissolved gases to exsolve and be separated as bubbles in the tailrace. In effect, the capacity for the water to dissolve gas in the downcomer process is regenerated in the riser. Yield loss is assumed to be small and relatively non-responsive to changes in water flow rate. Separator effectiveness is assumed to be responsible for the remainder of the difference.

1. Complete the separator experiment for Baby HAC;
2. Identify the most accurate bubble size model from that test;
3. Using the vertical velocity model at increments along the experimental range of water flow rates, produce a separator effectiveness curve;
4. Run one or more benchmark tests and calculate air productivity;
5. Identify the solubility yield loss at the lowest water flow rate point(s);
6. Correct the modeled separator effectiveness curve using the measured solubility yield loss to produce an air productivity model curve; and
7. Compare the separator effectiveness (air productivity) model result to the measured air productivity.

The separator model depends on a reasonably accurate prediction of the bubble size distribution. A non-visual method to measure bubble size distribution is currently under development. The

use of the bubble model determined most accurate at Baby HAC is currently the only reasonable method of estimation valid here.

5.3 Summary

Two experimental HACs were built and used to test a variety of mixing heads and both gravity separator models. Due to the time constraint after construction, the majority of the experiments were performed on Baby HAC. The mixing head comparison work has not yet been expanded to Dynamic Earth HAC. The larger scale and better instrument accuracy of Dynamic Earth HAC enabled some specialist tests to be run to validate the independence of the air entrainment equation from driving head and to observe the air detrainment zone in the downcomer below the mixing head.

The horizontal gravity separator on Baby HAC is the test platform for the bubble displacement separator model. While it is not possible to perform a true quantitative evaluation of the model, the length and shape of the bubble plume in photographs should agree with where the air mass is predicted to move in the model. The bubble size distribution measured in this test will also identify the best prediction model to predict the separator inlet size distribution at Dynamic Earth HAC.

The vertical gravity separator on Dynamic Earth HAC is the test platform for the vertical velocity separator model. In this case, an undersized separator has near-perfect separator effectiveness at low flow and only fair separator effectiveness at high water flow rate. The solubility yield loss can be canceled from the measurement by subtracting the outlet air flow from the inlet air flow at the low water flow rate operating point. The remaining difference

between inlet and outlet air flow rate is due to separator effectiveness, which can be used to generate the experimental effectiveness curve to be compared to the model curve.

Chapter 6

6. Results

This chapter reports the modeling results and the results and observations of the experiments performed to test the hypotheses presented in this thesis. These experiments measure mixing head performance and separator effectiveness on both functional HACs described in chapter 5. An additional experiment intended to detect air detrainment and re-entrainment in the downcomer at Dynamic Earth HAC is reported in brief. Mass flow rate is preferred over volume flow rate where flow measurements are reported. For air, mass flow rate is conserved when the pressure is increased volume flow rate is not. It is also preferred for water the air production rate scales to hydropower, which is proportional to the mass flow rate.

Most of the mixing head evaluations were performed on Baby HAC. Time constraints on Dynamic Earth HAC and the ease and low cost of mixing head fabrication and replacement on Baby HAC made that platform ideal for experiments to compare mixing head geometries against one another. Dynamic Earth HAC was operated under a greater variety of conditions including variable water load, which was used to test the hypothesis that the forebay tank level was a function of water flow rate and not driving head.

Separator pressure drop was not directly measured on either HAC. The instrument package required to measure pressure drop at Dynamic Earth HAC was not yet installed. The model results and relevance to the design effort are presented in section 6.3. Separator effectiveness was modeled and tested on a horizontal gravity separator (Baby HAC) and a vertical gravity separator (Dynamic Earth HAC). Bubble size was measured manually from a photograph at Baby HAC to

identify the closest size prediction model for use at Dynamic Earth HAC, where measurement is not feasible.

6.1 Baby HAC mixing head comparison

The target for each mixing head test is to have 50 data points that capture the full range of water flow rate from around 3 kg/s to the maximum flow at 8 kg/s. For some mixing heads, up to 100 points were required to complete the test, particularly when problems with the water flow meter led to imprecise measurement and excessive point scatter. The comparison is made on the basis of water level over the lip of the mixing head, which is a function of the irreversibility associated with the entrainment and inlet occurring above that position and air flow rate, which is proportional to mechanical efficiency (see: section 1.1). Each set of tests are presented first in terms of air flow rate against water flow rate and second as water level over the lip of the mixing head against water flow rate. These data are presented graphically in this section. Appendix H contains the full data set in tabular form. The experimental procedure for these tests is found in section 5.1.3.

6.1.1 Snorkel head configuration comparison

The snorkel head was tested in several configurations: no snorkel, using the original large diameter snorkel, and with a narrower snorkel at several fixed positions (see: Figure 6.1). Table 6.1 contains the complete list of snorkel head configurations evaluated on Baby HAC. It was clear during preliminary testing that the original (large diameter) snorkel performed poorly, such that at high water flow rate the water level in the forebay had risen so high that water was

bypassing the process through the tank overflow. Only the first intended test was ever completed on it.

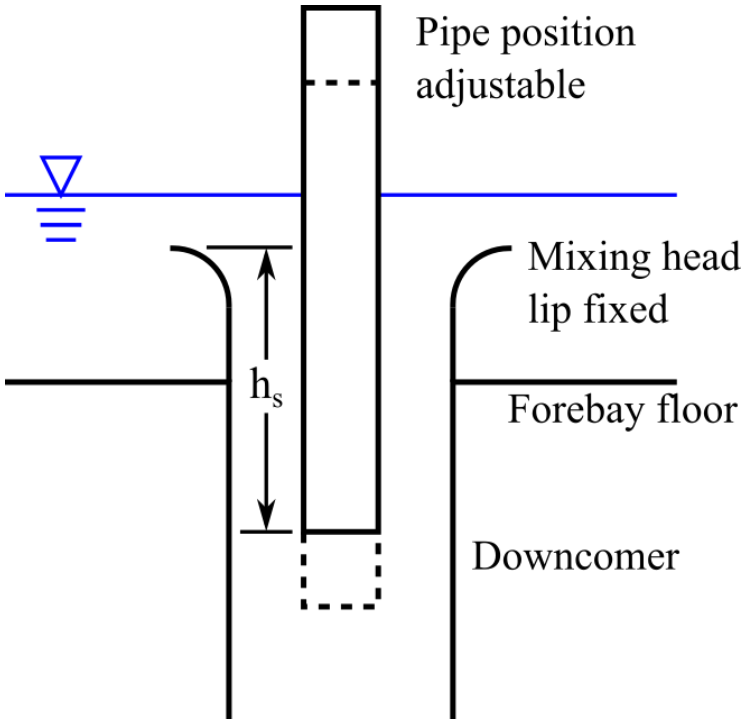

Figure 6.1: The adjustment of the snorkel head (h_s) is only made on the snorkel in the centre and not the main body.

Because there were so many configurations, only the best one was tested with the same number of points as the other heads. The target for the remainder was to have 30 data points across the same water flow rate range as above. That the head has the best performance without the snorkel was apparent early in the test series based on visual observation of the forebay water level at high water flow rates.

Table 6.1: Snorkel test configurations on Baby HAC. The test at position 2 was not completed

Configuration	Snorkel OD	Snorkel end position (h_s)	Number of test points
No snorkel	N/A	N/A	101
Large snorkel	51 mm (2 in)	~50 mm (2 in)	39
Position 1	32 mm (1.25 in)	202 mm (7.94 in)	26
Position 3	32 mm (1.25 in)	143 mm (5.63 in)	34
Position 4	32 mm (1.25 in)	113 mm (4.44 in)	26
Position 5	32 mm (1.25 in)	90 mm (3.56 in)	29
Position 6	32 mm (1.25 in)	64 mm (2.50 in)	30
Position 7	32 mm (1.25 in)	35 mm (1.38 in)	32

The best indication that one configuration is better than another is the comparison of air flow rate at the same water flow rate. Irreversibility leaves less energy for air compression, so a mixing head associated with less irreversibility entrains more air, all other things being equal. From Figure 6.2, the no snorkel configuration entrains the most air across the entire range. In the middle of the range, placing the snorkel at position 3, 4, or 6 matches the air flow rate of the no snorkel configuration. Placing the snorkel at positions 1, 5, or 7 or using the large diameter snorkel results in the least air entrainment. These configurations are in rough agreement with each other through the entire range.

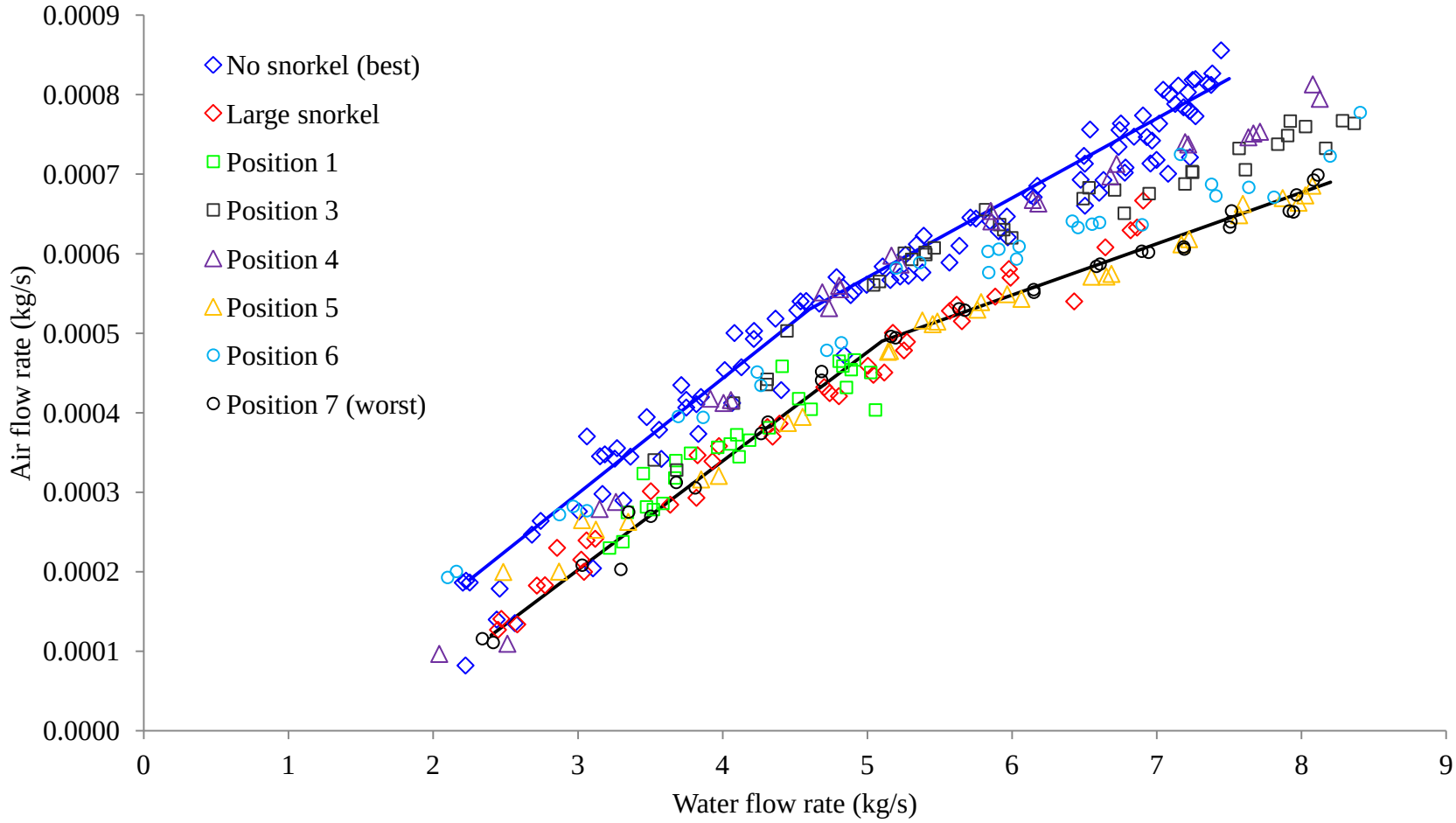

Figure 6.2: Air flow rate response to water flow rate control of all configurations of the snorkel head on Baby HAC. The performance envelope between best and worst snorkel configurations is bounded by the blue (best) and black (worst) lines

During the experimental design phase, the air entrainment irreversibility was assumed to be a small fraction of the driving head of the system such that the effect would not create clear distinctions between snorkel configurations in the air flow rate versus water flow rate relationship. Figure 6.3 reports the water level over the lip of the bellmouth inlet of the snorkel head for all configurations, where the water level over the lip of the mixing head was measured as the difference between the tank level measured by the forebay tank level instrument and the position of the lip of the mixing head over the floor of the tank measured with a tape when the head was installed. This quantity represents the water gauge pressure required to overcome the inlet losses, accelerate the water, and account for any entrainment irreversibility that occurs above that position. Recall from section 5.1.1 that the pressure in the forebay tank is depressed by the pressure drop of air flowing through the intake flow metering arrangement. The water level is measured low by as much as 3 mm water gauge (30 Pa) at maximum flow rate relative to no flow. The magnitude of this effect is not enough to account for the variability between mixing heads shown in Figure 6.3.

From section 3.5, the relationship between this level and the water flow rate was expected to be quadratic. However, it is clear that this relationship is linear in this case. For all configurations except the no snorkel configuration, there is a change in slope of the linear response after a threshold value.

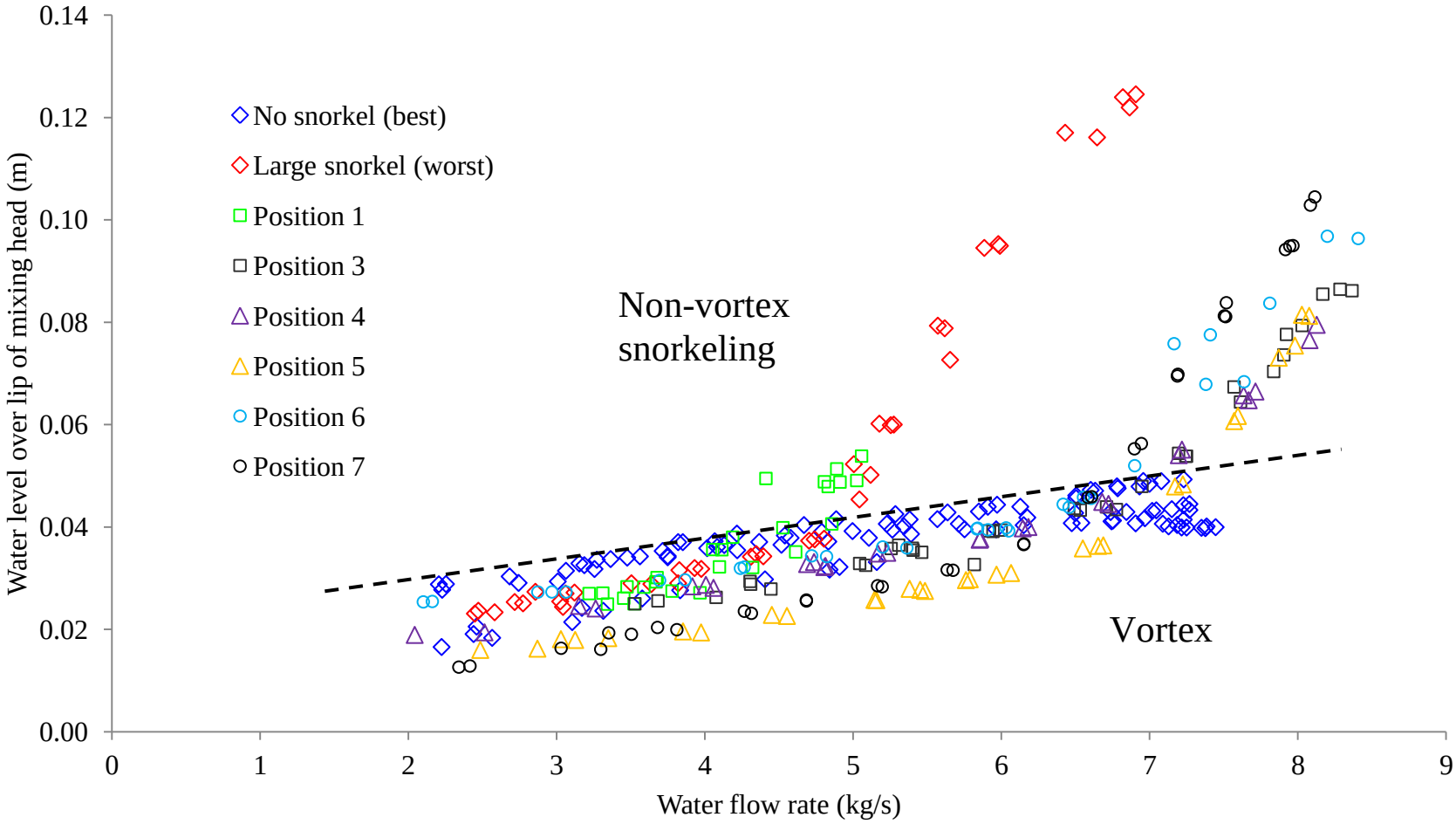

Figure 6.3: Water level over the lip of the mixing head increases with water flow rate. All configurations of the snorkel head on Baby HAC are represented in this figure

For example, when the snorkel is at position 7, the change in slope occurs between 6-7 kg/s water flow rate. The photographs in Figure 6.4 show a change of mechanism from vortex entrainment to some effect related to the snorkel, which appears to be Venturi entrainment, as the intermittent vortex through to the free surface is too small to account for the air flow into the system. Not clearly shown behind the snorkel in the maximum water flow rate photograph is a narrow, transient air entraining vortex that could only account for a small fraction of the air flow. All of the configurations that show the change of linear behaviour in Figure 6.3 exhibit the same change of mechanism as this example.

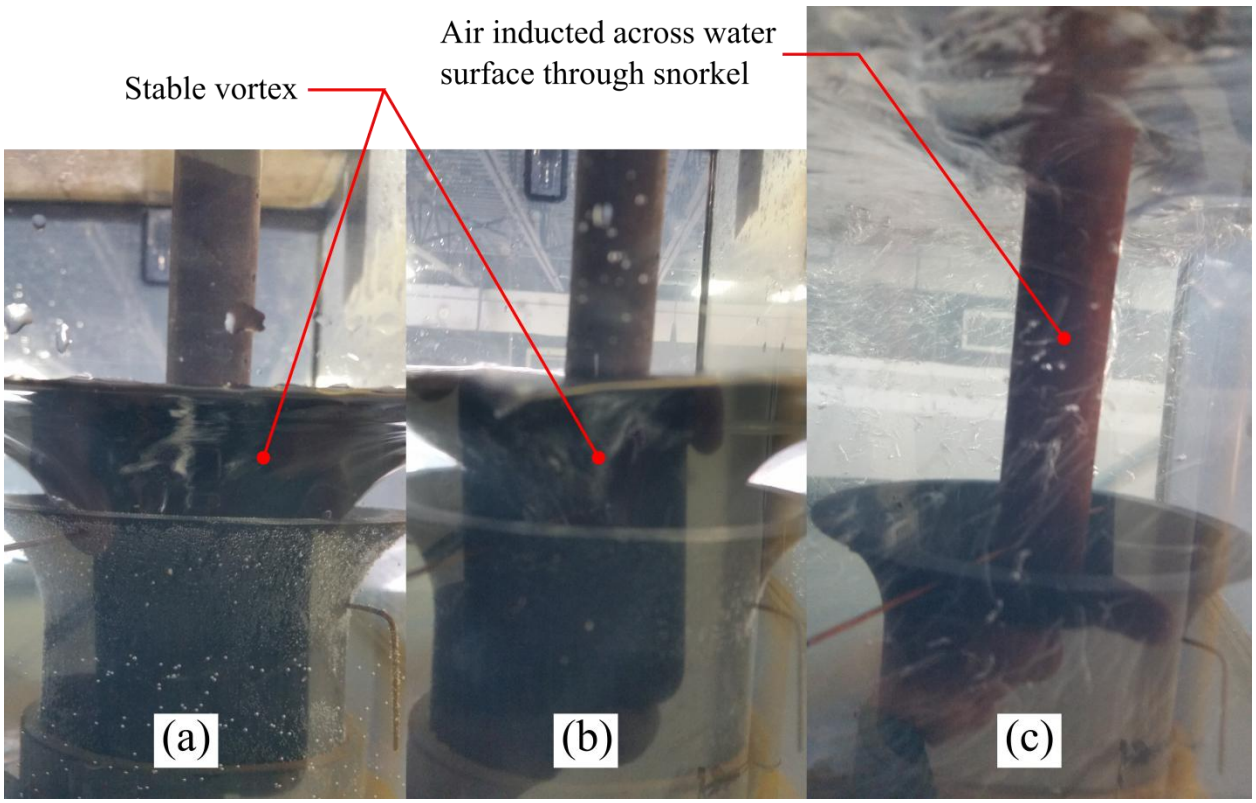

Figure 6.4: Snorkel at position 7 at the minimum (a, 3 kg/s), middle (b, 5 kg/s), and maximum (c, 8 kg/s) water flow rate

Only the no snorkel configuration exhibited vortex entrainment through the entire water flow rate range of the experiment. Figure 6.5 shows that the vortex became less smooth and more irregular with increasing water flow rate. In particular, the vortex was unstable and the air core was transient at the maximum water flow rate. A feature that is not clear in the photographs is that there is a set of vortex-breaking fins inside the mixing head just below the level of the bellmouth.

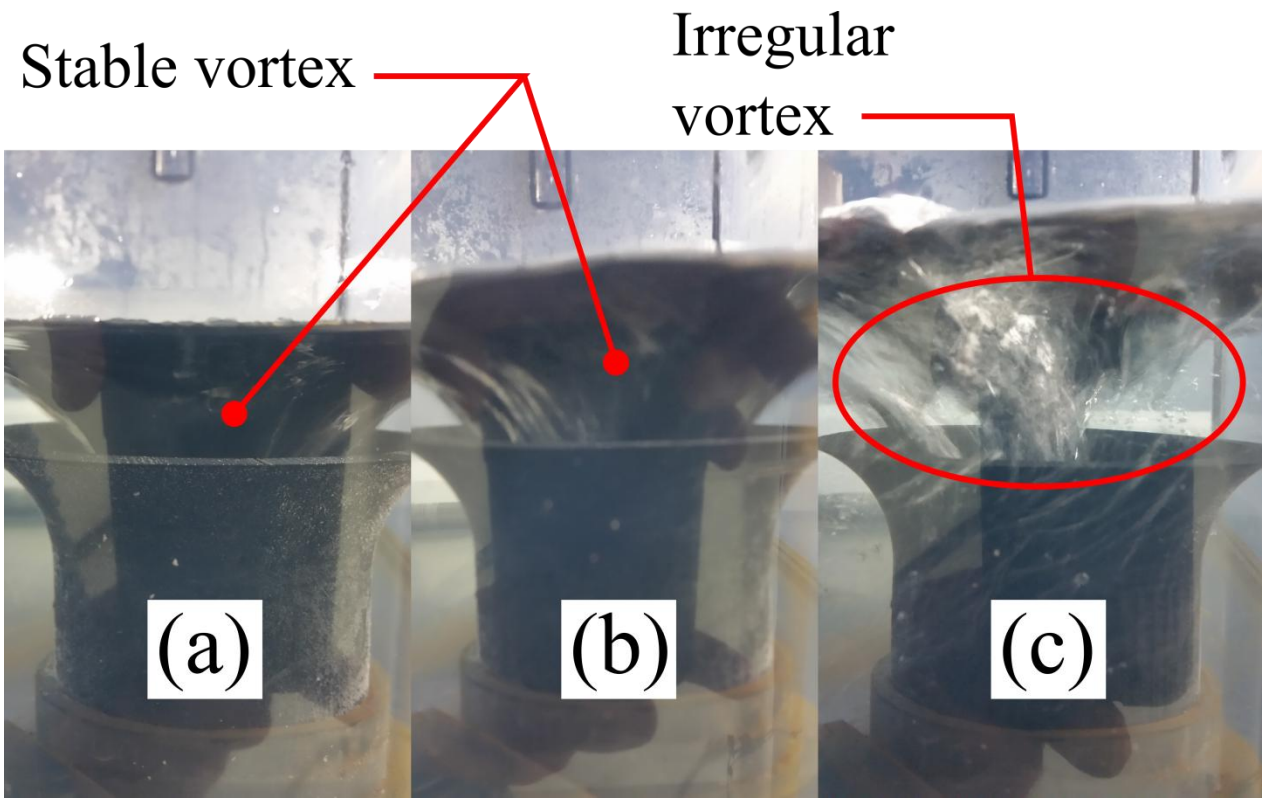

Figure 6.5: Snorkel head with the snorkel removed at the minimum (a, 3 kg/s), middle (b, 5 kg/s), and maximum (c, 8 kg/s) water flow rate

6.1.2 All other mixing heads including best snorkel head configuration

Four mixing heads were tested on Baby HAC: snorkel head, headless configuration, Peterborough head, and Ragged Chutes head. From the full range of snorkel head configuration tests reported in section 6.1.1, only the best configuration (the 'no snorkel' configuration) is repeated here for comparison against the others. Table 6.2 lists the mixing heads tested on Baby HAC and the number of data points for each. The Peterborough head and headless configuration were not favorable in comparison to the snorkel and Ragged Chutes heads, which received more attention. More data points were required to identify the trend for the headless test because it is unstable (and therefore more scattered) in the upper half of the flow rate range.

Table 6.2: Mixing head tests on Baby HAC including the no snorkel test from the snorkel head tests as the best performer of that series

Configuration	Mixing head lip position above floor of forebay tank	Number of test points
Snorkel	104 mm (4.09 in)	101
Headless	28 mm (1.09 in)	84
Peterborough	149 mm (5.88 in)	44
Ragged Chutes	152 mm (5.97 in)	101

The air flow rate versus water flow rate relationship is shown in Figure 6.6. All four heads perform similarly in the lower end of the water flow rate range. The snorkel head has the tightest spread, but the Ragged Chutes head is close to the same trend. The Peterborough head and headless option result in less air entrainment. A common inflection point was observed in the trend of all four mixing heads, though least apparent for the Peterborough head. The same trend

was observed in the snorkel head configurations at the same point (5 kg/s water flow rate and 0.0005 kg/s air flow rate), visible in Figure 6.2. The cause of this change in pattern is unknown.

In the snorkel head tests (per section 6.1.1), the elevation of the mixing head lip was fixed for all configurations (see: Figure 6.1). In the current series of tests, the position is fixed for all tests on each mixing head but not fixed across mixing heads. The maximum difference is 124 mm (4.88 in) between the headless configuration (lowest lip) and Ragged Chutes head (highest lip). Excluding the headless configuration, the maximum difference is 48 mm (1.88 in) between the snorkel and Ragged Chutes heads. The latter figure corresponds to approximately 5% of the driving head.

Figure 6.7 reports the water level over the lip of each of the four heads. All of the trends are linear or close to linear and only the Peterborough head has a change of slope after a similar threshold to those exhibited by most of the snorkel head configurations. For both pattern A and pattern B, the entrainment mechanism shifts from vortex entrainment to snorkeling, where snorkeling is air drawn through a pipe or manifold into the water flow below the surface by the Venturi effect. The dataset consists of two test series performed over two days with operating points from both test series appearing in both pattern A and pattern B. Both days produced a similar number of test points and occurred in the middle of a week-long test series of other heads, suggesting a metastable physical phenomenon rather than coincidence or error. Further, each of these points represents an average condition of 150 seconds of data. The patterns must be stable for at least that long or else there would be data points between the two lines. The cause of these patterns was not clear. However, the water level at which both inflection points appear was at the lower surface of the air manifold (1 in, 2.5 cm).

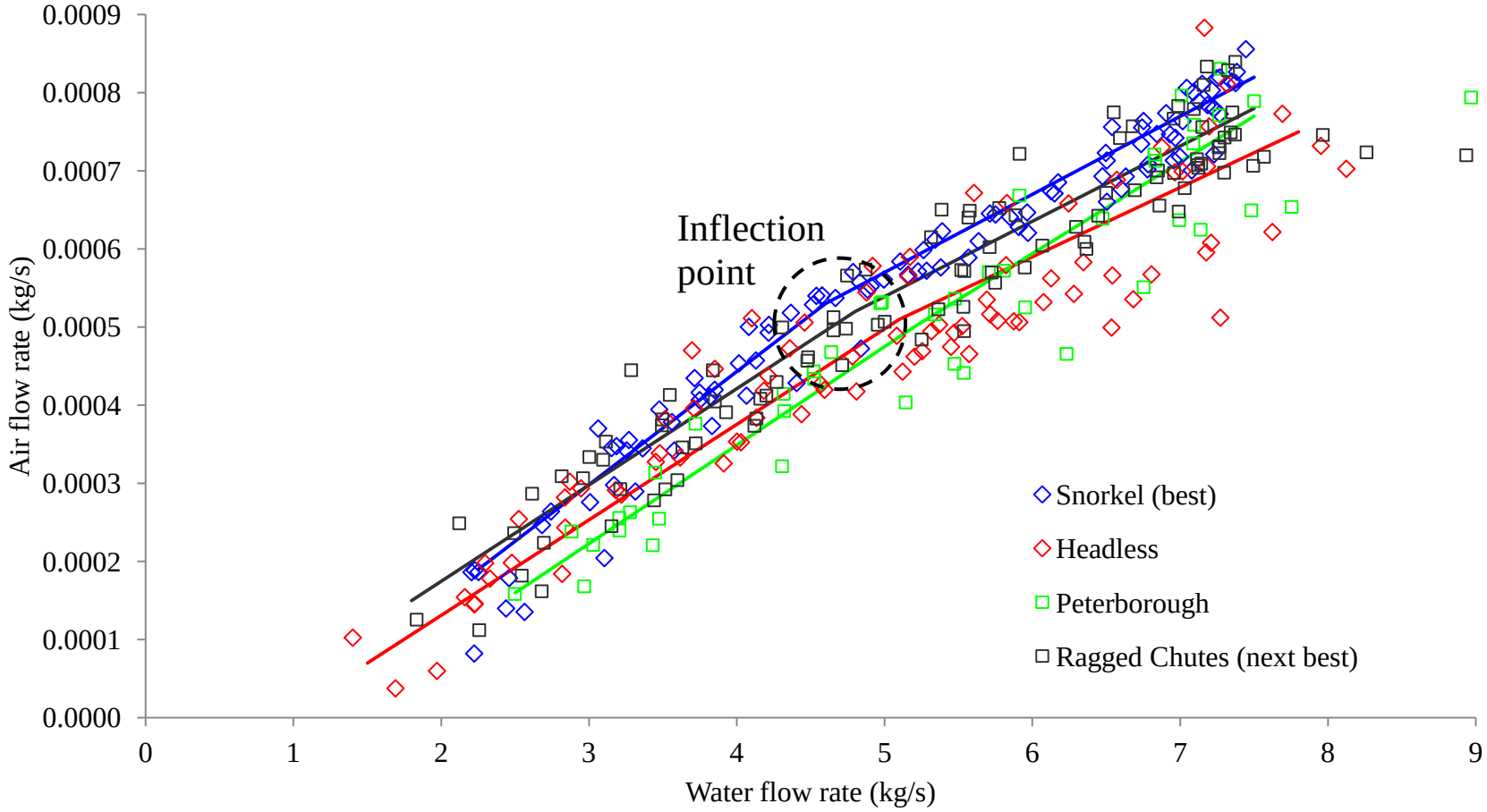

Figure 6.6: Air flow rate response to water flow rate control of all heads on Baby HAC. There is an inflection point in the trend for all four mixing heads around 5 kg/s water flow rate at 0.0005 kg/s air flow rate

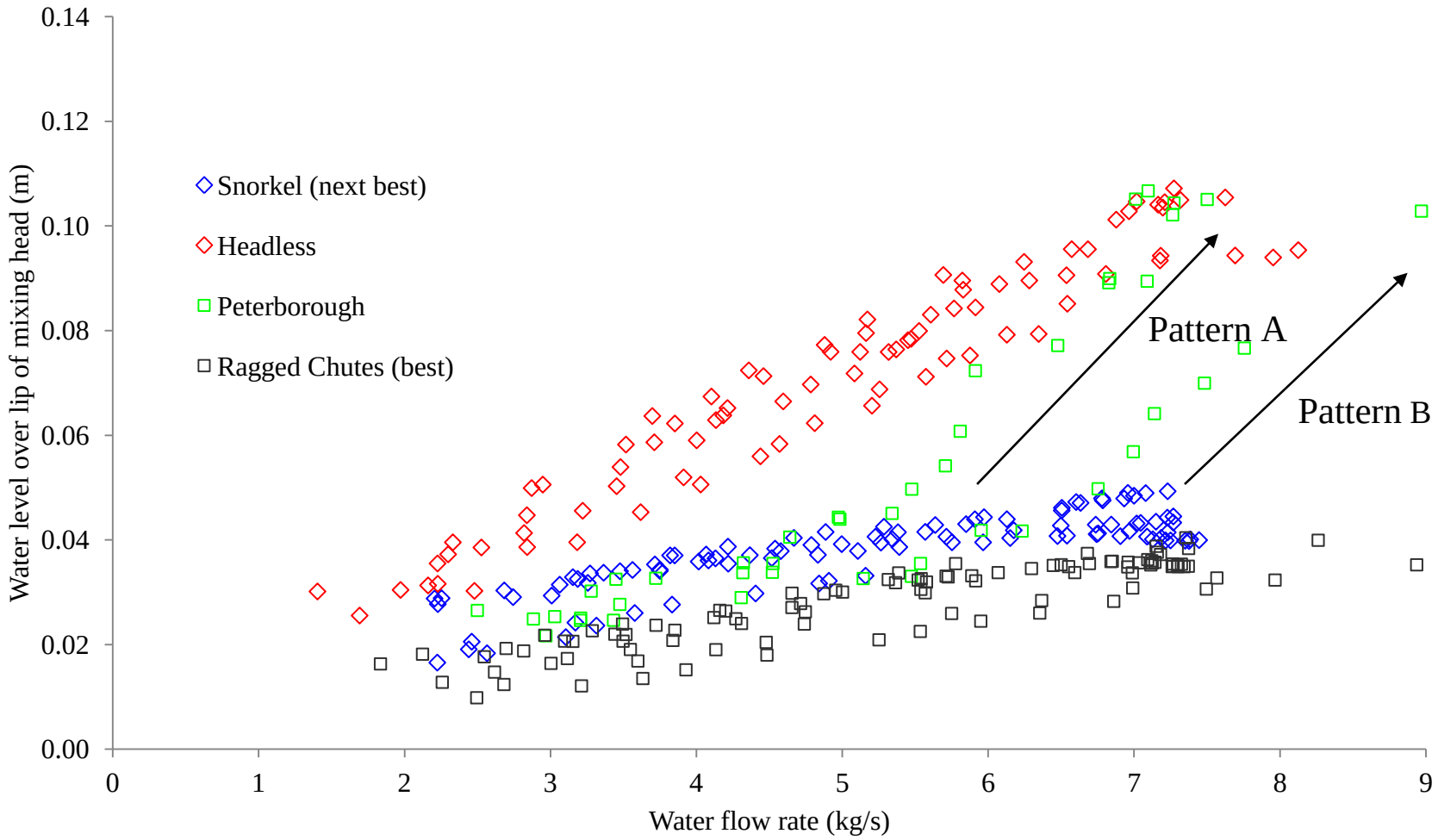

Figure 6.7: Water level over the lip of the mixing head increases with water flow rate. Two distinct patterns were identified for the Peterborough head. The flow changes from vortex to snorkeling at 5.5 kg/s for pattern A and 6.5 kg/s for Pattern B

By the water level metric, the Ragged Chutes head is visibly superior to the snorkel head. However, the Ragged Chutes head has more flow restriction below the lip of the intake pipes than the snorkel head.

At the top of the water flow rate range, the headless configuration experiences periodic stalls (see: Figure 6.8). The stall condition is caused by over-entrainment of air into the downcomer, which generates air lift. Air lift is the result of drag produced by bubbles rising relative to the water flow. It slows or reverses the flow and allows air to escape back into the forebay tank (b). The pump builds head in the forebay tank, which eventually overcomes the air lift effect in the downcomer and rushes downward (a). High transient water flow rate entrains excess air in the downcomer flow, resetting the stall cycle. At lower flow rates, the vortex is more stable and does not generate the surge/stall behaviour (see: Figure 6.9).

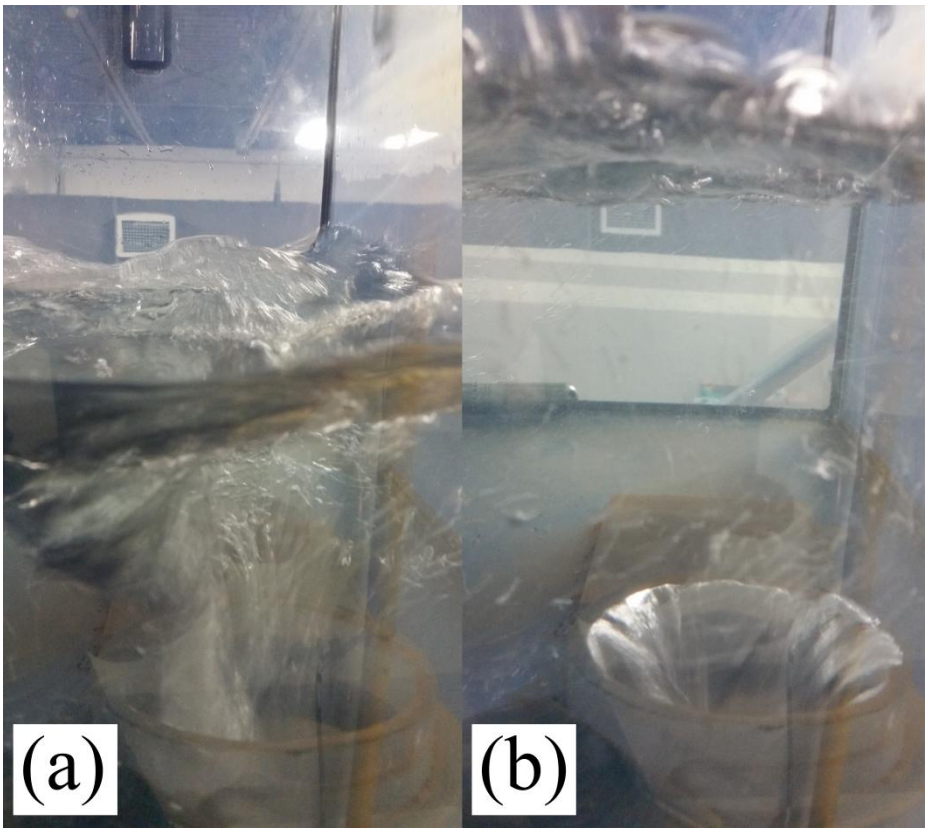

Figure 6.8: In the upper end of the water flow rate range when there is no mixing head, the flow oscillates. These photographs were taken at the extremes of the oscillation at the maximum water flow rate (8kg/s). In (a), the water level is dropping rapidly, entraining large quantities of air. In (b), the gas volume fraction in the downcomer has risen and the compressor has stalled, causing water to build up in the forebay

Figure 6.9: In the lower and middle portion of the water flow rate range, the headless inlet has a stable vortex

The Peterborough head exhibits the same change in entrainment mechanism as the snorkel head. The shift occurs when the water level increases above the lower plate of the air manifold (visible in Figure 6.10). At lower water flow rate, when the water level above the lip is below the underside of the air manifold, there is a vortex visible in the space under the manifold. The air manifold and hydrofoils act as a vortex breaker so that the appearance of the water surface is similar to that of the Ragged Chutes head (note the shape of the water surface around the air pipes on the left photograph in Figure 6.10 and compare it to the center photograph in Figure 6.11). Once the level increases above the manifold plate, the vortex can no longer form and the manifold must be the source of air into the downcomer.

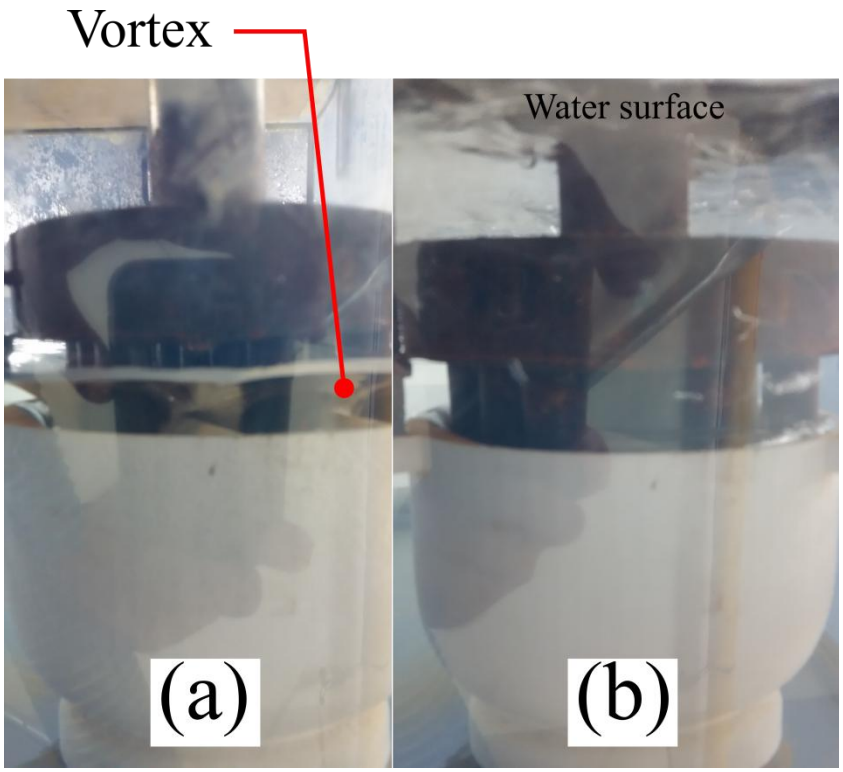

Figure 6.10: Peterborough head at the minimum (a, 3 kg/s) and maximum (b, 8 kg/s) water flow rate. At high water flow rate, the air manifold (cylindrical steel section above hydrofoils) blocks vortex formation

The Ragged Chutes head operates with a flattened vortex over the intake pipes. Across the entire flow rate range, the large, flat vortex has several small vortices that bridge the surface into the intake pipes. Note that all three photographs in Figure 6.11 show that these smaller vortices preferentially enter the middle pipes where there is a straight run into the downcomer.

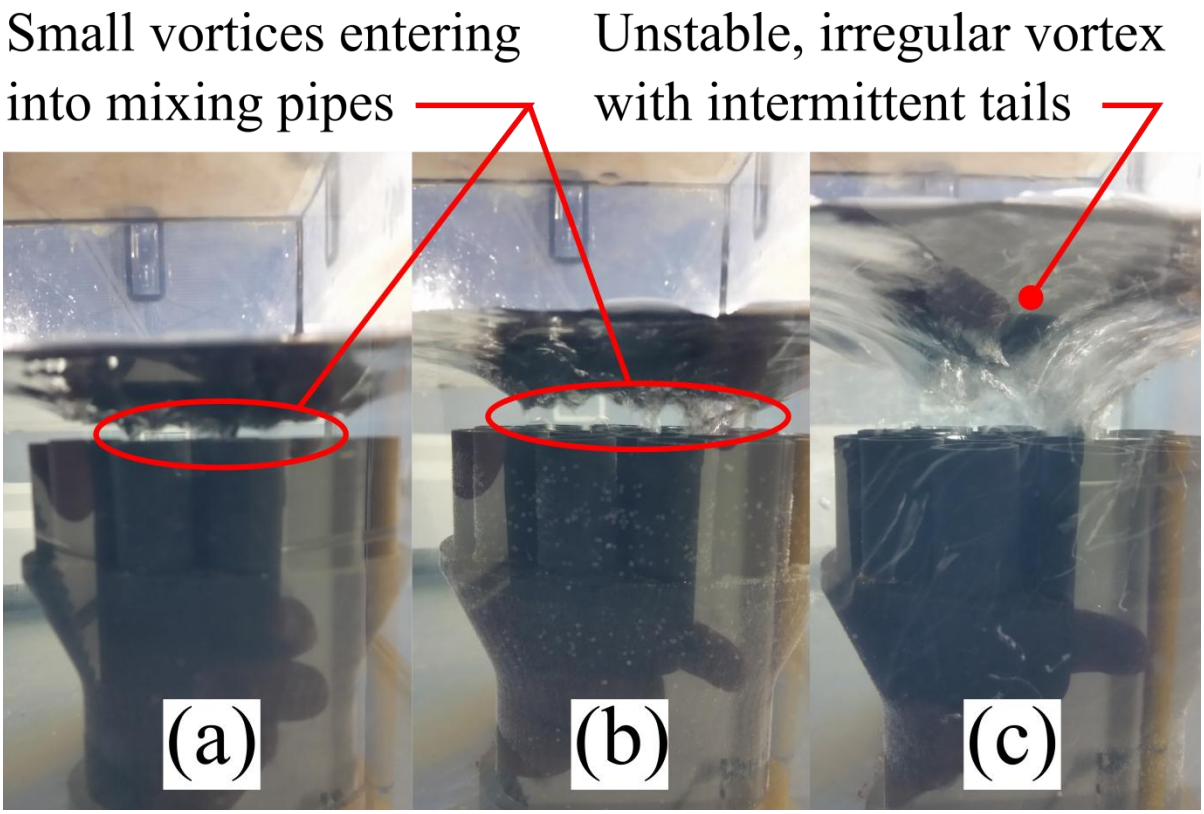

Figure 6.11: Ragged Chutes head at the minimum (a, 3 kg/s), middle (b, 5 kg/s), and maximum (c, 8 kg/s) water flow rate

From these experiments, there are three poor performers: the snorkel head with any snorkel in place (excepting the 'no snorkel' case from section 6.1.1 compared against the others in this section as 'snorkel'), the headless configuration, and the Peterborough head. All of the snorkel head configurations with the snorkel produced less air than the 'no snorkel' configuration and showed a similar pattern of rapidly increasing water level at high flow rates where they shifted from vortex entrainment to snorkeling. The headless configuration produced less air than the snorkel and Ragged Chutes heads, required more water over the inlet across all flow rates, and was unstable in the upper flow rates. The Peterborough head also produced less air than the

snorkel and Ragged Chutes heads and showed the same water level discontinuity as the snorkel head configurations with the snorkel installed.

The remaining two are the snorkel head (without snorkel) and the Ragged Chutes head. The snorkel head produced more air than the Ragged Chutes head on average. On its own, this metric is sufficient to rule in favour of this configuration of the snorkel head over the Ragged Chutes head. However, the Ragged Chutes head had less water over the ends of its pipes than the snorkel head had over its lip, indicating less irreversibility occurring above it. Shortening and increasing the diameter of the mixing pipes at the top of the Ragged Chutes head should improve its performance, particularly where it diverges from the performance of the snorkel head at increasing flow rates after the inflection point (see: Figure 6.6) A hybrid between the two with a vortex-breaking grille positioned up at the lip of the mixing head should combine the efficient over-lip entrainment of the Ragged Chutes head with the lower irreversibility of the snorkel head (without snorkel).

6.2 Dynamic Earth HAC forebay water level hypothesis validation

Only one mixing head has been fabricated and tested (see: Figure 6.12), so it has not been possible to perform a comparison between heads at this scale. However, the Dynamic Earth HAC is more flexible in water fill quantity so that the forebay tank level can be measured under a systematic series of water flow rate and water load conditions. Water fill quantity is the total amount of water in the HAC. During operation, the separator level is held at a single fixed set point, so adding water to the system has the primary effect of raising the water level in the tailrace tank. Driving head is the head faced by the pumps that is also a component of the hydropower consumed by the compression process. When the tailrace level is raised, the driving

head is decreased and the pumps deliver more water flow. The hypothesis for this evaluation is that the forebay level is a function of water flow rate and not driving head.

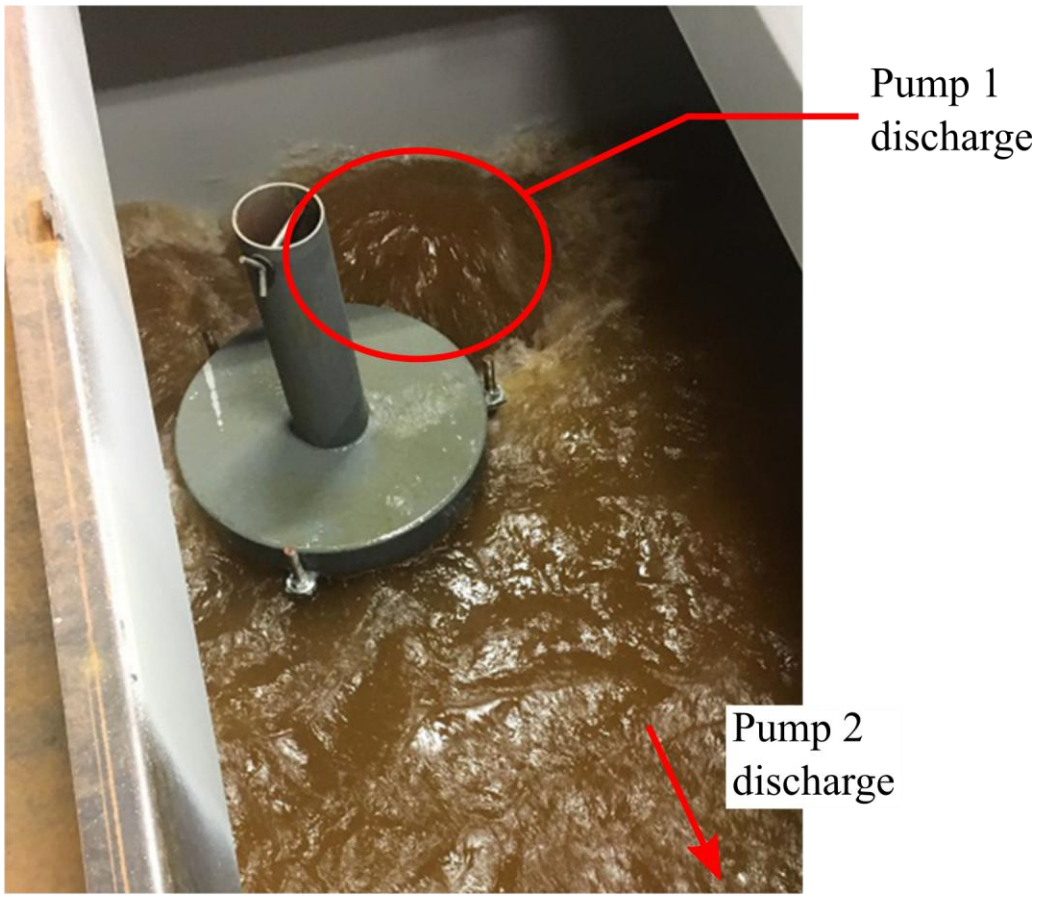

Figure 6.12: View through the lid of the forebay tank at Dynamic Earth HAC at a moderate flow rate on both pumps (modified from Electrale Innovation Limited, 2017)

A series of benchmark tests (numbered 68-90) were performed to identify the optimum water fill quantity for the Dynamic Earth HAC (Sivret, 2018). The 68th-80th tests were performed on two pumps and the 81st-90th tests were performed on a single pump (with the discharge port for pump 1 blocked off to prevent backflow) to capture a lower range of water flow rate. For the 81st-83rd tests, the flow meter on the blocked pump had a nonzero reading. These readings were ignored in

this result, which brought those tests into line with the other single pump tests (see: Figure 6.13). The maximum variation of water load is approximately 9 tonnes of water, which corresponds to 1.04 m of tank level between the forebay and tailrace tanks. The greatest difference occurs between the 68th and 80th tests on two pumps. This adjustment of water load changes the range of water flow rate of each of the tests, because the pumps face different head with changing tank levels. Both series of tests are presented in Figure 6.13. Despite changing water load, the two-pump and single pump test series each follow a single trend of forebay water level with water flow rate.

The single pump test series followed a similar linear trend to that observed at Baby HAC, passing through zero (red line in Figure 6.13). In the range of higher flow rates from the two-pump test series, the trend was quadratic (6.1), which is more in line with the expectation from section 3.5.

$$h_{inlet} = 3.20 \cdot Q_l^2 - 0.531 \cdot Q_l + 0.143 \quad (6.1)$$

There are three points in the two pump data at the top end of the water flow rate range that do not follow the same trend as the others, corresponding to the maximum pump speed for the three highest levels of water fill quantity. It was not possible to further increase the water fill quantity or pump speed to follow this shift further, but this may reflect a change in the operation of the mixing head. It is not a shift from vortex entrainment to snorkeling, as was observed with the similar head at Baby HAC (see: section 6.1.2). That was caused by the base of the air manifold being submerged, which is at 0.32 metres for this head, too low to be of relevance.

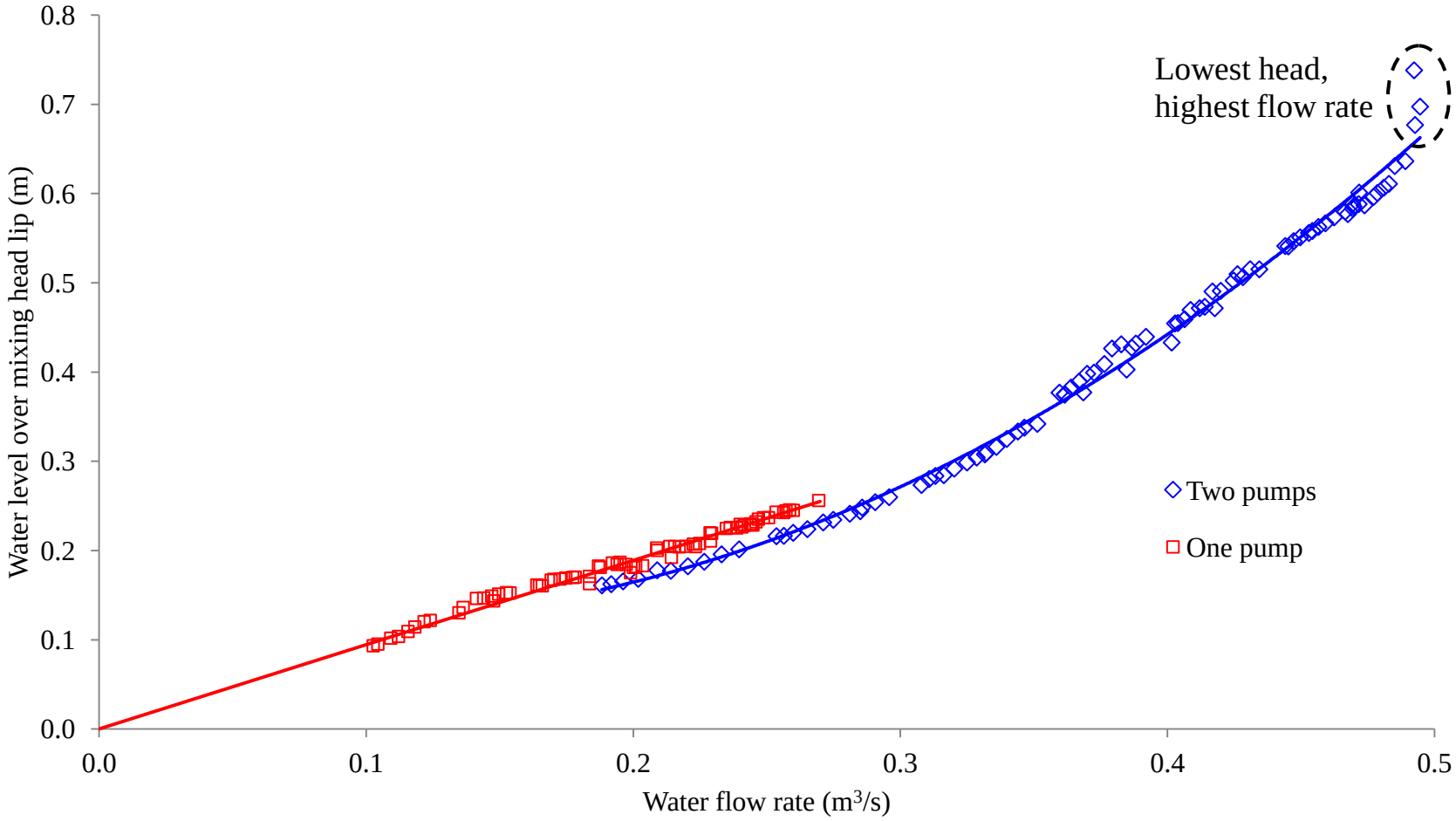

Figure 6.13: Water level over the mixing head lip on one pump and two pumps at Dynamic Earth HAC. The dataset for this test series is published in Sivret (2018)

6.3 Separator pressure drop

As with the mixing head, any irreversibility that is generated in the separator is energy unavailable for air compression. The curves presented in Figure 6.14 are the results of one dimensional fluid flow models for water flow in the main components of Baby HAC. The downcomer loss is underestimated because the effect of air is ignored in this simplistic analysis. The separator loss was evaluated using the pipe flow equation for head loss in the flow from the outlet of the downcomer, around the baffle, and up to the inlet of the riser pipe. Low flow velocity limited the loss such that the total head loss in the Baby HAC separator constitutes less than 1% of the nominal driving head (1 m) for this prototype at maximum water flow rate (8 kg/s). Head loss in this separator is too low to measure reliably with low-cost instruments and is not expected to account for enough energy to be worth investigating in detail, so it has been disregarded.

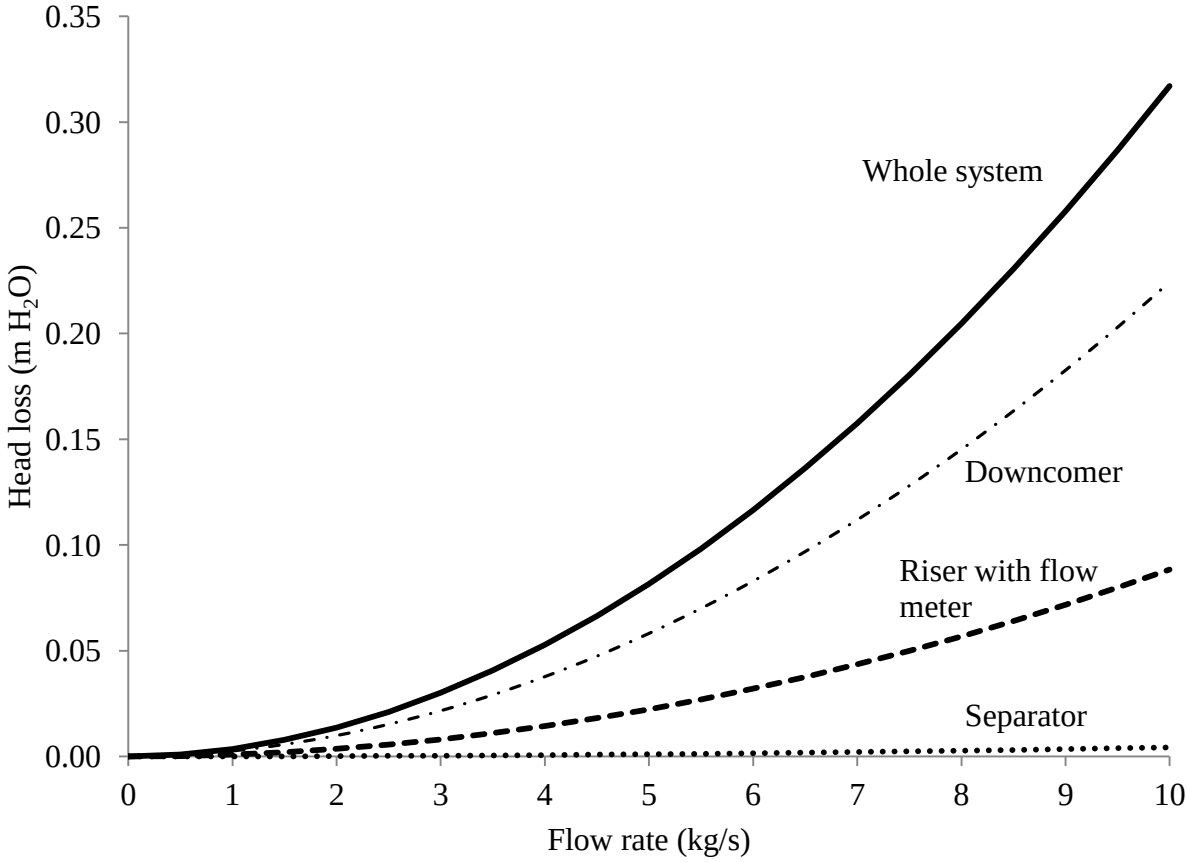

Figure 6.14: Baby HAC head loss breakdown

Pressure drop in the Dynamic Earth HAC separator eliminated the potential selection of a centrifugal separator (see: section 4.1). The analysis also highlighted the potential for excessive head loss in the downcomer outlet into the separator if the downcomer was not first increased in diameter immediately above the separator (see: section 4.2). The CFD results in Table 6.3 are consistent with the expected quadratic relationship between flow rate and pressure drop. The average Atkinson resistance (McPherson, 2003) of the Dynamic Earth separator is 20,669 kg/m^7, where the Atkinson resistance ($\mathcal{R}$) relates pressure drop (ΔP) to flow rate (Q_l):

$$\Delta P = \mathcal{R} \cdot Q_l^2 \tag{6.2}$$

Table 6.3: Atkinson resistance for Dynamic Earth HAC separator based on CFD model

Total flow rate (m^3/s)	Pressure drop (Pa)	Head loss (m H_2O)	Atkinson resistance (kg/m^7)
0.200	832	0.085	20,734
0.301	1,870	0.191	20,698
0.401	3,319	0.339	20,672
0.501	5,177	0.529	20,635
0.601	7,445	0.761	20,605

During the design and construction of Dynamic Earth HAC, no provision was made to directly measure the pressure drop across the separator. With a nominal head of 5 metres, the separator on Dynamic Earth HAC accounts for a greater potential fraction of the total head loss in the compression loop than does the Baby HAC separator, where the loss was on the order of 1% of the total. Without direct measurement, this value can only be confirmed by matching the

mechanistic HAC simulation model to the actual performance, after accounting for the separator pressure drop (see: section 6.5).

6.4 Separator model verification

The separator effectiveness models rely on two input parameters: the flow field inside the separator interrogated at pre-determined interrogation planes and the bubble size distribution at the inlet. The flow field result was produced using the CFD models described in chapter 4. At Baby HAC, the bubble size distribution was measured manually in a photograph of the downcomer immediately above the separator inlet. That measurement was used to select the closest bubble size model, which was used to predict the bubble size at the Dynamic Earth HAC separator inlet.

These inlet parameters were fed into one of two models, which predicted the bubble motion inside the separators: the displacement model was used for the horizontal gravity separator at Baby HAC and the vertical velocity model was used for the vertical gravity separator at Dynamic Earth HAC. The displacement model result was compared to the actual separator visually on photographs at minimum (3 kg/s), middle (5 kg/s), and maximum (8 kg/s) flow rate. The vertical velocity model result was compared to the actual measured separator effectiveness at Dynamic Earth HAC calculated as the ratio of air flow rate measured at outlet over the air flow rate measured at inlet.

6.4.1 Bubble size measurement

The bubble size distribution at Baby HAC was measured in a photograph of the downcomer above the separator inlet using the Ragged Chutes head at a flow rate of 5 kg/s, using the

measurement procedure originally established by Akita and Yoshida (1974), outlined in section 5.1.5. The diameters of a total of 566 bubbles were measured on their long and short axes and the average of the two values was taken to be the equivalent bubble diameter for each one. The bubbles were sorted in ascending order of diameter (volume) and the cumulative distribution is presented in Figure 6.15. Percent passing is a volume fraction relative to a given diameter, which is the sum of volumes of all bubbles with lesser or equal diameter divided by the sum of volumes for all bubbles in the distribution. Recall from section 2.3.6 that the Rosin-Rammler distribution (6.3) calculates percent passing (Y) using two fit parameters: Rosin-Rammler mean diameter ($\bar{d}$) and a spread parameter (n). The Rosin-Rammler distribution line is the minimum RMS fit between the distribution and all measurement points, where both parameters of the distribution were allowed to flex.

$$Y = 1 - \exp\left[-\left(\frac{d}{\bar{d}}\right)^{n}\right] \tag{6.3}$$

Note that the Rosin-Rammler distribution presented in Figure 6.15 fits the measured distribution well when the bubble diameter is smaller than 3.5 mm and more poorly in the upper range. There are three primary reasons for this imperfect fit: (i) the unmodified Rosin-Rammler (two-parameter) distribution is not a perfect fit for bubble distributions, (ii) many observable bubbles were missed in the measurement (presented in Appendix I), and (iii) larger bubbles tend not to sit against the pipe wall and were more difficult to spot in the bubble-dense image.

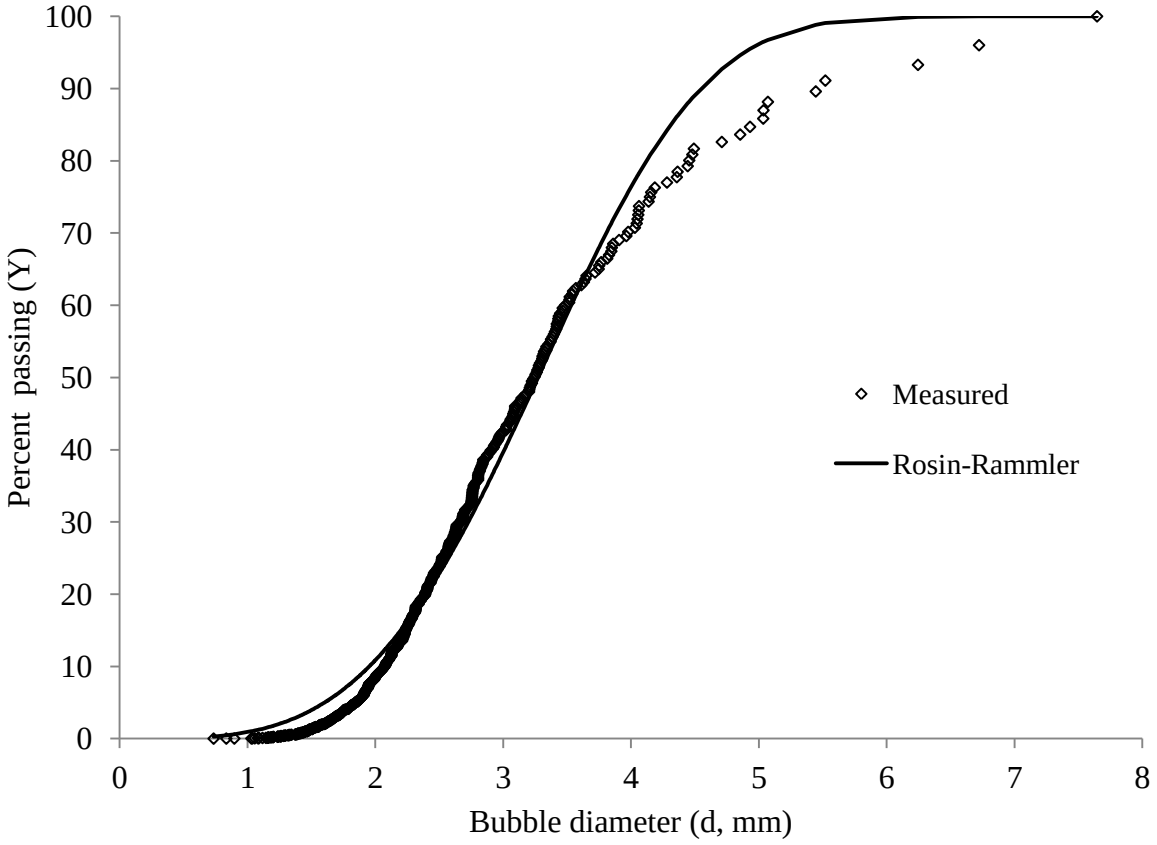

Figure 6.15: Cumulative bubble size plot from measurement at Baby HAC using the Ragged Chutes head at 5 kg/s water flow rate. Each data point represents a bubble

Figure 6.16 compared the parameters of the best-fit Rosin-Rammler distribution from Figure 6.15 to the linear distribution of fit parameters of air bubbles in water from the literature. This fit is consistent with the pattern, which means that the bubble distribution can be defined with a single parameter. With this relationship, only one parameter needs to be estimated as an input for the design of separators for future HACs.

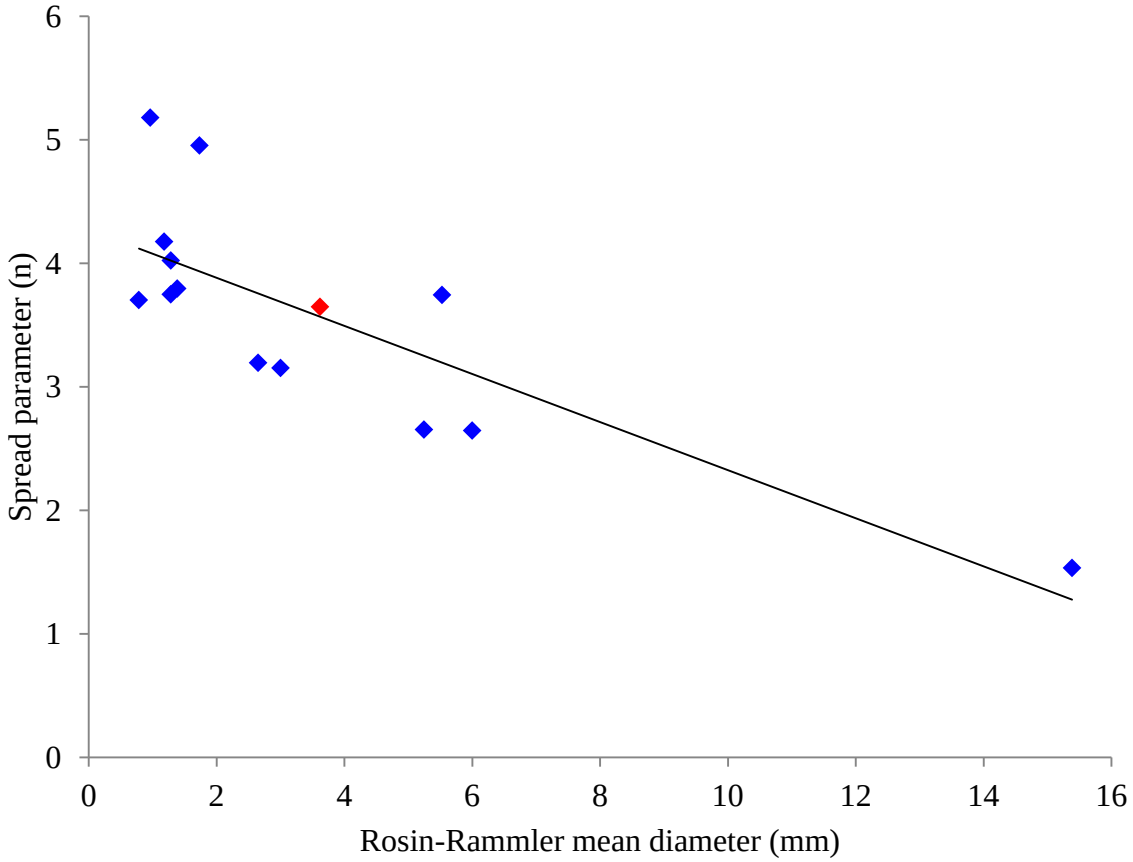

Figure 6.16: The red point is the measured bubble distribution added to the distributions from the literature first presented in Figure 4.8

The Ragged Chutes head was used for these tests. It has a reliable linear relationship between water and air mass flow rate:

$$\dot{m}_g = 0.000103 \cdot \dot{m}_l - 7.80 \times 10^{-6} \tag{6.4}$$

At 5 kg/s water flow rate, the air flow rate is 0.000509 kg/s. Assuming a temperature of 20°C, and using the normal separator pressure of 130 kPa (absolute) and internal pipe diameter of 102 mm provides enough information to calculate all of the bubble size model results (see: Table

6.4). For Baby HAC, only the Wilkinson et al. (1994) model produces sensible results, with an error of +27% on the Rosin-Rammler mean diameter. None of the other three models work correctly at this scale. The model presented in Hesketh et al. (1987) assumes that the bubble size is being limited by bubble breakup. That model overestimates the bubble size relative to the measurement, indicating that the bubble size at Baby HAC is being limited by coalescence. The Kobus (1984) model was developed for open channel flow at larger scale and this is outside its empirical range. The scale in size and flow rate of Baby HAC is within the top end of the range of experiments by Akita and Yoshida (1974). It is not clear why the bubble size predicted by this model matches so poorly.

Table 6.4: Comparison of the measured bubble distribution to the four bubble models presented in section 4.3.2

Source	Maximum bubble size, d_{99}	Rosin-Rammler mean, $\bar{d}$	Rosin-Rammler spread parameter, n
Measured	N/A	3.62	3.65
Akita and Yoshida (1974)	24.2	11.4	2.04
Wilkinson et al. (1994)	7.23	4.60	3.38
Hesketh et al. (1987)	25.2	11.7	1.99
Kobus (1984)	0.170	0.118	4.25

The models predict results closer to one another at the Dynamic Earth scale (see: section 4.3.2). However, the Wilkinson et al. (1994) model was used as the initial best estimate of bubble size distribution for the vertical velocity model. Table 6.5 shows that the bubble size distribution by this model is nearly constant across the full flow rate range on two pumps. Therefore, the bubble

size distribution used for modeling should be constant with a Rosin-Rammler mean diameter ($\bar{d}$) of 4.13 mm and a spread parameter (n) of 3.47.

Table 6.5: Wilkinson et al. (1994) bubble size model result for the average conditions in the 106th-109th benchmark tests of the Dynamic Earth HAC. During the tests, the average water temperature was 295 K and the average separator pressure was 316 kPa (absolute). The internal pipe diameter at the separator inlet is 0.575 m

Water flow rate (m3/s)	Air flow rate		Wilkinson bubble model			
	(m^3/s)	(m/s)	d_{99} (mm)	$\bar{d}$ (mm)	n	Residual
0.239	0.0140	0.0539	6.45	4.15	3.46	3.65E-08
0.295	0.0169	0.0651	6.43	4.14	3.47	2.91E-08
0.357	0.0191	0.0737	6.41	4.13	3.47	-5.74E-07
0.371	0.0197	0.0760	6.41	4.13	3.47	4.85E-08
0.425	0.0217	0.0836	6.40	4.12	3.47	2.84E-08
0.466	0.0229	0.0882	6.39	4.12	3.47	2.67E-08
0.490	0.0233	0.0899	6.39	4.11	3.47	2.79E-08

6.4.2 Baby HAC displacement model verification

The separator was modeled and photographed at three water flow rates: 3, 5, and 8 kg/s. The experiments were performed with the Ragged Chutes-type mixing head and the air flow rate has been calculated for each set point using equation (6.4). The CFD flow field model does not include the air fraction of the total flow. The gas volume fraction is small (see: Table 6.6) and decreases as the air separates, so the total flow rate was assumed to be equal to the water flow rate for the purposes of modeling for this experiment.

Table 6.6: Gas volume fraction calculation for Baby HAC

Flow rate (kg/s)		Flow rate (m3/s)		Gas volume fraction
Water	Air	Water	Air	
3	3.02E-04	3.01E-03	2.01E-04	0.0625
5	5.09E-04	5.01E-03	3.38E-04	0.0631
8	8.19E-04	8.02E-03	5.44E-04	0.0635

The separator effectiveness simulation for horizontal separators (such as the one installed at Baby HAC) tracks bubbles of a uniform size through space. To accommodate this method, the bubble size distribution was divided into a histogram consisting of 11 bins (see: Figure 6.17). Each bin is associated with a single, fixed bubble diameter. A volume fraction was calculated for each bin, using the measured size distribution presented in section 6.4.1.

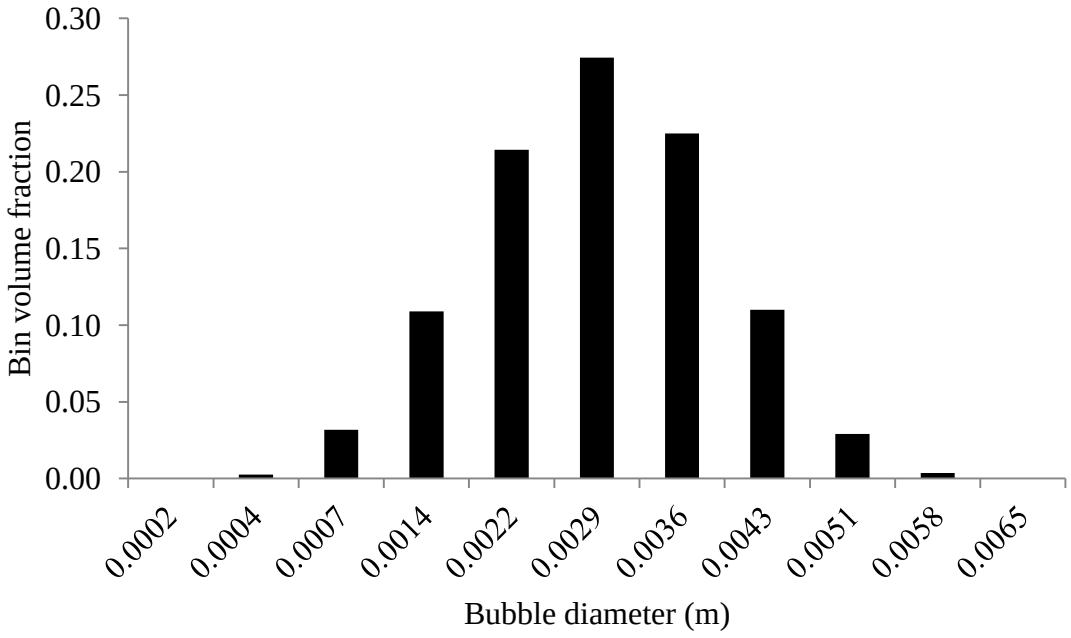

Figure 6.17: Bubble size histogram used for Baby HAC simulations. The sum of all bin volume fractions is 1

The model independently calculated the fraction of each bin present at each segment on an interrogation plane (see: Appendix J), by the procedure described in section 4.3.4. These results were volume-weighted and averaged to produce a distribution of the air by volume across the segments of each of the interrogation planes of the solution grid plus an additional segment denoting the separated air. The segment distributions were linearly interpolated to identify the position above which 95% and 99% of the original air volume was located for each of the interrogation planes. Those positions have been superimposed over photographs from the experiments at each of the modeled water flow rates: 3 (Figure 6.18), 5 (Figure 6.19), and 8 kg/s (Figure 6.20). The interrogation planes are labelled in millimeters from the inside surface of the wall behind the downcomer pipe. The first interrogation plane was moved to the centreline of the

downcomer in order to produce a useful model for the low and middle water flow rates. A consequence was that the constant velocity assumption between interrogation planes poorly matched the actual conditions close to the downcomer pipe, where there was high acceleration within the flow (changing both direction and speed).

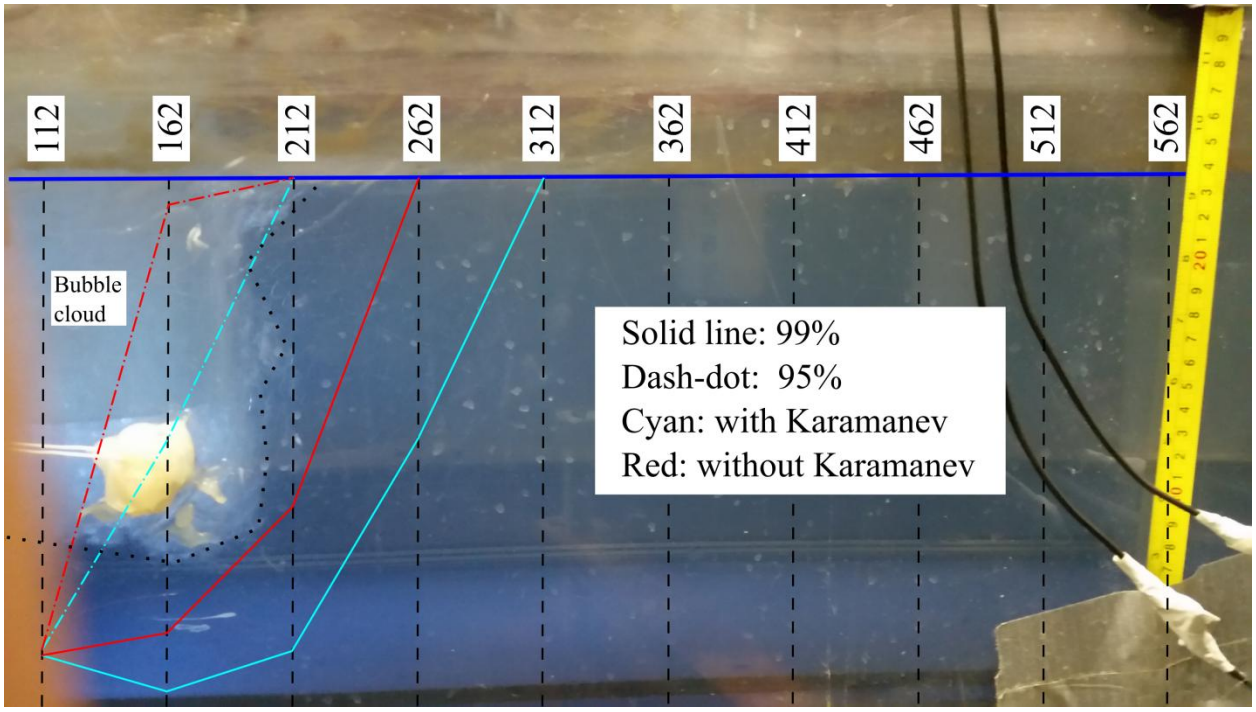

Figure 6.18: Separator at 3 kg/s water flow rate with model results superimposed

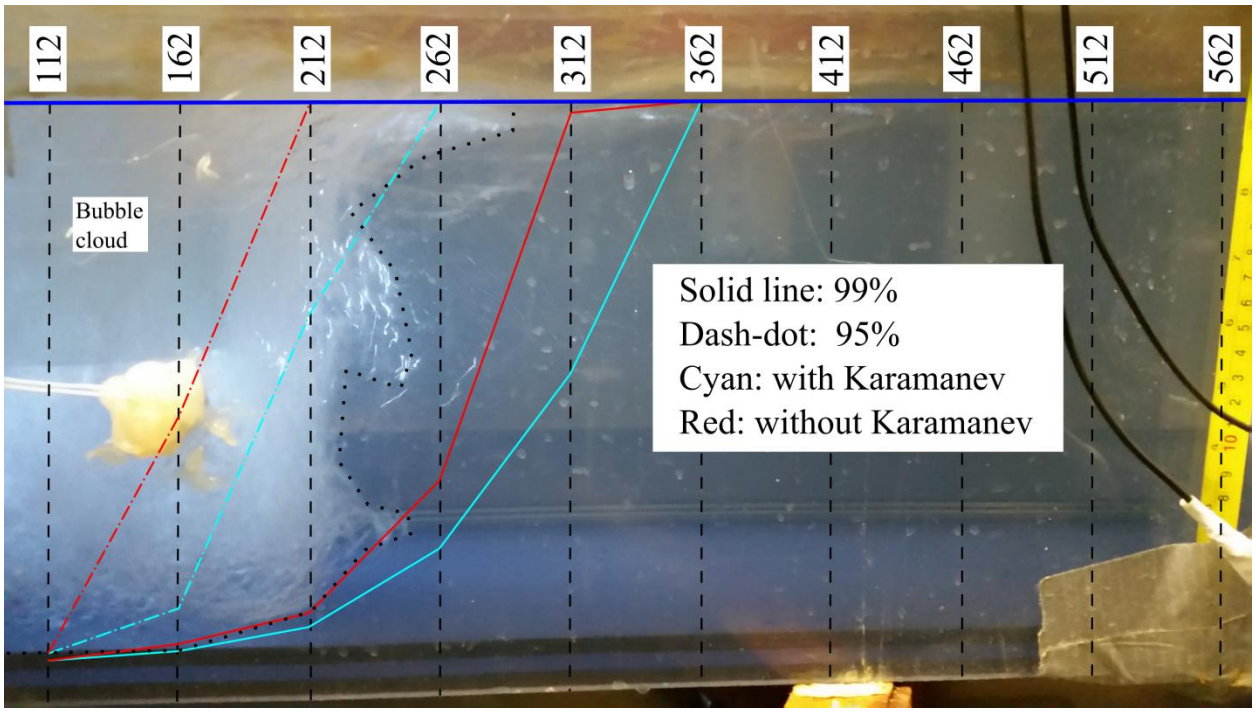

Figure 6.19: Separator at 5 kg/s water flow rate with model results superimposed

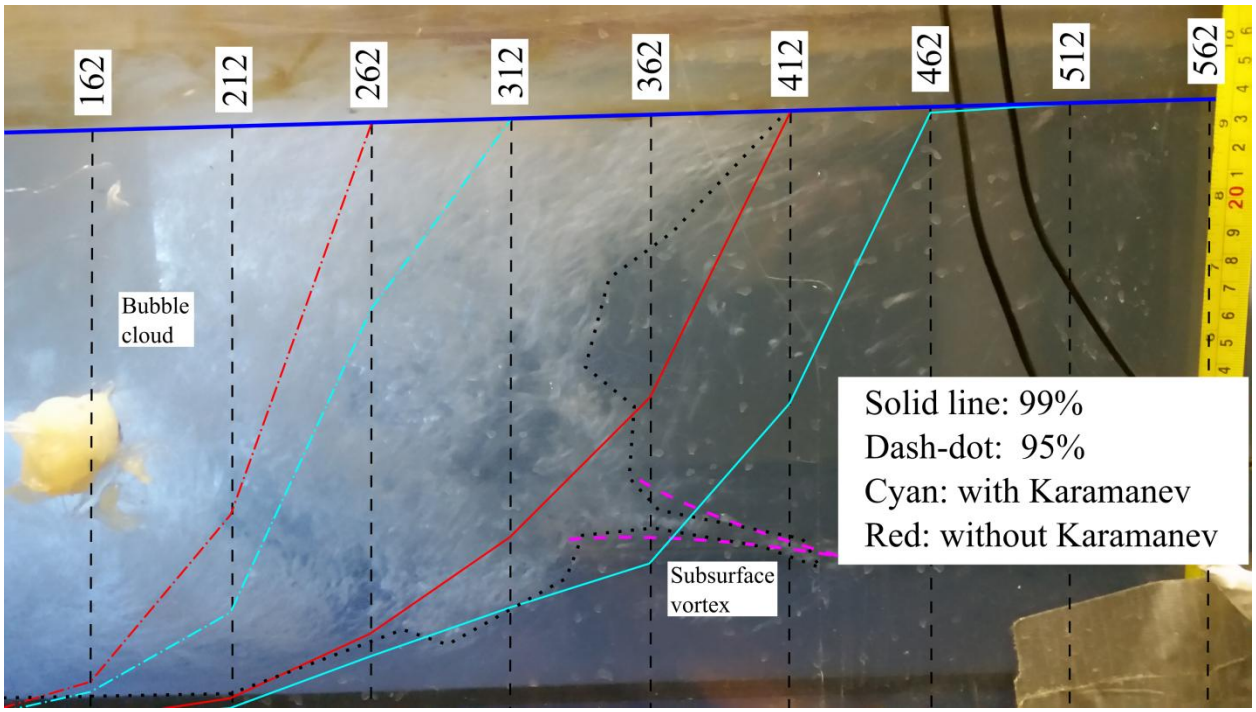

Figure 6.20: Separator at 8 kg/s water flow rate with model results superimposed

The bubbles visible at the bottom of the separator between planes 312 and 412 in Figure 6.20 form part of the core of a subsurface vortex not otherwise visible. The vortex may have been shed by the flow rapidly turning around the sharp edge of the downcomer pipe outlet or generated by the air moving vertically relative to the dominant horizontal motion of the water. Neither the flow field CFD model nor the bubble displacement model is capable of predicting this behaviour. In all three cases of mass flow rate of water, the 99% envelope includes almost all of the bubbles visible in the photographs. This means that although the approach is crude, it would nevertheless prove effective for design purposes. The horizontal flow path length at which 99% of the bubbles clear the water and coalesce with the compressed air plenum would be accurately predicted. The Karamanev and Nikolov (1992) drag correction (from section 2.3.4) systematically over-predicts the flow path length. In effect, the correction increases the bubble drag coefficient and reduces the predicted relative velocity, particularly for large bubbles.

6.4.3 Dynamic Earth HAC vertical velocity model verification

Four tests were selected from the Dynamic Earth HAC benchmark series for the separator model verification: the 106^{th}-109^{th} benchmark tests were performed in the middle of the range of water fill quantity of the second performance map measurement. The first performance map (68^{th}-90^{th} benchmark tests) was plagued by air leaks through the lid seal on the forebay tank, which made the air flow metering at the inlet unreliable. These four tests were selected from the two-pump runs where the range of water flow rates was near its maximum. The conditions (in terms of head and flow rate) for these tests were similar enough that all of them could be compared to one another using a single bubble size distribution and, therefore, a single set of separator model runs. The CFD flow field model uses total volume flow rate, so the air and water volume flow

rates have been added together to compare on an even footing (see: Table 6.7). The air flow rate reported below is the inlet flow rate, so that the total flow rate is that at the separator inlet.

Table 6.7: Total flow rate for separator modeling. Each flow rate value is an average of the 106th-109th benchmark tests of the Dynamic Earth HAC. Inlet air flow rate is reported

Pump speed (rpm)	Flow rate (m3/s)			Gas volume fraction
	Water	Air	Total	
600	0.205	0.0147	0.220	0.0669
650	0.267	0.0197	0.287	0.0687
700	0.319	0.0229	0.342	0.0670
750	0.364	0.0256	0.389	0.0657
800	0.405	0.0275	0.432	0.0636
850	0.445	0.0288	0.474	0.0608
880	0.470	0.0299	0.500	0.0599

Air productivity at Dynamic Earth HAC was calculated as the ratio of air flow rate measured at the outlet to the air flow rate measured at the inlet. The average measured productivity for the four benchmark tests at the lowest total flow rate (0.22 m^3/s) was 94.9%. Solubility yield accounts for the 5.1% loss of air, assuming perfect or near-perfect separator effectiveness at this low flow rate. From section 1.1.2, the air productivity is the product of yield (from solubility) and separator effectiveness. Yield was assumed to be constant for the calculation of air productivity from the separator effectiveness model for comparison to measured results; decreasing air productivity with increasing water flow rate is ascribed to a reduction of separator effectiveness. Each model result reported in Figure 6.21 below has been normalized (i.e.

multiplied by 94.9%, the yield) to convert the modeled value of separator effectiveness to air productivity.

This simple conversion is crude but produces an approximation of yield close to the model predictions by Young (2017). Table 6.8 contains modeling results of yield in downcomer models by downcomer length and water to air mass flow ratio. The water to air mass flow ratio at Dynamic Earth HAC is in the range of 4,000-5,000 (Sivret, 2018). Linear interpolation of the table for gas composed only of nitrogen and oxygen and with a downcomer length of 26 metres and mass flow ratio of 4,500 predicts a yield of 95.7%. The yield model produces reasonable agreement with the measured air productivity at the lowest water flow rate being attributable fully to solubility. A more detailed bivariate analysis of yield and separator effectiveness is the subject of future work to be conducted pending the addition of dissolved gas species instruments to Dynamic Earth HAC.

Table 6.8: Yield simulation results from Young (2017) at 10°C (close to the actual conditions of the experiments in this chapter). The Dynamic Earth HAC downcomer is 26 metres long. The column labels under gas yield are the mass flow ratio (water to air)

Downcomer length [m]	Gas Species	Gas yield, $\dot{n}_{j,out} / \dot{n}_{j,in}$ [%]				
		500	1,000	2,000	7,000	20,000
1	N2	100.00	100.00	100.00	99.99	99.99
1	O2	100.00	100.00	99.99	99.98	99.97
1	Ar	100.00	100.00	99.99	99.98	99.98
1	CO2	100.02	99.90	99.74	99.45	99.33
10	N2	99.95	99.81	99.61	99.26	99.11
10	O2	99.88	99.56	99.07	98.25	97.90
10	Ar	99.90	99.62	99.21	98.54	98.24
10	CO2	96.83	89.90	81.69	71.67	68.20
20	N2	99.75	99.25	98.55	97.48	97.08
20	O2	99.42	98.25	96.64	94.16	93.22
20	Ar	99.50	98.48	97.10	95.06	94.32
20	CO2	86.86	69.70	56.01	44.33	41.26
50	N2	98.35	95.99	93.06	88.91	87.43
50	O2	96.33	91.25	85.04	76.31	73.18
50	Ar	96.59	91.92	86.49	79.33	76.91
50	CO2	51.18	32.95	24.02	17.78	16.22
100	N2	94.55	88.30	80.67	70.13	66.54
100	O2	88.74	76.83	63.25	45.68	39.84
100	Ar	88.84	77.50	65.25	50.32	45.63
100	CO2	26.37	15.68	10.64	7.07	6.19
200	N2	85.35	70.66	53.31	32.35	26.38
200	O2	72.77	51.02	30.18	10.78	6.35
200	Ar	72.20	51.01	31.27	12.92	8.66
200	CO2	11.62	6.10	3.40	1.55	1.16

The flow field CFD model was run for total flow rates between 0.1-0.6 m^3/s at an increment of 0.1 m^3/s. Three vertical velocity model separator effectiveness curves are reported: (i) Wilkinson et al. (1994) bubble diameter with the Karamanev and Nikolov (1992) drag coefficient correction, (ii) Wilkinson et al. (1994) bubble diameter without the drag coefficient correction, and (iii) manual selection of the Rosin-Rammler mean bubble diameter ($\bar{d}$) with the best visual fit of the measured data to the nearest 0.25 mm without the drag coefficient correction. The mean diameter selected for the third curve was 8.25 mm, which is 106% higher than the Wilkinson et al. (1994) diameter of 4.13 mm (see: section 6.4.1).

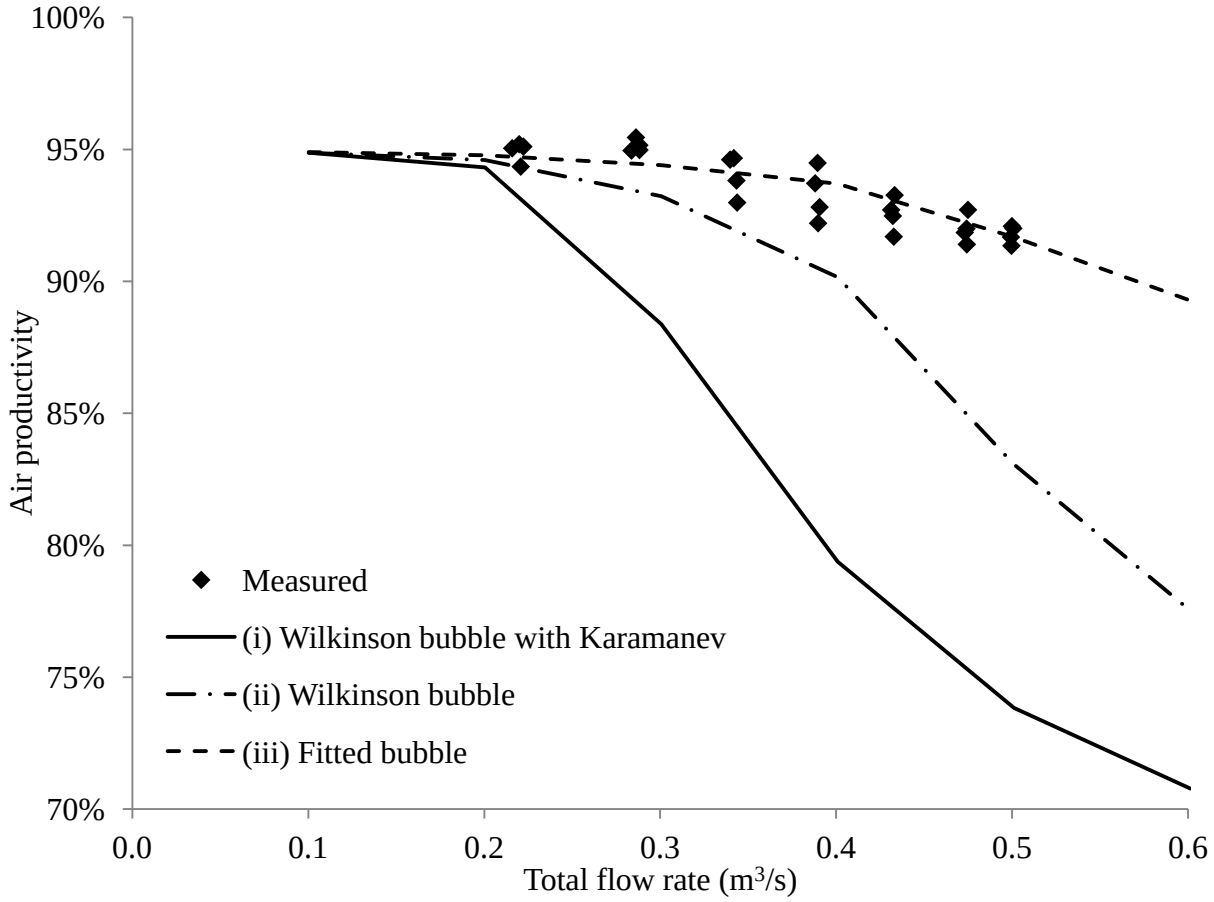

Figure 6.21: Separator effectiveness with total (combined water and air) flow rate from the 106th-109th benchmark tests and three variants of the vertical velocity model

The Karamanev and Nikolov (1992) drag coefficient correction resulted in under-prediction of separator effectiveness for both Baby HAC and Dynamic Earth HAC. The Wilkinson et al. (1994) bubble model was the closest match to the Baby HAC measured value, but significantly under-predicts the bubble size at Dynamic Earth HAC. From Figure 4.7, the only model that predicted a larger bubble diameter for Dynamic Earth HAC was the Akita and Yoshida (1974) model, which predicted roughly double the bubble diameter (consistent with Table 6.9 below).

Table 6.9: Akita and Yoshida (1974) bubble size model result for the average conditions in the 106th-109th benchmark tests of the Dynamic Earth HAC. During the tests, the average water temperature was 295 K and the average separator pressure was 316 kPa (absolute). The internal pipe diameter at the separator inlet is 0.575 m

Flow rate (m^3/s)			Akita & Yoshida bubble model			
Water	Air	Total	d_{99} (mm)	$\bar{d}$ (mm)	n	Error
0.205	0.0147	0.220	13.71	7.86	2.74	6.10E-07
0.267	0.0197	0.287	13.24	7.65	2.78	5.24E-07
0.319	0.0229	0.342	13.00	7.54	2.80	4.64E-07
0.364	0.0256	0.389	12.83	7.47	2.82	8.03E-07
0.405	0.0275	0.432	12.72	7.41	2.83	4.43E-07
0.445	0.0288	0.474	12.65	7.38	2.84	7.93E-07
0.470	0.0299	0.500	12.59	7.36	2.84	3.24E-07

The vertical velocity model was recalculated using the Akita and Yoshida (1974) bubble model. The Rosin-Rammler mean flexes more with changing flow rate with this model than for the Wilkinson et al. (1994) model. Therefore, the bubble diameter inputs for the vertical velocity separator model have been set to the nearest result from Table 6.9 based on total flow rate (e.g. $\bar{d}$ = 7.86 for a total flow rate of 0.2 m^3/s). Because the Karamanev and Nikolov (1992) drag coefficient correction has proven to effectively shrink the bubble size distribution, it has not been included in this model (see: Figure 6.22).

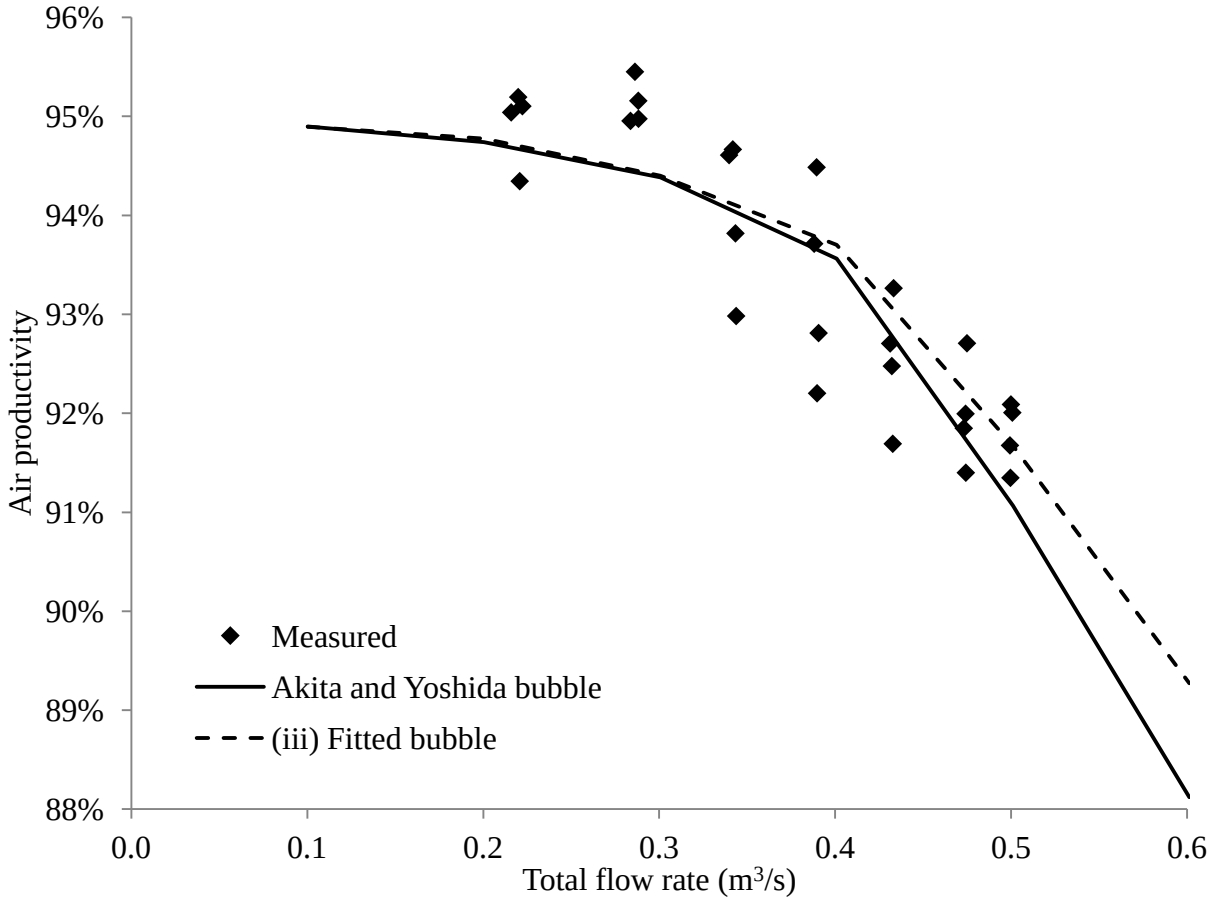

Figure 6.22: Separator effectiveness with total (combined water and air) flow rate from the 106th-109th benchmark tests against the vertical velocity model using the Akita and Yoshida (1974) bubble model and including curve (iii) from Figure 6.21

Using the Wilkinson et al. (1994) bubble size model (case (ii) from Figure 6.21) for design of a Dynamic Earth-scale HAC separator would significantly under-predict bubble size and result in an oversized separator, resulting in increased capital cost. The Akita and Yoshida (1974) model produces a much closer prediction, which is ~5% less than the fitted separator model (iii) using a Rosin-Rammler mean bubble diameter of 8.25 mm at the maximum total flow rate of 0.5 m^3/s.

6.5 Air detrainment in the downcomer

The model of Dynamic Earth HAC was predicting greater air flow rate than measured during the benchmark tests. A zone of air detrainment had been previously observed in the downcomer immediately below the mixing head at Baby HAC. The HAC performance model assumes bubbly flow along the full length of the downcomer, where the pressure increases with depth by the weight of the continuous column of water above. In a length of the downcomer where there is a continuous pocket of air and free-falling water beside it (as is the case for annular flow), there is no continuous column of water. The pressure would not substantially increase down this length. Fundamentally, this phenomenon represents an energy correction to the system. The energy wasted in free-fall and air re-entrainment is unavailable for air compression. The presence of a detrainment zone at Dynamic Earth HAC could explain the discrepancy between the model and measured result.

6.5.1 Visual observation at Baby HAC

Figure 6.23 shows the appearance of the detrainment zone in the downcomer immediately below the forebay tank at Baby HAC. This is the result of air bubbles coalescing after first being entrained at the mixing head and forming a pocket inside the downcomer. The water falls around the wall of the pipe in a falling film flow regime, where the water is accelerating in free-fall except for the friction along the wall boundary layer. The pressure does not increase in this section because of the coherent air pocket. At the base of the detrainment zone, the falling film impacts a static or slow-moving surface and re-entrains the air into bubbles by the impinging jet mechanism.

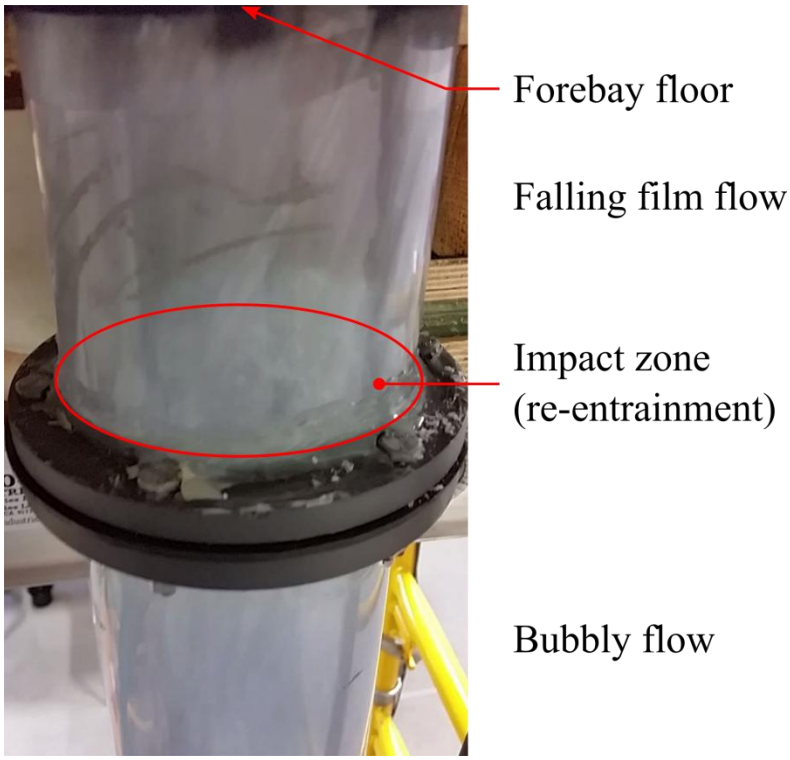

Figure 6.23: Air detrainment in the downcomer at Baby HAC at 5 kg/s water flow rate. The re-entrainment site is an impinging jet

The detrainment zone is visible in Baby HAC at all water flow rates and for all mixing heads (including no head), but is only recognizable in photographs at the lower flow rates. In the upper end of the water flow rate range, the falling film is nearly opaque. The top of the detrainment zone is not visible because it occurs inside or at the base of the mixing head, which is not transparent. However, the bottom of the zone tends to occur within 10 cm of the flange (pictured in Figure 6.23) and fluctuates over time. At low water flow rate (e.g. 3 kg/s), the zone tends to be more stable in that the bottom of the zone moves upward slowly and lowers suddenly when it merges with slugs of air migrating against the flow. At middle water flow rate (e.g. 5 kg/s), there are no air slugs successfully migrating against the flow, but the bottom of the detrainment zone

moves more rapidly than at low water flow rate and unpredictably. At high water flow rate (e.g. 8 kg/s), the detrainment zone appears less like falling film flow and more like a stationary churning slug, which occasionally shrinks enough to be pulled whole down the downcomer. When that occurs, a new pocket rapidly forms and the process is repeated.

The detrainment zone is visibly smaller with increasing flow rate across most mixing heads, except those where snorkeling was occurring. The snorkel head (configurations with the snorkel installed) and the Peterborough head had visibly larger detrainment zones at the highest flow rates. In one experiment with a de-foaming agent (using the Ragged Chutes head at 6 kg/s water flow rate), the length of the detrainment zone was on the order of 0.5 metres and the air flow rate through the system was halved, compared to the operating condition prior to adding the de-foamer. With the de-foamer, the process appeared to have some difficulty encapsulating the air into bubbles or slugs small enough to be dragged down the pipe instead of remerging with the air mass in the detrainment zone. The bubbles being formed were an order of magnitude larger than normal. Increasing the velocity in the downcomer would have increased its capacity to transport the air down (further discussion on this effect in section 7.7), but the increased water flow rate would also increase the flow rate of air into the system to be transported, making the size of and loss associated with the detrainment zone difficult to predict.

6.5.2 Pressure observation at Dynamic Earth HAC

The downcomer at Dynamic Earth HAC is opaque, so it is not possible to observe this effect visually. Instead, the pressure profile was measured in the upper section of the downcomer (see: Table 6.10) to detect the detrainment zone by the presence of a constant pressure section or interval where the pressure does not consistently increase as predicted by the bubbly flow model.

Experimental results are available from the 46th and 47th benchmark tests. Prior to each test, the instrument offsets were calibrated against the measured static water column over the respective pressure ports while the system was not running. The water level was inferred from the separator gauge pressure, which had been previously calibrated for this purpose against manual dipping of the water level in the surge pipe and pump #1 delivery line (Millar, 2017).

Table 6.10: List of pressure instruments and the port position relative to the base of the forebay tank (Millar, 2017)

Instrument name	Position (m)
P1P1	-0.72
P1P2	-1.50
P2P2	-2.25
P2P1	-3.00

The pressure profiles for the 46th benchmark test are presented in Figure 6.24 and the profiles for the 47th test in Figure 6.25. Each point is the time averaged pressure measured by the instrument at that elevation at the pump speed listed in the legend. The expected discontinuity in the pressure profile appears in every one of the tests. The effect is not immediately clear for the low pump speed (600 rpm) profiles, but projecting the profile up at constant slope intersects the zero gauge pressure line well below the bottom of the forebay tank. The base of the forebay tank sits 0.15 metres (6 inches) below the face of the flange at the base of the mixing head and the lip of the mixing head sits another 0.5 metres further up.

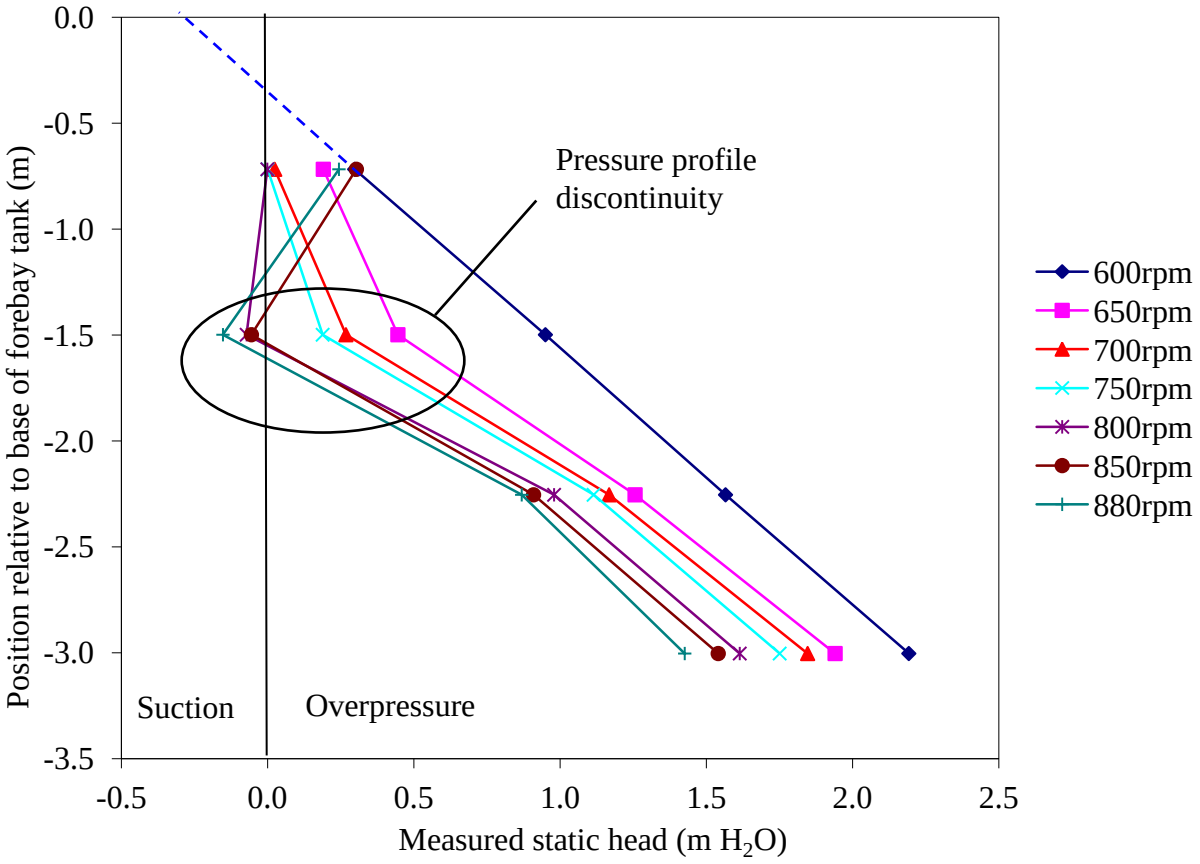

Figure 6.24: Pressure profiles from 46th benchmark test (modified from Millar, 2017)

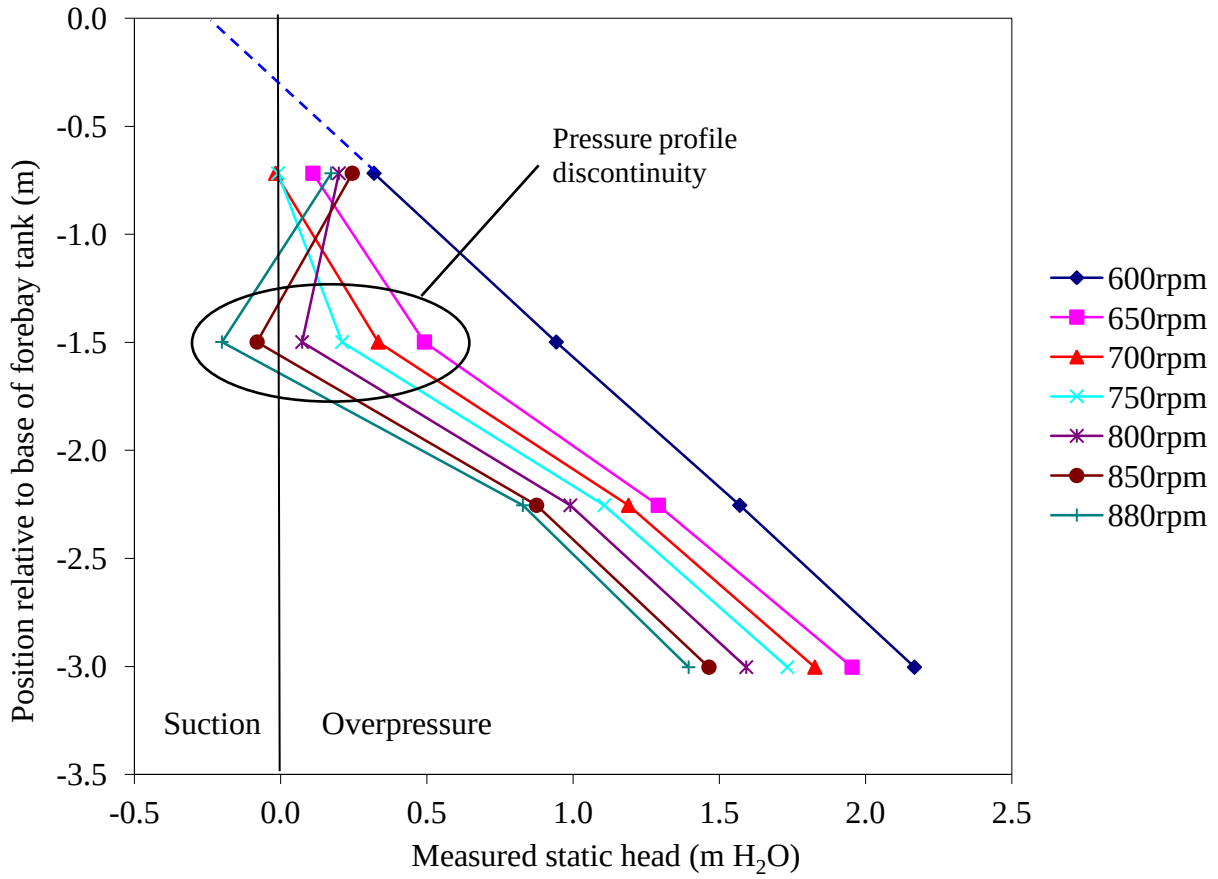

Figure 6.25: Pressure profiles from 47th benchmark test (modified from Millar, 2017)

The suction pressure inside the forebay tank at high pump speed was reaching around 1700 Pa (0.17 m H_2O) at the highest pump speed at the time this experiment was conducted. It is not clear whether the measured suction pressure at high flow rate at the P1P2 instrument location is actually greater than that in the forebay tank; however, there is no net static pressure increase to that point at the highest pump speeds (see: Figure 6.26). The rapid gain in pressure below the lowest point is probably from energy recovery at the point of impact of the free-falling jet against the slow-moving surface at which the bubbly flow resumes (May and Willoughby, 1991).

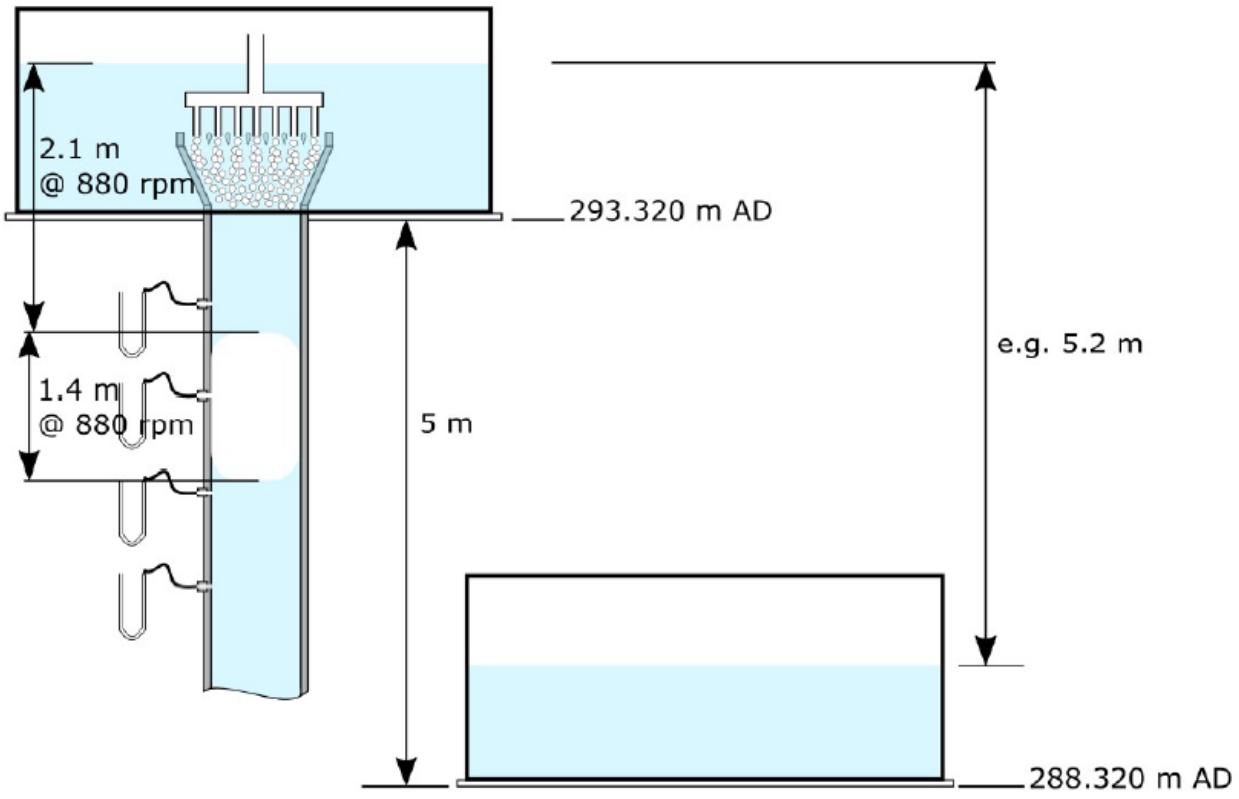

Figure 6.26: The local low pressure at the P1P2 instrument location is interpreted as direct observation of the air void in a free-fall detrainment zone (Millar, 2017)

The hypothesis for the cause of the detrainment zone is that too much air is being inducted in the initial entrainment process to be successfully transported down the downcomer. The flow passing the end of the hydrofoils at the bottom of the air manifold is immediately constricted in a nozzle arrangement (see: Figure 6.26) to increase the flow velocity to drag the bubbles down in the downcomer process. There are two potential problems with this arrangement. Firstly, the velocity at the end of the hydrofoils may be too low to transport some of the bubbles (as low as 0.5 m/s at a water flow rate of 0.2 m^3/s). This relatively low velocity is ideal for bubbles to coalesce into larger bubbles and slugs, which require a higher water velocity to properly entrain into the flow. Secondly, the pressure through the convergent section drops substantially,

especially at higher flow rates. If the pressure is low enough, bubble volume (and therefore buoyancy) increases and there may be more air inducted by the Venturi effect than the system can handle. Both of these problems lead to larger gas volume fractions in the flow, more bubble collisions, and more coalescence. Excessive air entrainment followed by coalescence, culminating in an annular flow regime beneath the convergent section (observed experimentally in the pressure profile) could be responsible for the poor performance of this mixing head.

6.6 Preliminary effects of salt co-solute

Adding a salt co-solute to the water circulating in a HAC is one of the interventions proposed to control gas solubility yield. The target concentration for most co-solutes is around 1 molal (mol solute/kg solvent), which corresponds to approximately 10% by weight.

Dissolving a co-solute has a small, linear, effect on HAC hydropower provided, and the pressure of the air delivered by increasing the water density. Most dissolved ionic salts increase the surface tension of water (Dutcher et al., 2010), increasing the maximum stable bubble diameter with reference to bubble breakup (Hesketh et al., 1987), suggesting that the HAC bubble sizes will increase. However, Craig et al. (1993) found that the phenomenon of bubble coalescence was greatly reduced by the presence of most dissolved salts, at concentrations much lower than 1 molal. In particular, common, cheap salts such as Na_2SO_4 are among those to inhibit coalescence. Coalescence inhibition reduces the bubble size at formation (Lessard and Zieminski, 1971) and prevents bubble collisions in the downcomer from increasing the distribution size. Consequently, addition of salts to control gas solubility must also allow for shrinking the bubble size distribution. The sensitivity analysis in section 7.6 shows that shrinking the bubble size distribution (model curves with negative flex parameter) will tend to reduce

separator effectiveness. In turn, this implies that separator diameters will be larger, and separator heights deeper to bring separator effectiveness back up to acceptable levels.

According to Chanson (2009), another effect of increased surface tension may be to reduce the entrainment quantity in impinging jets by ‘hardening’ the induction trumpet (see: Figure 6.27), and this will in turn affect air-water mixing processes. It is expected that what Chanson means by induction trumpet hardening is that the trailing edge of the surface in the elongated cavity (labeled in Figure 6.27) is more difficult to rupture, hindering air entrainment. With less air entrained per unit of surface discontinuity, more surface disruption is required to entrain the same amount of air, compared to the fresh water case. Therefore, the cost of air entrainment is expected to increase in the presence of co-solutes that increase surface tension.

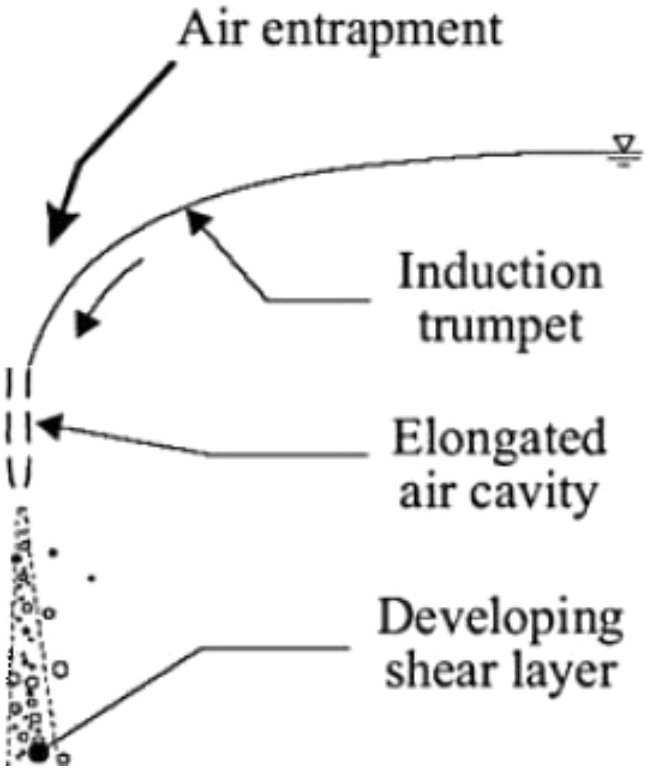

Figure 6.27: The induction trumpet is the water surface including the elongated air cavity leading to the site of air entrainment (modified from Chanson, 2009)

The biggest limitation of the separator effectiveness experiments and models to date is that only city water without added salt has been checked. The flow field CFD model is not expected to change significantly, but the bubble size distribution has been observed to be smaller at Baby HAC (see: Figure 6.28) where salt was used in several experiments to modify the yield of CO_2, in addition to the literature described above. Both of the bubble size models (Wilkinson et al. (1994) and Akita and Yoshida (1974)) predict larger bubbles for liquids with higher surface tension (e.g. salt water), so neither can be used unmodified. The linear relationship between

Rosin-Rammler mean bubble diameter ($\bar{d}$) and spread parameter (n) has not been validated for salt water.

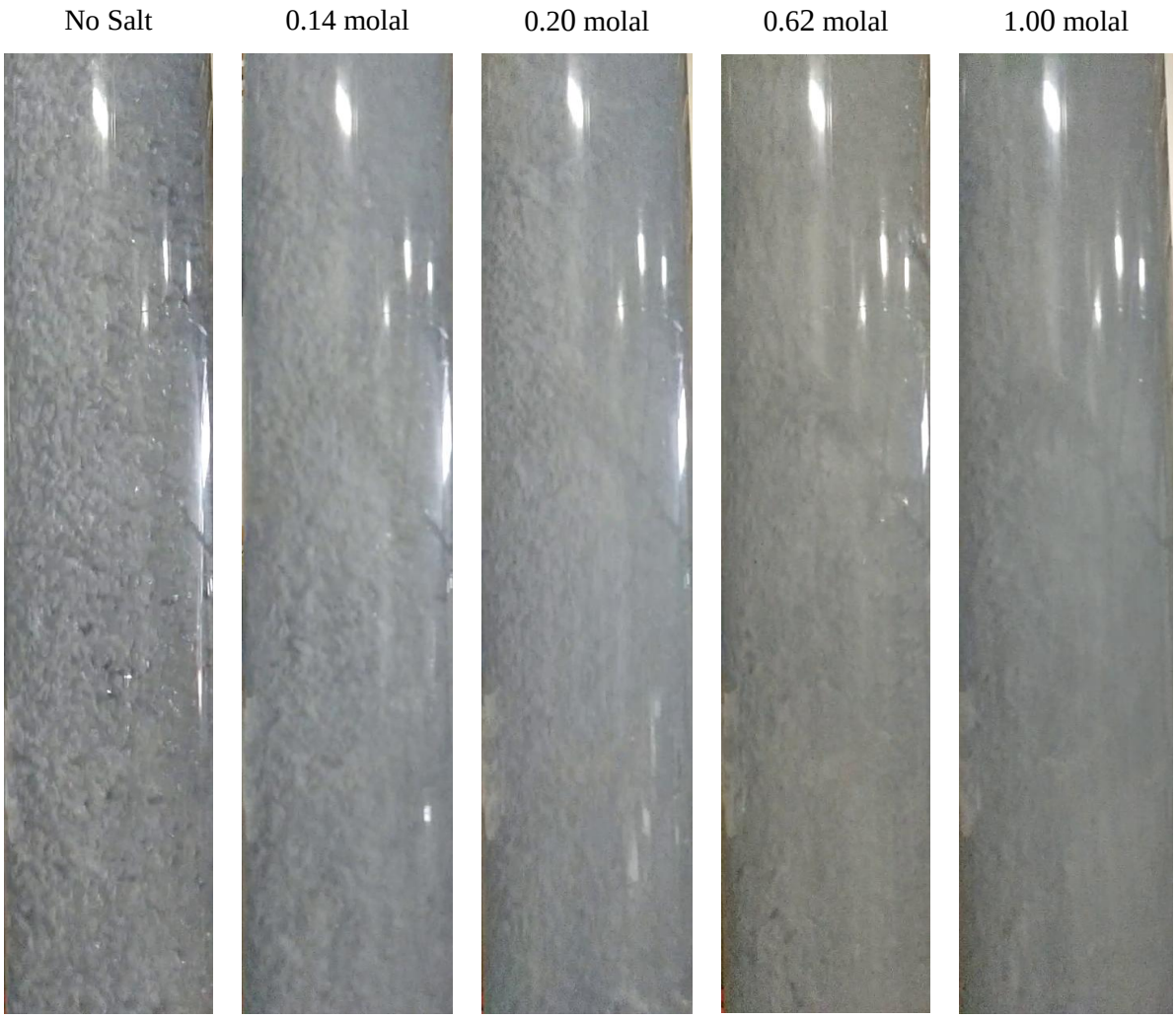

Figure 6.28: Downcomer pipe near the separator at Baby HAC during a recent salt (sodium chloride) experiment using air enriched with CO_2. The bubble distribution visibly shrinks with increasing salt molality and the water is cloudy with tiny bubbles which repeatedly bypass the separator at high salt concentrations

Some preliminary testing circulating salt water within at Baby HAC has been undertaken simply to confirm these expected trends or otherwise. The recent experiments were performed at a fixed water flow rate of 6 L/s (mass flow varied with sodium chloride concentration) using the Ragged Chutes mixing head. The temperature was held constant using a refrigeration loop connected to city water at 11°C. Salt concentration was incremented up to a 1 molal solution (see: Table 6.11).

Table 6.11: Experimental setup with incremental salt addition

Time start (hh:mm)	NaCl concentration (mol/kg solution)	Gas
11:27	0.00	Lab air
11:59	0.10	CO_2 enriched air (~10%)
13:30	0.14	CO_2 enriched air
14:19	0.18	CO_2 enriched air
15:04	0.20	CO_2 enriched air
15:45	0.35	CO_2 enriched air
16:31	0.62	CO_2 enriched air
17:16	0.80	CO_2 enriched air
18:00	1.00	CO_2 enriched air
18:57	1.00	Lab air

Bubbles were observed in every pipe (including the blow-off and riser) and tank through the entire compressor loop. The bubble size distribution was shifted smaller. With salt in the HAC, the smallest bubbles on the tail of the new size distribution were unable to separate and created a recirculating bubble load observed throughout the compression loop. The largest fraction of bubbles, visible in Figure 6.28, (a), disappeared from the distribution, along with most of the slugs previously observed in the flow. Confirmation of whether the spread parameter relationship identified in section 4.3.2 still applies requires quantitative assessment.

An additional consequence of increasing salt concentration is that the increase in water density led to an increase in air flow rate (see: Figure 6.29) and delivery pressure (see: Figure 6.30). Increasing the water density increases the mass flow rate of water for the same volume flow rate. With a higher mass flow rate, the hydropower, and therefore the air flow rate is increased. Delivery pressure is also increased for the same height of water columns when the density of the water is increased.

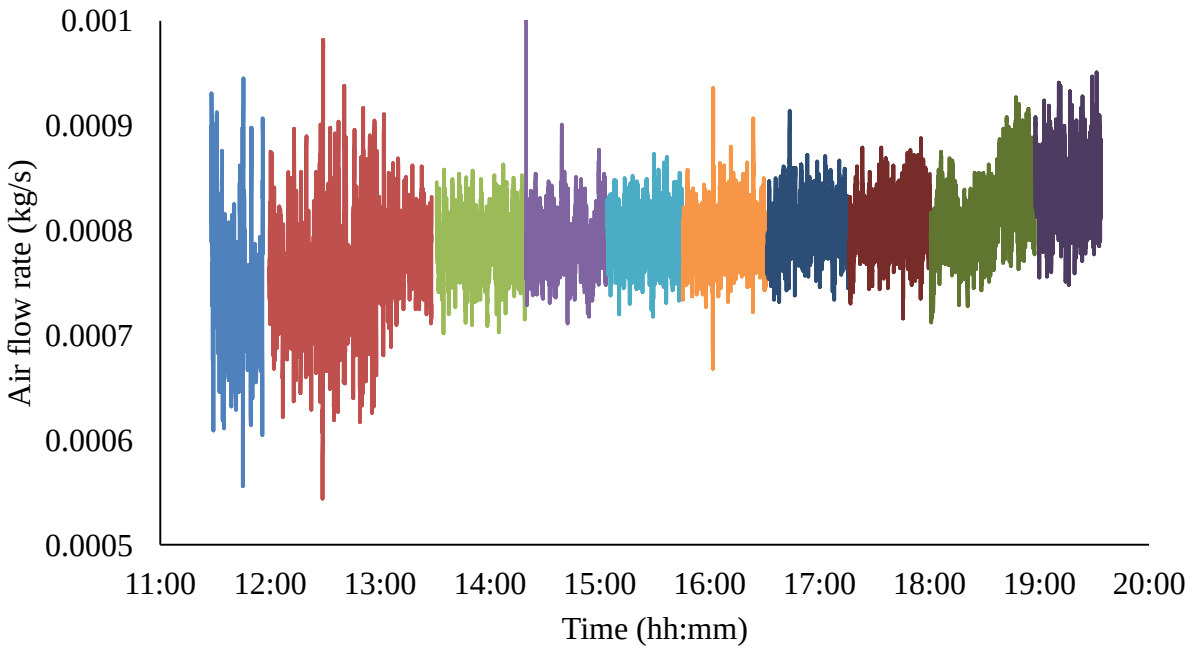

Figure 6.29: Air flow increases with increasing salt concentration; each colour change indicates incrementing salt concentration

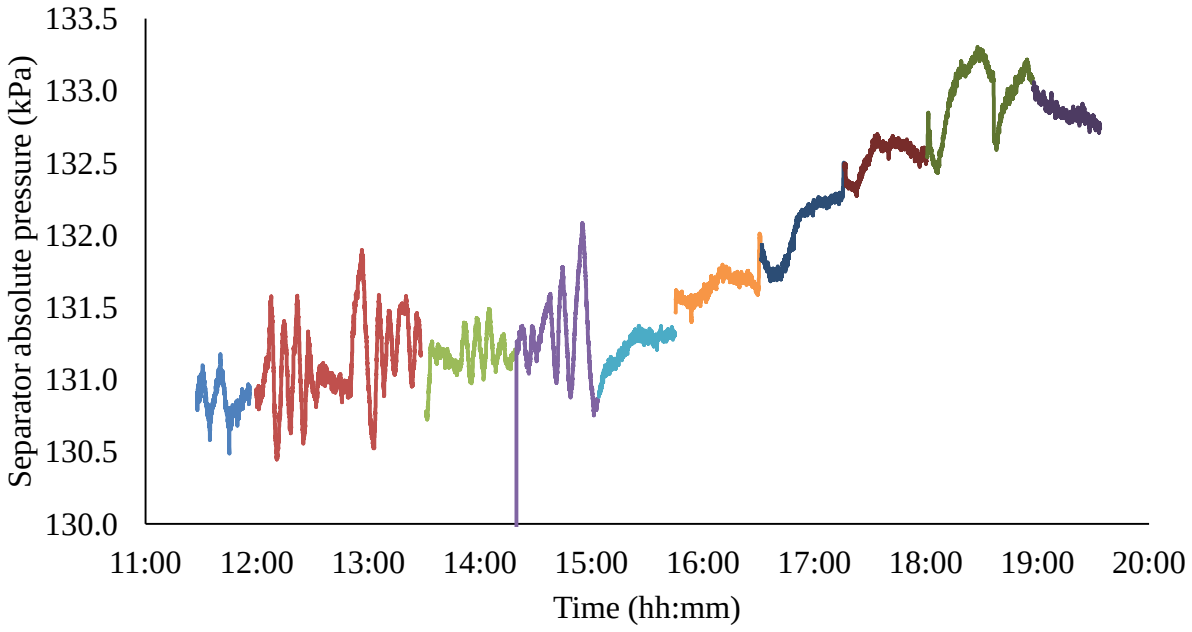

Figure 6.30: Separator pressure increases with increasing salt concentration; each colour change indicates incrementing salt concentration

When the co-solute intervention was originally proposed (Millar, 2014), no mention of the likely effects on bubble size distribution arising from changes in the surface tension of the water was articulated. While use of co-solute may reduce the dissolution potential for solute gas, the rate of dissolution is also known to be affected by the surface area available to mediate the mass transfer. A shrunken bubble size distribution will definitely lead to higher surface area for mass transfer and thus may defeat the intention of the intervention. Heat transfer would also be enhanced, but it is unlikely that it would affect the efficiency, because the kinetics are such that the system is already nearly isothermal. It may be possible to at least partially offset the shrinking bubble size with other additives, but that is part of future work after more testing has been completed with salt.

Chapter 7

7. Discussion

A series of experiments were performed to identify the design features of mixing heads associated with the lowest overall air entrainment irreversibility and to validate the separator effectiveness models for horizontal and vertical gravity separators. The mixing head tests on Baby HAC identified that the best designs prevented the formation of large, deep vortices (as observed in the 'no head' case) and did not rely on Venturi effect snorkeling to draw air in (observed at high flow rate for the Peterborough head and the snorkel head in configurations with its snorkels installed). The tests on Dynamic Earth HAC confirmed that the water level in the forebay tank follows the same trend with water flow rate regardless of the driving head of the system.

The objective of separator effectiveness modeling was to determine a method of predicting bubble size at the inlet and to correctly characterize the mechanics of bubble motion in order to establish the design methodology for HAC separators. The experiments validated the bubble size and motion models such that the design methodology is suitable for effective design.

At both Baby HAC and Dynamic Earth HAC, a detrainment effect was observed in the downcomer close to the mixing head. This is probably created in the convergent section of the mixing head below the hydrofoils where the low flow velocity limited the air transport capacity of the water flow and the low pressure encouraged over-entrainment of air. When crowded bubbles start to coalesce, the relative velocity increases and the bubbles collide more frequently, making the problem of coalescence and detrainment worse.

7.1 Mixing head evaluation metric agreement

There is an apparent disagreement between the water-air flow and water flow-level metrics for mixing head comparison. The snorkel head without snorkel performed better than all of the other snorkel head configurations on the basis of the air flow rate versus water flow rate relationship. Recall that the air mass flow rate ($\dot{m}_g$) is proportional to the numerator and the water mass flow rate ($\dot{m}_l$) is proportional to the denominator of the mechanical efficiency of the compression loop of a HAC:

$$\eta_{mech} = \frac{\text{indicated air power}}{\text{hydropower}} = \frac{\dot{m}_g \cdot \int V dP}{\dot{m}_l \cdot g \cdot h} \tag{7.1}$$

On the basis of forebay water level, this configuration required a higher level over its lip to achieve the same flow as the snorkel-in configurations until the mechanism switched away from vortex entrainment at high water flow rates. This behaviour is likely due to more of the losses occurring below the lip of the mixing head for the snorkel-in configurations, where the flow obstruction created by the snorkels served as a better vortex break but created downstream losses by pipe friction on the snorkel itself and the sudden flow expansion at the air outlet. Preventing the formation of larger vortices at the same flow rate would tend to reduce the inlet irreversibility cost, which is more than offset by the additional flow obstruction and minor loss.

A similar disagreement was measured between the snorkel head and the Ragged Chutes head. In this case, the protruding pipes of the Ragged Chutes head created a flattened vortex with small, air entraining vortices below it. The friction rubbing along the length of the protruding pipes and the sudden expansion at the end would again create downstream losses not accounted for by the

water level metric. The performance of the Ragged Chutes and snorkel heads on the air flow rate basis was close, however, so an improved version of the Ragged Chutes head would likely perform better than both. Removing the protruding pipes and instead employing a vortex-interrupting grate with minimum length in the flow direction and minimum obstruction at the lip of the downcomer inlet should produce a similar, flattened vortex as observed with the Ragged Chutes head but without the accompanying enhanced downstream losses.

The original expectation was that the air entrainment loss would be sufficiently small that it would be impractical to measure using the water-air flow metric. It appears instead that the difference of entrainment irreversibility of one mixing head to another was sufficiently large with respect to the compression energy on Baby HAC that it could be observed as a reduction of air flow rate for the mixing head causing higher irreversibility. A further advantage of the water-air flow metric is that it includes any difference in behaviour of the detrainment zone between mixing heads. Recall from section 3.5 that the water level measurement method can only capture the irreversibility that occurs above the lip of the mixing head. Therefore, disagreement between the water-air flow and water flow-level metrics should indicate increased downstream irreversibility for heads that perform better on the water flow-level metric than on the water-air flow metric. The water flow-level metric was particularly useful in the case of the Ragged Chutes head, and should be useful for future mixing head designs to identify which mixing heads generate irreversibility below the lip and how those heads might be improved.

7.2 Length scale effect on entrainment mechanism

Two of the air entrainment mechanisms were observable in the Baby HAC mixing head comparison tests: Venturi and vortex. Except in the headless case (addressed in section 7.3

below), the vortex was a better entrainment mechanism based on the minimum irreversibility criterion for mixing head design described above. The length scale (diameter) of the Baby HAC downcomer is the probable reason that impinging jet entrainment (the third entrainment mechanism in addition to vortex and Venturi entrainment from section 2.2) was not observed at the mixing head. It was observed at the bottom of the air detrainment zone in the downcomer where the air is re-entrained (see: section 6.5.1).

7.3 Problem of large vortex entrainment

The entrainment irreversibility equation presented in section 3.5 implies a metastable condition where both entraining and non-entraining flows could satisfy the energy balance at the downcomer inlet with the same water level. Entraining air increases the inlet loss, which allows a smaller water flow rate to develop the pressure drop necessary to entrain air. Alternatively, the same system with a higher water flow rate and no air entrainment (reducing the inlet loss coefficient) can satisfy the energy balance. There is a question of which of these cases dominates in practice and what determines that behaviour.

This effect was observed in two ways at Baby HAC: the transition from vortex to Venturi entrainment in the snorkeling heads and the unstable vortex at high water flow rate in the headless configuration. Baby HAC is different from the reservoir case in that it has constant flow rate rather than constant head. The pump provides flow and the water level in the forebay is free to flex. In the reservoir case (which assumes no flow control into the forebay), for which the entrainment irreversibility equation was developed, the water flow rate is free to flex but the water level is fixed. At Baby HAC, the increasing water level with water flow rate was associated with less stable vortices that became more intermittent (see: Figure 7.1). In a reservoir

HAC, the mixing head can be adjusted vertically to control the water flow rate (Schulze, 1954). One could determine the transitional behaviour between single phase and air entraining flow by starting with the mixing head sufficiently submerged to satisfy the system energy balance with water alone and then pulling the head up until it reaches the critical depth where air entrainment starts. A second test would involve starting the head at surface and lowering it until the critical depth from the opposite direction. Would the critical depth be the same from both directions? The two-pattern behaviour of the vortex to snorkeling transition observed with the Peterborough head on Baby HAC (see: section 6.1.2) suggests that a vortex may be bi-stable or metastable when the water level passes the point where a stable, steady vortex can form. Vortices in this condition can be unstable (e.g. ‘no head’ configuration at high water flow rate), irregular (e.g. Ragged Chutes head at high flow rate), or transient (e.g. Figure 7.1).

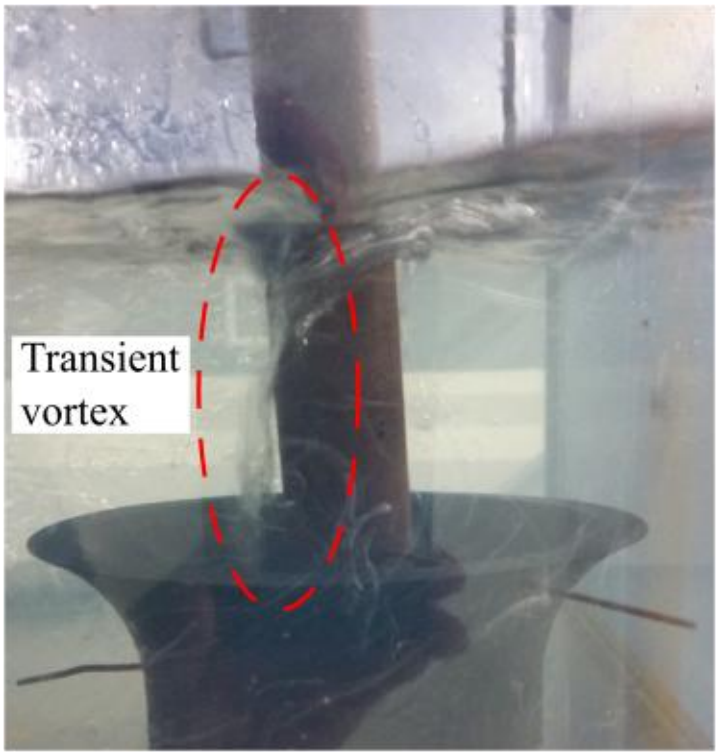

Figure 7.1: Snorkel head with a transient vortex at the water flow rate where the entrainment mechanism transitions from vortex to Venturi

At Baby HAC, the ‘no head’ configuration exhibited the most extreme variability in vortex entrainment. The plot in Figure 7.2 was generated using the fast Fourier transform tool in Excel on a decimated dataset (one measurement in four from the log over a running time of 82 s at 50 Hz, for a total of 4,096 of each of the flow and level measurements) of a high flow rate operating point of the ‘no head’ configuration. The pattern of compressor stall occurred on a regular period, which affected forebay water level and water flow rate. The variability in air flow rate was predominantly controlled by a piston effect of the changing water level, where increasing water level reduces or reverses air flow into the forebay tank and decreasing water level increases air flow. Both Quick (1970) and Shakerin (2008, 2010) observed that transitional

vortices are metastable and tend to be intermittent or cyclical. In the headless testing reported in section 6.1.2, the cyclical interruption of the vortex produced surging flow in the downcomer and large amplitude oscillations in the forebay water level and water flow rate. The compressor stall in the 'no head' configuration appears to be a forced oscillation behaviour created by the interaction between the pump and the vortex at the downcomer inlet.

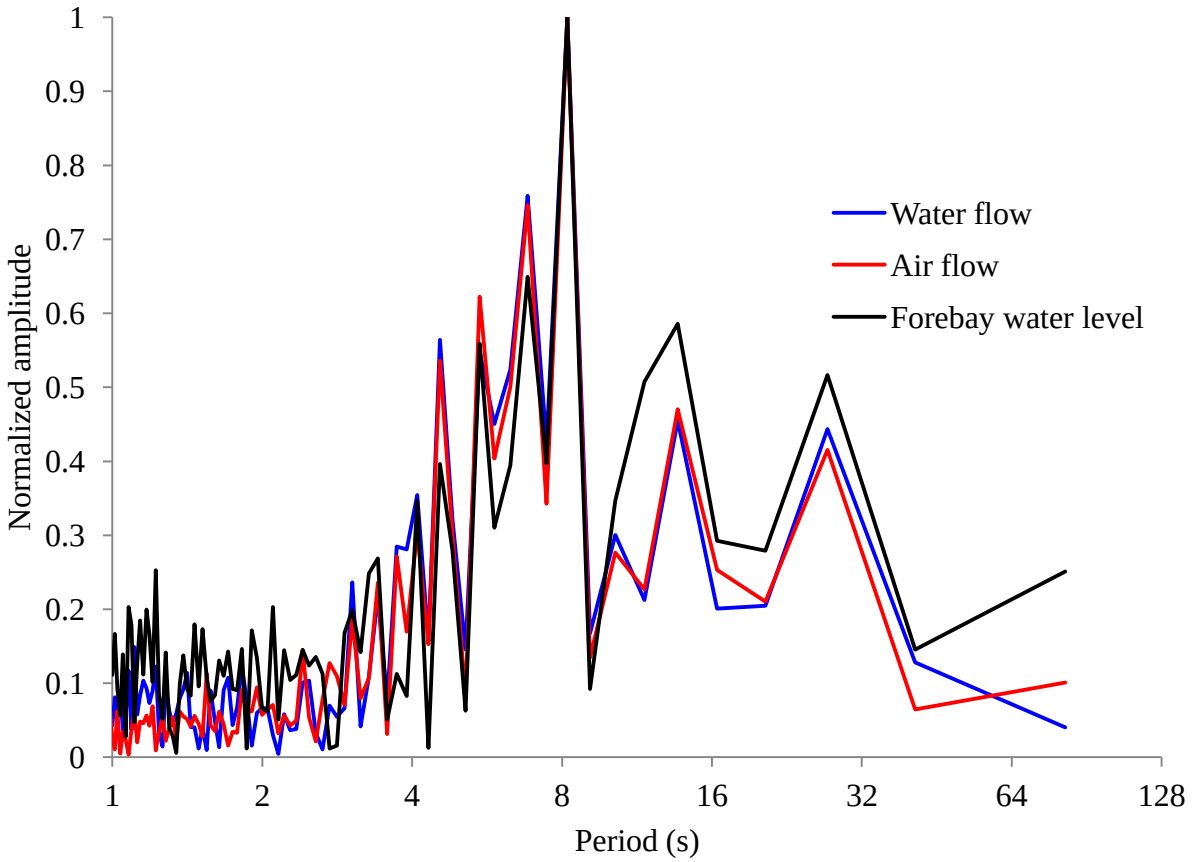

Figure 7.2: Period domain Fourier transform of decimated dataset from the headless configuration showing periodic vortex cycles centering on 8 seconds at an average water flow rate of 7.2 kg/s

Figure 7.3 compares the period and amplitude of water flow rate of the ‘no head’ configuration in the cyclic stall operating condition against the snorkel head without snorkel at the same average water flow rate of 7.2 kg/s. The Fourier transform for the snorkel head operating condition was generated using the same parameters and procedure as for the ‘no head’ configuration. The period with the largest amplitude is in a similar range of 4-16 seconds; however, the scale of the amplitude of flow rate for the snorkel head is one quarter that of the peak at 8 seconds for the ‘no head’ configuration.

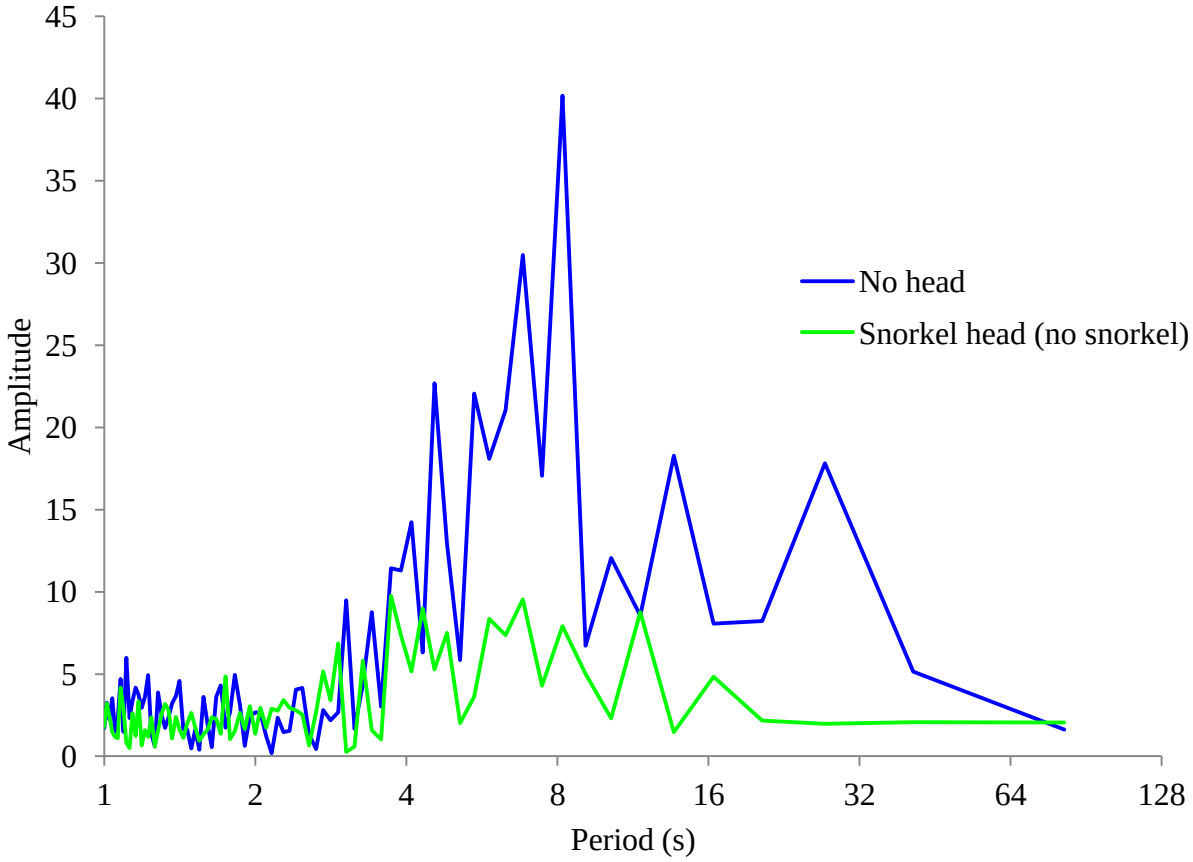

Figure 7.3: Comparison of amplitude of the period domain Fourier transform of decimated water flow rate dataset between the snorkel head (without snorkel) and the 'no head' test from Figure 7.2 at the same average water flow rate of 7.2 kg/s

It is possible that this effect also occurs at large scale. The Ragged Chutes compressor experienced an explosive blowback of compressed air in the enclosure around the mixing heads shortly after first operation in the fall of 1910 (Schulze, 1954). This had previously been observed at the Victoria installation, where freezing of the blow-off pipe (the separator level control mechanism for historic HACs) prevented the safe venting of excess compressed air, allowing it to accumulate and vent explosively in a blowback up the downcomer and back

through the mixing heads (Schulze, 1954). Freezing of the blow-off pipe is unlikely to have been the culprit at Ragged Chutes, considering the explosion occurred in fall and there are no reports of repeat occurrences in any of the subsequent winters. If the mixing head ever did operate as it was originally designed with water entering from inlet ports in the side (see: Figure 7.4), then it is possible that a large, unstable vortex formed on the inside of the mixing head with the air manifold supplying air above a free surface. An uncontrolled vortex of that size could be unstable, leading to compressor stall not visible from the surface. The release of upward moving slugs of air from the downcomer at Baby HAC during the compressor stall was relatively gentle, but at very large scale in both flow rate and pressure, could have been responsible for the explosive blowback.

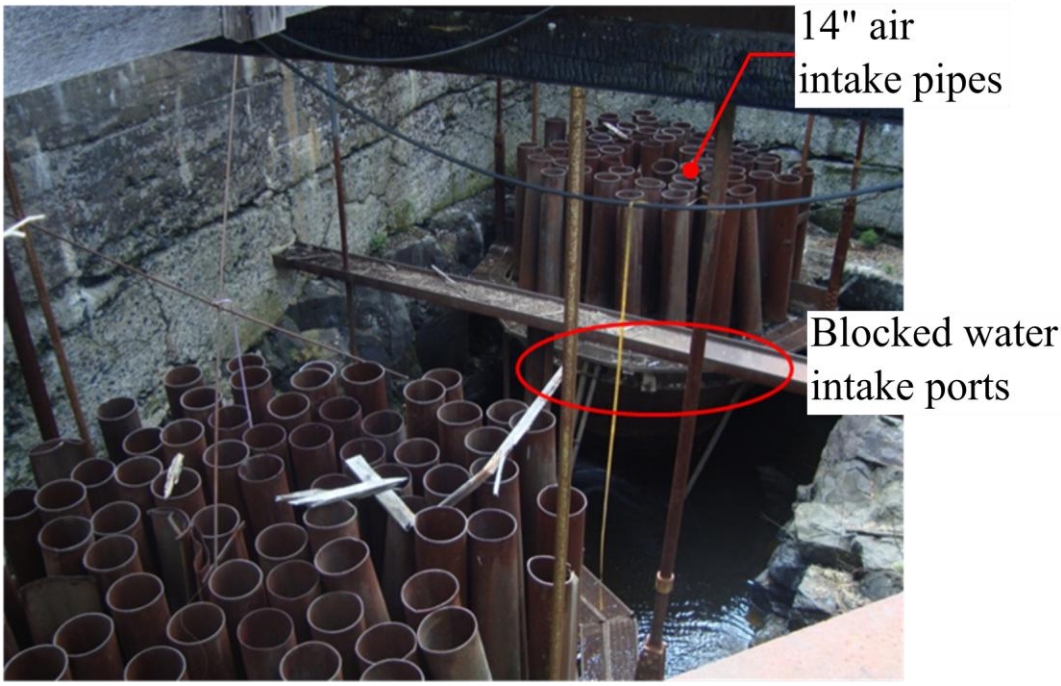

Figure 7.4: The water inlet ports around the circumference of the mixing heads at Ragged Chutes are stopped up with wooden blocks

7.4 Best practice design of mixing heads

The unstable vortex observed at Baby HAC in the headless configuration is tall and narrow, which is probably contributes to its instability in the irregular flow around the mixing head at high water flow rate. Above a mixing head with a vortex breaker (e.g. Ragged Chutes head), the vortex is shorter and wider. Smaller vortices protruding from the bottom of the large, broken vortex generate the air entrainment. The superior performance of the no-snorkel configuration and the Ragged Chutes head suggests that, at least at small scale, this is the ideal entrainment mechanism. All of the heads and configurations are more consistent with one another at low water flow rate than at high water flow rate. Under low flow conditions, all of the mixing heads have vortex entrainment with stable, smooth-walled vortices that are visually similar to one another. With increasing water flow rate, the no-snorkel configuration and the Ragged Chutes head remain visually the most similar to this condition, up to and beyond the transition to Venturi entrainment for the other heads and configurations.

On Dynamic Earth HAC, the premise that the forebay water level is a quadratic function of water flow rate was confirmed only for high water flow rate. It seems likely that the linear trend observed at Baby HAC reflects the linear trend observed at Dynamic Earth HAC at low water flow rate. It is possible that the linear trend indicates vortex entrainment (i.e. two-phase flow over the lip of the mixing head) and that the quadratic trend indicates a shift to Venturi entrainment (i.e. single phase flow over the lip of the mixing head). If so, the entrainment irreversibility equation (3.16) is useable with a constant loss coefficient only in the latter case or where no surface irregularity is entraining air above the lip, per the assumptions used to derive it.

The performance similarity across mixing heads of varied geometry on Baby HAC indicates that the hypothesis that the system drives air entrainment rather than local geometry is correct. The fact that the headless configuration operated at all, vortex instability notwithstanding, confirms this. The fact that any local geometry entrains air indicates that a closed pipe mixing head (see: section 3.7) should not require carefully-designed Venturi geometry to induct air. By opening a closed loop downcomer pipe to atmosphere, the delivery head on the pump is increased and air is drawn into the water stream as a consequence of the system energy balance. A pipe segment with holes drilled around the perimeter to admit air should be a perfectly suitable mixing head.

7.5 Applicability of separator effectiveness measure at Dynamic Earth HAC

The ratio of measured air flow rate at inlet and outlet at low pump speed was approximately 95%. From section 6.4.3, yield loss was assumed not to change with water flow rate at similar water fill quantities on Dynamic Earth HAC. The measured effectiveness (after the linear yield correction) was close to 100% at the lowest two water flow rates (presented in Figure 6.21), indicating that the separator effectiveness does not contribute to the ~5% yield loss. After applying the yield correction to produce a measured separator effectiveness curve and using the Akita and Yoshida (1974) bubble size model, the vertical velocity separator model agreed with the measured results. Further, at least in this case, the Akita and Yoshida (1974) was close but slightly conservative, which is ideal for the design of future separators.

For the Dynamic Earth HAC considered a vertical separator, the Karamanev and Nikolov (1992) correction resulted in the underestimation of separator effectiveness (compared to measured effectiveness), in comparison to predictions without the correction. For this reason, the

correction was not tested with the Akita and Yoshida (1974) model. The displacement model on the Baby HAC horizontal separator also better matched the visible bubble plume when the correction was not applied. Therefore, it is asserted that this correction could be discarded from the models for separator design.

7.6 Separator effectiveness sensitivity analysis

The spreadsheet models of bubble motion have several advantages over simulation in CFD modeling: they are conceptually similar but do not create numerical instability in the solution and are much faster to solve. These advantages make it relatively simple to perform multiple runs of the model to flex the total flow rate (combined water and air flow rate) to produce the separator effectiveness curve for the operational range of the HAC and to flex the bubble size distribution to show the effect of bubble size mis-estimation on the curve. The flex parameter adjusts the Rosin-Rammler mean diameter of the bubble size distribution used in the separator effectiveness model from the base case in a range of ±40%. The base case (0 in Table 7.1) is the Akita and Yoshida (1974) effectiveness curve from Figure 6.22. Recall from section 6.4.3 that this bubble model flexes with total flow rate; sample bubble flex parameters at a total flow rate of 0.4 m^3/s (from the range 0.1-0.6 m^3/s) are presented in Table 7.1 for the separator effectiveness sensitivity analysis of the Dynamic Earth HAC separator. The vertical velocity separator model was recalculated for each of these flexed inlet bubble size distributions. This analysis is an extension of the selected (fixed) mean diameter presented in Figure 6.21 (case iii), except the Akita and Yoshida (1974) bubble diameter is flexed at each total flow rate (0.1-0.6 m^3/s in increments of 0.1 m^3/s).

Table 7.1: Flex of Rosin-Rammler mean diameter for sensitivity analysis of vertical velocity model of Dynamic Earth HAC

Flex	Rosin-Rammler mean diameter ($\bar{d}$, mm)	Spread parameter (n)
+40%	10.37	2.25
+25%	9.26	2.47
+10%	8.15	2.69
0	7.41	2.83
-10%	6.67	2.97
-25%	5.56	3.19
-40%	4.45	3.41

At higher water flow rate, the separator effectiveness is more sensitive to small changes in bubble size (see: Figure 7.5). Despite their scatter, the data points are clustered around the middle of the sensitivity analysis, indicating that the Akita and Yoshida (1974) bubble model is a good predictor of bubble size at this scale. An accurate bubble size distribution is required to reliably and accurately characterize separator performance at high total flow rates.

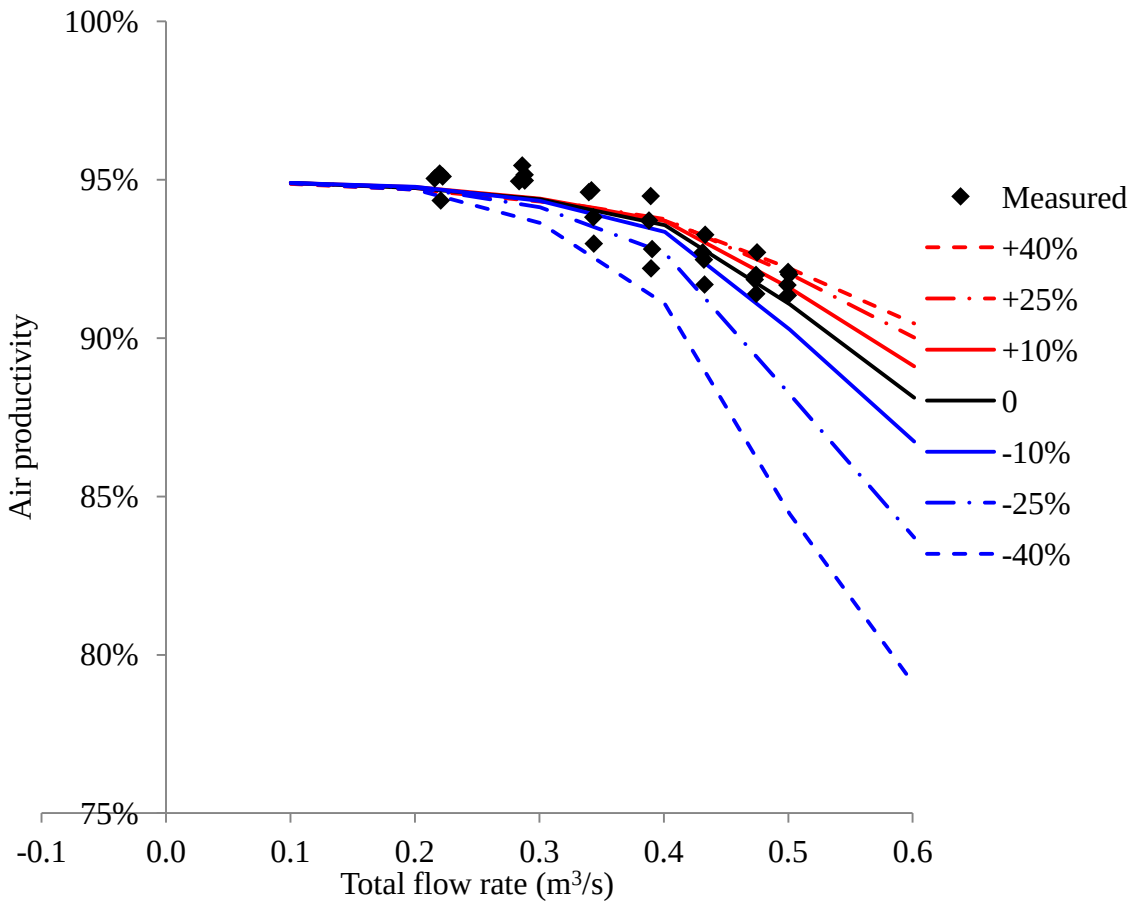

Figure 7.5: Sensitivity analysis of air productivity flexing Rosin-Rammler mean bubble diameter in the vertical velocity separator model for Dynamic Earth HAC, including measured air productivity reported in section 6.4.1

Adoption of the best bubble size distribution leads to underestimates of separator effectiveness at high total flow rates. At low total flow rates, it is valuable to note that all of the modelled separator effectiveness curves converge. Consequently, when the separator is adequately sized for the total flow rate, the separator effectiveness is not particularly sensitive to moderate changes in bubble size – within the same order of magnitude. Further, the separator model is more inaccurate when the bubble size is underestimated than when it is overestimated. In the

worst-case scenario for design, where the bubble size is substantially overestimated, this lower sensitivity limits the impact to air productivity. At least in this case, the Akita and Yoshida (1974) bubble size model is conservative and should be adequate to engage in separator design.

7.7 Air detrainment is caused by insufficient transport capacity

The HAC performance model is a mechanistic model that solves the two-phase flow in the downcomer using energy, momentum, and mass conservation equations using an assumption of bubbly flow (Millar, 2014). The air flow rate is solved to make the pressure at the end of the downcomer agree with the pressure calculated 'upstream' from the outlet at the tailrace. The latter is solved using single phase pipe flow equations. In Figure 7.6, the performance model agrees with the physical measurement in terms of mechanical efficiency and air delivery rate, across the whole performance map of water flow rate and applied head between forebay tank and tailrace tank, when a constant 0.9 metres is subtracted from the driving head across the entire range of water flow rate for one- and two-pump operation (0.1-0.5 m^3/s), including the position and magnitude of the maximum efficiency, at slightly above 0.2 m^3/s water flow rate. This is an indication that the bubbly flow assumption in the model is reasonable except for some head correction mechanism that is not accounted for.

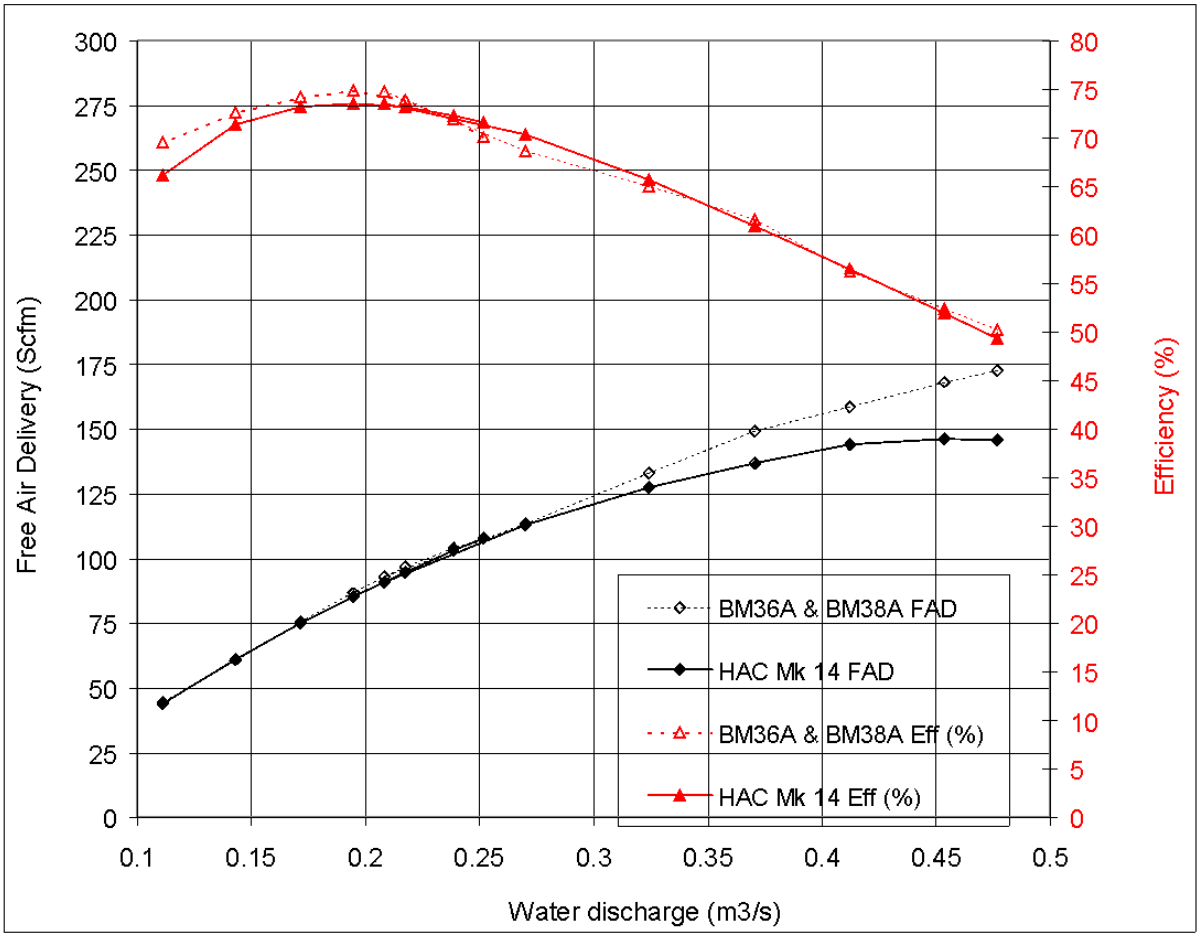

Figure 7.6: The HAC performance model agrees with the measured performance in terms of air flow rate and mechanical efficiency after the head correction is applied. Solid lines represent the model and dashed lines the measured (Millar and Muller presentation, 2017)

By locally lowering the pressure at the end of the mixing head air manifold with the Venturi effect, it is possible that too much air is being entrained in the flow. If the downstream water velocity is not sufficient to prevent the bubbles from coalescing into slugs, then local air recirculation and coalescence is responsible for detrainment at the top of the downcomer. The air transport capacity of flowing water is minimized for vertically downward flows (Kobus, 1984).

The minimum velocity of 0.3 m/s observed by Rice (1976) is likely due to bubble drag (corresponding to a bubble diameter of 3.2 mm) rather than the transport limit. In his experiments, he either did not experience air detrainment or was unable to detect it.

If excessive entrainment driven by Venturi suction is at least partially responsible for the detrainment zone in the downcomer, then adjusting the mixing head geometry so that it does not create local low pressure should mitigate the problem. The best style of mixing head design at Baby HAC scale was determined to be one where the local geometry features avoid Venturi snorkeling and control vortices or other large, air entraining surface discontinuities. Any part of the 'correction' that is not attributable to the mixing head geometry must be a system effect.

The hydropower available is determined by the driving head of the system and the water flow rate. The transport capacity is determined by the velocity of the water flowing in the downcomer (Kobus, 1984). For design, the hydropower and water flow rate are determined by the pump selection and relative elevations of the forebay and tailrace, and the downcomer velocity is determined by the water flow rate and the internal pipe area. These variables inform how much energy is available for air compression and what limits are imposed by the system on air flow rate. Recall from section 6.5.2 that the geometry of the mixing head at Dynamic Earth HAC created or exacerbated the detrainment problem at the top of the downcomer. Without a model of this behavior, it is not possible to predict the optimal conditions under which the system would normally induct just the right amount of air to balance the energy equation with air compression and without the detrainment correction except that accelerating the flow after the entrainment zone is likely to result in some detrainment. This problem has yet to be solved and will be the subject of future investigation.

Chapter 8

8. Conclusions and future work

The primary objectives of this thesis were to identify the minimum irreversibility design principles for mixing heads and to accurately model separator effectiveness. Experimental work on mixing heads did not result in an effective predictive model for performance but did:

i) validate the concept of designing for minimum irreversibility,
ii) confirm the idea that the overall system energy balance drives air entrainment, and
iii) highlight the importance of transport capacity of the water in the downcomer.

Furthermore, as vortices were clearly visible in the Baby HAC platform, at small scales (i.e. small downcomer diameter), vortex entrainment was identified as the best prospect where the vortex is broken at the inlet and not allowed to continue coherent swirl below the inlet.

Accurate prediction of separator effectiveness with the mechanistic bubble models relied heavily on accuracy of the input variables, particularly the bubble size distribution. Separator effectiveness has been found to be sensitive to the bubble size distribution. The Wilkinson et al. (1994) bubble size model was identified as the most accurate of the four identified in the literature review for consideration in this work, for the platform scale of Baby HAC. Similarly, the Akita and Yoshida (1974) was identified as the most accurate for the platform scale of Dynamic Earth HAC.

8.1 Research questions

The questions below represent the uncertainties from early in the project that needed to be addressed in order to be able to design the air entrainment and air-water separation processes for commercial HACs. Not all of these questions have been fully answered as a consequence of the research reported herein, but the most critical ones for basic design have been progressed. Some of those that are less important or where time constraints have limited work on the larger scale Dynamic Earth HAC have been delegated to future work.

8.1.1 Air entrainment

1. What drives air entrainment in a HAC?

   Air entrainment is driven by energy conservation; the falling water in the downcomer generates low pressure at the inlet, which provides the motive force for the surface discontinuity at the top (see: section 3.5). Adding air to the system increases the pressure at the downcomer inlet (as more energy is consumed below for air compression), resulting in a self-correcting balance where that pressure is maintained at the level necessary to induct enough air to consume the ‘excess’ energy set up in pumping. It is possible that forcing air entrainment with local low pressure in Venturi geometry may actually contribute to the detrainment problem observed in both experimental HACs (see: section 7.7).

2. Can a HAC in the closed loop configuration (i.e. no forebay tank) induct air without the Venturi effect?

   The indication from the open loop headless test on Baby HAC is that air entrainment occurs regardless of the local geometry at the downcomer inlet (see: section 6.1). No

experiments have yet been run to specifically confirm the operation of the closed loop configuration, however there is nothing to indicate that this case should be different from the open loop configuration (see: section 3.7).

3. Does air entrainment without a vortex create less flow irreversibility? Is any difference between vortex entrainment and other processes sufficiently significant to be relevant to engineering design?

   Vortex entrainment was observed to create less flow irreversibility than Venturi entrainment at small scale (see: section 6.1). Only the unbroken vortex in the headless case performed worse than the Venturi snorkels, but the metastability of the vortex led to flow surging in the entire compression loop (see: section 7.3), that most likely should be regarded as undesirable. Impinging jet entrainment has not been observed to-date at the downcomer inlet of either Baby HAC or Dynamic Earth HAC.

4. Under what conditions is a vortex likely to form?

   Vortices formed at least at low water flow rate for all of the mixing heads and configurations on Baby HAC (see: section 6.1) and probably also at Dynamic Earth HAC (see: section 7.4), although it was less visually apparent there. The vortex is apparently too unstable at higher water flow rates where the ratio of depth to rotational diameter and the air flow rate demanded by the system energy balance increase. The non-snorkeling mixing heads did not limit the rotational diameter of the vortex above the mixing head.

8.1.2 Air-water separation

1. How does one predict the size distribution of bubbles entering the separator without a reliable coalescence model?

   Mechanistic methods of prediction relying on the balance between coalescence and breakup cannot be reliable, owing to the unreliability of coalescence modeling (see: section 2.3.8). Instead, several empirical bubble diameter models were evaluated against photographic measurement made on Baby HAC and the comparison between the modeled and measured separator effectiveness (see: section 4.3.2). The Wilkinson et al. (1994) model was found to be the only one that came close to the measured value for Baby HAC and produced model results close to the actual for Dynamic Earth HAC (see: sections 6.4.3 and 7.6).

2. How much do dissolved salts affect separator effectiveness?

   The bubble size distribution is visibly smaller in salt water than in clean water (see: section 6.6). The Wilkinson et al. (1994) model was intended to predict bubble size in salt water, so the Rosin-Rammler mean bubble diameter may be correct. However, it is not clear whether or not the linear relationship between the Rosin-Rammler mean diameter and the spread parameter (see: section 4.3.2) holds in salt water.

3. What is the effect of swirling flow in gravity separators?

   The swirling flow in a vertical gravity separator with a full admission inlet has a greater impact on the direction than the magnitude of the resultant field acceleration (see: section 2.3.1). Bubbles in this field would tend to migrate upward and toward the axis of the separator. The vertical gravity separation model developed in this work does not include

this centrifugal acceleration, yet it produces a result that is at least close to the actual performance (see: section 6.4.3), subject to the uncertainty on the bubble size distribution prediction.

4. Under what economic conditions, if any, is the selection of a centrifugal separator preferable over a gravity separator?

   The centrifugal separator option was rejected for the Dynamic Earth HAC because the head loss across the separator would have consumed a significant fraction of the total driving head available for the compression loop (see: section 4.1). At least for HACs with low hydraulic head, the centrifugal separator is likely to be impractical and uneconomical.

8.1.3 Control and operation

1. What is the cause of the extreme flow surging observed at Baby HAC in the headless configuration at high water flow rate?

   The large vortex formed without a mixing head is unstable. The depth of the water above the downcomer inlet at high water flow rate creates regular interruptions of the tail of the vortex which blocks air induction, and causes the gas compression process to be interrupted. The continuous water influx by the pump produces a forced oscillation with a regular period (see: section 7.3).

2. What is the effect of gas solubility on bubble size distribution?

   The measured effect of yield reduction by gas solubility is small for Dynamic Earth HAC, even if the air leakage through the forebay tank lid bypassing measurement is larger than expected. If the solubility effect is small, the bubbles should not be

significantly affected by it. Given the smaller pressure swing at Baby HAC, the effect of solubility is smaller still. In a run-of-river HAC, the water coming in at the forebay is at or very near equilibrium with atmospheric air in terms of dissolved gases. In a pumped HAC, there is system equilibrium, where there is not enough residence time in the riser and tailrace tanks for the water to fully equilibrate with the atmosphere before being pumped back into the forebay. This generates a circulating load of dissolved gases, which should retard the gas solvation in the downcomer.

8.2 Original contributions

The following original contributions have been made over the course of this research:

- The driver of air entrainment in a HAC was determined to be the system energy balance. Taylor and the other designers of historic HACs were evidently unaware of this principle. None of the original HAC designers ever settled on a single form for mixing head design. Some mixing head designs (e.g. Ragged Chutes) did not operate as intended, but did entrain air despite not operating on the intended design principle (Venturi induction by speeding up flow through a narrow aperture)..
- The lowest irreversibility geometry of an air-water mixing head for an open loop HAC at small scale, as at Baby HAC, is a bellmouth inlet with a vortex-breaking grate at the lip. This is expected to hold true at larger scale but has yet to be confirmed experimentally.
- The Wilkinson et al. (1994) model produces a reasonable Rosin-Rammler mean bubble diameter in clean water (i.e. without co-solutes) at both small and large scale when the Hesketh et al. (1987) conversion is used to determine the 99^{th} percentile diameter from the Sauter mean diameter produced by the original model.

- There is a relationship between the Rosin-Rammler mean diameter and the spread parameter that converts the distribution into a single-parameter fit for gas bubbles in water.
- Two high-speed, explicit, mechanistic models were developed for two different types of gravity separators. Both models produce reasonably accurate results with no risk of numerical divergence or failure to converge as in a CFD model. After the single phase solution and model setup are complete, the solution time for both models is of the order of a few seconds on a 2014 model laptop PC. This modeling technique requires less skill with CFD software, but greater understanding of separator mechanics than direct CFD modeling of the bubble motion.
- The Karamanev and Nikolov (1992) drag coefficient correction for rising spheres does not lead to improved predictions of separator effectiveness in a gravity separator.
- Air detrainment was discovered in the downcomer of both experimental HACs, which may be a property of all HACs. Without modern modeling and instrumentation as well as the clear downcomer pipe of Baby HAC, it would not have been detectable.

8.3 Future work

Several tasks remain incomplete from the original scope of work proposed for this thesis and from the more recent discoveries made over the course of this investigation:

- The best design practices for mixing heads needs to be confirmed experimentally at large scale (i.e. Dynamic Earth HAC scale). The design is not expected to change significantly except that the entrainment mechanism is expected to shift from vortex to impinging jet, which may require an adjustment.

- Closed loop operation needs to be confirmed experimentally. In particular, the air entrainment needs to be validated against the open loop case with the forebay water level at the same elevation as the air inlet in the closed-loop downcomer pipe. Removing a heavy water tank at the top of the compressor would significantly reduce the cost of any superstructure otherwise necessary to support it.
- The irreversibility of air entrainment should be verified for salt water against a mixing head with known performance in order to determine if the hardening of the water surface by increased surface tension has a significant impact.
- Both Wilkinson et al. (1994) and Akita and Yoshida (1974) bubble models and the linear relationship with spread parameter for the Rosin-Rammler distribution need to be checked for salt water. Without accurate bubble size prediction, or accurate measurement, the separator models contain residual uncertainty that can only be accommodated through selection of larger diameter and deeper height separator designs – increasing their capital cost.
- The air detrainment problem in the downcomer needs to be more fully characterized in terms of how it is affected by driving head and changing mixing head geometry. It can only be visually inspected on Baby HAC, but further instrumented experiments on Dynamic Earth HAC should be definitive.
- Assuming the air detrainment problem is related to coalescence and local recirculation of air bubbles in the downcomer after the mixing head, what effect does salt have? Coalescence should be appreciably inhibited and detrainment may be avoided.
- What effect would coupling the suction side of the pumps to the riser have on HAC operation? Apart from the potential problem of ingesting exsolved air bubbles into the

pump, the system may be unstable in this configuration. The pump curve (i.e. the characteristic relationship between head and flow rate for a pump) should determine the flow rate and the location of the atmospheric pressure horizon in the riser, upstream of the air inlet at the top of the downcomer. Without opening the pipe to a fixed pressure at a second point in the riser, the pressure at the pump suction side may vary or oscillate. It is possible that there are many operating conditions that would satisfy the steady flow energy equation for the system in this configuration. On the other hand, removing the tailrace tank would reduce the construction cost and simplify the system to a pipe loop with a separator. If the pump is moved to the bottom near the separator or if it can cope with some air ingestion, there should be a further enhancement of gas yield by removing the significant residence time in the tailrace that would allow more of the dissolved gases (acting to prevent further dissolution in the downcomer) to evolve.

References

Akita, K., Yoshida, F., 1974. Bubble size, interfacial area, and liquid-phase mass transfer coefficient in bubble columns. Industrial & Engineering Chemistry Process Design and Development 13, 84–91.

Aliseda, A., Lasheras, J.C., 2011. Preferential concentration and rise velocity reduction of bubbles immersed in a homogeneous and isotropic turbulent flow. Physics of Fluids 23, 093301-1-093301–11.

Allsensors, 2014. Amplified low pressure sensors [WWW Document]. URL https://www.allsensors.com/datasheets/DS-0368_Rev_A.PDF (accessed 8.20.14).

ANSYS, 2009. ANSYS Fluent 12.0 user's guide [WWW Document]. URL http://users.ugent.be/~mvbelleg/flug-12-0.pdf (accessed 10.13.17).

Arnold, K., Stewart, M., 2008. Surface production operations, 3rd ed. Elsevier, Amsterdam.

Bhagwat, S.M., Ghajar, A.J., 2012. Similarities and differences in the flow patterns and void fraction in vertical upward and downward two phase flow. Experimental Thermal and Fluid Science 39, 213–227.

Bhargava, P.K., Vittal, N., Ranga Raju, K.G., 1984. Vortex formation at pipe-offtake in an open channel, in: Smith, K.V.H. (Ed.), Channels and Channel Control Structures: Proceedings of the 1st International Conference on Hydraulic Design in Water Resources Engineering. Presented at the 1st International Conference on Hydraulic Design in Water Resources Engineering, Computational Mechanics Cent, Southampton, UK, pp. 1.91-1.101.

Bidini, G., Grimaldi, C.N., Postrioti, L., 1999. Performance analysis of a hydraulic air compressor. Proceedings of the Institution of Mechanical Engineers, Part A 213, 191–203.

Biswal, S.K., Reddy, P.S.R., Bhaumik, S.K., 1994. Bubble size distribution in a flotation column. The Canadian Journal of Chemical Engineering 72, 148–152.

Brennen, C.E., 2005. Fundamentals of multiphase flows. Cambridge University Press.

Brown, P.P., Lawler, D.F., 2003. Sphere drag and settling velocity revisited. Journal of Environmental Engineering 129, 222–231.

Burdin, F., Tsochatzidis, N.A., Guiraud, P., Wilhelm, A.M., Delmas, H., 1999. Characterization of the acoustic cavitation cloud by two laser techniques. Utrasonics Sonochemistry 6, 43–51.

Çengel, Y.A., Cimbala, J.M., 2010. Fluid mechanics: fundamentals and applications, 2nd ed. McGraw-Hill, New York.

Chanson, H., 2009. Turbulent air-water flows in hydraulic structures: dynamic similarity and scale effects. Environ. Fluid Mech. 9, 125–142.

Chanson, H., 1995. Air bubble entrainment in free-surface turbulent flows (No. CH46/95). University of Queensland, Brisbane.

Chen, P., Sanyal, J., Dudoković, M.P., 2005. Numerical simulation of bubble columns flows: effect of different breakup and coalescence flows. Chemical Engineering Science 60, 1085–1101.

Chen, Y.N., 1979. From bath-tub vortex to pump-intake vortex: axial-flow-induced instability as their formation mechanism. Schweiz. Ing. Archit. 97, 845–852.

Cheng, N.-S., 2009. Comparison of formulas for drag coefficient and settling velocity of spherical particles. Powder Technology 189, 395–398.

Craig, V.S.J., Ninham, B.W., Pashley, R.M., 1993. The effect of electrolytes on bubble coalescence in water. J. Phys. Chem. 97, 10192–10197.

Clift, R., Grace, J.R., Weber, M.E., 1978. Bubbles, drops, and particles. Academic Press, London.

Cristofano, L., Nobili, M., Caruso, G., 2014. Experimenal study on unstable free surface vortices and gas entrainment onset conditions. Experimental Thermal and Fluid Science 52, 221–229.

Dankert, D., 1997. NTC Thermistor [WWW Document]. URL http://www.littelfuse.com/~/media/electronics/engineering_drawings/leaded_thermistors/littelfuse_leaded_thermistors_interchangeable_thermistors_ps103j2_engineering_drawing.pdf.pdf (accessed 8.20.14).

Daycounter, Inc., 2016. AWG - American wire gauge [WWW Document]. AWG - American wire gauge. URL http://www.daycounter.com/Calculators/AWG.phtml (accessed 11.27.17).

Dutcher, C.S., Wexler, A.S., Clegg, S.L., 2010. Surface tensions of inorganic multicomponent aqueous electrolyte solutions and melts. The Journal of Physical Chemistry A 12216–12230.

Electrale Innovation Limited, 2017. Latest news on Dynamic Earth HAC [WWW Document]. URL www.electrale.com (accessed 9.6.17).

Freescale Semiconductor, 2009. Integrated silicon pressure sensor manifold absolute pressure sensor, on-chip signal conditioned, temperature compensated and calibrated [WWW Document]. URL http://www.mouser.com/ds/2/302/MPX4250A-783416.pdf (accessed 8.20.14).

Grace, J.R., 1973. Shapes and velocities of bubbles rising in infinite liquids. Transactions of the Institution of Chemical Engineers 51, 116–120.

Gulliver, J.S., Rindels, A.J., 1987. Weak vortices at vertical intakes. J. Hydraul. Eng. 113, 1101–1116.

Hesketh, R.P., Russell, T.W.F., Etchells, A.W., 1987. Bubble size in horizontal pipelines. AIChE Journal 33, 663–667.

Howe, W.H., Lipták, B.G., 2003. Orifices, in: Lipták, B.G. (Ed.), Instrument Engineers' Handbook. CRC Press, p. 1824.

Iida, Y., Ashokkumar, M., Tuziuti, T., Kozuka, T., Yasui, K., Towata, A., Lee, J., 2010. Bubble population phenomena in sonochemical reactor: i. estimation of bubble size distribution and its number density with pulsed sonication - laser diffraction method. Ultrasonics Sonochemistry 17, 473–479.

Impress Sensors & Systems, 2014. IMSL submersible level transmitter - silicon sensor [WWW Document]. URL https://www.impress-sensors.co.uk/images/products/Datasheets/Impress/D-IMSL-Submersible-hydrostatic-level-transmitter-silicon-sensor.pdf (accessed 8.20.14).

Innopharma Technology, 2017. Innopharma Education Site [WWW Document]. Particle size distribution. URL https://www.innopharmalabs.com/tech/applications-and-processes/particle-size-distribution (accessed 9.12.17).

Jain, A.K., Garde, R.J., Ranga Raju, K.G., 1978. Vortex formation at vertical pipe intakes. Journal of the Hydraulics Division 104, 1429–1445.

Johansen, Ø., Rye, H., Melbye, A.G., Jensen, H.V., Seristgad, B., Knutsen, T., 2001. Experimental discharges of gas and oil at Helland Hansen - June 2000 (Technical Report No. STF66 F01082). SINTEF Applied Chemistry, Trondheim.

Karamanev, D.G., Nikolov, L.N., 1992. Free rising spheres do not obey Newton's law for free settling. AIChE Journal 38, 1843–1846.

Kharoua, N., Khezzar, L., Saadawi, H., 2013. CFD modelling of a horizontal three-phase separator: a population balance approach. American Journal of Fluid Mechanics 3, 101–118.

Knauss, J. (Ed.), 1987. Swirling flow problems at intakes, IAHR Design Manual. CRC Press.

Kobus, H., 1984. Local air entrainment and detrainment, in: Kobus, H. (Ed.), Proceedings of the Symposium on Scale Effects in Modelling Hydraulic Structures. Presented at the Symposium on scale effects in modelling hydraulic structures, Technische Akademie Esslingen, Esslingen am Necklar, FRG, pp. 4.10-1-4.10-10.

Kouba, G.E., Shoham, O., Shirazi, S., 1995. Design and performance of gas liquid cylindrical cyclone separators, in: Proceedings of the BHR Group 7th International Meeting on Multiphase Flow. Presented at the BHR Group 7th International Conference on "Multiphase 95," Cannes, France, pp. 307–329.

Krohne, 2017. OPTIMASS 6400 - S 25 [WWW Document]. URL https://krohne.com/en/products/flow-measurement/flowmeters/coriolis-mass-flowmeters/optimass-6400/ (accessed 1.26.17).

Krohne, 2016. OPTIFLUX 2300 - 12" [WWW Document]. URL https://krohne.com/en/products/flow-measurement/flowmeters/electromagnetic-flowmeters/optiflux-2300/ (accessed 12.6.16).

Kurokawa, J., Ohtaki, T., 1995. Gas-liquid flow characteristics and gas-separation efficiency in a cyclone separator. ASME FED 225, 51–57.

Laleh, A.P., 2010. CFD simulation of multiphase separators (PhD). University of Calgary, Calgary.

Laleh, A.P., Svrcek, W.Y., Monnery, W.D., 2012a. Computational fluid dynamics-based study of an oilfield separator - part i: a realistic simulation. Oil and Gas Facilities 57–68.

Laleh, A.P., Svrcek, W.Y., Monnery, W.D., 2012b. Design and CFD studies of multiphase separators - a review. The Canadian Journal of Chemical Engineering 90, 1547–1560.

Lessard, R.R., Zieminski, S.A., 1971. Bubble coalescence and gas transfer in aqueous electrolytic solutions. Industrial & Engineering Chemistry Fundamentals 10, 260–269.

Liao, Y., Lucas, D., 2009. A literature review of theoretical models for drop and bubble breakup in turbulent dispersions. Chemical Engineering Science 64, 3389–3406.

Majumder, S.K., Kundu, G., Mukherjee, D., 2006. Bubble size distribution and gas-liquid interfacial area in a modified downflow bubble column. Chemical Engineering Journal 122, 1–10.

Mantilla, I., Shirazi, S.A., Shoham, O., 1999. Flow field prediction and bubble trajectory model in gas-liquid cylindrical cyclone (GLCC) separators, in: Proceedings of ETCE '99: Energy Sources Technology Conference & Exhibition. Presented at the Energy Sources Technology Conference & Exhibition, Houston, Texas.

Mantilla Sanmiguel, I., 1998. Bubble trajectory analysis in gas-liquid cylindrical cyclone separators (MSc). The University of Tulsa, Tulsa, OK.

Martin, C.S., 1976. Vertically downward two-phase slug flow. Journal of Fluids Engineering 98, 715–722.

May, R.W.P., Willoughby, I.R., 1991. Impact pressures in plunge basins due to vertical plunging jets (Research No. SR242). Hydraulics Research Limited, Wallingford, Oxfordshire.

McNair, F.W., Koenig, G.A., 1911. Candle tests of air from a hydraulic air compressor. Compressed air magazine 16, 5963–5965.

McPherson, M.J., 2003. Chapter 5: Incompressible flow relationships [WWW Document]. Mine Ventilation Services, Incorporated. URL https://www.mvsengineering.com/files/Subsurface-Book/MVS-SVE_Chapter05.pdf (accessed 2.23.18).

Millar, D., Muller, E., 2017. Hydraulic air compressor (HAC) demonstrator project, in: Advancing Industrial Energy Efficiency through Collaboration. Presented at the 2017 ACEEE Summer Study on Energy Efficiency in Industry, ACEEE, Denver, Colorado, pp. 85–101.

Millar, D.L., 2017. Discussion document: Preliminary synthesis from results deployment of logging pressure probes in the first 4 sample tappings of the Dynamic Earth HAC downcomer (Internal document). Laurentian University, Dynamic Earth, Sudbury, Ontario.

Millar, D.L., 2014. A review of the case for modern-day adoption of hydraulic air compressors. Applied Thermal Engineering 69, 55–77.

Muñoz-Cobo, J.L., Chiva, S., Méndez, S., Monrós, G., Escrivá, A., Cuadros, J.L., 2017. Development of conductivity sensors for multi-phase flow local measurements at the Polytechnic University of Valencia (UPV) and University Jaume I of Castellon (UJI). Sensors 17, 35. https://doi.org/10.3390/s17051077

National Instruments, 2014. NI USB-6211 Device Specifications [WWW Document]. URL http://www.ni.com/pdf/manuals/375195d.pdf (accessed 8.20.14).

Nguyen, V.T., Song, C.-H., Bae, B.-U., Euh, D.-J., 2013. Modeling of bubble coalescense and break-up considering turbulent suppression phenomena in bubbly two-phase flow. International Journal of Multiphase Flow 54, 31–42.

NIST, 2018. REFPROP [WWW Document]. Standard reference data. URL https://www.nist.gov/srd/refprop (accessed 2.23.18).

Omega, 2016. PC mountable wet/wet differential pressure sensor [WWW Document]. URL https://www.omega.ca/pptst_eng/PX26.html (accessed 11.25.16).

Orvalho, S., Ruzicka, M.C., Giuseppe, O., Marzocchella, A., 2015. Bubble coalescence: effect of bubble approach velocity and liquid viscosity. Chemical Engineering Science 134, 205–216.

Parks Canada, 2013. Unpublished drawings and documents from Parks Canada.

Pavese, V., 2015. Energy and exergy analysis of a hydraulic air compressor for mining industry application (MSc). Politechnico di Torino, Turin, Italy.

Pavese, V., Millar, D., Verda, V., 2016. Mechanical efficiency of hydraulic air compressors. Journal of Energy Resources Technology 138, 062005-1-062005–11. https://doi.org/10.1115/1.4033623

Prosser, M.J., 1977. The hydraulic design of pump sumps and intakes. British Hydromechanics Research Association, Bedford.

Quick, M.C., 1970. Efficiency of air-entraining vortex formation at water intakes. Journal of the Hydraulics Division 96, 1403–1416.

Rice, W., 1976. Performance of hydraulic gas compressors. Journal of Fluids Engineering 98, 645–652.

Riventa Limited, 2017. FreeFlow temperature sensor [WWW Document]. FreeFlow temperature sensor. URL http://www.panakorea.co.kr/bbs/data/file/product/3731711948_yTB1ixVQ_TT-G2_Temperature_Sensor_-_Appendix1_V1.5.pdf (accessed 9.26.17).

Roghair, I., Lau, Y.M., Deen, N.G., Slagter, M.W., Van Sint Annaland, M., Kuipers, J.A.M., 2011. On the drag force of bubbles in bubble swarms at intermediate and high Reynolds numbers. Chemical Engineering Science 66, 3204–3211.

Sander, R., 2015. Compilation of Henry's law constants (version 4.0) for water as solvent. Atmospheric Chemistry and Physics 15, 4399–4981.

Schulze, L.E., 1954. Hydraulic air compressors. United States Department of the Interior. Bureau of Mines information circular 7683.

Shakerin, S., 2010. Vortex apparatus and demonstrations. The Physics Teacher 48, 316–318.

Shakerin, S., 2008. Self-induced vibration in whirlpool. Cornell University, Portland, OR.

Sivret, J., 2018. Commissioning and verification of compressed air yield on the hydraulic air compressor demonstrator (MASc). Laurentian University, Sudbury, Ontario.

Taya, C., Maeda, Y., Hosokawa, S., Tomoyama, A., Yoshihiro, I., Shibata, N., 2012. Size distribution of micro-bubbles generated by a pressurized dissolution method. Japanese Journal of Multiphase Flow 25, 407–414.

Taylor, C.H., 1897. Illustrated description of the Taylor hydraulic air compressor and transmission of power by compressed air. URL https://archive.org/stream/IllustratedDescriptionOfTheTaylorHydraulicAirCompressorAndTransmission/49590#page/n0 (accessed 8.25.16).

USSensor, 2014. Thermistor PN PT103J2 (resistance vs. temperature table) [WWW Document]. URL http://www.littelfuse.com/~/media/electronics/rt_tables/leaded_thermistors/littelfuse_leaded_thermistors_interchangeable_thermistors_ps103j2_rt_table.xlsx.xlsx (accessed 8.20.14).

Usui, K., 1989. Vertically downward two-phase flow, (II). Journal of Nuclear Science and Technology 26, 1013–1022.

Usui, K., Sato, K., 1989. Vertically downward two-phase flow, (I). Journal of Nuclear Science and Technology 26, 670–680.

Werth, D., Frizzell, C., 2009. Minimum pump submergence to prevent surface vortex formation. J. Hydraul. Res. 47, 142–144.

W.H.B., 1903. Trent canal hydraulic lock no. 1 air compressor drawing no. 12.

Wilkinson, P.M., Haringa, H., Van Dierendonck, L.L., 1994. Mass transfer and bubble size in a bubble column under pressure. Chemical Engineering Science 49, 1417–1427.

Wilkinson, P.M., Spek, A.P., Van Dierendonck, L.L., 1992. Design parameters estimation for scale-up of high-pressure bubble columns. AIChE Journal 38, 544–554.

Wilkinson, P.M., Van Dierendonck, L.L., 1990. Pressure and gas density effects of bubble break-up and gas hold-up in bubble columns. Chemical Engineering Science 45, 2309–2315.

Young, S., Hutchison, A., Sengupta, S., Clifford, T., Pavese, V., Noula, C., Myre, M., Vitone, D.M.A., Chiasson, J.P., Millar, D.L., 2015. Conceptual design of a modern-day hydraulic air compressor. Presented at the ECOS 2015 28th International Conference on Efficiency, Cost, Optimization, Simulation and Environmental Impact of Energy Systems, Pau, France.

Young, S.M., 2017. Simulating air absorption in a hydraulic air compressor (HAC) (MASc). Laurentian University, Sudbury, Ontario.

Zheng, Y., Werth, D., 2008. Optimize pump intake design with formed suction inlets, in: Babcock, R.W.J., Walton, R. (Eds.), World Environmental and Water Resources Congress 2008: Ahupa'A. Presented at the 2008 World Environmental and Water Resources Congress, ASCE, Honolulu, HI, pp. 1–11.

Appendices

Appendix A: Separator model code

This appendix contains the complete VBA code required to run both the vertical velocity and the horizontal displacement separator models. Both models require the velocity components (vertical only for the vertical velocity model or vertical and horizontal along flow direction for the horizontal displacement mode) to be imported into Excel from the CFD results and sorted by interrogation plane to solve (see: chapter 5). The horizontal displacement model requires some additional setup to enable sequential bubble tracking. A sample of the tracking sheet is included in Appendix J.

Vertical velocity model gravity separator effectiveness code

```
Option Explicit

'This function interfaces with the CritDiameter function and spreadsheet parameters to report cell-by-cell
'separation efficiency using only a single column.
Function SeparationEfficiency(verticalVelocity As Double, mixtureDensity As Double, airDensity As Double, _
                              bulkViscosity As Double, meanDiameter As Double, spreadIndex As Double)
    'if verticalVelocity is positive, the separation efficiency is 100% for that cell (short circuit)
    If verticalVelocity >= 0# Then
        SeparationEfficiency = 1
    Else
        'calculate critical diameter
        Dim criticalDiameter As Double
        criticalDiameter = CritDiameter(-verticalVelocity, mixtureDensity, airDensity, bulkViscosity)

        'use critical diameter to calculate separation efficiency
        SeparationEfficiency = Exp(-(criticalDiameter / meanDiameter) ^ spreadIndex)
    End If
End Function
```

```
'This function takes the critical terminal velocity, water density, air density, and water dynamic viscosity
'and returns the critical diameter of the smallest bubble that can separate out of the mixture.
'The function uses an iterative process to solve the system of equations, and can take an optional tolerance
'variable to control this process.
Function CritDiameter(critVelocity As Double, densWater As Double, densAir As Double, viscWater As Double,_
                      Optional tolerance As Double = 0.00001)

    'create drag coefficient with initial value = 0.95
    Dim dragCoeff As Double
    dragCoeff = 0.95

    'set gravitational acceleration constant
    Dim grav As Double
    grav = 9.80665

    'iterate to solve for critical diameter
    Dim currentDiam As Double
    currentDiam = 1
    Dim prevDiam As Double
    Do
        prevDiam = currentDiam
        Call BubbleDiameter(currentDiam, critVelocity, dragCoeff, densWater, densAir, grav)
        dragCoeff = DragCoefficient(currentDiam, densWater, critVelocity, viscWater)
    Loop Until Math.Abs(currentDiam - prevDiam) < tolerance

    'return diameter
    CritDiameter = prevDiam 'currentDiam
End Function

'single iteration of critical bubble diameter calculation
Sub BubbleDiameter(ByRef currentDiam As Double, critVelocity As Double, dragCoeff As Double, _
                   densWater As Double, densAir As Double, grav As Double)
    currentDiam = (3 * critVelocity ^ 2 * dragCoeff * densWater) / (4 * grav * (densWater - densAir))
End Sub
```

```
'calculate drag coefficient with bubble diameter
Function DragCoefficient(bubbleDiam As Double, densWater As Double, critVelocity As Double, _
                         viscWater As Double)
    'particle Reynold's number
    Dim Rep As Double
    Call ParticleReynolds(Rep, bubbleDiam, densWater, critVelocity, viscWater)


    'Cheng (2009) relationship for drag coefficient valid up to Rep = 2E5
    DragCoefficient = (24 / Rep) * (1 + 0.27 * Rep) ^ 0.43 + 0.47 * (1 - Exp(-0.04 * Rep ^ 0.38))

    'Karamanev and Nikolov (1992) correction for rising bubbles
    If DragCoefficient < 0.95 Then
        DragCoefficient = 0.95
    End If
End Function

'calculate particle Reynold's number for drag coefficient
Sub ParticleReynolds(ByRef Rep As Double, bubbleDiam As Double, densWater As Double, _
                     critVelocity As Double, viscWater As Double)
    Rep = bubbleDiam * densWater * critVelocity / viscWater
End Sub
```

This segment commented out for models excluding this correction.

Horizontal gravity separator effectiveness code:

The code calculates only displacement. Separator effectiveness is calculated iteratively between this code and values stored in the spreadsheet from interrogation plane to interrogation plane of the separator. A sample of the spreadsheet is included in Appendix J.

```
Option Explicit

'This is the master function that tracks displacement of bubbles of a uniform size in a horizontal
'separator. Rise velocity (of the bubble) interacts with vertical velocity (of the matrix fluid) and
'residence time (within the separator channel interval) to determine total vertical displacement for
```

```
'that cell. That displacement is checked against the start position (vertical bin) and other available
'vertical bins to determine the final vertical position of the bubbles from that cell. The bubbles are
'assumed to be uniformly distributed within each vertical bin. The proportion of bubbles that migrate
'as calculated for each cell is weighted by the area of that cell relatice to the total for the slice.
'The output is reported as a new distribution of bubbles across the vertical bins included in the
'input plus a quantity for bubbles completely separated from the mixture.
Function HorizontalSeparator(verticalBins As Range, currentPosition As Range, riseVelocity As Double, _
                             area As Range, verticalVelocity As Range, residenceTime As Range, _
                             elevation As Range)

    'row count is used to collect area, vertical velocity, and residence time by vertical slice interval
    Dim nRows As Integer
    nRows = area.Rows.Count
    'number of vertical slices and interval
    Dim nVerticalSlices As Integer
    nVerticalSlices = verticalBins.Columns.Count - 1
    Dim sliceHeight As Double
    sliceHeight = verticalBins(2) - verticalBins(1)

    'these vectors get used to compute and employ area weighting of displacement figures
    Dim areaSum() As Double
    ReDim areaSum(1 To nVerticalSlices) As Double
    Dim sliceStartPosition() As Integer
    ReDim sliceStartPosition(1 To nVerticalSlices) As Integer
    Dim nCellsBySlice() As Integer
    ReDim nCellsBySlice(1 To nVerticalSlices) As Integer

    'outer loop iterates through vertical intervals, inner loop used to track j index to identify
    'members of each slice
    Dim i As Integer
    Dim j As Integer
    j = 1
    For i = 1 To nVerticalSlices
        sliceStartPosition(i) = j
        Do
            areaSum(i) = areaSum(i) + area(j)
            j = j + 1
```

```
    Loop Until (j > nRows Or elevation(j) > i * sliceHeight + 0.000001)
    nCellsBySlice(i) = j - sliceStartPosition(i)
Next i

'these variables used to track slice redistribution of bubbles
Dim newVerticalBins() As Double
ReDim newVerticalBins(1 To nVerticalSlices + 1)
newVerticalBins(nVerticalSlices + 1) = currentPosition(nVerticalSlices + 1)
Dim displacement As Double
Dim weightFactor As Double
Dim cell As Integer
Dim k As Integer

'current slice redistribution of bubbles for every slice, cells weighted by current bubble fraction
'in each slice and cell area divided by total slice area
For i = 1 To nVerticalSlices
    For j = 1 To nCellsBySlice(i)
        'which cell to interrogate?
        cell = sliceStartPosition(i) + j - 1

        'final position unbounded
        displacement = verticalBins(i) + (verticalVelocity(cell) + riseVelocity) * _
                       residenceTime(cell)
        weightFactor = (area(cell) / areaSum(i)) * currentPosition(i)

        'add fraction of bubbles represented by current cell to new position
        If displacement < 0 Then
            'bubble cannot go below lowest slice
            newVerticalBins(1) = newVerticalBins(1) + weightFactor
        ElseIf displacement > verticalBins(nVerticalSlices) + sliceHeight / 2 Then
            'bubble above uppermost slice is separated
            newVerticalBins(nVerticalSlices + 1) = newVerticalBins(nVerticalSlices + 1) + _
                                                   weightFactor
        Else
            'bubble falls into any slice
            For k = 2 To nVerticalSlices
                'find correct interval
```

```
                    If (displacement > verticalBins(k - 1) And displacement < verticalBins(k)) Then
                        'find which one is closer and plug it in there
                        If (displacement - verticalBins(k - 1) > verticalBins(k) - displacement) Then
                            newVerticalBins(k) = newVerticalBins(k) + weightFactor
                            Exit For
                        Else
                            newVerticalBins(k - 1) = newVerticalBins(k - 1) + weightFactor
                            Exit For
                        End If

                    'above top slice midpoint but below free surface level
                    ElseIf k = nVerticalSlices Then
                        newVerticalBins(k) = newVerticalBins(k) + weightFactor
                    End If
                Next k
            End If
        Next j
    Next i

    HorizontalSeparator = newVerticalBins
End Function
```

```
'different length, the program may crash.
Function Interpolate(target As Double, searchRange As Range, interpolateRange As Range)
    'convert both ranges to variant array: this allows the program to treat ranges of any
    'format and orientation as equivalent
    Dim convertedSearch() As Variant
    convertedSearch = RangeToArray(searchRange)
    Dim convertedInterpolate() As Variant
    convertedInterpolate = RangeToArray(interpolateRange)

    'convert variant arrays to double arrays
    Dim nElements As Long
    nElements = UBound(convertedSearch)
    Dim searchArray() As Double
    ReDim searchArray(1 To nElements) As Double
```

```
    Dim interpolateArray() As Double
    ReDim interpolateArray(1 To nElements) As Double
    Dim i As Long
    For i = 1 To nElements
        searchArray(i) = convertedSearch(i)
        interpolateArray(i) = convertedInterpolate(i)
    Next i

    'interval of search array to find value
    Dim interval() As Long
    interval = BinarySearch(searchArray, target)
    Dim searchElements() As Double
    ReDim searchElements(1 To 2) As Double
    Dim interpolateElements() As Double
    ReDim interpolateElements(1 To 2) As Double
    For i = 1 To 2
        searchElements(i) = searchArray(interval(i))
        interpolateElements(i) = interpolateArray(interval(i))
    Next i

    'solve interpolation
    Interpolate = interpolateElements(1) - ((interpolateElements(1) - interpolateElements(2)) / _
                  (searchElements(1) - searchElements(2))) * (searchElements(1) - target)
End Function
```

```
'Returns the index interval within the search array where the value is found. It requires
'a sorted array (ascending or descending order) and a value within the range. Throws an
'error when the value is out of range. The function cannot detect whether or not the input
'array is sorted and will converge without error in that case on an arbitrary interval.
Function BinarySearch(searchArray() As Double, target As Double)
    'prepare output variable
    Dim indexRange() As Long
    ReDim indexRange(1 To 2) As Long

    'check ascending or descending order
    Dim isAscending As Boolean
```

```
Dim nElements As Long
nElements = UBound(searchArray)
If searchArray(1) < searchArray(nElements) Then
    isAscending = True
Else
    isAscending = False
End If

'check out of range
Dim isInRange As Boolean
If (isAscending) Then
    isInRange = target >= searchArray(1) And target <= searchArray(nElements)
Else
    isInRange = target <= searchArray(1) And target >= searchArray(nElements)
End If

'set bad indices and kick out of function if out of range
If (Not isInRange) Then
    indexRange(1) = -1
    indexRange(2) = -1
    BinarySearch = indexRange
    Exit Function
End If

'set indices for search
indexRange(1) = 1 'minimum
indexRange(2) = nElements 'maximum
Dim mid As Long

'conduct search
Do While (indexRange(2) > indexRange(1) + 1)
    'set midpoint
    mid = Int((indexRange(1) + indexRange(2)) / 2)

    'mid replaces min or max? depends on ascending or descending order
    If (isAscending) Then
        If (target > searchArray(mid)) Then
```

```
                indexRange(1) = mid
            Else
                indexRange(2) = mid
            End If
        Else
            If (target < searchArray(mid)) Then
                indexRange(1) = mid
            Else
                indexRange(2) = mid
            End If
        End If
    Loop

    BinarySearch = indexRange
End Function
```

```
'Converts range to an array. It assumes the range is 1D, but will construct an array from
'the first row or column (whichever is bigger) of a 2D range. Output is a variant array.
Function RangeToArray(rangeIn As Range)
    'determine whether or not range is column vector and determine maximum range length
    Dim nRows As Long
    Dim nColumns As Long
    Dim rangeLength As Long
    Dim isColumnVector As Boolean
    nRows = rangeIn.Rows.Count
    nColumns = rangeIn.Columns.Count
    If (nRows > nColumns) Then
        isColumnVector = True
        rangeLength = nRows
    Else
        isColumnVector = False
        rangeLength = nColumns
    End If

    'convert range to 1D variant array
    Dim arrayOut() As Variant
```

```
    ReDim arrayOut(1 To rangeLength) As Variant
    Dim i As Long
    For i = 1 To rangeLength
        'row array and column array are different
        If (isColumnVector) Then
            arrayOut(i) = rangeIn(i, 1)
        Else
            arrayOut(i) = rangeIn(1, i)
        End If
    Next i

    RangeToArray = arrayOut
End Function
```

```
'This function takes the critical terminal velocity, water density, air density, water dynamic viscosity,
'and (optional) void ratio and returns the critical diameter, which is smallest bubble that can separate
'out of the mixture. The function uses an iterative process to solve the system of equations, and can take
'an optional tolerance variable to control this process (default = 10E-8)
Function CritDiameter(criticalVelocity As Double, waterDensity As Double, airDensity As Double, _
                      waterViscosity As Double, Optional voidRatio As Double = 0, _
                      Optional tolerance As Double = 0.0000001)
    'create drag coefficient with initial value = 0.2
    Dim dragCoeff As Double
    dragCoeff = 0.2

    'set gravitational acceleration constant
    Dim gravity As Double
    gravity = 9.80665

    'set mixture density based on void ratio and air and water densities (if void ratio is 0, no weight
    'to air density)
    Dim mixtureDensity As Double
    mixtureDensity = (1 - voidRatio) * waterDensity + voidRatio * airDensity

    'iterate to solve for critical diameter to within tolerance
    Dim currentDiameter As Double
```

```
    currentDiameter = 0.001
    Dim previousDiameter As Double
    Do
        previousDiameter = currentDiameter
        Call CalculateDiameter(currentDiameter, criticalVelocity, dragCoeff, mixtureDensity, _
                               airDensity, gravity)
        dragCoeff = DragCoefficient(currentDiameter, mixtureDensity, criticalVelocity, waterViscosity)
    Loop Until Math.Abs(currentDiameter - previousDiameter) < tolerance


    CritDiameter = currentDiameter 'return diameter
End Function

'This function takes the bubble diameter, water density, air density, water dynamic viscosity, and
'(optional) void ratio and returns the vertical velocity that the bubble has relative to that of the
'water. The function uses an iterative process to solve the system of equations, and can take an
'optional tolerance variable to control this process.
Function critVelocity(bubbleDiameter As Double, waterDensity As Double, airDensity As Double, _
                      waterViscosity As Double, Optional voidRatio As Double = 0, _
                      Optional tolerance As Double = 0.0000001)
    'create drag coefficient with initial value = 0.2
    Dim dragCoeff As Double
    dragCoeff = 0.2

    'set gravitational acceleration constant
    Dim gravity As Double
    gravity = 9.80665

    'set mixture density based on void ratio and air and water densities (if void ratio is 0, no weight
    'to air density)
    Dim mixtureDensity As Double
    mixtureDensity = (1 - voidRatio) * waterDensity + voidRatio * airDensity

    'iterate to solve for relative vertical velocity to within tolerance
    Dim currentVelocity As Double
    currentVelocity = 0.3
    Dim previousVelocity As Double
```

```
    Do
        previousVelocity = currentVelocity
        Call CalculateVelocity(currentVelocity, bubbleDiameter, dragCoeff, mixtureDensity, airDensity, _
                               gravity)
        dragCoeff = DragCoefficient(bubbleDiameter, mixtureDensity, currentVelocity, waterViscosity)
    Loop Until Math.Abs(currentVelocity - previousVelocity) < tolerance

    'return velocity
    critVelocity = currentVelocity
End Function

'single iteration of critical bubble diameter calculation
Sub CalculateDiameter(ByRef currentDiameter As Double, bubbleVelocity As Double, dragCoeff As Double, _
                      mixtureDensity As Double, airDensity As Double, gravity As Double)
    currentDiameter = (3 * bubbleVelocity ^ 2 * dragCoeff * mixtureDensity) / _
                      (4 * gravity * (mixtureDensity - airDensity))
End Sub

'single iteration of critical bubble diameter calculation
Sub CalculateVelocity(ByRef currentVelocity As Double, bubbleDiameter As Double, dragCoeff As Double, _
                      mixtureDensity As Double, airDensity As Double, gravity As Double)
    currentVelocity = ((4 * bubbleDiameter * gravity * (mixtureDensity - airDensity)) / _
                      (3 * dragCoeff * mixtureDensity)) ^ 0.5
End Sub
```

```
'calculate drag coefficient with bubble diameter
Function DragCoefficient(bubbleDiam As Double, densWater As Double, critVelocity As Double, _
                         viscWater As Double)
    'particle Reynold's number
    Dim Rep As Double
    Call ParticleReynolds(Rep, bubbleDiam, densWater, critVelocity, viscWater)

    'Cheng (2009) relationship for drag coefficient valid up to Rep = 2E5
    DragCoefficient = (24 / Rep) * (1 + 0.27 * Rep) ^ 0.43 + 0.47 * (1 - Exp(-0.04 * Rep ^ 0.38))

    'Karamanev and Nikolov (1992) correction for rising bubbles
```

```
    If DragCoefficient < 0.95 Then
        DragCoefficient = 0.95
    End If
End Function

'calculate particle Reynold's number for drag coefficient
Sub ParticleReynolds(ByRef Rep As Double, bubbleDiam As Double, densWater As Double, _
                     critVelocity As Double, viscWater As Double)
    Rep = bubbleDiam * densWater * critVelocity / viscWater
End Sub
```

This segment commented out for models excluding this correction.

Appendix B: Full fabrication drawings Baby HAC

All drawings except separator and mixing head (at bottom) were prepared by Diogo Oliveira.

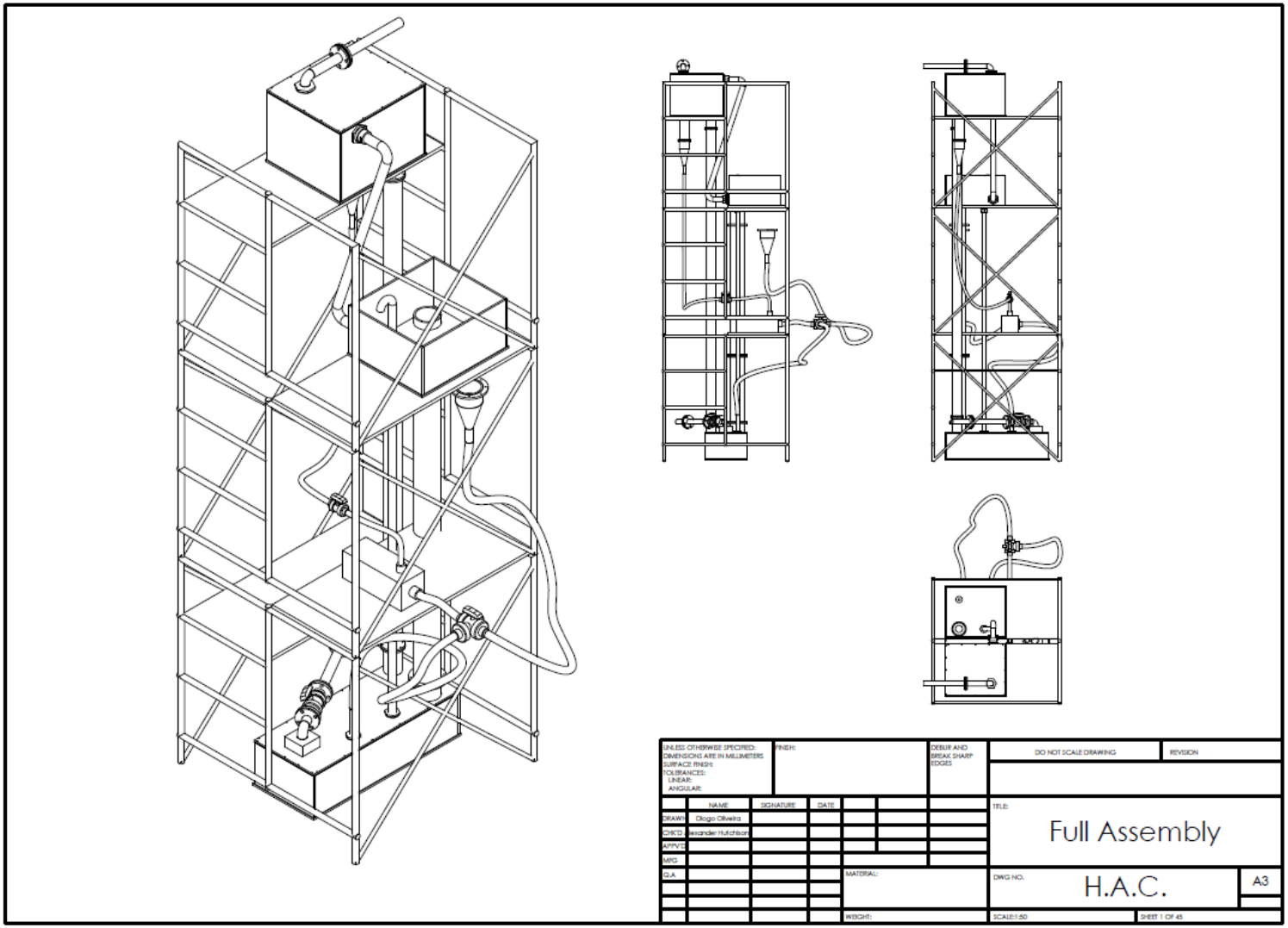

Part List	#
2" pipe sch 40 250mm long	1
2" pipe flange	1
2" Elbow	1
2" pipe Sch 40 70mm long	1

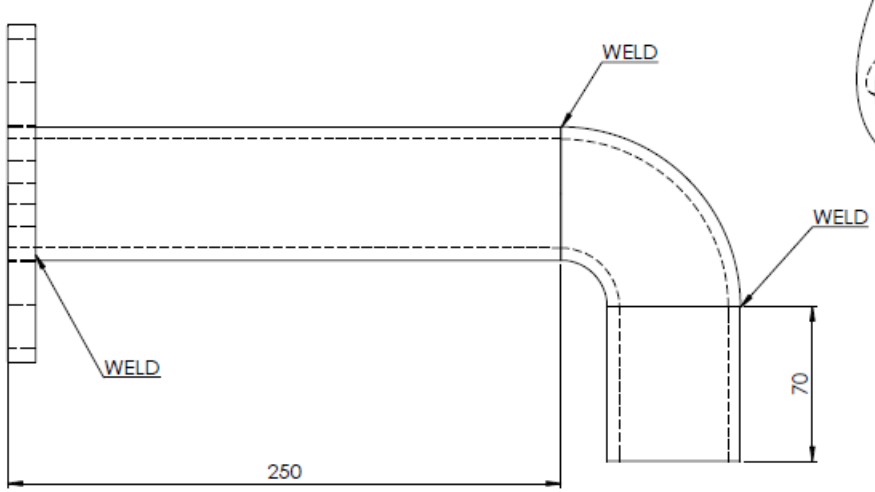

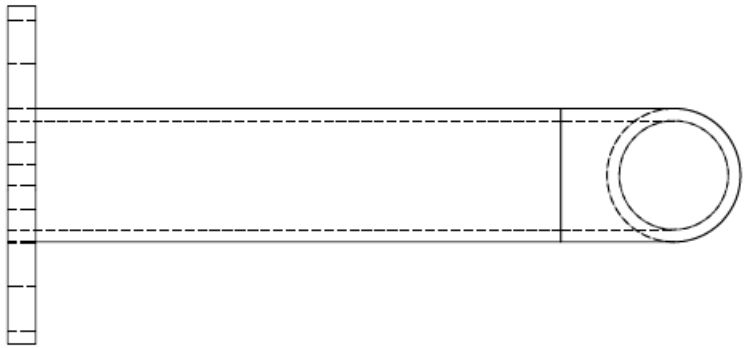

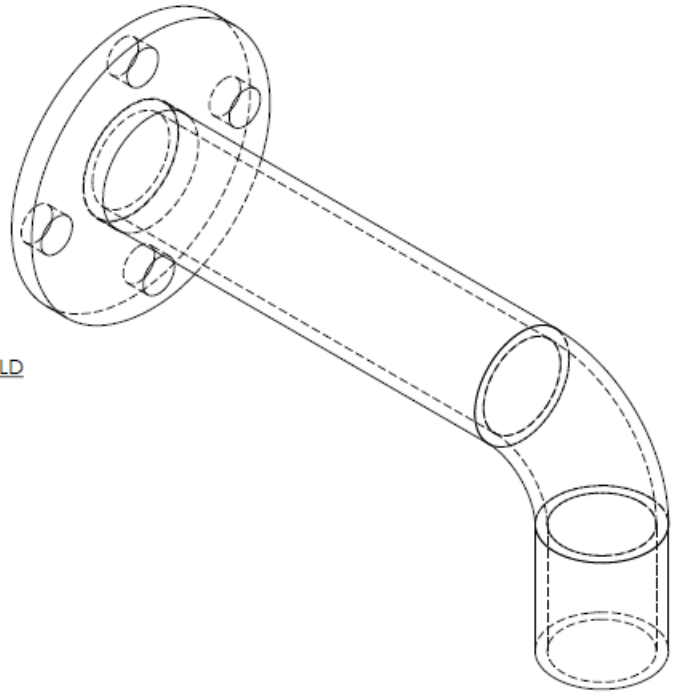

UNLESS OTHERWISE SPECIFIED: DIMENSIONS ARE IN MILLIMETERS SURFACE FINISH: TOLERANCES: LINEAR: ANGULAR:	FINISH:		DEBUR AND BREAK SHARP EDGES	DO NOT SCALE DRAWING	REVISION	
	NAME	SIGNATURE	DATE	TITLE: 2" pipe Weldment #1		
DRAWN	Diogo Oliveira					
CHK'D	Alexander Hutchison					
APPV'D						
MFG						
Q.A				MATERIAL:	DWG NO. H.A.C.	A3
				WEIGHT:	SCALE:1:5	SHEET 23 OF 45

Parts List	#
2" pipe sch 40 500mm long	1
2" pipe Flange	1

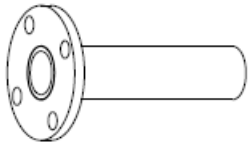

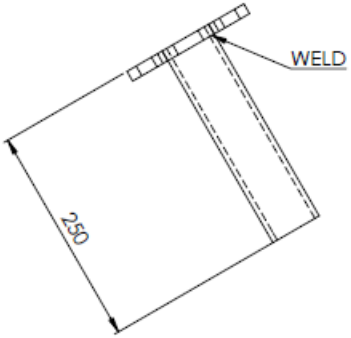

UNLESS OTHERWISE SPECIFIED: DIMENSIONS ARE IN MILLIMETERS SURFACE FINISH: TOLERANCES: LINEAR: ANGULAR:	FINISH:				DEBUR AND BREAK SHARP EDGES	DO NOT SCALE DRAWING / REVISION
	NAME	SIGNATURE	DATE			TITLE: 2" pipe Weldment #2
DRAWN	Diogo Oliveira					
CHECD	Alexandre Hutchinson					
APPVD						
MFG						
Q.A				MATERIAL:		DWG NO. H.A.C. / A3
				WEIGHT:		SCALE:1:10 / SHEET 28 OF 45

Parts List	#
2" pipe sch 40 500mm long	2
2" pipe Flange	2

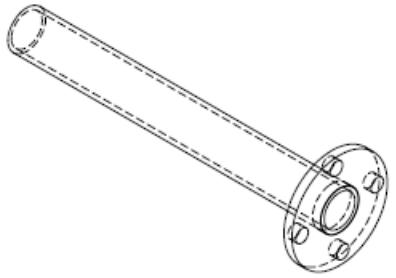

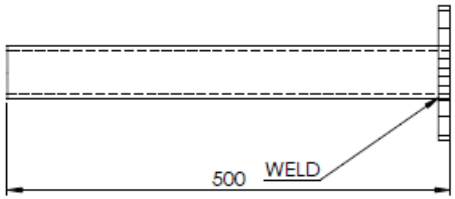

UNLESS OTHERWISE SPECIFIED:
DIMENSIONS ARE IN MILLIMETERS
SURFACE FINISH:
TOLERANCES:
LINEAR:
ANGULAR:

FINISH:

DEBUR AND BREAK SHARP EDGES

DO NOT SCALE DRAWING

REVISION

	NAME	SIGNATURE	DATE
DRAWN	Diogo Oliveira		
CHK'D	Alexander Hutchison		
APPV'D			
MFG			
Q.A.			

MATERIAL:

WEIGHT:

TITLE:

2" pipe Weldment #3

DWG NO. H.A.C.

A3

SCALE:1:5

SHEET 24 OF 45

Parts List	#
2" pipe sch 40 500mm long	1
2" pipe Flange	2

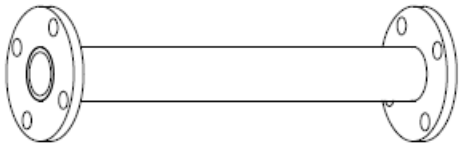

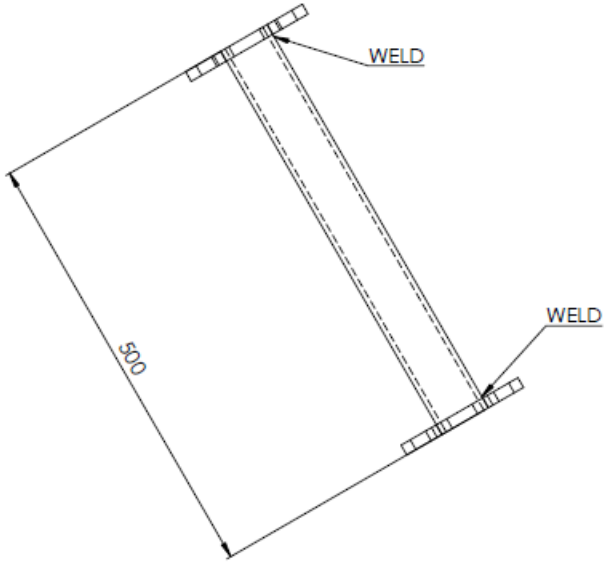

UNLESS OTHERWISE SPECIFIED:
DIMENSIONS ARE IN MILLIMETERS
SURFACE FINISH:
TOLERANCES:
LINEAR:
ANGULAR:

FINISH:

DEBUR AND BREAK SHARP EDGES

DO NOT SCALE DRAWING | REVISION

	NAME	SIGNATURE	DATE
DRAWN	Diogo Oliveira		
CHKD	Alexander Hutchison		
APPVD			
MFG			
Q.A			

MATERIAL:

WEIGHT:

TITLE:
2" pipe Weldment #4

DWG NO. H.A.C.

A3

SCALE:1:20

SHEET 27 OF 45

Parts List	#
2" pipe sch 40 3200mm long	1
2" U tube sch 40	1

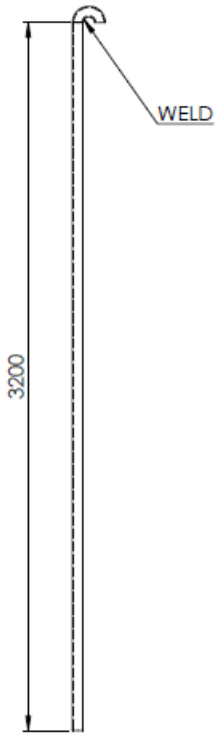

UNLESS OTHERWISE SPECIFIED:
DIMENSIONS ARE IN MILLIMETERS
SURFACE FINISH:
TOLERANCES:
LINEAR:
ANGULAR:

FINISH:

DEBUR AND BREAK SHARP EDGES

DO NOT SCALE DRAWING | REVISION

	NAME	SIGNATURE	DATE
DRAWN	Diogo Oliveira		
CHK'D	Alexander Hutchison		
APPV'D			
MFG			
Q.A.			

MATERIAL:

WEIGHT:

TITLE:

Blowoff Pipe

DWG NO. H.A.C.

A3

SCALE:1:50

SHEET 41 OF 45

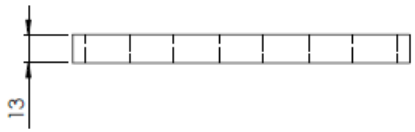

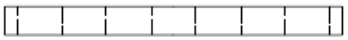

FLANGE 2" X 4

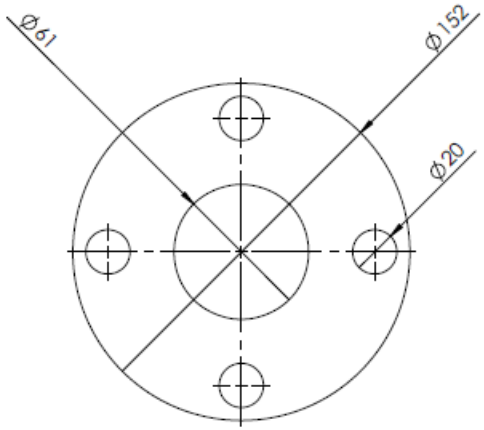

UNLESS OTHERWISE SPECIFIED: DIMENSIONS ARE IN MILLIMETERS SURFACE FINISH: TOLERANCES: LINEAR: ANGULAR:				FINISH:		DEBUR AND BREAK SHARP EDGES	DO NOT SCALE DRAWING / REVISION
	NAME	SIGNATURE	DATE				TITLE: 2" pipe Flange
DRAWN	Diogo Oliveira						
CHK'D	Alexander Hutchison						
APPV'D							
MFG							
Q.A				MATERIAL:			DWG NO. H.A.C. / A3
				WEIGHT:			SCALE:1:2 / SHEET 22 OF 45

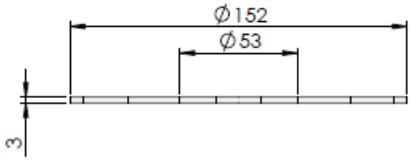

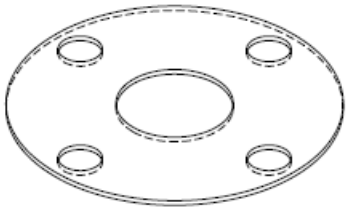

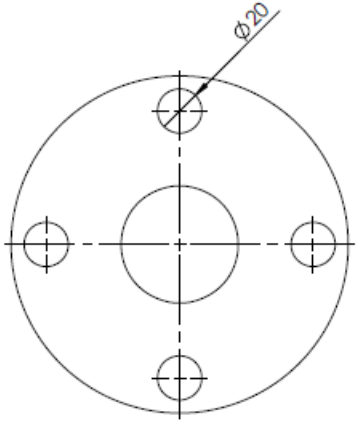

UNLESS OTHERWISE SPECIFIED: DIMENSIONS ARE IN MILLIMETERS SURFACE FINISH: TOLERANCES: LINEAR: ANGULAR:		FINISH:			DEBUR AND BREAK SHARP EDGES	DO NOT SCALE DRAWING	REVISION
	NAME	SIGNATURE	DATE			TITLE: Gasket 2"	
DRAWN	Diogo Oliveira						
CHKD	Alexander Hutchison						
APPVD							
MFG							
QA				MATERIAL:		DWG NO. H.A.C.	A3
				WEIGHT:		SCALE:1:2	SHEET 42 OF 44

Parts List	#
4" pipe sch 40 387mm long	1
4" pipe Flange	1

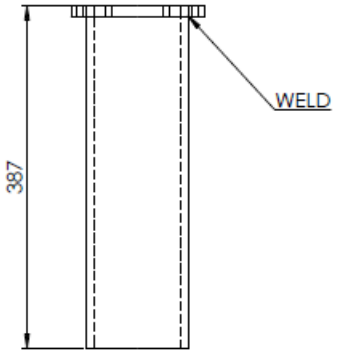

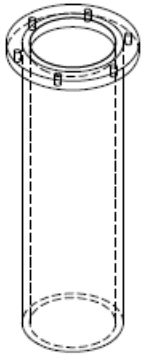

UNLESS OTHERWISE SPECIFIED: DIMENSIONS ARE IN MILLIMETERS SURFACE FINISH: TOLERANCES: LINEAR: ANGULAR:	FINISH:			DEBUR AND BREAK SHARP EDGES	DO NOT SCALE DRAWING	REVISION
	NAME	SIGNATURE	DATE		TITLE: 4" pipe Weldment #1	
DRAWN	Diogo Oliveira					
CHK'D	Alexander Hutchison					
APPV'D						
MFG						
Q.A				MATERIAL:	DWG NO. H.A.C.	A3
				WEIGHT:	SCALE:1:5	SHEET 33 OF 45

Parts List	#
4" pipe Flange	1
4" sch 40 pipe 300mm Long	1

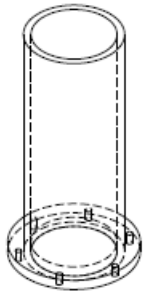

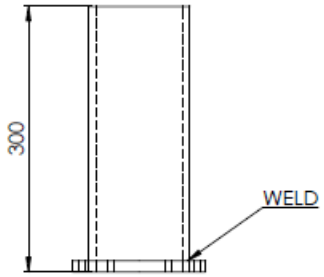

UNLESS OTHERWISE SPECIFIED:
DIMENSIONS ARE IN MILLIMETERS
SURFACE FINISH:
TOLERANCES:
LINEAR:
ANGULAR:

FINISH:

DEBUR AND BREAK SHARP EDGES

DO NOT SCALE DRAWING | REVISION

	NAME	SIGNATURE	DATE
DRAWN	Diogo Oliveira		
CHK'D	Alexander Hutchison		
APPV'D			
MFG			
Q.A			

MATERIAL:

WEIGHT:

TITLE:
4" pipe Weldment #3

DWG NO. H.A.C.

A3

SCALE:1:20

SHEET 30 OF 44

Parts List	#
4" pipe sch 40 3474mm Long	1
4" pipe Flange	2

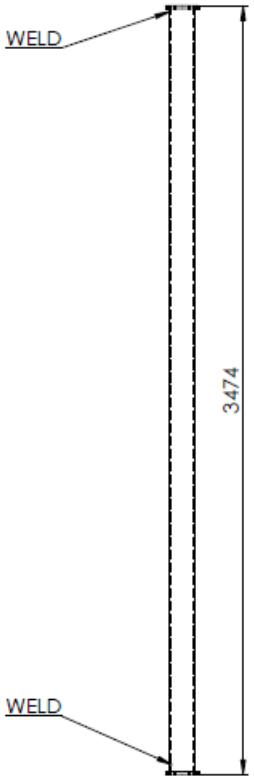

UNLESS OTHERWISE SPECIFIED: DIMENSIONS ARE IN MILLIMETERS SURFACE FINISH: TOLERANCES: LINEAR: ANGULAR:	FINISH:		DEBUR AND BREAK SHARP EDGES		DO NOT SCALE DRAWING	REVISION
	NAME	SIGNATURE	DATE		TITLE: 4" pipe Weldment #4	
DRAWN	Diogo oliveira					
CHK'D	Alexander Hutchison					
APPV'D						
MFG						
Q.A				MATERIAL:	DWG NO. H.A.C.	A3
				WEIGHT:	SCALE:1:50	SHEET 32 OF 45

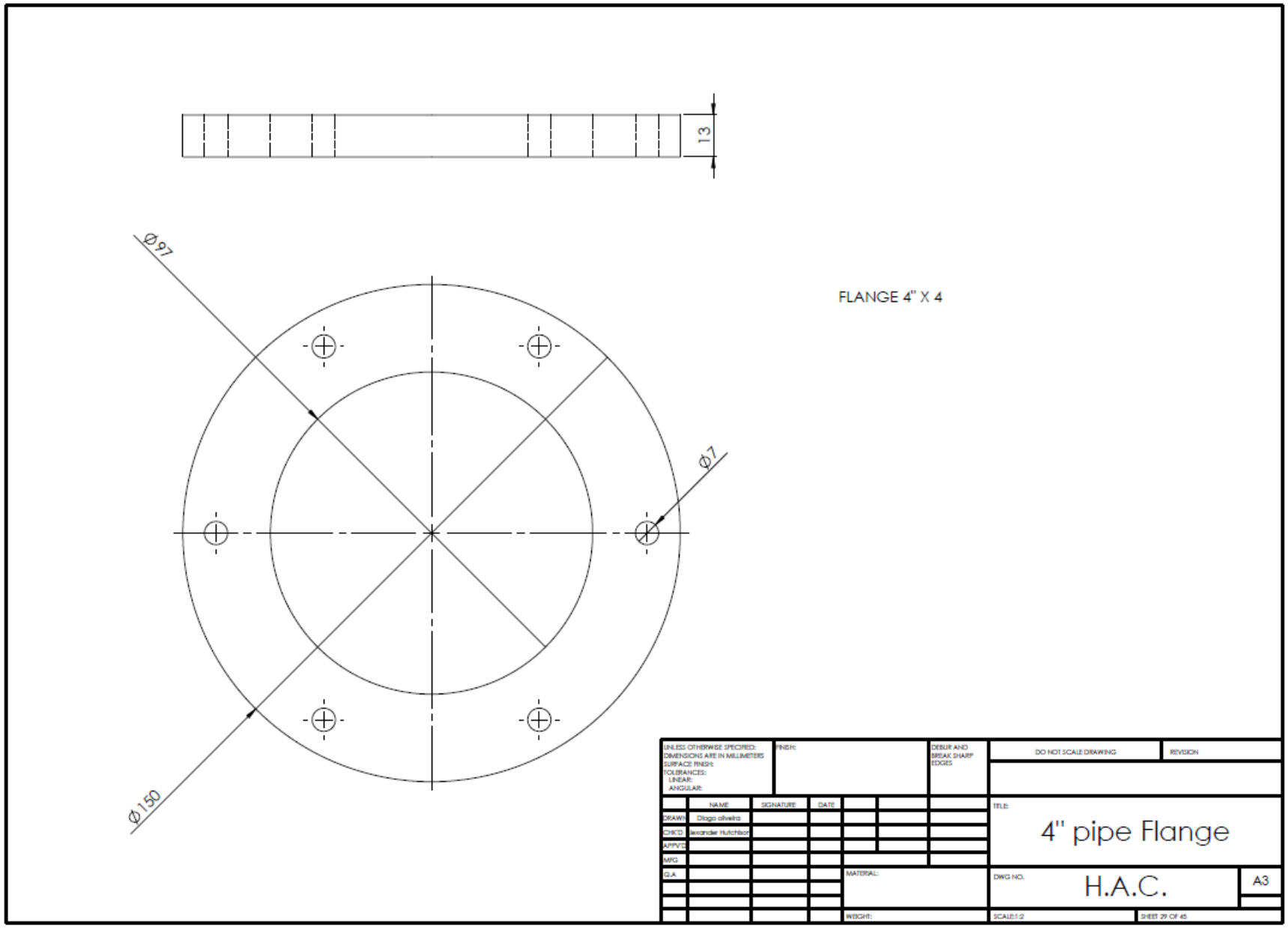
13
Ø97
Ø7
Ø150
FLANGE 4" X 4
UNLESS OTHERWISE SPECIFIED:
DIMENSIONS ARE IN MILLIMETERS
SURFACE FINISH:
TOLERANCES:
LINEAR:
ANGULAR:
FINISH:
DEBUR AND BREAK SHARP EDGES
DO NOT SCALE DRAWING
REVISION
NAME
SIGNATURE
DATE
DRAWN
Diogo oliveira
CHK'D
Alexander Hutchison
APP'V'D
MFG
Q.A.
MATERIAL:
WEIGHT:
TITLE:
4" pipe Flange
DWG NO.
H.A.C.
A3
SCALE:1:2
SHEET 29 OF 45

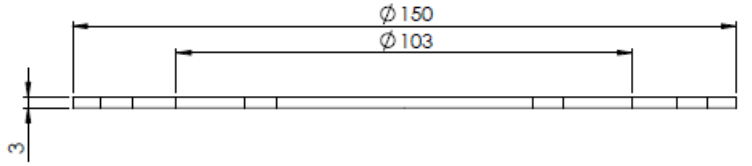

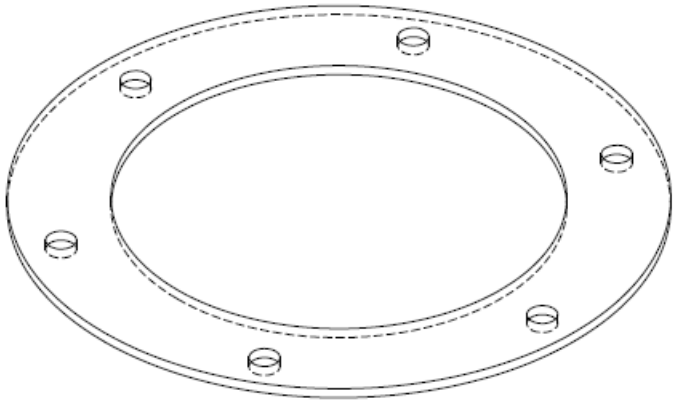

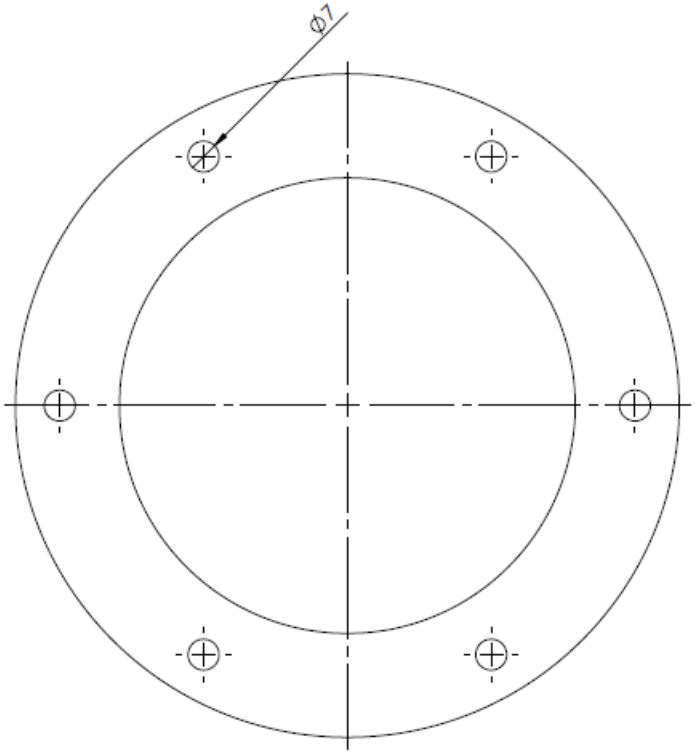

UNLESS OTHERWISE SPECIFIED: DIMENSIONS ARE IN MILLIMETERS SURFACE FINISH: TOLERANCES: LINEAR: ANGULAR:	FINISH:		DEBUR AND BREAK SHARP EDGES	DO NOT SCALE DRAWING	REVISION	
	NAME	SIGNATURE	DATE	TITLE: Gasket 4"		
DRAWN	Diogo Oliveira					
CHK'D	Alexander Hutchison					
APPV'D						
MFG						
Q.A.				MATERIAL:	DWG NO. H.A.C.	A3
				WEIGHT:	SCALE:1:2	SHEET 44 OF 44

Parts List	#
6" pipe sch 40 387mm long	1
6" pipe Flange	1

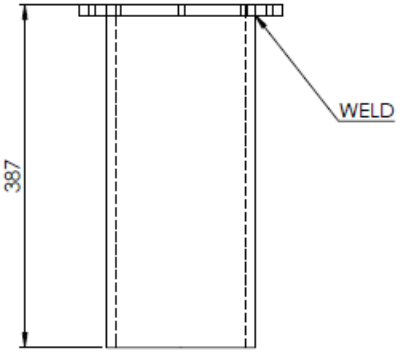

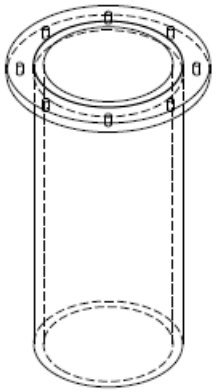

UNLESS OTHERWISE SPECIFIED: DIMENSIONS ARE IN MILLIMETERS SURFACE FINISH: TOLERANCES: LINEAR: ANGULAR:	FINISH:		DEBUR AND BREAK SHARP EDGES	DO NOT SCALE DRAWING	REVISION	
	NAME	SIGNATURE	DATE	TITLE: 6" pipe Weldment #1		
DRAWN	Diogo oliveira					
CHK'D	Alexander Hutchison					
APPV'D						
MFG						
Q.A.						
				MATERIAL:	DWG NO. H.A.C.	A3
				WEIGHT:	SCALE:1:20	SHEET 37 OF 45

Parts List	#
6" pipe sch 40 300mm Long	1
6" pipe Flange	1

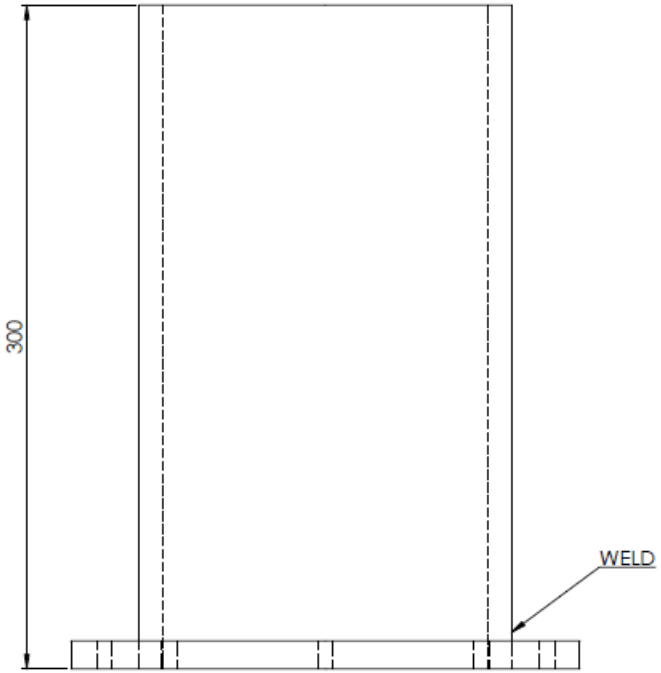

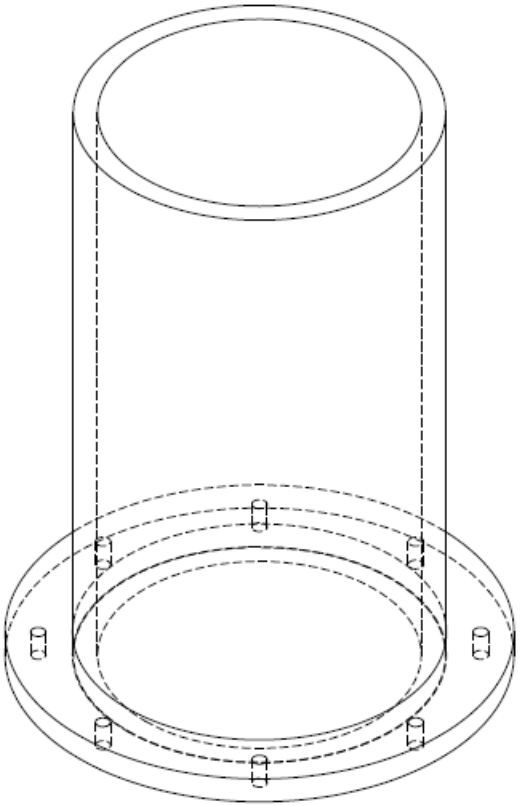

UNLESS OTHERWISE SPECIFIED: DIMENSIONS ARE IN MILLIMETERS SURFACE FINISH: TOLERANCES: LINEAR: ANGULAR:	FINISH:	DEBUR AND BREAK SHARP EDGES	DO NOT SCALE DRAWING	REVISION	
	NAME	SIGNATURE	DATE	TITLE: 6" pipe Weldment #2	
DRAWN	Diogo Oliveira				
CHK'D	Alexander Hutchison				
APPV'D					
MFG					
Q.A					
			MATERIAL:	DWG NO. H.A.C.	A3
			WEIGHT:	SCALE:1:10	SHEET 40 OF 45

Parts List	#
6" pipe sch 40 800mm Long	1
6" pipe Flange	2

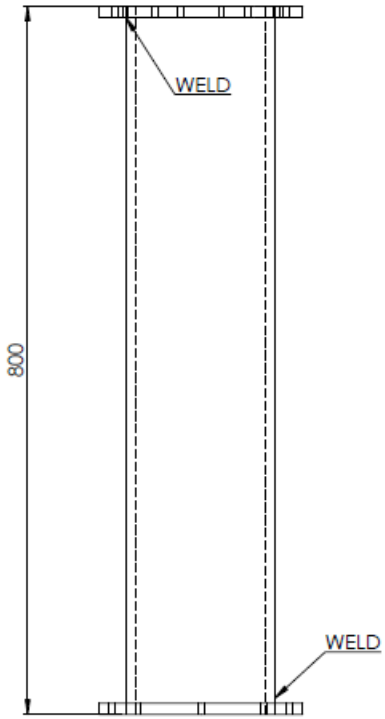

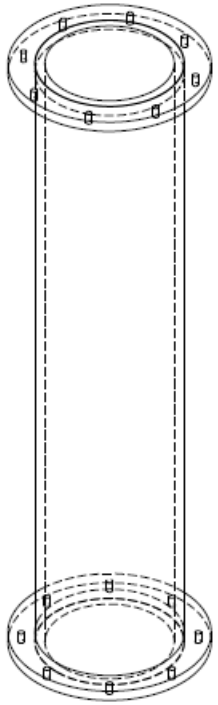

UNLESS OTHERWISE SPECIFIED:
DIMENSIONS ARE IN MILLIMETERS
SURFACE FINISH:
TOLERANCES:
LINEAR:
ANGULAR:

FINISH:

DEBUR AND BREAK SHARP EDGES

DO NOT SCALE DRAWING | REVISION

	NAME	SIGNATURE	DATE
DRAWN	Diogo Oliveira		
CHK'D	Alexander Hutchison		
APPV'D			
MFG			
Q.A			

MATERIAL:

WEIGHT:

TITLE:

6" pipe Weldment #3

DWG NO. H.A.C.

A3

SCALE:1:20

SHEET 38 OF 45

Parts List	#
6" pipe sch 40 1568mm Long	1
6" pipe Flange	2

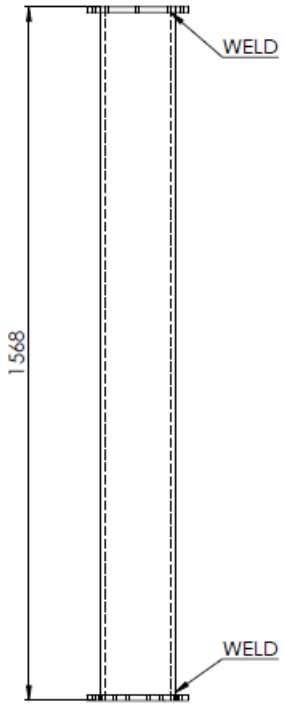

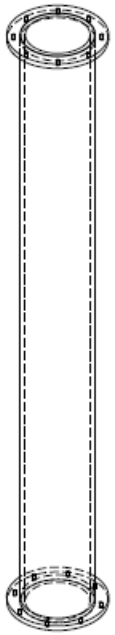

UNLESS OTHERWISE SPECIFIED:
DIMENSIONS ARE IN MILLIMETERS
SURFACE FINISH:
TOLERANCES:
LINEAR:
ANGULAR:

FINISH:

DEBUR AND BREAK SHARP EDGES

DO NOT SCALE DRAWING | REVISION

	NAME	SIGNATURE	DATE
DRAWN	Diogo Oliveira		
CHK'D	Alexander Hutchison		
APPV'D			
MFG			
Q.A.			

MATERIAL:

WEIGHT:

TITLE:

6" pipe Weldment #4

DWG NO. H.A.C.

A3

SCALE:1:20

SHEET 39 OF 45

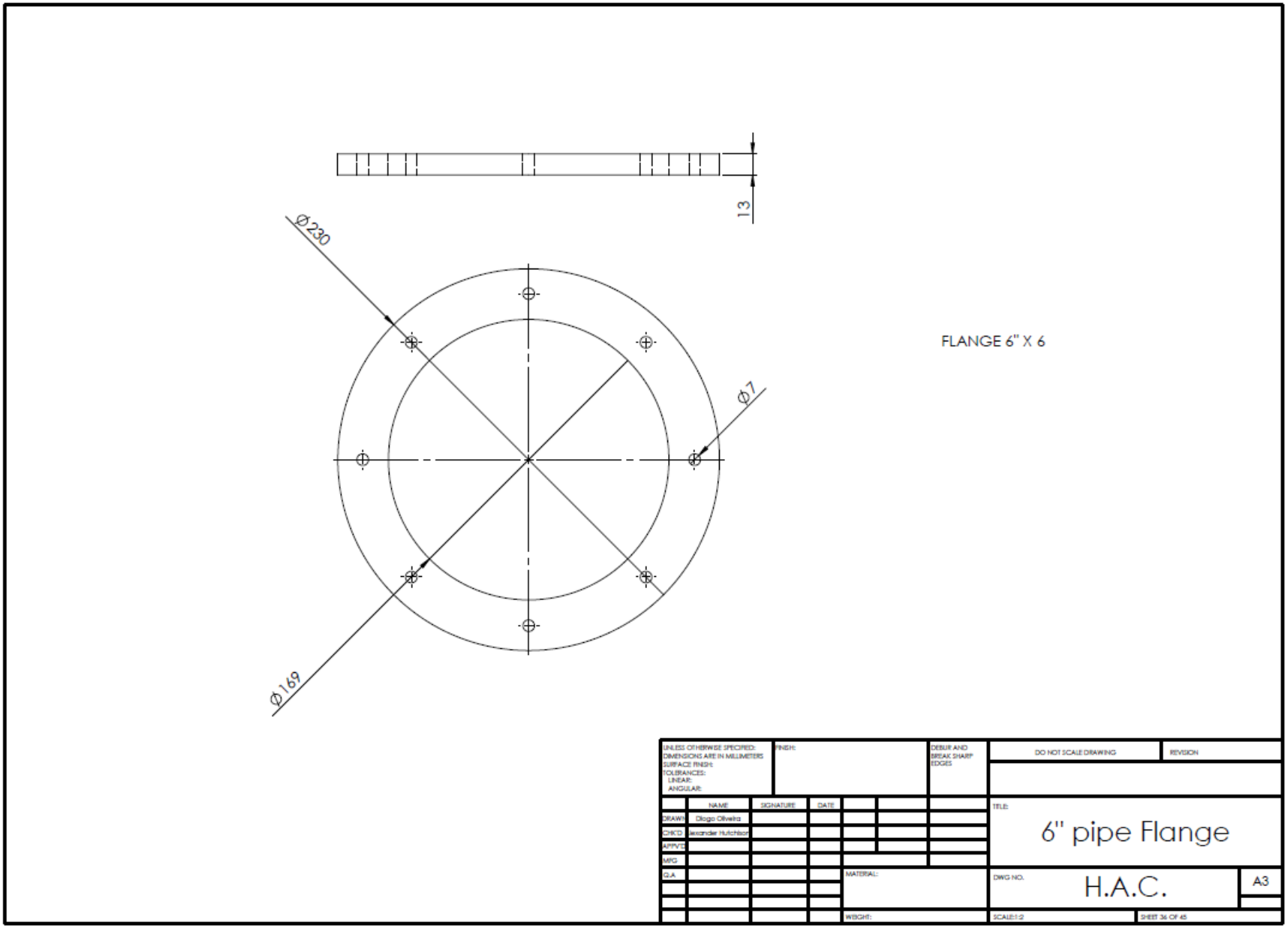
13
Ø230
Ø7
Ø169
FLANGE 6" X 6
UNLESS OTHERWISE SPECIFIED:
DIMENSIONS ARE IN MILLIMETERS
SURFACE FINISH:
TOLERANCES:
LINEAR:
ANGULAR:
FINISH:
DEBUR AND BREAK SHARP EDGES
DO NOT SCALE DRAWING
REVISION
NAME
SIGNATURE
DATE
DRAWN
Diogo Oliveira
CHK'D
Alexander Hutchison
APPV'D
MFG
Q.A.
MATERIAL:
WEIGHT:
TITLE:
6" pipe Flange
DWG NO.
H.A.C.
A3
SCALE:1:2
SHEET 36 OF 45

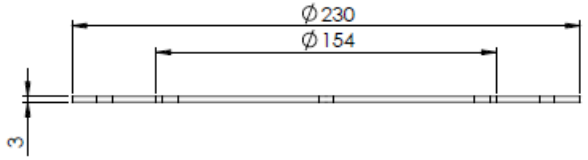

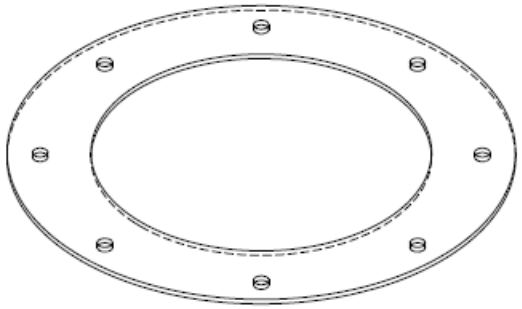

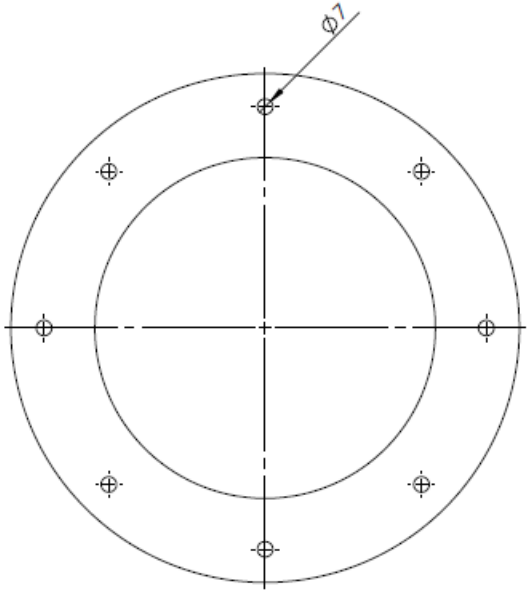

UNLESS OTHERWISE SPECIFIED: DIMENSIONS ARE IN MILLIMETERS SURFACE FINISH: TOLERANCES: LINEAR: ANGULAR:			FINISH:			DEBUR AND BREAK SHARP EDGES	DO NOT SCALE DRAWING
	NAME	SIGNATURE	DATE				TITLE: Gasket 6"
DRAWN	Diogo Oliveira						
CHK'D	Alexander Hutchison						
APPV'D							
MFG							
Q.A.				MATERIAL:			DWG NO. H.A.C.
							A3
				WEIGHT:			SCALE:1:2 SHEET 43 OF 44

Parts List	#
Downcomer Lid Plate	1
Downcomer Box Weldment	1
Toggle Latch	8

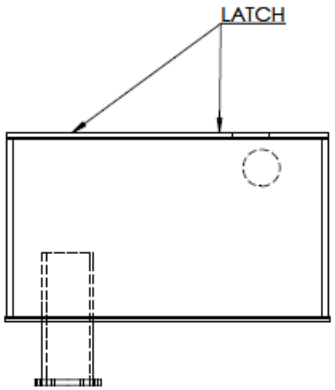

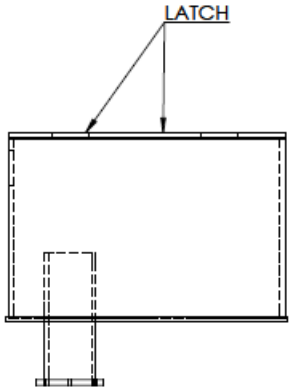

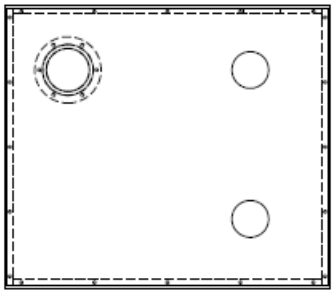

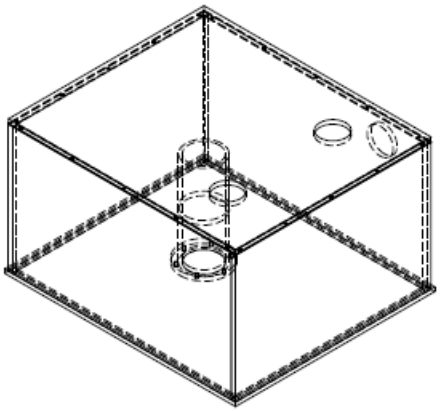

UNLESS OTHERWISE SPECIFIED: DIMENSIONS ARE IN MILLIMETERS SURFACE FINISH: TOLERANCES: LINEAR: ANGULAR:	FINISH:			DEBUR AND BREAK SHARP EDGES	DO NOT SCALE DRAWING	REVISION
	NAME	SIGNATURE	DATE		TITLE: Downcomer Box Assembly	
DRAWN	Diogo Oliveira					
CHK'D	Alexander Hutchison					
APPV'D						
MFG						
Q.A.				MATERIAL:	DWG NO. H.A.C.	A3
				WEIGHT:	SCALE:1:10	SHEET 9 OF 44

Parts List	#
Downcomer Box Bottom Plate	1
4" pipe weldment #2	1
4" pipe weldment #3	1

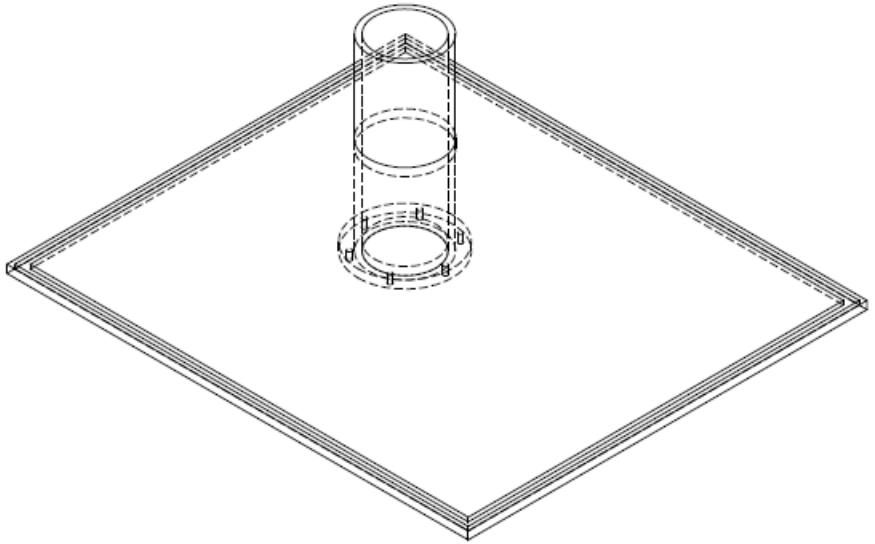

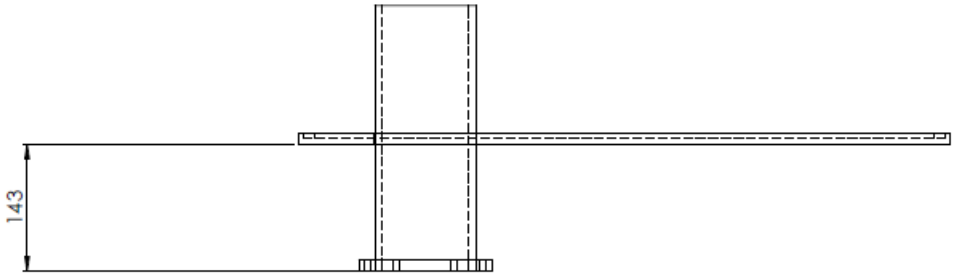

UNLESS OTHERWISE SPECIFIED: DIMENSIONS ARE IN MILLIMETERS SURFACE FINISH: TOLERANCES: LINEAR: ANGULAR:	FINISH:		DEBUR AND BREAK SHARP EDGES	DO NOT SCALE DRAWING	REVISION	
	NAME	SIGNATURE	DATE	TITLE: Downcomer Box Botton Weldment		
DRAWN	Diogo Oliveira					
CHK'D	Alexander Hutchison					
APPV'D						
MFG						
Q.A				MATERIAL:	DWG NO. H.A.C.	A3
				WEIGHT:	SCALE:1:20	SHEET 10 OF 44

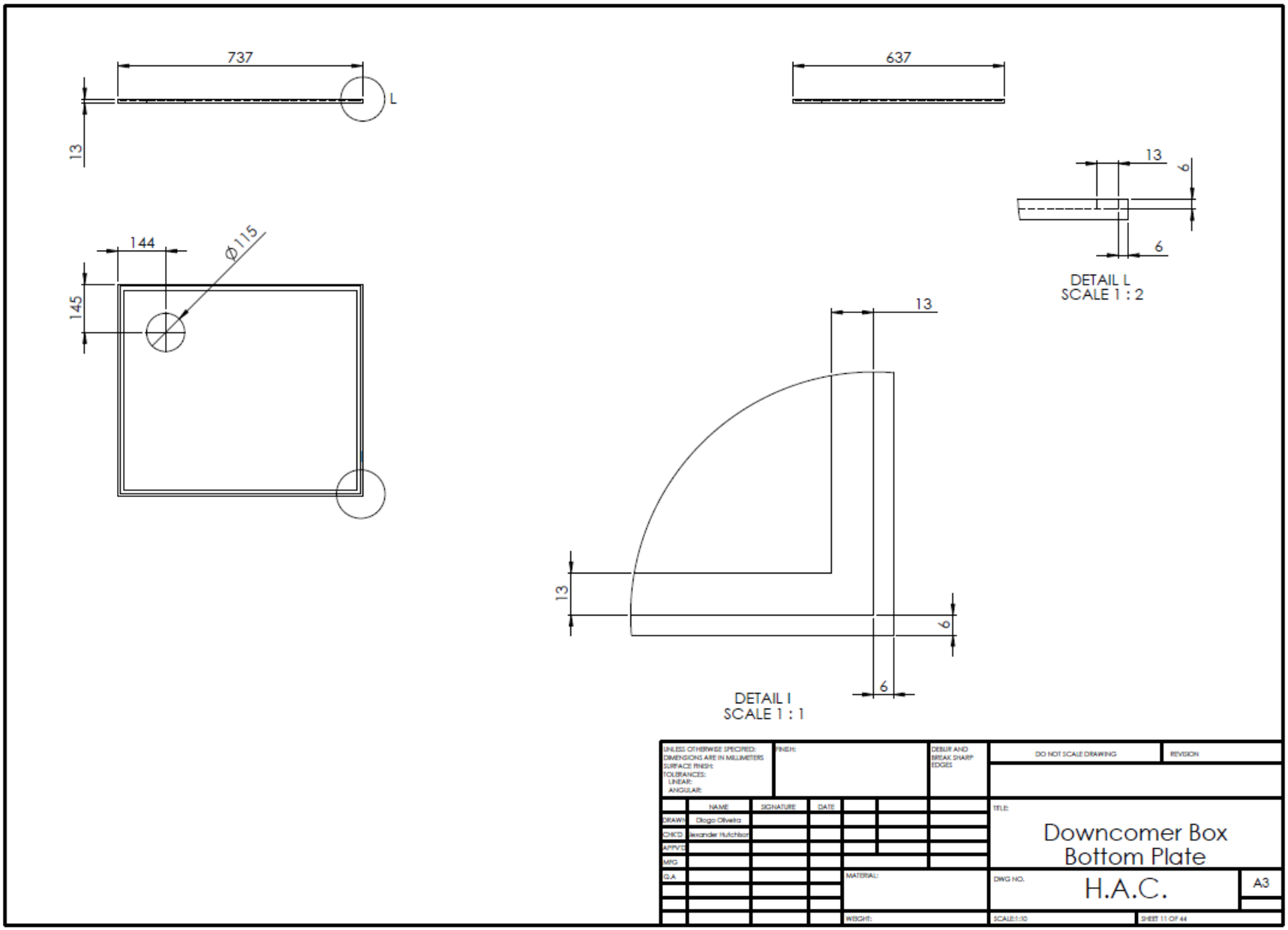
737
L
13
637
13
6
6
DETAIL L
SCALE 1 : 2
144
Ø115
145
13
13
6
6
DETAIL I
SCALE 1 : 1
UNLESS OTHERWISE SPECIFIED:
DIMENSIONS ARE IN MILLIMETERS
SURFACE FINISH:
TOLERANCES:
LINEAR:
ANGULAR:
FINISH:
DEBUR AND BREAK SHARP EDGES
DO NOT SCALE DRAWING
REVISION
NAME
SIGNATURE
DATE
DRAWN
Diogo Oliveira
CHKD
Alexander Hutchison
APPVD
MFG
Q.A.
MATERIAL:
WEIGHT:
TITLE:
Downcomer Box Bottom Plate
DWG NO.
H.A.C.
A3
SCALE:1:10
SHEET 11 OF 44

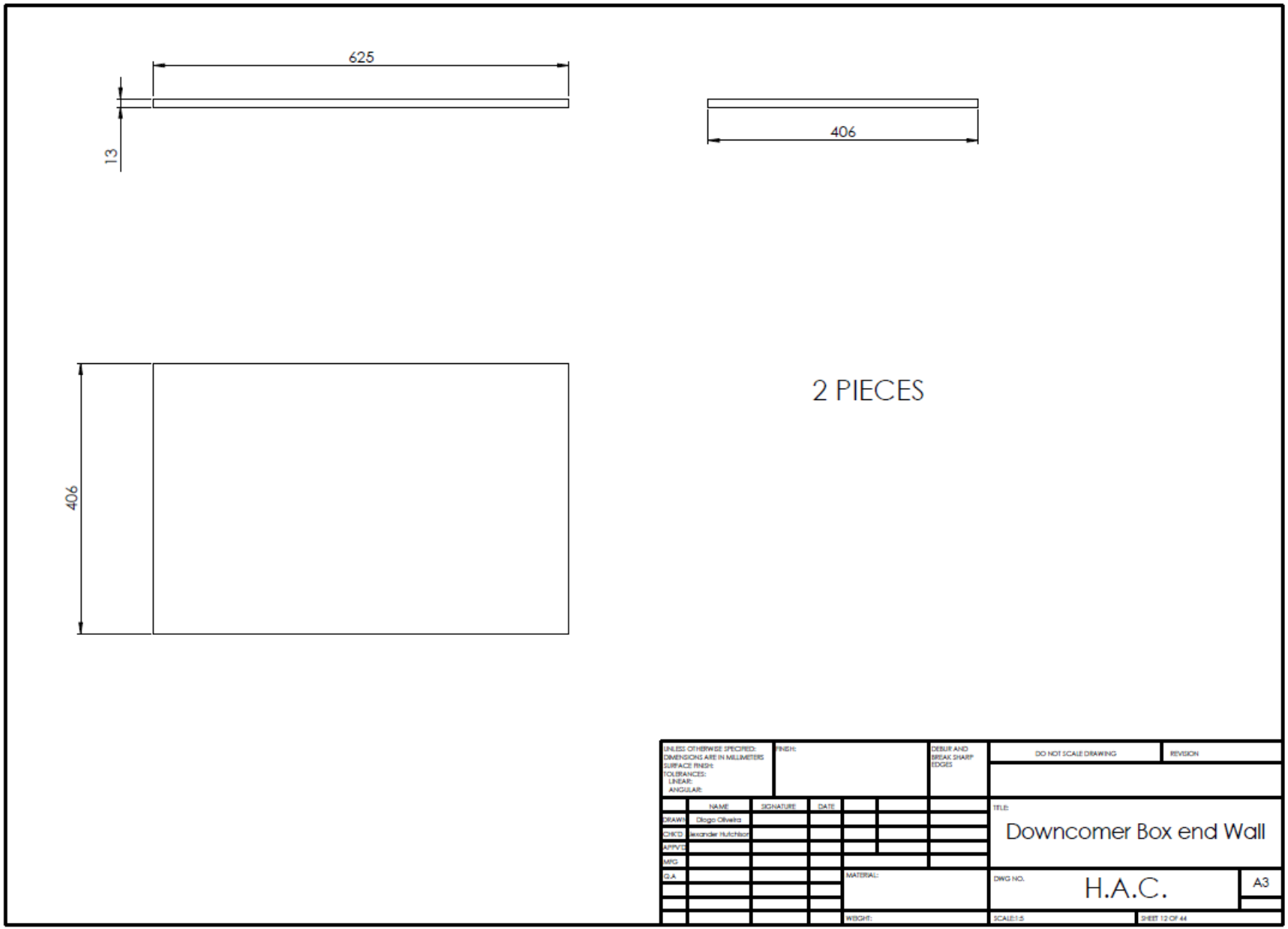
625
13
406
406
2 PIECES
UNLESS OTHERWISE SPECIFIED:
DIMENSIONS ARE IN MILLIMETERS
SURFACE FINISH:
TOLERANCES:
LINEAR:
ANGULAR:
FINISH:
DEBUR AND BREAK SHARP EDGES
DO NOT SCALE DRAWING
REVISION
NAME
SIGNATURE
DATE
DRAWN
Diogo Oliveira
CHK'D
Alexander Hutchison
APPV'D
MFG
Q.A
MATERIAL:
WEIGHT:
TITLE:
Downcomer Box end Wall
DWG NO.
H.A.C.
A3
SCALE:1:5
SHEET 12 OF 44

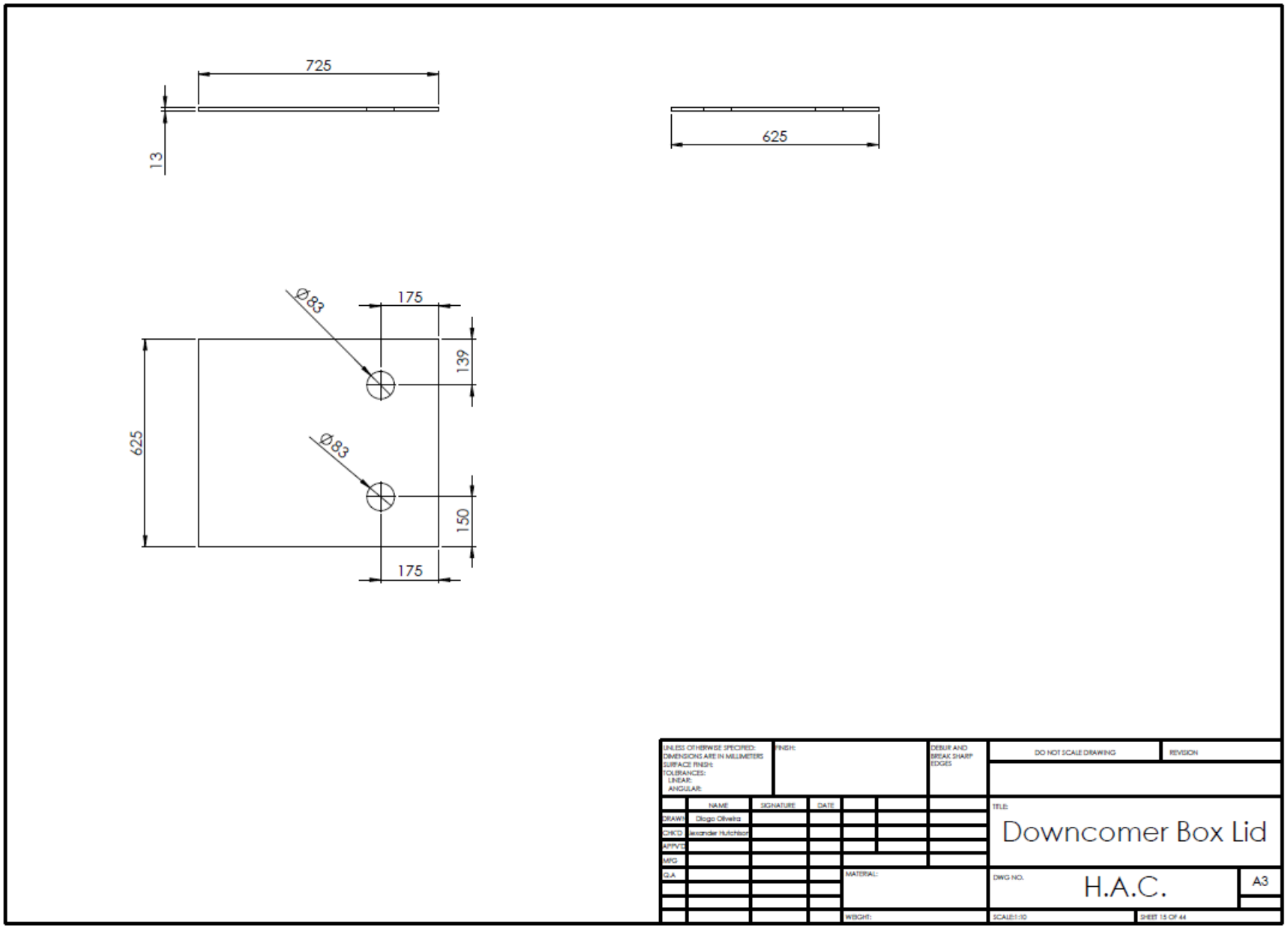
725
13
625
Ø83
175
139
625
Ø83
150
175
UNLESS OTHERWISE SPECIFIED:
DIMENSIONS ARE IN MILLIMETERS
SURFACE FINISH:
TOLERANCES:
LINEAR:
ANGULAR:
FINISH:
DEBUR AND BREAK SHARP EDGES
DO NOT SCALE DRAWING
REVISION
NAME
SIGNATURE
DATE
DRAWN
Diogo Oliveira
CHKD
Alexander Hutchison
APPVD
MFG
Q.A.
MATERIAL:
WEIGHT:
TITLE:
Downcomer Box Lid
DWG NO.
H.A.C.
A3
SCALE:1:10
SHEET 15 OF 44

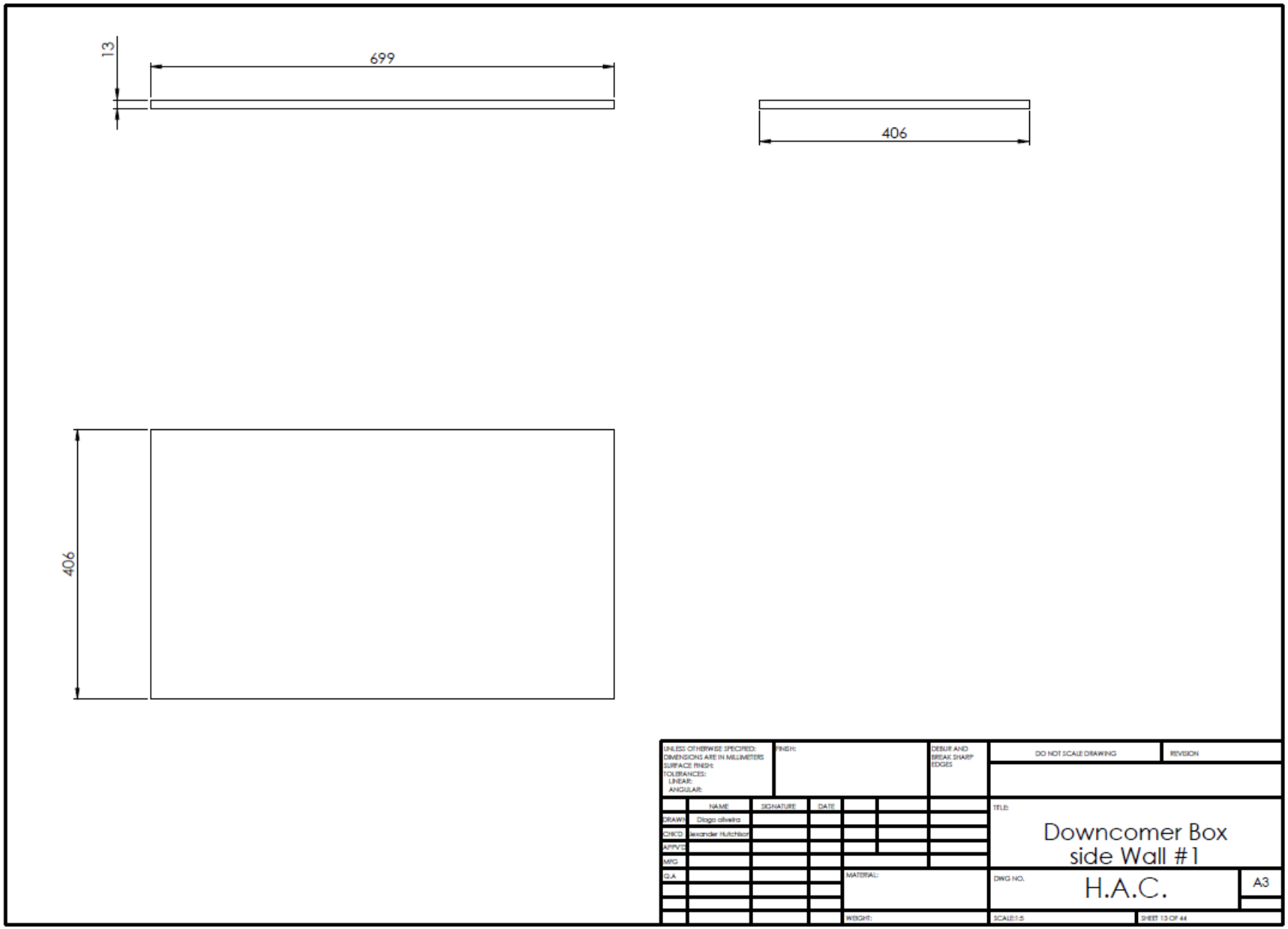
13
699
406
406
UNLESS OTHERWISE SPECIFIED:
DIMENSIONS ARE IN MILLIMETERS
SURFACE FINISH:
TOLERANCES:
LINEAR:
ANGULAR:
FINISH:
DEBUR AND BREAK SHARP EDGES
DO NOT SCALE DRAWING
REVISION
NAME
SIGNATURE
DATE
DRAWN
Diogo oliveira
CHK'D
Alexander Hutchison
APPV'D
MFG
Q.A
MATERIAL:
WEIGHT:
TITLE:
Downcomer Box
side Wall #1
DWG NO.
H.A.C.
A3
SCALE:1:5
SHEET 13 OF 44

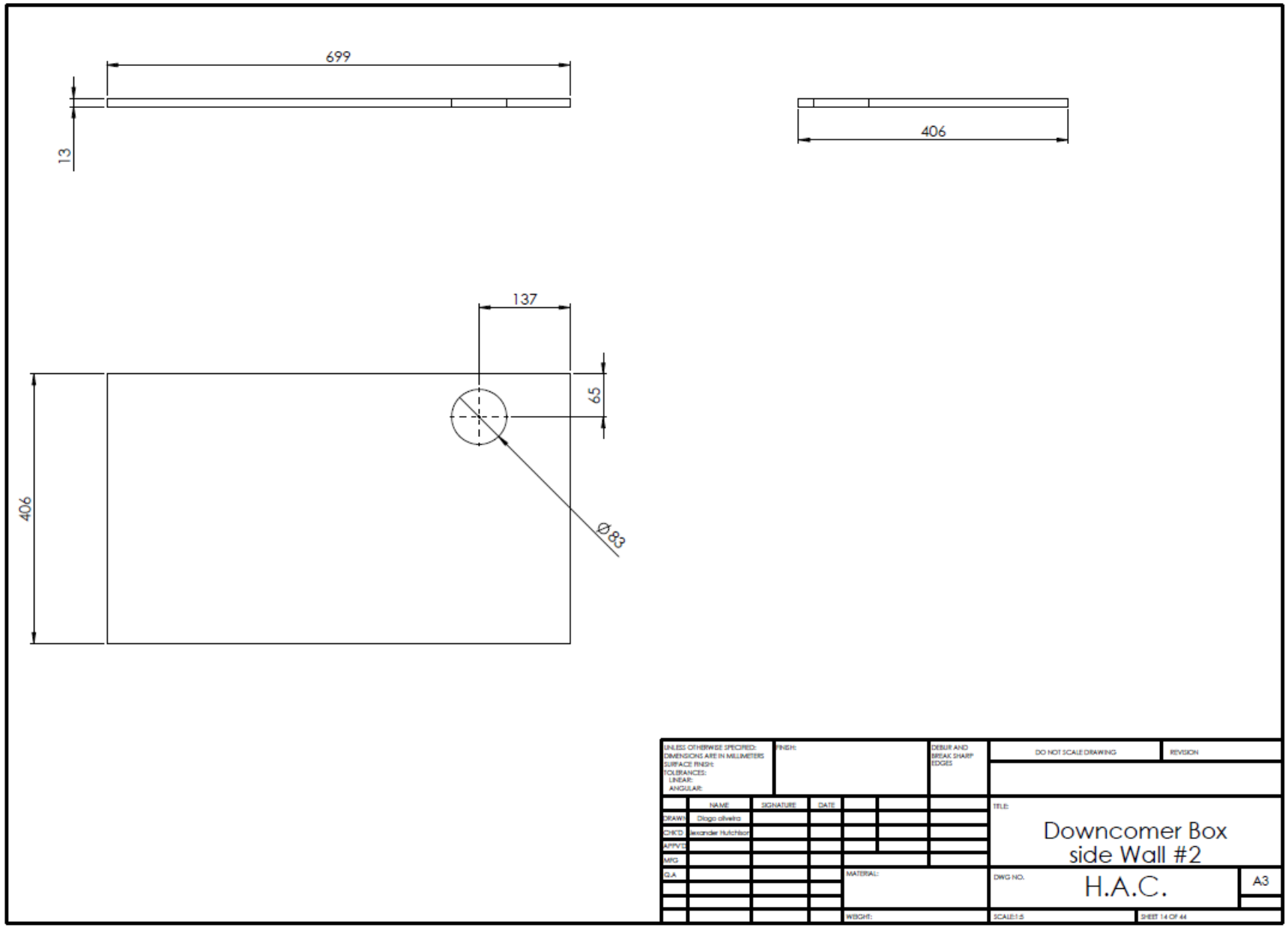
699
13
406
137
65
406
Ø83
UNLESS OTHERWISE SPECIFIED:
DIMENSIONS ARE IN MILLIMETERS
SURFACE FINISH:
TOLERANCES:
LINEAR:
ANGULAR:
FINISH:
DEBUR AND BREAK SHARP EDGES
DO NOT SCALE DRAWING
REVISION
NAME
SIGNATURE
DATE
DRAWN
Diogo oliveira
CHK'D
Alexander Hutchison
APPV'D
MFG
Q.A
MATERIAL:
WEIGHT:
TITLE:
Downcomer Box
side Wall #2
DWG NO.
H.A.C.
A3
SCALE:1:5
SHEET 14 OF 44

Parts List	#
Riser Box end Wall	2
Riser Box side Wall #1	1
Riser Box side Wall #2	1
Riser Bottom Weldment	1

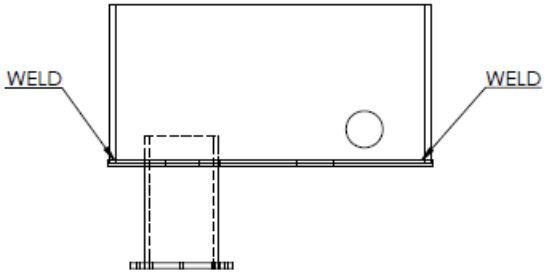

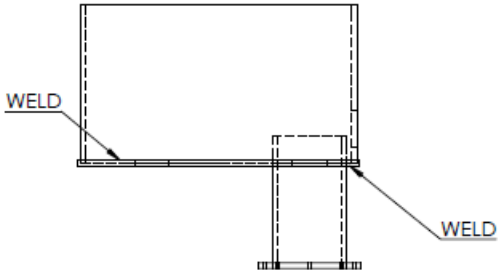

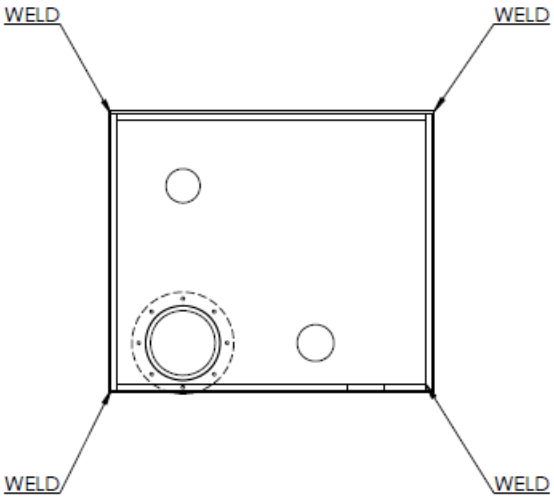

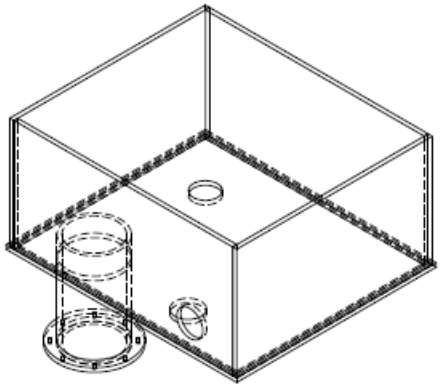

UNLESS OTHERWISE SPECIFIED: DIMENSIONS ARE IN MILLIMETERS SURFACE FINISH: TOLERANCES: LINEAR: ANGULAR:	FINISH:				DEBUR AND BREAK SHARP EDGES	DO NOT SCALE DRAWING
	NAME	SIGNATURE	DATE			TITLE: Riser Box Weldment
DRAWN	Diogo Oliveira					
CHK'D	Alexander Hutchison					
APPV'D						
MFG						
Q.A				MATERIAL:		DWG NO. H.A.C. A3
				WEIGHT:		SCALE:1:10 SHEET 16 OF 45

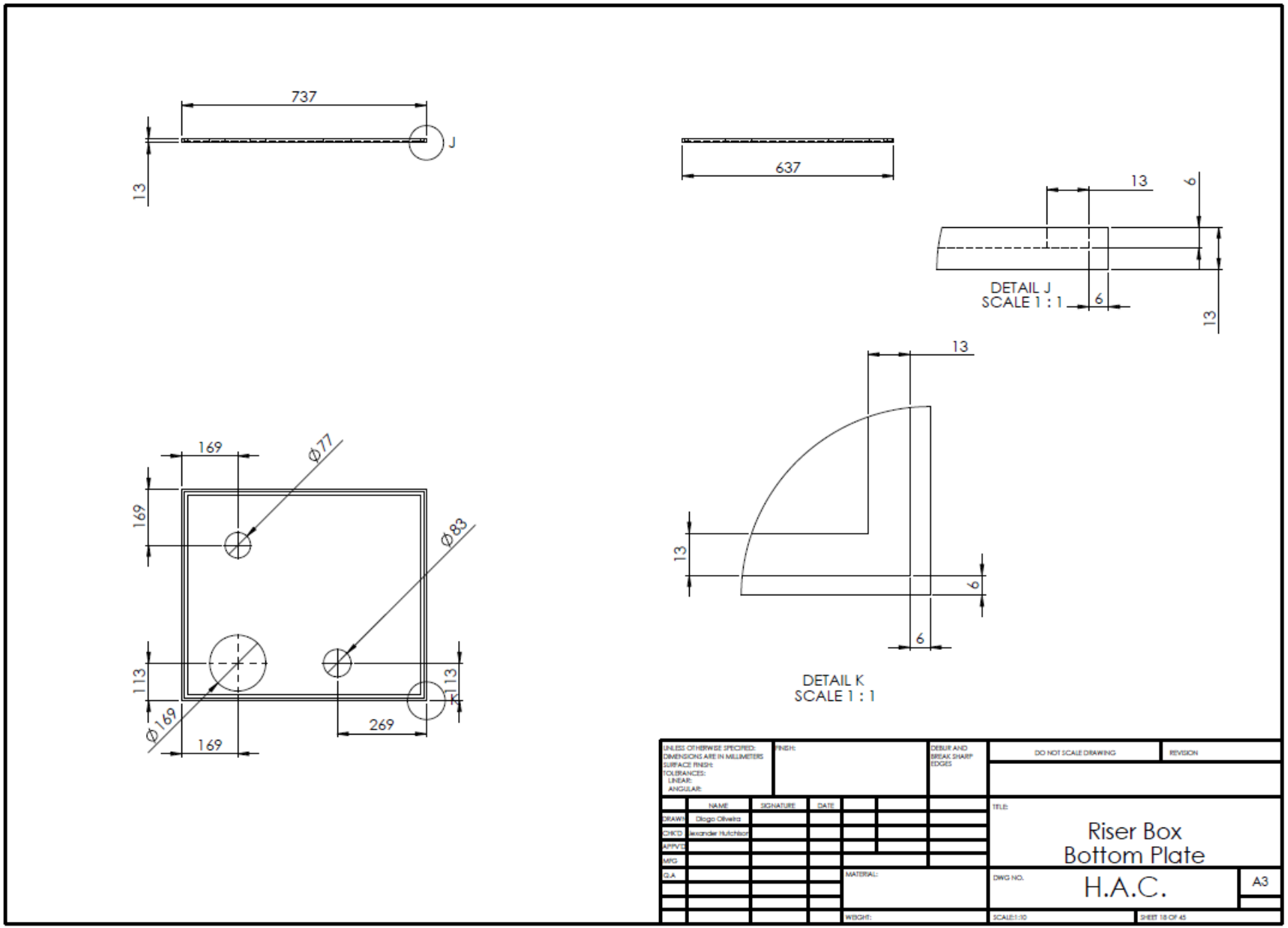
737
J
13
637
13
6
DETAIL J
SCALE 1 : 1
6
13
169
Ø77
169
Ø83
113
113
Ø169
169
269
13
13
6
6
DETAIL K
SCALE 1 : 1
UNLESS OTHERWISE SPECIFIED:
DIMENSIONS ARE IN MILLIMETERS
SURFACE FINISH:
TOLERANCES:
LINEAR:
ANGULAR:
FINISH:
DEBUR AND BREAK SHARP EDGES
DO NOT SCALE DRAWING
REVISION
NAME
SIGNATURE
DATE
DRAWN
Diogo Oliveira
CHK'D
Alexander Hutchison
APPV'D
MFG
Q.A.
MATERIAL:
WEIGHT:
TITLE:
Riser Box
Bottom Plate
DWG NO.
H.A.C.
A3
SCALE:1:10
SHEET 18 OF 45

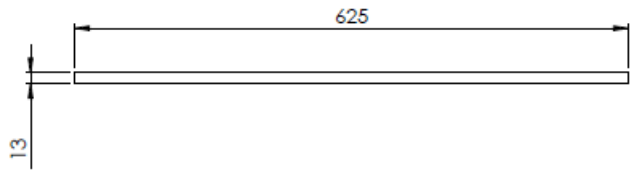

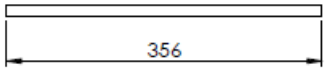

2 PIECES

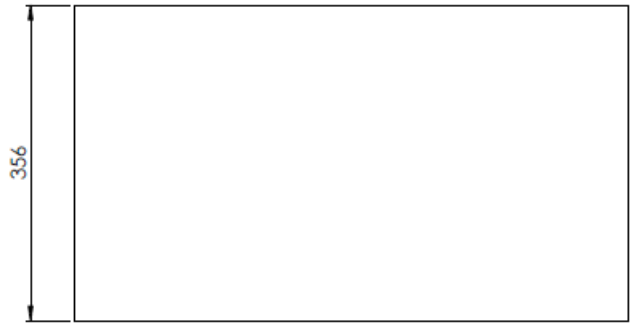

UNLESS OTHERWISE SPECIFIED: DIMENSIONS ARE IN MILLIMETERS SURFACE FINISH: TOLERANCES: LINEAR: ANGULAR:		FINISH:		DEBUR AND BREAK SHARP EDGES		DO NOT SCALE DRAWING	REVISION
	NAME	SIGNATURE	DATE			TITLE: Riser Box end Wall	
DRAWN	Diogo Oliveira						
CHK'D	Alexander Hutchison						
APPV'D							
MFG							
Q.A				MATERIAL:		DWG NO. H.A.C.	A3
				WEIGHT:		SCALE:1:5	SHEET 19 OF 45

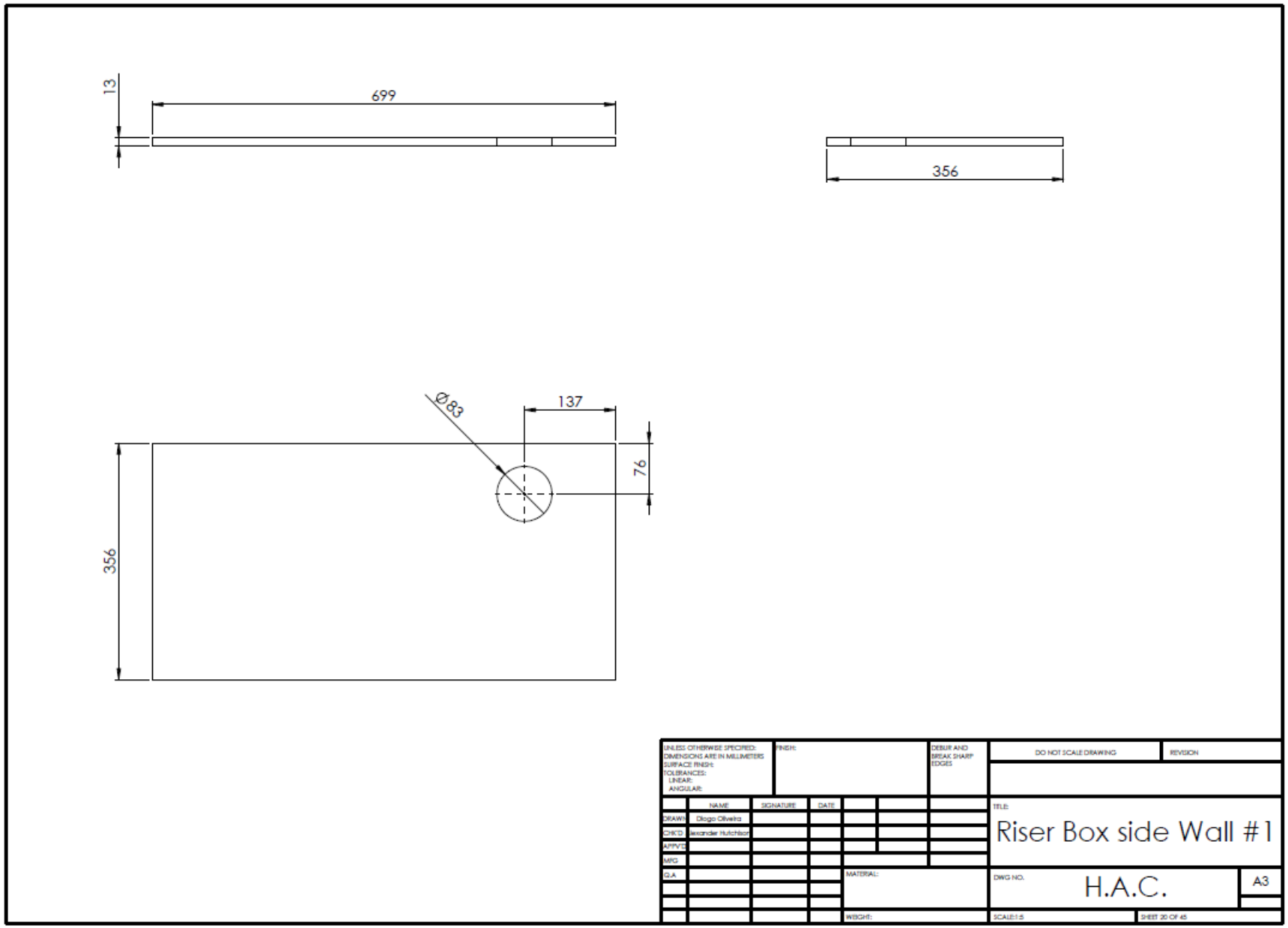
13
699
356
Ø83
137
76
356
UNLESS OTHERWISE SPECIFIED:
DIMENSIONS ARE IN MILLIMETERS
SURFACE FINISH:
TOLERANCES:
LINEAR:
ANGULAR:
FINISH:
DEBUR AND BREAK SHARP EDGES
DO NOT SCALE DRAWING
REVISION
NAME
SIGNATURE
DATE
DRAWN
Diogo Oliveira
CHK'D
Alexander Hutchison
APPV'D
MFG
Q.A
MATERIAL:
WEIGHT:
TITLE:
Riser Box side Wall #1
DWG NO.
H.A.C.
A3
SCALE:1:5
SHEET 20 OF 45

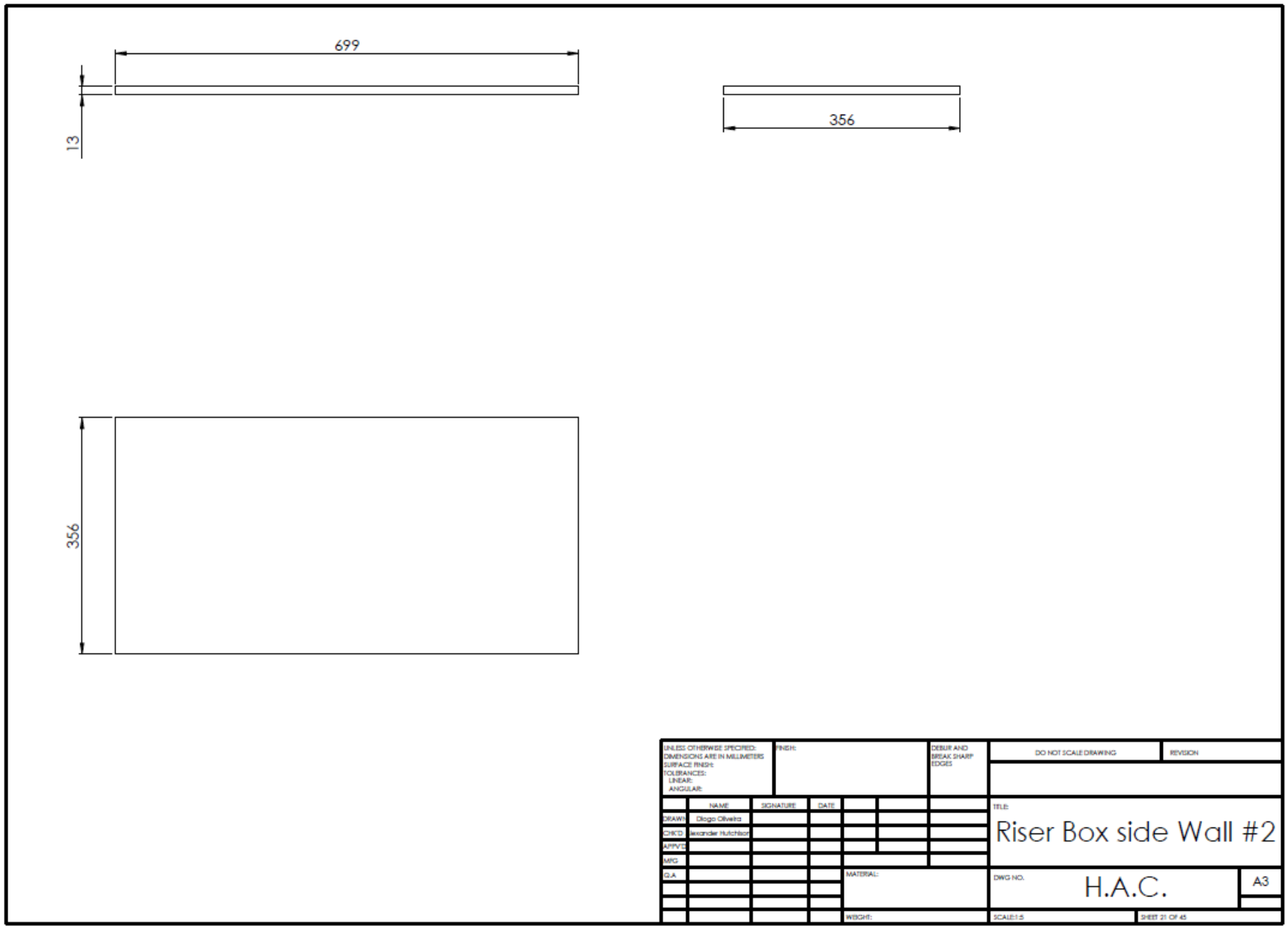
699
13
356
356
UNLESS OTHERWISE SPECIFIED:
DIMENSIONS ARE IN MILLIMETERS
SURFACE FINISH:
TOLERANCES:
LINEAR:
ANGULAR:
FINISH:
DEBUR AND BREAK SHARP EDGES
DO NOT SCALE DRAWING
REVISION
NAME
SIGNATURE
DATE
DRAWN
Diogo Oliveira
CHKD
Alexander Hutchison
APPVD
MFG
Q.A.
MATERIAL:
WEIGHT:
TITLE:
Riser Box side Wall #2
DWG NO.
H.A.C.
A3
SCALE:1:5
SHEET 21 OF 45

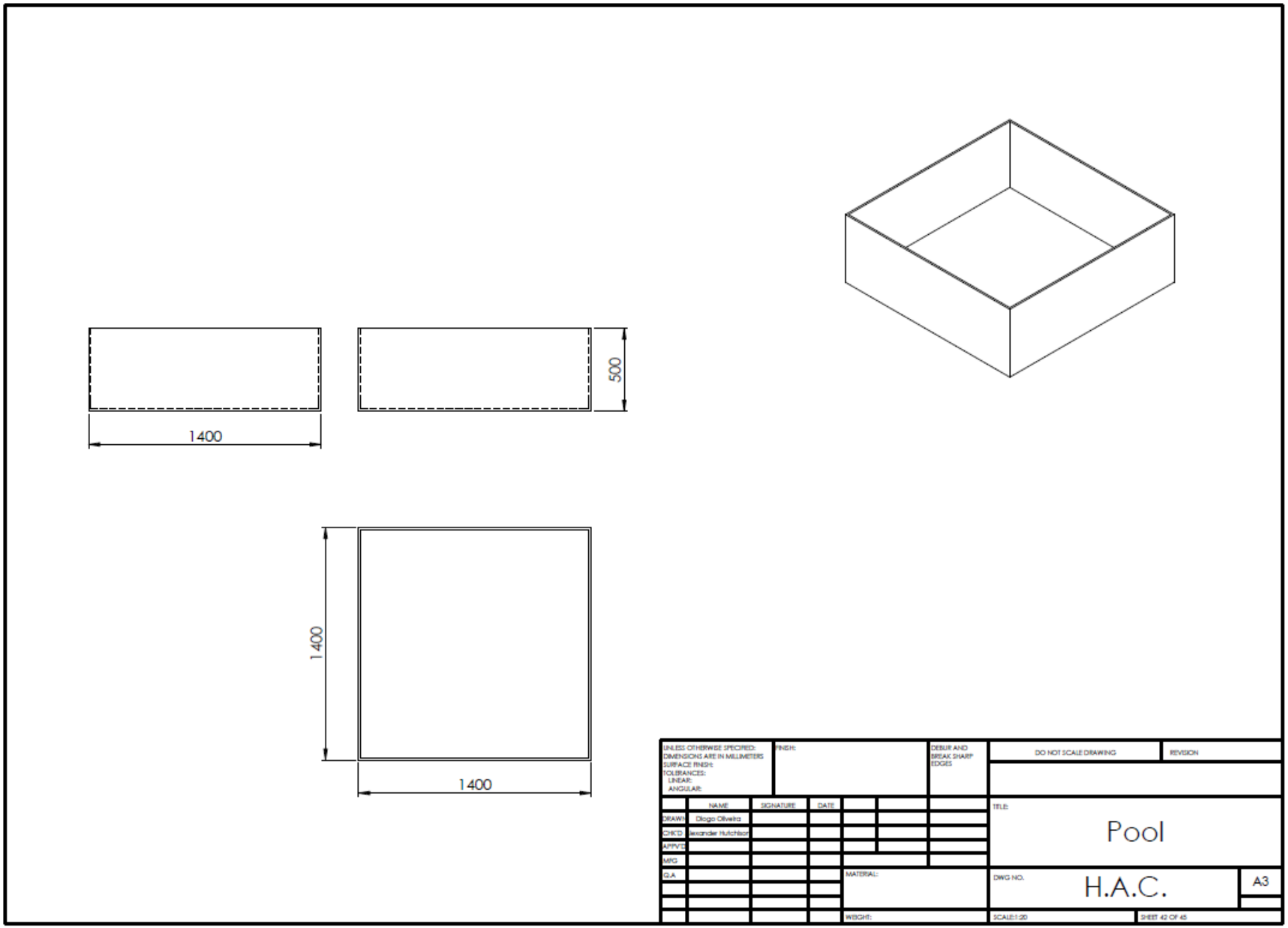

UNLESS OTHERWISE SPECIFIED: DIMENSIONS ARE IN MILLIMETERS SURFACE FINISH: TOLERANCES: LINEAR: ANGULAR:	FINISH:		DEBUR AND BREAK SHARP EDGES		DO NOT SCALE DRAWING	REVISION
	NAME	SIGNATURE	DATE			
DRAWN	Diogo Oliveira				TITLE: Pool	
CHK'D	Alexander Hutchison					
APPV'D						
MFG						
Q.A				MATERIAL:	DWG NO. H.A.C.	A3
				WEIGHT:	SCALE:1:20	SHEET 42 OF 45

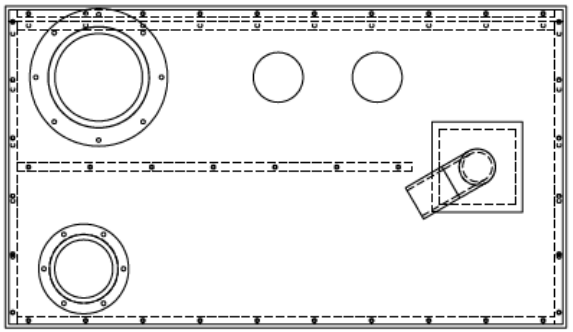

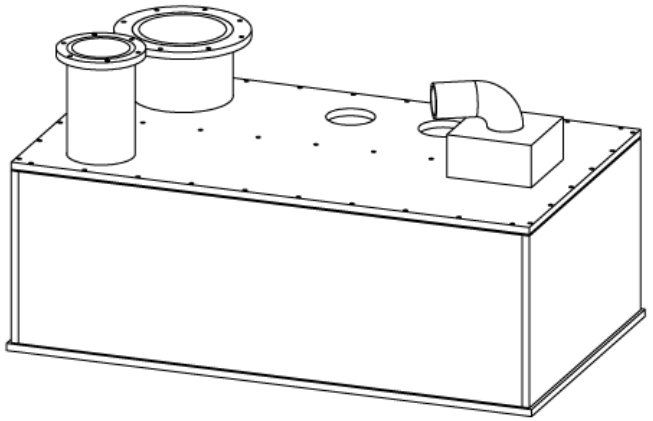

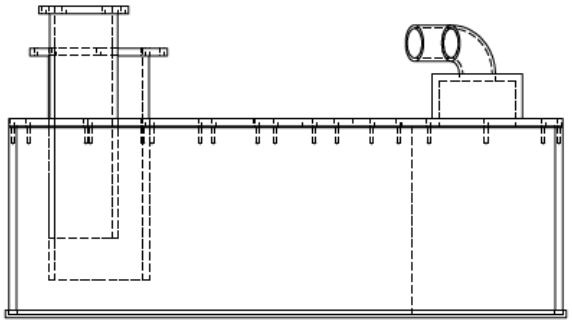

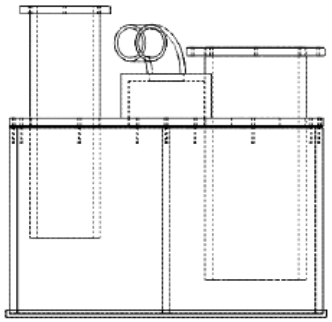

ITEM NO.	DESCRIPTION	QTY.
1	separator box weldment	1
2	separator box gasket	1
3	separator lid weldment	1

		NAME	DATE
UNLESS OTHERWISE SPECIFIED:			
DIMENSIONS ARE IN MILLIMETRES TOLERANCES: ±1MM	DRAWN		
	CHECKED		
	ENG APPR.		
	MFG APPR.		
INTERPRET GEOMETRIC TOLERANCING PER:	Q.A.		
MATERIAL	COMMENTS:		
FINISH			
DO NOT SCALE DRAWING			

TITLE:

Separator tank assembly

SIZE	DWG. NO.	REV
A		

SCALE: 1:10	WEIGHT:	SHEET 1 OF 1

ITEM NO.	DESCRIPTION	QTY.
1	small box	1
2	2in pipe sch 40 70mm long	1
3	2in standard elbow	1

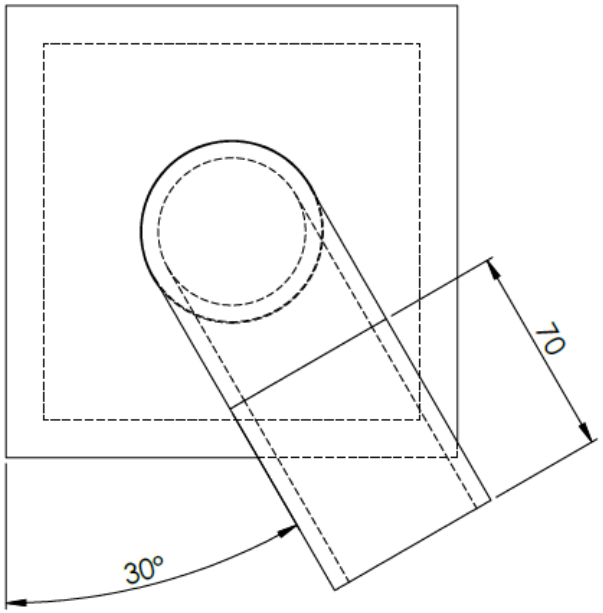

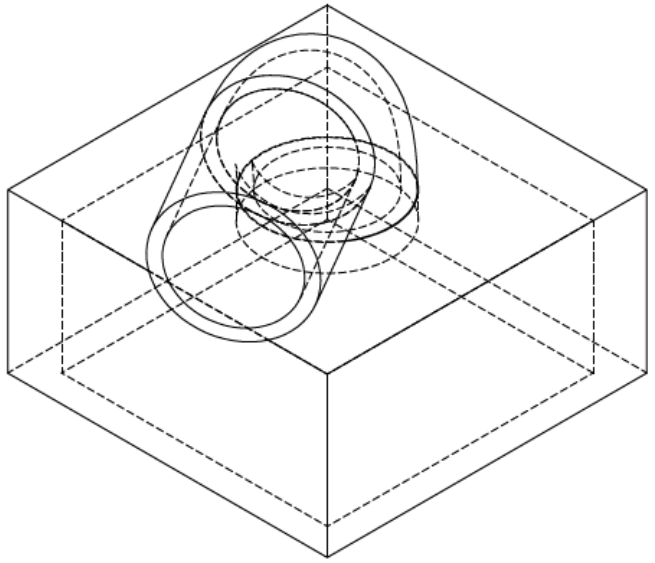

UNLESS OTHERWISE SPECIFIED:		NAME	DATE
DIMENSIONS ARE IN MILLIMETRES TOLERANCES: ±1MM	DRAWN		
	CHECKED		
	ENG APPR.		
	MFG APPR.		
INTERPRET GEOMETRIC TOLERANCING PER:	Q.A.		
MATERIAL	COMMENTS:		
FINISH			
DO NOT SCALE DRAWING			

TITLE: Raised pipe weldment

SIZE	DWG. NO.	REV
A		

SCALE: 1:2	WEIGHT:	SHEET 1 OF 1

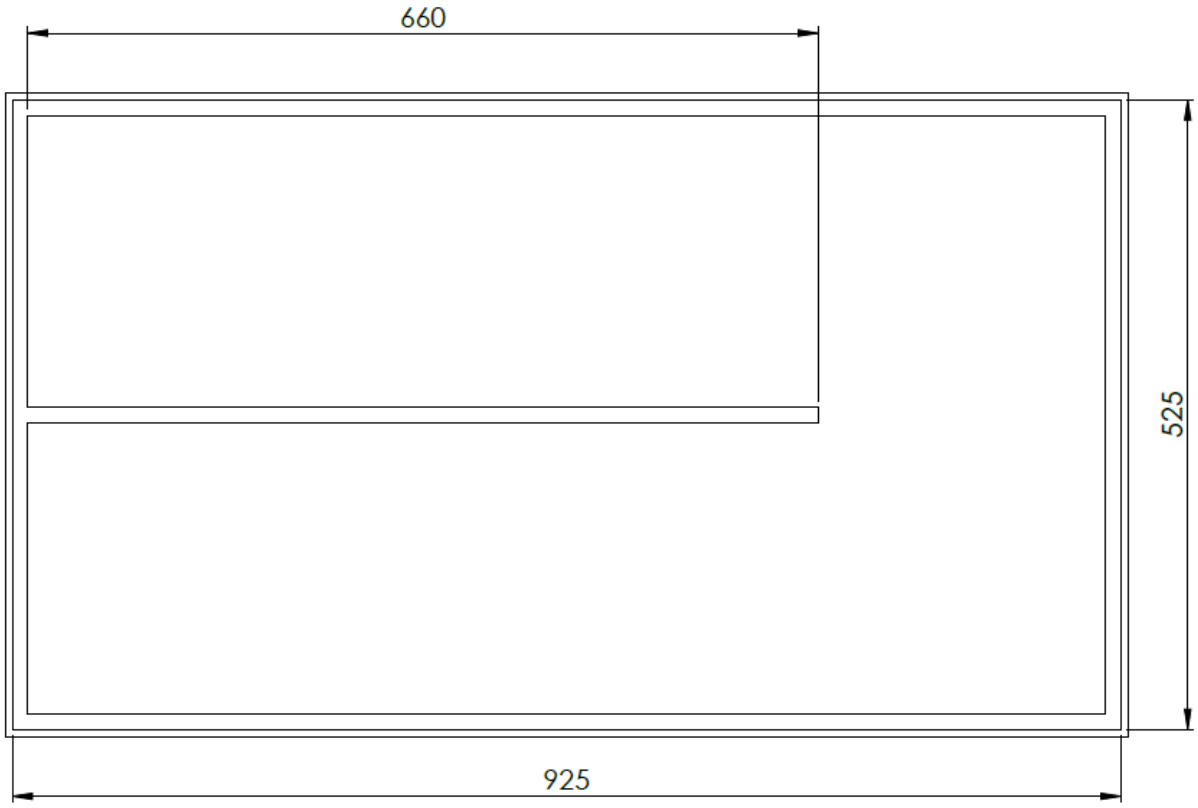

UNLESS OTHERWISE SPECIFIED:		NAME	DATE
DIMENSIONS ARE IN MILLIMETRES TOLERANCES: ±1MM	DRAWN		
	CHECKED		
	ENG APPR.		
	MFG APPR.		
INTERPRET GEOMETRIC TOLERANCING PER:	Q.A.		
MATERIAL 1/2 INCH CLEAR PVC	COMMENTS:		
FINISH			
DO NOT SCALE DRAWING			

TITLE:

Separator bottom plate

SIZE	DWG. NO.	REV
A		

SCALE: 1:5	WEIGHT:	SHEET 1 OF 1

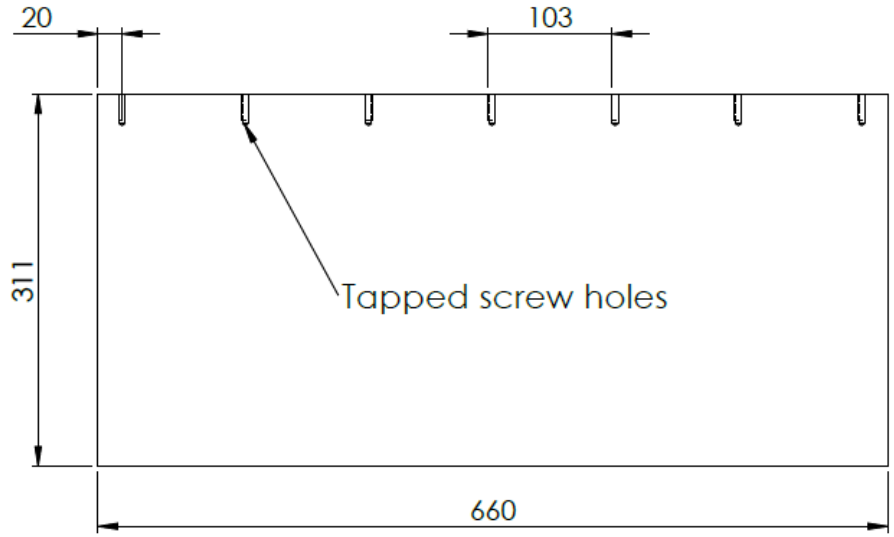

UNLESS OTHERWISE SPECIFIED:		NAME	DATE
DIMENSIONS ARE IN MILLIMETRES TOLERANCES: ±1MM	DRAWN		
	CHECKED		
	ENG APPR.		
	MFG APPR.		
INTERPRET GEOMETRIC TOLERANCING PER:	Q.A.		
MATERIAL 1/2 INCH CLEAR PVC	COMMENTS:		
FINISH			
DO NOT SCALE DRAWING			

TITLE: Separator divider

SIZE	DWG. NO.	REV
A		

SCALE: 1:5 | WEIGHT: | SHEET 1 OF 1

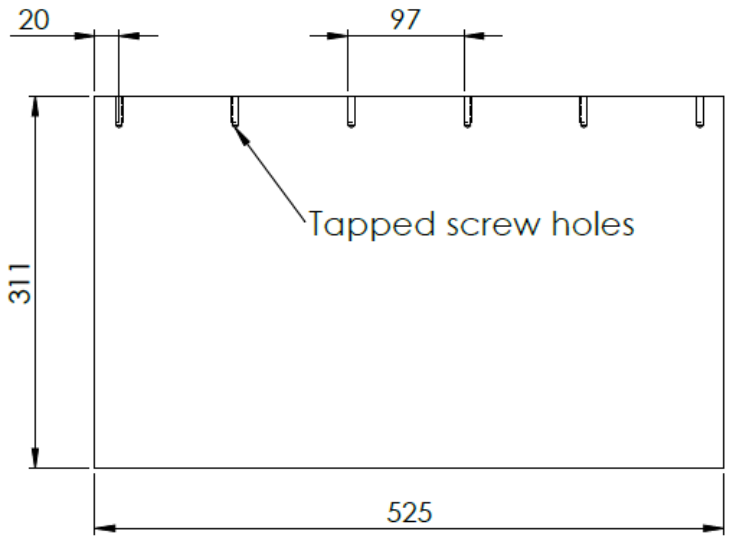

UNLESS OTHERWISE SPECIFIED:		NAME	DATE
DIMENSIONS ARE IN MILLIMETRES TOLERANCES: ±1MM	DRAWN		
	CHECKED		
	ENG APPR.		
	MFG APPR.		
INTERPRET GEOMETRIC TOLERANCING PER:	Q.A.		
MATERIAL 1/2 INCH CLEAR PVC	COMMENTS:		
FINISH			
DO NOT SCALE DRAWING			

TITLE: Separator end plate

SIZE	DWG. NO.	REV
A		

SCALE: 1:5	WEIGHT:	SHEET 1 OF 1

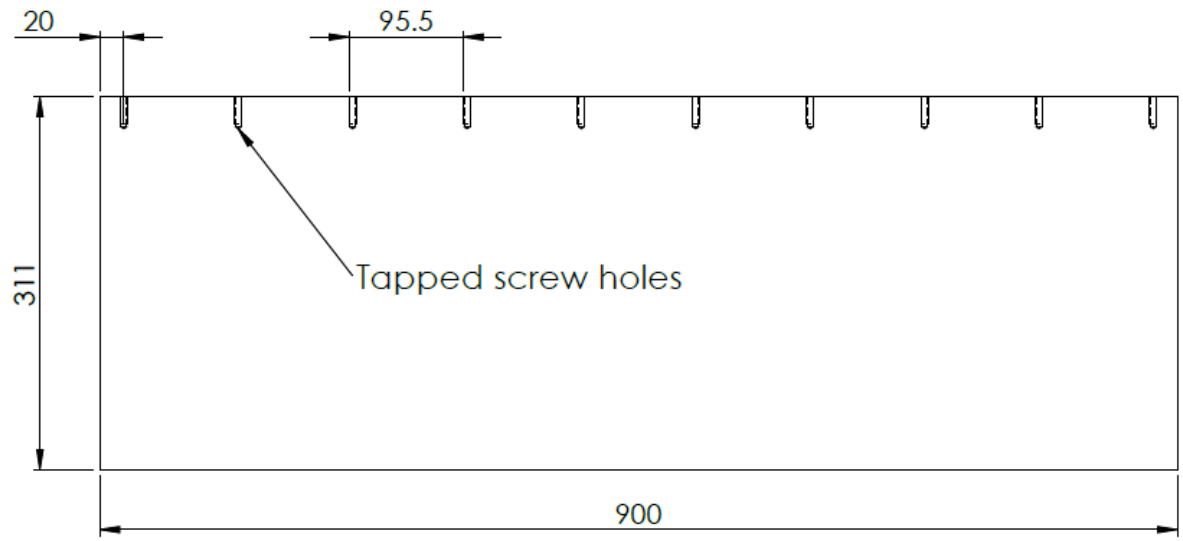

UNLESS OTHERWISE SPECIFIED:		NAME	DATE
DIMENSIONS ARE IN MILLIMETRES TOLERANCES: ±1MM	DRAWN		
	CHECKED		
	ENG APPR.		
	MFG APPR.		
INTERPRET GEOMETRIC TOLERANCING PER:	Q.A.		
MATERIAL 1/2 INCH CLEAR PVC	COMMENTS:		
FINISH			
DO NOT SCALE DRAWING			

TITLE: Separator side plate

SIZE	DWG. NO.	REV
A		

SCALE: 1:5 | WEIGHT: | SHEET 1 OF 1

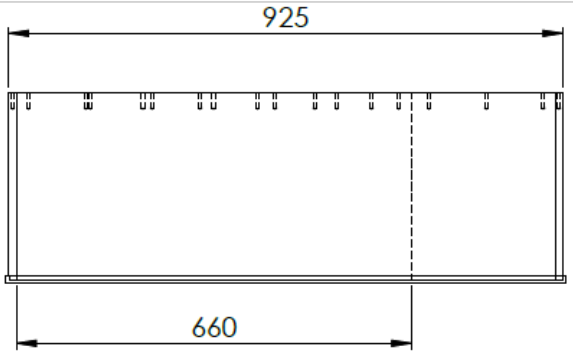

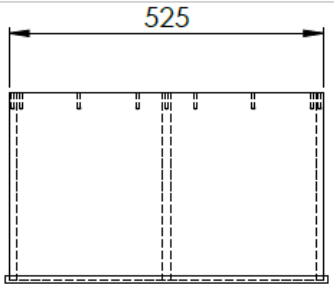

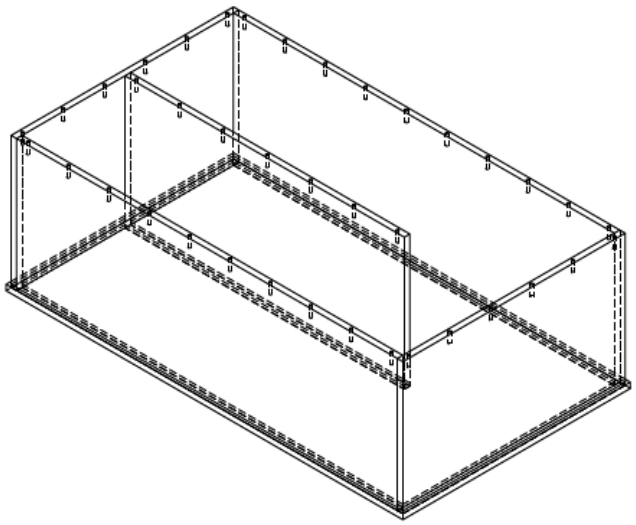

ITEM NO.	DESCRIPTION	QTY.
1	separator bottom plate	1
2	separator box divider	1
3	separator box end wall	2
4	separator box side wall	2

		NAME	DATE
UNLESS OTHERWISE SPECIFIED:			
DIMENSIONS ARE IN MILLIMETRES TOLERANCES: ±1MM	DRAWN		
	CHECKED		
	ENG APPR.		
	MFG APPR.		
INTERPRET GEOMETRIC TOLERANCING PER:	Q.A.		
MATERIAL	COMMENTS:		
FINISH			
DO NOT SCALE DRAWING			

TITLE: Separator box weldment

SIZE	DWG. NO.	REV
A		

SCALE: 1:10	WEIGHT:	SHEET 1 OF 1

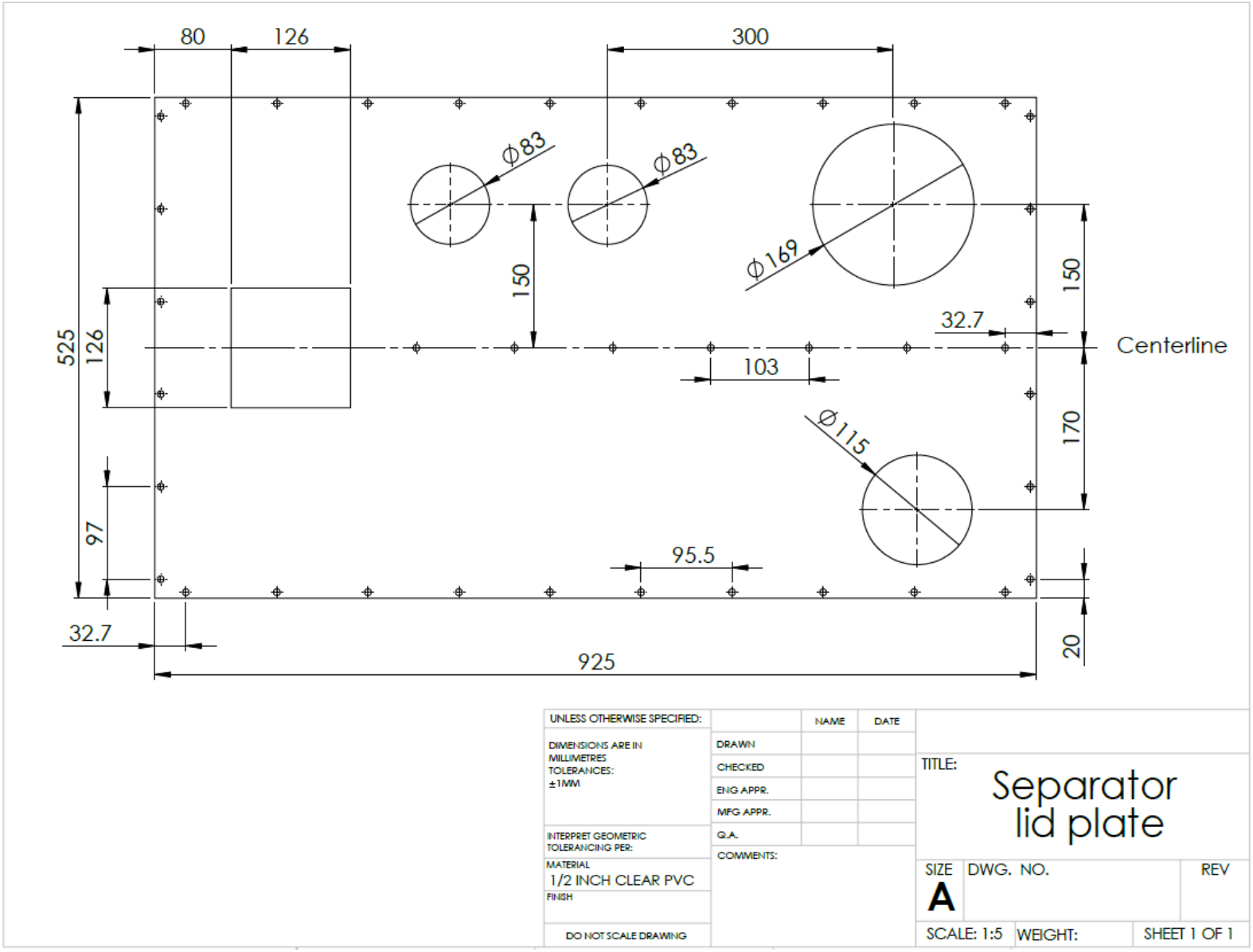
80
126
300
Ø83
Ø83
Ø169
150
150
32.7
Centerline
525
126
103
Ø115
170
97
95.5
32.7
925
20
UNLESS OTHERWISE SPECIFIED:
DIMENSIONS ARE IN MILLIMETRES
TOLERANCES: ±1MM
INTERPRET GEOMETRIC TOLERANCING PER:
MATERIAL
1/2 INCH CLEAR PVC
FINISH
DO NOT SCALE DRAWING
NAME
DATE
DRAWN
CHECKED
ENG APPR.
MFG APPR.
Q.A.
COMMENTS:
TITLE:
Separator lid plate
SIZE
A
DWG. NO.
REV
SCALE: 1:5
WEIGHT:
SHEET 1 OF 1

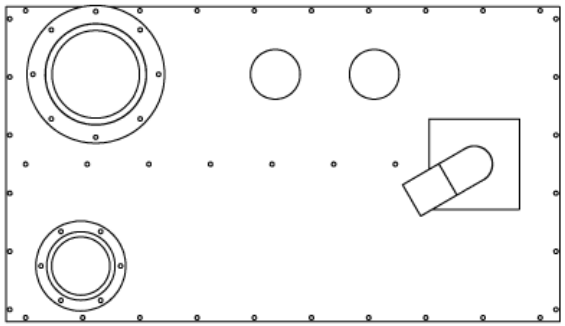

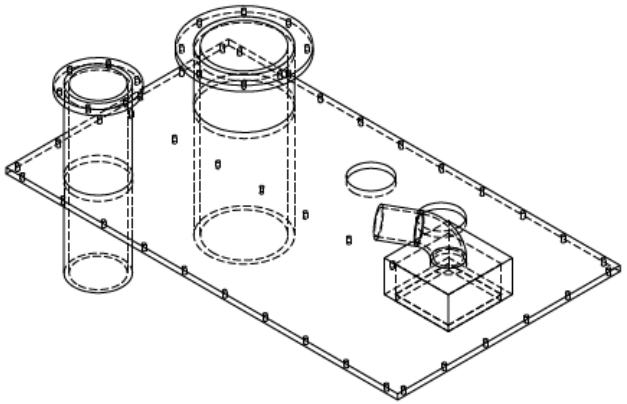

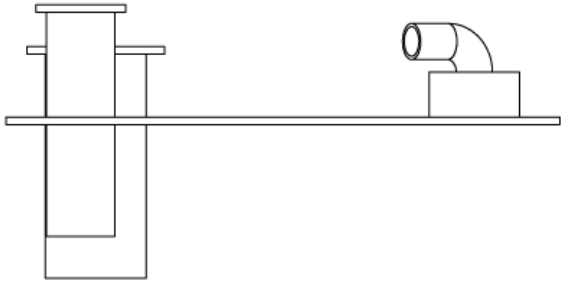

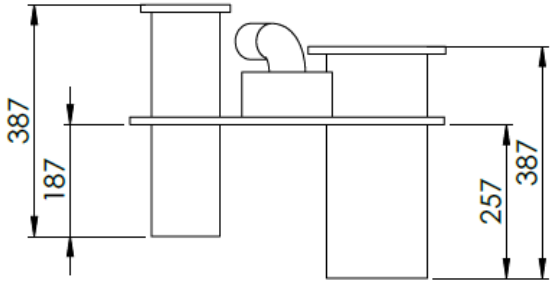

ITEM NO.	PART NUMBER	QTY.
1	6in pipe flange	1
2	4in pipe flange	1
3	raised pipe weldment	1
4	6in pipe sch 40 387mm long	1
5	4in pipe sch 40 387mm long	1
6	separator lid plate	1

UNLESS OTHERWISE SPECIFIED:		NAME	DATE
DIMENSIONS ARE IN MILLIMETRES TOLERANCES: ±1MM	DRAWN		
	CHECKED		
	ENG APPR.		
	MFG APPR.		
INTERPRET GEOMETRIC TOLERANCING PER:	Q.A.		
MATERIAL	COMMENTS:		
FINISH			
DO NOT SCALE DRAWING			

TITLE: Separator lid weldment

SIZE	DWG. NO.	REV
A		

SCALE: 1:10	WEIGHT:	SHEET 1 OF 1

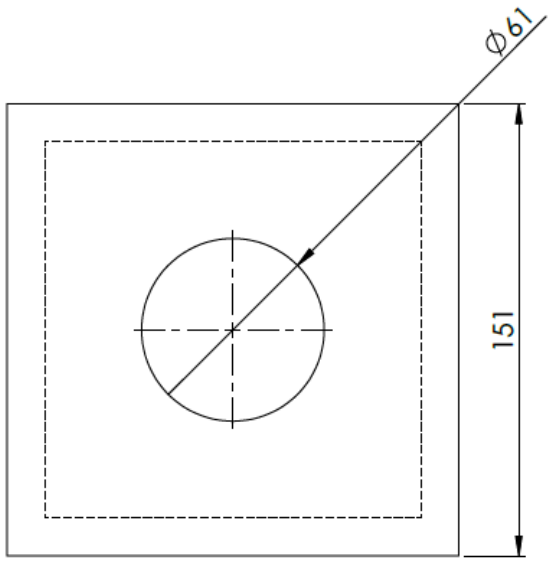

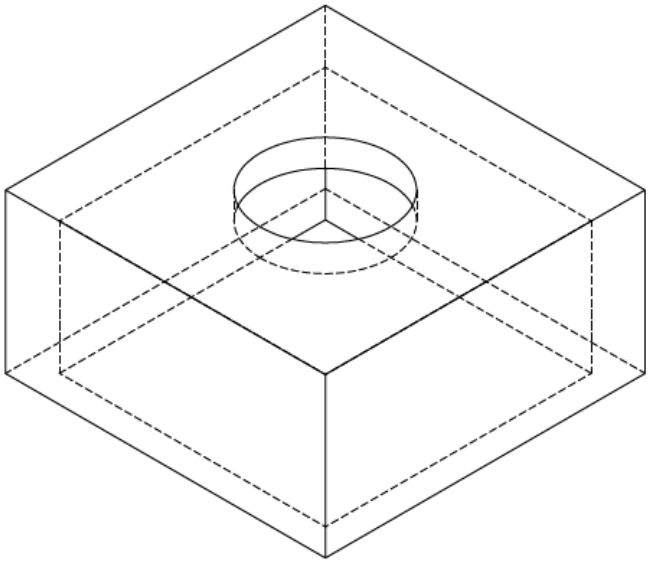

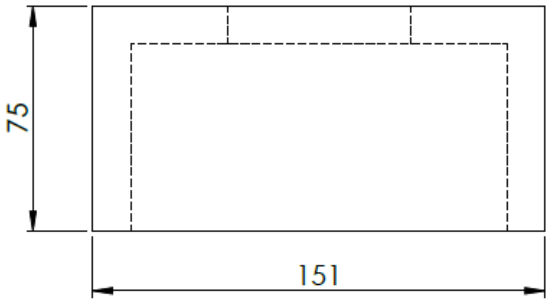

UNLESS OTHERWISE SPECIFIED:		NAME	DATE
DIMENSIONS ARE IN MILLIMETRES TOLERANCES: ±1MM	DRAWN		
	CHECKED		
	ENG APPR.		
	MFG APPR.		
INTERPRET GEOMETRIC TOLERANCING PER:	Q.A.		
MATERIAL 1/2 INCH CLEAR PVC	COMMENTS:		
FINISH			
DO NOT SCALE DRAWING			

TITLE: Small box

SIZE	DWG. NO.	REV
A		

SCALE: 1:2	WEIGHT:	SHEET 1 OF 1

Ragged Chutes head

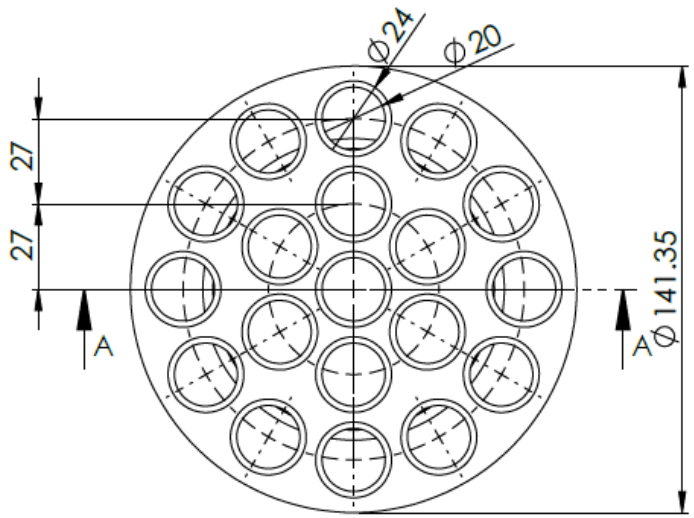

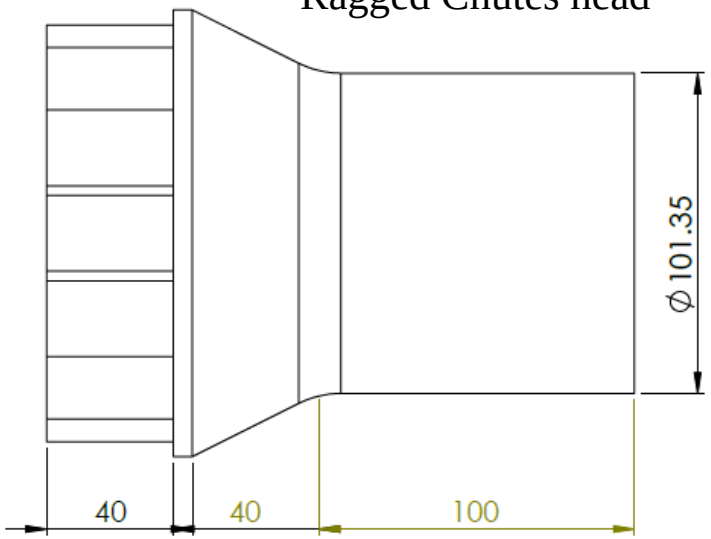

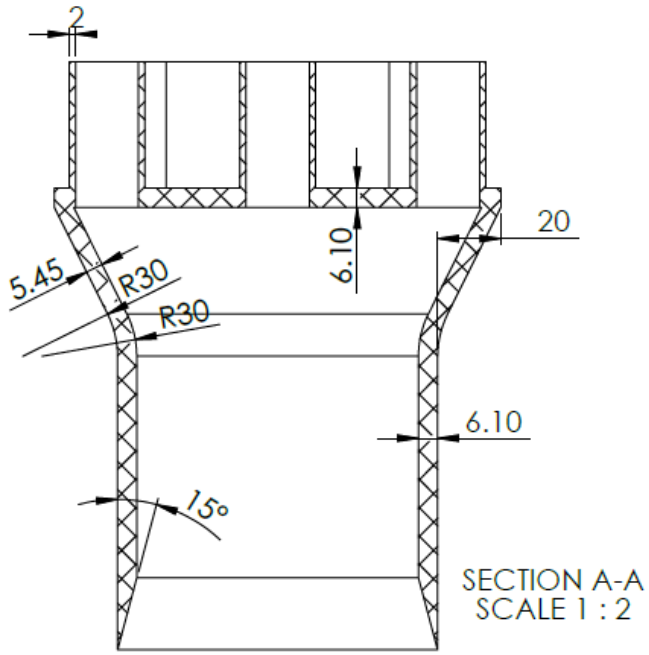

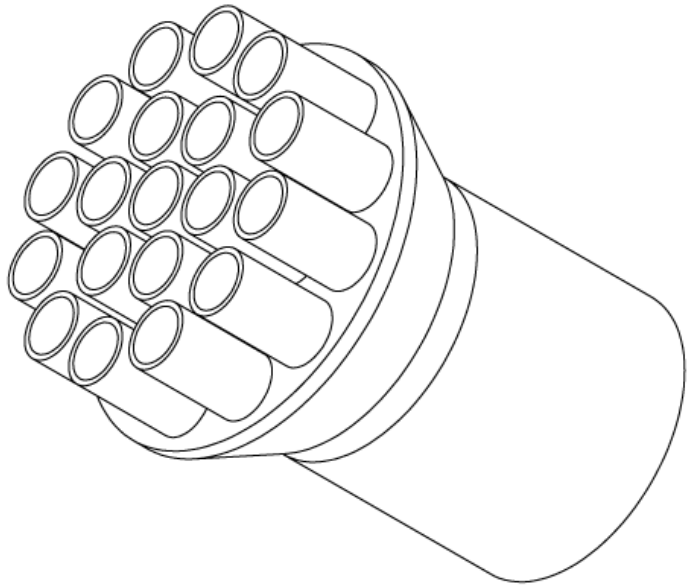

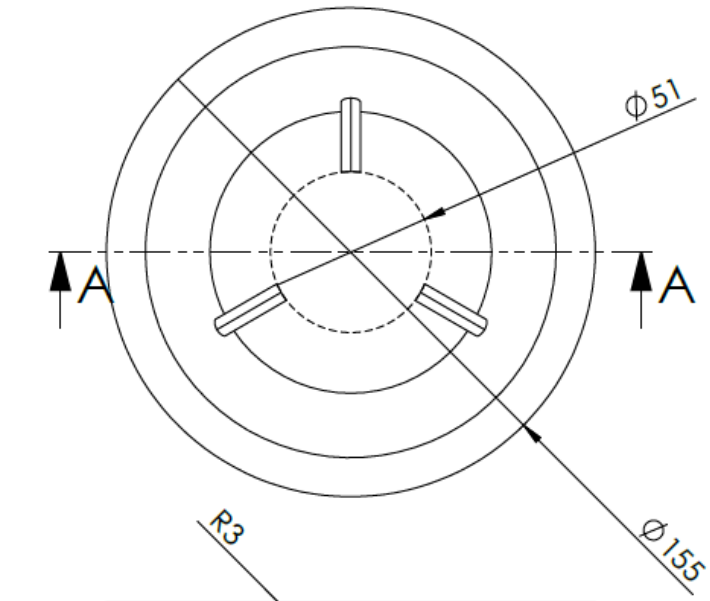

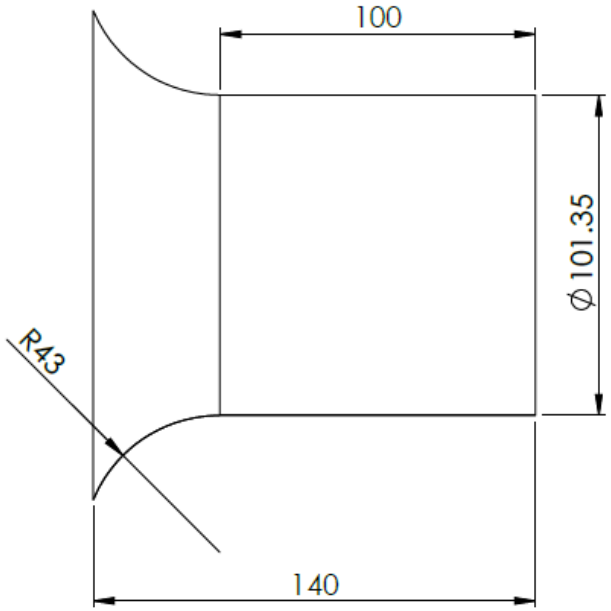

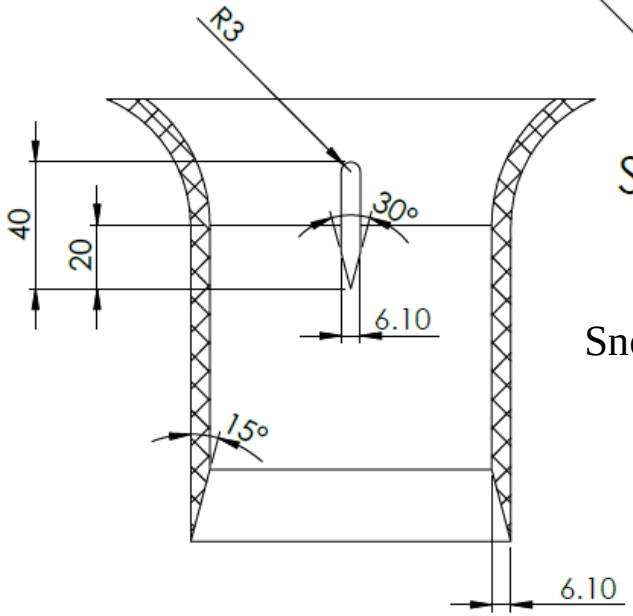

SECTION A-A

SCALE 1 : 2

Snorkel head (base)

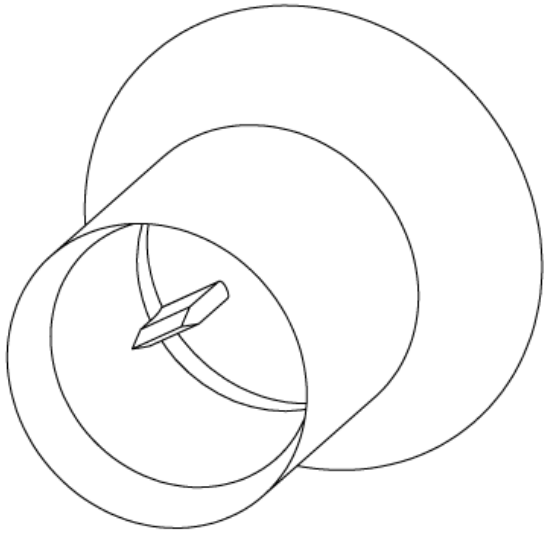

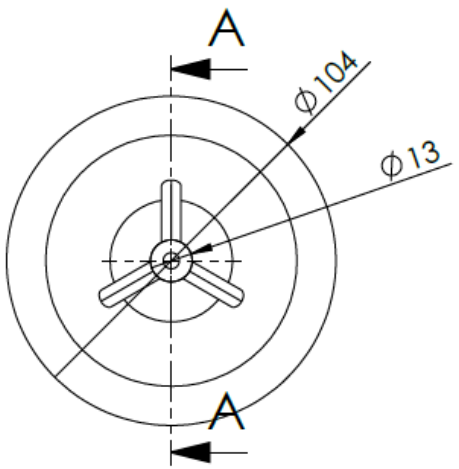

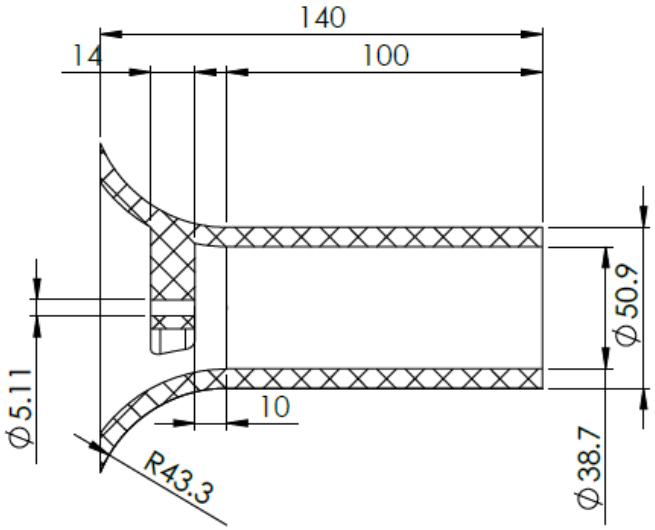

SECTION A-A

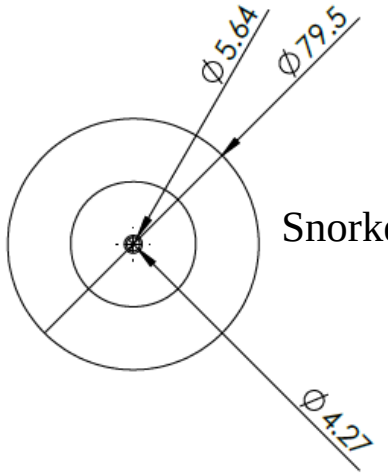

Snorkel head (large snorkel)

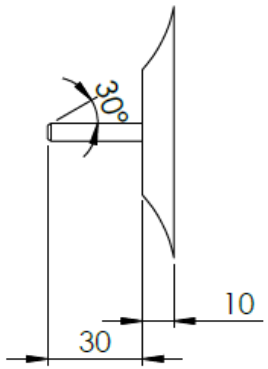

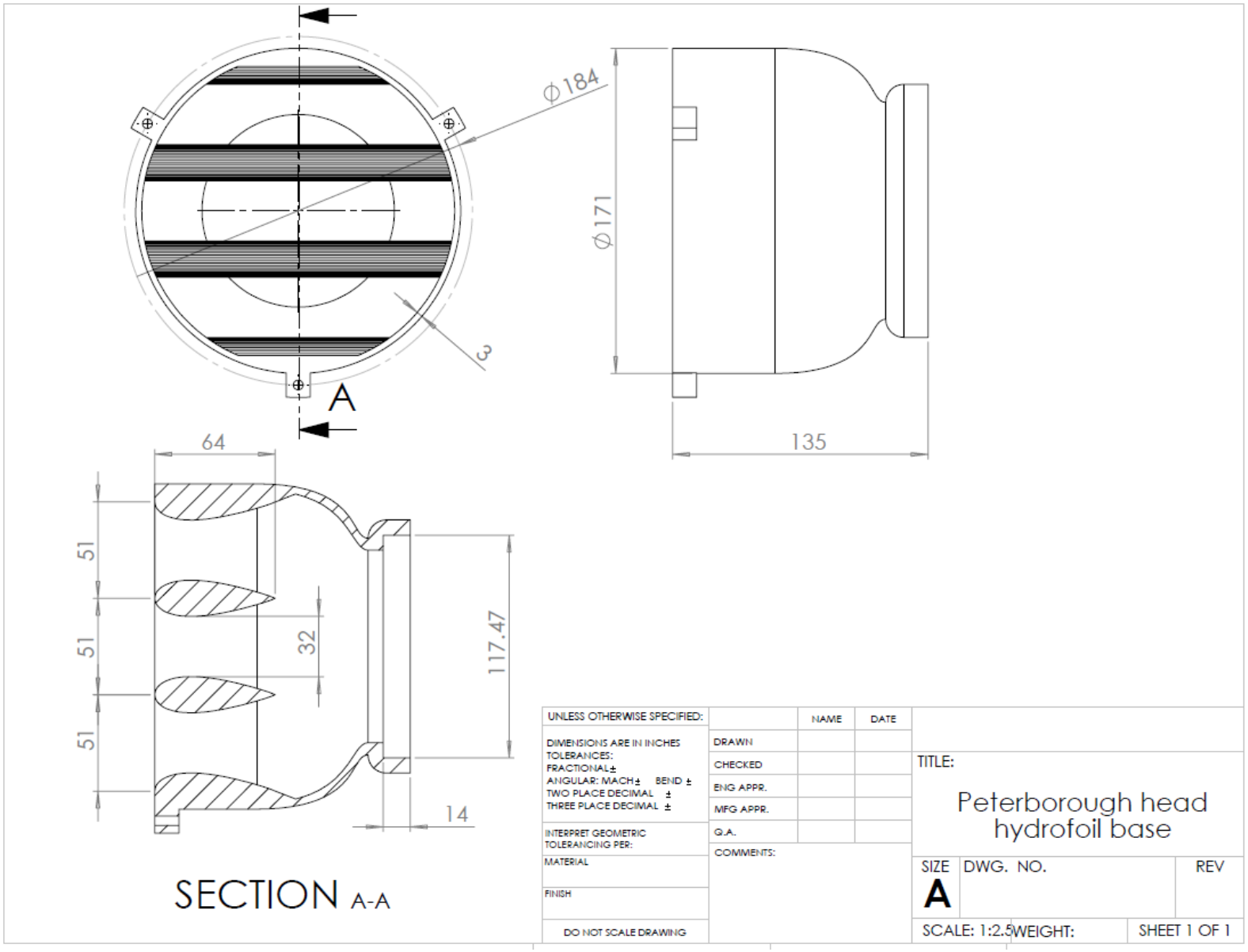
ϕ184
ϕ171
135
3
A
64
51
51
51
32
117.47
14
SECTION A-A
UNLESS OTHERWISE SPECIFIED:
DIMENSIONS ARE IN INCHES
TOLERANCES:
FRACTIONAL ±
ANGULAR: MACH ± BEND ±
TWO PLACE DECIMAL ±
THREE PLACE DECIMAL ±
INTERPRET GEOMETRIC TOLERANCING PER:
MATERIAL
FINISH
DO NOT SCALE DRAWING
NAME
DATE
DRAWN
CHECKED
ENG APPR.
MFG APPR.
Q.A.
COMMENTS:
TITLE:
Peterborough head hydrofoil base
SIZE
A
DWG. NO.
REV
SCALE: 1:2.5
WEIGHT:
SHEET 1 OF 1

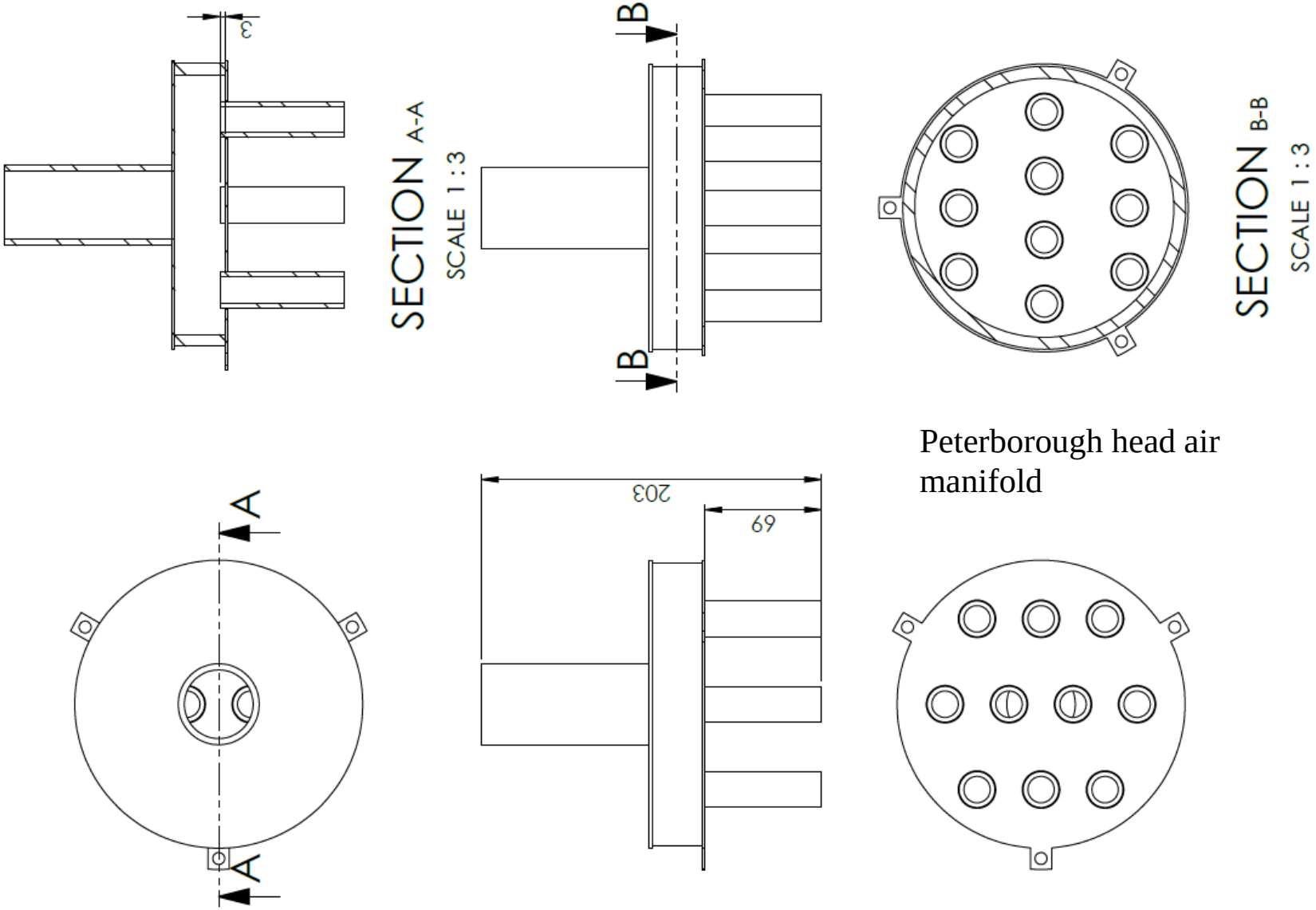

Peterborough head air manifold

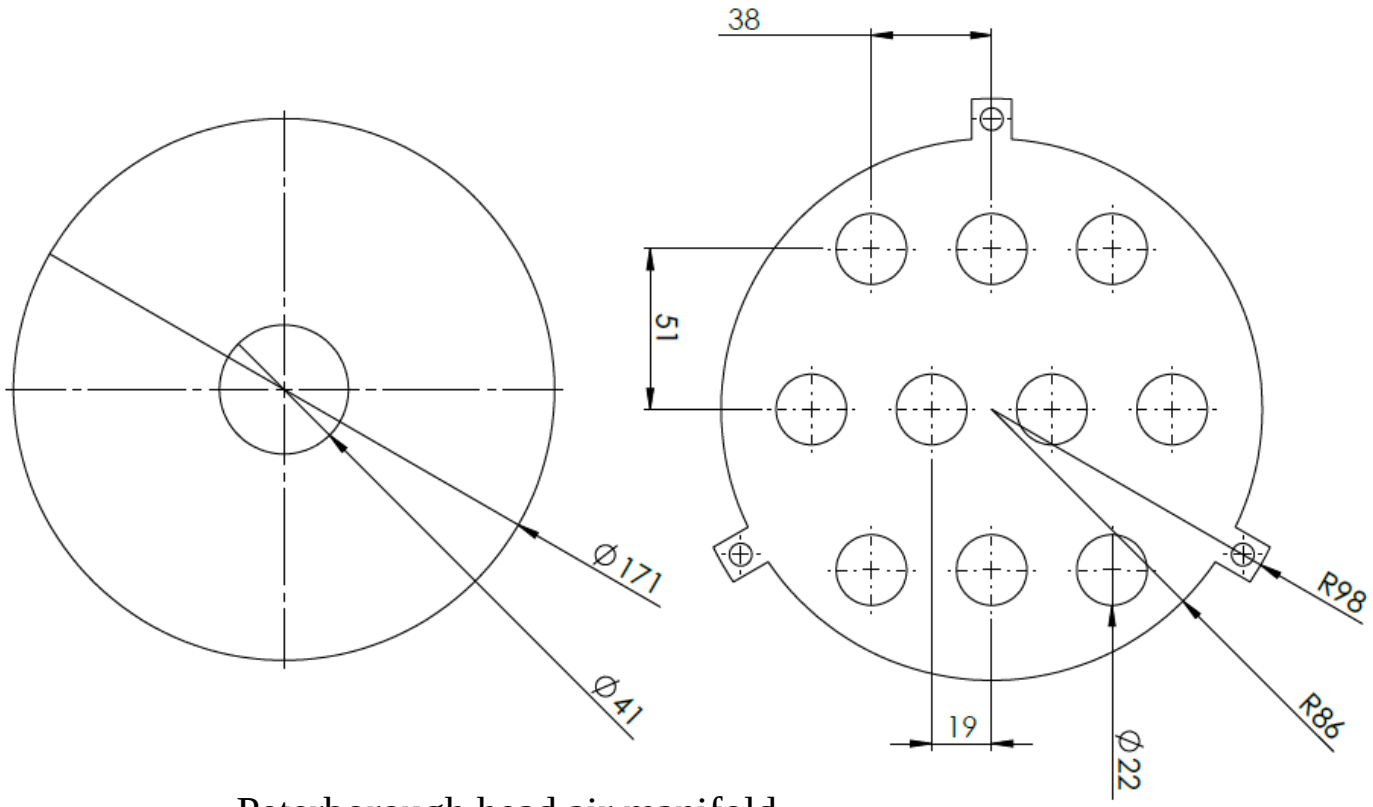

Peterborough head air manifold bounding plates

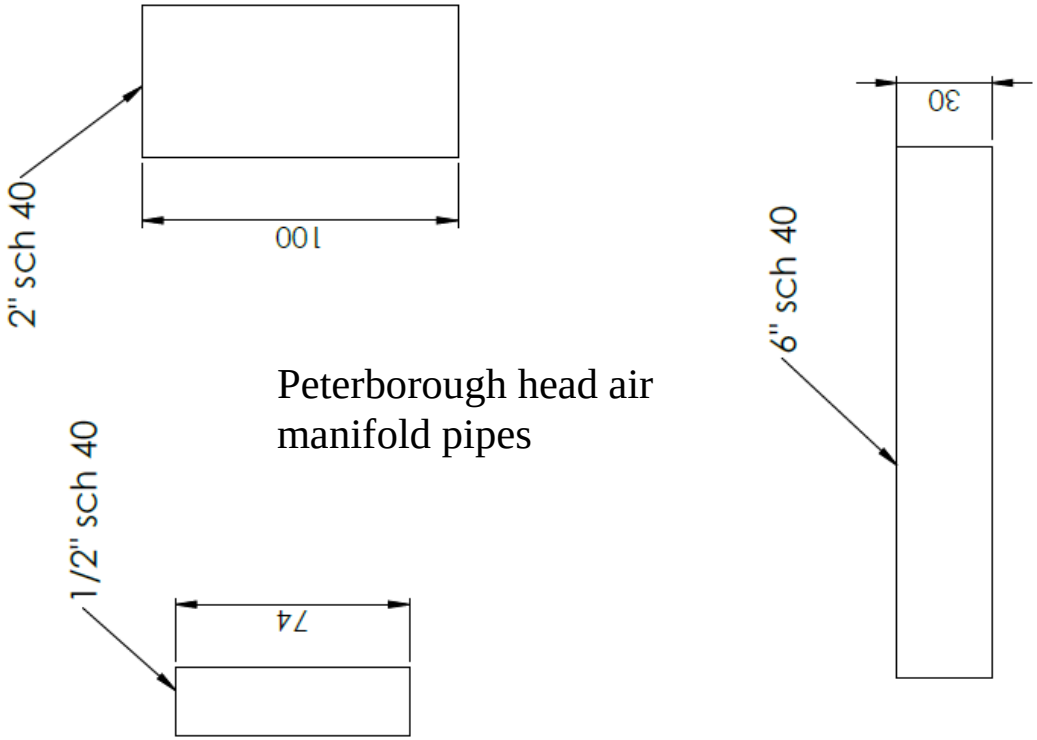

Peterborough head air manifold pipes

Appendix C: Sample code Baby HAC (LabVIEW)

The program presented in this appendix was written to view and log the instrument readings from Baby HAC from a single main interface. Above each sub-program here is a brief description of its function. The instrumentation package for Baby HAC is described in section 5.1.1.

Main interface for prototype data acquisition

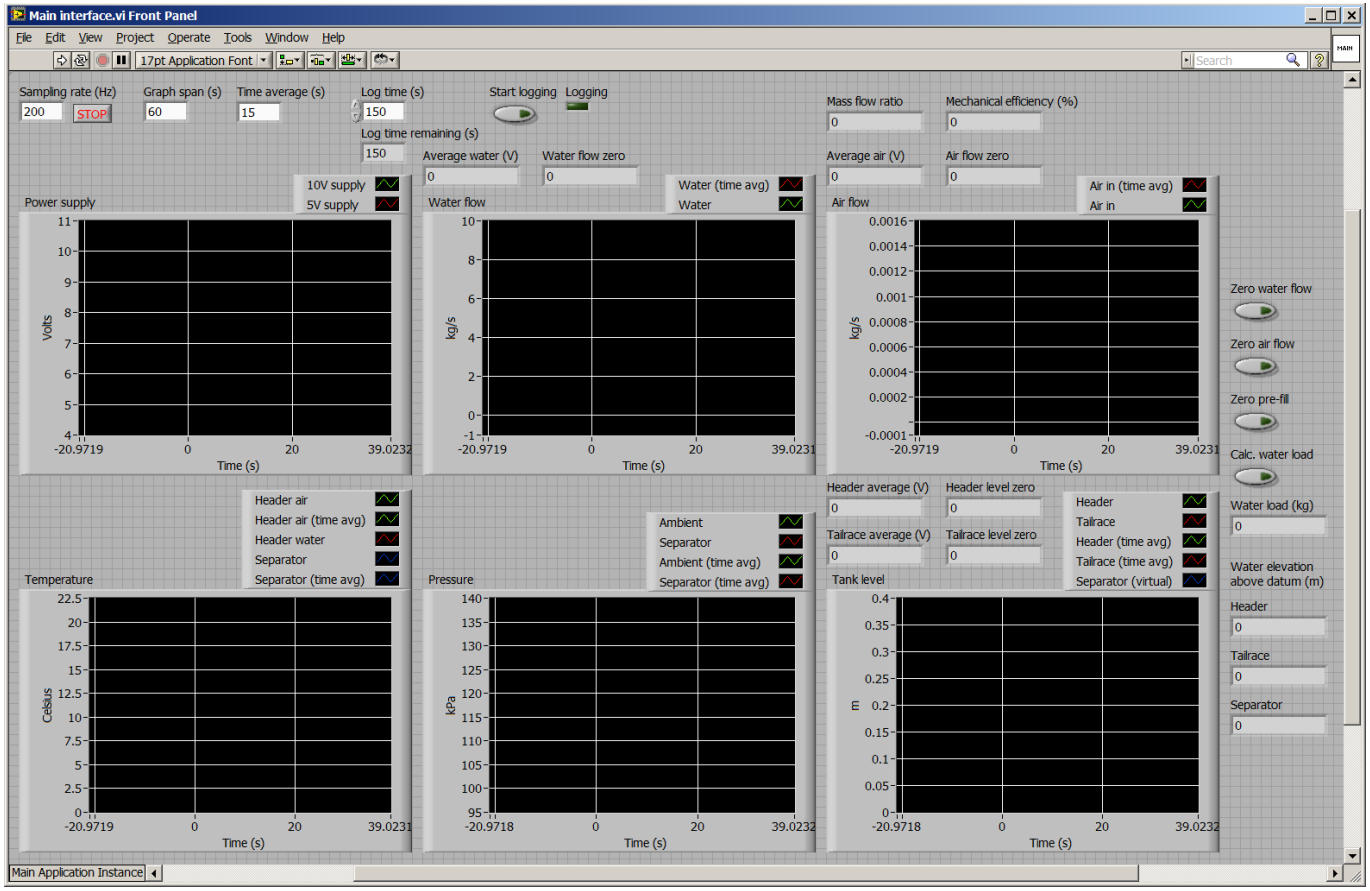

Main interface code

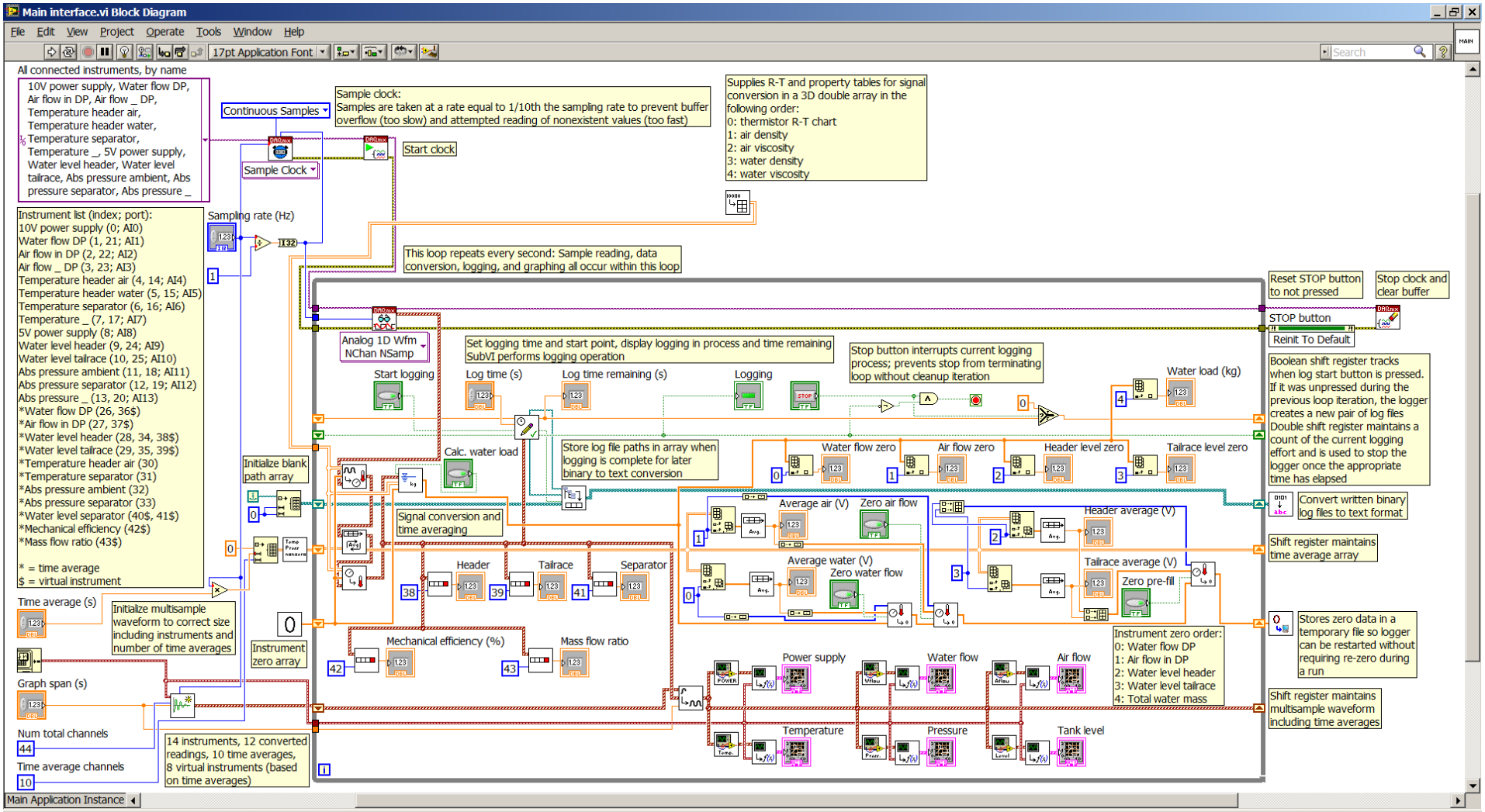

Logging handler: data are streamed into binary .tdms files to avoid slowdown created by opening and closing text files at every iteration

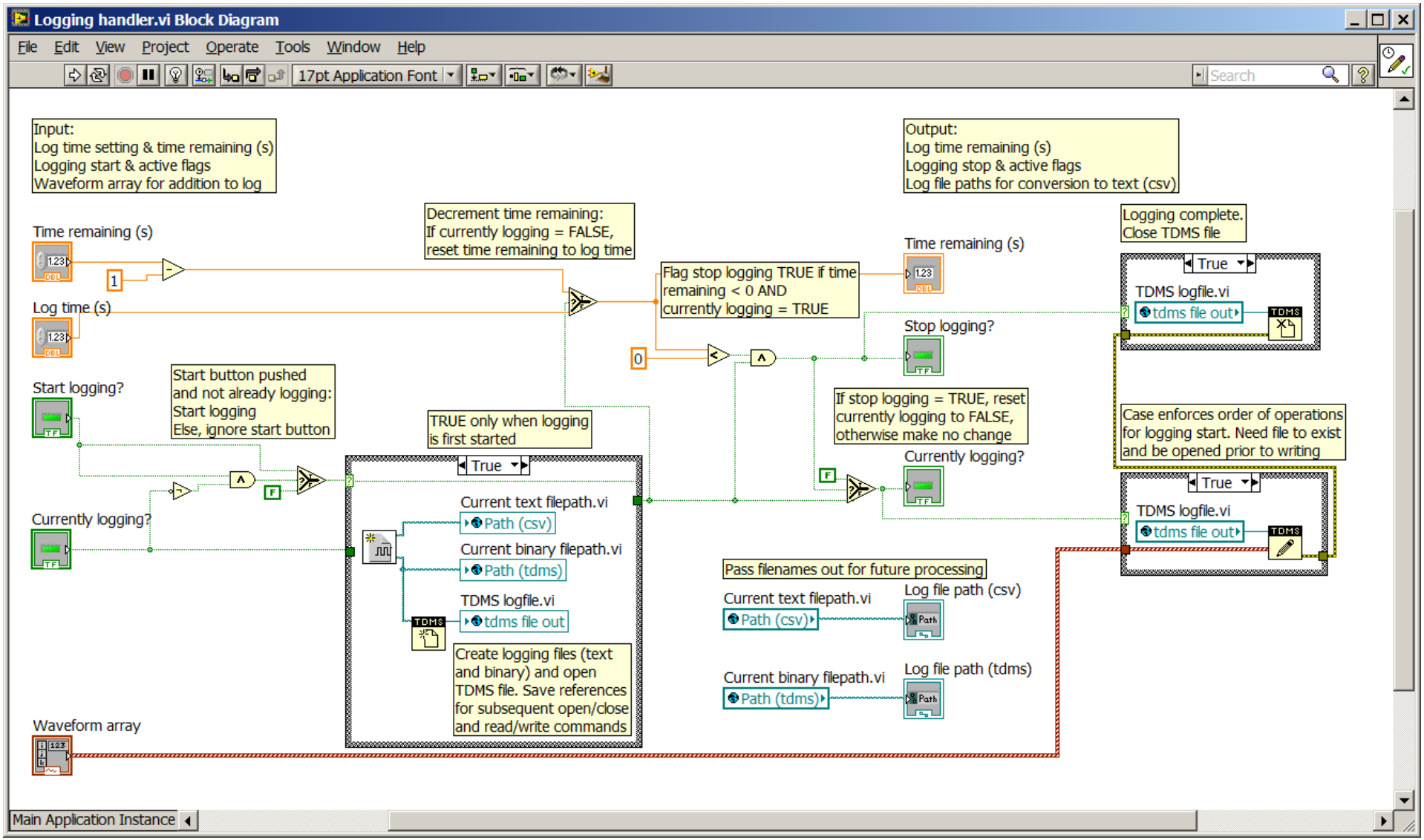

Logging conversion from binary file to text format executed after the measurement loop is stopped to prevent update interruption

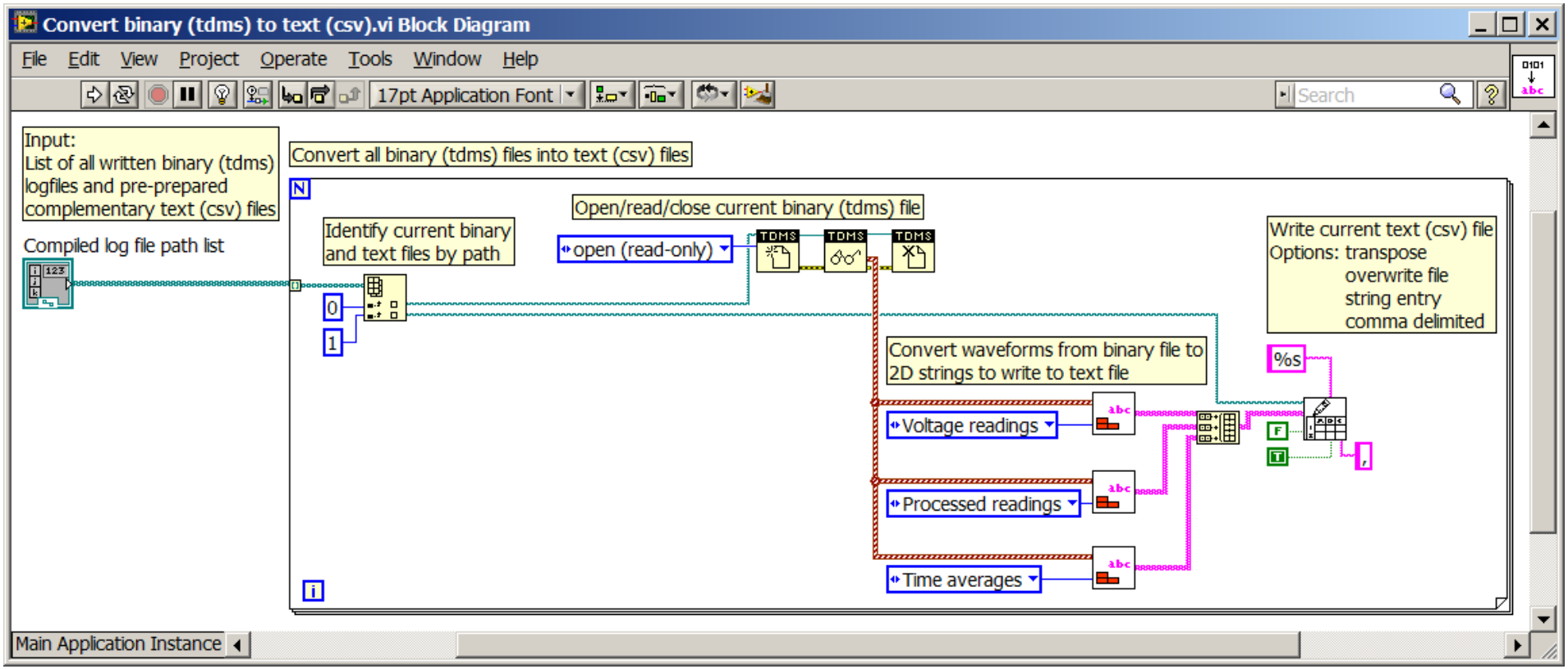

Voltage to variable converter currently showing the water flow rate orifice meter; this function controls all instrument conversions, including virtual instruments. A total of 22 instruments and virtual instruments are included in this converter. The numeric dropdown at the top centre of the selection box changes which instrument code is displayed on the page. All instruments share common input and output formats

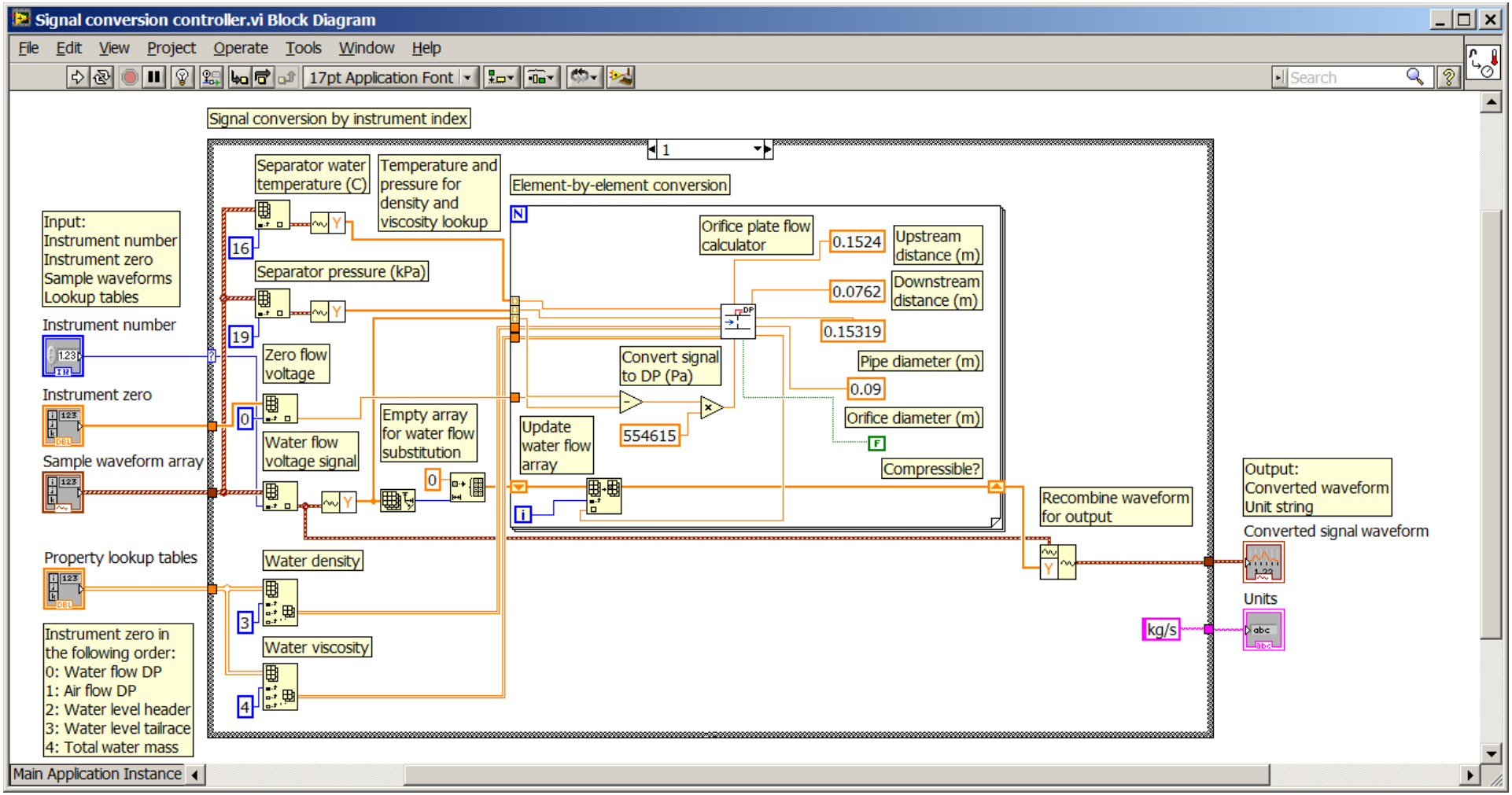

Orifice calculator for air and water flow rate

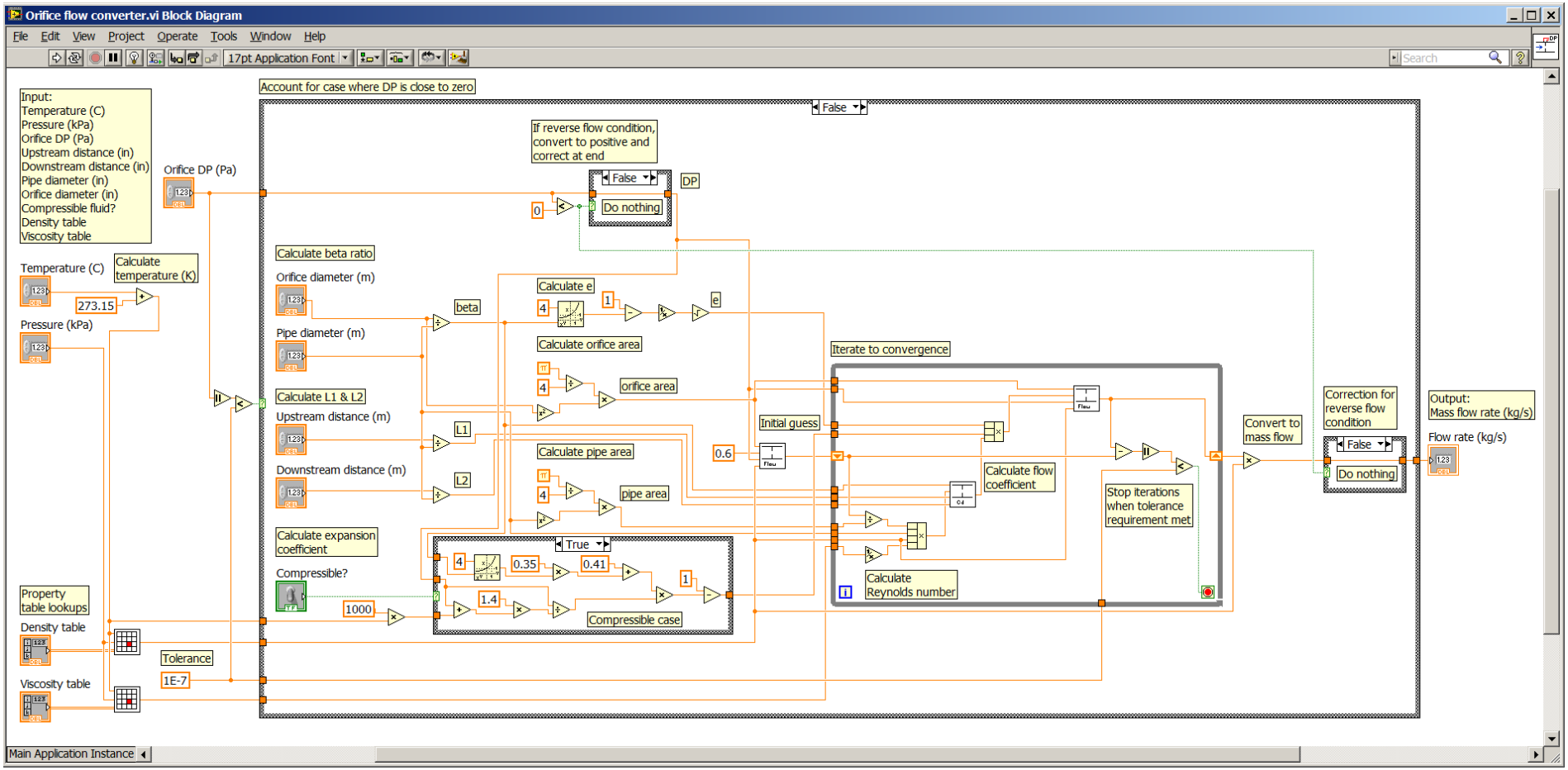

Time average calculation handler function: produces time average functions for display on the interface used for manual control and live instrument zeroing

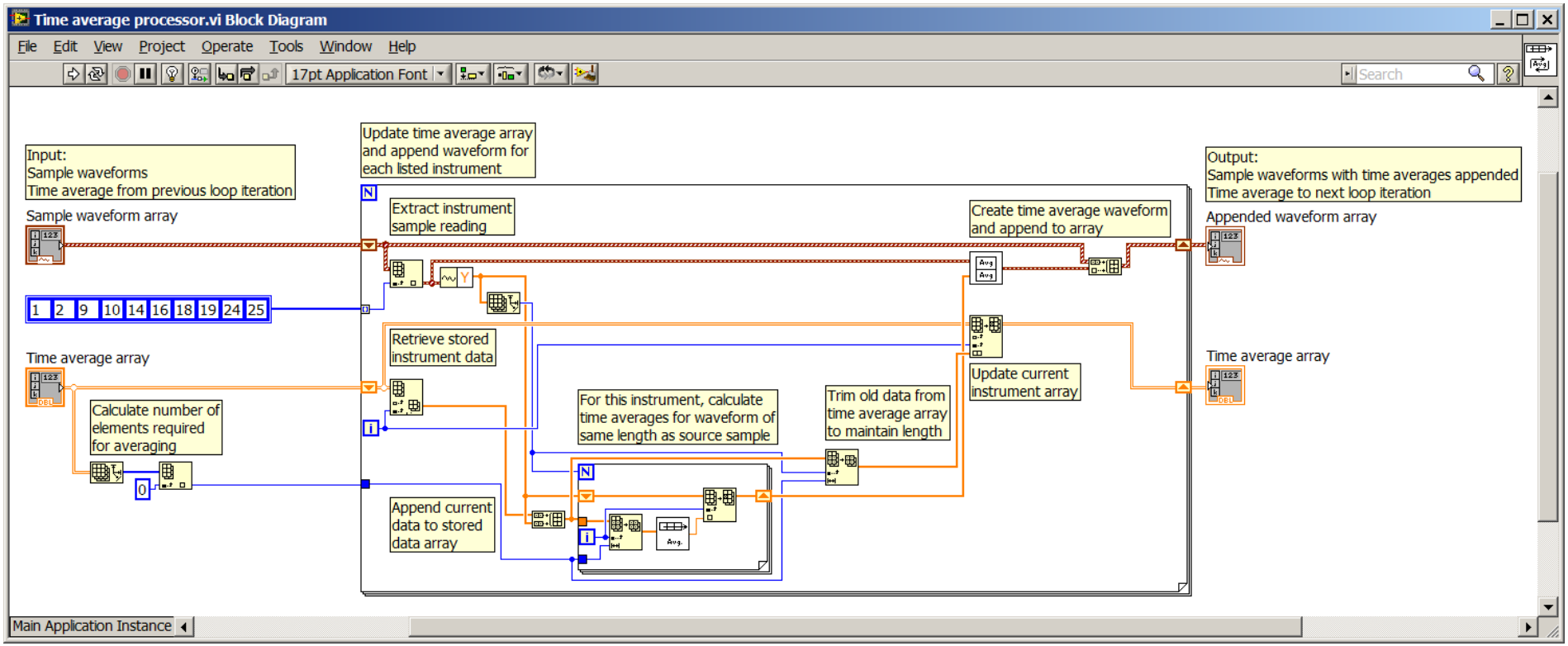

Virtual instrument handler: controls the calculation of virtual instruments in the voltage to variable converter displayed above

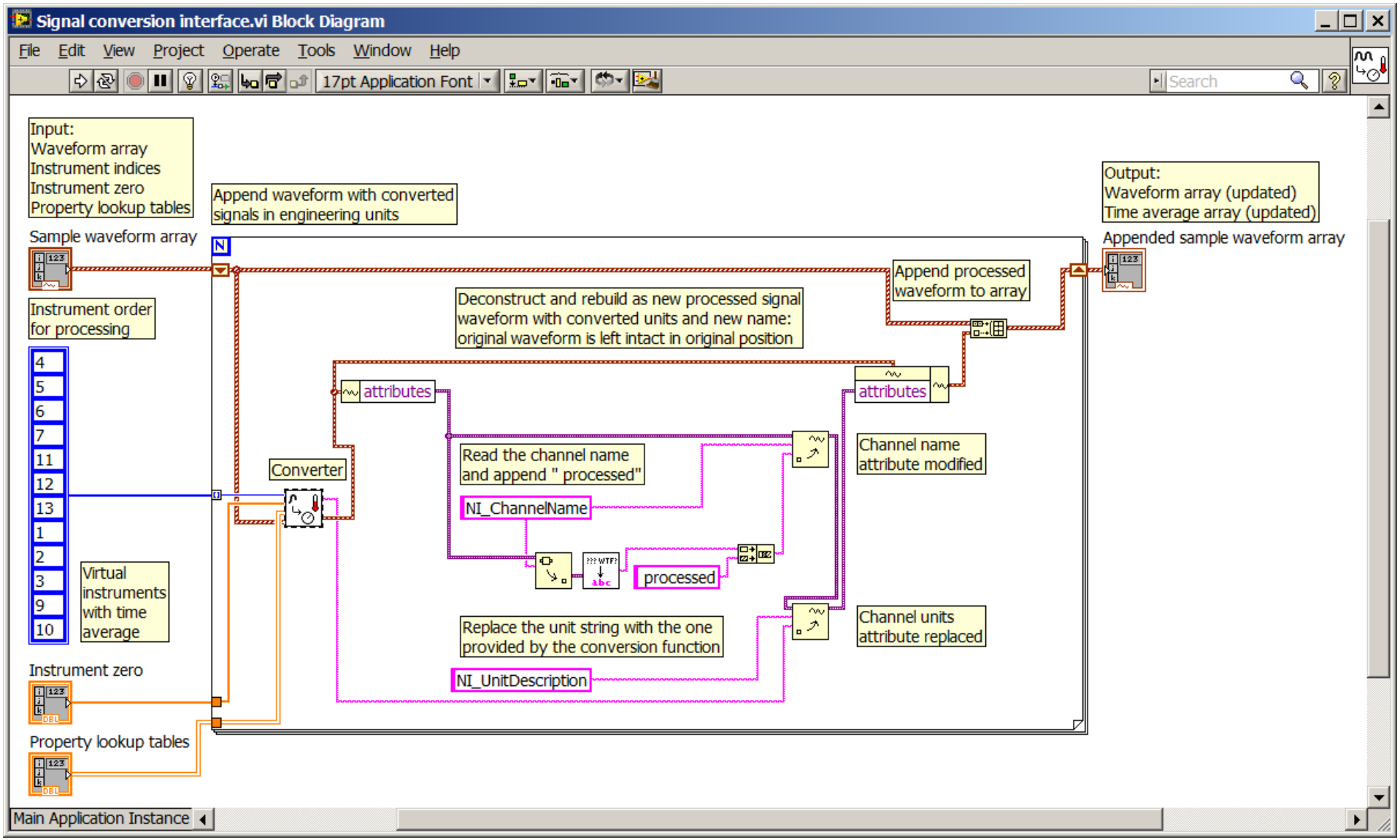

Water load calculator used to compute separator level and for solubility experiments

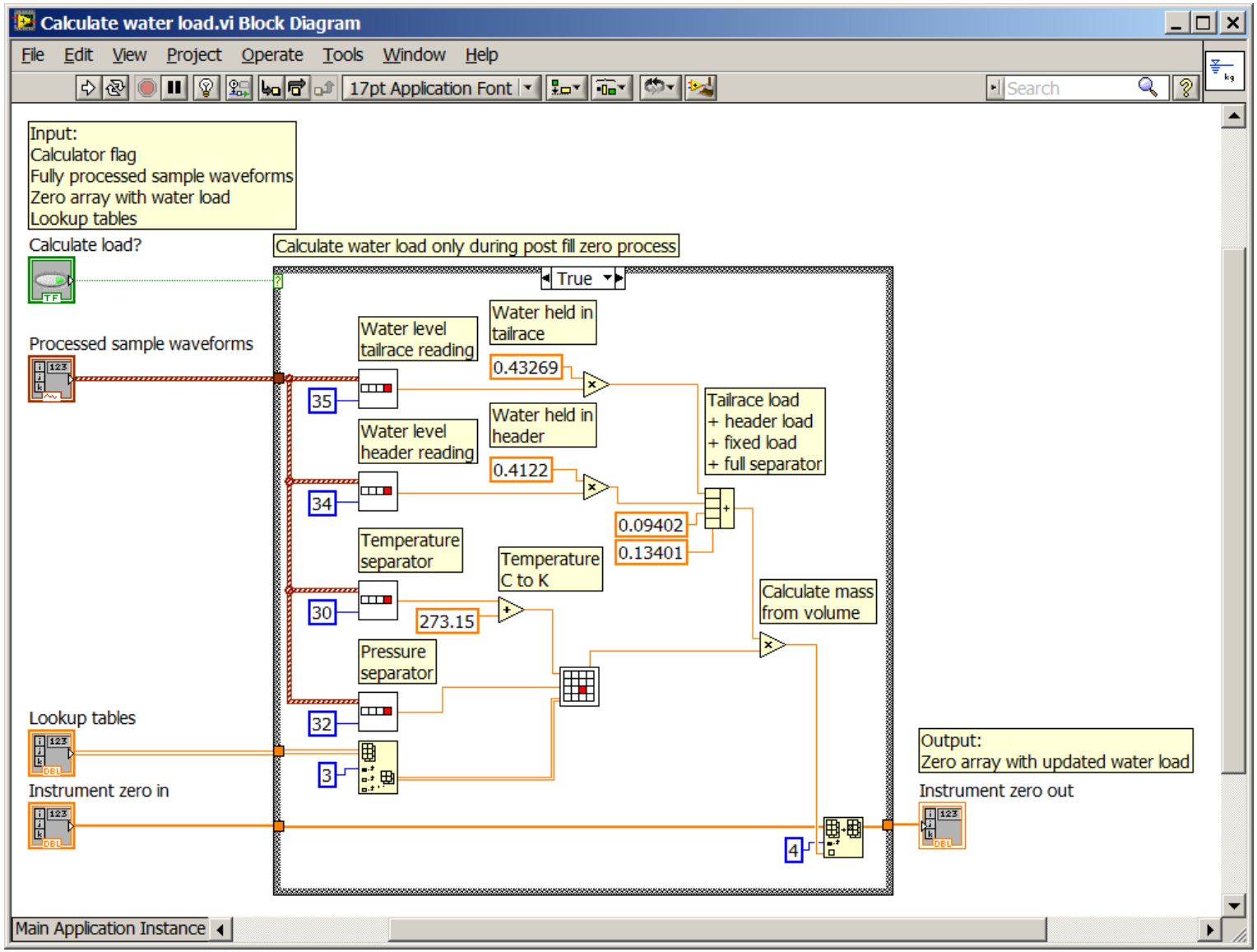

Appendix D: Baby HAC instrumentation calibration

This appendix presents the full calibration information for the instruments used at Baby HAC, described in the same order in section 5.1.1. Each calibration is presented in table format, followed by a graph showing the function and linearity of the voltage response for the given instrument(s).

Water flow rate differential pressure instrument

Water level above centreline		DP reading	deltaV/deltaH
(inches)	(cm)	(V)	(V/cm)
0.00	0.00	2.37330	-
28.13	71.44	2.38612	1.79E-04
26.00	66.04	2.38520	1.70E-04
23.19	58.90	2.38425	1.33E-04
22.31	56.67	2.38345	3.60E-04
20.50	52.07	2.38271	1.61E-04
18.88	47.94	2.38192	1.91E-04
17.13	43.50	2.38126	1.48E-04
15.38	39.05	2.38051	1.69E-04
12.88	32.70	2.37932	1.87E-04
11.00	27.94	2.37862	1.47E-04
9.19	23.34	2.37783	1.72E-04
6.88	17.46	2.37692	1.55E-04
5.81	14.76	2.37624	2.52E-04
4.63	11.75	2.37549	2.49E-04
3.69	9.37	2.37510	1.64E-04
2.31	5.87	2.37455	1.57E-04
1.06	2.70	2.37406	1.54E-04
0.38	0.95	2.37357	2.81E-04
0.00	0.00	2.37346	1.15E-04

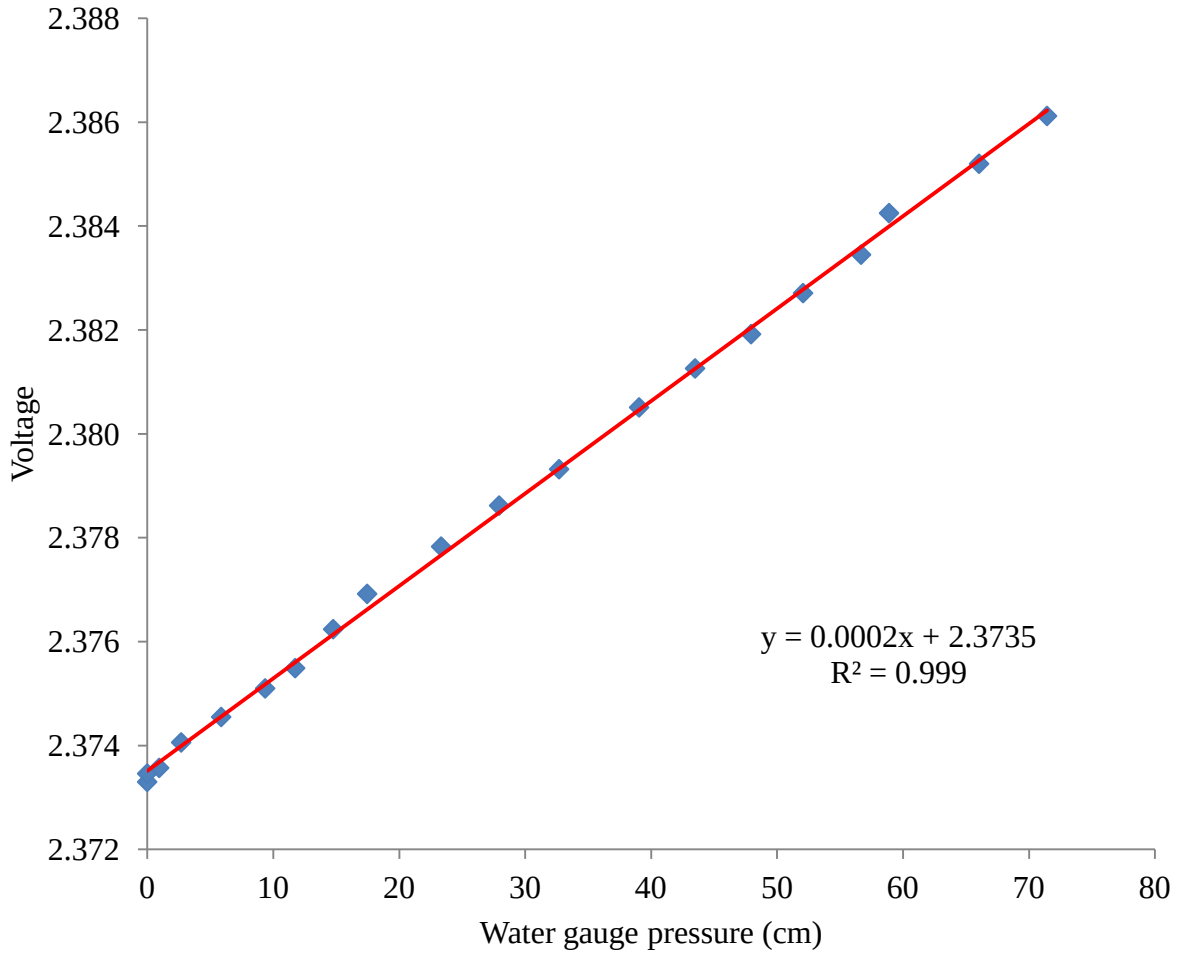
2.388
2.386
2.384
2.382
2.380
2.378
2.376
2.374
2.372
Voltage
0
10
20
30
40
50
60
70
80
Water gauge pressure (cm)
y = 0.0002x + 2.3735
R² = 0.999

Air flow rate differential pressure instrument

Gauge pressure (+ Port A, Pa)	Voltage (V)	deltaH/deltaP (V/Pa)
-244	4.25	-
-225	4.16	-4.74E-03
-207	3.96	-1.11E-02
-186	3.80	-7.62E-03
-176	3.75	-5.00E-03
-173	3.72	-1.00E-02
-149	3.53	-7.92E-03
-128	3.33	-9.52E-03
-112	3.15	-1.13E-02
-102	3.07	-8.00E-03
-95	3.05	-2.86E-03
-75	2.85	-1.00E-02
-72	2.83	-6.67E-03
0	2.25	-8.06E-03
98	1.45	-8.16E-03
104	1.41	-6.33E-03
136	1.12	-9.11E-03
139	1.12	-1.83E-03
146	1.04	-1.10E-02
153	0.95	-1.25E-02
176	0.78	-7.37E-03
189	0.68	-7.54E-03
204	0.58	-7.03E-03
226	0.29	-1.29E-02
243	0.26	-1.94E-03

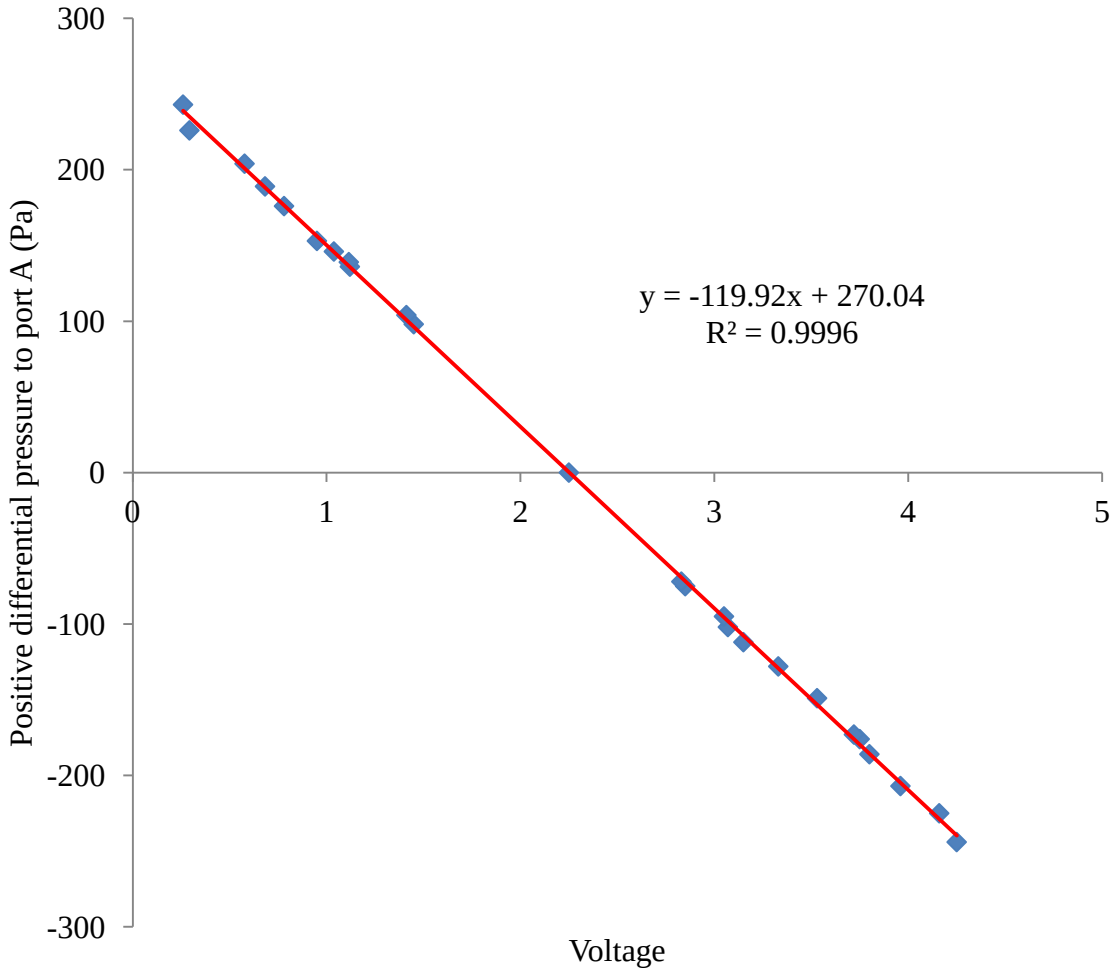
300
200
100
0
-100
-200
-300
0
1
2
3
4
5
Positive differential pressure to port A (Pa)
Voltage
y = -119.92x + 270.04
R² = 0.9996

Separator absolute pressure sensor

Water level (cm)	Pressure (kPa)	Voltage (V)	deltaP/deltaV (kPa/V)
0.0	99.13	1.754	-
14.8	99.58	1.780	17.3
31.2	101.18	1.813	48.5
49.9	103.01	1.850	49.5
68.6	104.84	1.886	50.8
97.0	107.61	1.941	50.4
114.7	109.34	1.976	49.4
144.3	112.21	2.035	48.6
171.7	114.92	2.090	49.3
197.5	117.44	2.139	51.4
216.4	119.29	2.198	31.4
250.9	122.66	2.247	68.8
271.1	124.64	2.288	48.3
291.8	126.66	2.323	57.7

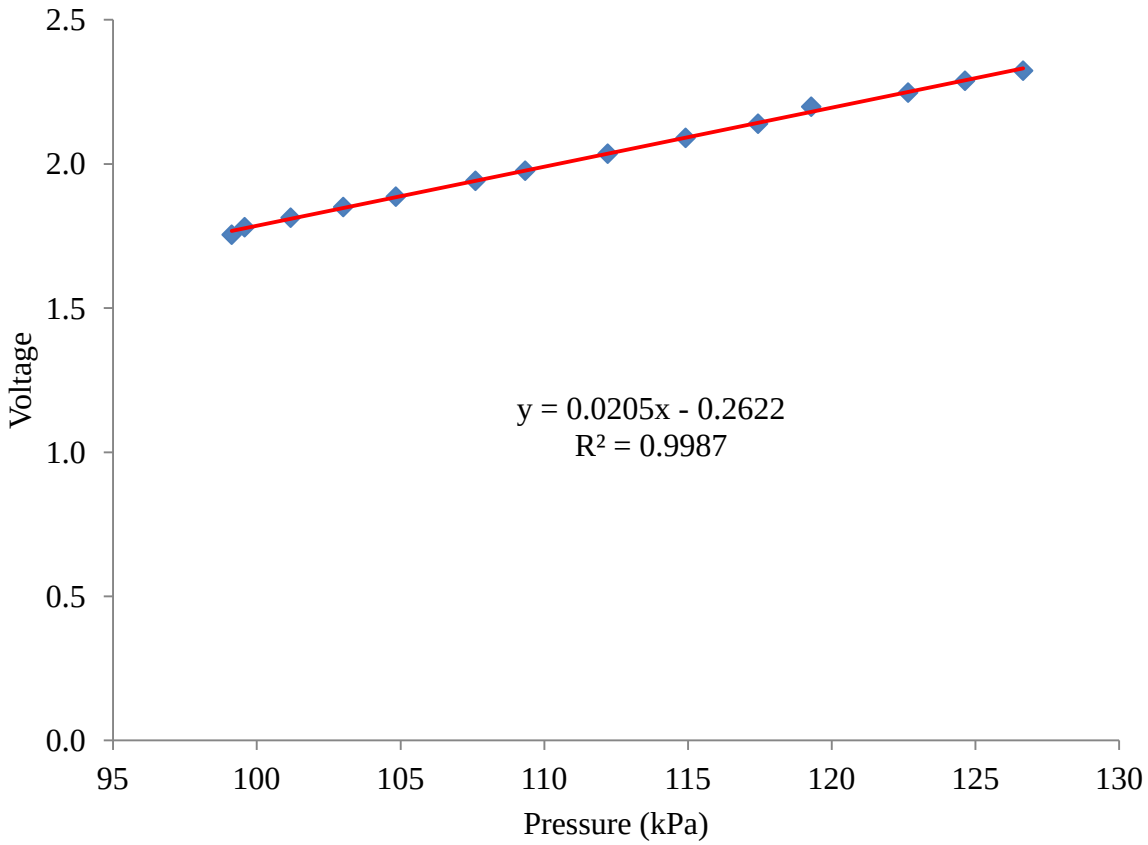

Water level sensors

Water level (cm)	Voltage (V)		deltaH/deltaV (cm/V)	
	#1	#2	#1	#2
0.0	-0.114	0.001	-	-
4.8	0.265	0.384	12.7	12.5
9.9	0.827	0.916	9.1	9.6
15.1	1.310	1.468	10.8	9.4
20.7	1.871	1.993	10.0	10.7
25.9	2.310	2.485	11.8	10.6
30.7	2.835	2.975	9.1	9.8
0.0	-0.119	0.003	10.4	10.3

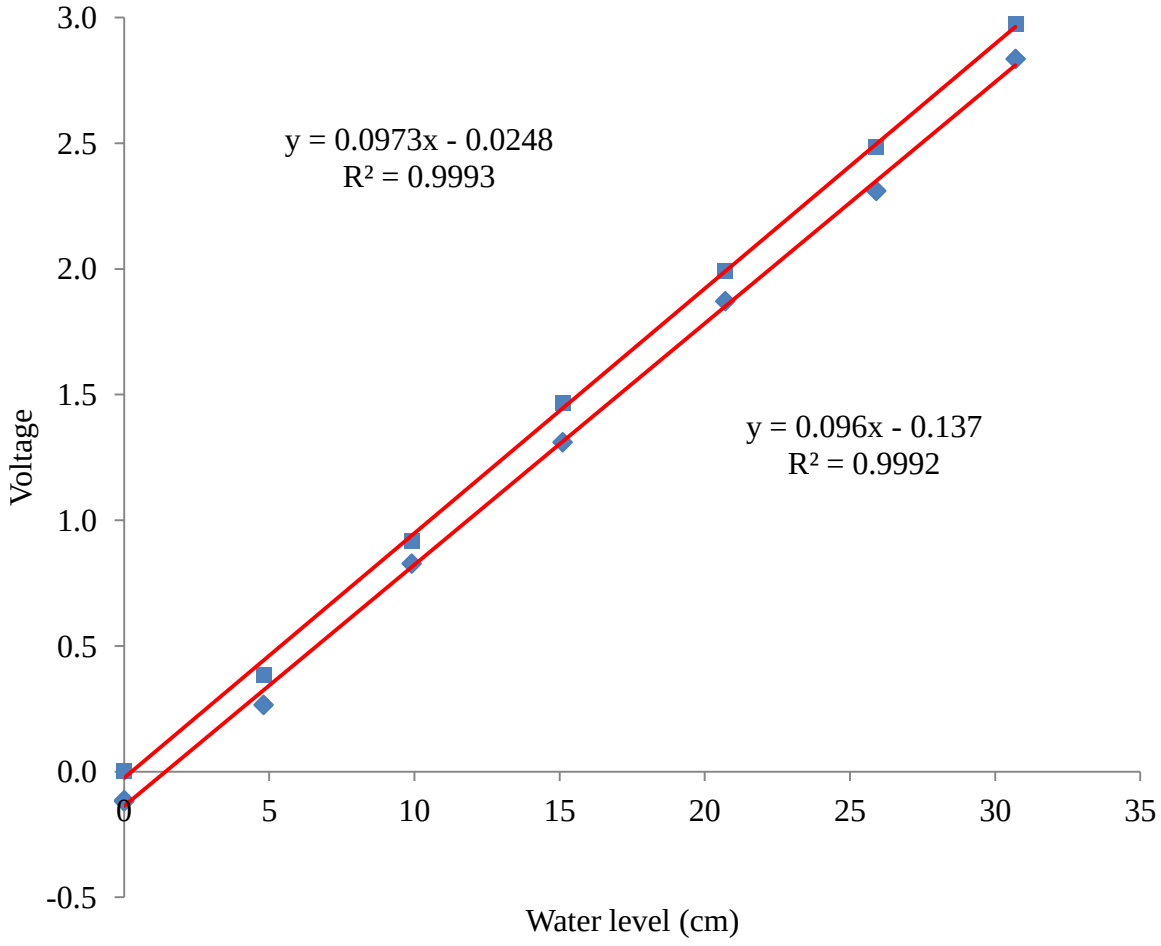

Appendix E: Orifice flow conversion

This orifice flow calculator is a copy into VBA of the LabVIEW code that converts differential pressure into mass flow rate for air and water flow rate measurement at Baby HAC.

```
Option Explicit

'calculate volumetric flow rate from orifice observation (air and water)
Function OrificeFlow(temp As Double, fluidPress As Double, fluidName As String, _
                     deltaPress As Double, pipeDiam As Double, orificeDiam As Double, _
                     upstreamDist As Double, downstreamDist As Double, _
                     Optional tolerance As Double = 0.000000001)
    'declare coefficients
    Dim flowCoeff As Double
    flowCoeff = 0.6
    Dim expansCoeff As Double
    Dim e As Double
    Dim dischargeCoeff As Double


    'adjust for negative differential pressure - initial flag
    Dim ReverseFlow As Boolean
    ReverseFlow = False
    If deltaPress < 0 Then
        deltaPress = -deltaPress
        ReverseFlow = True
    End If

    'declare geometry vars
    Dim beta As Double
    Dim L1 As Double
    Dim L2 As Double
    Dim pipeArea As Double

    'declare fluid property vars
```

```
Dim dynViscosity As Double
Dim dens As Double
Dim Re As Double
Dim velocity As Double

'calculate thermodynamic properties by fluid
dynViscosity = Viscosity(fluidName, "PT", "mks", fluidPress / 1000, temp + 273.15) / 1000000
dens = density(fluidName, "PT", "mks", fluidPress / 1000, temp + 273.15)

'calculate geometry parameters
L1 = upstreamDist / pipeDiam
L2 = downstreamDist / pipeDiam
pipeArea = Excel.WorksheetFunction.pi() / 4 * pipeDiam ^ 2

'calculate static coefficients
beta = orificeDiam / pipeDiam
e = Sqr(1 / (1 - beta ^ 4))
If fluidName = "air" Then
    expansCoeff = 1 - (deltaPress / (1.4 * (fluidPress + deltaPress))) * (0.41 + 0.35 * beta ^ 4)
Else
    expansCoeff = 1
End If
'solve for orifice flow
'initial conditions
Dim currentFlow As Double
Dim previousFlow As Double
currentFlow = OrificeEquation(orificeDiam, flowCoeff, deltaPress, dens)

'iterative solution
Do
    previousFlow = currentFlow

    'recalculate coefficient of flow
    velocity = currentFlow / pipeArea
    Re = dens * pipeDiam * velocity / dynViscosity
    dischargeCoeff = Cd(beta, Re, L1, L2)
    flowCoeff = dischargeCoeff * e * expansCoeff
```

```
        'final calculation
        currentFlow = OrificeEquation(orificeDiam, flowCoeff, deltaPress, dens)
    Loop Until Abs(currentFlow - previousFlow) < tolerance

    'adjust for negative differential pressure - final correction
    If ReverseFlow Then
        OrificeFlow = -currentFlow
    Else
        OrificeFlow = currentFlow
    End If
End Function

'calculate flow coefficient for orifice plate measurement
Function Cd(beta As Double, Re As Double, L1 As Double, L2 As Double) As Double
    Dim A As Double
    Dim b As Double
    Dim c As Double

    A = ((19000 * beta) / Re) ^ 0.8
    c = (2 * L2) / (1 - beta)
    b = beta ^ 4 / (1 - beta ^ 4)

    Cd = 0.5961 + 0.0261 * beta ^ 2 - 0.216 * beta ^ 8 + 0.000521 * ((1000000# * beta) / Re) ^ 0.7
    Cd = Cd + (0.0188 + 0.0063 * A) * (1000000# / Re) ^ 0.3 * beta ^ 3.5
    Cd = Cd + (0.043 + 0.08 * Exp(-10 * L1) - 0.123 * Exp(-7 * L1)) * (1 - 0.11 * A) * b
    Cd = Cd - 0.031 * (c - 0.8 * c ^ 1.1) * beta ^ 1.3
End Function

'for repeated calls of orifice equation
Function OrificeEquation(orificeDiam As Double, flowCoeff As Double, deltaPress As Double, density As Double)
    Dim orificeArea As Double

    orificeArea = Excel.WorksheetFunction.pi() / 4 * orificeDiam ^ 2
    OrificeEquation = orificeArea * flowCoeff * Sqr((2 * deltaPress) / density)
End Function
```

Appendix F: Additional operating procedures Baby HAC

Control software setup

Note: this code must be run in the development environment of LabVIEW. The compiler leaves the code working but breaks some of the built-in functions so that the wrong channels are read.

1. Install LabVIEW on the control PC
2. Download a copy of the control software folder: \\192.168.20.2\Projects\ERCM\Projects\HAC\Baby HAC\LabVIEW code\
3. Create a logging folder in a location of your choice (preferably local)
4. Open the program “Folder setup.vi” from the project explorer
5. Navigate to the “CSV Data” folder in the “Control software LabView” parent folder using the “CSV data folder” select folder dialog button
6. Navigate to the logging folder created in step 3 using the “Root logging folder” select folder dialog button
7. Right click each path field>Data Operations>Make Current Value Default
8. Save the program “Folder setup.vi”
9. Press the run button (right arrow in toolbar)
10. Close the program “Folder setup.vi”
11. Verify that there are now 5 .llb files in the logging folder. If not, return to step 4

Start-up

1. Plug in instrument power supply cable
2. Run the file “BabyHAC DAQ.lvproj” from your local control software folder

3. Open the program “Folder setup.vi” from the project explorer. If steps 7 and 8 above were properly followed, the path fields should point to the correct local folders
4. Press the run button (right arrow in toolbar)
5. Close the program “Folder setup.vi”
6. Open the program “Main interface.vi” from the project explorer. Note: this program can be opened directly from the folder but will not operate properly unless it is opened from the project explorer
7. Set sampling rate (default 100 Hz), graph span, and time average duration (default 15 seconds). Log time can be adjusted while the program is running. Sampling rate should be high enough that higher-frequency noise can be adequately captured. Time averaging is used as a low-pass filter to accurately eliminate this noise for several instruments. Using a higher sample rate enables flow rate integration with superior accuracy over the time average period. The default time average duration is a balance between smoothing the average flow signal to a more constant value and maintaining a reasonable response time for simulated instruments (e.g. separator level)
8. If changing the mixing head, open the header tank and insert the new head
9. Close, latch, and tape header tank. If this has already been done, verify that the tape seal is intact. The tape seal prevents air from entering an alternate route so that all inlet air is metered
10. If the header tank contains water, open the header tank drain valve and wait for the water to flow out. If the stop button is pushed or the program stops for any reason after this point or during operation, you must restart the procedure from this point
11. Close the header tank drain valve

12. Cover the air inlet. The position of the scaffold is in the line-of-fire from the ventilation system blower. Air moving across the opening creates a small flow through the orifice. This step is only necessary for accurate measurement of low air flows. I don't know whether or not it is important when accounting for cyclical (pulsing) flows as are typical during operation
13. If there is water in the tailrace tank above the level sensor port (1.2 cm depth), remove the sensor from the tank
14. Wait for level time average readings to settle (at least time average duration from sensor removal from water)
15. Press the "Zero pre-fill" button
16. Uncover the air inlet
17. Return the tailrace level sensor to the tank
18. Verify hoses and pipes are properly connected
19. Close fill hose valve
20. Connect water fill line to tap
21. Run out blue discharge hose to sink. Ensure there are no significant kinks or loops along its length
22. Set fill/empty 3-way valve to the discharge closed position
23. Set pump discharge 3-way valve to all open
24. Set pump suction 3-way valve to all open
25. Close both air valves at separator air offtake
26. Close all sampling ports and bleed valves that can drain to atmosphere
27. Open fill hose valve

28. Turn on water. The hoses and pipes around the pump will fill first. Verify that water is not leaking from these connections. If significant leaks do appear, stop filling
29. Fill system until separator is full (it may be necessary to bleed air from the separator) and tailrace tank is 80% full. While filling, it is safe to complete some of the steps below short of adjusting 3-way valves, zeroing the water flow instrument, and turning on the pump
30. Turn off water
31. Close fill hose valve
32. Verify pump switch is set to off position
33. Set pump circuit breaker to on position
34. Set pump choke valve to 50%
35. Bleed air from the water DP instrument lines. Crack open the bleed valves on the tees to drain air. Close both valves when the water lines leading to the valve tees are free of air. The limited opening of these valves is intended to reduce the pressure difference across the sensor to within its operating range
36. Press the "Zero water flow" button. Watch that the flow readings and time average converge on zero (at least time average duration from zeroing). Do not zero the flow while filling is underway. The flow in the riser is nonzero at this time
37. Verify the water flow readings remain stable around zero. If not, return to step 35. It may be necessary to repeat this procedure a few times to achieve a stable zero. Remember that the signal conversion is highly nonlinear so that relatively large deviations around zero flow translate into only small deviations in the upper range. Air flow will likely not read zero, owing to the covered port zeroing procedure

38. Set pump suction 3-way valve to pull from separator position
39. Set pump discharge 3-way valve to fill/empty line closed position
40. Turn on pump for a short 3-4 second burst to put a few centimetres of water into the header tank (i.e. enough to cover the level sensor without pouring down the downcomer in any significant quantity). If following the top-off procedure, a trickle of water is acceptable in the downcomer
41. Wait until the time average levels settle (i.e. at least the time average duration from the last signal blip in the level) then press the "Calc. water load" button. This figure is used to calculate the separator level. Any air gap in the separator or zeroing error in the level sensors will result in error in this figure
42. Turn on pump
43. Run until the water level in the separator has dropped to a reasonable level. It should be several centimetres below the lid and above the 18-19 cm mark on the tape, where it blows off
44. If the water level in the tailrace tank is 50% or more, there is sufficient water in the HAC to operate properly. If not, there is sufficient dead water in the header tank to account for the missing quantity. Bleed the air from the separator, close the air valves, turn off the pump, and return to step 22 for water top-off
45. Open the air valve(s) to stabilize the separator water level. It is not necessary to perfectly stabilize the level: just enough that it will not blow off frequently or fill the separator with water. In the latter case, the pump is likely to suck air and stop moving water as the tailrace water level drops
46. Set pump suction 3-way valve to pull from tailrace tank position

47. Operate normally

Troubleshooting

Pump making unusual or excessive sound:

When this happens, rapid action is required. Do not allow this condition to persist for long, or else you risk damage to the pump. The first action is to switch the pump suction 3-way valve to the pull from separator position. Note that this will disable water flow metering until the valve is restored to its normal position. DO NOT turn off the pump. If the noise continues, follow the shutdown procedure (steps 2-4) immediately and attempt a more comprehensive inspection.

Otherwise, there are two likely causes to this problem: the vortex breaker at the pump suction side may be out of place or the water level in the tailrace tank may be too low.

First, check the tailrace water level. If it is low and the level in the separator tank is high, then you have been venting too much air from the separator. Close down the valve until the levels rebalance and then switch the pump suction 3-way valve to pull from tailrace tank position. Return to normal operation.

If the tailrace water level is low and the separator tank level is in the normal position (a few centimetres above the 18-19 cm level on the tape), then there is too little water in the system. Follow the shutdown procedure (steps 2-4) then go to step 22 in the start-up procedure.

If both levels are in the normal range, then there is a problem with the vortex breaker in the tailrace tank. It has either fallen off the suction hose opening (and the pump is pulling air, which results in a distinctive “slurping” suction noise combined with the sound of the pump struggling)

or has fallen on top of the opening to block it (and the pump will make the struggling sound without the accompanying suction noise). Replace the vortex breaker sideways on top of the opening. Switch the pump suction 3-way valve to pull from tailrace tank position. Return to normal operation.

Shutdown (from operating normally)

1. Run out blue discharge hose to sink. Ensure there are no significant kinks along its length
2. Bleed air from the separator to fill it with water. This step is important because there is an additional load of water in the header tank that will ultimately flow into the tailrace tank after the pump is turned off. By filling the separator with water, the tailrace tank level is dropped to accommodate it
3. Close air valves
4. Turn off pump
5. Press “STOP” button on control software (NOT “abort execution” button)
6. Close fill hose valve
7. Set fill/empty 3-way valve to discharge closed position
8. Set pump suction 3-way valve to all open
9. Set pump discharge 3-way valve to all open
10. Place end of hose in sink
11. Set fill/empty 3-way valve to all open
12. Open header tank drain valve
13. Allow water to passively drain until it stops flowing
14. Set pump suction 3-way valve to pull from separator position

15. Set pump discharge 3-way valve to header tank line closed position
16. Set fill/empty 3-way valve to discharge mostly closed position. This serves to choke the flow coming from the discharge line when the pump is turned on. The closed fill hose valve will prevent water from exiting the other direction. Take this step seriously unless you want to get very wet
17. Hold end of hose in sink
18. Turn on pump
19. The pump will overwhelm the sink drain and the overflow between the two sides of the sink. Turn off the pump when switching sides to avoid a soaking. Repeat until the pump starts drawing air and the flow stops
20. Turn off pump
21. Empty discharge hose into sink
22. Reroll discharge hose for next use
23. Set pump circuit breaker to off position
24. Unplug instrument power supply cable

Appendix G: Selected design drawings Dynamic Earth HAC

Engineering drawing by Blackrock Engineering

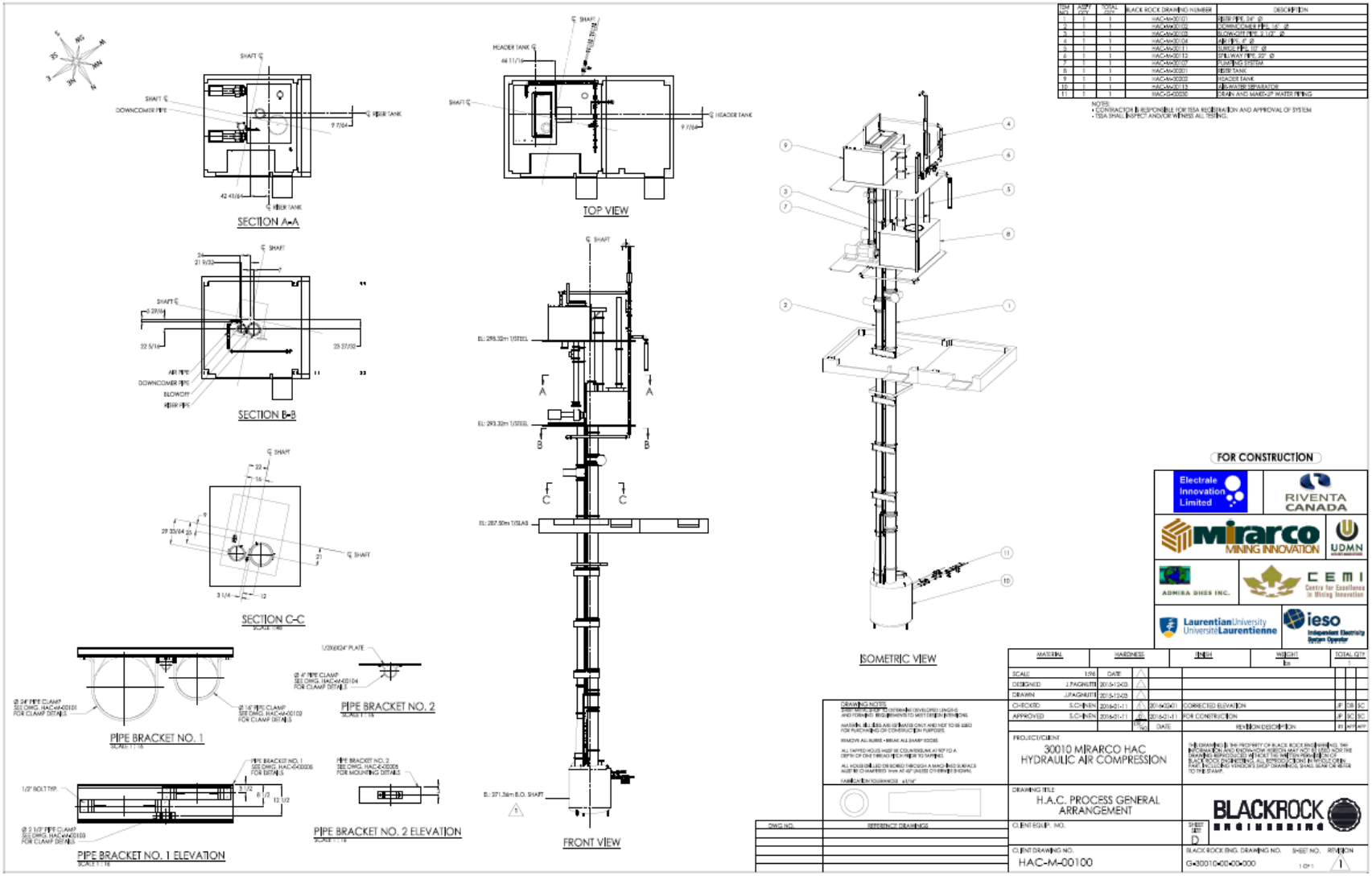

Engineering drawing by Blackrock Engineering

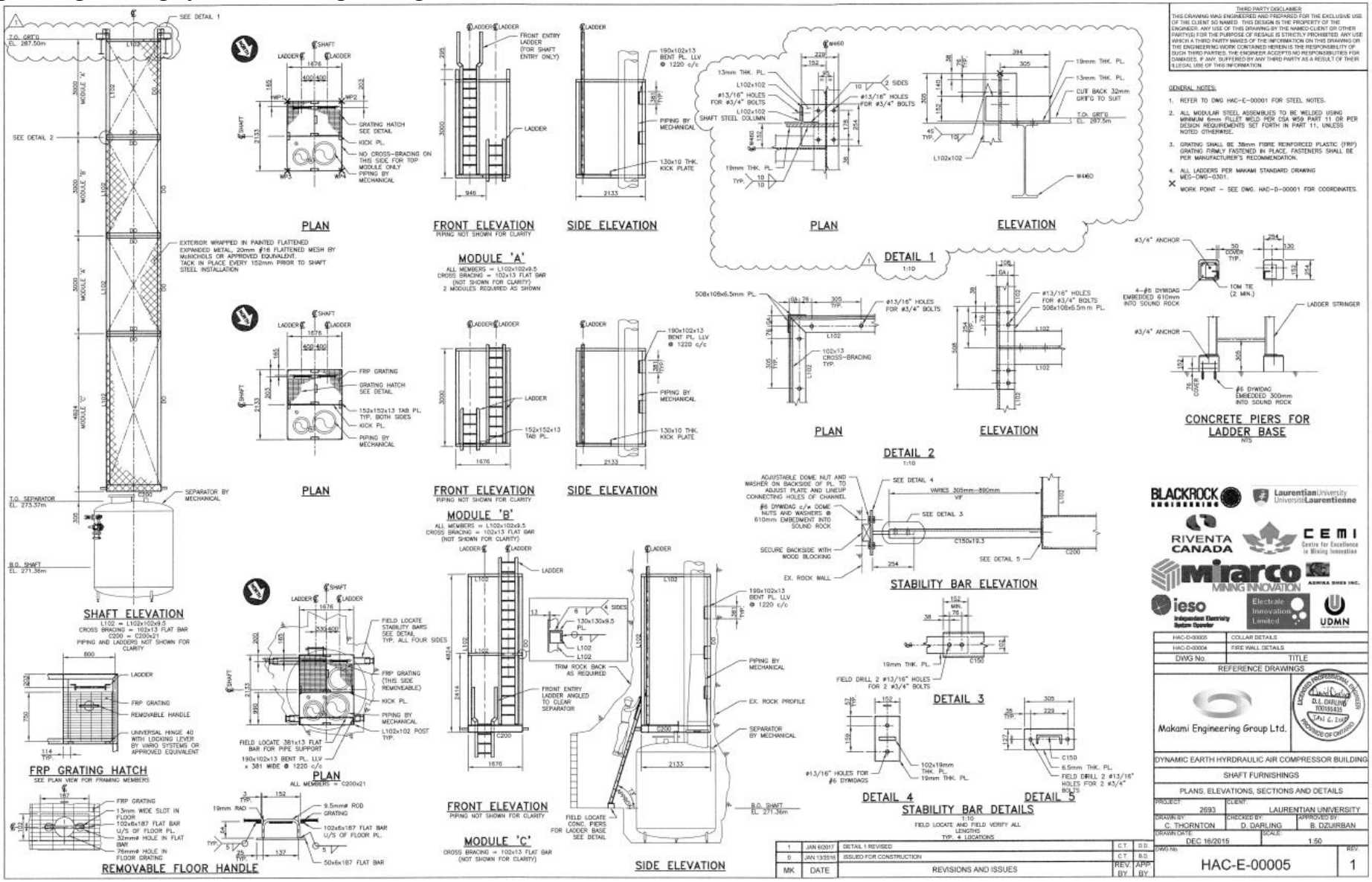

Fabrication drawing by Specialty Alloys and Stainless

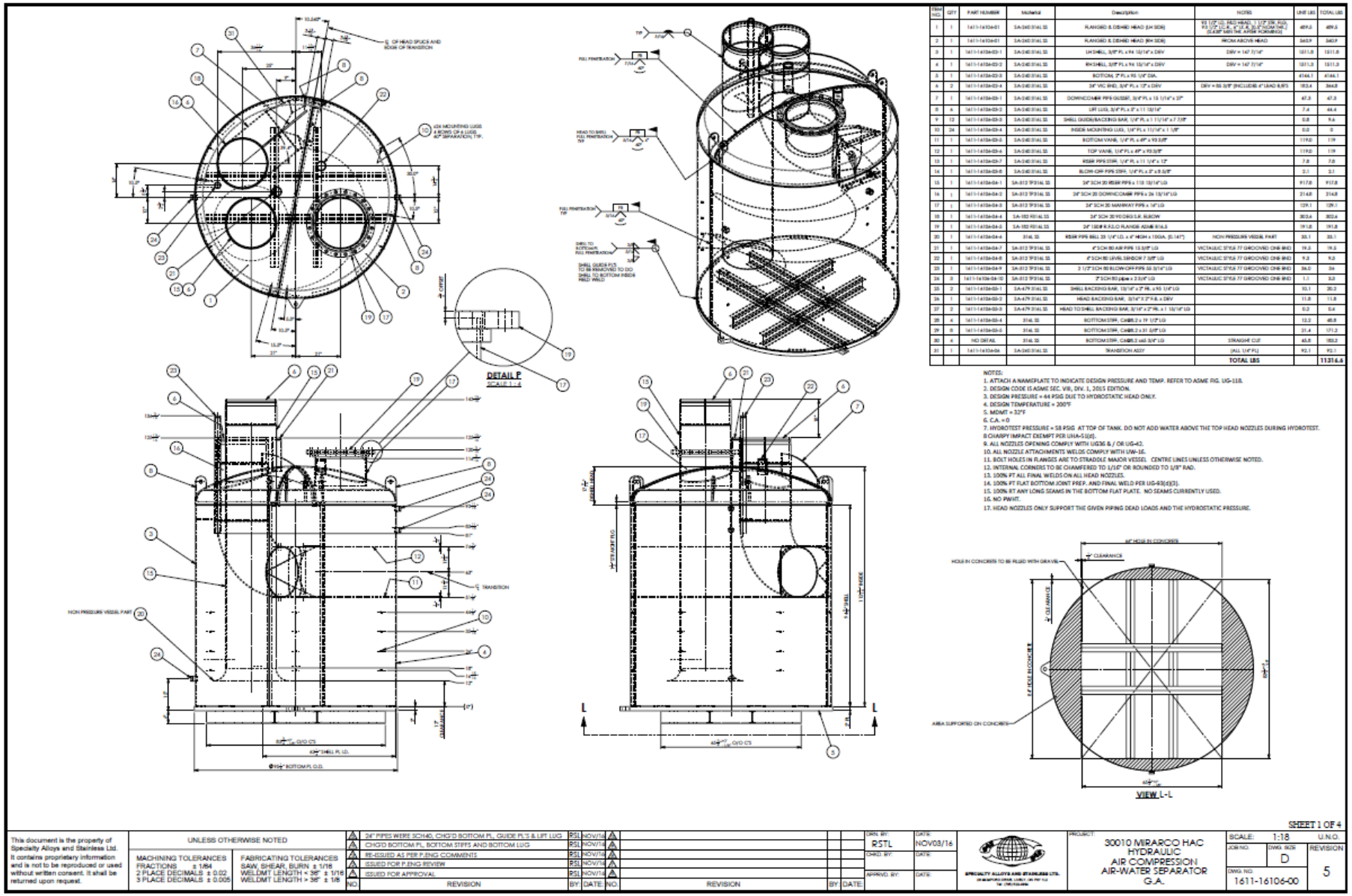

ITEM NO.	QTY	PART NUMBER	Material	Description	NOTES	UNIT LBS	TOTAL LBS
1	1	1611-16104-01	SA-240 316L SS	FLANGED & DISHED HEAD (LH SIDE)	93 1/2" I.D. MED HEAD, 1 1/2" 25# RWD, 93 1/2" I.D. x 1" LIP, 90° SEGMENTS (4pc), (LASP MIN THK AFTER FORMING)	489.0	489.0
2	1	1611-16104-01	SA-240 316L SS	FLANGED & DISHED HEAD (RH SIDE)	FROM ABOVE HEAD	540.9	540.9
3	1	1611-16104-03-1	SA-240 316L SS	LH SHELL, 3/8" PL x 94 13/16" x DRV	DRV = 147 7/16"	1311.8	1311.8
4	1	1611-16104-03-2	SA-240 316L SS	RH SHELL, 3/8" PL x 94 13/16" x DRV	DRV = 147 7/16"	1311.8	1311.8
5	1	1611-16104-03-3	SA-240 316L SS	BOTTOM, 2" PL x 93 1/4" DIA.		4144.1	4144.1
6	2	1611-16104-03-4	SA-240 316L SS	24" VIC BND, 3/8" PL x 12" x DRV	DRV = 55 3/8" (INCLUDES 4" LEAD 8.9°)	183.4	366.8
7	1	1611-16104-03-1	SA-240 316L SS	DOWNCOMER PIPE GUSSET, 3/4" PL x 15 1/16" x 27"		47.3	47.3
8	4	1611-16104-03-2	SA-240 316L SS	LIFT LUG, 3/4" PL x 9" x 11 13/16"		7.4	44.4
9	12	1611-16104-03-3	SA-240 316L SS	SHELL GUIDE/BACKING BAR, 1/4" PL x 1 11/16" x 7 7/8"		0.8	9.6
10	24	1611-16104-03-4	SA-240 316L SS	INSIDE MOUNTING LUG, 1/4" PL x 11 1/4" x 1 1/8"		0.3	5
11	1	1611-16104-03-5	SA-240 316L SS	BOTTOM VANE, 1/4" PL x 49" x 93 3/8"		119.0	119
12	1	1611-16104-03-6	SA-240 316L SS	TOP VANE, 1/4" PL x 49" x 93 3/8"		119.0	119
13	1	1611-16104-03-7	SA-240 316L SS	RISER PIPE STIFF, 3/4" PL x 11 1/4" x 12"		7.8	7.8
14	1	1611-16104-03-8	SA-240 316L SS	BLOW-OFF PIPE STIFF, 1/4" PL x 3" x 8 3/8"		3.1	3.1
15	1	1611-16104-04-1	SA-312 TP316L SS	24" SCH 20 RISER PIPE x 113 13/16" LG		917.8	917.8
16	1	1611-16104-04-2	SA-312 TP316L SS	24" SCH 20 DOWNCOMER PIPE x 24 13/16" LG		314.8	314.8
17	1	1611-16104-04-3	SA-312 TP316L SS	24" SCH 20 MANWAY PIPE x 14" LG		129.1	129.1
18	1	1611-16104-04-4	SA-182 F316L SS	24" SCH 20 90 DEG S.R. ELBOW		302.4	302.4
19	1	1611-16104-04-5	SA-182 F316L SS	24" 150# R.F.S.O. FLANGE ASME B16.5		19.1.8	191.8
20	1	1611-16104-04-6	316L SS	RISER PIPE BELL 23 1/4" I.D. x 4" HIGH x 100GA. (0.147")	NON PRESSURE VESSEL PART	33.1	33.1
21	1	1611-16104-04-7	SA-312 TP316L SS	4" SCH 80 AIR PIPE 13 3/8" LG	VICTAULIC ST'316 77 GROOVND ONE END	19.3	19.3
22	1	1611-16104-04-8	SA-312 TP316L SS	4" SCH 80 LEVEL SENSOR 7 3/8" LG	VICTAULIC ST'316 77 GROOVND ONE END	9.2	9.2
23	1	1611-16104-04-9	SA-312 TP316L SS	3 1/2" SCH 80 BLOW-OFF PIPE 33 3/16" LG	VICTAULIC ST'316 77 GROOVND ONE END	36.0	36
24	2	1611-16106-04-10	SA-312 TP316L SS	2" SCH 80 pipe x 2 3/4" LG	VICTAULIC ST'316 77 GROOVND ONE END	1.7	3.3
25	2	1611-16104-05-1	SA-479 316L SS	SHELL BACKING BAR, 13/16" x 2" PL x 93 13/16" LG		10.1	20.2
26	1	1611-16104-05-2	SA-479 316L SS	HEAD BACKING BAR, 3/16" x 2" PL x DRV		11.8	11.8
27	2	1611-16104-05-3	SA-479 316L SS	HEAD TO SHELL BACKING BAR, 3/16" x 2" PL x 1 13/16" LG		0.2	0.4
28	4	1611-16104-06-4	316L SS	BOTTOM STIFF, CHRD 2 x 19 1/2" LG		12.3	49.3
29	8	1611-16104-06-5	316L SS	BOTTOM STIFF, CHRD 2 x 31 3/8" LG		31.4	171.2
30	8	NO DETAIL	316L SS	BOTTOM STIFF, CHRD 2 x 6 3/8" LG	STRAIGHT CUT	6.0	120.2
31	1	1611-16104-06	SA-240 316L SS	TRANSITION ASSY	(ALL 1/4" PL)	92.1	92.1
					TOTAL LBS		11314.6

NOTES:
1. ATTACH A NAMEPLATE TO INDICATE DESIGN PRESSURE AND TEMP. REFER TO ASME FIG. UG-118.
2. DESIGN CODE IS ASME SEC. VIII, DIV. 1, 2015 EDITION.
3. DESIGN PRESSURE = 44 PSIG DUE TO HYDROSTATIC HEAD ONLY.
4. DESIGN TEMPERATURE = 200°F
5. MDMT = 32°F
6. C.A. = 0
7. HYDROTEST PRESSURE = 58 PSIG AT TOP OF TANK. DO NOT ADD WATER ABOVE THE TOP HEAD NOZZLES DURING HYDROTEST.
8 CHARPY IMPACT EXEMPT PER UHA-51(d).
9. ALL NOZZLES OPENING COMPLY WITH UG36 & / OR UG-42.
10. ALL NOZZLE ATTACHMENTS WELDS COMPLY WITH UW-16.
11. BOLT HOLES IN FLANGES ARE TO STRADDLE MAJOR VESSEL CENTRE LINES UNLESS OTHERWISE NOTED.
12. INTERNAL CORNERS TO BE CHAMFERED TO 1/16" OR ROUNDED TO 1/8" RAD.
13. 100% PT ALL FINAL WELDS ON ALL HEAD NOZZLES.
14. 100% PT FLAT BOTTOM JOINT PREP. AND FINAL WELD PER UG-93(d)(3).
15. 100% RT ANY LONG SEAMS IN THE BOTTOM FLAT PLATE. NO SEAMS CURRENTLY USED.
16. NO PWHT.
17. HEAD NOZZLES ONLY SUPPORT THE GIVEN PIPING DEAD LOADS AND THE HYDROSTATIC PRESSURE.

Fabrication drawing by Specialty Alloys and Stainless

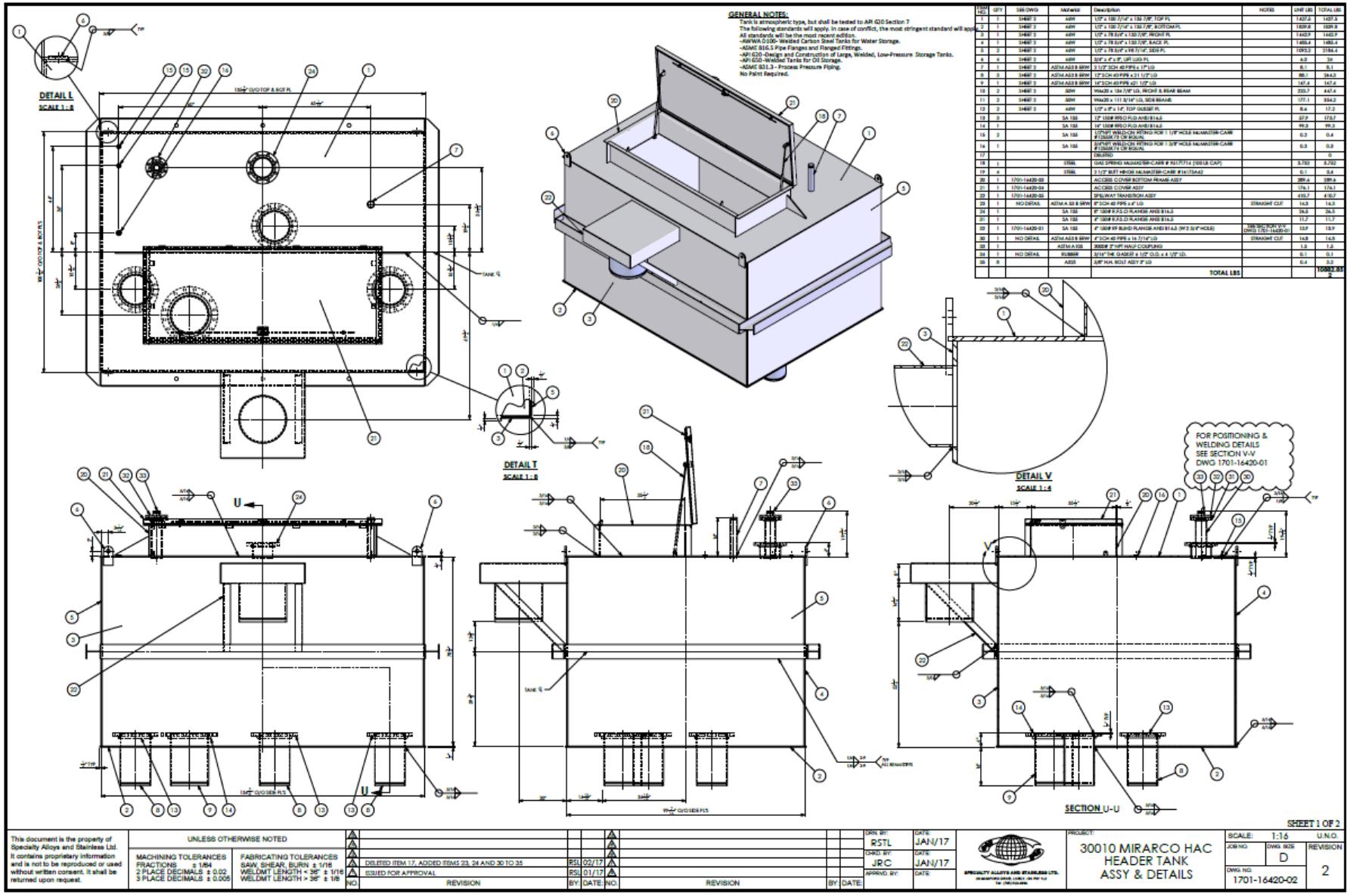

Fabrication drawing by Specialty Alloys and Stainless

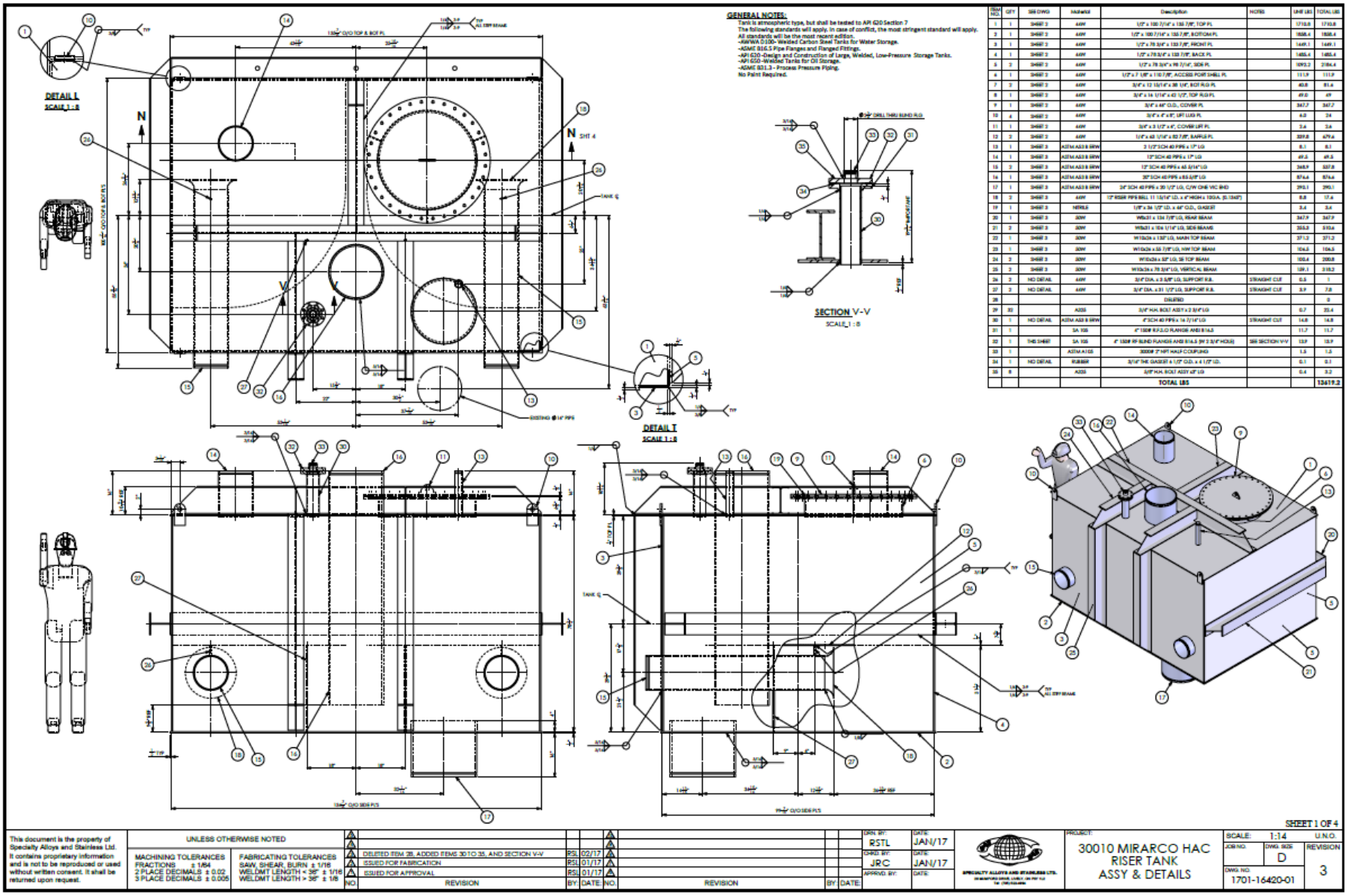

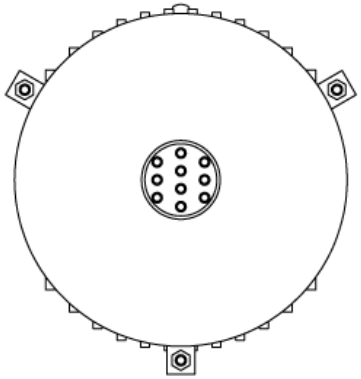

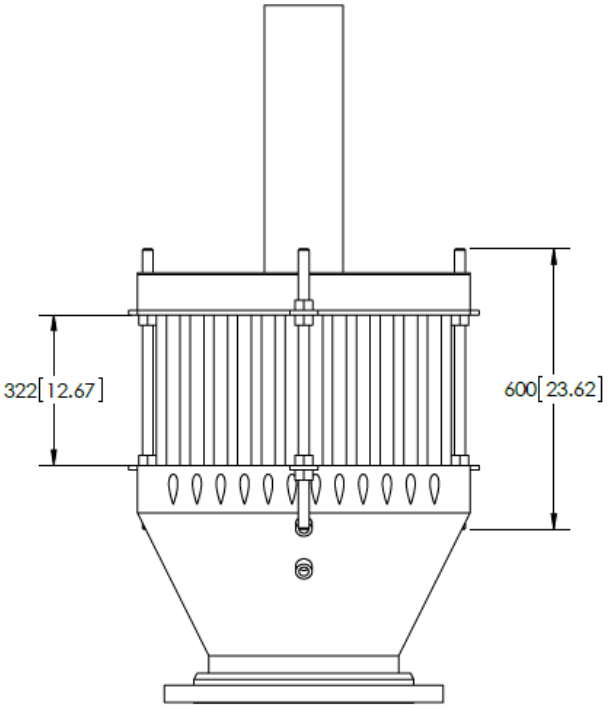

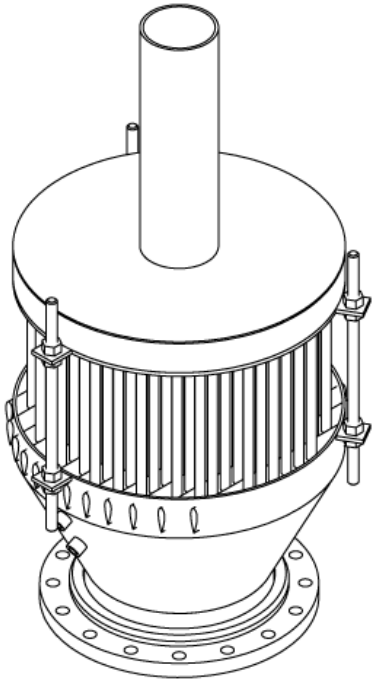

Test assembly fit

DO NOT TRANSPORT ASSEMBLED

ITEM NO.	DESCRIPTION	QTY.
1	Lower head weldment	1
2	Upper head weldment	1
3	threaded support & positioning rod	3
4	1-8 hex nut	12

		NAME	DATE
UNLESS OTHERWISE SPECIFIED:			
DIMENSIONS ARE IN MILLIMETRES [INCHES] TOLERANCE: ± 1 MM UNLESS OTHERWISE NOTED	DRAWN		
	CHECKED		
	ENG APPR.		
	MFG APPR.		
	Q.A.		
MATERIAL: See table	COMMENTS:		
FINISH			
DO NOT SCALE DRAWING			

TITLE: Full head assembly

SIZE	DWG. NO.	REV
B		
SCALE: 1:10	WEIGHT:	SHEET 1 OF 1

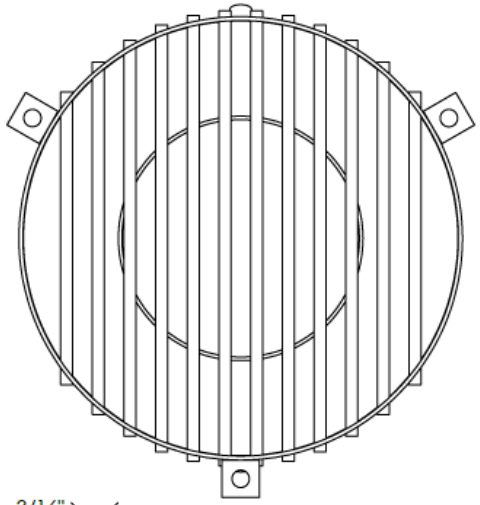

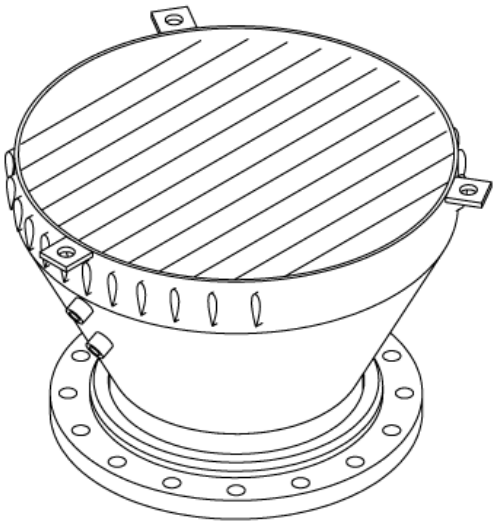

Use a minumum 3/16" fillet weld per CSA W59 Part 11 along bottom and both sides of each support tab. Use a 3/16" V weld on the upper surface

Use a minumum 3/16" V weld per CSA W59 Part 11 to attach hydrofoil weldment and flange attachment ring to 28 to 16 transition piece

Use a minumum 3/16" fillet weld per CSA W59 Part 11 to attach the top of the slip-on flange to the flange attachment ring. Use a 3/16" V weld between the face of the slip-on flange and the bottom end of the flange attachment ring. Grind the weld flush with the face of the flange.

Sand blast clean and paint. Note: do not paint the face of the slip-on flange

Line up couplings with hydrofoils, drill through couplings into shell to minimum diameter of 21 mm (0.82 in)

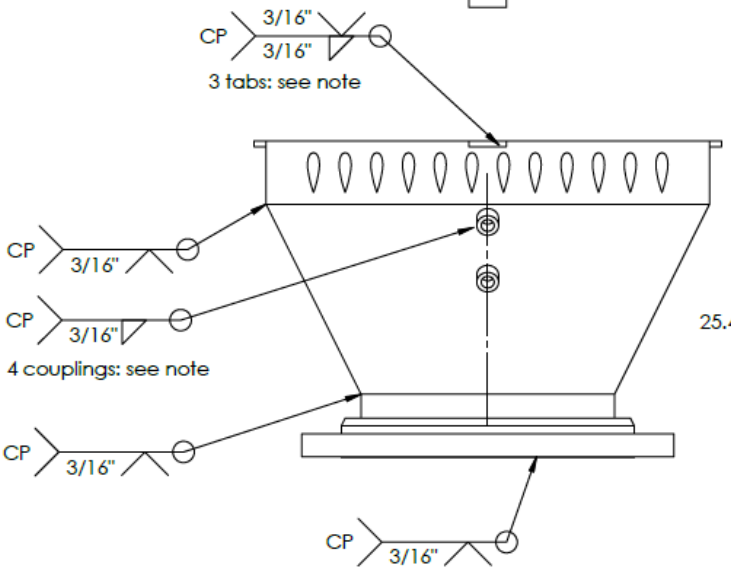

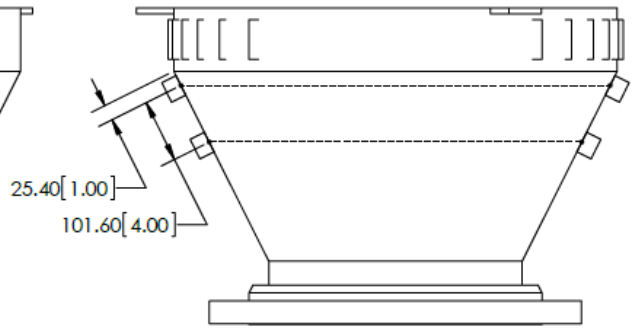

ITEM NO.	PART NUMBER	QTY.
1	28 to 16 transition piece	1
2	Flange attachment ring	1
3	150 class slip on flange	1
4	support tab	3
5	Hydrofoil weldment	1
6	3/4" class 3000 NPT half coupling	4

		NAME	DATE
UNLESS OTHERWISE SPECIFIED:			
DIMENSIONS ARE IN MILLIMETRES [INCHES] TOLERANCE: ± 1 MM UNLESS OTHERWISE NOTED	DRAWN		
	CHECKED		
	ENG APPR.		
	MFG APPR.		
	Q.A.		
MATERIAL: See table	COMMENTS:		
FINISH			
DO NOT SCALE DRAWING			

TITLE:

Lower head weldment

SIZE	DWG. NO.	REV
B		
SCALE: 1:7.5	WEIGHT:	SHEET 1 OF 1

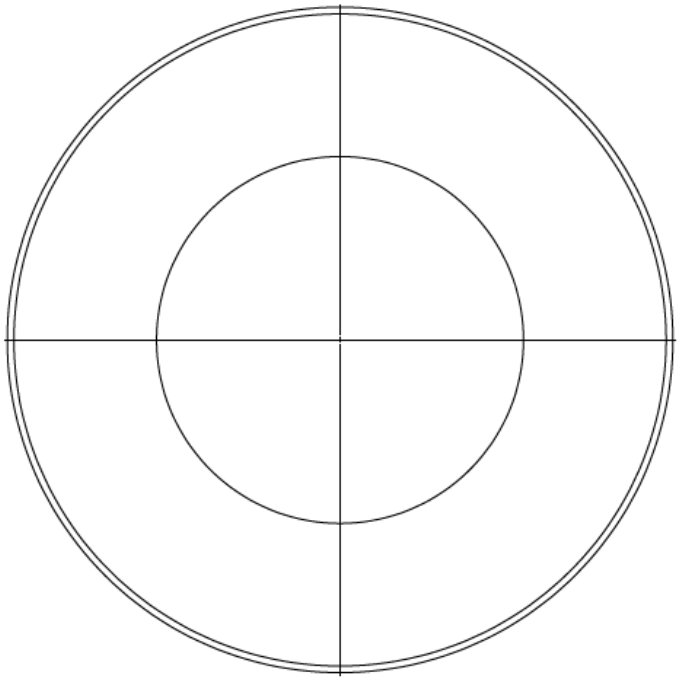

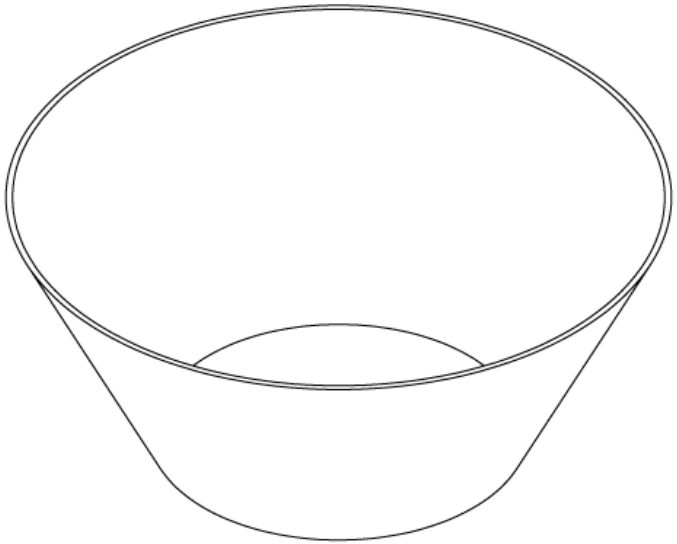

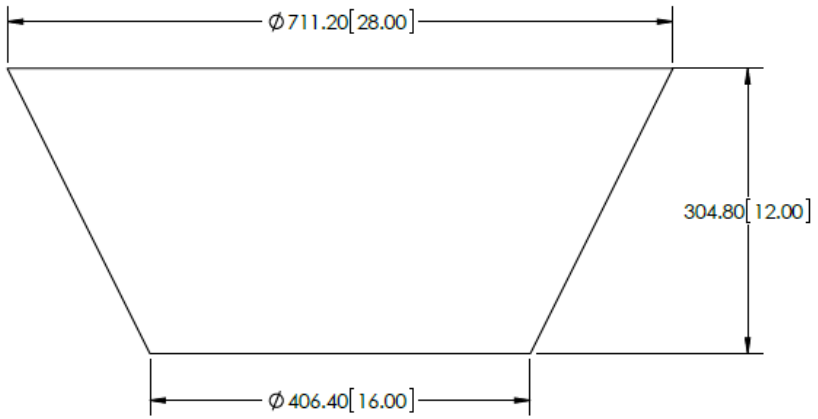

UNLESS OTHERWISE SPECIFIED:		NAME	DATE
DIMENSIONS ARE IN MILLIMETRES [INCHES] TOLERANCE: ± 1 MM UNLESS OTHERWISE NOTED	DRAWN		
	CHECKED		
	ENG APPR.		
	MFG APPR.		
	Q.A.		
MATERIAL: 1/4" mild steel plate	COMMENTS:		
FINISH			
DO NOT SCALE DRAWING			

TITLE:

28" to 16" transition piece

SIZE	DWG. NO.	REV
B		
SCALE: 1:5	WEIGHT:	SHEET 1 OF 1

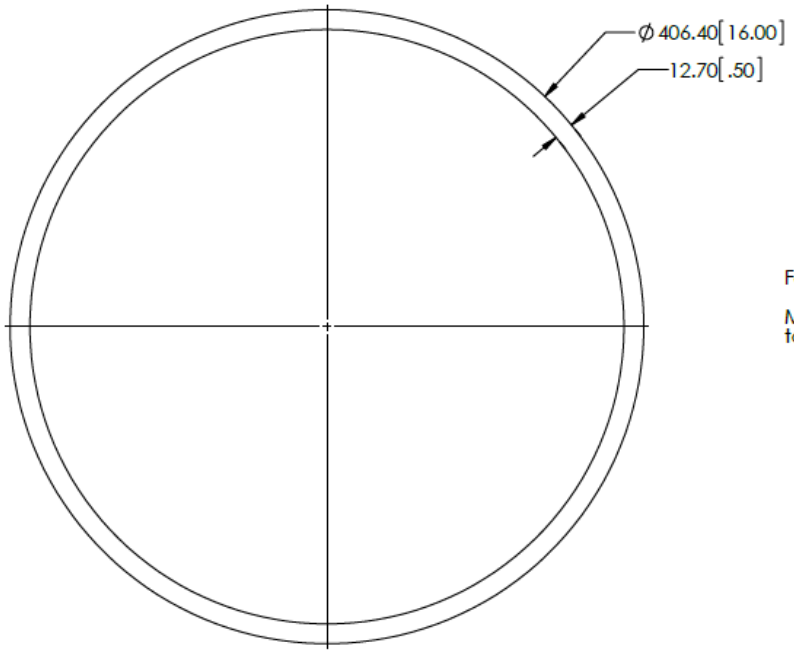

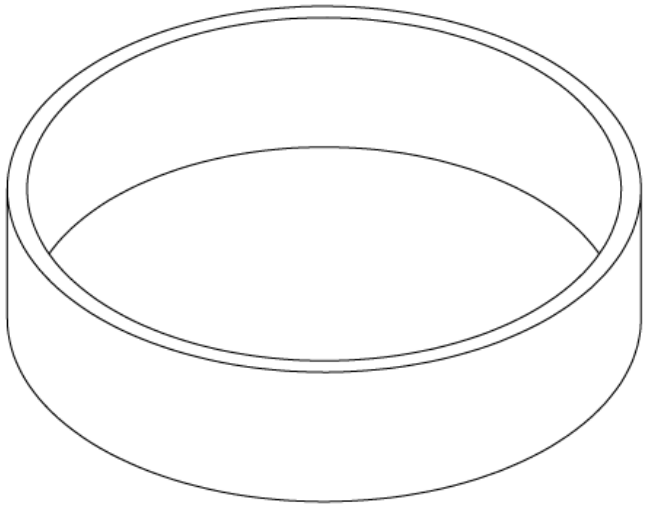

Fabricate from plate or 16" pipe

Material thickness required for smooth flow transition to pipe below head

UNLESS OTHERWISE SPECIFIED:		NAME	DATE
DIMENSIONS ARE IN MILLIMETRES [INCHES] TOLERANCE: ± 1 MM UNLESS OTHERWISE NOTED	DRAWN		
	CHECKED		
	ENG APPR.		
	MFG APPR.		
	Q.A.		
MATERIAL: Mild steel (see note)	COMMENTS:		
FINISH			
DO NOT SCALE DRAWING			

TITLE: Flange attachment ring

SIZE B	DWG. NO.	REV
SCALE: 1:3	WEIGHT:	SHEET 1 OF 1

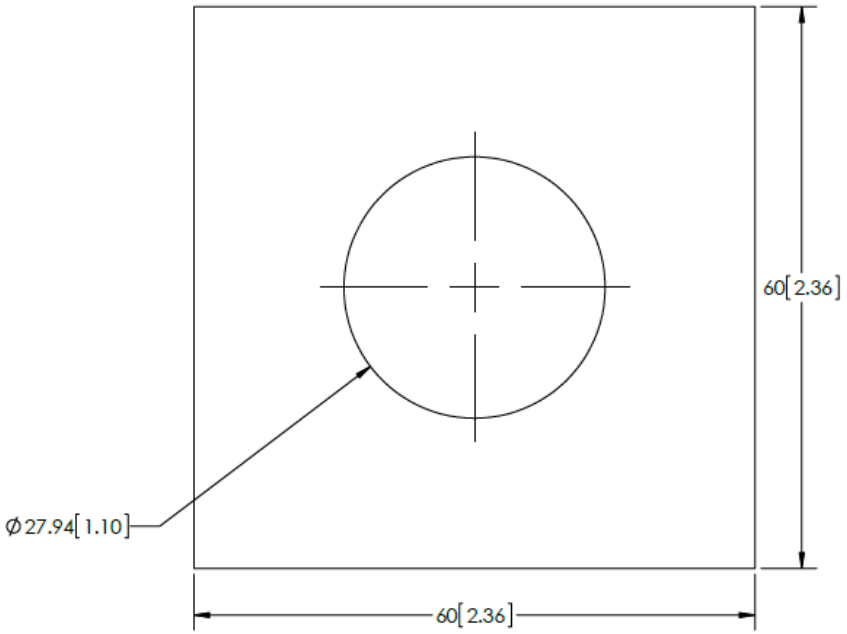

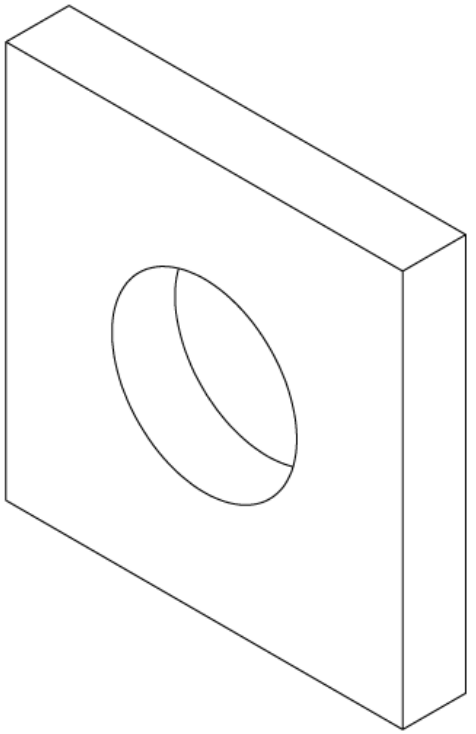

UNLESS OTHERWISE SPECIFIED:		NAME	DATE
DIMENSIONS ARE IN MILLIMETRES [INCHES] TOLERANCE: ± 1 MM UNLESS OTHERWISE NOTED	DRAWN		
	CHECKED		
	ENG APPR.		
	MFG APPR.		
	Q.A.		
MATERIAL: 3/8" mild steel plate	COMMENTS:		
FINISH			
DO NOT SCALE DRAWING			

TITLE: Support tab

SIZE	DWG. NO.	REV
B		
SCALE: 2:1	WEIGHT:	SHEET 1 OF 1

Use a minumum 3/16" fillet weld per CSA W59 Part 11 on both ends of each hydrofoil

Holes required to place hydrofoils not included in hydrofoil holder ring drawing. Cut to fit

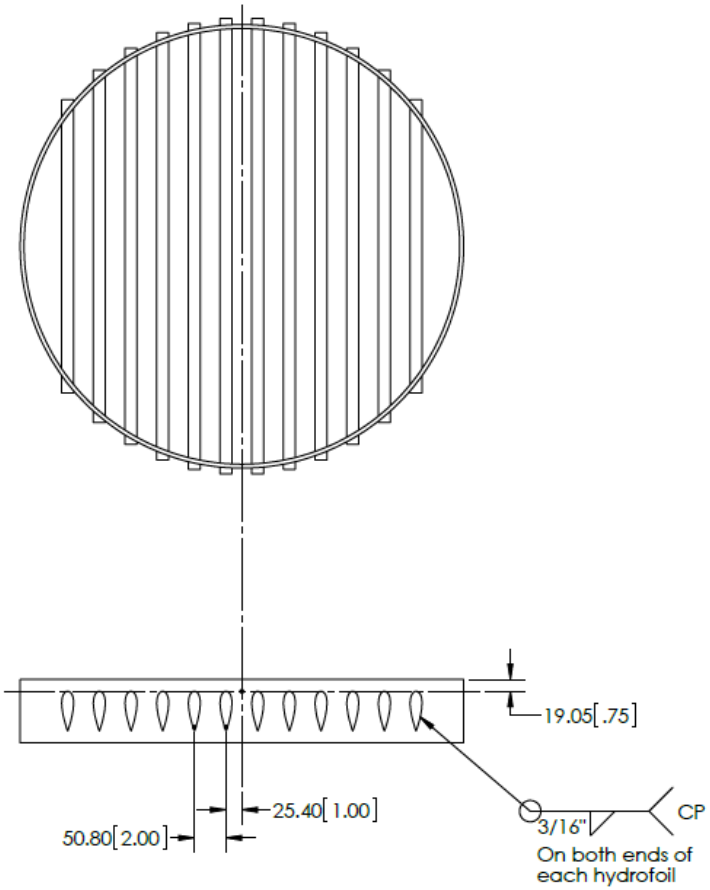

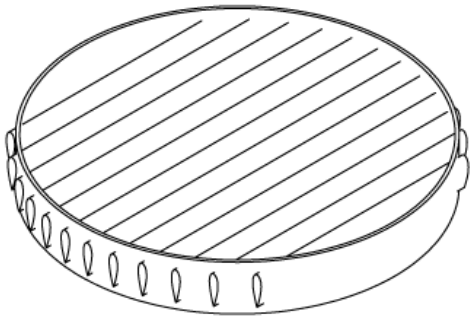

ITEM NO.	DESCRIPTION	QTY.
1	Hydrofoil holder ring	1
2	Hydrofoil 470	2
3	Hydrofoil 565	2
4	Hydrofoil 635	2
5	Hydrofoil 685	2
6	Hydrofoil 715	2
7	Hydrofoil 730	2

		NAME	DATE
UNLESS OTHERWISE SPECIFIED:			
DIMENSIONS ARE IN MILLIMETRES [INCHES] TOLERANCE: ± 1 MM UNLESS OTHERWISE NOTED	DRAWN		
	CHECKED		
	ENG APPR.		
	MFG APPR.		
	Q.A.		
MATERIAL: See table	COMMENTS:		
FINISH			
DO NOT SCALE DRAWING			

TITLE: Hydrofoil weldment

SIZE	DWG. NO.	REV
B		

SCALE: 1:7.5 WEIGHT: SHEET 1 OF 1

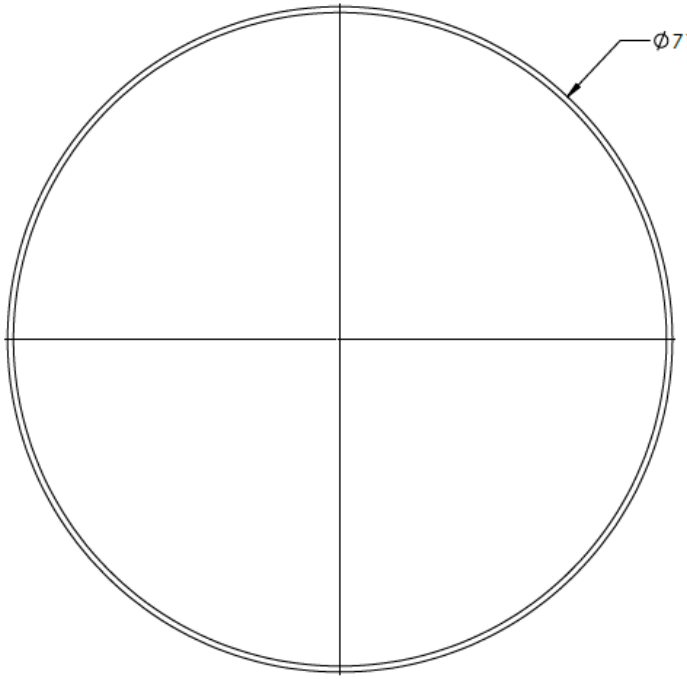

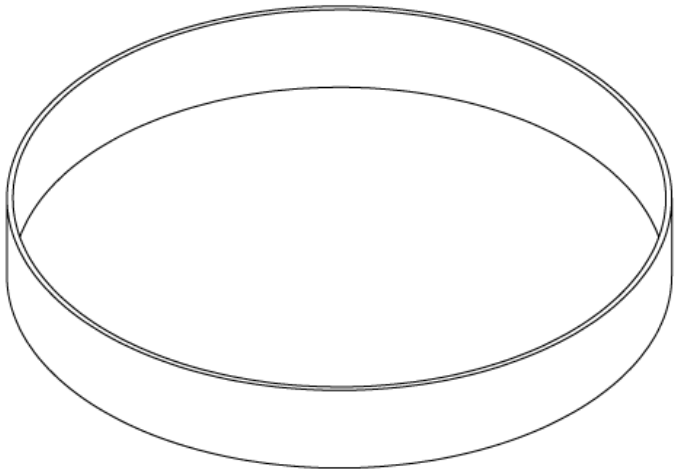

Fabricate from plate or 28" pipe
Minimum thickness: 1/4"

UNLESS OTHERWISE SPECIFIED:		NAME	DATE
DIMENSIONS ARE IN MILLIMETRES [INCHES] TOLERANCE: ± 1 MM UNLESS OTHERWISE NOTED	DRAWN		
	CHECKED		
	ENG APPR.		
	MFG APPR.		
	Q.A.		
MATERIAL: Mild steel (see note)	COMMENTS:		
FINISH			
DO NOT SCALE DRAWING			

TITLE:

Hydrofoil holder ring

SIZE B	DWG. NO.	REV
SCALE: 1:5	WEIGHT:	SHEET 1 OF 1

Hydrofoil length (mm)	Quantity
470	2
565	2
635	2
685	2
715	2
730	2

Length is projected out of page

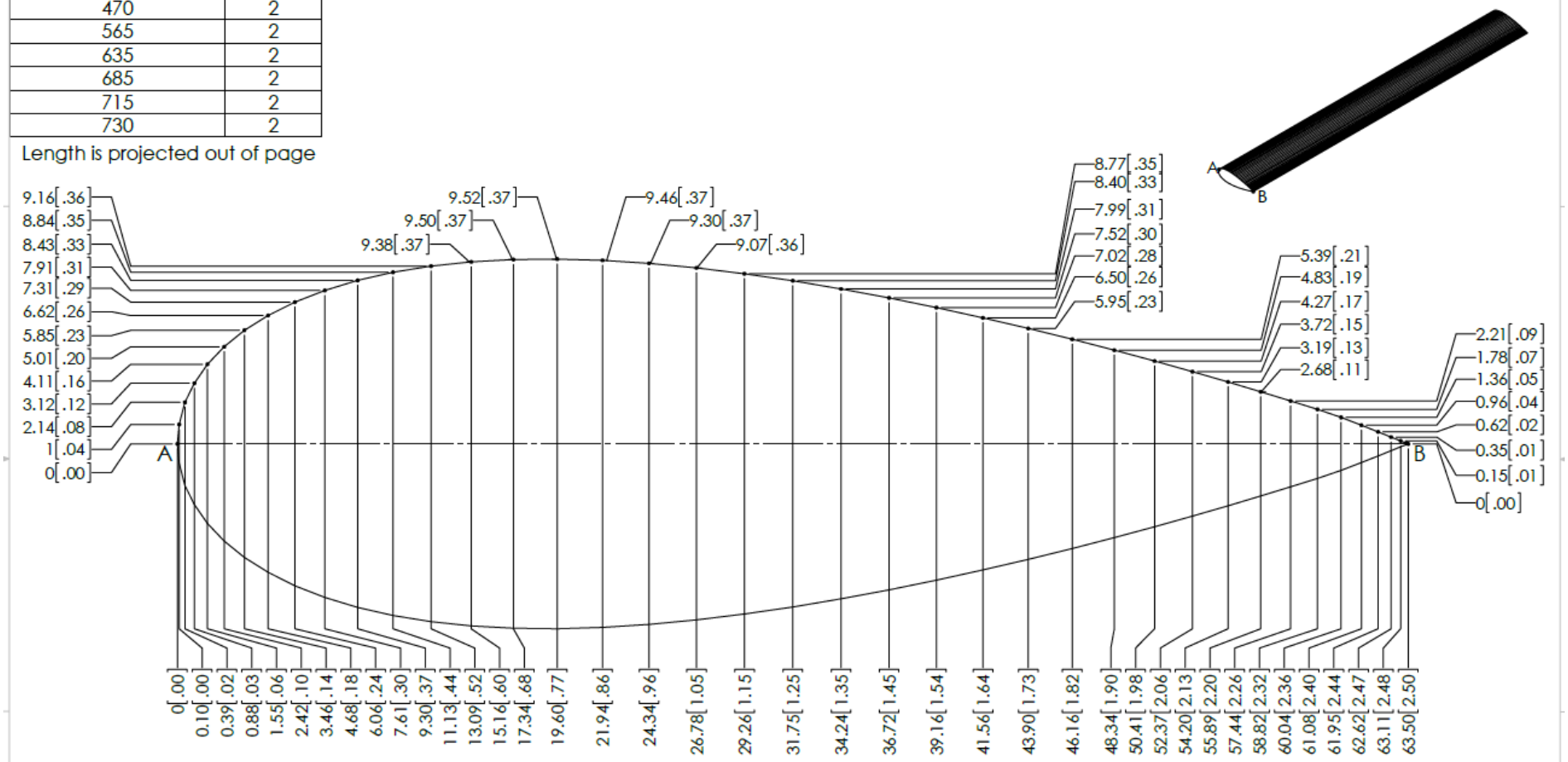

Scale 5:1

UNLESS OTHERWISE SPECIFIED:		NAME	DATE
DIMENSIONS ARE IN MILLIMETRES [INCHES] TOLERANCE: ± 1 MM UNLESS OTHERWISE NOTED	DRAWN		
	CHECKED		
	ENG APPR.		
	MFG APPR.		
	Q.A.		
MATERIAL: Mild steel flat bar	COMMENTS:		
FINISH			
DO NOT SCALE DRAWING			

TITLE: Hydrofoil

SIZE	DWG. NO.	REV
B		

SCALE: 1:5 | WEIGHT: | SHEET 1 OF 1

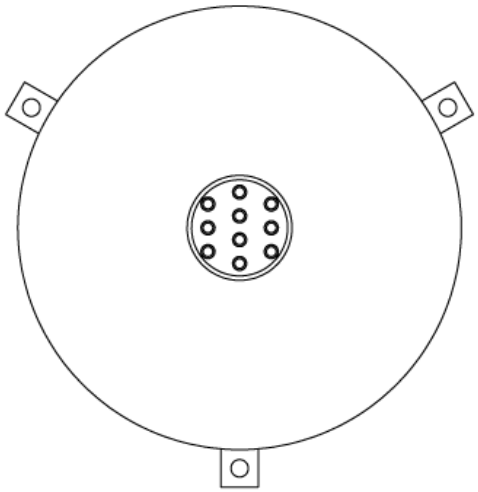

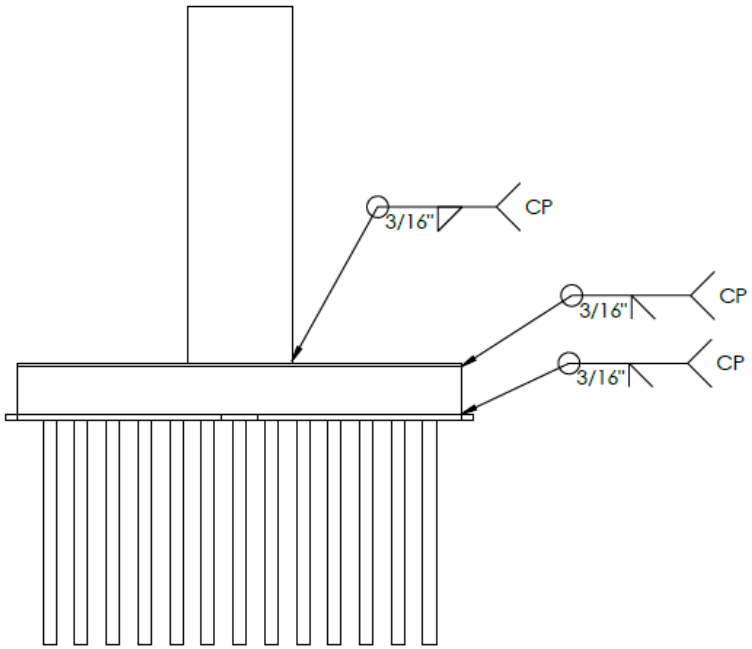

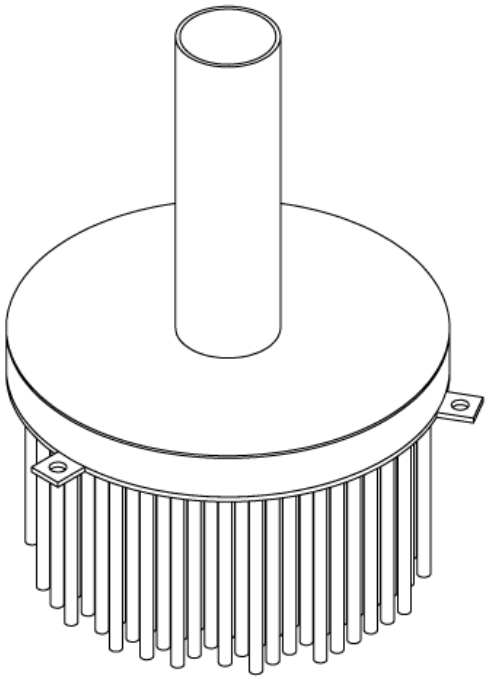

Use a minumum 3/16" fillet weld per CSA W59 Part 11 to attach snorkel pipe to air chamber upper plate

Use a minumum 3/16" bevel weld per CSA W59 Part 11 to attach air pipe weldment and air chamber upper plate to air chamber container ring

Sand blast clean and paint. Note: do not paint the inside of the air pipes, snorkel, or air chamber

ITEM NO.	DESCRIPTION	QTY.
1	Air pipe weldment	1
2	air chamber upper plate	1
3	snorkel pipe	1
4	Air chamber container ring	1

		NAME	DATE
UNLESS OTHERWISE SPECIFIED:			
DIMENSIONS ARE IN MILLIMETRES [INCHES] TOLERANCE: ± 1 MM UNLESS OTHERWISE NOTED	DRAWN		
	CHECKED		
	ENG APPR.		
	MFG APPR.		
	Q.A.		
MATERIAL: See table	COMMENTS:		
FINISH			
DO NOT SCALE DRAWING			

TITLE:

Upper head weldment

SIZE	DWG. NO.	REV
B		
SCALE: 1:7.5	WEIGHT:	SHEET 1 OF 1

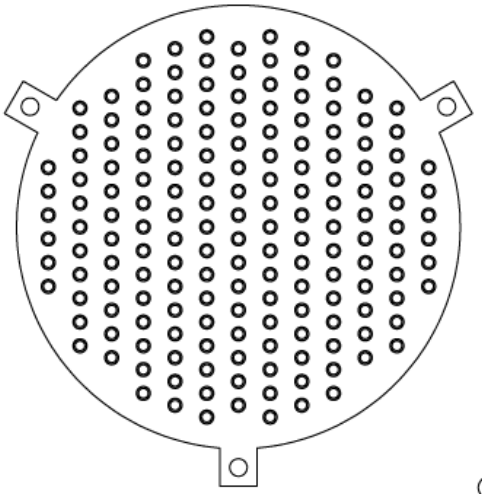

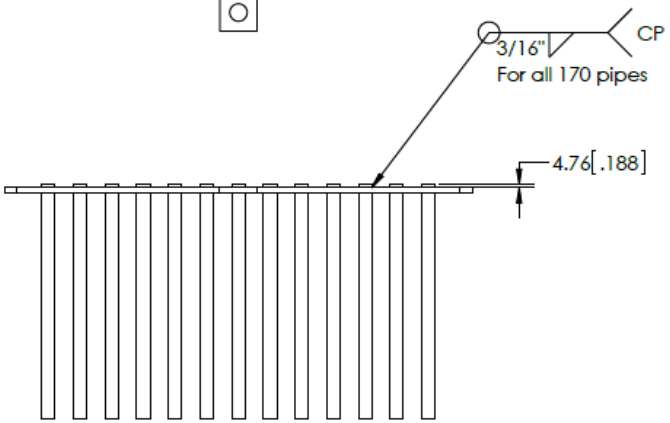

Use a minumum 3/16" fillet weld per CSA W59 Part 11 for all pipes

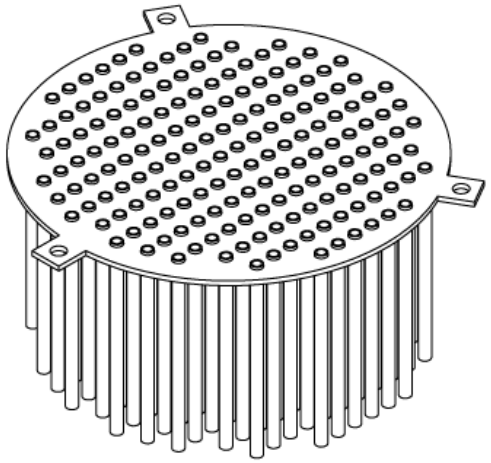

ITEM NO.	DESCRIPTION	QTY.
1	air pipe	170
2	air chamber lower plate	1

		NAME	DATE
UNLESS OTHERWISE SPECIFIED:			
DIMENSIONS ARE IN MILLIMETRES [INCHES] TOLERANCE: ± 1 MM UNLESS OTHERWISE NOTED	DRAWN		
	CHECKED		
	ENG APPR.		
	MFG APPR.		
	Q.A.		
MATERIAL: See table	COMMENTS:		
FINISH			
DO NOT SCALE DRAWING			

TITLE:

Air pipe weldment

SIZE	DWG. NO.	REV
B		
SCALE: 1:7.5	WEIGHT:	SHEET 1 OF 1

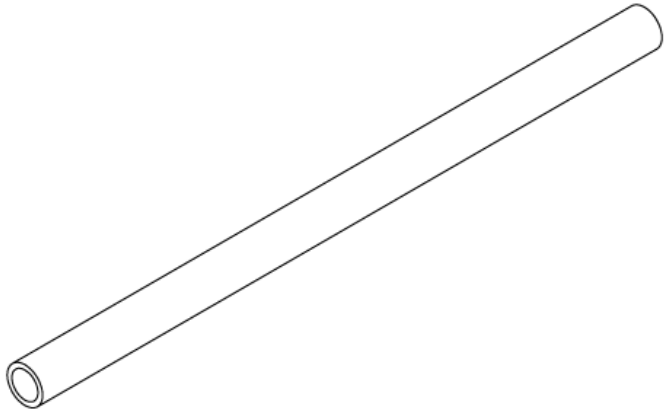

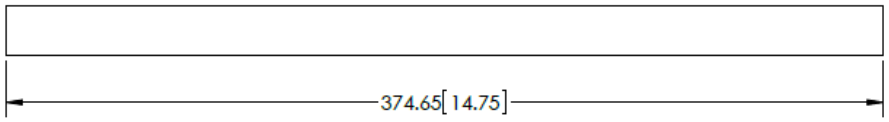

UNLESS OTHERWISE SPECIFIED:		NAME	DATE
DIMENSIONS ARE IN MILLIMETRES [INCHES] TOLERANCE: ± 1 MM UNLESS OTHERWISE NOTED	DRAWN		
	CHECKED		
	ENG APPR.		
	MFG APPR.		
	Q.A.		
MATERIAL 1/2" pipe sch 40	COMMENTS:		
FINISH			
DO NOT SCALE DRAWING			

TITLE: Air pipe

SIZE	DWG. NO.	REV
B		

SCALE: 1:2	WEIGHT:	SHEET 1 OF 1

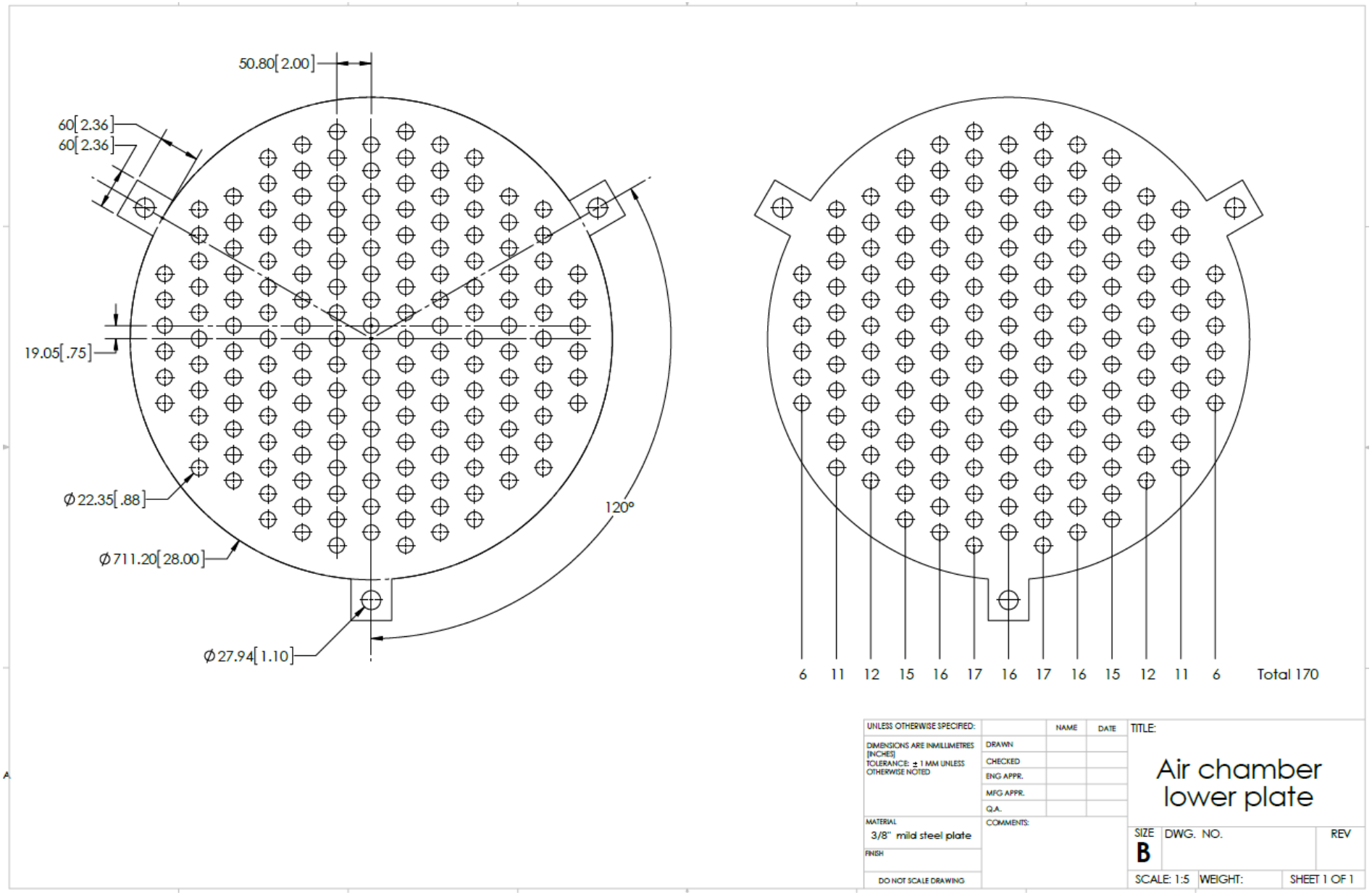

UNLESS OTHERWISE SPECIFIED:		NAME	DATE
DIMENSIONS ARE IN MILLIMETRES [INCHES] TOLERANCE: ± 1 MM UNLESS OTHERWISE NOTED	DRAWN		
	CHECKED		
	ENG APPR.		
	MFG APPR.		
	Q.A.		
MATERIAL: 3/8" mild steel plate	COMMENTS:		
FINISH			
DO NOT SCALE DRAWING			

TITLE: Air chamber lower plate

SIZE	DWG. NO.	REV
B		

SCALE: 1:5 | WEIGHT: | SHEET 1 OF 1

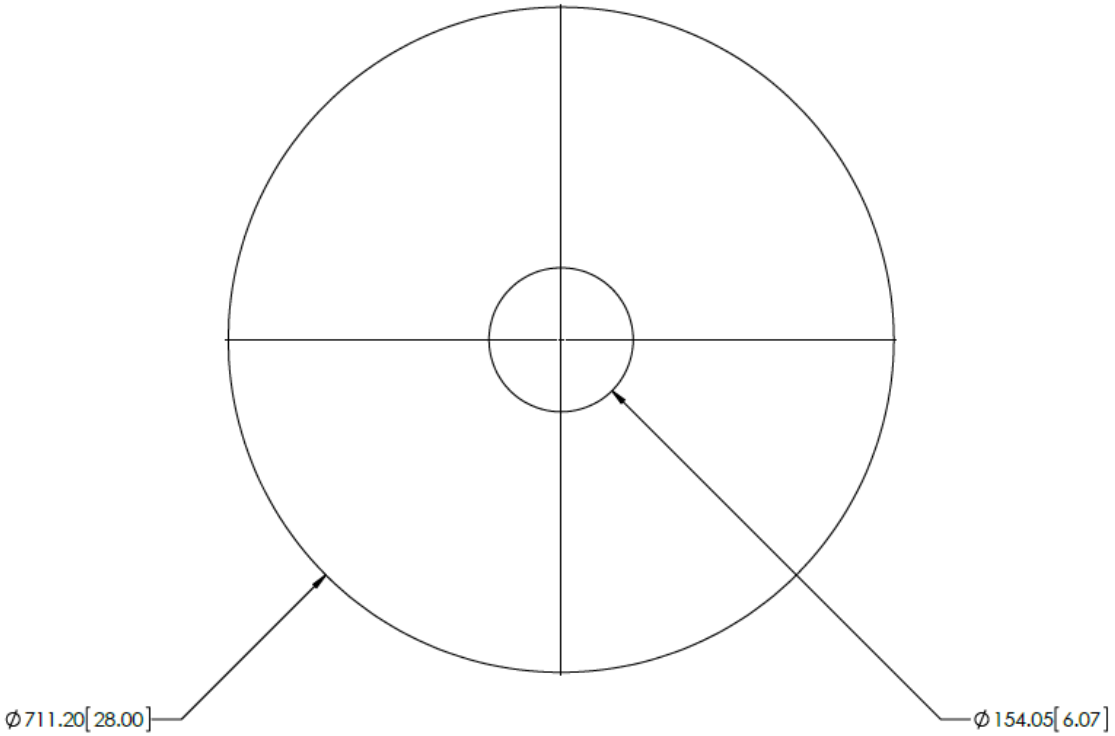

UNLESS OTHERWISE SPECIFIED:		NAME	DATE
DIMENSIONS ARE IN MILLIMETRES [INCHES] TOLERANCE: ± 1 MM UNLESS OTHERWISE NOTED	DRAWN		
	CHECKED		
	ENG APPR.		
	MFG APPR.		
	Q.A.		
MATERIAL: 3/16" mild steel plate	COMMENTS:		
FINISH			
DO NOT SCALE DRAWING			

TITLE:

Air chamber upper plate

SIZE	DWG. NO.	REV
B		
SCALE: 1:5	WEIGHT:	SHEET 1 OF 1

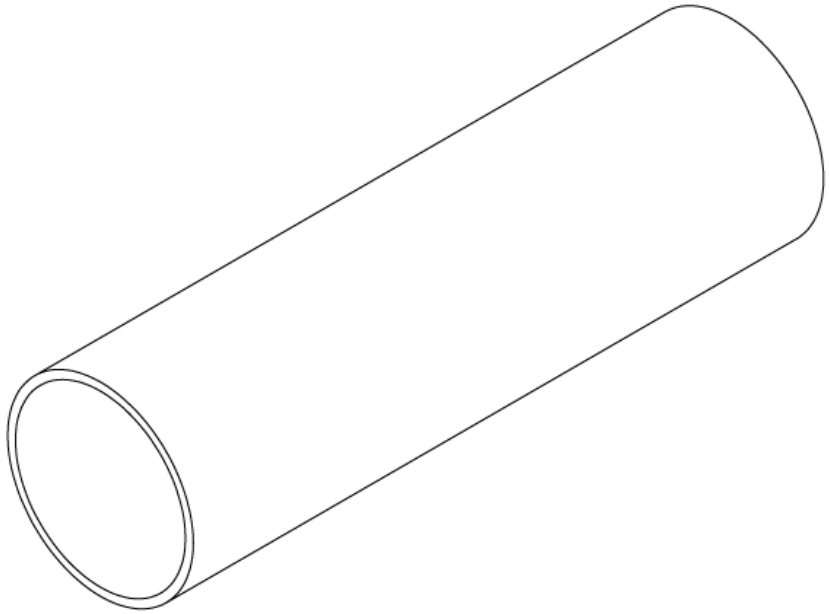

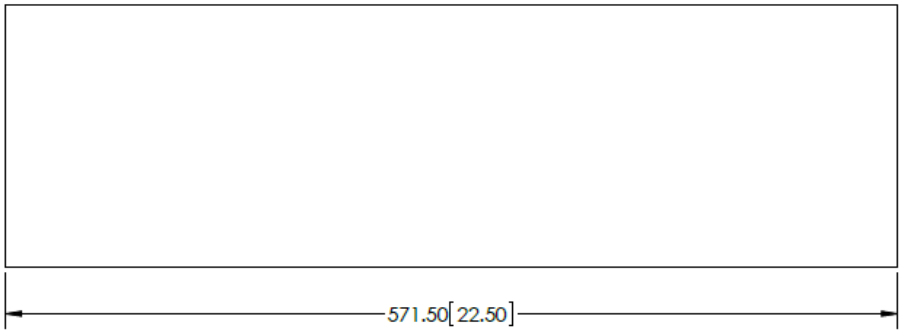

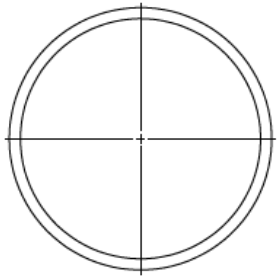

UNLESS OTHERWISE SPECIFIED:		NAME	DATE
DIMENSIONS ARE IN MILLIMETRES [INCHES] TOLERANCE: ± 1 MM UNLESS OTHERWISE NOTED	DRAWN		
	CHECKED		
	ENG APPR.		
	MFG APPR.		
	Q.A.		
MATERIAL 6" pipe sch 40	COMMENTS:		
FINISH			
DO NOT SCALE DRAWING			

TITLE:

Snorkel pipe

SIZE	DWG. NO.	REV
B		
SCALE: 1:3	WEIGHT:	SHEET 1 OF 1

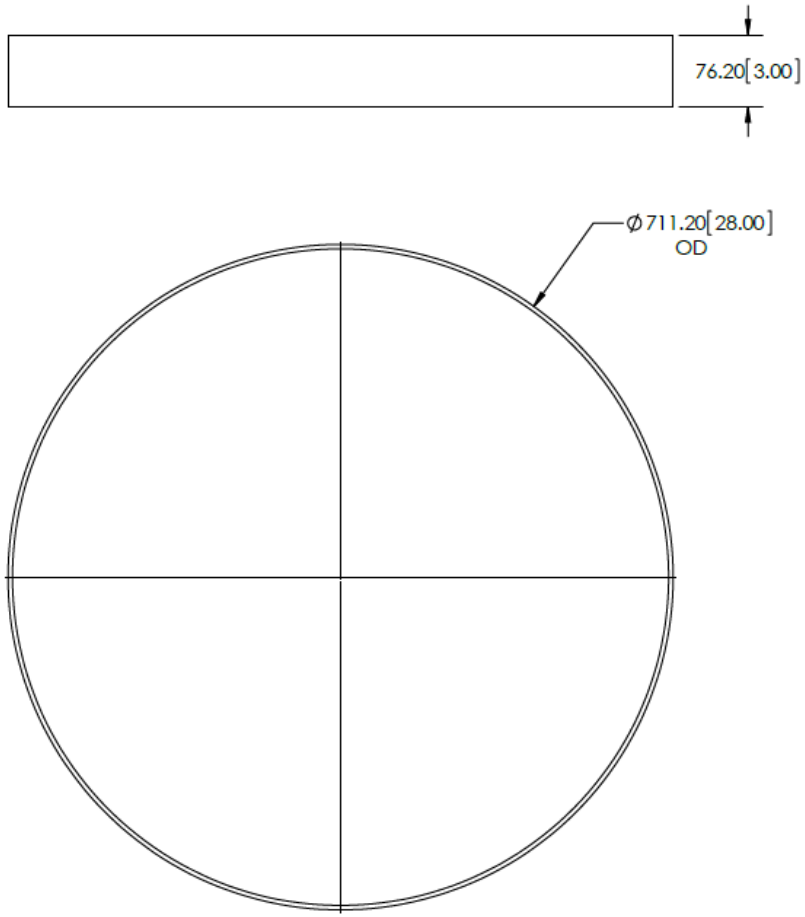

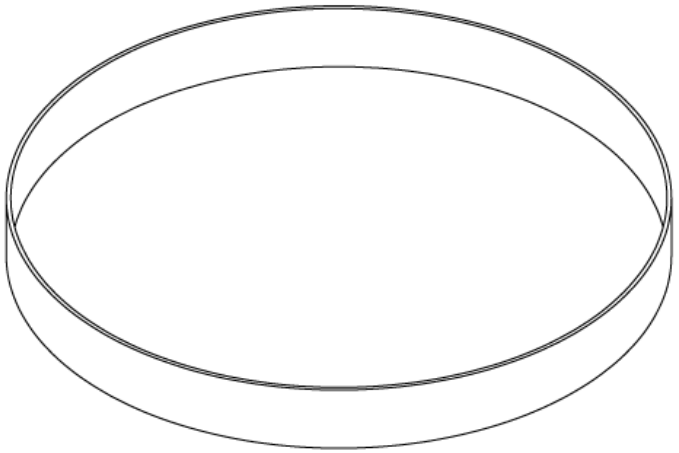

Fabricate from plate or 28" pipe
Minimum thickness: 3/16"

UNLESS OTHERWISE SPECIFIED:		NAME	DATE
DIMENSIONS ARE IN MILLIMETRES [INCHES] TOLERANCE: ± 1 MM UNLESS OTHERWISE NOTED	DRAWN		
	CHECKED		
	ENG APPR.		
	MFG APPR.		
	Q.A.		
MATERIAL: Mild steel (see note)	COMMENTS:		
FINISH			
DO NOT SCALE DRAWING			

TITLE:

Air chamber container ring

SIZE	DWG. NO.	REV
B		

SCALE: 1:5	WEIGHT:	SHEET 1 OF 1

Appendix H: Mixing head comparison data from Baby HAC

The tables below present the relevant variables from the mixing head comparison tests on Baby HAC. Measured values from the instrument log are presented in *italics*. The temperatures and pressures used to derive the densities reported here are not included in the tables. The mass flow of air in is equal to the mass flow of air out (i.e. air productivity is close to unity). Descriptions for these mixing heads can be found in sections 5.1.2 and 6.1.1.

Snorkel head: no snorkel configuration

Density (kg/m3)		Water flow rate		Air flow rate			Water elevation header (m)	Mixing head lip elevation (m)	Water level over mixing head lip (m)	Water elevation tailrace (m)
Air (in)	Water	(kg/s)	(m3/s)	(kg/s)	in (m3/s)	out (m3/s)				
1.161	999.3	*2.2*	0.0022	*0.000082*	0.000071	0.000053	*4.281*	4.264	0.017	*3.301*
1.165	999.2	*2.6*	0.0026	*0.000135*	0.000116	0.000088	*4.282*	4.264	0.018	*3.299*
1.166	999.2	*2.4*	0.0024	*0.000140*	0.000120	0.000091	*4.283*	4.264	0.019	*3.295*
1.167	999.1	*2.5*	0.0025	*0.000179*	0.000153	0.000116	*4.285*	4.264	0.021	*3.294*
1.168	999.1	*3.1*	0.0031	*0.000204*	0.000175	0.000133	*4.285*	4.264	0.021	*3.301*
1.168	999.0	*3.3*	0.0033	*0.000290*	0.000248	0.000188	*4.288*	4.264	0.024	*3.294*
1.168	999.0	*3.2*	0.0032	*0.000298*	0.000255	0.000193	*4.288*	4.264	0.024	*3.300*
1.168	998.9	*3.6*	0.0036	*0.000342*	0.000293	0.000222	*4.290*	4.264	0.026	*3.311*
1.168	998.9	*3.8*	0.0038	*0.000373*	0.000320	0.000243	*4.292*	4.264	0.028	*3.285*
1.168	998.8	*4.4*	0.0044	*0.000428*	0.000367	0.000279	*4.294*	4.264	0.030	*3.290*
1.168	998.7	*4.8*	0.0048	*0.000473*	0.000405	0.000308	*4.296*	4.264	0.032	*3.283*
1.168	998.7	*4.9*	0.0049	*0.000552*	0.000473	0.000360	*4.296*	4.264	0.032	*3.293*
1.168	998.6	*5.2*	0.0052	*0.000567*	0.000486	0.000369	*4.297*	4.264	0.033	*3.306*
1.171	999.1	*7.4*	0.0074	*0.000812*	0.000693	0.000518	*4.304*	4.264	0.040	*3.325*
1.173	999.0	*7.4*	0.0075	*0.000856*	0.000730	0.000549	*4.304*	4.264	0.040	*3.305*
1.173	999.0	*7.4*	0.0074	*0.000827*	0.000705	0.000531	*4.304*	4.264	0.040	*3.314*
1.173	998.9	*7.3*	0.0074	*0.000814*	0.000694	0.000522	*4.304*	4.264	0.040	*3.327*
1.174	998.8	*7.2*	0.0073	*0.000819*	0.000697	0.000527	*4.304*	4.264	0.040	*3.314*
1.174	998.8	*7.2*	0.0072	*0.000803*	0.000684	0.000516	*4.304*	4.264	0.040	*3.327*
1.174	998.7	*7.1*	0.0071	*0.000788*	0.000671	0.000507	*4.304*	4.264	0.040	*3.335*
1.175	998.6	*7.1*	0.0071	*0.000800*	0.000681	0.000517	*4.305*	4.264	0.041	*3.313*

Density (kg/m3)		Water flow rate		Air flow rate			Water elevation header (m)	Mixing head lip elevation (m)	Water level over mixing head lip (m)	Water elevation tailrace (m)
Air (in)	Water	(kg/s)	(m3/s)	(kg/s)	in (m3/s)	out (m3/s)				
1.175	998.5	*6.9*	0.0069	*0.000774*	0.000659	0.000501	*4.305*	4.264	0.041	*3.309*
1.173	998.5	*7.0*	0.0070	*0.000742*	0.000633	0.000478	*4.306*	4.264	0.042	*3.359*
1.172	998.4	*6.8*	0.0068	*0.000764*	0.000652	0.000495	*4.305*	4.264	0.041	*3.321*
1.171	998.3	*6.7*	0.0068	*0.000756*	0.000645	0.000490	*4.305*	4.264	0.041	*3.326*
1.172	998.2	*6.5*	0.0066	*0.000756*	0.000645	0.000492	*4.305*	4.264	0.041	*3.316*
1.170	998.2	*6.5*	0.0065	*0.000693*	0.000592	0.000450	*4.305*	4.264	0.041	*3.338*
1.169	998.1	*6.2*	0.0062	*0.000671*	0.000574	0.000437	*4.304*	4.264	0.040	*3.337*
1.169	998.0	*6.0*	0.0060	*0.000647*	0.000553	0.000421	*4.304*	4.264	0.040	*3.341*
1.169	998.0	*5.8*	0.0058	*0.000644*	0.000551	0.000423	*4.304*	4.264	0.040	*3.308*
1.167	997.9	*5.4*	0.0054	*0.000623*	0.000533	0.000409	*4.303*	4.264	0.039	*3.314*
1.166	997.8	*5.1*	0.0051	*0.000584*	0.000501	0.000383	*4.302*	4.264	0.038	*3.331*
1.166	997.8	*4.8*	0.0048	*0.000558*	0.000478	0.000366	*4.301*	4.264	0.037	*3.335*
1.167	997.7	*4.5*	0.0045	*0.000529*	0.000453	0.000347	*4.301*	4.264	0.037	*3.346*
1.167	997.7	*4.2*	0.0042	*0.000503*	0.000431	0.000330	*4.299*	4.264	0.035	*3.343*
1.166	997.6	*3.7*	0.0038	*0.000416*	0.000357	0.000274	*4.298*	4.264	0.034	*3.332*
1.166	997.6	*3.1*	0.0031	*0.000370*	0.000318	0.000246	*4.295*	4.264	0.031	*3.306*
1.165	997.5	*2.7*	0.0027	*0.000264*	0.000227	0.000176	*4.293*	4.264	0.029	*3.297*
1.165	997.5	*2.2*	0.0022	*0.000189*	0.000162	0.000126	*4.292*	4.264	0.028	*3.307*
1.163	997.4	*3.0*	0.0030	*0.000276*	0.000237	0.000184	*4.293*	4.264	0.029	*3.297*
1.163	997.3	*3.3*	0.0033	*0.000342*	0.000294	0.000228	*4.296*	4.264	0.032	*3.293*
1.162	997.3	*3.7*	0.0038	*0.000407*	0.000350	0.000271	*4.298*	4.264	0.034	*3.296*
1.162	997.2	*4.1*	0.0041	*0.000500*	0.000431	0.000333	*4.300*	4.264	0.036	*3.315*
1.161	997.2	*4.6*	0.0046	*0.000540*	0.000465	0.000359	*4.302*	4.264	0.038	*3.317*
1.162	997.1	*4.8*	0.0048	*0.000570*	0.000491	0.000379	*4.303*	4.264	0.039	*3.311*
1.161	997.0	*5.2*	0.0052	*0.000571*	0.000492	0.000379	*4.305*	4.264	0.041	*3.321*
1.161	997.0	*5.6*	0.0056	*0.000589*	0.000507	0.000389	*4.306*	4.264	0.042	*3.354*
1.160	996.9	*5.8*	0.0059	*0.000641*	0.000553	0.000424	*4.307*	4.264	0.043	*3.336*
1.160	996.8	*6.1*	0.0061	*0.000674*	0.000581	0.000448	*4.308*	4.264	0.044	*3.319*
1.159	996.8	*6.5*	0.0065	*0.000713*	0.000615	0.000473	*4.310*	4.264	0.046	*3.319*

Density (kg/m3)		Water flow rate		Air flow rate			Water elevation header (m)	Mixing head lip elevation (m)	Water level over mixing head lip (m)	Water elevation tailrace (m)
Air (in)	Water	(kg/s)	(m3/s)	(kg/s)	in (m3/s)	out (m3/s)				
1.164	998.9	*7.2*	0.0072	*0.000784*	0.000674	0.000502	*4.304*	4.264	0.040	*3.340*
1.166	998.9	*7.2*	0.0072	*0.000780*	0.000669	0.000499	*4.305*	4.264	0.041	*3.349*
1.167	998.8	*7.3*	0.0073	*0.000820*	0.000702	0.000528	*4.307*	4.264	0.043	*3.313*
1.167	998.7	*7.2*	0.0072	*0.000779*	0.000668	0.000502	*4.308*	4.264	0.044	*3.333*
1.168	998.7	*7.3*	0.0073	*0.000773*	0.000662	0.000496	*4.308*	4.264	0.044	*3.354*
1.168	998.6	*7.1*	0.0072	*0.000811*	0.000695	0.000525	*4.307*	4.264	0.043	*3.318*
1.168	998.5	*7.0*	0.0071	*0.000806*	0.000690	0.000523	*4.307*	4.264	0.043	*3.312*
1.168	998.5	*7.0*	0.0070	*0.000764*	0.000654	0.000494	*4.307*	4.264	0.043	*3.332*
1.168	998.4	*6.8*	0.0069	*0.000747*	0.000640	0.000484	*4.307*	4.264	0.043	*3.331*
1.167	998.3	*6.7*	0.0067	*0.000734*	0.000629	0.000477	*4.307*	4.264	0.043	*3.337*
1.167	998.3	*6.5*	0.0065	*0.000723*	0.000620	0.000470	*4.307*	4.264	0.043	*3.332*
1.166	998.2	*6.2*	0.0062	*0.000685*	0.000588	0.000447	*4.306*	4.264	0.042	*3.334*
1.166	998.1	*5.7*	0.0057	*0.000645*	0.000554	0.000422	*4.305*	4.264	0.041	*3.326*
1.165	998.1	*5.3*	0.0053	*0.000599*	0.000514	0.000392	*4.303*	4.264	0.039	*3.325*
1.165	998.0	*5.3*	0.0054	*0.000612*	0.000525	0.000403	*4.304*	4.264	0.040	*3.301*
1.164	997.9	*5.0*	0.0050	*0.000561*	0.000482	0.000367	*4.303*	4.264	0.039	*3.350*
1.163	997.8	*4.5*	0.0045	*0.000540*	0.000464	0.000356	*4.302*	4.264	0.038	*3.330*
1.163	997.8	*4.4*	0.0044	*0.000518*	0.000446	0.000341	*4.301*	4.264	0.037	*3.343*
1.162	997.7	*4.1*	0.0041	*0.000457*	0.000393	0.000301	*4.300*	4.264	0.036	*3.337*
1.162	997.7	*3.7*	0.0037	*0.000435*	0.000374	0.000288	*4.299*	4.264	0.035	*3.318*
1.162	997.6	*4.0*	0.0040	*0.000454*	0.000390	0.000303	*4.300*	4.264	0.036	*3.283*
1.161	997.5	*3.6*	0.0036	*0.000379*	0.000326	0.000252	*4.298*	4.264	0.034	*3.294*
1.160	997.5	*3.5*	0.0035	*0.000395*	0.000340	0.000262	*4.298*	4.264	0.034	*3.317*
1.159	997.4	*3.2*	0.0032	*0.000348*	0.000300	0.000232	*4.297*	4.264	0.033	*3.295*
1.158	997.4	*3.2*	0.0032	*0.000345*	0.000298	0.000231	*4.297*	4.264	0.033	*3.291*
1.158	997.2	*2.7*	0.0027	*0.000247*	0.000213	0.000165	*4.294*	4.264	0.030	*3.299*
1.157	997.2	*2.2*	0.0022	*0.000186*	0.000161	0.000125	*4.293*	4.264	0.029	*3.303*
1.157	997.2	*2.3*	0.0023	*0.000187*	0.000161	0.000125	*4.293*	4.264	0.029	*3.295*
1.157	997.1	*3.3*	0.0033	*0.000356*	0.000307	0.000237	*4.298*	4.264	0.034	*3.314*

Density (kg/m3)		Water flow rate		Air flow rate			Water elevation header (m)	Mixing head lip elevation (m)	Water level over mixing head lip (m)	Water elevation tailrace (m)
Air (in)	Water	(kg/s)	(m3/s)	(kg/s)	in (m3/s)	out (m3/s)				
1.156	997.1	*3.4*	0.0034	*0.000345*	0.000298	0.000230	*4.298*	4.264	0.034	*3.333*
1.156	997.0	*3.8*	0.0038	*0.000411*	0.000355	0.000274	*4.301*	4.264	0.037	*3.329*
1.155	997.0	*3.9*	0.0039	*0.000420*	0.000363	0.000280	*4.301*	4.264	0.037	*3.320*
1.155	996.9	*4.1*	0.0041	*0.000412*	0.000357	0.000275	*4.301*	4.264	0.037	*3.322*
1.154	996.9	*4.2*	0.0042	*0.000493*	0.000427	0.000329	*4.303*	4.264	0.039	*3.335*
1.155	996.9	*4.7*	0.0047	*0.000537*	0.000465	0.000359	*4.304*	4.264	0.040	*3.315*
1.154	996.8	*4.9*	0.0049	*0.000548*	0.000475	0.000365	*4.305*	4.264	0.042	*3.335*
1.153	996.7	*5.3*	0.0053	*0.000572*	0.000496	0.000382	*4.306*	4.264	0.043	*3.325*
1.153	996.6	*5.4*	0.0054	*0.000576*	0.000500	0.000386	*4.305*	4.264	0.041	*3.308*
1.152	996.6	*5.6*	0.0057	*0.000610*	0.000530	0.000409	*4.307*	4.264	0.043	*3.306*
1.152	996.5	*5.9*	0.0059	*0.000628*	0.000545	0.000421	*4.308*	4.264	0.044	*3.311*
1.151	996.4	*6.0*	0.0060	*0.000621*	0.000539	0.000415	*4.308*	4.264	0.044	*3.327*
1.151	996.4	*6.5*	0.0065	*0.000660*	0.000574	0.000443	*4.310*	4.264	0.046	*3.305*
1.151	996.3	*6.6*	0.0067	*0.000693*	0.000602	0.000462	*4.311*	4.264	0.047	*3.335*
1.150	996.3	*6.6*	0.0066	*0.000677*	0.000588	0.000451	*4.311*	4.264	0.047	*3.339*
1.150	996.2	*6.8*	0.0068	*0.000702*	0.000610	0.000469	*4.312*	4.264	0.048	*3.323*
1.149	996.1	*6.8*	0.0068	*0.000708*	0.000616	0.000474	*4.312*	4.264	0.048	*3.328*
1.149	996.1	*6.9*	0.0070	*0.000747*	0.000650	0.000502	*4.312*	4.264	0.048	*3.295*
1.149	996.0	*7.0*	0.0070	*0.000718*	0.000625	0.000481	*4.312*	4.264	0.048	*3.323*
1.148	995.9	*7.1*	0.0071	*0.000701*	0.000610	0.000468	*4.313*	4.264	0.049	*3.340*
1.147	995.9	*7.0*	0.0070	*0.000713*	0.000622	0.000478	*4.313*	4.264	0.049	*3.323*
1.147	995.8	*7.2*	0.0073	*0.000721*	0.000629	0.000483	*4.313*	4.264	0.049	*3.329*

Snorkel head: large diameter snorkel

Density (kg/m3)		Water flow rate		Air flow rate			Water elevation header (m)	Mixing head lip elevation (m)	Water level over mixing head lip (m)	Water elevation tailrace (m)
Air (in)	Water	(kg/s)	(m3/s)	(kg/s)	in (m3/s)	out (m3/s)				
1.149	998.4	*3.0*	0.0030	*0.000200*	0.000174	0.000132	*4.288*	4.264	0.024	*3.314*
1.150	998.3	*3.0*	0.0030	*0.000215*	0.000187	0.000142	*4.289*	4.264	0.025	*3.310*
1.151	998.2	*2.4*	0.0025	*0.000127*	0.000110	0.000084	*4.287*	4.264	0.023	*3.312*
1.152	998.2	*2.6*	0.0026	*0.000134*	0.000116	0.000089	*4.287*	4.264	0.023	*3.307*
1.153	998.1	*2.5*	0.0025	*0.000141*	0.000122	0.000093	*4.288*	4.264	0.024	*3.311*
1.153	998.1	*2.8*	0.0028	*0.000183*	0.000159	0.000121	*4.289*	4.264	0.025	*3.312*
1.153	998.0	*2.7*	0.0027	*0.000183*	0.000158	0.000121	*4.289*	4.264	0.025	*3.312*
1.153	998.0	*3.1*	0.0031	*0.000239*	0.000208	0.000158	*4.291*	4.264	0.027	*3.303*
1.153	997.9	*3.1*	0.0031	*0.000242*	0.000209	0.000160	*4.291*	4.264	0.027	*3.309*
1.153	997.9	*2.9*	0.0029	*0.000230*	0.000200	0.000152	*4.291*	4.264	0.027	*3.323*
1.153	997.8	*3.6*	0.0036	*0.000284*	0.000247	0.000188	*4.293*	4.264	0.029	*3.305*
1.153	997.8	*3.5*	0.0035	*0.000301*	0.000261	0.000199	*4.293*	4.264	0.029	*3.309*
1.153	997.7	*3.8*	0.0038	*0.000293*	0.000254	0.000194	*4.293*	4.264	0.029	*3.307*
1.152	997.7	*3.8*	0.0038	*0.000347*	0.000301	0.000230	*4.296*	4.264	0.032	*3.304*
1.152	997.6	*4.0*	0.0040	*0.000358*	0.000311	0.000238	*4.296*	4.264	0.032	*3.297*
1.153	997.6	*3.9*	0.0039	*0.000339*	0.000294	0.000225	*4.296*	4.264	0.032	*3.311*
1.153	997.5	*4.3*	0.0043	*0.000382*	0.000331	0.000253	*4.298*	4.264	0.034	*3.304*
1.153	997.5	*4.4*	0.0044	*0.000386*	0.000335	0.000256	*4.298*	4.264	0.034	*3.317*
1.153	997.4	*4.3*	0.0044	*0.000370*	0.000321	0.000246	*4.299*	4.264	0.035	*3.306*
1.152	997.3	*4.7*	0.0047	*0.000432*	0.000375	0.000286	*4.301*	4.264	0.037	*3.338*
1.152	997.3	*4.8*	0.0048	*0.000421*	0.000365	0.000278	*4.302*	4.264	0.038	*3.347*
1.152	997.2	*4.7*	0.0048	*0.000425*	0.000369	0.000280	*4.302*	4.264	0.038	*3.348*
1.151	997.2	*5.0*	0.0051	*0.000448*	0.000389	0.000296	*4.309*	4.264	0.045	*3.334*
1.151	997.1	*5.1*	0.0051	*0.000451*	0.000391	0.000298	*4.314*	4.264	0.050	*3.343*
1.151	997.1	*5.0*	0.0050	*0.000459*	0.000399	0.000304	*4.316*	4.264	0.052	*3.339*
1.150	997.0	*5.2*	0.0052	*0.000500*	0.000435	0.000333	*4.324*	4.264	0.060	*3.296*
1.150	997.0	*5.3*	0.0053	*0.000478*	0.000416	0.000317	*4.324*	4.264	0.060	*3.334*

Density (kg/m3)		Water flow rate		Air flow rate			Water elevation header (m)	Mixing head lip elevation (m)	Water level over mixing head lip (m)	Water elevation tailrace (m)
Air (in)	Water	(kg/s)	(m3/s)	(kg/s)	in (m3/s)	out (m3/s)				
1.149	996.9	*5.3*	0.0053	*0.000489*	0.000426	0.000325	*4.324*	4.264	0.060	*3.303*
1.149	996.8	*5.7*	0.0057	*0.000515*	0.000448	0.000342	*4.337*	4.264	0.073	*3.317*
1.150	996.9	*5.6*	0.0056	*0.000536*	0.000466	0.000356	*4.343*	4.264	0.079	*3.317*
1.149	996.8	*5.6*	0.0056	*0.000528*	0.000460	0.000350	*4.343*	4.264	0.079	*3.329*
1.148	996.7	*6.0*	0.0060	*0.000570*	0.000496	0.000378	*4.359*	4.264	0.095	*3.301*
1.148	996.7	*6.0*	0.0060	*0.000581*	0.000506	0.000386	*4.359*	4.264	0.095	*3.289*
1.148	996.6	*5.9*	0.0059	*0.000546*	0.000476	0.000362	*4.359*	4.264	0.095	*3.328*
1.148	996.5	*6.6*	0.0067	*0.000608*	0.000530	0.000404	*4.380*	4.264	0.116	*3.301*
1.149	996.5	*6.4*	0.0065	*0.000540*	0.000470	0.000357	*4.381*	4.264	0.117	*3.317*
1.149	996.4	*6.9*	0.0069	*0.000633*	0.000551	0.000419	*4.386*	4.264	0.122	*3.312*
1.149	996.3	*6.8*	0.0068	*0.000629*	0.000548	0.000416	*4.388*	4.264	0.124	*3.330*
1.147	996.3	*6.9*	0.0069	*0.000667*	0.000581	0.000444	*4.389*	4.264	0.125	*3.278*

Snorkel head: position 1

Density (kg/m3)		Water flow rate		Air flow rate			Water elevation header (m)	Mixing head lip elevation (m)	Water level over mixing head lip (m)	Water elevation tailrace (m)
Air (in)	Water	(kg/s)	(m3/s)	(kg/s)	in (m3/s)	out (m3/s)				
1.159	998.8	*4.9*	0.0049	*0.000454*	0.000392	0.000294	*4.315*	4.264	0.051	*3.323*
1.159	998.8	*4.4*	0.0044	*0.000458*	0.000395	0.000297	*4.313*	4.264	0.049	*3.322*
1.160	998.7	*4.9*	0.0049	*0.000466*	0.000402	0.000303	*4.313*	4.264	0.049	*3.306*
1.160	998.7	*5.0*	0.0050	*0.000451*	0.000389	0.000293	*4.313*	4.264	0.049	*3.316*
1.159	998.6	*4.8*	0.0048	*0.000459*	0.000396	0.000298	*4.312*	4.264	0.048	*3.313*
1.159	998.6	*4.8*	0.0048	*0.000465*	0.000401	0.000302	*4.313*	4.264	0.049	*3.314*
1.158	998.6	*4.5*	0.0045	*0.000418*	0.000361	0.000272	*4.304*	4.264	0.040	*3.322*
1.159	998.5	*4.9*	0.0049	*0.000432*	0.000373	0.000281	*4.305*	4.264	0.041	*3.319*
1.158	998.5	*4.6*	0.0046	*0.000404*	0.000349	0.000264	*4.299*	4.264	0.035	*3.322*
1.157	998.4	*4.1*	0.0041	*0.000372*	0.000322	0.000243	*4.296*	4.264	0.032	*3.321*

Density (kg/m3)		Water flow rate		Air flow rate			Water elevation header (m)	Mixing head lip elevation (m)	Water level over mixing head lip (m)	Water elevation tailrace (m)
Air (in)	Water	(kg/s)	(m3/s)	(kg/s)	in (m3/s)	out (m3/s)				
1.157	998.4	*4.3*	0.0043	*0.000381*	0.000329	0.000249	*4.296*	4.264	0.032	*3.315*
1.157	998.4	*4.0*	0.0040	*0.000356*	0.000308	0.000234	*4.291*	4.264	0.027	*3.310*
1.158	998.3	*3.8*	0.0038	*0.000349*	0.000302	0.000229	*4.291*	4.264	0.027	*3.317*
1.158	998.3	*3.5*	0.0035	*0.000324*	0.000279	0.000212	*4.290*	4.264	0.026	*3.314*
1.159	998.2	*3.3*	0.0033	*0.000275*	0.000237	0.000180	*4.289*	4.264	0.025	*3.328*
1.159	998.2	*3.5*	0.0035	*0.000278*	0.000240	0.000182	*4.289*	4.264	0.025	*3.329*
1.151	997.5	*3.3*	0.0033	*0.000238*	0.000207	0.000158	*4.291*	4.264	0.027	*3.322*
1.154	997.5	*3.2*	0.0032	*0.000230*	0.000199	0.000153	*4.291*	4.264	0.027	*3.309*
1.153	997.5	*3.6*	0.0036	*0.000286*	0.000248	0.000190	*4.292*	4.264	0.028	*3.310*
1.152	997.5	*3.5*	0.0035	*0.000282*	0.000245	0.000187	*4.292*	4.264	0.028	*3.318*
1.152	997.4	*3.7*	0.0037	*0.000318*	0.000276	0.000211	*4.293*	4.264	0.029	*3.321*
1.151	997.4	*3.7*	0.0037	*0.000340*	0.000295	0.000226	*4.294*	4.264	0.030	*3.311*
1.151	997.4	*4.1*	0.0041	*0.000361*	0.000313	0.000239	*4.300*	4.264	0.036	*3.320*
1.151	997.4	*4.1*	0.0041	*0.000345*	0.000300	0.000228	*4.300*	4.264	0.036	*3.325*
1.150	997.4	*4.2*	0.0042	*0.000366*	0.000318	0.000242	*4.302*	4.264	0.038	*3.319*
1.151	997.3	*5.1*	0.0051	*0.000404*	0.000351	0.000267	*4.318*	4.264	0.054	*3.304*

Snorkel head: position 3

Density (kg/m3)		Water flow rate		Air flow rate			Water elevation header (m)	Mixing head lip elevation (m)	Water level over mixing head lip (m)	Water elevation tailrace (m)
Air (in)	Water	(kg/s)	(m3/s)	(kg/s)	in (m3/s)	out (m3/s)				
1.171	998.7	*5.8*	0.0058	*0.000655*	0.000560	0.000423	*4.297*	4.264	0.033	*3.298*
1.172	998.6	*4.4*	0.0045	*0.000503*	0.000429	0.000326	*4.292*	4.264	0.028	*3.297*
1.173	998.6	*4.1*	0.0041	*0.000412*	0.000351	0.000268	*4.290*	4.264	0.026	*3.302*
1.173	998.5	*3.5*	0.0035	*0.000341*	0.000290	0.000222	*4.289*	4.264	0.025	*3.291*
1.176	998.4	*3.7*	0.0037	*0.000328*	0.000279	0.000212	*4.290*	4.264	0.026	*3.340*
1.174	998.4	*4.3*	0.0043	*0.000442*	0.000376	0.000288	*4.293*	4.264	0.029	*3.299*

Density (kg/m3)		Water flow rate		Air flow rate			Water elevation header (m)	Mixing head lip elevation (m)	Water level over mixing head lip (m)	Water elevation tailrace (m)
Air (in)	Water	(kg/s)	(m3/s)	(kg/s)	in (m3/s)	out (m3/s)				
1.176	998.3	*4.3*	0.0043	*0.000436*	0.000371	0.000283	*4.293*	4.264	0.029	*3.319*
1.176	998.2	*5.1*	0.0051	*0.000565*	0.000481	0.000366	*4.297*	4.264	0.033	*3.336*
1.176	998.2	*5.0*	0.0051	*0.000561*	0.000477	0.000363	*4.297*	4.264	0.033	*3.335*
1.175	998.1	*5.5*	0.0055	*0.000607*	0.000517	0.000396	*4.299*	4.264	0.035	*3.309*
1.176	998.0	*5.4*	0.0054	*0.000599*	0.000509	0.000390	*4.299*	4.264	0.035	*3.322*
1.175	997.9	*5.3*	0.0053	*0.000601*	0.000511	0.000393	*4.300*	4.264	0.036	*3.306*
1.175	997.8	*5.4*	0.0054	*0.000602*	0.000512	0.000393	*4.300*	4.264	0.036	*3.308*
1.176	997.7	*5.3*	0.0053	*0.000593*	0.000504	0.000387	*4.300*	4.264	0.036	*3.325*
1.175	997.7	*5.9*	0.0060	*0.000630*	0.000536	0.000412	*4.303*	4.264	0.039	*3.316*
1.174	997.6	*5.9*	0.0059	*0.000637*	0.000542	0.000417	*4.303*	4.264	0.039	*3.310*
1.175	997.5	*6.0*	0.0060	*0.000620*	0.000528	0.000405	*4.303*	4.264	0.039	*3.332*
1.173	997.5	*6.7*	0.0067	*0.000680*	0.000580	0.000446	*4.308*	4.264	0.044	*3.296*
1.174	997.4	*6.5*	0.0065	*0.000669*	0.000570	0.000438	*4.308*	4.264	0.044	*3.318*
1.174	997.3	*6.8*	0.0068	*0.000651*	0.000554	0.000426	*4.307*	4.264	0.043	*3.330*
1.172	997.2	*6.5*	0.0066	*0.000683*	0.000583	0.000450	*4.307*	4.264	0.043	*3.290*
1.173	997.2	*6.9*	0.0070	*0.000676*	0.000576	0.000443	*4.312*	4.264	0.048	*3.316*
1.170	997.1	*7.2*	0.0073	*0.000702*	0.000600	0.000462	*4.318*	4.264	0.054	*3.296*
1.170	997.1	*7.2*	0.0073	*0.000703*	0.000601	0.000462	*4.318*	4.264	0.054	*3.304*
1.172	997.0	*7.2*	0.0072	*0.000688*	0.000587	0.000451	*4.318*	4.264	0.054	*3.322*
1.169	996.9	*7.6*	0.0076	*0.000732*	0.000626	0.000482	*4.331*	4.264	0.067	*3.297*
1.171	996.9	*7.6*	0.0076	*0.000706*	0.000603	0.000463	*4.328*	4.264	0.064	*3.324*
1.169	996.8	*7.8*	0.0079	*0.000738*	0.000631	0.000486	*4.334*	4.264	0.070	*3.289*
1.168	996.8	*7.9*	0.0079	*0.000749*	0.000641	0.000494	*4.338*	4.264	0.074	*3.286*
1.167	996.7	*8.0*	0.0081	*0.000760*	0.000651	0.000501	*4.343*	4.264	0.079	*3.290*
1.168	996.7	*7.9*	0.0079	*0.000767*	0.000656	0.000506	*4.342*	4.264	0.078	*3.272*
1.168	996.6	*8.3*	0.0083	*0.000767*	0.000657	0.000506	*4.350*	4.264	0.086	*3.278*
1.167	996.5	*8.4*	0.0084	*0.000764*	0.000655	0.000503	*4.350*	4.264	0.086	*3.294*
1.167	996.4	*8.2*	0.0082	*0.000733*	0.000628	0.000482	*4.349*	4.264	0.085	*3.314*

Snorkel head: position 4

Density (kg/m3)		Water flow rate		Air flow rate			Water elevation header (m)	Mixing head lip elevation (m)	Water level over mixing head lip (m)	Water elevation tailrace (m)
Air (in)	Water	(kg/s)	(m3/s)	(kg/s)	in (m3/s)	out (m3/s)				
1.170	998.7	*2.0*	0.0020	*0.000097*	0.000083	0.000063	*4.283*	4.264	0.019	*3.287*
1.170	998.6	*2.5*	0.0025	*0.000110*	0.000094	0.000071	*4.283*	4.264	0.019	*3.289*
1.171	998.6	*3.3*	0.0033	*0.000288*	0.000246	0.000188	*4.288*	4.264	0.024	*3.301*
1.171	998.5	*3.2*	0.0032	*0.000279*	0.000238	0.000182	*4.289*	4.264	0.025	*3.298*
1.173	998.5	*4.1*	0.0041	*0.000416*	0.000355	0.000269	*4.292*	4.264	0.028	*3.335*
1.173	998.4	*3.9*	0.0039	*0.000418*	0.000356	0.000271	*4.292*	4.264	0.028	*3.338*
1.173	998.4	*4.0*	0.0040	*0.000412*	0.000352	0.000267	*4.293*	4.264	0.029	*3.338*
1.174	998.3	*4.8*	0.0048	*0.000560*	0.000477	0.000362	*4.296*	4.264	0.032	*3.344*
1.174	998.2	*4.8*	0.0048	*0.000555*	0.000473	0.000360	*4.296*	4.264	0.032	*3.340*
1.174	998.2	*4.7*	0.0047	*0.000551*	0.000470	0.000358	*4.297*	4.264	0.033	*3.350*
1.174	998.1	*4.7*	0.0047	*0.000532*	0.000453	0.000345	*4.297*	4.264	0.033	*3.343*
1.173	998.1	*5.2*	0.0052	*0.000598*	0.000510	0.000389	*4.299*	4.264	0.035	*3.329*
1.172	998.0	*5.2*	0.0052	*0.000586*	0.000500	0.000382	*4.299*	4.264	0.035	*3.325*
1.172	998.0	*5.9*	0.0059	*0.000654*	0.000558	0.000426	*4.301*	4.264	0.038	*3.317*
1.172	997.9	*5.9*	0.0059	*0.000641*	0.000547	0.000417	*4.302*	4.264	0.038	*3.338*
1.172	997.9	*6.1*	0.0062	*0.000668*	0.000570	0.000435	*4.304*	4.264	0.040	*3.333*
1.172	997.8	*6.2*	0.0062	*0.000663*	0.000566	0.000432	*4.304*	4.264	0.040	*3.339*
1.170	997.7	*6.7*	0.0067	*0.000713*	0.000609	0.000466	*4.308*	4.264	0.045	*3.308*
1.171	997.7	*6.7*	0.0067	*0.000697*	0.000595	0.000455	*4.309*	4.264	0.045	*3.328*
1.169	997.6	*7.2*	0.0072	*0.000740*	0.000633	0.000484	*4.318*	4.264	0.054	*3.305*
1.169	997.5	*7.2*	0.0072	*0.000737*	0.000631	0.000483	*4.319*	4.264	0.055	*3.308*
1.168	997.4	*7.7*	0.0077	*0.000751*	0.000643	0.000492	*4.329*	4.264	0.065	*3.302*
1.169	997.3	*7.7*	0.0077	*0.000753*	0.000645	0.000491	*4.330*	4.264	0.066	*3.337*
1.168	997.3	*7.6*	0.0077	*0.000746*	0.000639	0.000487	*4.330*	4.264	0.066	*3.337*
1.167	997.2	*8.1*	0.0081	*0.000813*	0.000697	0.000532	*4.340*	4.264	0.077	*3.317*
1.166	997.1	*8.1*	0.0082	*0.000795*	0.000682	0.000521	*4.343*	4.264	0.079	*3.309*

Snorkel head: position 5

Density (kg/m3)		Water flow rate		Air flow rate			Water elevation header (m)	Mixing head lip elevation (m)	Water level over mixing head lip (m)	Water elevation tailrace (m)
Air (in)	Water	(kg/s)	(m3/s)	(kg/s)	in (m3/s)	out (m3/s)				
1.152	998.8	*2.5*	0.0025	*0.000200*	0.000173	0.000131	*4.280*	4.264	0.016	*3.313*
1.152	998.7	*2.9*	0.0029	*0.000200*	0.000174	0.000132	*4.280*	4.264	0.016	*3.294*
1.153	998.7	*3.1*	0.0031	*0.000253*	0.000219	0.000166	*4.282*	4.264	0.018	*3.301*
1.153	998.6	*3.0*	0.0030	*0.000265*	0.000230	0.000175	*4.282*	4.264	0.018	*3.295*
1.154	998.6	*3.3*	0.0034	*0.000263*	0.000228	0.000173	*4.282*	4.264	0.018	*3.302*
1.156	998.6	*4.0*	0.0040	*0.000321*	0.000277	0.000210	*4.283*	4.264	0.019	*3.333*
1.156	998.5	*3.9*	0.0039	*0.000316*	0.000273	0.000207	*4.284*	4.264	0.020	*3.348*
1.156	998.5	*4.6*	0.0046	*0.000395*	0.000341	0.000259	*4.287*	4.264	0.023	*3.334*
1.157	998.4	*4.5*	0.0045	*0.000387*	0.000335	0.000254	*4.287*	4.264	0.023	*3.322*
1.157	998.4	*5.2*	0.0052	*0.000478*	0.000413	0.000313	*4.290*	4.264	0.026	*3.337*
1.158	998.3	*5.1*	0.0052	*0.000477*	0.000412	0.000312	*4.290*	4.264	0.026	*3.348*
1.158	998.3	*5.5*	0.0055	*0.000515*	0.000445	0.000337	*4.291*	4.264	0.028	*3.335*
1.158	998.2	*5.5*	0.0055	*0.000511*	0.000442	0.000336	*4.292*	4.264	0.028	*3.329*
1.158	998.2	*5.4*	0.0054	*0.000516*	0.000446	0.000339	*4.292*	4.264	0.028	*3.324*
1.158	998.1	*5.8*	0.0058	*0.000530*	0.000457	0.000348	*4.294*	4.264	0.030	*3.320*
1.158	998.0	*5.8*	0.0058	*0.000539*	0.000466	0.000355	*4.294*	4.264	0.030	*3.318*
1.158	998.0	*6.0*	0.0060	*0.000549*	0.000474	0.000362	*4.295*	4.264	0.031	*3.310*
1.158	997.9	*6.1*	0.0061	*0.000543*	0.000469	0.000358	*4.295*	4.264	0.031	*3.321*
1.158	997.8	*6.7*	0.0067	*0.000571*	0.000493	0.000376	*4.300*	4.264	0.036	*3.324*
1.157	997.8	*6.5*	0.0066	*0.000571*	0.000493	0.000376	*4.300*	4.264	0.036	*3.330*
1.158	997.7	*6.7*	0.0067	*0.000575*	0.000496	0.000378	*4.300*	4.264	0.036	*3.331*
1.158	997.7	*7.2*	0.0072	*0.000612*	0.000528	0.000402	*4.312*	4.264	0.048	*3.333*
1.156	997.6	*7.2*	0.0072	*0.000618*	0.000535	0.000409	*4.312*	4.264	0.048	*3.292*
1.155	997.5	*7.6*	0.0076	*0.000648*	0.000561	0.000428	*4.325*	4.264	0.061	*3.294*
1.156	997.5	*7.6*	0.0076	*0.000663*	0.000573	0.000439	*4.326*	4.264	0.062	*3.281*
1.155	997.4	*8.0*	0.0080	*0.000664*	0.000575	0.000439	*4.339*	4.264	0.075	*3.284*
1.155	997.4	*7.9*	0.0079	*0.000670*	0.000580	0.000444	*4.337*	4.264	0.073	*3.279*

Density (kg/m3)		Water flow rate		Air flow rate			Water elevation header (m)	Mixing head lip elevation (m)	Water level over mixing head lip (m)	Water elevation tailrace (m)
Air (in)	Water	(kg/s)	(m3/s)	(kg/s)	in (m3/s)	out (m3/s)				
1.155	997.3	*8.0*	0.0080	*0.000673*	0.000583	0.000445	*4.345*	4.264	0.081	*3.291*
1.154	997.2	*8.1*	0.0081	*0.000686*	0.000594	0.000454	*4.345*	4.264	0.081	*3.283*

Snorkel head: position 6

Density (kg/m3)		Water flow rate		Air flow rate			Water elevation header (m)	Mixing head lip elevation (m)	Water level over mixing head lip (m)	Water elevation tailrace (m)
Air (in)	Water	(kg/s)	(m3/s)	(kg/s)	in (m3/s)	out (m3/s)				
1.162	997.8	*2.2*	0.0022	*0.000200*	0.000172	0.000132	*4.289*	4.264	0.025	*3.350*
1.164	997.8	*2.1*	0.0021	*0.000193*	0.000166	0.000126	*4.289*	4.264	0.025	*3.388*
1.163	997.8	*2.9*	0.0029	*0.000272*	0.000234	0.000179	*4.291*	4.264	0.027	*3.360*
1.161	997.7	*3.1*	0.0031	*0.000277*	0.000238	0.000182	*4.291*	4.264	0.027	*3.339*
1.161	997.7	*3.0*	0.0030	*0.000282*	0.000243	0.000187	*4.291*	4.264	0.027	*3.325*
1.161	997.6	*3.7*	0.0037	*0.000395*	0.000340	0.000262	*4.294*	4.264	0.030	*3.316*
1.161	997.6	*3.9*	0.0039	*0.000394*	0.000339	0.000261	*4.294*	4.264	0.030	*3.316*
1.162	997.6	*4.2*	0.0042	*0.000451*	0.000388	0.000299	*4.296*	4.264	0.032	*3.316*
1.162	997.5	*4.3*	0.0043	*0.000434*	0.000374	0.000288	*4.296*	4.264	0.032	*3.318*
1.161	997.5	*4.8*	0.0048	*0.000488*	0.000420	0.000324	*4.298*	4.264	0.034	*3.288*
1.162	997.5	*4.7*	0.0047	*0.000479*	0.000412	0.000317	*4.298*	4.264	0.034	*3.302*
1.162	997.4	*5.4*	0.0054	*0.000589*	0.000507	0.000390	*4.300*	4.264	0.036	*3.302*
1.163	997.4	*5.2*	0.0052	*0.000582*	0.000501	0.000385	*4.300*	4.264	0.036	*3.314*
1.163	997.3	*6.0*	0.0061	*0.000609*	0.000524	0.000402	*4.303*	4.264	0.039	*3.328*
1.163	997.3	*5.9*	0.0059	*0.000606*	0.000521	0.000399	*4.303*	4.264	0.039	*3.338*
1.163	997.2	*5.8*	0.0059	*0.000576*	0.000495	0.000380	*4.304*	4.264	0.040	*3.331*
1.163	997.2	*6.6*	0.0066	*0.000637*	0.000548	0.000421	*4.310*	4.264	0.046	*3.321*
1.163	997.1	*6.6*	0.0066	*0.000639*	0.000550	0.000421	*4.310*	4.264	0.046	*3.336*
1.162	997.1	*5.8*	0.0059	*0.000603*	0.000519	0.000399	*4.304*	4.264	0.040	*3.331*
1.162	997.0	*6.0*	0.0060	*0.000593*	0.000510	0.000393	*4.304*	4.264	0.040	*3.324*

Density (kg/m3)		Water flow rate		Air flow rate			Water elevation header (m)	Mixing head lip elevation (m)	Water level over mixing head lip (m)	Water elevation tailrace (m)
Air (in)	Water	(kg/s)	(m3/s)	(kg/s)	in (m3/s)	out (m3/s)				
1.161	997.0	*6.4*	0.0064	*0.000641*	0.000552	0.000425	*4.308*	4.264	0.044	*3.307*
1.162	996.9	*6.5*	0.0065	*0.000633*	0.000545	0.000419	*4.308*	4.264	0.044	*3.319*
1.162	996.9	*6.9*	0.0069	*0.000636*	0.000548	0.000419	*4.316*	4.264	0.052	*3.345*
1.160	996.8	*7.6*	0.0077	*0.000683*	0.000589	0.000454	*4.332*	4.264	0.068	*3.287*
1.160	996.8	*7.4*	0.0074	*0.000687*	0.000592	0.000455	*4.332*	4.264	0.068	*3.311*
1.159	996.7	*7.2*	0.0072	*0.000725*	0.000626	0.000481	*4.340*	4.264	0.076	*3.296*
1.160	996.6	*7.4*	0.0074	*0.000673*	0.000580	0.000445	*4.342*	4.264	0.078	*3.311*
1.159	996.5	*7.8*	0.0078	*0.000671*	0.000579	0.000443	*4.348*	4.264	0.084	*3.321*
1.158	996.5	*8.4*	0.0084	*0.000778*	0.000672	0.000516	*4.360*	4.264	0.096	*3.280*
1.158	996.4	*8.2*	0.0082	*0.000723*	0.000624	0.000478	*4.361*	4.264	0.097	*3.301*

Snorkel head: position 7

Density (kg/m3)		Water flow rate		Air flow rate			Water elevation header (m)	Mixing head lip elevation (m)	Water level over mixing head lip (m)	Water elevation tailrace (m)
Air (in)	Water	(kg/s)	(m3/s)	(kg/s)	in (m3/s)	out (m3/s)				
1.189	998.8	*2.3*	0.0023	*0.000116*	0.000097	0.000075	*4.277*	4.264	0.013	*3.305*
1.189	998.8	*2.4*	0.0024	*0.000111*	0.000093	0.000072	*4.277*	4.264	0.013	*3.310*
1.190	998.7	*3.3*	0.0033	*0.000203*	0.000171	0.000131	*4.280*	4.264	0.016	*3.324*
1.191	998.7	*3.0*	0.0030	*0.000208*	0.000175	0.000134	*4.280*	4.264	0.016	*3.327*
1.191	998.6	*3.5*	0.0035	*0.000270*	0.000227	0.000174	*4.283*	4.264	0.019	*3.312*
1.192	998.5	*3.4*	0.0034	*0.000275*	0.000231	0.000178	*4.283*	4.264	0.019	*3.311*
1.192	998.5	*3.8*	0.0038	*0.000306*	0.000256	0.000198	*4.284*	4.264	0.020	*3.305*
1.193	998.5	*3.7*	0.0037	*0.000312*	0.000262	0.000202	*4.284*	4.264	0.020	*3.315*
1.194	998.4	*4.3*	0.0043	*0.000388*	0.000325	0.000250	*4.287*	4.264	0.023	*3.325*
1.195	998.4	*4.3*	0.0043	*0.000374*	0.000313	0.000240	*4.288*	4.264	0.024	*3.357*
1.195	998.3	*4.7*	0.0047	*0.000452*	0.000378	0.000290	*4.290*	4.264	0.026	*3.358*
1.195	998.3	*4.7*	0.0047	*0.000441*	0.000369	0.000283	*4.290*	4.264	0.026	*3.353*

Density (kg/m3)		Water flow rate		Air flow rate			Water elevation header (m)	Mixing head lip elevation (m)	Water level over mixing head lip (m)	Water elevation tailrace (m)
Air (in)	Water	(kg/s)	(m3/s)	(kg/s)	in (m3/s)	out (m3/s)				
1.194	998.3	*5.2*	0.0052	*0.000494*	0.000414	0.000318	*4.292*	4.264	0.028	*3.339*
1.194	998.2	*5.2*	0.0052	*0.000496*	0.000415	0.000320	*4.293*	4.264	0.029	*3.338*
1.193	998.1	*5.7*	0.0057	*0.000529*	0.000443	0.000342	*4.296*	4.264	0.032	*3.327*
1.192	998.0	*5.6*	0.0056	*0.000531*	0.000445	0.000344	*4.296*	4.264	0.032	*3.320*
1.192	998.0	*6.2*	0.0062	*0.000555*	0.000466	0.000359	*4.301*	4.264	0.037	*3.326*
1.192	997.9	*6.2*	0.0062	*0.000551*	0.000463	0.000357	*4.301*	4.264	0.037	*3.328*
1.191	997.9	*6.6*	0.0066	*0.000584*	0.000490	0.000378	*4.310*	4.264	0.046	*3.323*
1.190	997.8	*6.6*	0.0066	*0.000587*	0.000493	0.000380	*4.310*	4.264	0.046	*3.322*
1.189	997.8	*6.9*	0.0070	*0.000602*	0.000506	0.000390	*4.320*	4.264	0.056	*3.309*
1.189	997.7	*6.9*	0.0069	*0.000603*	0.000507	0.000390	*4.319*	4.264	0.055	*3.321*
1.188	997.7	*7.2*	0.0072	*0.000606*	0.000510	0.000393	*4.334*	4.264	0.070	*3.307*
1.188	997.6	*7.2*	0.0072	*0.000609*	0.000512	0.000394	*4.333*	4.264	0.070	*3.310*
1.186	997.6	*7.5*	0.0075	*0.000633*	0.000534	0.000411	*4.345*	4.264	0.081	*3.292*
1.186	997.5	*7.5*	0.0075	*0.000640*	0.000540	0.000415	*4.345*	4.264	0.081	*3.302*
1.184	997.4	*7.5*	0.0075	*0.000654*	0.000552	0.000426	*4.348*	4.264	0.084	*3.283*
1.185	997.4	*7.9*	0.0079	*0.000654*	0.000552	0.000425	*4.358*	4.264	0.094	*3.292*
1.184	997.3	*8.0*	0.0080	*0.000674*	0.000569	0.000439	*4.359*	4.264	0.095	*3.285*
1.184	997.3	*7.9*	0.0080	*0.000653*	0.000551	0.000425	*4.359*	4.264	0.095	*3.287*
1.182	997.1	*8.1*	0.0081	*0.000693*	0.000586	0.000452	*4.367*	4.264	0.103	*3.272*
1.182	997.0	*8.1*	0.0081	*0.000699*	0.000591	0.000456	*4.368*	4.264	0.104	*3.281*

Headless (‘no head’ configuration)

Density (kg/m3)		Water flow rate		Air flow rate			Water elevation header (m)	Mixing head lip elevation (m)	Water level over mixing head lip (m)	Water elevation tailrace (m)
Air (in)	Water	(kg/s)	(m3/s)	(kg/s)	in (m3/s)	out (m3/s)				
1.170	998.2	*2.8*	0.0028	*0.000184*	0.000157	0.000120	*4.229*	4.188	0.041	*3.373*
1.169	998.2	*2.9*	0.0029	*0.000302*	0.000259	0.000198	*4.238*	4.188	0.050	*3.339*
1.168	998.1	*3.5*	0.0035	*0.000382*	0.000328	0.000250	*4.246*	4.188	0.058	*3.328*
1.167	998.1	*3.7*	0.0037	*0.000470*	0.000403	0.000309	*4.251*	4.188	0.064	*3.302*
1.166	998.0	*4.1*	0.0041	*0.000511*	0.000438	0.000336	*4.255*	4.188	0.067	*3.300*
1.166	998.0	*4.5*	0.0045	*0.000506*	0.000434	0.000332	*4.259*	4.188	0.071	*3.313*
1.165	997.9	*4.9*	0.0049	*0.000578*	0.000496	0.000378	*4.264*	4.188	0.076	*3.335*
1.165	997.9	*5.2*	0.0052	*0.000565*	0.000485	0.000370	*4.267*	4.188	0.080	*3.332*
1.164	997.8	*5.6*	0.0056	*0.000672*	0.000577	0.000442	*4.271*	4.188	0.083	*3.296*
1.164	997.7	*5.8*	0.0058	*0.000659*	0.000566	0.000434	*4.276*	4.188	0.088	*3.297*
1.164	997.7	*6.2*	0.0063	*0.000658*	0.000566	0.000433	*4.281*	4.188	0.093	*3.302*
1.163	997.6	*6.6*	0.0066	*0.000688*	0.000592	0.000451	*4.283*	4.188	0.096	*3.329*
1.162	997.5	*6.9*	0.0069	*0.000730*	0.000628	0.000479	*4.289*	4.188	0.101	*3.312*
1.162	997.5	*7.2*	0.0072	*0.000757*	0.000652	0.000496	*4.291*	4.188	0.104	*3.324*
1.161	997.4	*7.2*	0.0072	*0.000883*	0.000760	0.000579	*4.292*	4.188	0.104	*3.326*
1.161	997.3	*7.0*	0.0070	*0.000698*	0.000601	0.000460	*4.291*	4.188	0.103	*3.298*
1.160	997.2	*7.0*	0.0070	*0.000699*	0.000603	0.000460	*4.292*	4.188	0.105	*3.322*
1.160	997.2	*7.2*	0.0072	*0.000608*	0.000524	0.000399	*4.292*	4.188	0.105	*3.333*
1.159	997.1	*7.3*	0.0073	*0.000512*	0.000442	0.000338	*4.295*	4.188	0.107	*3.305*
1.158	997.0	*7.6*	0.0076	*0.000622*	0.000537	0.000410	*4.293*	4.188	0.105	*3.313*
1.167	999.1	*2.0*	0.0020	*0.000060*	0.000051	0.000039	*4.218*	4.188	0.030	*3.360*
1.169	999.1	*2.3*	0.0023	*0.000178*	0.000152	0.000115	*4.227*	4.188	0.040	*3.362*
1.170	999.1	*2.5*	0.0025	*0.000198*	0.000170	0.000127	*4.218*	4.188	0.030	*3.356*
1.171	999.1	*3.2*	0.0032	*0.000291*	0.000249	0.000188	*4.227*	4.188	0.040	*3.339*
1.172	999.0	*3.6*	0.0036	*0.000333*	0.000284	0.000215	*4.233*	4.188	0.045	*3.324*
1.172	999.0	*4.0*	0.0040	*0.000353*	0.000301	0.000228	*4.238*	4.188	0.051	*3.316*
1.173	998.9	*3.9*	0.0039	*0.000326*	0.000278	0.000210	*4.240*	4.188	0.052	*3.324*

Density (kg/m3)		Water flow rate		Air flow rate			Water elevation header (m)	Mixing head lip elevation (m)	Water level over mixing head lip (m)	Water elevation tailrace (m)
Air (in)	Water	(kg/s)	(m3/s)	(kg/s)	in (m3/s)	out (m3/s)				
1.173	998.9	*4.4*	0.0044	*0.000389*	0.000331	0.000251	*4.244*	4.188	0.056	*3.322*
1.173	998.8	*4.6*	0.0046	*0.000427*	0.000364	0.000276	*4.246*	4.188	0.058	*3.320*
1.173	998.8	*4.8*	0.0048	*0.000418*	0.000356	0.000271	*4.250*	4.188	0.062	*3.305*
1.173	998.7	*5.2*	0.0052	*0.000462*	0.000394	0.000300	*4.253*	4.188	0.066	*3.305*
1.173	998.6	*5.3*	0.0053	*0.000469*	0.000400	0.000305	*4.257*	4.188	0.069	*3.301*
1.173	998.5	*5.6*	0.0056	*0.000466*	0.000397	0.000303	*4.259*	4.188	0.071	*3.296*
1.172	998.5	*5.7*	0.0057	*0.000516*	0.000441	0.000336	*4.262*	4.188	0.075	*3.300*
1.172	998.4	*5.9*	0.0059	*0.000507*	0.000433	0.000331	*4.263*	4.188	0.075	*3.296*
1.172	998.4	*6.1*	0.0061	*0.000562*	0.000480	0.000367	*4.267*	4.188	0.079	*3.287*
1.172	998.3	*6.3*	0.0064	*0.000583*	0.000498	0.000381	*4.267*	4.188	0.079	*3.288*
1.170	998.1	*6.5*	0.0066	*0.000566*	0.000484	0.000370	*4.273*	4.188	0.085	*3.309*
1.170	998.0	*6.8*	0.0068	*0.000568*	0.000485	0.000370	*4.279*	4.188	0.091	*3.323*
1.170	997.9	*7.2*	0.0072	*0.000596*	0.000509	0.000389	*4.281*	4.188	0.093	*3.312*
1.169	997.8	*7.7*	0.0077	*0.000773*	0.000661	0.000505	*4.282*	4.188	0.094	*3.318*
1.169	997.7	*8.0*	0.0080	*0.000732*	0.000626	0.000477	*4.282*	4.188	0.094	*3.336*
1.168	997.6	*8.1*	0.0081	*0.000703*	0.000602	0.000458	*4.283*	4.188	0.095	*3.336*
1.167	997.5	*7.2*	0.0072	*0.000706*	0.000605	0.000462	*4.282*	4.188	0.094	*3.324*
1.165	997.6	*1.7*	0.0017	*0.000038*	0.000032	0.000025	*4.213*	4.188	0.026	*3.329*
1.165	997.5	*2.2*	0.0022	*0.000146*	0.000125	0.000097	*4.219*	4.188	0.032	*3.322*
1.165	997.5	*2.5*	0.0025	*0.000254*	0.000218	0.000169	*4.226*	4.188	0.039	*3.320*
1.165	997.4	*2.3*	0.0023	*0.000198*	0.000170	0.000131	*4.225*	4.188	0.037	*3.316*
1.164	997.4	*2.8*	0.0028	*0.000282*	0.000242	0.000188	*4.232*	4.188	0.045	*3.307*
1.163	997.3	*2.9*	0.0030	*0.000294*	0.000252	0.000196	*4.238*	4.188	0.051	*3.300*
1.162	997.2	*3.7*	0.0037	*0.000396*	0.000341	0.000264	*4.246*	4.188	0.059	*3.295*
1.162	997.1	*3.9*	0.0039	*0.000446*	0.000384	0.000298	*4.250*	4.188	0.062	*3.288*
1.161	997.1	*4.2*	0.0042	*0.000438*	0.000377	0.000291	*4.253*	4.188	0.065	*3.318*
1.161	997.0	*4.4*	0.0044	*0.000473*	0.000407	0.000314	*4.260*	4.188	0.072	*3.323*
1.161	996.9	*4.9*	0.0049	*0.000544*	0.000469	0.000362	*4.265*	4.188	0.077	*3.310*
1.160	996.9	*5.2*	0.0052	*0.000590*	0.000508	0.000392	*4.270*	4.188	0.082	*3.317*

Density (kg/m3)		Water flow rate		Air flow rate			Water elevation header (m)	Mixing head lip elevation (m)	Water level over mixing head lip (m)	Water elevation tailrace (m)
Air (in)	Water	(kg/s)	(m3/s)	(kg/s)	in (m3/s)	out (m3/s)				
1.160	996.8	*5.7*	0.0057	*0.000535*	0.000461	0.000355	*4.278*	4.188	0.091	*3.318*
1.160	996.7	*5.8*	0.0058	*0.000579*	0.000499	0.000384	*4.277*	4.188	0.090	*3.334*
1.173	999.3	*1.4*	0.0014	*0.000103*	0.000087	0.000066	*4.218*	4.188	0.030	*3.321*
1.176	999.2	*2.2*	0.0022	*0.000145*	0.000123	0.000093	*4.223*	4.188	0.036	*3.321*
1.178	999.1	*2.2*	0.0022	*0.000154*	0.000131	0.000099	*4.219*	4.188	0.031	*3.320*
1.179	999.1	*2.8*	0.0028	*0.000243*	0.000206	0.000157	*4.226*	4.188	0.039	*3.311*
1.179	998.9	*3.2*	0.0032	*0.000286*	0.000242	0.000184	*4.233*	4.188	0.046	*3.311*
1.178	998.9	*3.5*	0.0035	*0.000327*	0.000278	0.000212	*4.238*	4.188	0.050	*3.299*
1.178	998.8	*3.5*	0.0035	*0.000339*	0.000287	0.000219	*4.242*	4.188	0.054	*3.295*
1.178	998.8	*4.0*	0.0040	*0.000353*	0.000300	0.000229	*4.247*	4.188	0.059	*3.290*
1.178	998.7	*4.1*	0.0041	*0.000384*	0.000326	0.000249	*4.251*	4.188	0.063	*3.293*
1.178	998.7	*4.2*	0.0042	*0.000419*	0.000356	0.000272	*4.252*	4.188	0.064	*3.283*
1.176	998.6	*4.6*	0.0046	*0.000420*	0.000357	0.000273	*4.254*	4.188	0.066	*3.279*
1.175	998.5	*4.8*	0.0048	*0.000462*	0.000393	0.000301	*4.257*	4.188	0.070	*3.275*
1.174	998.4	*5.1*	0.0051	*0.000489*	0.000416	0.000319	*4.260*	4.188	0.072	*3.271*
1.174	998.3	*5.1*	0.0051	*0.000443*	0.000377	0.000289	*4.264*	4.188	0.076	*3.267*
1.173	998.3	*5.3*	0.0053	*0.000495*	0.000422	0.000324	*4.264*	4.188	0.076	*3.266*
1.174	998.2	*5.4*	0.0054	*0.000503*	0.000429	0.000328	*4.264*	4.188	0.076	*3.301*
1.172	998.1	*5.4*	0.0055	*0.000475*	0.000405	0.000309	*4.266*	4.188	0.078	*3.321*
1.171	998.0	*5.5*	0.0055	*0.000493*	0.000421	0.000322	*4.266*	4.188	0.078	*3.301*
1.170	997.9	*5.5*	0.0055	*0.000501*	0.000429	0.000327	*4.268*	4.188	0.080	*3.321*
1.169	997.9	*5.8*	0.0058	*0.000508*	0.000434	0.000331	*4.272*	4.188	0.084	*3.320*
1.169	997.8	*5.9*	0.0059	*0.000506*	0.000433	0.000330	*4.272*	4.188	0.084	*3.329*
1.168	997.7	*6.1*	0.0061	*0.000532*	0.000455	0.000348	*4.277*	4.188	0.089	*3.319*
1.167	997.6	*6.3*	0.0063	*0.000543*	0.000465	0.000355	*4.277*	4.188	0.090	*3.325*
1.167	997.5	*6.5*	0.0066	*0.000499*	0.000428	0.000326	*4.278*	4.188	0.091	*3.347*
1.166	997.4	*6.7*	0.0067	*0.000536*	0.000459	0.000351	*4.283*	4.188	0.096	*3.319*
1.165	997.2	*7.3*	0.0073	*0.000811*	0.000696	0.000532	*4.293*	4.188	0.105	*3.305*

Peterborough head

Density (kg/m3)		Water flow rate		Air flow rate			Water elevation header (m)	Mixing head lip elevation (m)	Water level over mixing head lip (m)	Water elevation tailrace (m)
Air (in)	Water	(kg/s)	(m3/s)	(kg/s)	in (m3/s)	out (m3/s)				
1.168	997.8	*5.5*	0.0055	*0.000453*	0.000388	0.000297	*4.342*	4.309	0.033	*3.361*
1.166	997.6	*7.0*	0.0070	*0.000637*	0.000546	0.000418	*4.366*	4.309	0.057	*3.329*
1.166	997.5	*9.0*	0.0090	*0.000794*	0.000681	0.000516	*4.412*	4.309	0.103	*3.340*
1.164	997.4	*3.0*	0.0030	*0.000168*	0.000145	0.000111	*4.331*	4.309	0.022	*3.369*
1.161	997.4	*3.2*	0.0032	*0.000256*	0.000220	0.000170	*4.334*	4.309	0.025	*3.327*
1.163	997.3	*6.0*	0.0060	*0.000525*	0.000452	0.000346	*4.351*	4.309	0.042	*3.355*
1.162	997.1	*7.5*	0.0075	*0.000649*	0.000559	0.000425	*4.379*	4.309	0.070	*3.368*
1.161	997.0	*7.3*	0.0073	*0.000831*	0.000716	0.000546	*4.414*	4.309	0.104	*3.327*
1.158	996.9	*2.9*	0.0029	*0.000238*	0.000206	0.000160	*4.334*	4.309	0.025	*3.318*
1.157	996.9	*3.2*	0.0032	*0.000240*	0.000207	0.000160	*4.334*	4.309	0.025	*3.330*
1.157	996.8	*4.5*	0.0045	*0.000443*	0.000383	0.000296	*4.343*	4.309	0.034	*3.334*
1.158	996.7	*5.0*	0.0050	*0.000532*	0.000459	0.000354	*4.353*	4.309	0.044	*3.346*
1.158	996.6	*7.1*	0.0071	*0.000735*	0.000635	0.000486	*4.399*	4.309	0.089	*3.349*
1.154	996.4	*3.0*	0.0030	*0.000221*	0.000192	0.000149	*4.335*	4.309	0.025	*3.309*
1.154	996.3	*4.3*	0.0043	*0.000415*	0.000359	0.000278	*4.343*	4.309	0.034	*3.338*
1.155	996.2	*5.0*	0.0050	*0.000531*	0.000459	0.000353	*4.354*	4.309	0.044	*3.372*
1.154	996.1	*7.3*	0.0073	*0.000771*	0.000668	0.000514	*4.411*	4.309	0.102	*3.315*
1.157	997.0	*3.4*	0.0034	*0.000221*	0.000191	0.000147	*4.334*	4.309	0.025	*3.346*
1.156	997.0	*4.3*	0.0043	*0.000322*	0.000279	0.000215	*4.338*	4.309	0.029	*3.332*
1.156	996.9	*5.1*	0.0052	*0.000404*	0.000349	0.000270	*4.342*	4.309	0.033	*3.315*
1.156	996.8	*5.5*	0.0056	*0.000441*	0.000382	0.000295	*4.345*	4.309	0.035	*3.324*
1.157	996.8	*6.2*	0.0063	*0.000466*	0.000403	0.000307	*4.351*	4.309	0.042	*3.405*
1.155	996.7	*6.8*	0.0068	*0.000551*	0.000477	0.000367	*4.359*	4.309	0.050	*3.328*
1.154	996.7	*7.1*	0.0072	*0.000625*	0.000541	0.000416	*4.373*	4.309	0.064	*3.316*
1.154	996.6	*7.8*	0.0078	*0.000654*	0.000567	0.000434	*4.386*	4.309	0.077	*3.334*
1.153	996.5	*7.5*	0.0075	*0.000789*	0.000685	0.000525	*4.414*	4.309	0.105	*3.311*
1.151	996.5	*3.5*	0.0035	*0.000255*	0.000221	0.000172	*4.337*	4.309	0.028	*3.325*

Density (kg/m3)		Water flow rate		Air flow rate			Water elevation header (m)	Mixing head lip elevation (m)	Water level over mixing head lip (m)	Water elevation tailrace (m)
Air (in)	Water	(kg/s)	(m3/s)	(kg/s)	in (m3/s)	out (m3/s)				
1.151	996.4	*3.7*	0.0037	*0.000376*	0.000327	0.000253	*4.342*	4.309	0.033	*3.331*
1.151	996.4	*4.5*	0.0045	*0.000434*	0.000377	0.000292	*4.345*	4.309	0.035	*3.329*
1.152	996.3	*5.3*	0.0054	*0.000516*	0.000448	0.000346	*4.354*	4.309	0.045	*3.340*
1.151	996.3	*5.7*	0.0057	*0.000571*	0.000496	0.000383	*4.363*	4.309	0.054	*3.323*
1.150	996.2	*5.9*	0.0059	*0.000668*	0.000581	0.000448	*4.382*	4.309	0.072	*3.323*
1.149	996.1	*6.8*	0.0069	*0.000721*	0.000627	0.000483	*4.398*	4.309	0.089	*3.320*
1.148	996.0	*7.0*	0.0070	*0.000796*	0.000693	0.000533	*4.414*	4.309	0.105	*3.307*
1.147	996.0	*2.5*	0.0025	*0.000159*	0.000138	0.000108	*4.336*	4.309	0.027	*3.312*
1.146	996.0	*3.3*	0.0033	*0.000263*	0.000230	0.000179	*4.339*	4.309	0.030	*3.308*
1.146	995.9	*3.4*	0.0035	*0.000314*	0.000274	0.000213	*4.342*	4.309	0.032	*3.308*
1.145	995.9	*4.3*	0.0043	*0.000393*	0.000343	0.000267	*4.345*	4.309	0.036	*3.300*
1.146	995.8	*4.6*	0.0047	*0.000468*	0.000409	0.000318	*4.350*	4.309	0.041	*3.303*
1.145	995.8	*5.5*	0.0055	*0.000536*	0.000468	0.000364	*4.359*	4.309	0.050	*3.308*
1.146	995.8	*5.8*	0.0058	*0.000572*	0.000499	0.000386	*4.370*	4.309	0.061	*3.327*
1.146	995.8	*6.5*	0.0065	*0.000639*	0.000558	0.000429	*4.386*	4.309	0.077	*3.335*
1.145	995.8	*6.8*	0.0069	*0.000713*	0.000622	0.000479	*4.399*	4.309	0.090	*3.317*
1.144	995.8	*7.1*	0.0071	*0.000759*	0.000663	0.000511	*4.416*	4.309	0.107	*3.295*

Ragged chutes head

Density (kg/m3)		Water flow rate		Air flow rate			Water elevation header (m)	Mixing head lip elevation (m)	Water level over mixing head lip (m)	Water elevation tailrace (m)
Air (in)	Water	(kg/s)	(m3/s)	(kg/s)	in (m3/s)	out (m3/s)				
1.149	999.2	*2.5*	0.0025	*0.000236*	0.000206	0.000154	*4.321*	4.312	0.010	*3.302*
1.152	999.2	*3.2*	0.0032	*0.000293*	0.000254	0.000189	*4.324*	4.312	0.012	*3.326*
1.153	999.1	*3.6*	0.0036	*0.000346*	0.000300	0.000226	*4.325*	4.312	0.014	*3.283*
1.154	999.1	*3.9*	0.0039	*0.000391*	0.000339	0.000255	*4.327*	4.312	0.015	*3.285*
1.153	999.0	*4.5*	0.0045	*0.000461*	0.000400	0.000300	*4.330*	4.312	0.018	*3.307*

Density (kg/m3)		Water flow rate		Air flow rate			Water elevation header (m)	Mixing head lip elevation (m)	Water level over mixing head lip (m)	Water elevation tailrace (m)
Air (in)	Water	(kg/s)	(m3/s)	(kg/s)	in (m3/s)	out (m3/s)				
1.155	999.0	*5.3*	0.0053	*0.000484*	0.000419	0.000315	*4.333*	4.312	0.021	*3.320*
1.155	998.9	*5.5*	0.0055	*0.000526*	0.000456	0.000342	*4.334*	4.312	0.023	*3.324*
1.155	998.8	*5.9*	0.0060	*0.000576*	0.000499	0.000374	*4.336*	4.312	0.024	*3.334*
1.155	998.7	*6.4*	0.0064	*0.000609*	0.000528	0.000396	*4.338*	4.312	0.026	*3.323*
1.153	998.6	*6.9*	0.0069	*0.000656*	0.000568	0.000427	*4.340*	4.312	0.028	*3.315*
1.154	998.5	*7.5*	0.0075	*0.000706*	0.000612	0.000460	*4.342*	4.312	0.031	*3.333*
1.153	998.4	*8.0*	0.0080	*0.000746*	0.000647	0.000486	*4.344*	4.312	0.032	*3.324*
1.152	998.3	*7.0*	0.0070	*0.000783*	0.000680	0.000512	*4.345*	4.312	0.034	*3.322*
1.151	998.3	*7.3*	0.0073	*0.000829*	0.000720	0.000544	*4.347*	4.312	0.035	*3.309*
1.151	998.2	*2.6*	0.0026	*0.000287*	0.000249	0.000190	*4.326*	4.312	0.015	*3.307*
1.151	998.1	*3.0*	0.0030	*0.000334*	0.000290	0.000222	*4.328*	4.312	0.016	*3.296*
1.150	998.1	*3.1*	0.0031	*0.000353*	0.000307	0.000235	*4.329*	4.312	0.017	*3.309*
1.151	998.0	*3.5*	0.0036	*0.000413*	0.000359	0.000273	*4.331*	4.312	0.019	*3.338*
1.150	997.9	*3.8*	0.0038	*0.000445*	0.000387	0.000295	*4.332*	4.312	0.021	*3.326*
1.149	997.9	*4.3*	0.0043	*0.000500*	0.000435	0.000332	*4.336*	4.312	0.024	*3.319*
1.149	997.8	*4.7*	0.0048	*0.000566*	0.000493	0.000376	*4.338*	4.312	0.026	*3.321*
1.150	997.7	*5.6*	0.0056	*0.000640*	0.000557	0.000423	*4.341*	4.312	0.030	*3.342*
1.148	997.6	*5.9*	0.0059	*0.000722*	0.000629	0.000479	*4.344*	4.312	0.032	*3.319*
1.147	997.6	*6.6*	0.0066	*0.000775*	0.000675	0.000514	*4.347*	4.312	0.035	*3.316*
1.148	997.5	*7.2*	0.0072	*0.000833*	0.000726	0.000554	*4.349*	4.312	0.037	*3.294*
1.146	997.4	*7.4*	0.0074	*0.000840*	0.000732	0.000557	*4.350*	4.312	0.038	*3.309*
1.146	997.3	*2.8*	0.0028	*0.000309*	0.000270	0.000207	*4.330*	4.312	0.019	*3.315*
1.146	997.3	*3.5*	0.0035	*0.000382*	0.000333	0.000256	*4.332*	4.312	0.021	*3.299*
1.146	997.2	*3.3*	0.0033	*0.000445*	0.000388	0.000299	*4.334*	4.312	0.023	*3.294*
1.150	998.4	*2.7*	0.0027	*0.000162*	0.000141	0.000107	*4.324*	4.312	0.012	*3.323*
1.149	998.3	*3.6*	0.0036	*0.000304*	0.000265	0.000200	*4.328*	4.312	0.017	*3.336*
1.149	998.3	*4.1*	0.0041	*0.000383*	0.000333	0.000252	*4.331*	4.312	0.019	*3.330*
1.148	998.2	*4.5*	0.0045	*0.000457*	0.000398	0.000303	*4.332*	4.312	0.020	*3.293*
1.149	998.1	*4.7*	0.0047	*0.000498*	0.000434	0.000330	*4.336*	4.312	0.024	*3.295*

Density (kg/m3)		Water flow rate		Air flow rate			Water elevation header (m)	Mixing head lip elevation (m)	Water level over mixing head lip (m)	Water elevation tailrace (m)
Air (in)	Water	(kg/s)	(m3/s)	(kg/s)	in (m3/s)	out (m3/s)				
1.148	998.1	*5.7*	0.0058	*0.000557*	0.000485	0.000367	*4.338*	4.312	0.026	*3.320*
1.147	998.0	*6.4*	0.0064	*0.000600*	0.000523	0.000396	*4.340*	4.312	0.028	*3.318*
1.147	998.0	*7.0*	0.0070	*0.000648*	0.000565	0.000426	*4.342*	4.312	0.031	*3.324*
1.147	997.9	*7.6*	0.0076	*0.000718*	0.000626	0.000473	*4.344*	4.312	0.033	*3.311*
1.146	997.8	*6.6*	0.0066	*0.000742*	0.000647	0.000490	*4.345*	4.312	0.034	*3.325*
1.146	997.8	*7.0*	0.0070	*0.000767*	0.000669	0.000507	*4.346*	4.312	0.035	*3.319*
1.145	997.7	*7.1*	0.0071	*0.000779*	0.000680	0.000514	*4.348*	4.312	0.036	*3.329*
1.145	997.6	*7.2*	0.0072	*0.000810*	0.000707	0.000537	*4.349*	4.312	0.038	*3.309*
1.144	997.5	*2.3*	0.0023	*0.000112*	0.000098	0.000075	*4.324*	4.312	0.013	*3.338*
1.141	997.1	*2.1*	0.0021	*0.000249*	0.000218	0.000169	*4.330*	4.312	0.018	*3.251*
1.141	997.1	*3.1*	0.0031	*0.000330*	0.000290	0.000223	*4.332*	4.312	0.021	*3.296*
1.141	997.0	*3.9*	0.0039	*0.000405*	0.000355	0.000272	*4.334*	4.312	0.023	*3.318*
1.140	997.0	*4.3*	0.0043	*0.000430*	0.000377	0.000288	*4.337*	4.312	0.025	*3.326*
1.140	996.9	*4.7*	0.0047	*0.000496*	0.000435	0.000333	*4.339*	4.312	0.027	*3.321*
1.140	996.9	*4.9*	0.0049	*0.000574*	0.000503	0.000385	*4.341*	4.312	0.030	*3.317*
1.141	996.8	*5.6*	0.0056	*0.000649*	0.000569	0.000436	*4.344*	4.312	0.032	*3.300*
1.140	996.7	*5.4*	0.0054	*0.000650*	0.000570	0.000435	*4.345*	4.312	0.034	*3.335*
1.140	996.7	*6.7*	0.0067	*0.000757*	0.000664	0.000509	*4.349*	4.312	0.037	*3.300*
1.140	996.6	*7.2*	0.0072	*0.000756*	0.000664	0.000507	*4.350*	4.312	0.039	*3.309*
1.138	996.5	*7.4*	0.0074	*0.000775*	0.000681	0.000519	*4.352*	4.312	0.040	*3.314*
1.138	996.5	*1.8*	0.0018	*0.000126*	0.000110	0.000085	*4.328*	4.312	0.016	*3.322*
1.138	996.5	*2.5*	0.0026	*0.000182*	0.000160	0.000124	*4.329*	4.312	0.018	*3.274*
1.137	996.4	*2.7*	0.0027	*0.000224*	0.000197	0.000153	*4.331*	4.312	0.019	*3.282*
1.138	996.4	*3.0*	0.0030	*0.000307*	0.000270	0.000209	*4.333*	4.312	0.022	*3.276*
1.137	996.4	*3.5*	0.0035	*0.000374*	0.000329	0.000255	*4.336*	4.312	0.024	*3.278*
1.136	996.3	*4.2*	0.0042	*0.000408*	0.000359	0.000276	*4.338*	4.312	0.027	*3.318*
1.136	996.3	*4.7*	0.0047	*0.000513*	0.000451	0.000347	*4.341*	4.312	0.030	*3.317*
1.136	996.2	*5.3*	0.0053	*0.000615*	0.000542	0.000416	*4.344*	4.312	0.032	*3.315*
1.136	996.1	*5.8*	0.0058	*0.000652*	0.000574	0.000440	*4.347*	4.312	0.035	*3.330*

Density (kg/m3)		Water flow rate		Air flow rate			Water elevation header (m)	Mixing head lip elevation (m)	Water level over mixing head lip (m)	Water elevation tailrace (m)
Air (in)	Water	(kg/s)	(m3/s)	(kg/s)	in (m3/s)	out (m3/s)				
1.136	996.0	*8.3*	0.0083	*0.000724*	0.000637	0.000488	*4.352*	4.312	0.040	*3.298*
1.167	998.2	*8.9*	0.0090	*0.000720*	0.000617	0.000466	*4.347*	4.312	0.035	*3.311*
1.167	998.1	*7.3*	0.0074	*0.000749*	0.000642	0.000486	*4.346*	4.312	0.035	*3.324*
1.166	998.1	*7.3*	0.0073	*0.000732*	0.000627	0.000474	*4.347*	4.312	0.035	*3.342*
1.165	998.0	*7.4*	0.0074	*0.000746*	0.000641	0.000484	*4.347*	4.312	0.035	*3.345*
1.164	997.9	*7.3*	0.0073	*0.000730*	0.000627	0.000475	*4.347*	4.312	0.035	*3.341*
1.164	997.9	*7.3*	0.0073	*0.000743*	0.000638	0.000484	*4.347*	4.312	0.035	*3.337*
1.164	997.8	*7.3*	0.0073	*0.000698*	0.000600	0.000453	*4.347*	4.312	0.035	*3.357*
1.163	997.7	*7.3*	0.0073	*0.000723*	0.000621	0.000473	*4.347*	4.312	0.035	*3.321*
1.162	997.7	*7.1*	0.0071	*0.000704*	0.000606	0.000460	*4.347*	4.312	0.036	*3.337*
1.161	997.6	*7.1*	0.0072	*0.000709*	0.000611	0.000464	*4.347*	4.312	0.036	*3.336*
1.161	997.5	*7.1*	0.0071	*0.000715*	0.000616	0.000469	*4.347*	4.312	0.035	*3.327*
1.160	997.5	*7.1*	0.0071	*0.000708*	0.000610	0.000464	*4.348*	4.312	0.036	*3.339*
1.160	997.4	*7.0*	0.0070	*0.000678*	0.000585	0.000444	*4.347*	4.312	0.036	*3.346*
1.159	997.3	*7.0*	0.0070	*0.000697*	0.000602	0.000459	*4.347*	4.312	0.036	*3.317*
1.158	997.3	*6.9*	0.0069	*0.000700*	0.000605	0.000461	*4.348*	4.312	0.036	*3.328*
1.158	997.2	*6.8*	0.0069	*0.000692*	0.000598	0.000456	*4.347*	4.312	0.036	*3.329*
1.157	997.1	*6.7*	0.0067	*0.000675*	0.000584	0.000446	*4.347*	4.312	0.035	*3.323*
1.156	997.1	*6.5*	0.0065	*0.000672*	0.000581	0.000443	*4.347*	4.312	0.035	*3.334*
1.156	997.0	*6.4*	0.0065	*0.000643*	0.000556	0.000424	*4.347*	4.312	0.035	*3.342*
1.155	996.9	*6.3*	0.0063	*0.000628*	0.000544	0.000416	*4.346*	4.312	0.035	*3.335*
1.155	996.9	*5.9*	0.0059	*0.000643*	0.000557	0.000428	*4.345*	4.312	0.033	*3.300*
1.154	996.8	*6.1*	0.0061	*0.000604*	0.000524	0.000401	*4.345*	4.312	0.034	*3.337*
1.154	996.7	*5.7*	0.0057	*0.000570*	0.000494	0.000378	*4.345*	4.312	0.033	*3.342*
1.153	996.7	*5.7*	0.0057	*0.000602*	0.000522	0.000401	*4.345*	4.312	0.033	*3.326*
1.153	996.6	*5.5*	0.0056	*0.000572*	0.000496	0.000380	*4.344*	4.312	0.033	*3.343*
1.152	996.6	*5.5*	0.0055	*0.000573*	0.000498	0.000383	*4.344*	4.312	0.032	*3.311*
1.152	996.5	*5.4*	0.0054	*0.000523*	0.000454	0.000347	*4.343*	4.312	0.032	*3.353*
1.151	996.5	*5.0*	0.0050	*0.000503*	0.000437	0.000336	*4.342*	4.312	0.030	*3.320*

Density (kg/m3)		Water flow rate		Air flow rate			Water elevation header (m)	Mixing head lip elevation (m)	Water level over mixing head lip (m)	Water elevation tailrace (m)
Air (in)	Water	(kg/s)	(m3/s)	(kg/s)	in (m3/s)	out (m3/s)				
1.150	996.4	*5.0*	0.0050	*0.000507*	0.000441	0.000339	*4.342*	4.312	0.030	*3.324*
1.150	996.4	*5.5*	0.0056	*0.000495*	0.000430	0.000329	*4.342*	4.312	0.031	*3.352*
1.149	996.3	*4.7*	0.0047	*0.000451*	0.000393	0.000305	*4.339*	4.312	0.028	*3.269*
1.149	996.3	*4.2*	0.0042	*0.000412*	0.000359	0.000279	*4.338*	4.312	0.026	*3.278*
1.148	996.2	*4.1*	0.0041	*0.000374*	0.000326	0.000252	*4.337*	4.312	0.025	*3.307*
1.148	996.2	*3.7*	0.0037	*0.000351*	0.000306	0.000238	*4.335*	4.312	0.024	*3.272*
1.147	996.1	*3.4*	0.0035	*0.000278*	0.000243	0.000189	*4.334*	4.312	0.022	*3.269*
1.147	996.1	*3.5*	0.0035	*0.000292*	0.000255	0.000198	*4.334*	4.312	0.022	*3.279*
1.146	996.0	*3.2*	0.0032	*0.000245*	0.000214	0.000167	*4.332*	4.312	0.021	*3.272*

Appendix I: Bubble size measurement raw data

The photograph below has each of the measured bubbles circled. It was taken at the middle flow rate of Baby HAC at 5 kg/s with the Ragged Chutes head. The identification and measurement of these bubbles was performed by Arnaud Kottas. The large bubbles in the bottom section look a bit like wishful thinking, but their inclusion does not seem to have badly affected the distribution. Further details are included in section 6.4.1.

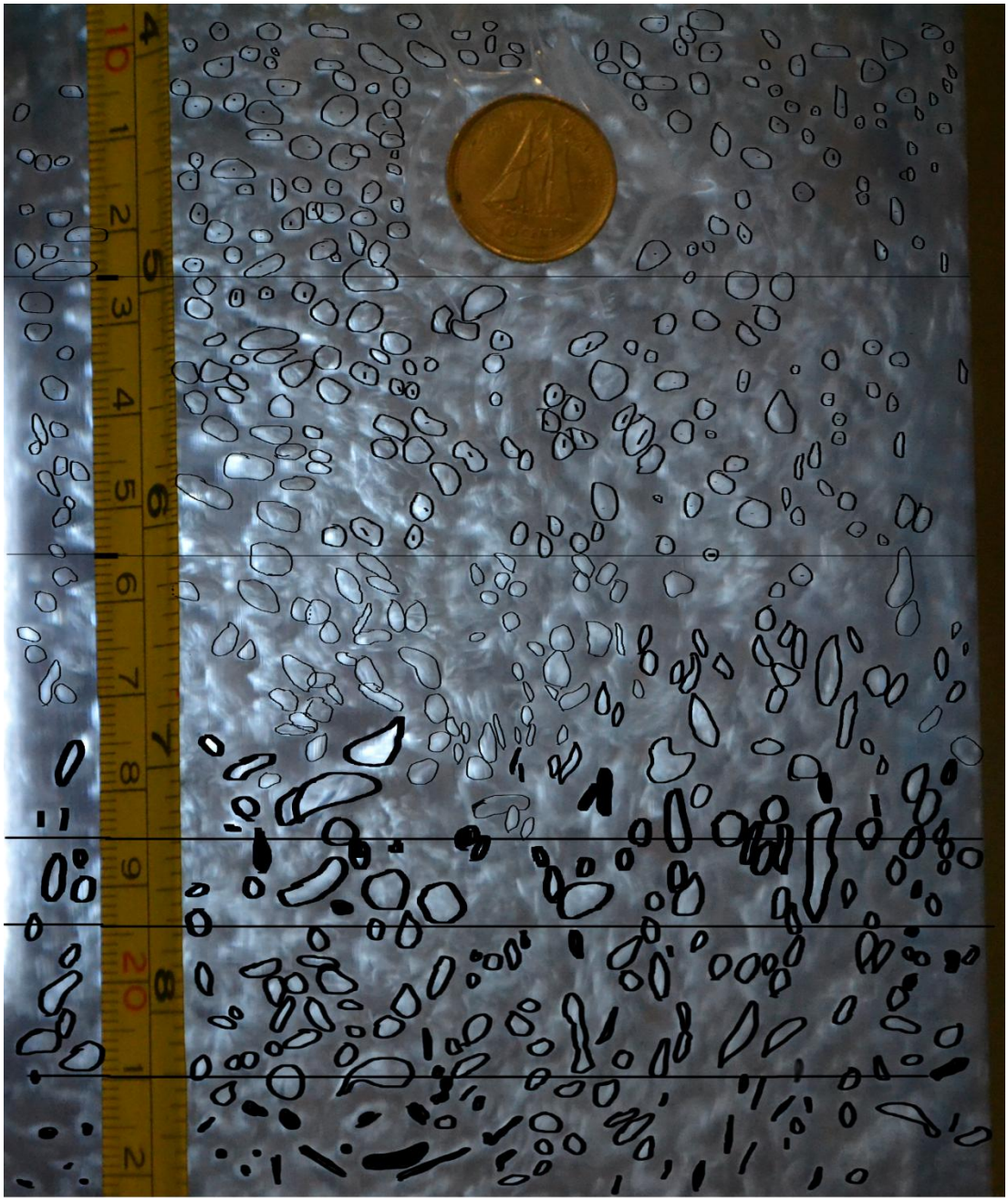

The scale on the raw image is 247 pixels to 10 mm. The table below is a list of all the bubbles measured in the photograph above ordered by the average axis diameter calculated per the Akita and Yoshida (1974) method cited in section 5.1.5.

#	Size (pixels)		Converted size (mm)			Volume (mm3)		Percent passing		
	short axis	long axis	short axis	long axis	average	bubble	cumulative	measured	R-R	Error
1	14	22	0.56	0.91	0.73	0.3	0.3	0.00	0.30	0.09
2	18	23	0.73	0.94	0.83	0.5	0.8	0.01	0.47	0.21
3	15	29	0.62	1.18	0.90	0.6	1.3	0.02	0.61	0.36
4	16	35	0.66	1.40	1.03	0.9	2.2	0.02	1.02	0.99
5	25	26	1.02	1.06	1.04	0.9	3.1	0.04	1.05	1.02
6	19	33	0.77	1.35	1.06	0.9	4.0	0.05	1.12	1.14
7	24	29	0.98	1.19	1.08	1.0	5.0	0.06	1.21	1.33
8	16	37	0.66	1.51	1.09	1.0	6.0	0.07	1.24	1.36
9	17	37	0.70	1.48	1.09	1.0	7.0	0.08	1.24	1.36
10	23	32	0.93	1.31	1.12	1.1	8.1	0.09	1.37	1.62
11	23	34	0.92	1.36	1.14	1.2	9.3	0.11	1.49	1.90
12	20	37	0.81	1.50	1.16	1.2	10.5	0.12	1.55	2.06
13	20	37	0.82	1.51	1.16	1.2	11.7	0.13	1.57	2.07
14	25	33	1.00	1.32	1.16	1.2	13.0	0.15	1.57	2.03
15	26	32	1.03	1.30	1.17	1.2	14.2	0.16	1.59	2.05
16	22	36	0.89	1.47	1.18	1.3	15.5	0.18	1.66	2.21
17	25	34	1.01	1.36	1.19	1.3	16.8	0.19	1.71	2.29
18	25	35	1.00	1.40	1.20	1.4	18.2	0.21	1.76	2.41
19	21	38	0.85	1.55	1.20	1.4	19.5	0.22	1.77	2.39
20	22	38	0.88	1.53	1.20	1.4	20.9	0.24	1.79	2.41
21	18	44	0.71	1.76	1.23	1.5	22.4	0.26	1.96	2.91
22	23	38	0.92	1.55	1.24	1.5	23.9	0.27	1.97	2.89
23	20	41	0.81	1.68	1.24	1.5	25.4	0.29	2.01	2.95
24	26	36	1.05	1.46	1.26	1.6	26.9	0.31	2.08	3.14
25	23	40	0.92	1.60	1.26	1.6	28.5	0.32	2.12	3.21
26	23	39	0.94	1.58	1.26	1.6	30.1	0.34	2.12	3.14
27	13	50	0.51	2.02	1.26	1.6	31.7	0.36	2.13	3.12
28	28	36	1.12	1.44	1.28	1.7	33.3	0.38	2.24	3.46
29	20	43	0.82	1.75	1.29	1.7	35.0	0.40	2.27	3.49
30	23	41	0.92	1.66	1.29	1.7	36.7	0.42	2.32	3.61
31	30	34	1.21	1.38	1.30	1.7	38.4	0.44	2.34	3.64
32	28	38	1.11	1.52	1.32	1.8	40.2	0.46	2.47	4.03
33	18	47	0.74	1.91	1.32	1.8	42.0	0.48	2.52	4.17
34	29	36	1.17	1.47	1.32	1.8	43.8	0.50	2.52	4.08
35	18	47	0.74	1.92	1.33	1.9	45.7	0.52	2.58	4.23

#	Size (pixels)		Converted size (mm)			Volume (mm3)		Percent passing		
	short axis	long axis	short axis	long axis	average	bubble	cumulative	measured	R-R	Error
36	27	40	1.08	1.61	1.34	1.9	47.6	0.54	2.66	4.49
37	28	40	1.11	1.63	1.37	2.0	49.6	0.57	2.87	5.31
38	25	43	1.00	1.76	1.38	2.1	51.7	0.59	2.92	5.41
39	23	45	0.94	1.83	1.38	2.1	53.8	0.61	2.95	5.44
40	20	49	0.82	1.96	1.39	2.1	55.9	0.64	3.01	5.63
41	33	36	1.32	1.47	1.39	2.1	58.0	0.66	3.02	5.59
42	24	45	0.96	1.83	1.39	2.1	60.1	0.69	3.04	5.55
43	25	44	1.01	1.79	1.40	2.2	62.3	0.71	3.09	5.66
44	30	39	1.22	1.60	1.41	2.2	64.5	0.73	3.14	5.77
45	19	51	0.77	2.06	1.41	2.2	66.7	0.76	3.20	5.96
46	23	47	0.92	1.91	1.42	2.2	68.9	0.79	3.22	5.92
47	22	48	0.91	1.94	1.42	2.3	71.2	0.81	3.27	6.03
48	28	43	1.14	1.72	1.43	2.3	73.5	0.84	3.33	6.24
49	34	37	1.36	1.51	1.43	2.3	75.8	0.86	3.35	6.19
50	30	41	1.20	1.68	1.44	2.3	78.2	0.89	3.40	6.31
51	23	48	0.94	1.95	1.45	2.4	80.5	0.92	3.45	6.44
52	15	57	0.60	2.30	1.45	2.4	82.9	0.94	3.49	6.48
53	31	40	1.27	1.63	1.45	2.4	85.3	0.97	3.51	6.43
54	29	43	1.18	1.73	1.45	2.4	87.7	1.00	3.52	6.38
55	29	43	1.19	1.75	1.47	2.5	90.2	1.03	3.65	6.87
56	19	53	0.78	2.16	1.47	2.5	92.7	1.06	3.65	6.72
57	31	41	1.27	1.67	1.47	2.5	95.2	1.08	3.67	6.67
58	24	48	0.99	1.96	1.47	2.5	97.7	1.11	3.69	6.62
59	28	45	1.14	1.82	1.48	2.5	100.2	1.14	3.76	6.85
60	21	52	0.85	2.11	1.48	2.5	102.8	1.17	3.76	6.70
61	18	55	0.74	2.21	1.48	2.5	105.3	1.20	3.76	6.55
62	31	42	1.25	1.72	1.48	2.6	107.9	1.23	3.80	6.59
63	26	48	1.03	1.94	1.49	2.6	110.5	1.26	3.81	6.53
64	31	43	1.25	1.72	1.49	2.6	113.1	1.29	3.83	6.48
65	24	50	0.98	2.03	1.50	2.7	115.7	1.32	3.98	7.10
66	27	47	1.11	1.91	1.51	2.7	118.4	1.35	4.00	7.04
67	34	40	1.38	1.64	1.51	2.7	121.1	1.38	4.02	6.98
68	24	50	0.98	2.03	1.51	2.7	123.8	1.41	4.02	6.82
69	23	52	0.92	2.11	1.51	2.7	126.5	1.44	4.08	6.96
70	33	42	1.32	1.71	1.52	2.7	129.3	1.47	4.10	6.90
71	30	45	1.21	1.83	1.52	2.8	132.0	1.50	4.16	7.05
72	30	45	1.22	1.83	1.52	2.8	134.8	1.54	4.18	6.99
73	25	51	1.00	2.07	1.53	2.8	137.6	1.57	4.26	7.24
74	33	43	1.34	1.73	1.53	2.8	140.5	1.60	4.26	7.07
75	30	47	1.21	1.89	1.55	2.9	143.4	1.63	4.42	7.77

#	Size (pixels)		Converted size (mm)			Volume (mm3)		Percent passing		
	short axis	long axis	short axis	long axis	average	bubble	cumulative	measured	R-R	Error
76	33	44	1.32	1.79	1.55	3.0	146.3	1.67	4.48	7.93
77	36	41	1.45	1.67	1.56	3.0	149.3	1.70	4.50	7.86
78	23	54	0.93	2.19	1.56	3.0	152.3	1.73	4.53	7.79
79	28	49	1.14	1.98	1.56	3.0	155.2	1.77	4.53	7.60
80	35	42	1.41	1.71	1.56	3.0	158.2	1.80	4.53	7.41
81	33	44	1.33	1.80	1.56	3.0	161.2	1.84	4.59	7.57
82	30	48	1.21	1.93	1.57	3.0	164.2	1.87	4.61	7.50
83	28	50	1.11	2.04	1.57	3.1	167.3	1.91	4.70	7.78
84	31	47	1.26	1.90	1.58	3.1	170.4	1.94	4.76	7.94
85	26	52	1.06	2.11	1.59	3.1	173.5	1.98	4.80	7.99
86	27	52	1.09	2.10	1.60	3.2	176.7	2.01	4.94	8.54
87	36	43	1.46	1.75	1.61	3.2	180.0	2.05	5.03	8.85
88	25	55	1.01	2.21	1.61	3.3	183.3	2.09	5.07	8.89
89	29	51	1.16	2.06	1.61	3.3	186.6	2.13	5.09	8.81
90	30	50	1.21	2.01	1.61	3.3	189.8	2.16	5.09	8.59
91	26	54	1.06	2.17	1.62	3.3	193.2	2.20	5.16	8.77
92	35	45	1.42	1.83	1.62	3.4	196.5	2.24	5.23	8.95
93	28	52	1.15	2.11	1.63	3.4	199.9	2.28	5.25	8.86
94	34	47	1.36	1.89	1.63	3.4	203.3	2.32	5.28	8.77
95	23	57	0.94	2.32	1.63	3.4	206.7	2.35	5.30	8.68
96	28	53	1.13	2.14	1.63	3.4	210.1	2.39	5.35	8.72
97	32	49	1.31	1.97	1.64	3.5	213.6	2.43	5.42	8.91
98	20	62	0.79	2.49	1.64	3.5	217.1	2.47	5.47	8.96
99	32	49	1.30	2.00	1.65	3.5	220.6	2.51	5.51	9.01
100	36	45	1.47	1.84	1.65	3.5	224.1	2.55	5.56	9.05
101	25	57	1.00	2.31	1.65	3.6	227.7	2.59	5.59	8.95
102	33	48	1.35	1.96	1.66	3.6	231.2	2.63	5.61	8.86
103	30	52	1.22	2.10	1.66	3.6	234.8	2.68	5.66	8.90
104	20	62	0.82	2.52	1.67	3.6	238.5	2.72	5.76	9.25
105	23	59	0.94	2.40	1.67	3.7	242.1	2.76	5.78	9.14
106	25	58	1.01	2.33	1.67	3.7	245.8	2.80	5.78	8.89
107	30	52	1.23	2.11	1.67	3.7	249.5	2.84	5.81	8.79
108	34	48	1.39	1.96	1.68	3.7	253.2	2.88	5.86	8.84
109	32	51	1.30	2.06	1.68	3.7	256.9	2.93	5.93	9.04
110	29	54	1.17	2.20	1.68	3.8	260.6	2.97	5.96	8.93
111	38	45	1.54	1.83	1.69	3.8	264.4	3.01	6.01	8.98
112	39	45	1.57	1.81	1.69	3.8	268.2	3.06	6.03	8.87
113	26	58	1.03	2.35	1.69	3.8	272.0	3.10	6.06	8.77
114	23	61	0.95	2.45	1.70	3.9	275.9	3.14	6.16	9.12
115	36	48	1.47	1.94	1.71	3.9	279.8	3.19	6.24	9.32

#	Size (pixels)		Converted size (mm)			Volume (mm3)		Percent passing		
	short axis	long axis	short axis	long axis	average	bubble	cumulative	measured	R-R	Error
116	39	46	1.57	1.84	1.71	3.9	283.7	3.23	6.24	9.05
117	32	53	1.30	2.14	1.72	4.0	287.7	3.28	6.40	9.75
118	25	60	1.01	2.43	1.72	4.0	291.7	3.32	6.43	9.63
119	40	45	1.61	1.83	1.72	4.0	295.7	3.37	6.45	9.51
120	21	64	0.85	2.59	1.72	4.0	299.7	3.41	6.45	9.23
121	32	53	1.30	2.15	1.73	4.0	303.8	3.46	6.51	9.28
122	40	45	1.63	1.83	1.73	4.1	307.8	3.51	6.53	9.16
123	27	59	1.09	2.39	1.74	4.1	311.9	3.55	6.67	9.70
124	29	57	1.16	2.32	1.74	4.1	316.1	3.60	6.70	9.58
125	30	56	1.22	2.26	1.74	4.1	320.2	3.65	6.70	9.29
126	31	55	1.25	2.24	1.74	4.2	324.4	3.70	6.75	9.34
127	38	49	1.52	1.97	1.74	4.2	328.6	3.74	6.75	9.05
128	42	44	1.72	1.78	1.75	4.2	332.8	3.79	6.78	8.93
129	34	52	1.38	2.11	1.75	4.2	337.0	3.84	6.81	8.81
130	38	48	1.54	1.96	1.75	4.2	341.2	3.89	6.83	8.69
131	30	56	1.22	2.28	1.75	4.2	345.4	3.94	6.83	8.41
132	32	55	1.28	2.24	1.76	4.3	349.7	3.98	6.95	8.78
133	31	57	1.24	2.30	1.77	4.3	354.0	4.03	7.06	9.16
134	37	51	1.50	2.05	1.78	4.4	358.4	4.08	7.17	9.55
135	28	61	1.12	2.46	1.79	4.5	362.9	4.13	7.38	10.51
136	39	49	1.59	2.00	1.79	4.5	367.4	4.19	7.41	10.37
137	33	55	1.34	2.24	1.79	4.5	371.9	4.24	7.44	10.23
138	35	54	1.41	2.18	1.79	4.5	376.5	4.29	7.44	9.90
139	44	45	1.78	1.82	1.80	4.6	381.0	4.34	7.49	9.95
140	29	60	1.19	2.41	1.80	4.6	385.6	4.39	7.55	9.99
141	22	67	0.89	2.72	1.80	4.6	390.2	4.45	7.58	9.85
142	31	58	1.26	2.35	1.81	4.6	394.9	4.50	7.61	9.71
143	31	59	1.25	2.37	1.81	4.6	399.5	4.55	7.64	9.56
144	24	65	0.98	2.65	1.81	4.7	404.2	4.60	7.70	9.61
145	37	52	1.51	2.12	1.82	4.7	408.9	4.66	7.76	9.65
146	18	73	0.71	2.95	1.83	4.8	413.7	4.71	7.95	10.47
147	30	60	1.22	2.45	1.83	4.8	418.5	4.77	8.01	10.51
148	30	61	1.20	2.47	1.83	4.8	423.3	4.82	8.04	10.35
149	32	59	1.28	2.40	1.84	4.9	428.2	4.88	8.10	10.40
150	45	46	1.82	1.86	1.84	4.9	433.1	4.93	8.17	10.44
151	39	52	1.60	2.09	1.84	4.9	438.0	4.99	8.17	10.08
152	38	53	1.55	2.15	1.85	5.0	443.0	5.05	8.26	10.32
153	27	65	1.09	2.61	1.85	5.0	448.0	5.10	8.29	10.16
154	32	60	1.29	2.44	1.86	5.1	453.1	5.16	8.52	11.25
155	34	59	1.36	2.37	1.87	5.1	458.2	5.22	8.55	11.07

#	Size (pixels)		Converted size (mm)		Volume (mm3)			Percent passing		
	short axis	long axis	short axis	long axis	average	bubble	cumulative	measured	R-R	Error
156	28	64	1.14	2.59	1.87	5.1	463.3	5.28	8.55	10.69
157	36	56	1.47	2.27	1.87	5.1	468.4	5.34	8.58	10.52
158	40	53	1.60	2.15	1.88	5.2	473.6	5.40	8.74	11.21
159	30	63	1.20	2.56	1.88	5.2	478.8	5.46	8.78	11.03
160	37	56	1.49	2.27	1.88	5.2	484.1	5.52	8.81	10.85
161	33	60	1.34	2.44	1.89	5.3	489.3	5.58	8.88	10.89
162	30	63	1.22	2.56	1.89	5.3	494.6	5.64	8.91	10.71
163	29	64	1.19	2.60	1.89	5.3	500.0	5.70	8.98	10.75
164	44	50	1.78	2.01	1.89	5.3	505.3	5.76	8.98	10.36
165	39	55	1.58	2.21	1.90	5.4	510.6	5.82	9.04	10.40
166	32	62	1.29	2.52	1.90	5.4	516.1	5.88	9.14	10.65
167	32	62	1.29	2.52	1.91	5.4	521.5	5.94	9.21	10.69
168	60	34	2.42	1.39	1.91	5.4	526.9	6.00	9.21	10.29
169	34	60	1.38	2.43	1.91	5.5	532.4	6.07	9.24	10.11
170	31	64	1.23	2.58	1.91	5.5	537.9	6.13	9.24	9.71
171	41	54	1.64	2.18	1.91	5.5	543.4	6.19	9.28	9.54
172	26	69	1.04	2.79	1.91	5.5	548.9	6.25	9.31	9.36
173	45	50	1.82	2.01	1.91	5.5	554.4	6.32	9.31	8.98
174	18	76	0.74	3.09	1.92	5.5	559.9	6.38	9.38	9.02
175	26	69	1.06	2.77	1.92	5.5	565.4	6.44	9.38	8.64
176	43	52	1.74	2.10	1.92	5.6	571.0	6.51	9.42	8.47
177	34	61	1.38	2.47	1.92	5.6	576.6	6.57	9.49	8.51
178	36	59	1.47	2.38	1.92	5.6	582.1	6.63	9.49	8.14
179	32	63	1.31	2.54	1.93	5.6	587.7	6.70	9.52	7.97
180	28	67	1.14	2.72	1.93	5.6	593.4	6.76	9.55	7.81
181	34	61	1.38	2.47	1.93	5.6	599.0	6.82	9.59	7.65
182	31	65	1.25	2.62	1.94	5.7	604.7	6.89	9.73	8.07
183	39	57	1.58	2.29	1.94	5.7	610.4	6.95	9.73	7.70
184	36	60	1.44	2.45	1.94	5.7	616.2	7.02	9.80	7.73
185	34	62	1.38	2.50	1.94	5.7	621.9	7.09	9.80	7.37
186	25	71	1.00	2.89	1.94	5.8	627.7	7.15	9.84	7.21
187	36	60	1.47	2.41	1.94	5.8	633.4	7.22	9.84	6.86
188	30	66	1.22	2.67	1.95	5.8	639.2	7.28	9.87	6.70
189	27	69	1.08	2.81	1.95	5.8	645.0	7.35	9.87	6.36
190	39	57	1.58	2.32	1.95	5.8	650.8	7.41	9.94	6.39
191	28	68	1.15	2.76	1.95	5.8	656.7	7.48	9.98	6.24
192	30	66	1.22	2.68	1.95	5.8	662.5	7.55	9.98	5.91
193	28	68	1.13	2.77	1.95	5.8	668.3	7.61	9.98	5.59
194	39	57	1.58	2.32	1.95	5.9	674.2	7.68	10.01	5.44
195	37	60	1.51	2.41	1.96	5.9	680.1	7.75	10.09	5.47

#	Size (pixels)		Converted size (mm)		Volume (mm3)			Percent passing		
	short axis	long axis	short axis	long axis	average	bubble	cumulative	measured	R-R	Error
196	36	61	1.47	2.47	1.97	6.0	686.0	7.82	10.23	5.83
197	40	57	1.64	2.30	1.97	6.0	692.0	7.88	10.27	5.68
198	34	64	1.36	2.58	1.97	6.0	698.0	7.95	10.34	5.70
199	41	56	1.68	2.27	1.97	6.0	704.1	8.02	10.38	5.55
200	38	61	1.52	2.45	1.99	6.2	710.2	8.09	10.60	6.29
201	39	59	1.58	2.40	1.99	6.2	716.4	8.16	10.67	6.31
202	20	78	0.81	3.17	1.99	6.2	722.6	8.23	10.71	6.14
203	37	62	1.49	2.50	1.99	6.2	728.8	8.30	10.71	5.80
204	28	71	1.13	2.86	1.99	6.2	735.1	8.37	10.75	5.64
205	46	53	1.87	2.13	2.00	6.3	741.3	8.45	10.82	5.66
206	45	54	1.81	2.19	2.00	6.3	747.6	8.52	10.86	5.50
207	30	69	1.23	2.78	2.00	6.3	753.9	8.59	10.94	5.52
208	28	71	1.14	2.87	2.00	6.3	760.3	8.66	10.94	5.18
209	48	51	1.95	2.07	2.01	6.4	766.6	8.73	11.05	5.37
210	40	59	1.62	2.40	2.01	6.4	773.0	8.81	11.05	5.04
211	39	61	1.57	2.45	2.01	6.4	779.4	8.88	11.09	4.89
212	38	61	1.55	2.49	2.02	6.4	785.8	8.95	11.17	4.90
213	36	64	1.44	2.61	2.02	6.5	792.4	9.03	11.32	5.27
214	32	68	1.30	2.76	2.03	6.6	798.9	9.10	11.40	5.28
215	41	59	1.66	2.40	2.03	6.6	805.5	9.18	11.40	4.95
216	48	53	1.92	2.15	2.04	6.7	812.1	9.25	11.60	5.50
217	35	66	1.42	2.66	2.04	6.7	818.8	9.33	11.68	5.51
218	46	56	1.85	2.25	2.05	6.8	825.6	9.41	11.80	5.71
219	40	61	1.63	2.47	2.05	6.8	832.3	9.48	11.80	5.35
220	38	63	1.54	2.57	2.05	6.8	839.1	9.56	11.92	5.55
221	35	67	1.40	2.72	2.06	6.8	846.0	9.64	11.96	5.37
222	40	62	1.60	2.51	2.06	6.9	852.8	9.72	12.00	5.20
223	30	72	1.23	2.90	2.06	6.9	859.7	9.79	12.12	5.39
224	28	75	1.11	3.02	2.07	7.0	866.7	9.87	12.20	5.40
225	30	72	1.22	2.92	2.07	7.0	873.7	9.95	12.24	5.23
226	47	56	1.89	2.26	2.07	7.0	880.7	10.03	12.32	5.23
227	28	74	1.14	3.01	2.08	7.0	887.7	10.11	12.36	5.06
228	43	60	1.74	2.42	2.08	7.1	894.8	10.19	12.40	4.88
229	34	69	1.38	2.78	2.08	7.1	901.8	10.27	12.45	4.71
230	39	64	1.56	2.60	2.08	7.1	908.9	10.36	12.49	4.54
231	46	57	1.87	2.30	2.09	7.1	916.1	10.44	12.53	4.37
232	48	55	1.93	2.24	2.09	7.1	923.2	10.52	12.53	4.04
233	29	75	1.16	3.02	2.09	7.2	930.3	10.60	12.61	4.05
234	42	62	1.69	2.49	2.09	7.2	937.5	10.68	12.69	4.05
235	48	55	1.96	2.23	2.10	7.2	944.8	10.76	12.74	3.89

#	Size (pixels)		Converted size (mm)		Volume (mm3)			Percent passing		
	short axis	long axis	short axis	long axis	average	bubble	cumulative	measured	R-R	Error
236	40	64	1.63	2.57	2.10	7.3	952.1	10.85	12.90	4.23
237	25	79	1.01	3.20	2.11	7.3	959.4	10.93	12.95	4.07
238	41	63	1.66	2.55	2.11	7.3	966.8	11.01	12.99	3.90
239	44	60	1.80	2.42	2.11	7.4	974.1	11.10	13.03	3.74
240	40	64	1.62	2.61	2.11	7.4	981.5	11.18	13.12	3.74
241	33	71	1.34	2.89	2.12	7.5	989.0	11.27	13.20	3.74
242	51	53	2.08	2.16	2.12	7.5	996.5	11.35	13.25	3.58
243	37	68	1.49	2.76	2.13	7.5	1004.0	11.44	13.37	3.75
244	28	77	1.12	3.13	2.13	7.5	1011.6	11.52	13.37	3.42
245	35	70	1.41	2.84	2.13	7.5	1019.1	11.61	13.37	3.11
246	47	58	1.89	2.36	2.13	7.5	1026.6	11.70	13.37	2.82
247	36	69	1.46	2.80	2.13	7.6	1034.2	11.78	13.42	2.67
248	50	56	2.01	2.25	2.13	7.6	1041.8	11.87	13.42	2.40
249	23	82	0.94	3.32	2.13	7.6	1049.4	11.96	13.50	2.40
250	50	55	2.03	2.23	2.13	7.6	1057.0	12.04	13.50	2.14
251	39	66	1.58	2.68	2.13	7.6	1064.6	12.13	13.50	1.89
252	41	64	1.66	2.61	2.13	7.6	1072.2	12.22	13.55	1.78
253	31	75	1.24	3.05	2.14	7.7	1080.0	12.30	13.77	2.14
254	39	67	1.57	2.72	2.15	7.8	1087.7	12.39	13.86	2.14
255	45	62	1.81	2.51	2.16	7.9	1095.6	12.48	14.08	2.54
256	25	82	1.02	3.32	2.17	8.0	1103.6	12.57	14.30	2.99
257	44	63	1.80	2.54	2.17	8.0	1111.7	12.67	14.35	2.83
258	38	69	1.54	2.81	2.17	8.0	1119.7	12.76	14.39	2.67
259	44	63	1.79	2.55	2.17	8.1	1127.8	12.85	14.44	2.52
260	48	59	1.96	2.40	2.18	8.1	1135.9	12.94	14.48	2.38
261	19	88	0.77	3.58	2.18	8.1	1144.0	13.03	14.48	2.10
262	47	61	1.91	2.45	2.18	8.1	1152.1	13.13	14.53	1.97
263	49	59	1.97	2.40	2.18	8.2	1160.2	13.22	14.62	1.96
264	38	70	1.54	2.83	2.19	8.2	1168.4	13.31	14.71	1.96
265	32	76	1.30	3.09	2.19	8.3	1176.7	13.41	14.89	2.21
266	40	69	1.62	2.80	2.21	8.5	1185.2	13.50	15.22	2.95
267	46	64	1.84	2.57	2.21	8.5	1193.7	13.60	15.22	2.63
268	31	78	1.27	3.15	2.21	8.5	1202.1	13.70	15.27	2.47
269	33	76	1.34	3.09	2.21	8.5	1210.7	13.79	15.31	2.31
270	53	56	2.15	2.28	2.21	8.5	1219.2	13.89	15.36	2.16
271	39	70	1.60	2.84	2.22	8.6	1227.8	13.99	15.46	2.15
272	50	60	2.03	2.41	2.22	8.6	1236.3	14.09	15.46	1.88
273	35	75	1.41	3.02	2.22	8.6	1244.9	14.18	15.46	1.62
274	35	74	1.43	3.01	2.22	8.6	1253.5	14.28	15.55	1.61
275	51	59	2.06	2.39	2.23	8.7	1262.2	14.38	15.64	1.60

#	Size (pixels)		Converted size (mm)			Volume (mm3)		Percent passing		
	short axis	long axis	short axis	long axis	average	bubble	cumulative	measured	R-R	Error
276	36	74	1.45	3.01	2.23	8.7	1270.9	14.48	15.69	1.47
277	46	64	1.85	2.61	2.23	8.7	1279.6	14.58	15.69	1.24
278	53	58	2.13	2.33	2.23	8.7	1288.3	14.68	15.69	1.03
279	45	65	1.84	2.62	2.23	8.7	1297.0	14.78	15.74	0.93
280	43	67	1.74	2.72	2.23	8.7	1305.7	14.88	15.74	0.75
281	55	56	2.21	2.26	2.24	8.8	1314.5	14.98	15.88	0.82
282	38	72	1.55	2.93	2.24	8.8	1323.3	15.08	15.93	0.73
283	39	72	1.56	2.92	2.24	8.8	1332.2	15.18	15.98	0.64
284	33	78	1.33	3.15	2.24	8.9	1341.0	15.28	16.03	0.56
285	45	66	1.81	2.68	2.24	8.9	1349.9	15.38	16.08	0.49
286	53	59	2.13	2.37	2.25	8.9	1358.8	15.48	16.13	0.41
287	38	73	1.54	2.96	2.25	9.0	1367.8	15.58	16.27	0.47
288	53	59	2.15	2.37	2.26	9.0	1376.8	15.69	16.37	0.47
289	50	61	2.04	2.47	2.26	9.0	1385.9	15.79	16.37	0.34
290	54	57	2.20	2.32	2.26	9.1	1395.0	15.89	16.52	0.39
291	54	58	2.17	2.35	2.26	9.1	1404.1	16.00	16.52	0.27
292	18	94	0.71	3.82	2.27	9.1	1413.2	16.10	16.57	0.22
293	28	84	1.13	3.40	2.27	9.2	1422.4	16.21	16.61	0.17
294	35	77	1.43	3.12	2.27	9.2	1431.6	16.31	16.76	0.20
295	45	67	1.83	2.72	2.27	9.2	1440.8	16.42	16.76	0.12
296	27	85	1.10	3.46	2.28	9.3	1450.1	16.52	16.91	0.15
297	27	86	1.10	3.47	2.29	9.4	1459.5	16.63	17.06	0.19
298	48	65	1.96	2.61	2.29	9.4	1468.9	16.73	17.06	0.11
299	38	75	1.54	3.03	2.29	9.4	1478.3	16.84	17.11	0.07
300	27	86	1.09	3.49	2.29	9.4	1487.7	16.95	17.16	0.05
301	42	72	1.68	2.90	2.29	9.5	1497.2	17.06	17.26	0.04
302	37	77	1.48	3.11	2.30	9.5	1506.7	17.17	17.31	0.02
303	35	79	1.40	3.19	2.30	9.6	1516.2	17.27	17.42	0.02
304	49	65	1.98	2.64	2.31	9.7	1525.9	17.38	17.62	0.06
305	47	68	1.88	2.74	2.31	9.7	1535.6	17.49	17.67	0.03
306	48	66	1.94	2.68	2.31	9.7	1545.3	17.61	17.72	0.01
307	32	83	1.28	3.35	2.31	9.7	1555.0	17.72	17.77	0.00
308	51	63	2.07	2.56	2.31	9.7	1564.7	17.83	17.77	0.00
309	32	83	1.28	3.35	2.32	9.8	1574.5	17.94	17.82	0.01
310	46	68	1.86	2.77	2.32	9.8	1584.2	18.05	17.82	0.05
311	42	72	1.71	2.92	2.32	9.8	1594.0	18.16	17.82	0.11
312	42	72	1.72	2.92	2.32	9.8	1603.8	18.27	17.88	0.16
313	39	76	1.57	3.06	2.32	9.8	1613.5	18.38	17.88	0.26
314	45	70	1.83	2.82	2.33	9.9	1623.4	18.50	18.08	0.17
315	35	80	1.43	3.24	2.34	10.0	1633.5	18.61	18.40	0.05

#	Size (pixels)		Converted size (mm)			Volume (mm3)		Percent passing		
	short axis	long axis	short axis	long axis	average	bubble	cumulative	measured	R-R	Error
316	35	80	1.42	3.26	2.34	10.0	1643.5	18.72	18.40	0.11
317	36	79	1.47	3.21	2.34	10.1	1653.6	18.84	18.45	0.15
318	31	85	1.25	3.44	2.34	10.1	1663.7	18.95	18.55	0.16
319	40	76	1.63	3.08	2.35	10.2	1673.9	19.07	18.82	0.06
320	56	61	2.26	2.46	2.36	10.3	1684.2	19.19	18.87	0.10
321	53	64	2.13	2.59	2.36	10.3	1694.5	19.31	18.87	0.19
322	47	70	1.90	2.83	2.37	10.4	1704.9	19.42	19.14	0.08
323	57	60	2.32	2.42	2.37	10.5	1715.3	19.54	19.24	0.09
324	46	71	1.87	2.89	2.38	10.5	1725.9	19.66	19.41	0.07
325	47	71	1.92	2.85	2.39	10.7	1736.6	19.78	19.68	0.01
326	44	74	1.79	2.98	2.39	10.7	1747.3	19.91	19.73	0.03
327	25	93	1.02	3.76	2.39	10.7	1758.0	20.03	19.79	0.06
328	57	61	2.31	2.47	2.39	10.7	1768.7	20.15	19.79	0.13
329	44	74	1.79	3.00	2.39	10.8	1779.5	20.27	19.84	0.19
330	57	62	2.31	2.49	2.40	10.8	1790.3	20.40	20.01	0.15
331	27	91	1.11	3.70	2.40	10.9	1801.2	20.52	20.12	0.16
332	42	77	1.71	3.10	2.40	10.9	1812.2	20.65	20.17	0.23
333	40	79	1.60	3.21	2.41	11.0	1823.1	20.77	20.23	0.30
334	50	69	2.01	2.80	2.41	11.0	1834.1	20.90	20.23	0.45
335	40	79	1.61	3.21	2.41	11.0	1845.0	21.02	20.28	0.55
336	44	75	1.80	3.02	2.41	11.0	1856.0	21.15	20.34	0.65
337	33	86	1.34	3.49	2.41	11.1	1867.1	21.27	20.45	0.68
338	50	69	2.04	2.81	2.42	11.1	1878.2	21.40	20.62	0.61
339	46	74	1.86	3.00	2.43	11.3	1889.5	21.53	20.90	0.40
340	34	86	1.37	3.49	2.43	11.3	1900.8	21.66	20.90	0.58
341	23	98	0.92	3.95	2.44	11.3	1912.2	21.79	21.01	0.60
342	58	63	2.34	2.53	2.44	11.3	1923.5	21.91	21.01	0.82
343	38	83	1.52	3.36	2.44	11.4	1934.9	22.04	21.12	0.85
344	49	71	1.99	2.89	2.44	11.4	1946.3	22.17	21.18	0.99
345	56	65	2.25	2.64	2.44	11.5	1957.8	22.31	21.24	1.14
346	46	75	1.87	3.04	2.46	11.6	1969.4	22.44	21.58	0.74
347	58	64	2.34	2.57	2.46	11.6	1981.0	22.57	21.58	0.98
348	48	73	1.95	2.96	2.46	11.6	1992.7	22.70	21.58	1.26
349	49	72	1.99	2.93	2.46	11.7	2004.4	22.84	21.69	1.31
350	41	81	1.64	3.28	2.46	11.7	2016.0	22.97	21.69	1.63
351	40	82	1.61	3.33	2.47	11.8	2027.9	23.10	21.98	1.26
352	23	99	0.92	4.02	2.47	11.9	2039.7	23.24	22.04	1.44
353	42	81	1.69	3.28	2.48	12.0	2051.8	23.38	22.39	0.97
354	52	71	2.09	2.88	2.49	12.1	2063.8	23.51	22.45	1.14
355	28	95	1.13	3.85	2.49	12.1	2075.9	23.65	22.57	1.18

#	Size (pixels)		Converted size (mm)		Volume (mm3)			Percent passing		
	short axis	long axis	short axis	long axis	average	bubble	cumulative	measured	R-R	Error
356	35	89	1.41	3.59	2.50	12.3	2088.2	23.79	22.86	0.87
357	38	86	1.54	3.47	2.50	12.3	2100.6	23.93	22.98	0.91
358	47	77	1.90	3.11	2.50	12.3	2112.9	24.07	22.98	1.20
359	54	70	2.19	2.83	2.51	12.4	2125.3	24.21	23.10	1.25
360	30	94	1.22	3.81	2.52	12.5	2137.8	24.36	23.34	1.04
361	41	83	1.67	3.36	2.52	12.5	2150.3	24.50	23.40	1.22
362	41	84	1.66	3.38	2.52	12.6	2162.9	24.64	23.46	1.41
363	59	65	2.40	2.64	2.52	12.6	2175.5	24.79	23.46	1.77
364	33	92	1.33	3.72	2.52	12.6	2188.1	24.93	23.52	2.00
365	40	84	1.63	3.41	2.52	12.6	2200.7	25.07	23.52	2.42
366	47	78	1.88	3.17	2.53	12.7	2213.3	25.22	23.64	2.50
367	58	68	2.33	2.76	2.55	13.0	2226.3	25.36	24.24	1.26
368	42	84	1.70	3.41	2.55	13.1	2239.4	25.51	24.49	1.06
369	37	89	1.50	3.61	2.55	13.1	2252.5	25.66	24.49	1.38
370	47	79	1.90	3.21	2.56	13.1	2265.6	25.81	24.55	1.60
371	38	88	1.54	3.57	2.56	13.1	2278.8	25.96	24.55	2.00
372	43	84	1.72	3.40	2.56	13.3	2292.0	26.11	24.79	1.74
373	43	84	1.76	3.38	2.57	13.3	2305.3	26.26	24.98	1.65
374	49	79	1.97	3.18	2.57	13.4	2318.7	26.42	25.04	1.89
375	48	79	1.95	3.19	2.57	13.4	2332.1	26.57	25.04	2.34
376	63	64	2.55	2.60	2.57	13.4	2345.5	26.72	25.10	2.62
377	25	102	1.02	4.14	2.58	13.4	2359.0	26.88	25.17	2.93
378	45	82	1.83	3.32	2.58	13.5	2372.4	27.03	25.23	3.25
379	57	71	2.31	2.86	2.58	13.5	2386.0	27.18	25.35	3.35
380	61	67	2.48	2.69	2.59	13.6	2399.5	27.34	25.41	3.70
381	59	69	2.40	2.80	2.60	13.8	2413.3	27.50	25.92	2.49
382	28	101	1.11	4.10	2.61	13.9	2427.2	27.65	26.04	2.59
383	40	89	1.63	3.59	2.61	13.9	2441.2	27.81	26.11	2.91
384	63	66	2.55	2.68	2.61	14.0	2455.2	27.97	26.30	2.81
385	40	90	1.60	3.63	2.61	14.0	2469.2	28.13	26.30	3.37
386	44	85	1.79	3.46	2.62	14.1	2483.3	28.29	26.55	3.03
387	42	88	1.69	3.55	2.62	14.1	2497.5	28.45	26.55	3.62
388	40	90	1.62	3.63	2.62	14.2	2511.7	28.62	26.62	4.00
389	52	78	2.11	3.15	2.63	14.3	2526.0	28.78	26.81	3.88
390	34	96	1.38	3.87	2.63	14.3	2540.2	28.94	26.81	4.55
391	46	85	1.85	3.42	2.63	14.3	2554.6	29.10	26.94	4.70
392	45	86	1.80	3.47	2.63	14.3	2568.9	29.27	26.94	5.44
393	61	69	2.47	2.80	2.64	14.4	2583.3	29.43	27.00	5.91
394	25	105	1.01	4.26	2.64	14.4	2597.7	29.60	27.06	6.41
395	50	81	2.03	3.29	2.66	14.8	2612.5	29.76	27.84	3.69

#	Size (pixels)		Converted size (mm)		Volume (mm3)			Percent passing		
	short axis	long axis	short axis	long axis	average	bubble	cumulative	measured	R-R	Error
396	34	98	1.36	3.97	2.66	14.8	2627.4	29.93	27.91	4.10
397	57	75	2.32	3.03	2.67	15.0	2642.4	30.10	28.17	3.74
398	55	78	2.21	3.14	2.67	15.0	2657.4	30.28	28.24	4.16
399	43	89	1.74	3.62	2.68	15.1	2672.5	30.45	28.43	4.05
400	42	90	1.72	3.65	2.68	15.2	2687.7	30.62	28.57	4.22
401	42	90	1.71	3.66	2.68	15.2	2702.9	30.79	28.57	4.96
402	46	87	1.85	3.53	2.69	15.3	2718.1	30.97	28.70	5.15
403	42	91	1.68	3.69	2.69	15.3	2733.4	31.14	28.70	5.97
404	49	84	1.98	3.41	2.70	15.4	2748.8	31.32	28.96	5.54
405	63	71	2.55	2.86	2.70	15.5	2764.3	31.49	29.16	5.43
406	37	96	1.51	3.89	2.70	15.5	2779.8	31.67	29.16	6.28
407	56	78	2.27	3.16	2.71	15.7	2795.5	31.85	29.57	5.21
408	54	80	2.19	3.26	2.72	15.9	2811.4	32.03	29.90	4.53
409	41	94	1.66	3.81	2.73	16.1	2827.5	32.21	30.24	3.89
410	39	97	1.56	3.92	2.74	16.2	2843.6	32.40	30.44	3.81
411	51	85	2.08	3.42	2.75	16.4	2860.0	32.58	30.79	3.23
412	44	92	1.77	3.73	2.75	16.4	2876.3	32.77	30.79	3.94
413	65	71	2.65	2.86	2.75	16.4	2892.7	32.96	30.85	4.42
414	36	100	1.45	4.06	2.76	16.4	2909.1	33.14	30.92	4.93
415	62	74	2.52	2.99	2.76	16.4	2925.6	33.33	30.92	5.80
416	24	112	0.98	4.53	2.76	16.5	2942.0	33.52	30.99	6.39
417	41	95	1.67	3.85	2.76	16.5	2958.5	33.71	30.99	7.37
418	35	101	1.42	4.10	2.76	16.5	2975.0	33.89	31.06	8.03
419	39	98	1.57	3.95	2.76	16.5	2991.5	34.08	31.06	9.13
420	62	75	2.49	3.03	2.76	16.5	3008.0	34.27	31.13	9.87
421	22	115	0.89	4.64	2.76	16.5	3024.6	34.46	31.13	11.09
422	58	79	2.36	3.18	2.77	16.6	3041.2	34.65	31.34	10.98
423	40	97	1.60	3.94	2.77	16.7	3057.9	34.84	31.40	11.80
424	51	86	2.07	3.47	2.77	16.7	3074.6	35.03	31.40	13.14
425	52	85	2.11	3.45	2.78	16.8	3091.3	35.22	31.61	13.02
426	43	94	1.75	3.82	2.78	16.9	3108.3	35.41	31.89	12.42
427	62	76	2.51	3.07	2.79	17.1	3125.4	35.61	32.17	11.84
428	33	105	1.34	4.26	2.80	17.3	3142.7	35.80	32.59	10.36
429	49	89	1.99	3.62	2.80	17.3	3160.0	36.00	32.59	11.67
430	38	100	1.55	4.06	2.80	17.3	3177.3	36.20	32.59	13.06
431	59	79	2.39	3.21	2.80	17.3	3194.6	36.40	32.59	14.52
432	24	115	0.98	4.64	2.81	17.3	3211.9	36.59	32.66	15.51
433	58	81	2.36	3.26	2.81	17.4	3229.3	36.79	32.73	16.53
434	42	97	1.71	3.92	2.82	17.5	3246.9	36.99	33.01	15.88
435	57	82	2.31	3.32	2.82	17.6	3264.4	37.19	33.08	16.93

#	Size (pixels)		Converted size (mm)		Volume (mm3)			Percent passing		
	short axis	long axis	short axis	long axis	average	bubble	cumulative	measured	R-R	Error
436	55	84	2.23	3.41	2.82	17.6	3282.1	37.39	33.22	17.43
437	48	91	1.96	3.70	2.83	17.8	3299.8	37.60	33.43	17.35
438	32	108	1.29	4.38	2.83	17.8	3317.7	37.80	33.57	17.87
439	62	78	2.52	3.16	2.84	18.0	3335.6	38.00	33.78	17.80
440	45	95	1.83	3.85	2.84	18.0	3353.6	38.21	33.86	18.94
441	40	100	1.63	4.06	2.84	18.1	3371.7	38.41	34.00	19.50
442	28	113	1.13	4.56	2.84	18.1	3389.8	38.62	34.00	21.36
443	70	72	2.83	2.89	2.86	18.4	3408.2	38.83	34.64	17.54
444	39	103	1.60	4.15	2.87	18.7	3426.8	39.04	35.07	15.76
445	61	81	2.45	3.30	2.87	18.7	3445.5	39.25	35.07	17.49
446	34	108	1.38	4.39	2.89	18.9	3464.4	39.47	35.51	15.72
447	54	89	2.18	3.62	2.90	19.1	3483.5	39.69	35.94	14.04
448	49	95	1.96	3.84	2.90	19.2	3502.7	39.91	36.09	14.60
449	47	97	1.91	3.93	2.92	19.5	3522.3	40.13	36.67	11.97
450	55	90	2.21	3.64	2.93	19.7	3542.0	40.35	36.96	11.50
451	72	73	2.92	2.94	2.93	19.7	3561.7	40.58	37.04	12.55
452	40	105	1.62	4.26	2.94	19.9	3581.6	40.81	37.40	11.57
453	54	92	2.18	3.72	2.95	20.1	3601.7	41.03	37.70	11.12
454	53	93	2.15	3.76	2.96	20.3	3622.1	41.27	38.07	10.22
455	51	96	2.05	3.88	2.96	20.4	3642.5	41.50	38.29	10.29
456	33	114	1.33	4.61	2.97	20.5	3663.0	41.73	38.44	10.84
457	73	74	2.94	3.00	2.97	20.7	3683.7	41.97	38.66	10.92
458	69	79	2.77	3.19	2.98	20.8	3704.5	42.21	38.96	10.52
459	42	106	1.68	4.30	2.99	21.1	3725.6	42.45	39.41	9.21
460	50	99	2.02	4.02	3.02	21.6	3747.2	42.69	40.39	5.31
461	58	91	2.36	3.68	3.02	21.7	3768.9	42.94	40.46	6.13
462	47	102	1.91	4.14	3.02	21.7	3790.6	43.19	40.54	7.01
463	62	88	2.50	3.56	3.03	21.9	3812.5	43.44	40.76	7.13
464	66	85	2.66	3.44	3.05	22.2	3834.7	43.69	41.37	5.37
465	51	100	2.07	4.04	3.05	22.4	3857.1	43.94	41.67	5.15
466	40	111	1.63	4.49	3.06	22.5	3879.6	44.20	41.83	5.63
467	39	112	1.59	4.55	3.07	22.7	3902.3	44.46	42.21	5.07
468	70	82	2.82	3.33	3.08	22.9	3925.1	44.72	42.51	4.87
469	52	100	2.12	4.04	3.08	22.9	3948.1	44.98	42.59	5.72
470	60	93	2.42	3.75	3.09	23.1	3971.1	45.24	42.82	5.88
471	59	94	2.38	3.81	3.09	23.2	3994.3	45.51	43.05	6.05
472	51	102	2.07	4.11	3.09	23.2	4017.6	45.77	43.13	7.01
473	62	90	2.53	3.66	3.09	23.2	4040.8	46.04	43.13	8.48
474	54	100	2.20	4.06	3.13	24.1	4064.9	46.31	44.51	3.25
475	52	103	2.11	4.17	3.14	24.3	4089.1	46.59	44.82	3.13

#	Size (pixels)		Converted size (mm)		Volume (mm3)			Percent passing		
	short axis	long axis	short axis	long axis	average	bubble	cumulative	measured	R-R	Error
476	34	121	1.38	4.89	3.14	24.3	4113.4	46.86	44.82	4.19
477	68	87	2.76	3.53	3.14	24.4	4137.8	47.14	45.05	4.38
478	31	125	1.27	5.07	3.17	25.0	4162.8	47.43	45.98	2.10
479	77	80	3.13	3.23	3.18	25.2	4187.9	47.71	46.29	2.03
480	65	93	2.63	3.77	3.20	25.8	4213.7	48.01	47.30	0.50
481	39	119	1.59	4.82	3.20	25.8	4239.6	48.30	47.38	0.85
482	69	90	2.79	3.63	3.21	25.9	4265.5	48.60	47.53	1.13
483	78	81	3.14	3.29	3.21	26.1	4291.6	48.89	47.77	1.27
484	55	104	2.22	4.23	3.22	26.3	4317.9	49.19	48.16	1.08
485	50	109	2.03	4.42	3.22	26.3	4344.3	49.49	48.16	1.79
486	79	81	3.19	3.28	3.23	26.6	4370.9	49.80	48.55	1.56
487	49	111	1.99	4.50	3.25	26.9	4397.7	50.10	49.02	1.18
488	46	115	1.87	4.64	3.25	27.0	4424.8	50.41	49.25	1.35
489	37	124	1.50	5.03	3.26	27.3	4452.1	50.72	49.64	1.17
490	75	86	3.04	3.49	3.27	27.4	4479.5	51.03	49.80	1.53
491	40	122	1.61	4.94	3.28	27.6	4507.1	51.35	50.19	1.35
492	39	123	1.60	4.96	3.28	27.7	4534.8	51.67	50.27	1.96
493	44	118	1.79	4.78	3.29	27.9	4562.7	51.98	50.58	1.97
494	48	115	1.94	4.66	3.30	28.2	4590.9	52.30	51.05	1.58
495	40	124	1.60	5.01	3.31	28.4	4619.3	52.63	51.28	1.81
496	80	83	3.25	3.37	3.31	28.4	4647.7	52.95	51.36	2.53
497	58	106	2.35	4.28	3.32	28.6	4676.4	53.28	51.67	2.57
498	52	112	2.10	4.54	3.32	28.7	4705.1	53.61	51.83	3.15
499	127	38	5.14	1.53	3.33	29.1	4734.1	53.94	52.30	2.67
500	58	107	2.36	4.32	3.34	29.2	4763.4	54.27	52.54	3.00
501	56	110	2.25	4.46	3.35	29.6	4793.0	54.61	53.16	2.09
502	51	115	2.07	4.67	3.37	30.1	4823.1	54.95	53.79	1.35
503	47	120	1.91	4.84	3.37	30.2	4853.2	55.29	53.94	1.82
504	68	99	2.75	4.02	3.39	30.5	4883.8	55.64	54.41	1.51
505	49	119	1.98	4.82	3.40	30.8	4914.5	55.99	54.80	1.41
506	62	106	2.51	4.30	3.40	31.0	4945.5	56.34	55.11	1.51
507	62	107	2.52	4.31	3.41	31.3	4976.8	56.70	55.50	1.43
508	56	113	2.25	4.59	3.42	31.4	5008.2	57.06	55.66	1.96
509	74	95	3.01	3.83	3.42	31.4	5039.6	57.42	55.66	3.08
510	57	112	2.32	4.54	3.43	31.7	5071.3	57.78	56.05	2.98
511	52	117	2.11	4.75	3.43	31.7	5103.0	58.14	56.13	4.04
512	72	98	2.90	3.97	3.44	31.8	5134.8	58.50	56.28	4.92
513	58	112	2.36	4.53	3.45	32.1	5167.0	58.87	56.67	4.82
514	55	116	2.23	4.70	3.47	32.7	5199.6	59.24	57.45	3.21
515	83	88	3.38	3.55	3.47	32.7	5232.3	59.61	57.45	4.69

#	Size (pixels)		Converted size (mm)		Volume (mm3)			Percent passing		
	short axis	long axis	short axis	long axis	average	bubble	cumulative	measured	R-R	Error
516	34	138	1.38	5.59	3.48	33.2	5265.5	59.99	58.14	3.41
517	83	91	3.36	3.68	3.52	34.1	5299.7	60.38	59.38	1.00
518	60	114	2.44	4.60	3.52	34.2	5333.9	60.77	59.45	1.73
519	60	114	2.44	4.60	3.52	34.3	5368.1	61.16	59.53	2.65
520	39	136	1.60	5.49	3.54	34.9	5403.0	61.56	60.30	1.59
521	65	110	2.64	4.45	3.55	35.0	5438.0	61.96	60.53	2.04
522	38	138	1.55	5.59	3.57	35.7	5473.7	62.36	61.37	0.99
523	58	120	2.35	4.87	3.61	37.0	5510.7	62.78	62.95	0.03
524	58	121	2.36	4.91	3.63	37.6	5548.3	63.21	63.70	0.24
525	44	136	1.79	5.50	3.64	38.0	5586.3	63.65	64.15	0.26
526	67	113	2.72	4.58	3.65	38.2	5624.6	64.08	64.45	0.14
527	61	122	2.48	4.96	3.72	40.4	5665.0	64.54	66.88	5.45
528	48	137	1.96	5.54	3.75	41.3	5706.3	65.01	67.89	8.28
529	74	111	3.00	4.50	3.75	41.5	5747.7	65.48	68.03	6.49
530	64	122	2.61	4.93	3.77	42.0	5789.7	65.96	68.60	6.98
531	46	142	1.87	5.76	3.81	43.6	5833.3	66.46	70.23	14.21
532	67	123	2.70	4.96	3.83	44.1	5877.4	66.96	70.72	14.10
533	42	148	1.72	5.98	3.85	44.7	5922.0	67.47	71.34	14.96
534	65	125	2.62	5.08	3.85	44.8	5966.9	67.98	71.47	12.21
535	67	124	2.70	5.02	3.86	45.2	6012.1	68.50	71.82	11.03
536	66	127	2.68	5.14	3.91	46.8	6058.9	69.03	73.37	18.83
537	62	134	2.51	5.42	3.96	48.9	6107.8	69.59	75.20	31.55
538	95	101	3.86	4.10	3.98	49.4	6157.2	70.15	75.65	30.28
539	40	159	1.64	6.43	4.03	51.4	6208.6	70.74	77.28	42.90
540	75	125	3.05	5.04	4.04	52.0	6260.6	71.33	77.71	40.80
541	78	122	3.17	4.93	4.05	52.2	6312.8	71.92	77.90	35.70
542	51	149	2.07	6.04	4.06	52.4	6365.2	72.52	78.08	30.91
543	62	138	2.53	5.60	4.06	52.6	6417.8	73.12	78.20	25.83
544	78	123	3.14	4.99	4.06	52.7	6470.5	73.72	78.26	20.63
545	81	124	3.27	5.01	4.14	55.6	6526.1	74.35	80.43	36.95
546	36	169	1.44	6.86	4.15	56.0	6582.2	74.99	80.71	32.76
547	49	156	1.99	6.32	4.16	56.5	6638.6	75.63	81.00	28.75
548	54	153	2.17	6.20	4.19	57.6	6696.2	76.29	81.77	30.04
549	61	150	2.48	6.08	4.28	61.6	6757.9	76.99	84.24	52.51
550	83	132	3.38	5.34	4.36	65.0	6822.9	77.73	86.08	69.62
551	47	169	1.90	6.83	4.36	65.3	6888.2	78.48	86.22	59.89
552	83	137	3.35	5.53	4.44	68.9	6957.1	79.26	87.94	75.38
553	82	138	3.33	5.58	4.46	69.5	7026.6	80.05	88.20	66.31
554	60	161	2.45	6.51	4.48	70.6	7097.2	80.86	88.69	61.36
555	109	113	4.43	4.55	4.49	71.2	7168.4	81.67	88.93	52.77

#	Size (pixels)		Converted size (mm)		Volume (mm3)			Percent passing		
	short axis	long axis	short axis	long axis	average	bubble	cumulative	measured	R-R	Error
556	56	177	2.27	7.15	4.71	82.1	7250.4	82.60	92.71	102.02
557	74	166	3.00	6.70	4.85	89.8	7340.3	83.63	94.61	120.69
558	43	200	1.75	8.11	4.93	94.2	7434.5	84.70	95.47	115.91
559	58	191	2.34	7.73	5.03	100.2	7534.7	85.84	96.44	112.41
560	48	201	1.95	8.13	5.04	100.3	7635.0	86.99	96.46	89.80
561	106	145	4.28	5.86	5.07	102.4	7737.4	88.15	96.75	73.87
562	41	228	1.68	9.21	5.45	126.8	7864.2	89.60	98.82	85.12
563	86	187	3.47	7.57	5.52	132.1	7996.3	91.10	99.06	63.36
564	95	214	3.85	8.64	6.24	191.3	8187.6	93.28	99.93	44.25
565	83	250	3.34	10.11	6.72	238.6	8426.3	96.00	99.99	15.94
566	69	309	2.78	12.51	7.65	351.0	8777.3	100.00	100.00	0.00

Appendix J: Sample of displacement model bubble tracking

The following tables present the bubble displacement model for Baby HAC at 5 kg/s without the Karamanev and Nikolov (1992) drag correction

Horiz. pos.	Bubble dia.	Bubble location by vertical bin centre (m)										
(m)	(m)	0.0125	0.0375	0.0625	0.0875	0.1125	0.1375	0.1625	0.1875	0.2125	0.2375	Separated
	1.81E-04	0.3333	0.3333	0.3333	0.0000	0.0000	0.0000	0.0000	0.0000	0.0000	0.0000	0.0000
	3.62E-04	0.3333	0.3333	0.3333	0.0000	0.0000	0.0000	0.0000	0.0000	0.0000	0.0000	0.0000
	7.24E-04	0.3333	0.3333	0.3333	0.0000	0.0000	0.0000	0.0000	0.0000	0.0000	0.0000	0.0000
	1.45E-03	0.3333	0.3333	0.3333	0.0000	0.0000	0.0000	0.0000	0.0000	0.0000	0.0000	0.0000
	2.17E-03	0.3333	0.3333	0.3333	0.0000	0.0000	0.0000	0.0000	0.0000	0.0000	0.0000	0.0000
0.112	2.90E-03	0.3333	0.3333	0.3333	0.0000	0.0000	0.0000	0.0000	0.0000	0.0000	0.0000	0.0000
	3.62E-03	0.3333	0.3333	0.3333	0.0000	0.0000	0.0000	0.0000	0.0000	0.0000	0.0000	0.0000
	4.34E-03	0.3333	0.3333	0.3333	0.0000	0.0000	0.0000	0.0000	0.0000	0.0000	0.0000	0.0000
	5.07E-03	0.3333	0.3333	0.3333	0.0000	0.0000	0.0000	0.0000	0.0000	0.0000	0.0000	0.0000
	5.79E-03	0.3333	0.3333	0.3333	0.0000	0.0000	0.0000	0.0000	0.0000	0.0000	0.0000	0.0000
	6.52E-03	0.3333	0.3333	0.3333	0.0000	0.0000	0.0000	0.0000	0.0000	0.0000	0.0000	0.0000
	1.81E-04	0.1974	0.0025	0.0000	0.1077	0.0225	0.0178	0.0000	0.0000	0.0000	0.5606	0.0915
	3.62E-04	0.1425	0.0106	0.0129	0.0025	0.0025	0.0109	0.0000	0.1024	0.0389	0.5782	0.0985
	7.24E-04	0.1076	0.0119	0.0199	0.0038	0.0031	0.0105	0.0068	0.0000	0.0096	0.5520	0.2747
	1.45E-03	0.0566	0.0081	0.0104	0.0043	0.0119	0.0122	0.0043	0.0031	0.0038	0.5569	0.3284
	2.17E-03	0.0489	0.0000	0.0082	0.0117	0.0000	0.0000	0.0165	0.0121	0.0068	0.5572	0.3386
0.162	2.90E-03	0.0253	0.0082	0.0043	0.0039	0.0159	0.0076	0.0037	0.0043	0.0121	0.5616	0.3531
	3.62E-03	0.0216	0.0000	0.0000	0.0088	0.0000	0.0121	0.0041	0.0076	0.0037	0.5572	0.3849
	4.34E-03	0.0043	0.0089	0.0000	0.0044	0.0045	0.0043	0.0042	0.0080	0.0118	0.5492	0.4003
	5.07E-03	0.0043	0.0000	0.0000	0.0045	0.0044	0.0089	0.0000	0.0086	0.0080	0.5492	0.4121
	5.79E-03	0.0043	0.0000	0.0000	0.0000	0.0000	0.0045	0.0045	0.0000	0.0173	0.5573	0.4121
	6.52E-03	0.0000	0.0000	0.0000	0.0000	0.0000	0.0000	0.0000	0.0090	0.0042	0.5536	0.4332

Horiz. pos.	Bubble dia.	Bubble location by vertical bin centre (m)										
(m)	(m)	0.0125	0.0375	0.0625	0.0875	0.1125	0.1375	0.1625	0.1875	0.2125	0.2375	Separated
	1.81E-04	0.1678	0.0217	0.0078	0.0605	0.0103	0.0024	0.0091	0.0091	0.0043	0.3675	0.3396
	3.62E-04	0.0667	0.0138	0.0079	0.0033	0.0039	0.0046	0.0162	0.0627	0.0229	0.3280	0.4698
	7.24E-04	0.0536	0.0156	0.0082	0.0090	0.0037	0.0047	0.0020	0.0036	0.0019	0.0183	0.8793
	1.45E-03	0.0240	0.0161	0.0073	0.0028	0.0042	0.0044	0.0035	0.0031	0.0021	0.0057	0.9267
	2.17E-03	0.0104	0.0135	0.0079	0.0041	0.0018	0.0029	0.0029	0.0019	0.0040	0.0039	0.9466
0.212	2.90E-03	0.0122	0.0053	0.0082	0.0035	0.0026	0.0013	0.0016	0.0040	0.0021	0.0017	0.9575
	3.62E-03	0.0060	0.0000	0.0060	0.0026	0.0022	0.0016	0.0006	0.0016	0.0020	0.0021	0.9752
	4.34E-03	0.0039	0.0001	0.0021	0.0038	0.0015	0.0011	0.0006	0.0007	0.0010	0.0013	0.9840
	5.07E-03	0.0043	0.0001	0.0004	0.0014	0.0007	0.0003	0.0008	0.0007	0.0012	0.0009	0.9893
	5.79E-03	0.0011	0.0000	0.0000	0.0011	0.0004	0.0003	0.0002	0.0002	0.0002	0.0004	0.9961
	6.52E-03	0.0000	0.0000	0.0000	0.0000	0.0000	0.0000	0.0000	0.0000	0.0000	0.0000	1.0000
	1.81E-04	0.0819	0.0420	0.0146	0.0539	0.0071	0.0078	0.0071	0.0036	0.0307	0.3102	0.4411
	3.62E-04	0.0291	0.0172	0.0100	0.0077	0.0052	0.0110	0.0078	0.0310	0.0293	0.1522	0.6995
	7.24E-04	0.0222	0.0187	0.0106	0.0082	0.0046	0.0029	0.0040	0.0025	0.0028	0.0031	0.9204
	1.45E-03	0.0044	0.0092	0.0093	0.0051	0.0037	0.0024	0.0020	0.0027	0.0033	0.0029	0.9550
	2.17E-03	0.0038	0.0029	0.0029	0.0053	0.0020	0.0023	0.0012	0.0027	0.0011	0.0016	0.9742
0.262	2.90E-03	0.0034	0.0014	0.0031	0.0021	0.0026	0.0006	0.0012	0.0009	0.0015	0.0014	0.9818
	3.62E-03	0.0025	0.0000	0.0019	0.0005	0.0007	0.0002	0.0002	0.0004	0.0002	0.0004	0.9930
	4.34E-03	0.0016	0.0000	0.0010	0.0004	0.0002	0.0005	0.0001	0.0002	0.0001	0.0001	0.9957
	5.07E-03	0.0006	0.0000	0.0008	0.0007	0.0003	0.0004	0.0001	0.0001	0.0002	0.0000	0.9967
	5.79E-03	0.0003	0.0000	0.0001	0.0002	0.0001	0.0001	0.0000	0.0000	0.0001	0.0000	0.9990
	6.52E-03	0.0000	0.0000	0.0000	0.0000	0.0000	0.0000	0.0000	0.0000	0.0000	0.0000	1.0000

Horiz. pos.	Bubble dia.	Bubble location by vertical bin centre (m)										
(m)	(m)	0.0125	0.0375	0.0625	0.0875	0.1125	0.1375	0.1625	0.1875	0.2125	0.2375	Separated
	1.81E-04	0.0594	0.0384	0.0276	0.0363	0.0127	0.0037	0.0074	0.0067	0.0220	0.2858	0.4999
	3.62E-04	0.0231	0.0158	0.0084	0.0067	0.0063	0.0048	0.0063	0.0171	0.0106	0.0827	0.8183
	7.24E-04	0.0084	0.0103	0.0133	0.0056	0.0070	0.0046	0.0030	0.0024	0.0012	0.0014	0.9427
	1.45E-03	0.0044	0.0016	0.0013	0.0024	0.0034	0.0027	0.0038	0.0027	0.0018	0.0019	0.9739
	2.17E-03	0.0029	0.0006	0.0012	0.0009	0.0005	0.0010	0.0009	0.0010	0.0022	0.0010	0.9879
0.312	2.90E-03	0.0019	0.0000	0.0011	0.0008	0.0004	0.0003	0.0005	0.0004	0.0004	0.0007	0.9936
	3.62E-03	0.0007	0.0000	0.0006	0.0006	0.0002	0.0001	0.0001	0.0001	0.0001	0.0001	0.9974
	4.34E-03	0.0004	0.0000	0.0003	0.0003	0.0003	0.0001	0.0001	0.0001	0.0001	0.0000	0.9984
	5.07E-03	0.0005	0.0000	0.0000	0.0001	0.0001	0.0000	0.0000	0.0000	0.0001	0.0000	0.9990
	5.79E-03	0.0001	0.0000	0.0000	0.0001	0.0001	0.0000	0.0000	0.0000	0.0000	0.0000	0.9997
	6.52E-03	0.0000	0.0000	0.0000	0.0000	0.0000	0.0000	0.0000	0.0000	0.0000	0.0000	1.0000
	1.81E-04	0.0516	0.0392	0.0223	0.0270	0.0122	0.0052	0.0055	0.0077	0.0238	0.2477	0.5578
	3.62E-04	0.0173	0.0130	0.0101	0.0053	0.0036	0.0028	0.0057	0.0090	0.0054	0.0521	0.8755
	7.24E-04	0.0073	0.0055	0.0045	0.0082	0.0062	0.0039	0.0018	0.0010	0.0008	0.0018	0.9589
	1.45E-03	0.0031	0.0010	0.0017	0.0006	0.0005	0.0012	0.0017	0.0015	0.0006	0.0004	0.9875
	2.17E-03	0.0009	0.0001	0.0012	0.0006	0.0003	0.0002	0.0003	0.0005	0.0004	0.0005	0.9949
0.362	2.90E-03	0.0006	0.0000	0.0004	0.0007	0.0002	0.0001	0.0001	0.0002	0.0003	0.0002	0.9973
	3.62E-03	0.0003	0.0000	0.0001	0.0002	0.0001	0.0001	0.0000	0.0001	0.0001	0.0002	0.9988
	4.34E-03	0.0002	0.0000	0.0000	0.0001	0.0001	0.0000	0.0000	0.0000	0.0000	0.0001	0.9993
	5.07E-03	0.0001	0.0000	0.0000	0.0001	0.0001	0.0001	0.0000	0.0000	0.0000	0.0000	0.9996
	5.79E-03	0.0000	0.0000	0.0000	0.0000	0.0000	0.0000	0.0000	0.0000	0.0000	0.0000	0.9999
	6.52E-03	0.0000	0.0000	0.0000	0.0000	0.0000	0.0000	0.0000	0.0000	0.0000	0.0000	1.0000

Horiz. pos.	Bubble dia.	Bubble location by vertical bin centre (m)										
(m)	(m)	0.0125	0.0375	0.0625	0.0875	0.1125	0.1375	0.1625	0.1875	0.2125	0.2375	Separated
	1.81E-04	0.0399	0.0377	0.0245	0.0265	0.0138	0.0050	0.0067	0.0058	0.0208	0.1888	0.6305
	3.62E-04	0.0104	0.0069	0.0116	0.0068	0.0037	0.0032	0.0036	0.0066	0.0045	0.0287	0.9141
	7.24E-04	0.0044	0.0044	0.0023	0.0027	0.0063	0.0035	0.0024	0.0013	0.0007	0.0009	0.9710
	1.45E-03	0.0009	0.0003	0.0015	0.0005	0.0004	0.0006	0.0007	0.0004	0.0005	0.0007	0.9935
	2.17E-03	0.0003	0.0000	0.0002	0.0003	0.0001	0.0001	0.0003	0.0002	0.0002	0.0002	0.9980
0.412	2.90E-03	0.0002	0.0000	0.0000	0.0002	0.0001	0.0001	0.0001	0.0002	0.0001	0.0001	0.9989
	3.62E-03	0.0001	0.0000	0.0000	0.0000	0.0001	0.0000	0.0000	0.0000	0.0000	0.0000	0.9996
	4.34E-03	0.0001	0.0000	0.0000	0.0000	0.0001	0.0000	0.0000	0.0000	0.0000	0.0000	0.9997
	5.07E-03	0.0001	0.0000	0.0000	0.0000	0.0000	0.0000	0.0000	0.0000	0.0000	0.0000	0.9998
	5.79E-03	0.0000	0.0000	0.0000	0.0000	0.0000	0.0000	0.0000	0.0000	0.0000	0.0000	0.9999
	6.52E-03	0.0000	0.0000	0.0000	0.0000	0.0000	0.0000	0.0000	0.0000	0.0000	0.0000	1.0000
	1.81E-04	0.0252	0.0223	0.0373	0.0281	0.0153	0.0076	0.0084	0.0087	0.0109	0.1495	0.6866
	3.62E-04	0.0027	0.0057	0.0077	0.0072	0.0062	0.0037	0.0026	0.0059	0.0038	0.0128	0.9417
	7.24E-04	0.0020	0.0022	0.0012	0.0028	0.0029	0.0028	0.0016	0.0014	0.0019	0.0009	0.9803
	1.45E-03	0.0003	0.0000	0.0003	0.0002	0.0003	0.0005	0.0005	0.0003	0.0003	0.0004	0.9969
	2.17E-03	0.0001	0.0000	0.0000	0.0001	0.0001	0.0001	0.0001	0.0001	0.0001	0.0000	0.9994
0.462	2.90E-03	0.0000	0.0000	0.0000	0.0000	0.0001	0.0000	0.0000	0.0001	0.0000	0.0000	0.9997
	3.62E-03	0.0000	0.0000	0.0000	0.0000	0.0000	0.0000	0.0000	0.0000	0.0000	0.0000	0.9999
	4.34E-03	0.0000	0.0000	0.0000	0.0000	0.0000	0.0000	0.0000	0.0000	0.0000	0.0000	0.9999
	5.07E-03	0.0000	0.0000	0.0000	0.0000	0.0000	0.0000	0.0000	0.0000	0.0000	0.0000	0.9999
	5.79E-03	0.0000	0.0000	0.0000	0.0000	0.0000	0.0000	0.0000	0.0000	0.0000	0.0000	1.0000
	6.52E-03	0.0000	0.0000	0.0000	0.0000	0.0000	0.0000	0.0000	0.0000	0.0000	0.0000	1.0000

Horiz. pos.	Bubble dia.	Bubble location by vertical bin centre (m)										
(m)	(m)	0.0125	0.0375	0.0625	0.0875	0.1125	0.1375	0.1625	0.1875	0.2125	0.2375	Separated
	1.81E-04	0.0179	0.0255	0.0291	0.0306	0.0170	0.0123	0.0064	0.0070	0.0051	0.1212	0.7280
	3.62E-04	0.0016	0.0029	0.0072	0.0050	0.0054	0.0037	0.0027	0.0039	0.0030	0.0056	0.9590
	7.24E-04	0.0011	0.0009	0.0012	0.0018	0.0015	0.0015	0.0017	0.0009	0.0008	0.0014	0.9873
	1.45E-03	0.0002	0.0000	0.0001	0.0001	0.0001	0.0002	0.0002	0.0002	0.0001	0.0002	0.9987
	2.17E-03	0.0000	0.0000	0.0000	0.0000	0.0000	0.0000	0.0000	0.0000	0.0000	0.0000	0.9998
0.512	2.90E-03	0.0000	0.0000	0.0000	0.0000	0.0000	0.0000	0.0000	0.0000	0.0000	0.0000	0.9999
	3.62E-03	0.0000	0.0000	0.0000	0.0000	0.0000	0.0000	0.0000	0.0000	0.0000	0.0000	1.0000
	4.34E-03	0.0000	0.0000	0.0000	0.0000	0.0000	0.0000	0.0000	0.0000	0.0000	0.0000	1.0000
	5.07E-03	0.0000	0.0000	0.0000	0.0000	0.0000	0.0000	0.0000	0.0000	0.0000	0.0000	1.0000
	5.79E-03	0.0000	0.0000	0.0000	0.0000	0.0000	0.0000	0.0000	0.0000	0.0000	0.0000	1.0000
	6.52E-03	0.0000	0.0000	0.0000	0.0000	0.0000	0.0000	0.0000	0.0000	0.0000	0.0000	1.0000
	1.81E-04	0.0152	0.0254	0.0279	0.0276	0.0160	0.0071	0.0082	0.0057	0.0071	0.1012	0.7586
	3.62E-04	0.0020	0.0034	0.0041	0.0044	0.0038	0.0034	0.0027	0.0025	0.0025	0.0028	0.9683
	7.24E-04	0.0007	0.0007	0.0007	0.0011	0.0009	0.0008	0.0009	0.0008	0.0008	0.0005	0.9922
	1.45E-03	0.0001	0.0000	0.0001	0.0001	0.0000	0.0000	0.0001	0.0000	0.0001	0.0001	0.9995
	2.17E-03	0.0000	0.0000	0.0000	0.0000	0.0000	0.0000	0.0000	0.0000	0.0000	0.0000	0.9999
0.562	2.90E-03	0.0000	0.0000	0.0000	0.0000	0.0000	0.0000	0.0000	0.0000	0.0000	0.0000	1.0000
	3.62E-03	0.0000	0.0000	0.0000	0.0000	0.0000	0.0000	0.0000	0.0000	0.0000	0.0000	1.0000
	4.34E-03	0.0000	0.0000	0.0000	0.0000	0.0000	0.0000	0.0000	0.0000	0.0000	0.0000	1.0000
	5.07E-03	0.0000	0.0000	0.0000	0.0000	0.0000	0.0000	0.0000	0.0000	0.0000	0.0000	1.0000
	5.79E-03	0.0000	0.0000	0.0000	0.0000	0.0000	0.0000	0.0000	0.0000	0.0000	0.0000	1.0000
	6.52E-03	0.0000	0.0000	0.0000	0.0000	0.0000	0.0000	0.0000	0.0000	0.0000	0.0000	1.0000

Horiz. pos.	Bubble dia.	Bubble location by vertical bin centre (m)										
(m)	(m)	0.0125	0.0375	0.0625	0.0875	0.1125	0.1375	0.1625	0.1875	0.2125	0.2375	Separated
	1.81E-04	0.0160	0.0316	0.0171	0.0207	0.0144	0.0066	0.0073	0.0045	0.0089	0.0822	0.7907
	3.62E-04	0.0015	0.0036	0.0040	0.0037	0.0018	0.0027	0.0019	0.0025	0.0015	0.0026	0.9742
	7.24E-04	0.0003	0.0005	0.0004	0.0006	0.0004	0.0005	0.0007	0.0003	0.0005	0.0003	0.9953
	1.45E-03	0.0000	0.0000	0.0000	0.0000	0.0000	0.0000	0.0000	0.0000	0.0000	0.0000	0.9998
	2.17E-03	0.0000	0.0000	0.0000	0.0000	0.0000	0.0000	0.0000	0.0000	0.0000	0.0000	1.0000
0.612	2.90E-03	0.0000	0.0000	0.0000	0.0000	0.0000	0.0000	0.0000	0.0000	0.0000	0.0000	1.0000
	3.62E-03	0.0000	0.0000	0.0000	0.0000	0.0000	0.0000	0.0000	0.0000	0.0000	0.0000	1.0000
	4.34E-03	0.0000	0.0000	0.0000	0.0000	0.0000	0.0000	0.0000	0.0000	0.0000	0.0000	1.0000
	5.07E-03	0.0000	0.0000	0.0000	0.0000	0.0000	0.0000	0.0000	0.0000	0.0000	0.0000	1.0000
	5.79E-03	0.0000	0.0000	0.0000	0.0000	0.0000	0.0000	0.0000	0.0000	0.0000	0.0000	1.0000
	6.52E-03	0.0000	0.0000	0.0000	0.0000	0.0000	0.0000	0.0000	0.0000	0.0000	0.0000	1.0000
	1.81E-04	0.0148	0.0379	0.0186	0.0160	0.0115	0.0055	0.0053	0.0057	0.0090	0.0477	0.8279
	3.62E-04	0.0010	0.0029	0.0051	0.0022	0.0017	0.0017	0.0009	0.0018	0.0013	0.0018	0.9794
	7.24E-04	0.0003	0.0003	0.0003	0.0005	0.0004	0.0003	0.0002	0.0003	0.0003	0.0002	0.9969
	1.45E-03	0.0000	0.0000	0.0000	0.0000	0.0000	0.0000	0.0000	0.0000	0.0000	0.0000	0.9999
	2.17E-03	0.0000	0.0000	0.0000	0.0000	0.0000	0.0000	0.0000	0.0000	0.0000	0.0000	1.0000
0.662	2.90E-03	0.0000	0.0000	0.0000	0.0000	0.0000	0.0000	0.0000	0.0000	0.0000	0.0000	1.0000
	3.62E-03	0.0000	0.0000	0.0000	0.0000	0.0000	0.0000	0.0000	0.0000	0.0000	0.0000	1.0000
	4.34E-03	0.0000	0.0000	0.0000	0.0000	0.0000	0.0000	0.0000	0.0000	0.0000	0.0000	1.0000
	5.07E-03	0.0000	0.0000	0.0000	0.0000	0.0000	0.0000	0.0000	0.0000	0.0000	0.0000	1.0000
	5.79E-03	0.0000	0.0000	0.0000	0.0000	0.0000	0.0000	0.0000	0.0000	0.0000	0.0000	1.0000
	6.52E-03	0.0000	0.0000	0.0000	0.0000	0.0000	0.0000	0.0000	0.0000	0.0000	0.0000	1.0000

The following table presents the bubble size with the relative proportions by volume fraction used to convert the displacement tracking data by bubble diameter above into separator effectiveness in the subsequent table

Bubble dia. (m)	Volume fraction			Rise vel. (m/s)
	Cumulative	Corrected	Bin	
1.81E-04	1.0000	1.0000	0.0002	0.014
3.62E-04	0.9998	0.9998	0.0026	0.037
7.24E-04	0.9972	0.9972	0.0319	0.080
1.45E-03	0.9653	0.9654	0.1089	0.159
2.17E-03	0.8564	0.8565	0.2143	0.224
2.90E-03	0.6422	0.6422	0.2743	0.278
3.62E-03	0.3679	0.3679	0.2250	0.323
4.34E-03	0.1429	0.1429	0.1100	0.362
5.07E-03	0.0329	0.0329	0.0290	0.397
5.79E-03	0.0039	0.0039	0.0037	0.428
6.52E-03	0.0002	0.0002	0.0002	0.456

Horizontal position (m)	Cumulative separator effectiveness by vertical bin centre (m)										
	0.013	0.038	0.063	0.088	0.113	0.138	0.163	0.188	0.213	0.238	0.250
0.112	1.000	0.667	0.333	0.000	0.000	0.000	0.000	0.000	0.000	0.000	0.000
0.162	1.000	0.967	0.963	0.958	0.951	0.945	0.937	0.931	0.924	0.916	0.358
0.212	1.000	0.988	0.981	0.975	0.971	0.969	0.967	0.965	0.962	0.960	0.956
0.262	1.000	0.996	0.994	0.990	0.987	0.986	0.984	0.983	0.982	0.981	0.979
0.312	1.000	0.998	0.997	0.996	0.995	0.994	0.993	0.992	0.991	0.991	0.990
0.362	1.000	0.999	0.999	0.998	0.997	0.997	0.996	0.996	0.996	0.995	0.995
0.412	1.000	1.000	0.999	0.999	0.999	0.998	0.998	0.998	0.998	0.998	0.997
0.462	1.000	1.000	1.000	1.000	0.999	0.999	0.999	0.999	0.999	0.999	0.999
0.512	1.000	1.000	1.000	1.000	1.000	1.000	1.000	0.999	0.999	0.999	0.999
0.562	1.000	1.000	1.000	1.000	1.000	1.000	1.000	1.000	1.000	1.000	1.000
0.612	1.000	1.000	1.000	1.000	1.000	1.000	1.000	1.000	1.000	1.000	1.000
0.662	1.000	1.000	1.000	1.000	1.000	1.000	1.000	1.000	1.000	1.000	1.000
Height fraction	0.050	0.150	0.250	0.350	0.450	0.550	0.650	0.750	0.850	0.950	1.000